HL–LHC PRELIMINARY DESIGN REPORT

EUROPEAN ORGANIZATION FOR NUCLEAR RESEARCH

ORGANISATION EUROPEENNE POUR LA RECHERCHE NUCLEAIRE

CERN EUROPEAN ORGANIZATION FOR NUCLEAR RESEARCH

HL-LHC
Preliminary Design
Report

Editorial Board

G. Apollinari, I. Béjar Alonso, O. Brüning, M. Lamont,
L. Rossi

GENEVA

2015

Abstract

The Large Hadron Collider (LHC) is one of the largest scientific instruments ever built. Since opening up a new energy frontier for exploration in 2010, it has gathered a global user community of about 7,000 scientists working in fundamental particle physics and the physics of hadronic matter at extreme temperature and density. To sustain and extend its discovery potential, the LHC will need a major upgrade in the 2020s. This will increase its luminosity (rate of collisions) by a factor of five beyond the original design value and the integrated luminosity (total collisions created) by a factor ten. The LHC is already a highly complex and exquisitely optimised machine so this upgrade must be carefully conceived and will require about ten years to implement. The new configuration, known as High Luminosity LHC (HL-LHC), will rely on a number of key innovations that push accelerator technology beyond its present limits. Among these are cutting-edge 11-12 tesla superconducting magnets, compact superconducting cavities for beam rotation with ultra-precise phase control, new technology and physical processes for beam collimation and 300 metre-long high-power superconducting links with negligible energy dissipation.

The present document describes the technologies and components that will be used to realise the project and is intended to serve as the basis for the detailed engineering design of HL-LHC

TABLE OF CONTENTS

TABLE OF FIGURES

9

TABLE OF TABLES

CONTRIBUTORS LIST

C. Adorisio	CERN, Accelerator & Technology Sector, CH-1211, Geneva, Switzerland
A. Adraktas	CERN, Accelerator & Technology Sector, CH-1211, Geneva, Switzerland
L. Alberty	CERN, Accelerator & Technology Sector, CH-1211, Geneva, Switzerland
D. Alesini	INFN-LNF, Via E. Fermi 40, 00044 Frascati, Rome, Italy
G. Ambrosio	FNAL, Fermi National Accelerator Laboratory, Batavia, P.O. Box 500, IL, USA
M. Anerella	BNL, Brookhaven National Laboratory, Upton, NY 11973, USA
D. Angal-Kalinin	ASTeC, STFC, Daresbury Laboratory, Warrington WA4 4AD, United Kingdom
G. Apollinari	FNAL, Fermi National Accelerator Laboratory, Batavia, P.O. Box 500, IL, USA
A. Apollonio	CERN, Accelerator & Technology Sector, CH-1211, Geneva, Switzerland
R.B. Appleby	UMAN, The University of Manchester and the Cockcroft Institute, United Kingdom
G. Arduini	CERN, Accelerator & Technology Sector, CH-1211, Geneva, Switzerland
K.Artoos	CERN, Accelerator & Technology Sector, CH-1211, Geneva, Switzerland
S. Atieh	CERN, Accelerator & Technology Sector, CH-1211, Geneva, Switzerland
B. Auchmann	CERN, Accelerator & Technology Sector, CH-1211, Geneva, Switzerland
T. Baer	CERN, Accelerator & Technology Sector, CH-1211, Geneva, Switzerland
V. Baglin	CERN, Accelerator & Technology Sector, CH-1211, Geneva, Switzerland
M. Bajko	CERN, Accelerator & Technology Sector, CH-1211, Geneva, Switzerland
A. Ballarino	CERN, Accelerator & Technology Sector, CH-1211, Geneva, Switzerland
D. Banfi	EPFL, Lausanne, Switzerland
R. Barlow	UHUD, University of Huddersfield, United Kingdom
M. Barnes	CERN, Accelerator & Technology Sector, CH-1211, Geneva, Switzerland
J. Barranco	EPFL, Lausanne, Switzerland
W. Bartmann	CERN, Accelerator & Technology Sector, CH-1211, Geneva, Switzerland
E. Barzi	FNAL, Fermi National Accelerator Laboratory, Batavia, P.O. Box 500, IL, USA
P. Baudrenghien	CERN, Accelerator & Technology Sector, CH-1211, Geneva, Switzerland
I. Bejar Alonso	CERN, Accelerator & Technology Sector, CH-1211, Geneva, Switzerland
S.Belomestnykh	BNL, Brookhaven National Laboratory, Upton, NY 11973, USA
A.Benoit	CERN, Accelerator & Technology Sector, CH-1211, Geneva, Switzerland
I.Ben-Zvi	BNL, Brookhaven National Laboratory, Upton, NY 11973, USA
A. Bertarelli	CERN, Accelerator & Technology Sector, CH-1211, Geneva, Switzerland
N. Biancacci	CERN, Accelerator & Technology Sector, CH-1211, Geneva, Switzerland
A. Bignami	INFN-LASA, Milan, Italy
N. Bliss	STFC, Daresbury Laboratory, Warrington WA4 4AD, United Kingdom
J. Borburgh	CERN, Accelerator & Technology Sector, CH-1211, Geneva, Switzerland
B. Bordini	CERN, Accelerator & Technology Sector, CH-1211, Geneva, Switzerland
R. Bossert	FNAL, Fermi National Accelerator Laboratory, Batavia, P.O. Box 500, IL, USA
L. Bottura	CERN, Accelerator & Technology Sector, CH-1211, Geneva, Switzerland
A.Boucherie	CERN, Accelerator & Technology Sector, CH-1211, Geneva, Switzerland
C. Bracco	CERN, Accelerator & Technology Sector, CH-1211, Geneva, Switzerland
E. Bravin	CERN, Accelerator & Technology Sector, CH-1211, Geneva, Switzerland

G. Bregliozzi	CERN, Accelerator & Technology Sector, CH-1211, Geneva, Switzerland
D. Brett	UMAN, The University of Manchester and the Cockcroft Institute, United Kingdom
K. Brodzinski	CERN, Accelerator & Technology Sector, CH-1211, Geneva, Switzerland
F. Broggi	INFN-LASA, Milan, Italy
R. Bruce	CERN, Accelerator & Technology Sector, CH-1211, Geneva, Switzerland
M. Brugger	CERN, Accelerator & Technology Sector, CH-1211, Geneva, Switzerland
O. Brüning	CERN, Accelerator & Technology Sector, CH-1211, Geneva, Switzerland
X. Buffat	CERN, Accelerator & Technology Sector, CH-1211, Geneva, Switzerland
H. Burkhardt	CERN, Accelerator & Technology Sector, CH-1211, Geneva, Switzerland
J.P. Burnet	CERN, Accelerator & Technology Sector, CH-1211, Geneva, Switzerland
A. Burov	FNAL, Fermi National Accelerator Laboratory, Batavia, P.O. Box 500, IL, USA
G. Burt	University of Lancaster, Lancaster, UK and Cockcroft Institute Sci-Tech Daresbury, Warrington UK
Y. Cai	SLAC National Accelerator Laboratory, 2575 Sand Hill Road, Menlo Park California 94025 USA
R. Calaga	CERN, Accelerator & Technology Sector, CH-1211, Geneva, Switzerland
S. Calatroni	CERN, Accelerator & Technology Sector, CH-1211, Geneva, Switzerland
O. Capatina	CERN, Accelerator & Technology Sector, CH-1211, Geneva, Switzerland
T. Capelli	CERN, Accelerator & Technology Sector, CH-1211, Geneva, Switzerland
E. Carlier	CERN, Accelerator & Technology Sector, CH-1211, Geneva, Switzerland
F. Carra	CERN, Accelerator & Technology Sector, CH-1211, Geneva, Switzerland
F. Caspers	CERN, Accelerator & Technology Sector, CH-1211, Geneva, Switzerland
F. Cerutti	CERN, Accelerator & Technology Sector, CH-1211, Geneva, Switzerland
A. Chancé	CEA/SACLAY, DSM/Irfu/SACM - 91191 Gif-sur-Yvette - France
S. Chemli	CERN, Accelerator & Technology Sector, CH-1211, Geneva, Switzerland
D. Cheng	LBNL, Lawrence Berkeley National Laboratory, Berkeley, CA 94720, USA
P. Chiggiato	CERN, Accelerator & Technology Sector, CH-1211, Geneva, Switzerland
G. Chlachidze	FNAL, Fermi National Accelerator Laboratory, Batavia, P.O. Box 500, IL, USA
S. Claudet	CERN, Accelerator & Technology Sector, CH-1211, Geneva, Switzerland
P. Costa Pinto	CERN, Accelerator & Technology Sector, CH-1211, Geneva, Switzerland
M. Crouch	UMAN, The University of Manchester and the Cockcroft Institute, United Kingdom
K. Dahlerup-Petersen	CERN, Accelerator & Technology Sector, CH-1211, Geneva, Switzerland
B. Dalena	CEA/SACLAY, DSM/Irfu/SACM - 91191 Gif-sur-Yvette - France
H. Day	CERN, Accelerator & Technology Sector, CH-1211, Geneva, Switzerland
J.P. De Carvalho Saraiva	CERN, Accelerator & Technology Sector, CH-1211, Geneva, Switzerland
R. De Maria	CERN, Accelerator & Technology Sector, CH-1211, Geneva, Switzerland
S. De Silva	ODU, Old Dominion University, 5115 Hampton Boulevard, Norfolk, VA 23529, USA
G. De Rijk	CERN, Accelerator & Technology Sector, CH-1211, Geneva, Switzerland
B. Dehning	CERN, Accelerator & Technology Sector, CH-1211, Geneva, Switzerland
J.Delayen	ODU, Old Dominion University, 5115 Hampton Boulevard, Norfolk, VA 23529, USA

B. Delille	CERN, Accelerator & Technology Sector, CH-1211, Geneva, Switzerland
R. Denz	CERN, Accelerator & Technology Sector, CH-1211, Geneva, Switzerland
A.Dexter	University of Lancaster, Lancaster, UK and Cockcroft Institute Sci-Tech Daresbury, Warrington UK
D. Dietderich	LBNL, Lawrence Berkeley National Laboratory, Berkeley, CA 94720, USA
A.Doherty	University of Lancaster, Lancaster, UK and Cockcroft Institute Sci-Tech Daresbury, Warrington UK
A. Drago	INFN-LNF, Via E. Fermi 40, 00044 Frascati, Rome, Italy
D Duarte Ramos	CERN, Accelerator & Technology Sector, CH-1211, Geneva, Switzerland
L. Ducimetière	CERN, Accelerator & Technology Sector, CH-1211, Geneva, Switzerland
I. Efthymiopoulos	CERN, Accelerator & Technology Sector, CH-1211, Geneva, Switzerland
L. Esposito	CERN, Accelerator & Technology Sector, CH-1211, Geneva, Switzerland
J. Esteban Muller	CERN, Accelerator & Technology Sector, CH-1211, Geneva, Switzerland
P. Fabbricatore	INFN, Sezione di Genova, I-16146 Genova, Italy
S. Farinon	INFN, Sezione di Genova, I-16146 Genova, Italy
S. Fartoukh	CERN, Accelerator & Technology Sector, CH-1211, Geneva, Switzerland
A. Faus-Golfe	IFIC, Instituto de Fısica Corpuscular, CSIC,E-46071 Valencia, Spain
G. Favre	CERN, Accelerator & Technology Sector, CH-1211, Geneva, Switzerland
H. Felice	LBNL, Lawrence Berkeley National Laboratory, Berkeley, CA 94720, USA
G. Ferlin	CERN, Accelerator & Technology Sector, CH-1211, Geneva, Switzerland
P. Ferracin	CERN, Accelerator & Technology Sector, CH-1211, Geneva, Switzerland
A. Ferrari	CERN, Accelerator & Technology Sector, CH-1211, Geneva, Switzerland
L. Ferreira	CERN, Accelerator & Technology Sector, CH-1211, Geneva, Switzerland
P. Fessia	CERN, Accelerator & Technology Sector, CH-1211, Geneva, Switzerland
L.Ficcadenti	CERN, Accelerator & Technology Sector, CH-1211, Geneva, Switzerland
L. Fiscarelli	CERN, Accelerator & Technology Sector, CH-1211, Geneva, Switzerland
R. Folch	CERN, Accelerator & Technology Sector, CH-1211, Geneva, Switzerland
G. Foffano	CERN, Accelerator & Technology Sector, CH-1211, Geneva, Switzerland
O. Frasciello	INFN-LNF, Via E. Fermi 40, 00044 Frascati, Rome, Italy
M. Fraser	CERN, Accelerator & Technology Sector, CH-1211, Geneva, Switzerland
P.Freijedo Menendez	CERN, Accelerator & Technology Sector, CH-1211, Geneva, Switzerland
A. Gallo	INFN-LNF, Via E. Fermi 40, 00044 Frascati, Rome, Italy
J. Garcia Matos	CIEMAT, Madrid, Spain
H. Garcia Morales	URHL, Royal Holloway, United Kingdom
J.C. Gascon	CERN, Accelerator & Technology Sector, CH-1211, Geneva, Switzerland
L. Gentini	CERN, Accelerator & Technology Sector, CH-1211, Geneva, Switzerland
A. Ghosh	BNL, Brookhaven National Laboratory, Upton, NY 11973, USA
K.Gibran Hernandez	CERN, Accelerator & Technology Sector, CH-1211, Geneva, Switzerland
S. M. Gibson	URHL, Royal Holloway, United Kingdom
C. Ginburg	FNAL, Fermi National Accelerator Laboratory, Batavia, P.O. Box 500, IL, USA
M. Giovannozzi	CERN, Accelerator & Technology Sector, CH-1211, Geneva, Switzerland
B. Goddard	CERN, Accelerator & Technology Sector, CH-1211, Geneva, Switzerland
P. Gomes	CERN, Accelerator & Technology Sector, CH-1211, Geneva, Switzerland

P.Goudket	ASTeC, STFC, Daresbury Laboratory, Warrington WA4 4AD, United Kingdom
P. Gradassi	CERN, Accelerator & Technology Sector, CH-1211, Geneva, Switzerland
L. Grand-Clément	CERN, Accelerator & Technology Sector, CH-1211, Geneva, Switzerland
M. Guinchard	CERN, Accelerator & Technology Sector, CH-1211, Geneva, Switzerland
P. Hagen	CERN, Accelerator & Technology Sector, CH-1211, Geneva, Switzerland
B.Hall	University of Lancaster, Lancaster, UK and Cockcroft Institute Sci-Tech Daresbury, Warrington UK
W. Herr	CERN, Accelerator & Technology Sector, CH-1211, Geneva, Switzerland
C.Hill	STFC, Daresbury Laboratory, Warrington WA4 4AD, United Kingdom
W. Höfle	CERN, Accelerator & Technology Sector, CH-1211, Geneva, Switzerland
B. Holzer	CERN, Accelerator & Technology Sector, CH-1211, Geneva, Switzerland
J. Hrivnak	CERN, Accelerator & Technology Sector, CH-1211, Geneva, Switzerland
G. Iadarola	CERN, Accelerator & Technology Sector, CH-1211, Geneva, Switzerland
S. Izquierdo Bermudez	CERN, Accelerator & Technology Sector, CH-1211, Geneva, Switzerland
E. Jensen	CERN, Accelerator & Technology Sector, CH-1211, Geneva, Switzerland
R. Jones	CERN, Accelerator & Technology Sector, CH-1211, Geneva, Switzerland
T. Jones	STFC, Daresbury Laboratory, Warrington WA4 4AD, United Kingdom
J.M. Jowett	CERN, Accelerator & Technology Sector, CH-1211, Geneva, Switzerland
M. Juchno	CERN, Accelerator & Technology Sector, CH-1211, Geneva, Switzerland
C. Julie	CERN, Accelerator & Technology Sector, CH-1211, Geneva, Switzerland
T. Junginger	CERN, Accelerator & Technology Sector, CH-1211, Geneva, Switzerland
V. Kain	CERN, Accelerator & Technology Sector, CH-1211, Geneva, Switzerland
P. Kardasopoulos	CERN, Accelerator & Technology Sector, CH-1211, Geneva, Switzerland
M. Karppinen	CERN, Accelerator & Technology Sector, CH-1211, Geneva, Switzerland
F. Kiling	CERN, Accelerator & Technology Sector, CH-1211, Geneva, Switzerland
M. Korostelev	University of Liverpool, Liverpool L69 7ZE, United Kingdom
N. Kos	CERN, Accelerator & Technology Sector, CH-1211, Geneva, Switzerland
S. Krave	FNAL, Fermi National Accelerator Laboratory, Batavia, P.O. Box 500, IL, USA
N. Kuder	CERN, Accelerator & Technology Sector, CH-1211, Geneva, Switzerland
R. Kwee-Hinzmann	URHL, Royal Holloway, United Kingdom
F. Lackner	CERN, Accelerator & Technology Sector, CH-1211, Geneva, Switzerland
M. Lamont	CERN, Accelerator & Technology Sector, CH-1211, Geneva, Switzerland
L. Lari	IFIC, Instituto de Fısica Corpuscular, CSIC,E-46071 Valencia, Spain (now at ESS)
A. Lechner	CERN, Accelerator & Technology Sector, CH-1211, Geneva, Switzerland
T. Lefevre	CERN, Accelerator & Technology Sector, CH-1211, Geneva, Switzerland
R. Leuxe	CERN, Accelerator & Technology Sector, CH-1211, Geneva, Switzerland
K. Li	CERN, Accelerator & Technology Sector, CH-1211, Geneva, Switzerland
Z. Li	SLAC National Accelerator Laboratory, 2575 Sand Hill Road, Menlo Park California 94025 USA
C. Lingwood	University of Lancaster, Lancaster, UK and Cockcroft Institute Sci-Tech Daresbury, Warrington UK
C. Löffler	CERN, Accelerator & Technology Sector, CH-1211, Geneva, Switzerland

F. Lorenzo Maciariello	CERN, Accelerator & Technology Sector, CH-1211, Geneva, Switzerland
R. Losito	CERN, Accelerator & Technology Sector, CH-1211, Geneva, Switzerland
P. Macintosh	ASTeC, STFC, Daresbury Laboratory, Warrington WA4 4AD, United Kingdom
A. Macpherson	CERN, Accelerator & Technology Sector, CH-1211, Geneva, Switzerland
P. Maesen	CERN, Accelerator & Technology Sector, CH-1211, Geneva, Switzerland
F. Marcellini	INFN-LNF, Via E. Fermi 40, 00044 Frascati, Rome, Italy
M. Marchevsky	LBNL, Lawrence Berkeley National Laboratory, Berkeley, CA 94720, USA
K. Marinov	ASTeC, STFC, Daresbury Laboratory, Warrington WA4 4AD, United Kingdom
T. Markiewicz	SLAC National Accelerator Laboratory, 2575 Sand Hill Road, Menlo Park California 94025 USA
A. Marsili	CERN, Accelerator & Technology Sector, CH-1211, Geneva, Switzerland
A. Masi	CERN, Accelerator & Technology Sector, CH-1211, Geneva, Switzerland
T. Mastoridis	California Polytechnic State University, San Luis Obispo, USA
A.May	ASTeC, STFC, Daresbury Laboratory, Warrington WA4 4AD, United Kingdom
J. Mazet	CERN, Accelerator & Technology Sector, CH-1211, Geneva, Switzerland
E. McIntosh	CERN, Accelerator & Technology Sector, CH-1211, Geneva, Switzerland
P. Menendez	CERN, Accelerator & Technology Sector, CH-1211, Geneva, Switzerland
M. Mensi	CERN, Accelerator & Technology Sector, CH-1211, Geneva, Switzerland
A. Mereghetti	CERN, Accelerator & Technology Sector, CH-1211, Geneva, Switzerland
T. Mertens	CERN, Accelerator & Technology Sector, CH-1211, Geneva, Switzerland
E. Métral	CERN, Accelerator & Technology Sector, CH-1211, Geneva, Switzerland
M. Migliorati	University of Rome "La Sapienza", Rome, Italy
P.Minginette	CERN, Accelerator & Technology Sector, CH-1211, Geneva, Switzerland
N.V. Mokhov	FNAL, Fermi National Accelerator Laboratory, Batavia, P.O. Box 500, IL, USA
J. Molson	UMAN, The University of Manchester and the Cockcroft Institute, United Kingdom
E. Montesinos	CERN, Accelerator & Technology Sector, CH-1211, Geneva, Switzerland
R. Moron-Ballester	CERN, Accelerator & Technology Sector, CH-1211, Geneva, Switzerland
A. Mostacci	University of Rome "La Sapienza", Rome, Italy
N. Mounet	CERN, Accelerator & Technology Sector, CH-1211, Geneva, Switzerland
B. Muratori	ASTeC, STFC, Daresbury Laboratory, Warrington WA4 4AD, United Kingdom
M. Navarro-Tapia	CERN, Accelerator & Technology Sector, CH-1211, Geneva, Switzerland
T. Nakamoto	KEK, Oho, Tsukuba, 305-0801, Japan
H. Neupert	CERN, Accelerator & Technology Sector, CH-1211, Geneva, Switzerland
L. J. Nevay	URHL, Royal Holloway, United Kingdom
T. Nicol	FNAL, Fermi National Accelerator Laboratory, Batavia, P.O. Box 500, IL, USA
C. Noels	CERN, Accelerator & Technology Sector, CH-1211, Geneva, Switzerland
E. Nolan	STFC, Daresbury Laboratory, Warrington WA4 4AD, United Kingdom
Y. Nosochkov	SLAC National Accelerator Laboratory, 2575 Sand Hill Road, Menlo Park California 94025 USA
L. Oberli	CERN, Accelerator & Technology Sector, CH-1211, Geneva, Switzerland
T. Ogitsu	KEK, Oho, Tsukuba, 305-0801, Japan
K. Ohmi	KEK, Oho, Tsukuba, 305-0801, Japan

R. Olave	ODU, Old Dominion University, 5115 Hampton Boulevard, Norfolk, VA 23529, USA
T. Otto	CERN, Accelerator & Technology Sector, CH-1211, Geneva, Switzerland
L. Palumbo	University of Rome "La Sapienza", Rome, Italy
Y. Papaphilippou	CERN, Accelerator & Technology Sector, CH-1211, Geneva, Switzerland
C. Parente	CERN, Accelerator & Technology Sector, CH-1211, Geneva, Switzerland
S. Paret	LBNL, Lawrence Berkeley National Laboratory, Berkeley, CA 94720, USA
H.Park	ODU, Old Dominion University, 5115 Hampton Boulevard, Norfolk, VA 23529, USA
S. Pattalwar	ASTeC, STFC, Daresbury Laboratory, Warrington WA4 4AD, United Kingdom
J. Payet	CEA/SACLAY, DSM/Irfu/SACM - 91191 Gif-sur-Yvette - France
G. Pechaud	CERN, Accelerator & Technology Sector, CH-1211, Geneva, Switzerland
J.C. Perez	CERN, Accelerator & Technology Sector, CH-1211, Geneva, Switzerland
J. Perez Espinos	CERN, Accelerator & Technology Sector, CH-1211, Geneva, Switzerland
A. Perillo Marcone	CERN, Accelerator & Technology Sector, CH-1211, Geneva, Switzerland
T. Peterson	FNAL, Fermi National Accelerator Laboratory, Batavia, P.O. Box 500, IL, USA
T. Pieloni	CERN, Accelerator & Technology Sector, CH-1211, Geneva, Switzerland
M. Pojer	CERN, Accelerator & Technology Sector, CH-1211, Geneva, Switzerland
H. Prin	CERN, Accelerator & Technology Sector, CH-1211, Geneva, Switzerland
J. Qiang	LBNL, Lawrence Berkeley National Laboratory, Berkeley, CA 94720, USA
E. Quaranta	CERN, Accelerator & Technology Sector, CH-1211, Geneva, Switzerland
H. Rafique	UHUD, University of Huddersfield, United Kingdom
I.L. Rakhno	FNAL, Fermi National Accelerator Laboratory, Batavia, P.O. Box 500, IL, USA
D. Ramos Duarte	CERN, Accelerator & Technology Sector, CH-1211, Geneva, Switzerland
A. Ratti	FNAL, Fermi National Accelerator Laboratory, Batavia, P.O. Box 500, IL, USA
S. Redaelli	CERN, Accelerator & Technology Sector, CH-1211, Geneva, Switzerland
T. Renaglia	CERN, Accelerator & Technology Sector, CH-1211, Geneva, Switzerland
J.M. Rifflet	CEA/SACLAY, DSM/Irfu/SACM - 91191 Gif-sur-Yvette - France
T. Rijoff	CERN, Accelerator & Technology Sector, CH-1211, Geneva, Switzerland
L. Rivkin	EPFL, Lausanne, Switzerland
S. Roesler	CERN, Accelerator & Technology Sector, CH-1211, Geneva, Switzerland
I. Romera Ramirez	CERN, Accelerator & Technology Sector, CH-1211, Geneva, Switzerland
L. Rossi	CERN, Accelerator & Technology Sector, CH-1211, Geneva, Switzerland
G. Rumolo	CERN, Accelerator & Technology Sector, CH-1211, Geneva, Switzerland
G.L. Sabbi	LBNL, Lawrence Berkeley National Laboratory, Berkeley, CA 94720, USA
T. Sahner	CERN, Accelerator & Technology Sector, CH-1211, Geneva, Switzerland
B. Salvant	CERN, Accelerator & Technology Sector, CH-1211, Geneva, Switzerland
I.Santillana	CERN, Accelerator & Technology Sector, CH-1211, Geneva, Switzerland
C. Santini	Politecnico of Milan, Italy
K. Sasaki	KEK, Oho, Tsukuba, 305-0801, Japan
F. Savary	CERN, Accelerator & Technology Sector, CH-1211, Geneva, Switzerland
M. Schaumann	CERN, Accelerator & Technology Sector, CH-1211, Geneva, Switzerland
J. Schmalzle	BNL, Brookhaven National Laboratory, Upton, NY 11973, USA

H. Schmickler	CERN, Accelerator & Technology Sector, CH-1211, Geneva, Switzerland
R. Schmidt	CERN, Accelerator & Technology Sector, CH-1211, Geneva, Switzerland
M. Segreti	CEA/SACLAY, DSM/Irfu/SACM - 91191 Gif-sur-Yvette - France
M. Serluca	UMAN, The University of Manchester and the Cockcroft Institute, United Kingdom
E. Shaposhnikova	CERN, Accelerator & Technology Sector, CH-1211, Geneva, Switzerland
D. Shatilov	BINP, Novosibirsk, Russia
A. Siemko	CERN, Accelerator & Technology Sector, CH-1211, Geneva, Switzerland
J. Skarita	BNL, Brookhaven National Laboratory, Upton, NY 11973, USA
E. Skordis	CERN, Accelerator & Technology Sector, CH-1211, Geneva, Switzerland
Z. Sobiech	CERN, Accelerator & Technology Sector, CH-1211, Geneva, Switzerland
B. Spataro	INFN-LNF, Via E. Fermi 40, 00044 Frascati, Rome, Italy
G. Spiezia	CERN, Accelerator & Technology Sector, CH-1211, Geneva, Switzerland
G. Stancari	FNAL, Fermi National Accelerator Laboratory, Batavia, P.O. Box 500, IL, USA
G. Steele	CERN, Accelerator & Technology Sector, CH-1211, Geneva, Switzerland
M. Sugano	KEK, Oho, Tsukuba, 305-0801, Japan
A. Szeberenyi	CERN, Accelerator & Technology Sector, CH-1211, Geneva, Switzerland
M. Taborelli	CERN, Accelerator & Technology Sector, CH-1211, Geneva, Switzerland
C. Tambasco	CERN, Accelerator & Technology Sector, CH-1211, Geneva, Switzerland
L. Tavian	CERN, Accelerator & Technology Sector, CH-1211, Geneva, Switzerland
B. Teissandier	CERN, Accelerator & Technology Sector, CH-1211, Geneva, Switzerland
N. Templeton	STFC, Daresbury Laboratory, Warrington WA4 4AD, United Kingdom
M. Therasse	CERN, Accelerator & Technology Sector, CH-1211, Geneva, Switzerland
H. Thiesen	CERN, Accelerator & Technology Sector, CH-1211, Geneva, Switzerland
A. Toader	UHUD, University of Huddersfield, United Kingdom
E. Todesco	CERN, Accelerator & Technology Sector, CH-1211, Geneva, Switzerland
R. Tomás	CERN, Accelerator & Technology Sector, CH-1211, Geneva, Switzerland
F. Toral	CIEMAT, Madrid, Spain
R. Torres-Sanchez	CERN, Accelerator & Technology Sector, CH-1211, Geneva, Switzerland
I.S. Tropin	FNAL, Fermi National Accelerator Laboratory, Batavia, P.O. Box 500, IL, USA
J. Tuckamantel	CERN, Accelerator & Technology Sector, CH-1211, Geneva, Switzerland
J. Uythoven	CERN, Accelerator & Technology Sector, CH-1211, Geneva, Switzerland
A. Valishev	INFN-LNF, Via E. Fermi 40, 00044 Frascati, Rome, Italy
E. Van Weelderen	CERN, Accelerator & Technology Sector, CH-1211, Geneva, Switzerland
F. Velotti	CERN, Accelerator & Technology Sector, CH-1211, Geneva, Switzerland
S. Verdu Andres	BNL, Brookhaven National Laboratory, Upton, NY 11973, USA
A. Verweij	CERN, Accelerator & Technology Sector, CH-1211, Geneva, Switzerland
N. Vittal Shetty	CERN, Accelerator & Technology Sector, CH-1211, Geneva, Switzerland
V. Vlachoudis	CERN, Accelerator & Technology Sector, CH-1211, Geneva, Switzerland
G. Volpini	INFN-LASA, Milan, Italy
U. Wagner	CERN, Accelerator & Technology Sector, CH-1211, Geneva, Switzerland
P. Wanderer	BNL, Brookhaven National Laboratory, Upton, NY 11973, USA

M.-H. Wang	SLAC National Accelerator Laboratory, 2575 Sand Hill Road, Menlo Park California 94025 USA
X. Wang	LBNL, Lawrence Berkeley National Laboratory, Berkeley, CA 94720, USA
R. Wanzenberg	DESY, Deutsches Elektronen-Synchrotron Notkestr. 85, 2000 Hamburg 52, Germany
R.V. Weelderen	CERN, Accelerator & Technology Sector, CH-1211, Geneva, Switzerland
S. Weisz	CERN, Accelerator & Technology Sector, CH-1211, Geneva, Switzerland
J. Wenninger	CERN, Accelerator & Technology Sector, CH-1211, Geneva, Switzerland
W. Weterings	CERN, Accelerator & Technology Sector, CH-1211, Geneva, Switzerland
S. White	CERN, Accelerator & Technology Sector, CH-1211, Geneva, Switzerland
G. Willering	CERN, Accelerator & Technology Sector, CH-1211, Geneva, Switzerland
D. Wollmann	CERN, Accelerator & Technology Sector, CH-1211, Geneva, Switzerland
A. Wolski	University of Liverpool, Liverpool L69 7ZE, United Kingdom
Q.Wu	BNL, Brookhaven National Laboratory, Upton, NY 11973, USA
B. Xiao	BNL, Brookhaven National Laboratory, Upton, NY 11973, USA
L.Xiao	SLAC National Accelerator Laboratory, 2575 Sand Hill Road, Menlo Park California 94025 USA
Q. Xu	KEK, Oho, Tsukuba, 305-0801, Japan
Y.Yakovlev	FNAL, Fermi National Accelerator Laboratory, Batavia, P.O. Box 500, IL, USA
Y. Yang	University of Southampton, Southampton SO17 1BJ, UK
M. Yu	FNAL, Fermi National Accelerator Laboratory, Batavia, P.O. Box 500, IL, USA
I. Zacharov	EPFL, Lausanne, Switzerland
O. Zagorodnova	DESY, Deutsches Elektronen-Synchrotron Notkestr. 85, 2000 Hamburg 52, Germany
C. Zannini	CERN, Accelerator & Technology Sector, CH-1211, Geneva, Switzerland
C. Zanoni	CERN, Accelerator & Technology Sector, CH-1211, Geneva, Switzerland
M. Zerlauth	CERN, Accelerator & Technology Sector, CH-1211, Geneva, Switzerland
F. Zimmermann	CERN, Accelerator & Technology Sector, CH-1211, Geneva, Switzerland
A. Zlobin	FNAL, Fermi National Accelerator Laboratory, Batavia, P.O. Box 500, IL, USA
M. Zobov	INFN-LNF, Via E. Fermi 40, 00044 Frascati, Rome, Italy
V. Vlachoudis	CERN, Accelerator & Technology Sector, CH-1211, Geneva, Switzerland

Chapter 1

High Luminosity Large Hadron Collider HL-LHC

G. Apollinari[10], O. Brüning[5], T Nakamoto [16], L. Rossi[5]
[10]Fermi National Accelerator Laboratory, Batavia, P.O. Box 500, IL, USA
[5]CERN, Accelerator & Technology Sector, CH-1211, Geneva, Switzerland
[16]KEK, Oho, Tsukuba, 305-0801, Japan

1   High Luminosity Large Hadron Collider HL-LHC

1.1   Introduction

The Large Hadron Collider (LHC) was successfully commissioned in 2010 for proton-proton collisions with a 7 TeV centre-of-mass energy and delivered 8 TeV centre-of-mass proton collisions from April 2012 to the end of 2013. The LHC is pushing the limits of human knowledge, enabling physicists to go beyond the Standard Model. The announcement given by CERN on 4 July 2012 about the discovery of a new boson at about 125 GeV, the long awaited Higgs particle, is the first fundamental discovery, hopefully the first of a series that LHC can deliver.

It is a remarkable era for cosmology, astrophysics and high energy physics and the LHC is at the forefront of attempts to understand the fundamental nature of the universe. The discovery of the Higgs boson in 2012 is undoubtedly a major milestone in the history of physics. Beyond this, the LHC has the potential to go on and help answer some of the key questions of the age: the existence, or not, of supersymmetry; the nature of dark matter; the existence of extra dimensions. It is also important to continue to the study the properties of the Higgs – here the LHC is well placed to do this in exquisite detail.

Thanks to the LHC, Europe has decisively regained world leadership in High Energy Physics (HEP), a key sector of knowledge and technology. The LHC can continue to act as catalyst for a global effort unrivalled by any other branch of science: out of the 10,000 CERN users, more than 7,000 are scientists and engineers using the LHC, half of which are from countries outside the EU.

The LHC will remain the most powerful accelerator in the world for at least the next two decades. Its full exploitation is the highest priority of the European Strategy for particle physics. This strategy has been adopted by the CERN Council, and is a reference point for the Particle Physics Strategy of the USA and, to a certain extent, Japan. To extend its discovery potential, the LHC will need a major upgrade in the 2020s to increase its luminosity (and thus collision rate) by a factor of five beyond its design value. The integrated luminosity goal is a factor ten times design. As a highly complex and optimized machine, such an upgrade must be carefully studied. The necessary developments will require about 10 years to prototype, test and realize. The novel machine configuration, the High Luminosity LHC (HL-LHC), will rely on a number of key innovative technologies representing exceptional technological challenges. These include among others: cutting-edge 11-12 tesla superconducting magnets; very compact with ultra-precise phase control superconducting cavities for beam rotation; new

technology for beam collimation; and long high-power superconducting links with zero energy dissipation.

HL-LHC federates efforts and R&D of a large international community towards the ambitious HL-LHC objectives and contributes to establishing the European Research Area (ERA) as a focal point of global research cooperation and a leader in frontier knowledge and technologies. HL-LHC relies on a strong participation from various partners, in particular leading US and Japanese laboratories. This participation will be required for the execution of the construction phase as a global project. In particular, the USA LHC Accelerator R&D Program (LARP) has developed some of the key technologies for the HL-LHC, such as the large aperture niobium-tin (Nb_3Sn) quadrupoles and the crab cavities. The proposed governance model is tailored accordingly and should pave the way for the organization of the construction phase.

1.1   HL-LHC in a nutshell

The LHC baseline programme until 2025 is shown schematically in Figure 1-1. After entering into the nominal energy regime of 13-14 TeV centre-of-mass energy in 2015, it is expected that the LHC will reach the design luminosity of 1×10^{34} cm^{-2} s^{-1}. This peak value should give a total integrated luminosity of about 40 fb^{-1} per year. In the period 2015-2022 LHC will hopefully further increase the peak luminosity. Margins in the design of the nominal LHC are expected to allow, in principle, about 2 times the nominal design performance. The baseline programme for the next ten years is depicted in Figure 1-1, while

Figure 1-2 shows of the possible evolution of peak and integrated luminosity.
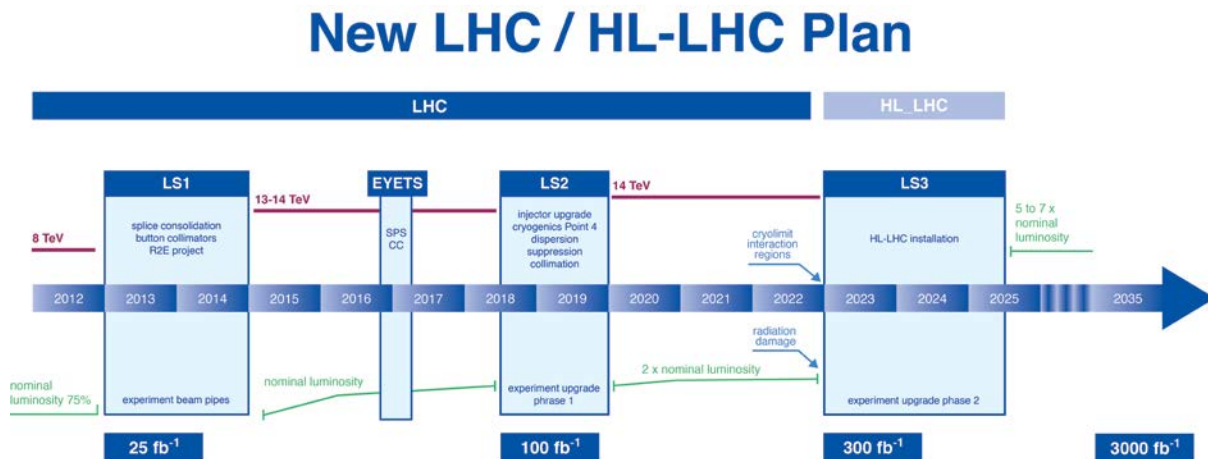
Figure 1-1: LHC baseline plan for the next decade and beyond showing the energy of the collisions (upper line - red) and luminosity (lower lines - green). The first long shutdown (LS1) in 2013-14 will allow design parameters of beam energy and luminosity to be reached. The second long shutdown (LS2) in 2018-19, will consolidate luminosity and reliability as well as upgrade the LHC Injectors. After LS3, 2023-2025, the machine will be in the High Luminosity configuration (HL-LHC).

After 2020 the statistical gain in running the accelerator without a significant luminosity increase beyond its design value will become marginal. The running time necessary to halve the statistical error in the measurements will be more than ten years after 2020. Therefore, to maintain scientific progress and to explore its full capacity, the LHC will need to have a decisive increase of its luminosity. This is why, when the CERN Council adopted the European Strategy for particle physics in 2006 [1], its first priority was agreed to be "*to fully exploit the physics potential of the LHC. A subsequent major luminosity upgrade, motivated by physics results and operation experience, will be enabled by focused R&D*". The European Strategy for particle physics has been integrated into the European Strategy Forum

on Research Infrastructures (ESFRI) Roadmap of 2006, as has the update of 2008 [2]. The priority to fully exploit the potential of the LHC has been recently confirmed as *first priority* among the "High priority large-scale scientific activities" in the new European Strategy for particle physics – Update 2013 [3]. This update was approved in Brussels on 30 May 2013 with the following wording: *"Europe's top priority should be the exploitation of the full potential of the LHC, including the high-luminosity upgrade of the machine and detectors with a view to collecting ten times more data than in the initial design, by around 2030"*.

The importance of the LHC luminosity upgrade for the future of High Energy Physics has been also recently re-affirmed by the May 2014 recommendation by the Particle Physics Project Prioritization Panel (P5) to the High Energy Physics Advisory Panel (HEPAP) which in turn advises the US Department of Energy (DOE) [4]. The recommendation, a critical step in the updating of the USA strategy for HEP, states the following: *"Recommendation 10: ... The LHC upgrades constitute our highest-priority near-term large project."*

In Japan, the 2012 report of a subcommittee in the HEP community concluded that an e^+e^- linear collider and a large scale neutrino detector be the core projects in Japan, with the assumption that the LHC and its upgrade are pursued de facto. The updated KEK roadmap in 2013 states that *"The main agenda at LHC/ATLAS is to continually participate in the experiment and to take a proactive initiative in upgrade programs within the international collaboration at both the accelerator and detector facilities."* Following these supports, The ATLAS-Japan group has been making intensive R&D's on the detector upgrades and the KEK cryogenic group has started the R&D of the LHC separation dipole magnet.
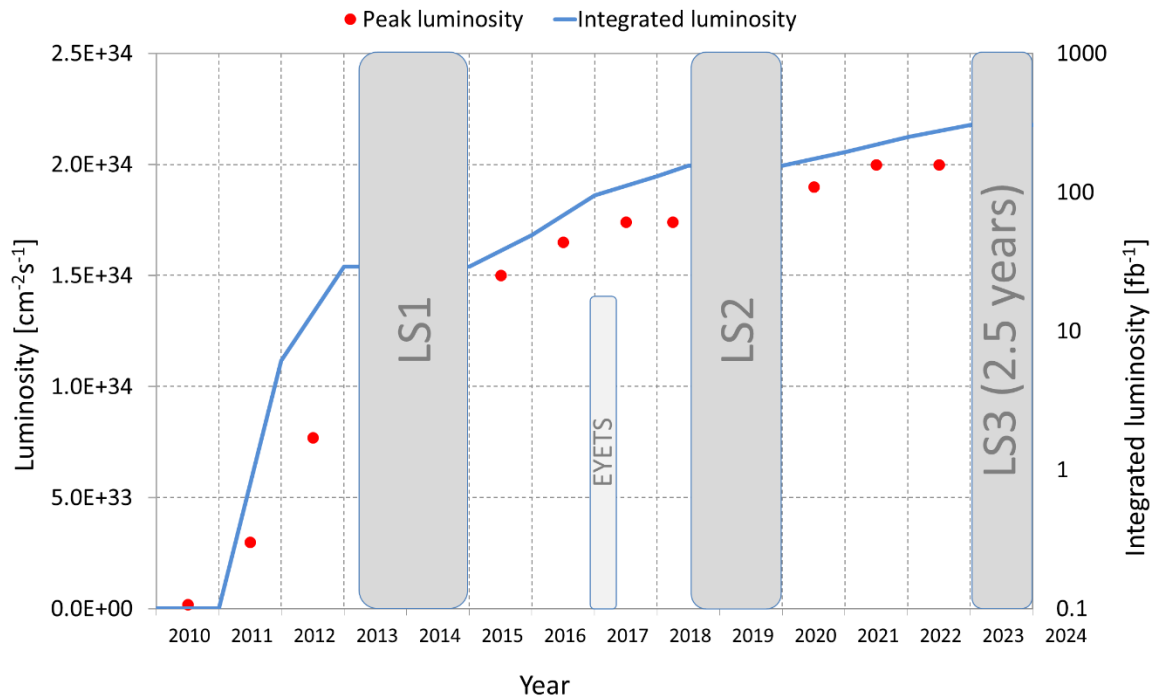
Figure 1-2: LHC luminosity plan for the next decade, both peak (red dots) and integrated (blue line). Main shutdown periods are indicated.

In this context, at the end of 2010 CERN created the High Luminosity LHC (HL-LHC) project [5]. Started as a design study, and after the approval of CERN Council of 30 May 2013 and the insertion of the budget in the CERN Medium Term Plan approved by Council in June 2014, HL-LHC has become CERN's major construction project for the next decade.

The main objective of High Luminosity LHC design study is to determine a set of beam parameters and the hardware configuration that will enable the LHC to reach the following targets:

- A peak luminosity of 5×10^{34} cm^{-2}s^{-1} with levelling, allowing:

- An integrated luminosity of 250 fb^{-1} per year with the goal of 3000 fb^{-1} in about a dozen years after the upgrade. This integrated luminosity is about ten times the expected luminosity reach of the first twelve years of the LHC lifetime.

The overarching goals are the installation of the main hardware for HL-LHC and the commissioning of the new machine configuration during LS3, scheduled for 2023-2025, while taking all actions to assure a high efficiency in operation until 2035.

Actually, in the last year, it emerged the necessity to aim at an enhanced goal in term of annual integrated luminosity. If the target of 3000 fb^{-1} should be reached by around 2035, as inferred by the European Strategy Update, the nominal goal of 250 fb^{-1}/year as fixed above is probably not adequate. However, since all equipment are being designed with a margin of 50%, for what concerns luminosity reach, we are defining the concept of *ultimate parameters*. By using the margins we should be able to push our machine to about *7-7.5 10^{34} cm^{-2} s^{-1}* of peak, levelling luminosity, of course increasing the total pile up in the detectors up to 200. This luminosity level should enable to collect up to 300-350 fb^{-1}/year. Also in terms of total integrated luminosity, we think we can define an ultimate value of about 4000 fb^{-1}. It must be said that while at a first examination there is no show-stopper to these performances, the ultimate parameters are not yet consolidated as the nominal parameters. Therefore, they will be thoroughly scrutinised and consolidated for the next version of the technical design report.

All the hadron colliders in the world before the LHC have produced a combined total integrated luminosity of about 10 fb^{-1}. The LHC delivered nearly 30 fb^{-1} by the end of 2012 and should reach 300 fb^{-1} in its first 13-15 years of operation. The High Luminosity LHC is a major, extremely challenging, upgrade. For its successful realization, a number of key novel technologies have to be developed, validated and integrated. The work was initiated quite early: ideas were circulating at the beginning of the LHC construction [6] and continued throughout the LHC construction [7]. From 2003 the U.S.-LARP (see 1.3.2) has been the main and continuous motor for technological development devoted to the LHC upgrade. After a period during which the upgrade was conceived in two phases, all studies were unified in 2010 under the newly formed High Luminosity Project. The first step consisted in launching a Design Study under the auspices of EC-FP7 with the nickname of **HiLumi LHC**, which following the approval by EC in 2011, has been is instrumental in initiating a new global collaboration for the LHC matching the spirit of the worldwide user community of the LHC experiments.

The High Luminosity LHC project is working in close collaboration with the CERN project for the LHC Injector complex Upgrade (LIU) [8], the companion ATLAS and CMS upgrade projects of 2018-19 and 2023-25 and the upgrade foreseen in 2018-19 for both LHCb and Alice.

1.1.1 Luminosity

The (instantaneous) luminosity L can be expressed as:

$$L = \gamma \frac{n_b N^2 f_{rev}}{4\pi \beta^* \varepsilon_n} R; \qquad R = 1 \Big/ \sqrt{1 + \frac{\theta_c \sigma_z}{2\sigma}} \qquad (1\text{-}1)$$

γ is the proton beam energy in unit of rest mass

n_b is the number of bunches per beam: 2808 (nominal LHC value) for 25 ns bunch spacing

N is the bunch population. N $_{nominal\ 25\ ns}$: 1.15×10^{11} p ($\Rightarrow$0.58 A of beam current at 2808 bunches)

f_{rev} is the revolution frequency (11.2 kHz)

β^* is the beam beta function (focal length) at the collision point (nominal design 0.55 m)

ε_n is the transverse normalized emittance (nominal design: 3.75 μm)

R is a luminosity geometrical reduction factor (0.85 at a β^* of 0.55 m of, down to 0.5 at 0.25 m)

θ_c is the full crossing angle between colliding beam (285 μrad as nominal design)

σ, σ_z are the transverse and longitudinal r.m.s. sizes, respectively (nominally 16.7 μm and 7.55 cm respectively)

With the nominal parameter values shown above, a luminosity of 1×10^{34} cm^{-2} s^{-1} is obtained, with an average pile-up (number of events in the same bunch crossing) of μ= 27 (although μ=19 was the original forecast at the LHC approval due to uncertainties in the total proton cross section at higher energies).

1.1.2 Present luminosity limitations and hardware constraints

There are various expected limitations to an increase in luminosity, either from beam characteristics (injector chain, beam impedance and beam-beam interactions in the LHC) or from technical systems. Mitigation of potential performance limitations arising from the LHC injector complex are addressed by the previously mentioned LIU project, which should be completed in 2019 (after LS2). Any potential limitations coming from the LHC injector complex aside, it is expected that the present LHC will reach a performance limitation from the beam current, from cleaning efficiency with 350 MJ beam stored energy, from e-clouds effects, from the maximum available cooling in the triplet magnets, from the magnet aperture (β* limit) and from the acceptable pile-up level. The ultimate value of bunch population with the nominal LHC should enable a peak luminosity of around 2×10^{34} cm^{-2}s^{-1} to be reached. Any further performance increase of the LHC will require significant hardware and beam parameter modifications with respect to the design LHC configuration.

Before discussing the new configuration it is useful to recall the systems that need to be changed, and possibly improved, because they become vulnerable to breakdown and accelerated aging, or because they may become a bottleneck for operation in a higher radiation environment. This goes well beyond the on-going basic consolidation.

- **Inner Triplet Magnets:** After about 300 fb^{-1} some components of the inner triplet quadrupoles and their corrector magnets will have received a dose of 30 MGy, entering into the region of possible radiation damage. The quadrupoles may withstand a maximum of 400-700 fb^{-1}, but some corrector magnets of nested type are likely to fail already at 300 fb^{-1}. Actual damage must be anticipated because the most likely failure mode is through sudden electric breakdown, entailing serious and long repairs. Thus the replacement of the triplet must be envisaged before damage occurs. Replacement of the low-beta triplet is a long intervention, requiring one to two years shutdown and must be coupled with a major detector upgrades.

- **Cryogenics:** To increase intervention flexibility and machine availability it is planned to install a new cryogenics plant for a full separation between SCRF and magnet cooling. In the long term, the cooling of the inner triplets and matching section magnets must be separated from the magnets of the arcs. This would avoid the need to warm-up an entire arc in the case of triplet region intervention.

- **Collimation:** The collimation system has been designed for the first operation phase of LHC. The present system was optimized for robustness and will need an upgrade that takes in account the need for the lower impedance required for the planned increased beam intensities. A new configuration will also be required to protect the new triplets in IR1 and IR5.
  Also requiring special attention are the Dispersion Suppressor (DS) regions, where a leakage of off-momentum particles into the first and second main superconducting dipoles has been already identified as a possible LHC performance limitation. The most promising concept is to substitute an LHC main dipole with dipoles of equal bending strength (~120 T·m) obtained by a higher field

(11 T) and shorter length (11 m) than those of the LHC dipoles (8.3 T and 14.2 m). The room gained is sufficient for installing special collimators.

- **R2E and SC links for remote powering of cold circuits**: considerable effort is under way to study how to replace the radiation sensitive electronic boards of the power converter system with radiation-hard cards. A complementary solution is also being pursued for special zones. This would entail removal of the power converters and associate DFBs (electrical feed-boxes, delicate equipment presently in line with the continuous cryostat) out of the tunnel, possibly to the surface. LHC availability should be improved. In particular in LHC point 7, where a set of 600 A power converters are placed near the betatron cleaning collimators, removal will be to a lateral tunnel because the surface is not accessible. Displacement of power converters to distant locations is possible only thanks to a novel technology: superconducting links (SCLs) made from HTS (YBCO or Bi-2223) or MgB_2 superconductors.

- **QPS, machine protection and remote manipulation**: Other systems will potentially become problematic, along with aging of the machine and the radiation level that comes with higher performance levels of 40 to 60 fb^{-1} per year:

  o **Quench Protection System** of the superconducting magnets, based on a design that is almost 20 years old.

  o **Machine protection:** improved robustness to mis-injected beams, to kickers sparks and asynchronous dumps will be required. The kicker system is, with collimation and the injection beam stopper, the main shield against severe beam induced damage. The kicker systems, along with the system will need renovation after 2020.

  o **Remote manipulation:** the level of activation from 2020 onwards, and perhaps even earlier, requires a careful study and the development of special equipment to allow replacing collimators, magnets, vacuum components etc., according to as low as reasonably achievable principle (ALARA). While full robotics is difficult to implement, given the conditions on the ground, remote manipulation, enhanced reality and supervision is the key to minimizing the radiation doses sustained during interventions.

1.1.3 Luminosity levelling, availability

Both the consideration of energy deposition by collision debris in the interaction region magnets, and the necessity to limit the peak pile up in the experimental detector, impose "a-priori" a limitation of the peak luminosity. The consequence is that the HL-LHC operation will have to rely on luminosity levelling. As shown in Figure 1-3 left, the luminosity profile without levelling quickly decreases from the initial peak value due to "luminosity burn" (protons consumed in the collisions). The collider is designed to operate with a constant luminosity at a value below the virtual maximum luminosity. The average luminosity achieved is almost the same as that without levelling, see Figure 1-3 right. However the advantage is that the maximum peak luminosity is lower.
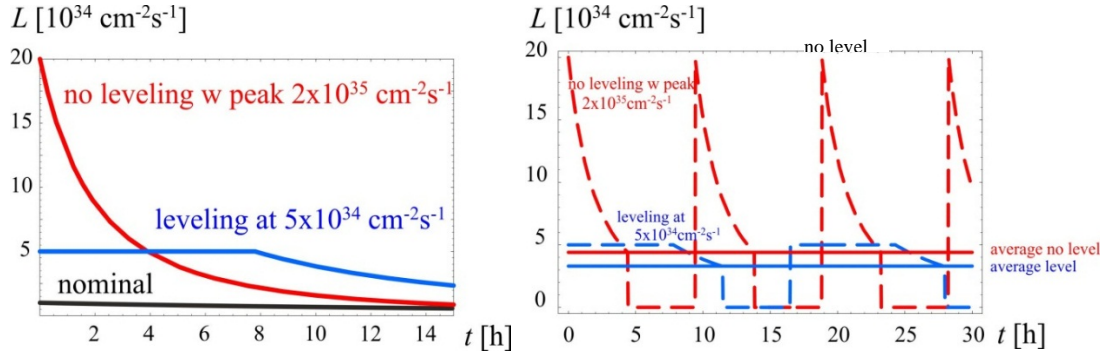
Figure 1-3: Left: luminosity profile for a single long fill: starting at nominal peak luminosity (black line), with upgrade no levelling (red line), with levelling (blue line). Right: luminosity profile with optimized run time, without and with levelling (blue and red dashed lines), and average luminosity in both cases (solid lines).

Because of the levelled luminosity limit, to maximize the integrated luminosity one needs to maximize the fill length. This can be achieved by maximizing the injected beam current. Other key factors for maximizing the integrated luminosity and obtaining the required 3 fb^{-1}/day (see Figure 1-4) are a short average machine turnaround time, an average operational fill length which exceeds the luminosity levelling time, and good overall machine efficiency. The machine efficiency is essentially the available time for physics after downtime for fault recovery is taken into account. Closely related is the physics efficiency – the fraction of time per year spent actually providing collisions to the experiments. For the integrated luminosity the efficiency counts almost as much as the virtual peak performance.

The HL-LHC with 160 days of physics operation a year needs a physics efficiency of about 40%. The overall LHC efficiency during the 2012 run, without luminosity levelling, was around 37%. The requirement of an efficiency higher than the one of the present LHC, with a (levelled) luminosity five times the nominal one, will be a real challenge. The project must foresee a vigorous consolidation for the high intensity and high luminosity regime: the High Luminosity LHC must also be a high availability LHC.
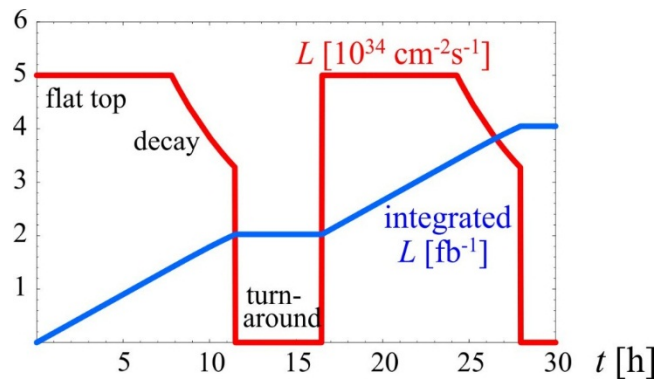
Figure 1-4: Luminosity cycle for HL-LHC with levelling and a short decay (optimized for integrated luminosity).

1.1.4 HL-LHC parameters and main systems for the upgrade

Table 1-1 lists the main parameters foreseen for the high luminosity operation. The 25 ns bunch spacing is the baseline operation mode; however, 50 ns bunch spacing is kept as a possible alternative in case the e-cloud or other unforeseen effects undermine the 25 ns performance. A slightly different parameter set at 25 ns (BCMS: Bach Compression and beam Merging Scheme) with very small transverse beam

emittance is also shown and might be interesting for the HL-LHC operation in case the operation with high beam intensities results in unforeseen emittance blow-up.

An upgrade should provide the potentiality of performance over a wide range of parameters, and eventually the machine and experiments will find the best practical set of parameters in actual operations.

Beam current and brightness: the total beam current may be a hard limit in the LHC since many systems are affected by this parameter: RF power system and RF cavities; Collimation; Cryogenics; Kickers; Vacuum; beam diagnostics; QPS etc. Radiation effects aside, all systems have been designed in principle for I_{beam}= 0.86 A, the so-called "ultimate" beam current. However the ability to go to the ultimate limit is still to be experimentally demonstrated and the HL-LHC will need to go 30% beyond ultimate with 25 ns bunch spacing.

For HL-LHC there is a need to increase the beam brightness, a beam characteristic that must be maximized at the beginning of the beam generation and then preserved throughout the entire injector chain and in LHC itself. The LIU project has as the primary objective of increasing the number of protons per bunch by a factor two above nominal design value while keeping the emittance at the present low value.

Table 1-1: High Luminosity LHC parameters.

Parameter	Nominal LHC (design report)	HL-LHC 25ns (standard)	HL-LHC 25ns (BCMS)	HL-LHC 50ns
Beam energy in collision [TeV]	7	7	7	7
N_b	1.15E+11	2.2E+11	2.2E+11	3.5E+11
n_b	2808	2748	2604	1404
Number of collisions in IP1 and IP5	2808	2736 [1]	2592	1404
N_{tot}	3.2E+14	6.0E+14	5.7E+14	4.9E+14
beam current [A]	0.58	1.09	1.03	0.89
x-ing angle [μrad]	285	590	590	590
beam separation [σ]	9.4	12.5	12.5	11.4
β^* [m]	0.55	0.15	0.15	0.15
ε_n [μm]	3.75	2.50	2.50	3
ε_L [eVs]	2.50	2.50	2.50	2.50
r.m.s. energy spread	1.13E-04	1.13E-04	1.13E-04	1.13E-04
r.m.s. bunch length [m]	7.55E-02	7.55E-02	7.55E-02	7.55E-02
IBS horizontal [h]	80 -> 106	18.5	18.5	17.2
IBS longitudinal [h]	61 -> 60	20.4	20.4	16.1
Piwinski parameter	0.65	3.14	3.14	2.87
Geometric loss factor R0 without crab-cavity	0.836	0.305	0.305	0.331
Geometric loss factor R1 with crab-cavity	(0.981)	0.829	0.829	0.838
beam-beam / IP without Crab Cavity	3.1E-03	3.3E-03	3.3E-03	4.7E-03
beam-beam / IP with Crab cavity	3.8E-03	1.1E-02	1.1E-02	1.4E-02
Peak Luminosity without crab-cavity [cm^{-2} s^{-1}]	1.00E+34	7.18E+34	6.80E+34	8.44E+34
Virtual Luminosity with crab-cavity: Lpeak*R1/R0 [cm^{-2} s^{-1}]	(1.18E+34)	19.54E+34	18.52E+34	21.38E+34
Events / crossing without levelling and without crab-cavity	27	198	198	454
Levelled Luminosity [cm^{-2} s^{-1}]	-	5.00E+34 [5]	5.00E+34	2.50E+34
Events / crossing (with leveling and crab-cavities for HL-LHC)	27	138	146	135
Peak line density of pile up event [event/mm] (max over stable beams)	0.21	1.25	1.31	1.20
Leveling time [h] (assuming no emittance growth)	-	8.3	7.6	18.0
Number of collisions in IP2/IP8	2808	2452/2524 [7]	2288/2396	0[4]/1404
N_b at SPS extraction [2]	1.20E+11	2.30E+11	2.30E+11	3.68E+11
n_b/ injection	288	288	288	144
N_{tot}/ injection	3.46E+13	6.62E+13	6.62E+13	5.30E+13
ε_n at SPS extraction [μm] [3]	3.40	2.00	< 2.00 [6]	2.30

β[*] and cancelling the reduction factor R: A classical route for a luminosity upgrade is to reduce β^* by means of stronger and larger aperture low-β triplet quadrupoles. However a reduction in β^* values implies not only larger beam sizes in the triplet magnets but also an increase in crossing angle. The increased crossing angle in turn requires even larger aperture triplet magnets, a larger aperture D1 (first separation dipole) and further modifications of the matching section. It also reduces the luminous region size and thus the gain in peak luminosity.

Stronger chromatic aberrations coming from the larger β-functions inside the triplet magnets may furthermore exceed the strength of the existing correction circuits. The peak β-function is also limited by the possibility to match the optics to the regular beta functions of the arcs. A previous study has shown that in the nominal LHC the practical limit for β^* is 30-40 cm cf. the nominal 55 cm. However, a novel scheme called Achromatic Telescopic Squeeze (ATS) [12] uses the adjacent arcs as enhanced matching sections. The increase of the beta-functions in these arcs can boost, at constant strength, the efficiency of the arc correction circuits. In this way a β^* value of 15 cm can be envisaged and a flat optics with a β^* as low as 5 cm in the plane perpendicular to the crossing plane could be realized. For such a β^* reduction the triplet quadrupoles need to double their aperture, and required a peak field 50% above the present LHC. This implies the use of new, advanced, superconducting technology based on Nb_3Sn.

The drawback of very small β^* is that it requires a larger crossing angle. This causes a reduction of the geometrical luminosity reduction factor R. In Figure 1-5 the reduction factor is plotted vs. β^* values.
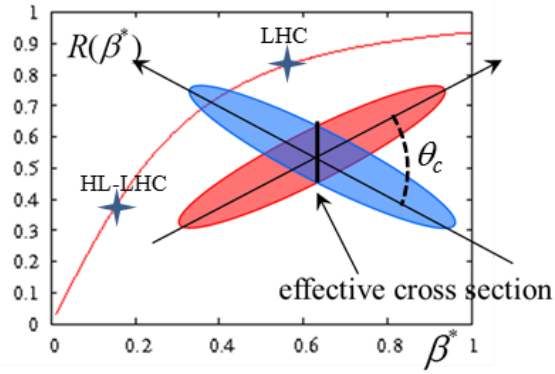
Figure 1-5: Behaviour of geometrical luminosity reduction factor vs. β* for a constant normalized beam separation with the indication of two operational points: nominal LHC and HL-LHC. The sketch of bunch crossing shows the reduction mechanism.

Various methods can be employed to counteract at least partially this effect. The most efficient and elegant solution for compensating the geometric reduction factor is the use of special superconducting RF crab cavities, capable of generating transverse electric fields that rotate each bunch longitudinally by $\theta_c/2$, such that they collide effectively head on, overlapping perfectly at the collision points, as illustrated in Figure 1-6. Crab cavities allow access to the full performance reach of the small β* values offered by the ATS scheme and the larger triplet quadrupole magnets. While the primary function of the crab cavities is to boost the virtual peak luminosity, they can also be used in combination with dynamic β* variation during the fill. This would allow optimization of the size of the luminous region and thus the pileup density through the fill. Finally, the Crab Cavities can be used to tilt the bunches in a direction perpendicular to the plane of crossing, providing pile-up control and an additional handle for luminosity levelling through the so called "crab-kissing" scheme.
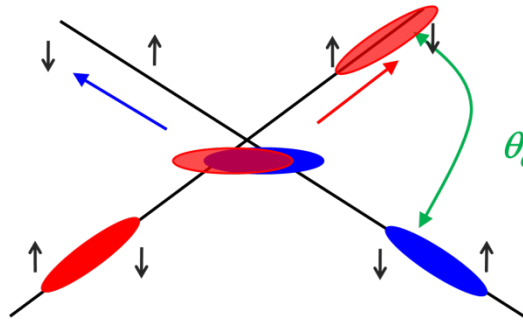
Figure 1-6: Effect of the crab cavity on the beam (small arrows indicate the torque on the bunch generated by the transverse RF field).

The layout and main hardware modifications required to produce the parameters listed in Table 1-1 are described in the chapter 2 of this report.

Given the yearly and long-term operations schedule, the targets of 250 fb[-1] per year and 3000 fb[-1] by the mid-2030s are very challenging. If the performance of the HL-LHC can go beyond the design levelled luminosity value of $L_{peak} = 5\times10^{34}$ cm[-2]s[-1] then these targets become more reasonable. Indeed, all systems will be designed with some margin. If the behaviour of the machine is such as to allow the utilization of these margins, and if the upgraded detectors will accept a higher pile-up, up to 200, then the performance could eventually reach 7.5×10^{34} cm^{-2}s[-1] with levelling. With a performance of 300 fb[-1]/year, this would allow almost 4000 fb[-1] to be obtained by 2037, as shown in Figure 1-7.
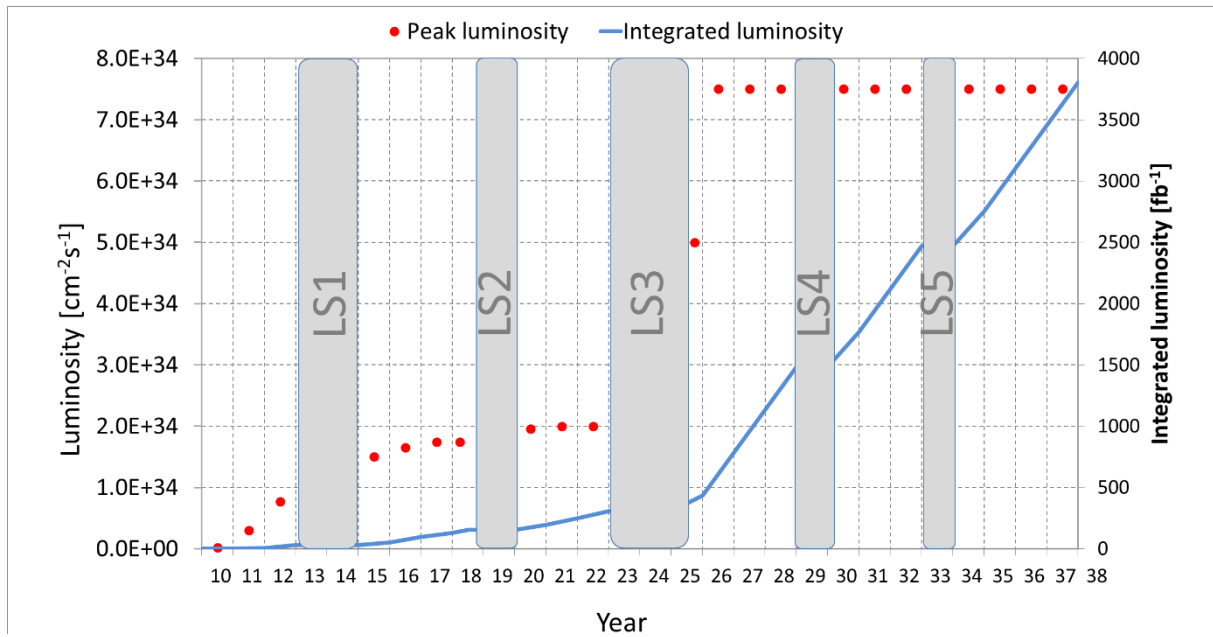
Figure 1-7: Forecast for peak luminosity (red dots) and integrated one (blue line) in the HL-LHC era, for the case of ultimate HL-LHC parameters. Note that for sake of simplicity there is no learning curve for the luminosity after LS3.

1.1.5 Plan and Cost

The HL-LHC schedule aims at the installation of the main HL-LHC hardware during LS3, together with the final upgrade of the experimental detectors (so-called Phase-II upgrade). However, a few items like the new cryogenic plant for P4, the 11 T dipole for DS collimation in P2 (for ions) and the SC links in P7 would be installed during LS2.

The HL-LHC schedule is based on the following milestones:

- 2014: Preliminary Design Report (PDR)

- 2015: end of design phase, release of the first Technical Design Report (TDR)

- 2016: Proof of main hardware components on test benches

- 2017: Testing of prototypes (including crab cavity test in SPS) and release of TDR_v2

- 2017-2021: Construction and test of long lead hardware components (e.g. magnets, crab cavities, SC links, collimators)

- 2018-2019: LS2 - Installation of Cryo-plant P4, DS collimators (11T) in P2, SC link in P7

- 2020-2022: String test of Inner triplet

- 2023-2025: LS3 – Main installation (new magnets, crab cavities, cryo-plants, collimators, absorbers, etc.) and commissioning
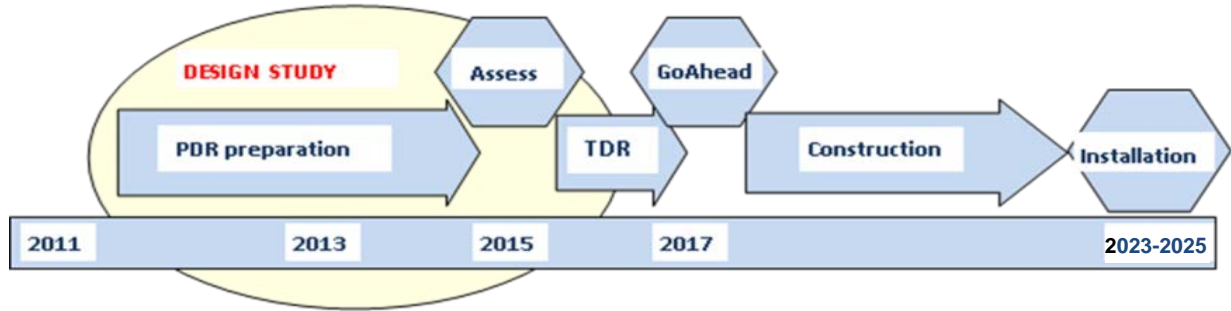
Figure 1-8: Schematic representation of the main HL-LHC milestones

The preliminary cost-to-completion (CtC) of the full HL-LHC project amounts to about 830 MCHF for Material (CERN accounting). A coarse evaluation of personnel requirements amounts to more than 1000 FTE-y. The cost-to-completion does not include the civil engineering works for the underground cavern (presently under evaluation) and non-baseline systems such as the long range beam-beam compensators and the RF harmonic system and the related infrastructures. The budget profile is shown in Figure 1-9.
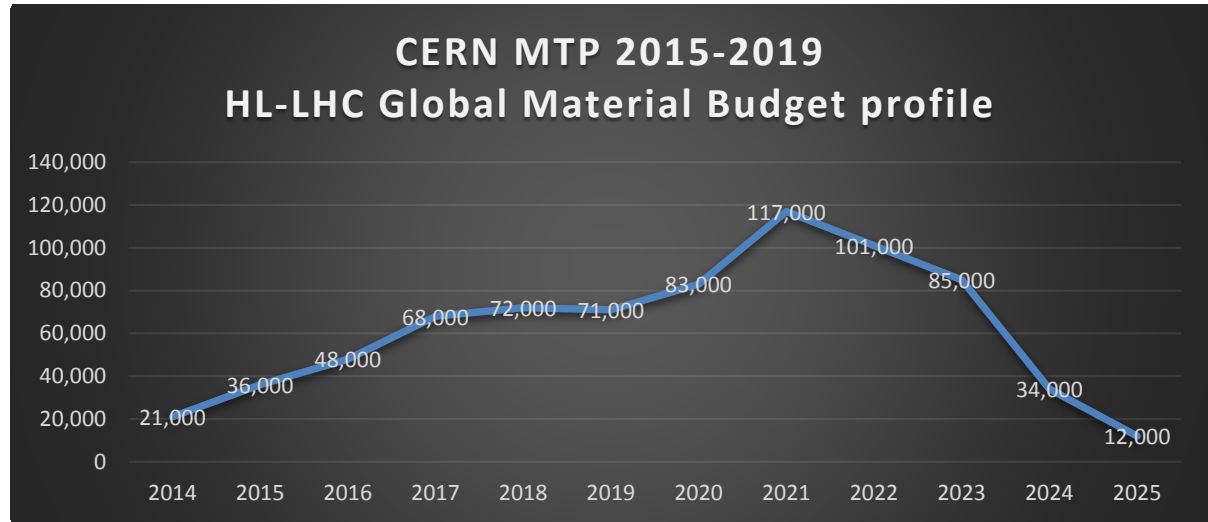
Figure 1-9: Budget allocation 2015 - 2025

Today the CERN draft budget attributes about 750 MCHF for the HL-LHC project until 2025, with certain assumptions of in-kind contributions from both the USA and Japan. The discrepancy is not critical at this stage, since modifications of certain systems are not yet fully defined. LHC operation at full energy and intensity will give important indications. The thorough investigation of potential synergy with the LHC consolidation project together with various studies should allow savings without compromising performance. Additional in-kind contributions to the hardware baseline would help alleviate the cost discrepancy and would also bring more personnel into the project.

A further possibility is to stage the project by using LS4, see Figure 1-7. Indeed the performance "forecast" of Figure 1-7 is somewhat theoretical: there will be certainly a learning curve to pass from 2 to (levelled) 5×10^{34} cm^{-2}s^{-1}, naturally favouring a staged approach. However, the 250 fb^{-1} annual integrated luminosity goal can only be attained, and possibly even surpassed, when installation of all equipment is completed.

1.2 The Collaboration

The LHC Luminosity Upgrade was conceived from the beginning as even more international than the LHC machine construction, since US laboratories started to work on it with considerable resources well

before CERN. In 2002-2003 collaboration between the US laboratories and CERN established the route for a machine upgrade [9]. The program LARP (LHC Accelerator Research Program) was then setup and approved by DOE. In the meantime, CERN was totally engaged in the LHC construction and commissioning: it could only participate in CARE, an EC-FP6 program, in 2004-2008. CARE contained a modest program for the LHC upgrade. Then two EC-FP7 programs (SLH-PP and EuCARD) helped to reinforce the design and R&D work for the LHC upgrade in Europe, although still at a modest level. KEK in Japan, in the frame of the permanent CERN-KEK collaboration, also engaged in activity for the LHC upgrade from 2008. LARP remained until 2011 the main R&D activity in the world for the LHC upgrade.
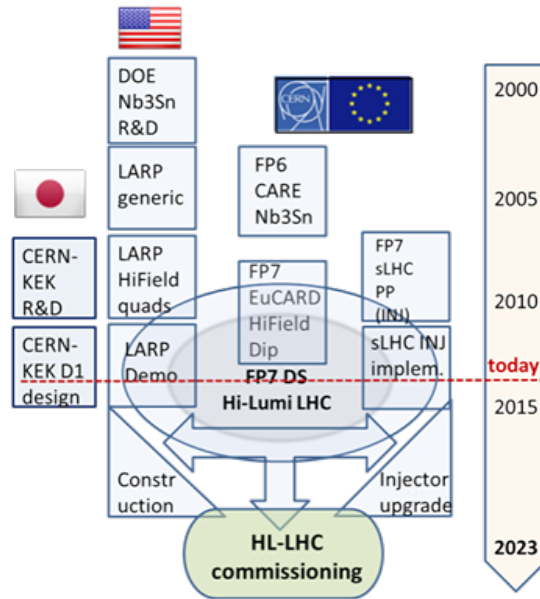
Figure 1-10: timeline of the various collaboration branches, converging toward the luminosity upgrade of the LHC

Finally, with the approval of the EC-FP7 Design Study *HiLumi LHC* in 2011, and the maturing of the main project lines considered in Section 1, the collaboration for HL-LHC took the present form. It is worth noticing that FP-HiLumi covers only the design of a few systems, given the limited amount of funding in such a program. It has however allowed the formation and structuring of a European participation to the LHC Upgrade from the very beginning of the project. In 2014, CEA (Saclay, FR), INFN (Milano and Genova, IT) and CIEMAT (Madrid, ES), have signed a further collaboration agreement to carry out design, engineering and prototyping work for HL-LHC magnets in addition to the FP7-EC commitment. In all three cases the CERN funding for the activities is approximately 50%, the rest being supported by the collaborating institutes. In **Error! Reference source not found.** a schematic indicating the various collaboration branches is shown.

1.2.1 FP7-Hilumi LHC

The "FP7 High Luminosity Large Hadron Collider Design Study", in short "HiLumi LHC" proposal was submitted on November 2010 to the EC Seventh Framework Programme. Approved with a full score of 15/15 it has been fully funded by EC. The contract was signed by the fifteen partners (beneficiaries). KEK is a partner without EC funding - all their funding is internal. The US laboratories were part of the proposal, without EC funding, but then for various reasons (mainly related to IP issues) they could not sign the FP7-HiLumi LHC Consortium Agreement, thus they are external associates with no formal obligations. In practice LARP is excellently coordinated with FP7Hilumi (see section on "governance") and the project heavily relies on LARP to reach the project goals.

The mechanism of FP7 is such that each of the thirteen European Institutions that are members of HiLumi LHC have to match the EC contribution with their own funding. In the case of FP7-HiLumi the matching funds equal the EC funds: each EU Institute receives 50% of the total cost (including overheads). The exception is CERN that receives only 17% of its total cost, mainly for management and coordination. In Figure 1-11 the funding mechanism is explained. Given the success of the evaluation, see above, the project was ranked first in its category and was fully financed, with a EU contribution of M€4.9 against a request of M€4.97.
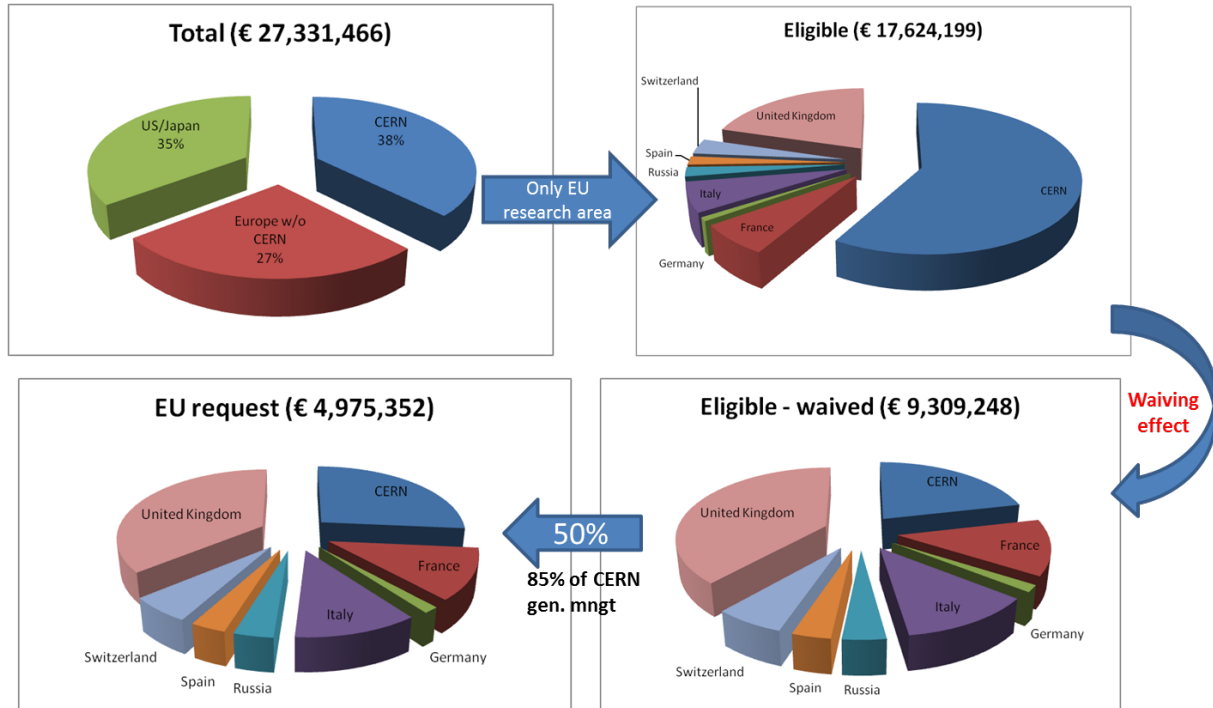
Figure 1-11: Top left: total estimation of the cost of the design study, subdivided by USA and Japan, EU Institutes and CERN. Top Right: total cost with USA and Japan removed (i.e. only costs that are eligible for funding by the EC). Bottom right: effect of CERN waiving the cost for technical works (recognizing that HL-LHC is part of the core CERN program financed via normal budget), while keeping the extra cost generated by the management and coordination of the project. This is the total cost declared to the E.C. Bottom right: cost claimed to EC: 50% of the declared cost (eligible cost reduced by CERN waiving action).

In Figure 1-12 the list of the 15 FP7-HiLumi Institutions is shown, followed by the list of the five USA collaborating institutes.

Short Name	Country	Logo
CERN	Geneva Switzerland	
CEA	Saclay France	
DESY	Hamburg Germany	
INFN	Frascati Italy	
CSIC	Madrid Spain	
EPFL	Lausanne Switzerland	
SOTON	Southampton United Kingdom	
RHUL	London United Kingdom	

Short Name	Country	Logo
STFC*	Daresbury United Kingdom	
ULANC*	Lancaster United Kingdom	
UNILIV*	Liverpool United Kingdom	
UNIMAN*	Manchester United Kingdom	
HUD	Huddersfield United Kingdom	
KEK	Tsukuba Japan	
BINP	Novosibirsk Russia	

*Members of Cockcroft Institute

Short Name	Country	Logo	
BNL	Upton, NY USA		
FNAL	Batavia, IL USA		LARP
LBNL	Berkeley, CA USA		
SLAC	Menlo Park, CA USA		
ODU	Norfolk, VA USA		

Figure 1-12: Table of the 15 members ("beneficiaries") of the FP7 HiLumi LHC design study and of the five U.S. LARP laboratories that are associated with the project.

1.2.2 U.S. LARP

The U.S. LARP (LHC Accelerator R&D Program) was initiated by the US Department of Energy (DOE) in 2003 to participate in the commissioning of the US-built interaction region triplets by bringing together and coordinating resources from the 4 US HEP laboratories (BNL, FNAL, LBNL and SLAC) with the inclusion of some universities as the program evolved. Already in 2003 it was recognized, based on the Tevatron experience, that an increase in LHC luminosity would become necessary after a decade of LHC operation to reduce the "halving time", i.e. the time needed to reduce statistical errors by a factor of two. Consequently the program focused - from the very beginning - on the design of improved focusing quadrupoles for the LHC low-β insertion regions, finding a synergy with the various DOE High Field Magnet (HFM) R&D programs at the participating Laboratories. The conductor of choice for this R&D program was selected to be Nb_3Sn and therefore LARP became synergetic with another DOE program, the Conductor Development Program (CDP), initiated in 1998 with the goal of improving the performance of Nb_3Sn. The LARP, CDP and US Labs HFM activities interacted in an extremely constructive way achieving a substantial increase in the critical current performance of Nb_3Sn

superconductor (Figure 1-13) and defining the assembly technique for accelerator quality high field Nb_3Sn magnets in different kind of configuration and with different apertures.

The LARP effort was funded at approximately 12-13 M$/year with 50% of the funding going directly to magnet development. Several magnets developed by LARP reached and surpassed the design field as shown in Figure 1-14 right for one of the latest models (HQ02, a 120 mm aperture quadrupole assembled in 2014 and tested at FNAL and CERN). Additionally, LARP has demonstrated the scale-up of the Nb_3Sn technology (i.e. the performance of the technology for magnets as long as 3 m) as shown in Figure 1-14 left for the LQ (90 mm aperture Long Quadrupole). The achievements of the US programs, in particular LARP but also of the general R&D high field magnet program, have led to the adoption of the Nb_3Sn superconductor solution as the baseline for the HL-LHC new focusing system and 11 T magnets.
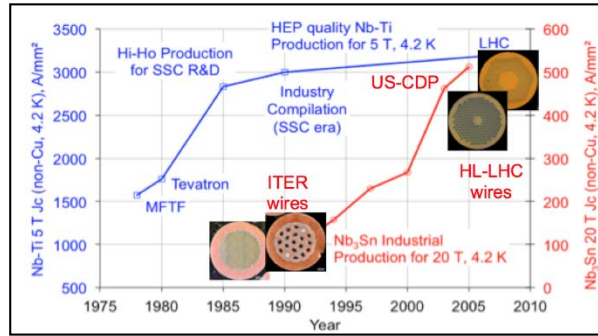
Figure 1-13: Left: Improvement in Jc (Current Density) in Nb3Sn superconductor during the last 3 decades compared with the NbTi Jc performance.
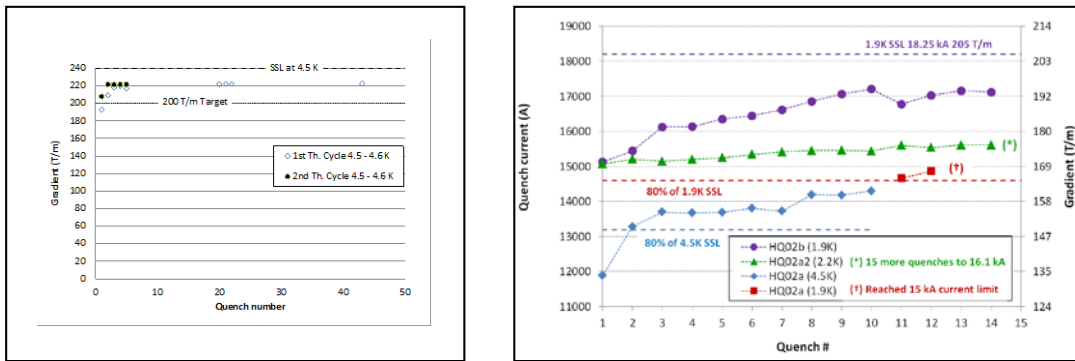
Figure 1-14: Left: Quench performance of LQ (Long Quadrupole), the first quadrupole demonstrating the scale-up of the Nb_3Sn technology to lengths of interest for LHC applications (~3 m). Right: Quench performance of HQ02 (120 mm aperture) after several re-assemblies, showing that in all cases the magnet achieved and passed the target (80% of the Short Sample Limit, SSL).

In addition to contributions to LHC commissioning and magnet development related activities, LARP was also tasked with the support and promotion of accelerator physics R&D activities at the LHC accelerator. An additional very important aspect of this commitment was the institution of the Toohig Fellowship (*http://www.interactions.org/toohig/*) to support young accelerator physicists and engineers wishing to pursue research at the LHC in the early years of their career.

Recently LARP has leveraged the superconducting RF capabilities and resources available at the US Laboratories and Universities to focus on the development of the Crab Cavities (Chapter 4) achieving transverse fields meeting the technical specifications for this system. In addition, a Wide Band Feedback System is being researched and developed within LARP with the goal of mitigating transverse instabilities in the SPS and, possibly, in the LHC.

DOE and CERN will negotiate the deliverables from the US in the coming years. In the CY15-CY17 period, LARP will concentrate on prototyping the elements needed by the HL-LHC project in which the US National Laboratories and Universities have demonstrated excellent capabilities. In particular - subject to funding availability - LARP plans to build 2 short (1m) and 3 long (4 m) QXF magnet models to demonstrate the final design and reduce the risk during the construction period. In addition LARP plans to deliver 4 fully-dressed SCRF Crab Cavities and a Wide Band Feedback System prototype for tests in the SPS. This phase is expected to continue until the start of construction in the 2018-2021 period.

1.2.3 KEK

Within the framework of the CERN-KEK collaboration, KEK has conducted the Nb_3Al superconductor R&D for the high field magnets aimed at the future LHC upgrade from the early 2000s in collaboration with the National Institute of Materials Science (NIMS) in Japan. The Nb_3Al superconductors are made by the "Rapid-Heating, Quenching Transformation (RHQT)" process, which was invented by NIMS. These superconductors have shown better critical current density and less strain dependence, and have been considered as one of the promising candidates for the high field accelerator magnet application. Nevertheless, KEK and NIMS faced technical difficulties in the long wire production and it was judged in 2011 that the Nb_3Al superconductor was unfortunately not ready for the industrialization for the HL-LHC upgrade anticipated around 2022.

KEK has officially participated in the FP7 HiLumi LHC design study since 2011 in the context of enhancing the Japanese contribution to the physics outcome from the ATLAS experiment. Following suppression of the research activities on the Nb_3Al superconductor development, the main effort was redirected to the conceptual design study of the beam separation dipole magnet, D1, situated immediately after the low-beta insertion quadrupoles in the HL-LHC machine. While the conceptual design study has been dominantly pursued by KEK, the close collaboration with CERN and other partners has strengthened the success of the design study. The D1 magnet is based on the mature Nb-Ti technology. Design challenges are the tight control of the field quality with the large iron saturation, and the accommodation of the heat load and the radiation dose. The research engagement includes the 2-m long model magnet development and its tests at 1.9 K. KEK has also contributed to the HiLumi LHC design study through beam dynamics studies and the cooperative work associated with the crab cavity.

Aside from the HiLumi LHC, KEK has also participated to the LHC Injectors Upgrade (LIU) project. The main collaboration items have been consolidation and upgrade of PS Booster RF systems using Finemet-FT3L technology and development of the longitudinal damper system.

1.2.4 Other Collaborations

In 2014, CEA (Saclay, FR), INFN (Milano and Genova, IT) and CIEMAT (Madrid, ES), have each signed a further collaboration agreement to carry out design, engineering and prototype work for HL-LHC magnets in addition to the FP7-EC commitment. In all three cases, the CERN funding is about 50%, the rest being at charge of the collaborating institutes.

1.2.4.1 CEA

The CEA agreement concerns "Research and Development for future LHC Superconducting Magnets". It has six technical work packages, covering R&D for HL-LHC and for post-LHC magnets. Among them, the following ones are of HL-LHC interest:

- Design and construction of a single aperture, 1 m long, full coil size model magnet of the first quadrupole of the matching section, Q4. The magnet is based on classical Nb-Ti technology but has very large aperture (90 mm) in a Two-in-One cold mass, and thus presents a number of design challenges.

- Completion of the 13 T, large aperture dipole Fresca2 (a technological Work Package of HL-LHC, that has served as promoter of Nb₃Sn at CERN).

- Studies on Nb₃Sn thermal properties and a finite element model of Nb₃Sn cabling.

1.2.4.2 INFN (Milano and Genova)

The INFN agreement is also related to R&D on Superconducting Magnets for HL-LHC and concerns two main items:

- Design and construction of a prototype of each of the six high order corrector magnets for the inner triplet, all with a single aperture of 150 mm. The work is based on Nb-Ti superferric technology and is carried out at INFN-LASA in Milano. An option based on MgB_2 superconductor is also considered as extra effort by INFN.

- Engineering Design of the superconducting recombination dipole magnet, D2, the first Two-in-One magnet, at the end of the common beam pipe. The work is based on Nb-Ti technology, with design challenges coming from the large aperture and the relatively high fields which have parallel direction in both apertures. The work is performed at INFN-Genova.

1.2.4.3 CIEMAT (Madrid)

The CIEMAT agreement concerns the design and construction of a 1 m-long prototype of the 150 mm aperture nested orbit corrector dipole for the inner triplet. It features two dipoles coils, rotated by 90 degree for simultaneous horizontal and vertical beam steering, in the same aperture. The main challenges is the mechanical structure to withstand the large torque and the unusual force distribution arising when both field directions are needed.

1.3 Governance and Project Structure

Given the fact that the application for the FP7 HiLumi LHC Design Study marked the start of the project in its present form, the structure and terminology are borrowed from the typical FP7 style. To avoid any duplication the governance of the whole HL-LHC project is conceived as an extension of the governance that has been instituted for the governance of the FP7-HiLumi LHC.

As noted above, the FP7-HiLumi LHC covers only a few work packages (WPs), although they are the backbone of the upgrade. The WP structure, with task arborescence, is the basic structure of the project. LARP is a parallel structure, independently funded, associated to FP7 with connections both at project management level as well as at WP/task level to maximize synergy. KEK is directly member of FP7-HiLumi. It is worth noting that HiLumi LHC is the nickname to indicate the part of HL-LHC that is covered by FP7 funds, even if in practice it has become a popular name to indicate the full project. In Figure 1-15 the general governance of the project is shown. Each body contains the FP7 part and the part that is not covered by FP7. The Steering Committee is the main managing body: it meets regularly every 2 months and all WPs are there represented, with the addition of the LARP representatives. It oversees the progress of the technical work and the planning, approving the milestones and deliverables. The Steering Committee usually meets in its "enlarged" form, including also the WPs not covered by FP7 and including the LARP leadership. The Collaboration Board is the highest-level governance body with representation from each institute.

In case of approval of formal acts for FP7, only the FP7-WP coordinators and FP7 Institutes can vote. It is worth noting that the collaboration is based on a Consortium Agreement, signed by the 15 members (beneficiaries in FP7 terminology) of FP7-HiLumi LHC. The USA laboratories are not members of FP7-HiLumi LHC, however representatives of each USA laboratory, included the LARP Director, are co-opted in the enlarged Collaboration Board. The formal link with the USA laboratories is assured by the recently signed CERN-DOE Protocol II concerning the LHC and its upgrades. Given

the fact that CERN is responsible for the LHC machine, the CERN DG, through his representative in the Collaboration Board, the Project Coordinator, has the right of veto.

The Parameter and Layout Committee and the Technical committee have mainly technical functions inside the project. The Coordination group, chaired by the HL-LHC leader, constitutes the meeting point between CERN Management, HL-LHC, LIU and Detector Management.

A new structure, more suited to a project that is passing from the design study phase to
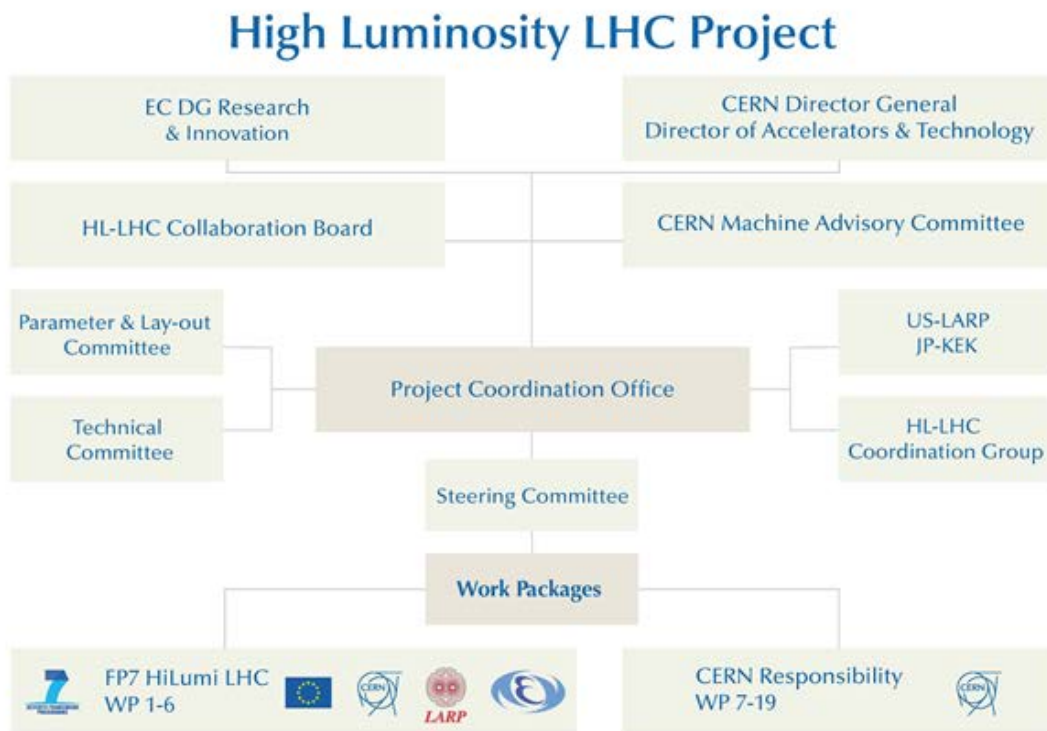
construction project status, is under study and will be operative from November 2015 when the FP7 Consortium Agreement comes to an end.

Figure 1-15: The general governance scheme of FP-7 HiLumi LHC, used for the whole HL-LHC project (see text for details)

In Figure 1-16 the project structure with all WPs and their coordinators, as well as the main collaborators, is shown. Typically, each WPs is assigned 3 to 6 tasks. The tasks are the core of the technical work.
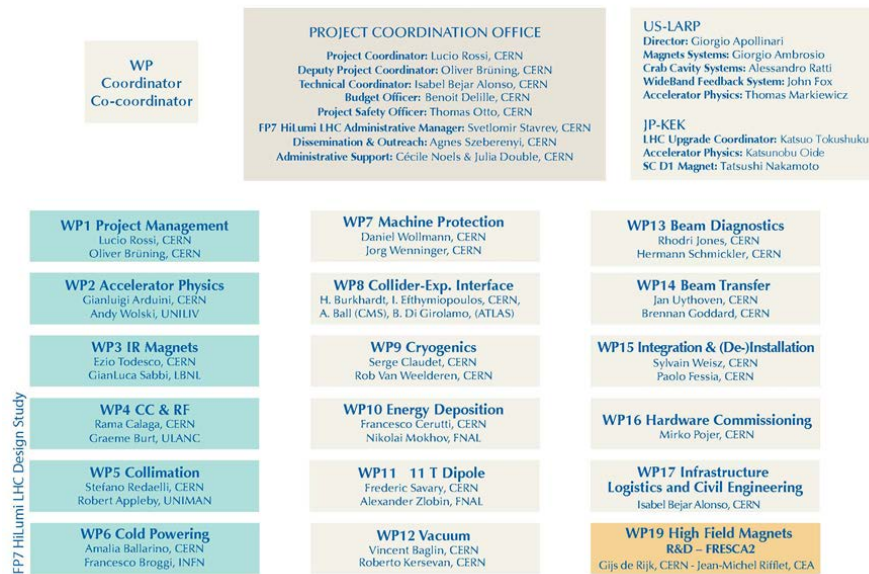
Figure 1-16: HL-LHC project structure, with FP7 part indicated in dark green. The orange box refers to the High Field Magnets work package, which was started before the HL-LHC in the framework of generic R&D for the LHC upgrade.

1.4 References

[1]   European Strategy for Particle Physics, adopted by the CERN Council at a special session at ministerial level in Lisbon in 2006. http://cern.ch/council/en/EuropeanStrategy/ESParticlePhysics.html

[2]   European Strategy Forum for Research Infrastructures, ESFRI, http://ec.europa.eu/research/esfri

[3]   The European Strategy for Particle Physics Update 2013, CERN-Council-S/106, adopted at a special session in the Brussels on 30 May 2013. http://cern.ch/council/en/EuropeanStrategy/ESParticlePhysics.html

[4]   Building for Discovery: Strategic Plan for U.S. Particle Physics in the Global Context, in http://science.energy.gov/hep/hepap/reports/

[5]   Lucio Rossi, "LHC Upgrade Plans: Options and Strategy", Proceedings of IPAC2011, San Sebastián, Spain, 01/09/2011, pp. 908-912

[6]   LHC Luminosity and Energy Upgrade: A Feasibility Study, O. Bruning, R. Cappi, R. Garoby, O. Grobner, W. Herr, T. Linnecar, R. Ostojic, K. Potter, L. Rossi, F. Ruggiero (editor), K. Schindl, G. Stevenson, L. Tavian, T. Taylor, E. Tsesmelis, E. Weisse, and F. Zimmermann

[7]   Towards a New LHC Interaction Region Design for a Luminosity Upgrade http://accelconf.web.cern.ch/AccelConf/p03/PAPERS/MOPA006.PDF

[8]   Project for the LHC Injector complex Upgrade (LIU)

[9]   Towards a new lhc interacton region design for a Luminosity upgrade. J. Strait, M. Lamm, P. Limon, N.V. Mokhov, T. Sen, A.V. Zlobin, O. Brüning, R. Ostojic, L. Rossi, F. Ruggiero, T. Taylor, H. ten Kate, A. Devred, R. Gupta, M. Harrison, S. Peggs, F. Pilat, S. Caspi, S. Gourlay, G. Sabbi. Proceedings of the 2003 Particle Accelerator Conference.

Chapter 2

Machine layout and performance

D. Angal-Kalinin[1], R. Appleby [21], G. Arduini [5], D. Banfi [9], J. Barranco [9], N. Biancacci [5], D. Brett [21], R. Bruce [5], O. Brüning [5], X. Buffat [5], A. Burov [10], Y. Cai [19], R. Calaga [5], A. Chancé [4], M. Crouch [21], B. Dalena [4], H. Day [5], R. de Maria [5], J. Esteban Muller [5], S. Fartoukh [5], O. Frasciello [15], M. Giovannozzi [5], W. Herr [5], W. Höfle [5], B. Holzer [5], G. Iadarola [5], J.M. Jowett [5], M. Korostelev [23], K. Li [5], E. McIntosh [5], E. Métral [5], A. Mostacci [24], N. Mounet [5], B. Muratori [1], Y. Nosochkov [19], K. Ohmi [16], Y. Papaphilippou[5], S. Paret [17], J. Payet [4], T. Pieloni [5], J. Qiang [17], T. Rijoff [5], L. Rossi [5], G. Rumolo [5], B. Salvant [5], M. Schaumann [5], E. Shaposhnikova [5], D. Shatilov [2], C. Tambasco [5], R. Tomás [5], A. Valishev[10], M.-H. Wang [19], R. Wanzenberg [8], S. White [5], A. Wolski [23], O. Zagorodnova [8], C. Zannini [5], F. Zimmermann [5], M. Zobov [15]

[1]ASTeC, STFC, Daresbury Laboratory, Warrington WA4 4AD, United Kingdom
[2]BINP, Novosibirsk, Russia
[4]CEA/SACLAY, DSM/Irfu/SACM - 91191 Gif-sur-Yvette - France
[5]CERN, Accelerator & Technology Sector, CH-1211, Geneva, Switzerland
[8]DESY, Deutsches Elektronen-Synchrotron   Notkestr. 85, 2000 Hamburg 52, Germany
[9]EPFL, Lausanne, Switzerland
[10]FNAL, Fermi National Accelerator Laboratory, Batavia, P.O. Box 500, IL, USA
[15]INFN-LNF, Via E. Fermi 40, 00044 Frascati, Rome, Italy
[16]KEK, Oho, Tsukuba, 305-0801, Japan
[17]LBNL, Lawrence Berkeley National Laboratory, Berkeley, CA 94720, USA
[19]SLAC National Accelerator Laboratory, 2575 Sand Hill Road, Menlo Park California 94025 USA
[21]UMAN, The University of Manchester and the Cockcroft Institute, United Kingdom
[23]University of Liverpool, Liverpool L69 7ZE, United Kingdom
[24]University of Rome "La Sapienza", Rome, Italy

2   Machine layout and performance

2.1   Performance goals (nominal scheme)

The goal of the High Luminosity upgrade of the LHC is to deliver an integrated luminosity of at least 250 fb^{-1} per year in each of the two high luminosity general purpose detectors, ATLAS and CMS, located at the interaction points (IP) 1 and 5, respectively. The other two experiments, ALICE and LHCb with detectors located at IP2 and IP8 respectively, are expecting to collect integrated luminosities of 100 pb^{-1} per year (of proton-proton data) and 5 to 10 fb^{-1} per year, respectively [1]. No operation for forward physics experiments is expected after the upgrade.

The ATLAS and CMS detectors will be upgraded to handle an average number of pile-up events per bunch crossing of at least 140, corresponding to an instantaneous luminosity of approximately 5×10^{34} cm^{-2}s^{-1} for operation with 25 ns beams at 7 TeV, for a visible cross section $\sigma_{vis} = 85$ mb. The

detectors are also expected to handle a line density of pile up events of 1.3 events per mm per bunch crossing. ALICE and LHCb will be upgraded to operate at instantaneous luminosities of up to 2×10^{31} $cm^{-2}s^{-1}$ and 2×10^{33} $cm^{-2}s^{-1}$, respectively.

The HL-LHC upgrade project aims to achieve a 'virtual' peak luminosity that is considerably higher than the maximum imposed by the acceptable event pile-up rate, and to control the instantaneous luminosity during the physics fill ("luminosity levelling") so that the luminosity production can be sustained over longer periods to maximize the integrated luminosity.

A simplified but realistic model of the luminosity evolution has been developed [2] taking into account the beam population N_{beam} reduction due to the collisions (the so called "burn-off") in nIP collision points with instantaneous luminosity L_{inst}:

$$\frac{dN_{beam}}{dt} = -n_{IP}\sigma_{tot}L_{inst} \tag{2-1}$$

where σ_{tot} is the total hadron cross-section (here assumed to be 100 mb). No other sources of intensity reduction or emittance blow-up are considered in this model. Figure 2-1 shows the expected yearly integrated luminosity as a function of the 'virtual' peak luminosity for three different values of the luminosity at which levelling is performed (see 1.2.3). In this figure the corresponding optimum fill length T_{fill} (i.e. the length of time for each fill that will maximize the average luminosity production rate) is also shown. In order to estimate the annual integrated luminosity, we assume a minimum turn-around time $T_{turnaround}$ of 3 hours (see Chapter 16), a scheduled physics time $T_{physics}$ for luminosity production of 160 days per year, with N_{fills} successful physics fills of duration T_{fill}, and a performance efficiency of 50% (in 2012 was 53.5%) where [3]:

$$\eta = N_{fills}\frac{T_{turnaround} + T_{fill}}{T_{physics}} \times 100\% \tag{2-2}$$

In order to reach the goal of integrating 250 fb-1/year levelling must be performed at luminosities larger than 5×10^{34} $cm^{-2}s^{-1}$ and peak virtual luminosities of more than 20×10^{34} $cm^{-2}s^{-1}$. Furthermore, the performance efficiency must be at least 50% and the typical fill length must be comparable with the estimated optimum fill length (for comparison the average fill length during the 2012 run was 6.1 hours). In this respect, levelling to higher luminosities will be beneficial because it would make it easier to reach and even exceed the integrated luminosity goal, with fill lengths comparable to the fill lengths of the 2012 run.
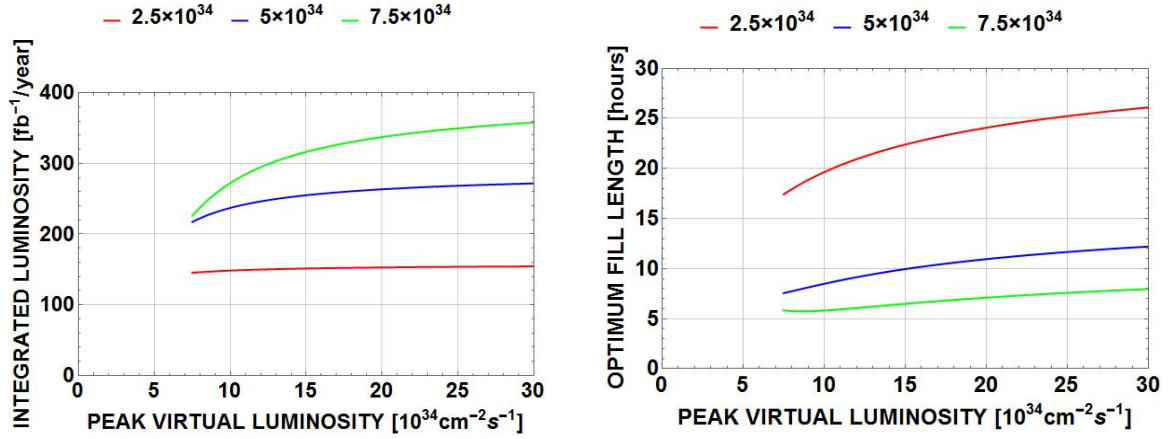
Figure 2-1: Expected annual integrated luminosity (left) and optimum fill length (right) as a function of the 'virtual' peak luminosity for three different values of the luminosity at which levelling is performed. A circulating current of 1.1 A (corresponding to $N_{beam}=6.1\times10^{14}$ p), a minimum turn-around time of 3 hours and a performance efficiency η of 50% have been assumed. Only burn-off for a total hadron cross-section of 100 mbarn has been considered for the estimate of the beam population and virtual luminosity evolution. Two high luminosity interaction points have been assumed.

2.1.1 Parameter space and basic parameter choices

The instantaneous luminosity L is given by equation:

$$L = \frac{n_b N^2 f_{\text{rev}} \gamma}{4\pi \beta^* \varepsilon_n} R(\beta^*, \sigma_z, d_{\text{bb}})$$

(2-3)

The r.m.s. normalized emittance ε_n in collision is assumed here to be equal for the two beams and for the horizontal and vertical planes. The T_{wiss} beta function β^* in collision at the IP determines, together with the normalized emittance, the r.m.s. beam size $\sigma^* = \sqrt{\varepsilon_n \beta^*/\gamma}$ at the IP (assuming that the contribution to the beam size due to the dispersion and the momentum spread of the beam can be neglected). Here and in the following it is assumed that the relativistic factor $\beta = 1$.

A crossing angle is needed to separate bunches immediately upstream and downstream of the collision point. This leads to a reduced geometric overlap between the colliding beams, and hence to a reduction in luminosity. The crossing angle needs to be increased when reducing the β^* in order to maintain a sufficiently large normalized beam-beam separation d_{bb}. The luminosity is also reduced by the "hourglass effect" that arises from the increase of the beta function upstream and downstream of the interaction point along the bunch longitudinal distribution. The hourglass effect is enhanced by a reduction in β^* and by an increase in bunch length. The luminosity reduction factor R in equation (2-3) takes both the crossing angle and the hourglass effect into account.

Equation (2-3) shows the parameters that can be varied to maximize the instantaneous luminosity. The considerations that constrain their values are briefly discussed below [4, 5]:

-   The maximum number of bunches n_b is limited by the minimum time interval between bunch crossings at the IP that can be handled by the detectors: this is limited to 25 ns. The maximum number of bunches that can be injected in the LHC is also limited by:

    o   The maximum number of bunches that can be transferred safely from the SPS to the LHC due to the maximum energy that can be deposited on the injection protection absorber (TDI) in case

the LHC injection kicker is not firing. The present limitation for the TDI is considered to be at maximum 288 bunches per SPS extraction for the ultimate bunch population [6].

- o The rise-time of the injection kickers in the SPS and LHC, extraction kickers in the PS and SPS and abort gap kicker in the LHC.

- o The need for injecting one train consisting of few bunches (typically 12 nominal bunches for 25 ns spacing) before injecting one nominal train for machine protection considerations [7]. For the same reason the last train must have the maximum number of bunches.

- o The constraints imposed by the experiments: need for non-colliding bunches for background evaluation, sufficient number of collisions for the lower luminosity experiments [1].

- The maximum bunch population N is limited in the LHC by the onset of the single bunch Transverse Mode Coupling Instability (TMCI), expected to occur at 3.5×10^{11} p/bunch [8].

- The total current of the beam circulating in the LHC $I_{\text{beam}} = e n_b N f_{\text{rev}}$ (where e is the proton charge) is expected to be limited to 1.1 A by the cryogenic power available to cool the beam screen. This assumes that a secondary electron yield (SEY) as low as 1.3 can be reached in the beam screen, to limit the heat load due to electron cloud in the arcs, and additional cryogenic plants are installed in points 1, 4 and 5 [4, 9].

- The beam brightness $B \equiv N/\varepsilon_n$ is limited by the following considerations [4]:

- o The total head-on beam-beam tune shift $\Delta Q_{\text{bbho}} \propto N/\varepsilon_n$ is expected to be limited to 0.02-0.03 based on experience gained (from operations and dedicated experiments) during the LHC Run 1. Its value is reduced in a similar fashion to the luminosity in the presence of a crossing angle [10].

- o Intra-beam scattering induces transverse and longitudinal emittance blow-up, particularly at injection (low energy) but also in the phases of acceleration, squeeze, and in collision. The evolution of the beam emittances can be described by the equations:

$$\frac{1}{\tau_H} = \frac{1}{\varepsilon_{nH}} \frac{d\varepsilon_{nH}}{dt} \text{ and } \frac{1}{\tau_L} = \frac{1}{\varepsilon_L} \frac{d\varepsilon_L}{dt} \text{ with } \frac{1}{\tau_d} \propto \frac{N}{\gamma \varepsilon_{nH} \varepsilon_{nV} \varepsilon_L} \text{ and } d = H, L, \qquad \textbf{(2-4)}$$

Where $\varepsilon_{nH,V}$ are the r.m.s. normalized horizontal and vertical emittances. Here we assume that vertical dispersion and coupling are negligible so that the vertical emittance blow-up can be neglected.

The minimum β^* is limited by [5]:

- The aperture at the triplet, taking into account that the maximum β function β_{max} at the triplet increases in inverse proportion to β^*, and that the crossing angle θ_C required to maintain a sufficiently large normalized beam-beam separation d_{bb} to minimize the long range beam-beam tune spread ΔQ_{bbLR} is $\theta_C = d_{\text{bb}} \sqrt{\varepsilon_n / \gamma \beta^*}$;

- The maximum β function at the triplet that can be matched to the regular optics of the arcs within the distance available in the matching section between the triplets and the arcs;

- The strengths of the arc sextupoles available to correct the chromaticity generated by the triplets (proportional to β_{max}) and, in general, the nonlinear chromaticities and off-momentum beta beating.

For a round optics (i.e. with equal β^* in the horizontal and vertical planes) in the presence of a crossing angle and at constant normalized long range beam-beam separation d_{bb}, the increase in luminosity saturates for values of $\beta^* < \sigma_z$, as shown in Figure 2-2, because of the corresponding reduction of the luminosity reduction factor R. The effect of the geometric reduction due to the crossing angle can be counteracted by means of crab cavities operated at the LHC main RF frequency [11] as shown in

Figure 1-6. The comparison of the two plots of Figure 2-2 also shows that the effect of crab cavities in enhancing the peak virtual luminosity becomes negligible, for β* greater than 30 to 40 cm.
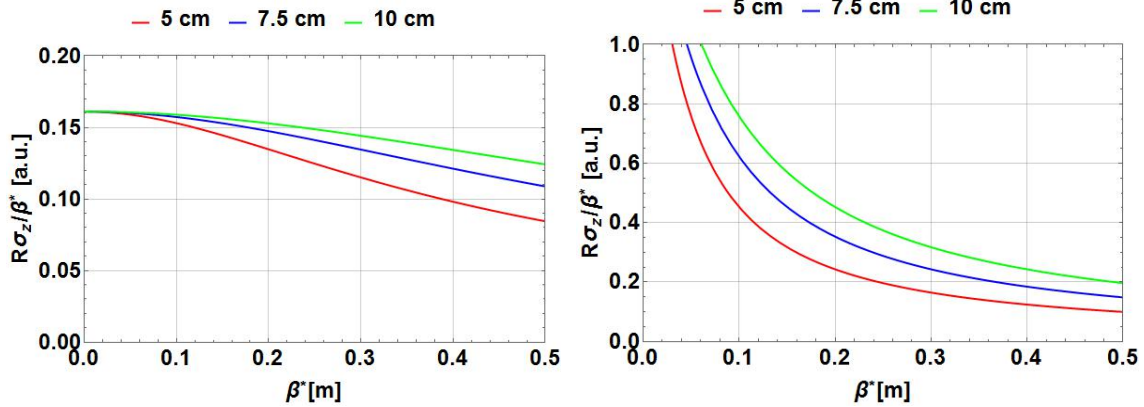
Figure 2-2: Parameter $R\sigma_z/\beta^*$ vs. β* for different bunch lengths for a round optics and constant normalized long range beam-beam separation d_{bb} without crab cavities (left) and with crab cavities (right). The small effect of RF curvature in the crab cavities is not included.

Even after their planned upgrades, the injectors will also constrain the parameters of the beam that can be expected in the LHC in collision. First, there is a maximum current $I_{RF} \approx 2N_{SPS}\,e/T_{bb}$ (where N_{SPS} is the bunch population in the SPS and T_{bb} is the bunch spacing) that can be accelerated per SPS cycle due to RF power limitations in the power amplifiers, power couplers and feeder lines of the main 200 MHz RF system. This maximum current is 2.6 A corresponding to $N_{SPS} = 2.0\times10^{11}$ particles at SPS extraction [12, 13]. The total number of bunches is also limited to 288 due to the thermal load on the power lines. Second, the brightness of the LHC beam in the injectors is expected to be limited by space charge effects at injection in the PSB, PS and SPS. From present experience it is expected that the maximum brightness of the LHC beams after the full injector upgrade will be $B_{SPS} \sim 1.5\times10^{11}$ p/μm [13].

Table 2-1 shows the beam parameters at collision, selected on the basis of the above considerations [3, 14]. The parameters in the table are consistent with the above constraints with the exception of the requested bunch population that can be delivered within the longitudinal acceptance of the LHC at injection. To avoid longitudinal instabilities in the SPS, a controlled longitudinal emittance blow-up needs to be applied for high bunch population, which would lead to longer bunches than acceptable for clean capture in the LHC with the main 400 MHz RF system (even with the maximum 200 MHz RF voltage available in the SPS at extraction). The identification of the elements contributing to the longitudinal impedance in the SPS and the reduction of their impedance might allow for this limit to be increased. In that case, the requirements in terms of bunch population for the HL-LHC could be met.

Table 2-1: HL-LHC nominal parameters for 25 ns operation [14] for two production modes of the LHC beam in the injectors described in [3].

Parameter	Nominal LHC (design report)	HL-LHC (standard)	HL-LHC (BCMS)
Beam energy in collision [TeV]	7	7	7
Particles per bunch, N $[10^{11}]$	1.15	2.2	2.2
Number of bunches per beam	2808	2748	2604
Number of collisions in IP1 and IP5[1]	2808	2736	2592
N_{tot} $[10^{14}]$	3.2	6.0	5.7
Beam current [A]	0.58	1.09	1.03
Crossing angle in IP1 and IP5 [μrad]	285	590	590
Normalized long range beam-beam separation $[\sigma]$	9.4	12.5	12.5
Minimum β^* [m]	0.55	0.15	0.15
ε_n [μm]	3.75	2.50	2.50
ε_L [eVs]	2.50	2.50	2.50
r.m.s. energy spread [0.0001]	1.13	1.13	1.13
r.m.s. bunch length [cm]	7.55	7.55	7.55
IBS horizontal [h]	105	18.5	18.5
IBS longitudinal [h]	63	20.4	20.4
Piwinski parameter	0.65	3.14	3.14
Total loss factor R_0 without crab-cavity	0.836	0.305	0.305
Total loss factor R_1 with crab-cavity	-	0.829	0.829
Beam-beam / IP without crab cavity	0.0031	0.0033	0.0033
Beam-beam / IP with crab cavity	0.0038	0.011	0.011
Peak luminosity without crab-cavity $[10^{34}$ cm^{-2}s$^{-1}]$	1.00	7.18	6.80
Virtual luminosity with crab-cavity $L_{peak}\times R_1/R_0$ $[10^{34}$ cm^{-2}s$^{-1}]$	(1.18)	19.54	18.52
Events/crossing without levelling and without crab-cavity	27	198	198
Levelled luminosity $[10^{34}$ cm^{-2}s$^{-1}]$	-	5.00[2]	5.00[2]
Events/crossing (with levelling and crab-cavities for HL-LHC)[3]	27	138	146
Maximum line density of pile up events during fill [event/mm]	0.21	1.25	1.31
Levelling time [h] (assuming no emittance growth)[3]	-	8.3	7.6
Number of collisions in IP2/IP8	2808	2452/2524[4]	2288/2396[4]
N at LHC injection $[10^{11}]$[5]	1.20	2.30	2.30
Maximum number of bunches per injection	288	288	288
N_{tot} / injection $[10^{13}]$	3.46	6.62	6.62
ε_n at SPS extraction [μm][6]	3.40	2.00	< 2.00[7]

2.2 Proposed Systems Upgrades and Improvements

The high luminosity configuration requires upgrades of numerous systems. In some cases, existing systems would not be able to face the increasingly harsh conditions that the highest luminosity performance will generate. Accelerated wear and radiation damage are serious concerns. Many changes will be necessary just in order to allow the machine to continue to run in a regime of nominal or ultimate

---

[1] Assuming one less batch from the PS for machine protection (pilot injection, TL steering with 12 nominal bunches) and non-colliding bunches for experiments (background studies etc.). Note that due to RF beam loading the abort gap length must not exceed the 3μs design value.

[2] For the design of the HL-LHC systems (collimators, triplet magnets, etc.), a margin of 50% on the stated peak luminosity has been agreed.

luminosity. For certain systems, a replacement could be made with equipment achieving a better performance, rather than with a spare of the same specification. This performance "improvement" goes well beyond the basic consolidation that is already planned for LHC.

For other systems, replacement, although triggered by technical reasons, is the chance to carry out a complete change of layout or performance and maybe considered a real upgrade. The most striking example is the replacement of the Inner Triplet magnets with new ones of different technology based on Nb_3Sn superconductor. This will constitute the backbone of the upgrade. Another case is the replacement of a good part of the present collimation system with an improved design with lower impedance jaws.

In other cases, new equipment not included in the present LHC layout will be installed in order to increase performance, either in terms of peak luminosity or availability. The most important example is the superconducting RF crab cavities, which in the form of compact design required of the HL-LHC comprise a completely new development and a first for a proton collider. A further example is the installation of collimation in the continuous cryostat in the dispersion suppressors.

In this section, we compile a list of the systems that will require an upgrade or at least a serious improvement in performance, to face the ambitious challenge of the High Luminosity LHC.

2.2.1 Insertion region magnets

It is expected that the LHC will reach an integrated luminosity of approximately 300 fb[-1] by 2022, resulting in doses up to 30 MGy to some components in the high luminosity interaction regions. The inner triplet quadrupoles should withstand the radiation resulting from 400 to 700 fb[-1] but some corrector magnets of nested type could fail at around 300 fb[-1]. The most likely failure mode is sudden electric breakdown, entailing serious and long repairs. Replacement of the triplet must be anticipated before radiation damage reaches the level that serious failure is a significant possibility.

The replacement can be coupled with an increase in the quadrupole aperture to allow room for an increase in the luminosity via a lower β^*. However, larger aperture inner triplet (IT) quadrupoles and the increased luminosity, with consequent higher radiation levels, imply the redesign of the whole Interaction Region (IR) zone. This redesign includes larger D1 and D2 dipoles, a new electrical feed-box (DFBX), and much better access to various components for maintenance. In addition, larger aperture magnets in the matching sections will be required, as well as a redesign of the collimation system in the high luminosity insertions.

To maximise the benefit of such a long shutdown, this work must be complemented by a series of improvements and upgrades for other systems, and must be coupled with a major upgrade of the experimental detectors. Both the machine and the detectors must be partially redesigned in order to

---

[3] The total number of events/crossing is calculated with an inelastic cross-section of 85 mb (also for nominal), while 100 mb is still assumed for calculating the proton burn off and the resulting levelling time.

[4] The lower number of collisions in IR2/8 compared to the general purpose detectors is a result of the agreed filling scheme, aiming as much as possible at a democratic sharing of collisions between the experiments.

[5] An intensity loss of 5% distributed along the cycle is assumed from SPS extraction to collisions in the LHC.

[6] A transverse emittance blow-up of 10 to 15% on the average H/V emittance in addition to that expected from intra-beam scattering (IBS) is assumed (to reach the 2.5 μm of emittance in collision for 25 ns operation).

[7] For the BCMS scheme emittances down to 1.4 μm have already been achieved at LHC injection which might be used to mitigate excessive emittance blow-up in the LHC during injection and ramp.

withstand the expected level of integrated luminosity. The upgrade should allow the delivery of 3000 fb^{-1}, i.e. one order of magnitude larger than the nominal LHC design goal.

It is clear that the change of the inner triplets in the high luminosity insertions is the cornerstone of the LHC upgrade. The decision for HL-LHC has been to rely on the success of the advanced Nb$_3$Sn technology that provides access to magnetic fields well beyond 9 T, allowing the maximization of the aperture of the IT quadrupoles. A 15-year-long study led by the DOE in the US under the auspices of the U.S. LARP programme (see chapter 1.3.2), and lately by other EU programmes, has shown the feasibility of Nb$_3$Sn accelerator magnets. For HL-LHC, some 24 IT Nb$_3$Sn quadrupoles are needed: they all feature 150 mm aperture and operating gradient of 140 T/m, which entails more than 12 T peak field on the coils. The Q1 and Q3 quadrupoles each consist of a pair of 4 m long magnets, while Q2a and Q2b each consist of a single unit almost 7 m long (see chapter 3.2). The same Nb$_3$Sn technology will be used to provide collimation in the DS, which will be achieved by replacing a number of selected main dipoles with two shorter 11 T Nb$_3$Sn dipoles (see Chapter 11.3). A collimator will be installed between the shorter dipoles (see e.g. [15] and references therein).

In addition to the IT quadrupoles, there are four new D1/D2 separation/recombination dipole pairs, a number of matching section (MS) quadrupoles, not only in IR1 and 5, but also in IR6, and a smaller number of lattice sextupoles that can be made with well-known Nb-Ti technology (see Table 2-3 and Table 2-4). These magnets will feature larger aperture and will be exposed to higher radiation dose if not properly protected, and thus will be more challenging than the present LHC equivalents (see chapter 3).

The corrector packages in the IT and in the MS regions need to be significantly upgraded to increase aperture and (where needed) strength. Some 70 corrector magnets of various orders (from dipole for orbit correction to dodecapole skew correctors) and typology (from superferric to nested cosθ) have to be installed with the new larger IR magnets.

2.2.2 TAXS/TAXN absorbers

The change of the IT aperture will require replacement of the TAS, the first absorber on either side of the high luminosity interaction points. The TAS protects the downstream magnets from the collision debris. Its aperture roughly scales with the IT aperture. The new absorber, renamed TAXS, will have an aperture of 54 mm (compared with 30 mm in the present TAS), and will have to withstand a flux of particles five times larger than in the present nominal design. In the present LHC, the TAS is probably the most highly activated component of the whole machine. The baseline choice at present is to replace the TAS with the TAXS during LS3 (see chapter 8).

Given the fact that the experimental detectors have reduced the size of the vacuum chamber by nearly 50% (from 55 mm down to about 35 mm) it is clear that all challenges at the machine-detector interface are increased. This includes keeping background in the detectors at acceptable levels.

2.2.3 Crab cavities

Superconducting (SC) RF crab cavities (CC) in HL-LHC are needed in order to compensate for the geometric reduction factor, thus making the very low β* fully useful for luminosity. HL-LHC crab cavities are beyond the state-of-the-art in terms of their unconventional, compact design that cannot be achieved with the well-known geometry of an elliptical cavity. They also demand a very precise control of the phase of the RF (to better than 0.001°) so that the beam rotation given before collision is exactly cancelled on the other side of the interaction point (IP). The crab cavities will also pose new challenges for machine protection. Compact crab cavities will be installed on both sides of IP1 and IP5 without additional magnetic doglegs (as in IP4 for the accelerating cavities). Each cavity is designed to provide a transverse kick voltage of 3.4 MV. There are four crab cavities per beam on each side of the IP. They will be assembled in cryomodules each containing two cavities. All four cavities may be used to rotate

the beam in the crossing plane; alternatively, a single cryomodule (two cavities) can be used for this task, with the cavities in the second cryomodule providing a deflection in the orthogonal plane, enabling the so-called crab kissing scheme for reducing the pile-up density [16]. At present, the baseline is to use all crab cavities for geometric compensation, i.e. rotation in the crossing plane.

The first generation, proof-of-principle, compact crab cavities have recently been tested successfully (see chapter 4). However, a second generation with machine-oriented characteristics are now under construction by LARP, CERN and UK Institutions (Lancaster University, STFC, and the Cockcroft Institute). A full cryomodule will be tested in the SPS before LS2, to investigate experimentally the effect on a proton beam and to gain the necessary experience in view of LHC operation.

2.2.4 Collimation

The collimation system has been designed for the first phase of LHC operation. Today it is operating according to design. However, the impedance of the collimation system may need to be reduced if beam instabilities are triggered at intensity close to, or just above, nominal. Hints of this behaviour have been already seen during Run 1: only operation near nominal conditions can dismiss or validate this hypothesis.

Safe handling of a beam of 1 A or more, with beta functions at collision beyond the design value will constitute new territory. The triplet must remain protected during the large change of the collision beam parameters (β^* transition from 6 m to 10-15 cm). This will be one of the most critical phases of HL-LHC operation: just the beam halo itself could be beyond the damage limit. An upgrade of the collimation system is thus required. The main additional needs associated with the upgrade are a better precision in alignment; and materials capable of withstanding higher power.

A second area that will require special attention in connection with the collimation system is the Dispersion Suppressor (DS), where leakage of off-momentum particles into the first and second main superconducting dipoles has already been identified as a possible LHC performance limitation. The most promising concept is to substitute an LHC main dipole with a dipole of equal bending strength (120 T·m) obtained by a higher field (11 T) and shorter magnetic length (11 m) than those of the LHC dipoles (8.3 T and 14.2 m). The space gained is sufficient for the installation of special collimators. This system is already needed for Run 3 ion operation in the DS region around IP2 following the upgrade of ALICE in LS2. It might also be needed in the DS around IP7 for HL-LHC operation. The requirements in other insertion regions have yet to be assessed.

2.2.5 New cold powering

While a considerable effort is under way to study how to replace the radiation-sensitive electronic boards with radiation-hard cards, another solution is also being pursued for special zones: removal of the power converters and DFBs (electrical feed-boxes, delicate equipment associated with the continuous cryostat) out of the tunnel. Besides improving LHC availability (fewer interruptions, faster interventions without the need for tunnel access), radiation dose to personnel would be reduced as well.

Removal of power converters and DFBs to locations far from the beam line, and possibly to the surface, is only possible through the use of a novel technology: superconducting links (SCLs) made out of high-temperature superconductor (YBCO or Bi-2223) or MgB_2 superconductors. Regions where this radical solution will be needed because of the high radiation load on electronics, and/or where the "as low as reasonably achievable" principle (ALARA) have been identified:

- The long straight section of IP7 where a 500 m cable rated at 20 kA is needed;

- The high luminosity Insertion Regions IR1 and IR5, where much higher current cables (150 and 164 kA) are needed for the IT magnets and the magnets in the MS region (i.e. from D2 to Q6). In

this latter case, the superconducting cable will link the magnets with power converters on the surface, with significant challenges to cryogenics and system integration resulting from the 100 m or so difference in altitude.

2.2.6 Enhanced machine protection and remote handling

Various systems will become a bottleneck with aging of the machine and higher performance beyond the 40 to 60 fb^{-1} per year envisaged in the original LHC design. One such system is the Quench Protection System (QPS) of the superconducting magnets. The QPS should: (i) become fully redundant in case of power loss; (ii) allow low energy discharge on quench heaters and easy adaption of the detection thresholds; (iii) provide an interlock for the quench heater discharge based on a sensor for quench heater integrity. In general, the QPS will need a complete revamping after 2020.

Machine protection will have to be improved not just because of the higher beam energy and energy density: it will have to cope with very fast events generated for example by crab cavities and by possible increase of the events generated by falling particles (UFOs).

LHC has not been designed specifically for remote handling. However the level of activation from 2020, and even earlier, requires a careful study and development of special equipment to allow replacing collimators, magnets, vacuum components etc. according to the ALARA principle. While full robotics is difficult to implement given the conditions, remote manipulation, enhanced reality and supervision are the key to minimize the radiation dose to personnel.

2.2.7 New cryogenics plants and distribution

To increase the flexibility for intervention and rapid restoration of availability (i.e. to minimise loss of integrated luminosity) it will be useful to install a new cryogenics plant in P4 for a full separation between Superconducting RF and magnet cooling. This should be done during LS2, to avoid a possible weak zone for Run 3. The new plant should also be able to provide cooling to new cryogenic equipment under consideration for IP4 i.e. a new SCRF harmonic system and the hollow e-lens for halo control, which requires a superconducting solenoid. For the time being, these two systems are not in the baseline; however, they constitute interesting options under study.

A further consolidation that is deemed necessary in the long term is the separation between the cooling of the inner triplets and the few stand-alone superconducting magnets in the MS from the magnets of the arc. The present coupling of IR and arc magnets means that an intervention in the triplet region requires warm up of the entire sector (an operation of 3 months, not without risk).

New power plants will be needed to cope with higher heat deposition from the high luminosity points. In particular, given the luminosity driven heat load in the cold magnets, and the cooling of superconducting crab cavities at 1.9 K, the power (at 4.2 K) of the new cryo-plant in IP1 and IP5 will have to be in the 15-18 kW range. The cooling scheme includes separation, with possible interconnection, between arc and IR cryogenics to gain in flexibility.

2.2.8 Enhanced beam instrumentation

Improving beam instrumentation is a continuous task during routine operation of an accelerator. HL-LHC will require improved or new equipment to monitor and act on proton beams with more challenging parameters than in LHC. A short illustrative list includes:

- New beam loss monitors for the IT quadrupoles.

- A radiation tolerant ASIC for the beam loss monitoring system;

- A new beam position monitoring system, including a high resolution orbit measurement system, and high-directivity strip-line pick-ups for the Insertion Regions;

- Emittance measurement: while improving the present system, a new concept based Beam Gas Vertex Emittance Monitor is envisaged for the HL-LHC;

- Halo diagnostics to control the halo in order to minimize losses (and especially loss peaks) in the presence of a beam with a stored energy close to 0.7 GJ. Synchrotron radiation imaging and possibly wire scanners, appear to be the only candidates for halo monitoring in the HL-LHC;

- Diagnostics for crab cavities: electromagnetic pick-ups and streak cameras are being studied for beam shape monitoring;

- Luminosity measurements with new radiation-hard devices (located in the new TAXN) capable of withstanding the ten times higher radiation level.

2.2.9 Beam transfer and kickers

The higher beam current significantly increases the beam-induced power deposited in many elements, including the injection kicker magnets in the LHC ring. New designs for several components in the dump system devices will probably be needed because of the increased energy deposition in the case of direct impact, and because of increased radiation background, which could affect the reliability of this key machine protection system.

A non-exhaustive list of the elements that could need an improvement or a more radical upgrade (based on the experience from Run 2) is listed below.

- Injector Kicker Magnets (better cooling of the magnets to cope with beam induced heating, different type of ferrites with higher critical temperature, coating of ceramic tubes to reduce SEY to suppress e-cloud effects).

- Beam dump block TDE with its N_2 overpressure system and window VDWB: if these are not compatible with HL-LHC intensities, extension of the dilution pattern may be the only practical and safe solution, implying the installation of additional dilution kicker systems MKB (up to 50%).

- Injection absorber, auxiliary protection collimators, protection masks.

- Beam dump absorber system.

2.3 Baseline Optics and Layout

2.3.1 Basic optics and layout choices for the High Luminosity insertions

The current baseline optics design (HLLHCV1.1) has evolved from the previous LHC Upgrade Phase I project [17-19]. A realistic, cost efficient and robust (achromatic) implementation of low β* collision optics requires the deployment of the Achromatic Telescopic Squeeze (ATS) scheme, together with the installation of insertion magnets of larger aperture [20-24]. Successful validation tests of the ATS with beam were achieved in 2011-2012 [25-29] in very specific conditions (low intensity, no crossing angle to save aperture, etc.). The corresponding number, type and specifications of the new magnets to reach low β* [20, 21] were then endorsed by the project (see, for example, [30] and references therein).

The historical development of the optics design is summarised in [31]; here, only the last three parts of this long chain are mentioned, namely the so-called SLHCV3.1b [32], HLLHCV1.0 [33], and HLLHCV1.1 (current baseline) optics. SLHCV3.1b uses ATS optics based on 150 T/m Nb_3Sn triplets and displacement of D2 for crab cavity integration [32]. HLLHCV1.0 is similar to SLHCV3.1b, but with a new triplet layout based on 140 T/m Nb3Sn triplets [33]. HLLHCV1.1, the new baseline, is based on HLLHCV1.0, but with some modifications to take into account the results of design studies for D2, energy deposition studies for the passive protection of the superconducting elements, hardware integration studies and updated naming conventions [34, 35]ponding optical configurations.

Table 2-2 presents an overview of the main features of the three layouts and of the corresponding optical configurations.

Table 2-2: Main HL-LHC optics variants currently under study. The baseline collision optics corresponds to $\beta^* = 15$ cm in both transverse planes (round optics) with a full crossing angle of 590 μrad. Other collision optics are available, round or flat, for dedicated studies.

	SLHC V3.1b	HLLHCV1.0	HLLHCV1.1 (Baseline)
Collision β* IP1,5	Round: 15cm, (10 cm, 33 cm, 40 cm). Flat: 30/7.5cm, (20/5 cm) with HV, VH crossing.	Round: 15cm, (10 cm). Flat: 30/7.5cm, (20/5 cm) with HV, VH crossing. Complete squeeze.	
Pre-squeeze β* IP1,5	40 cm, (2 m)	44 cm, (3 m) transition strengths.	44 cm
Injection β* IP1,5	5.5 m, (11 m)	6 m, (11 m, 18 m)	6 m (15 m)
Triplet gradient	150 T/m	140 T/m	140 T/m
Triplet magnetic length	Q1-Q3: 7.685 m Q2: 6.577 m	Q1-Q3: 4.002 m ×2 Q2: 6.792 m	Q1-Q3: 4.00 m ×2 Q2: 6.8 m
Triplet corrector package	Nested triplet nonlinear corrector package with new a_5, b_5, a_6 corrector coils	Super ferric, non-nested, nonlinear corrector package.	
Insertion region dipoles	D2 moved towards the IP by 15 m. For version HLLHCV1.1 the magnetic length of D1 [35] and D2 has been shortened.		
Insertion region quadrupoles	MQYY type for Q4 in IR1,5. Q5 moved towards arc by 11m. MQYL type for Q5 in IR1,5,6. Additional MS in Q10 of IR1 and IR5.	MQYY type for Q4 in IR1,5. Q5 moved towards the arc by 11m. MQYL type for Q5 in IR1,5,6. Additional MS in Q10 of IR1 and IR5.	Q4 moved towards arc by 8m. MQYY type for Q4 in IR1,5. Q5 moved towards arc by 11m. MQY at 1.9 K type for Q5 in IR1,5. Double MQY for Q5 in IR6. Additional MS in Q10 of IR1,5.
Crab cavities	3		4

The current baseline layout incorporates various optimisations, and in particular has been made compatible with the latest hardware parameters and constraints. The magnetic elements in the region between the IP and Q4 (Figure 2-3) have been positioned to optimise the strength requirements for the magnets and for ancillary equipment. For instance, moving the Q4 quadrupole changes the value of the beta functions at the location of the crab cavities, thus improving their efficiency.

In the triplet region (Figure 2-3, which is in the range of approximately 20 m to 80 m) the Q1 and Q3 magnets are split into two and the dipole corrector magnets (used to create the crossing and separation schemes) are implemented in a nested configuration for both planes. The corrector package close to Q3 consists of super ferric magnets. The specifications and performance of the non-linear correctors (used to compensate the field quality effects of the triplets and D1 separation dipoles on both sides of the IP) are reported in [36, 37]. Detailed numerical simulations indicate that additional corrector types are needed to cope with the pushed performance of HL-LHC, so the layout of the correctors will not be a simple carbon copy of the existing layout. Inclusion of the field quality of the D2 separation dipole has been considered, but is not trivial, due to the two-in-one structure of the D2.
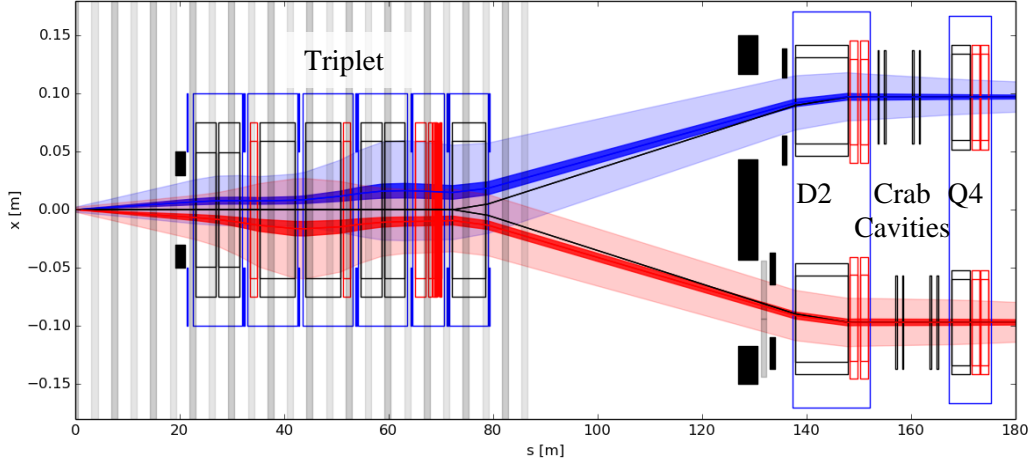
Figure 2-3: Overall layout of the insertion region between the IP and Q4. The dark blue and red areas represent the 2σ beam envelope. The light regions correspond to a 12σ value of the beam envelope for an emittance of 3.5 μm with a tolerance of 20% for beta-beating and 2 mm of closed orbit distortion. The shaded grey areas in the triplet region represent the locations of the parasitic beam-beam encounters.

The block of two separation dipoles has been changed with respect to the nominal LHC layout, decreasing their separation. The D2 area is particularly delicate for several reasons. First, there are space constraints because of the need for protection devices such as the absorber of neutral debris from the collisions. Second, the transverse separation is not yet optimal, leading to a reduction in the amount of iron between the two apertures of the D2, as well as to reduced beam and mechanical apertures because of the large values of the beta functions at this point. Downstream of D2, the situation is not much easier, as the crab cavities impose tight constraints on the space between D2 and Q4, as well as on the values of the beta functions.

Detailed work has been performed to specify the strengths of dipole orbit correctors in the triplets and the D2 and Q4 magnets [38, 39]. Initially, the required strength needed too long correctors, mainly because of the need to close the bumps at the D2 dipole in order to avoid a non-zero closed orbit at the location of the crab cavities. Detailed analysis of the RF aspects allowed the tight constraints to be relaxed (0.5 mm of closed orbit distortion can be tolerated at the crab cavities when operating and 2-3 mm when cavities are made transparent to the beam). The design now includes a correction scheme with magnets that are 1.5 to 2.5 m long. This makes it possible to close the orbit bumps further downstream from the D2 separation dipoles, thus reducing their overall strength. In the current layout, Q4 is a new magnet with larger aperture called MQYY, while Q5 is a MQY-type (the Q4 of the present LHC) operating at 1.9 K to provide the required gradient.

The implementation of the ATS scheme in the HLLHCV1.0 requires hardware changes in other parts of the LHC ring. In particular, an additional lattice sextupole (MS) magnet should be installed in Q10 in IR1 and 5. Moreover, Q5 in IR6 should be upgraded. The current baseline layout envisages the installation of a second MQY-type quadrupole close to each existing Q5.

Table 2-3 lists the key parameters of the quadrupoles (new or refurbished) to be installed in IR1 and 5, while Table 2-4 gives the corresponding parameters for the separation dipoles and orbit correctors. Table 2-5 gives the parameters for the multipolar correctors.

As already mentioned, protection devices are required for the new layout of the IR1 and IR5 regions. The current LHC layout has only a TAS in front of Q1, to protect this magnet from the collision debris, and a TAN to protect the D2 from the neutrals produced at the IP. For HL-LHC, these two

devices will have to be upgraded to withstand much larger luminosities. Furthermore, additional masks are envisaged to protect other magnets in the matching section. A summary of the characteristics of these devices can be found in Table 2-6

Table 2-3: New or refurbished quadrupoles for HL-LHC, all operating at 1.9 K. The orientation of the Rectellipse aperture ("R") [40] can be changed to optimise the mechanical aperture.

	Inner triplet (single aperture)			Matching section (2-in-1)		
Magnet	Q1	Q2	Q3	Q4	Q5	Q6
Number	2	2	2	1	1	1
Type	MQXFA	MQXFB	MQXFA	MQYY	MQY	MQML
Magnetic length [m]	4.0	6.8	4.0	3.8	3.4	4.8
Gradient [T/m]	140			115	200	200
Coil aperture [mm]	150			90	70	56
Aperture separation [mm]	n/a			194	194	194
Beam screen (BS) shape	Octagon			Rectellipse		
BS aperture (H/V) [mm]	98/98	118/118		64/74	44/57.8	35.3/45.1
Mech. tol. (R/H/V) [mm] [41]	0.6/1/1	0.6/1/1		0.84/1.26/0.6	0.84/1.26/0.6	as built

Table 2-4: New dipole magnets for HL-LHC, all operating at 1.9 K. The orientation of the Rectellipse ("R") aperture can be changed to optimise the mechanical aperture. The orbit correctors can be nested or consecutive as indicated.

	Separation/recombination dipoles		Orbit correctors			
Magnet	D1	D2	Q1/Q3	Q2	D2	Q4
Number per side per insertion	1	1	2 [HV nest]	1 [HV nest]	2 [HV consec.]	2 [HV consec.]
Type	MBXF	MBRD	MCBXFA	MCBXFB	MCBRD	MCBYY
Magnetic length [m]	6.27	7.78	1.2	2.2	1.5	1.5
Integrated field [Tm]	35	35	2.5	4.5	4.5	4.5
Coil aperture [mm]	150	105	150	150	100	100
Aperture separation [mm]	n/a	188	n/a		194	194
BS shape	Octagon					Rectellipse
BS aperture (H/V) [mm]	118/118	84/84	118/118		79/79	64/74
Mech. tol. (R/H/V) [mm]	0.6/1/1	0.84/1.36/1	0.6/1/1		0.84/1.36/1	0.84/1.26/0.6

Table 2-5: New multipolar superferric correctors for HL-LHC, all operating at 1.9 K.

Number	1	1	1	1	1	1	1	1	1
# poles	4	12	12	10	10	8	8	6	6
Normal/Skew	skew	normal	skew	normal	skew	normal	skew	normal	skew
Type	MQSXF	MCTXF	MCTSXF	MCDXF	MCDSXF	MCOXF	MCOSXF	MCSXF	MCSSXF
Mag. length [m]	0.807	0.43	0.089	0.095	0.095	0.087	0.087	0.111	0.111
Integrated field [mT·m] @50 mm	1000	86	17	25	25	46	46	63	63
Coil ap. [mm]	150								
BS shape	Octagon								
BS ap. (H/V) [mm]	118/118								
Mech. tolerances (R/H/V) [mm]	0.6/1/1								

Table 2-6: New absorbers for HL-LHC, all operating at 1.9 K. The orientation of the Rectellipse aperture can be changed to optimise the mechanical aperture.

	Inner triplet (single aperture)	Matching section (2-in-1)			
Absorber	TAS	TAN	Mask D2	Mask Q5	Mask Q6
Aperture	1	2	2	2	2
Type	TAXS	TAXN	TCLMA	TCLMB	TCLMC
L [m]	1.8	3.5	0.5	1.0	1.0
Aperture separation [mm]	n/a	149-159	188	194	194
Aperture (H/V) [mm]	54/54	80/80	84/84	44/57.8	35.3/45.1
Mech. tolerances (R/H/V) [mm]	2/0.5/0.5	0.6/1/1	0.6/1/1	0.6/1/1	0.6/1/1

Figure 2-4 shows example optics configurations for injection and collision. Several configurations can be provided apart from the nominal (i.e. round) optics.

Table 2-7 gives the main sets of β^* values (including the optical parameters corresponding to the ion runs). Since IR2 and IR8 are running with increased strength of the triplets at injection, a so-called pre-squeeze has to be applied at top energy to reduce the strength of the triplets at constant value of beta function at the IP.

The transition between the various optical configurations has been studied in detail [42, 43]. The sequence of gradients during the squeeze is available, and will be used to perform first estimates of the hysteresis effects. Moreover, it will be possible to evaluate the time required to accomplish the squeeze, which is essential information to determine specifications for the required power converters. Work is in progress to address these two points; results are expected in the coming months.

Finally, it is worth mentioning additional studies that have looked at alternative layouts. Options have been studied based on triplets using 120 T/m and 170 T/m gradients [44, 45], and an additional Q7 for crab cavity kick enhancements [46] without upgrading the matching section layout [47]. The latest results can be found in [48].

There are numerous constraints on the layout of components, arising from various considerations. The constraints and the associated issues are described in Chapter 15.
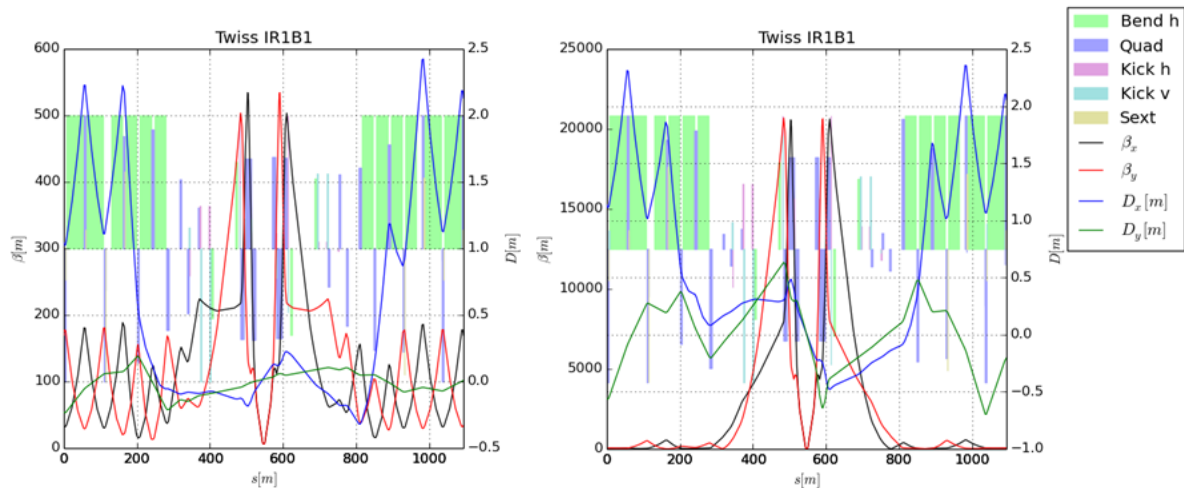
Figure 2-4: Optical functions at injection (left) and collision (right). Note the different vertical scales: at collision, the beta functions in the triplets are large, to provide the low β^* at the IP.

Table 2-7: Available optical configurations for the baseline layout. IR3 and IR7 are not reported here as they have static optics from injection to collision and do not take part in the ATS scheme. Some alternative configurations (other than the nominal) are also shown.

Optics	IR1	IR5	IR2	IR8	IR4	IR6
Injection	β^*=6 m, inj.	β^*=6 m, inj.	β^*=10 m, inj.	β^*=10 m, inj.	inj.	inj.
End of Ramp	β^*=6 m	β^*=6 m	β^*=10 m	β^*=10 m	inj.	inj.
Pre-squeeze	β^*=44 cm	β^*=44 cm	β^*=10 m	β^*=3 m	inj.	inj.
Collision Round	β^*_{ATS}=15 cm	β^*_{ATS}=15 cm	β^*=10 m, ATS (3×, 3×)	β^*=3 m, ATS (3×, 3×)	ATS (3×, 3×)	ATS (3×, 3×)
Collision Ions	β^*=44 cm	β^*=44 cm	β^*=50 cm	β^*=50 cm	inj.	inj.
Collision VDM	β^*=30 m	β^*=30 m	in preparation	in preparation	inj.	inj.
			Alternative configurations			
Collision Flat	β^*_{ATS}= 7.5/30 cm	β^*_{ATS}= 30/7.5 cm	β^*=10 m, ATS (1.5×, 6×)	β^*=3 m, ATS (1.5×, 6×)	ATS (1.5×, 6×)	ATS (1.5×, 6×)
Collision FlatHV	β^*_{ATS}= 30/7.5 cm	β^*_{ATS}= 7.5/30 cm	β^*=10 m, ATS (1.5×, 6×)	β^*=3 m, ATS (1.5×, 6×)	ATS (1.5×, 6×)	ATS (1.5×, 6×)
Collision sRound	β^*_{ATS}=10 cm	β^*_{ATS}=10 cm	β^*=10 m, ATS (4.5×, 4.5×)	β^*=3m, ATS (4.5×, 4.5×)	ATS (4.5×, 4.5×)	ATS (4.5×, 4.5×)
Collision sFlat	β^*_{ATS}= 5/20 cm	β^*_{ATS}= 20/5 cm	β^*=10 m, ATS (9×, 4.5×)	β^*=3 m, ATS (4.5×, 9×)	ATS (9×, 4.5×)	ATS (9×, 4.5×)
Collision sFlatHV	β^*_{ATS}= 20/5 cm	β^*_{ATS}= 5/20 cm	β^*=10 m, ATS (4.5×, 9×)	β^*=3 m, ATS (9×, 4.5×)	ATS (4.5×, 9×)	ATS (4.5×,9×)

2.3.2 Target field quality and dynamic aperture

The dynamic aperture (DA) has been used since the initial steps of the design of the LHC [40] to determine the required field quality of the various magnet classes. For computation of the DA in HL-LHC, particles are tracked over 10^6 or 10^5 turns, depending on whether beam-beam effects are included or neglected, respectively. The initial momentum co-ordinate is set to 2/3 of the bucket height (2.7×10^{-4} and 7.5×10^{-4} for collision and injection energy, respectively). Sixty implementations of the random components in the magnets, corresponding to sixty realisations of the LHC lattice, are considered in the numerical simulations. Eleven phase space angles have routinely been used (although for special studies up to 59 values have been probed), while thirty particle-pairs per 2σ amplitude step have been used. All these parameters have been specified during the design stage of the LHC. Since then, the amount of available computing power has increased, thanks to the increased CPU power of the CERN batch system and because of the use of volunteer-based computing resources [49]: this enabled the increase of the number of directions considered in the studies, making the DA estimate more accurate. Note that the number of turns and random seeds affects the accuracy of the DA calculation which is at least 0.1σ in this case.

For reference, the multipole expansion used to describe the magnetic field is given as [40]:

$$B_y + iB_x = B_{ref} \sum_{n=1}^{\infty} (b_n + ia_n) \left(\frac{x+iy}{r_0}\right)^{n-1} \tag{2-5}$$

where B_x, B_y and B_{ref} are the transverse magnetic field components and the reference field, respectively. The coefficients a_n, b_n are the skew and normal field components, and r_0 is a reference radius. In the framework of the LHC studies the magnetic errors are split into three components, namely mean (S), uncertainty (U), and random (R), such that a given multipole is obtained by:

$$b_n = b_{n_S} + \frac{\xi_U}{1.5} b_{n_U} + \xi_R b_{n_R} \tag{2-6}$$

where ξ_U, ξ_R are Gaussian-distributed random variables cut at 1.5σ and 3σ, respectively. The ξ_U variable is the same for all magnets of a given class, but changes from seed to seed and for the different multipoles. On the other hand, ξ_R changes also from magnet to magnet.

The target value of the DA differs between injection and collision energies. At injection, where the beam-beam effects can be safely neglected, the focus is on the impact of magnetic field quality. For the LHC design [40], a target value of 12σ (for a normalised emittance of 3.75 μm) was assumed. The best model of the LHC, including the measured field quality of the magnets and the sorting of magnets, provides a DA slightly lower than 11σ [50]. No signs of issues due to DA limitations have been observed during operation or dedicated studies in Run 1 although operation at high intensity has been conducted with beams with emittance smaller than nominal (2-2.5 μm rather than 3.75 μm).

At top energy, beam-beam effects cannot be neglected and the DA has to be evaluated including both magnetic field imperfections and head-on and long-range beam-beam phenomena (see 2.4.2). Hence, the approach taken consists of probing the impact on DA of the field quality of the new magnets, asking that all the new magnets have an impact on the DA that is in the shadow of the triplet quadrupoles. Eventually, the beam-beam effects are also included, providing the final DA value.

Studies for the field quality of the new magnets started from the top energy configuration and with an earlier version of the layout, namely the so-called SLHCV3.1b [32]. This allowed first estimates of the required field quality to be derived, which were then improved by including considerations for the injection energy, where the beam size reaches its maximum and the field quality is worse, due to the persistent current effect. The newer layout HLLHCV1.0 [33] has been used following its release.

In the numerical simulations the machine as-built is considered, i.e. the best knowledge of the measured magnetic errors is assigned to the magnets as-installed, while, for the magnets that will be replaced according to the upgrade plans, the expected error table, with statistical assignment of errors, is used. This is the baseline configuration of the LHC ring to which magnetic field errors of other classes of magnets can be selectively added.

In these studies the acceptable minimum DA was set to about 10.5σ at top energy, based on experience from the LHC. The DA calculation was performed using long-term tracking in SixTrack [51, 52], neglecting beam-beam effects. Determination of the required field quality based on DA computations is intrinsically a non-linear problem. The field quality obtained from electromagnetic simulations is used as an initial guess. Then, optimisation of the field quality essentially involves determining the Jacobian of the DA as a function of the multipoles around the initial value of field quality. For this reason, it is of paramount importance to have a reliable estimate of the expected field quality from detailed electromagnetic simulations and measurements (see chapter 3). The resulting error tables can be found in the official optics repositories [53, 54] and are also collected in Ref. [55].

The previous IT specifications at 7 TeV [56] were updated to take into account the additional IT correctors for a_5, b_5, a_6 errors. It is worth mentioning that in all the studies reported in this document, the IT correctors have been considered as ideal devices, i.e. exactly correcting the field quality of the IT and D1 magnets, without any error due to uncertainty in the transfer function of the correctors. These specifications will be referred to as IT_errortable_v66. Estimate of the D1 field quality is based on

magnet design and referred to as D1_errortable_v1 [57]. Due to the evolution of the D2 dipole design, three versions of the D2 field quality were used in the study: these are referred to as D2_errortable_v3, _v4 [58], and _v5 [59]. The D2 low order terms at 7 TeV are shown in Table 2-8. Estimates for the Q4 and Q5 magnets are based on a scaling of the measured field of the existing MQY quadrupole and referred to as Q4_errortable_v1 and Q5_errortable_v0, respectively.

Table 2-8: Evolution of low order terms of the estimated D2 field quality at 7 TeV (r_0 = 35 mm).

n	a_{nS}	a_{nU}	a_{nR}	b_{nS}	b_{nU}	b_{nR}
			D2_errortable_v3			
2	0.0	0.679	0.679	65.0	3.000	3.000
3	0.0	0.282	0.282	-30.0	5.000	5.000
4	0.0	0.444	0.444	25.0	1.000	1.000
5	0.0	0.152	0.152	-4.0	1.000	1.000
6	0.0	0.176	0.176	0.0	0.060	0.060
			D2_errortable_v4			
2	0.0	0.679	0.679	25.0	2.500	2.500
3	0.0	0.282	0.282	3.0	1.500	1.500
4	0.0	0.444	0.444	2.0	0.200	0.200
5	0.0	0.152	0.152	-1.0	0.500	0.500
6	0.0	0.176	0.176	0.0	0.060	0.060
			D2_errortable_v5			
2	0.0	0.679	0.679	1.0	1.000	1.000
3	0.0	0.282	0.282	1.0	1.667	1.667
4	0.0	0.444	0.444	-3.0	0.600	0.600
5	0.0	0.152	0.152	-1.0	0.500	0.500
6	0.0	0.176	0.176	2.0	0.060	0.060

The SLHCV3.1b collision optics features $\beta^* = 15$ cm. The desired minimum DA (among all seeds and phase angles) at collision energy is about 10σ. Tracking simulations performed with the error table IT_errortable_v66 and without the D1, D2, Q4, Q5 magnetic errors give $DA_{min} = 10.4\sigma$, which is acceptable. Note that DA_{min} stands for the minimum DA over all seeds and angles, while DA_{ave} represents the minimum over all angles of the DA averaged over the seeds.

As a next step, the impact on DA of the field quality in the D1, D2, Q4, Q5 magnets was verified. The Q4 and Q5 estimated magnetic errors produced negligible effect on the DA, hence their field quality is acceptable. Impact of the D1 estimated errors is mostly due to the relatively large allowed multipoles b_{nS}. It is found that the largest DA reduction is caused by b_{7S} and b_{9S}. The low order D1 errors have negligible effect since they are compensated by the included IT correctors of order n between 3 and 6. To reduce the impact of b_{7S} and b_{9S} while keeping them realistic, it is proposed to reduce them by a factor of 2 (to 0.2 and -0.295, respectively) relative to D1_errortable_v1.

Two versions of the estimated D2 field quality were used for the SLHCV3.1b tracking: D2_errortable_v3 and D2_errortable_v4. These tables were produced during successive iterations for the field quality optimization. The b_2 to b_4 terms are rather large due to field saturation. These terms showed a strong impact on the DA. The b_2 affected the linear optics by increasing β^*, thus resulting in a too optimistic DA value. To avoid this effect, the b_2 was set to zero for subsequent tracking campaigns, on the assumption that it can be reduced by appropriate design and that β^* will be corrected after measurements. It is found that the D2 b_3 and b_4 have a strong effect on the DA. Effects of feed-down due to the orbit in the straight D1 and D2 magnets were found very small. To maintain the DA_{min} close to 10σ, b_3 and b_4 must be reduced by an order of magnitude relative to D2_errortable_v3. These terms had been, indeed, much improved in the updated error table, D2_errortable_v4 (see Table 2-8). Following the tracking results, the proposed further adjustment for D2_errortable_v4 is

to reduce b_2 to about 1 unit and b_{3S} from 3.0 to 1.5. The resulting DA_{min} and DA_{ave} at 7 TeV, with all new magnet errors and adjustments, are 9.90σ and 11.64σ, respectively, which is still acceptable.

The β^* for SLHCV3.1b lattice at 450 GeV is 5.5 m, with peak beta functions in the IR magnets lower by a factor of 35 than those in the collision optics. Beam sizes in these magnets are also reduced even though the emittance is larger by a factor of 16. Therefore, the impact of field errors of the new magnets will be much smaller, and the use of the IT correctors is *a priori* not needed: these results are confirmed by tracking studies. Hence, their field quality at injection based on the present estimates is acceptable. The resulting DA_{min} and DA_{ave} with all errors are 10.16σ and 10.5σ, respectively, and are also acceptable. Another option of the injection optics, with β^* of 11 m, was verified and showed very similar DA.

The injection DA, however, is about 1σ smaller than the DA of the nominal LHC. Since it is not limited by the IR magnets, other improvements (e.g. in the arcs) may need to be considered. Possible options include a larger integer tune split and adjustment of the working point. Tune scans indicate an effect of the 7th order horizontal resonance close to the current tune (62.28, 60.31). Reducing the horizontal and vertical tunes by about 0.01 would increase the DA by about 0.5σ.

HLLHCV1.0 is the latest version of the HL-LHC lattice that has been considered in numerical simulations so far. Some of the differences relative to the SLHCV3.1b include: a longer IT with a lower gradient of 140 T/m and higher peak beta function (7%) at collision, adjusted orientation of magnets in the cryostat, new IT corrector positions, and different phase advance between IP1 and IP5. Using the previously optimized field quality of the new magnets, the collision DA of the HLLHCV1.0 lattice is reduced by about 1σ relative to the SLHCV3.1b, i.e. with DA_{min} and DA_{ave} of 8.8σ and 10.4σ, respectively. A stronger impact of the D2 b_3 and b_4 terms of the previously adjusted `D2_errortable_v4` was noticed. Since b_{3S} had been already reduced in this table, the next step was to reduce b_{4S} by half. This improved the DA to $DA_{min} = 9.1\sigma$ and $DA_{ave} = 11.1\sigma$. Further improvement was achieved when using the most recent D2 field estimate `D2_errortable_v5` [59] (see Table 2-8), where the b_2 and b_3 terms are reduced at the expense of somewhat larger higher-order terms. In this case, $DA_{min} = 9.8\sigma$ and $DA_{ave} = 12.5\sigma$, as shown in Figure 2-5 (left), which is acceptable and rather comparable to the DA of the SLHCV3.1b. The reasons for such noticeable improvement will need to be further analysed.
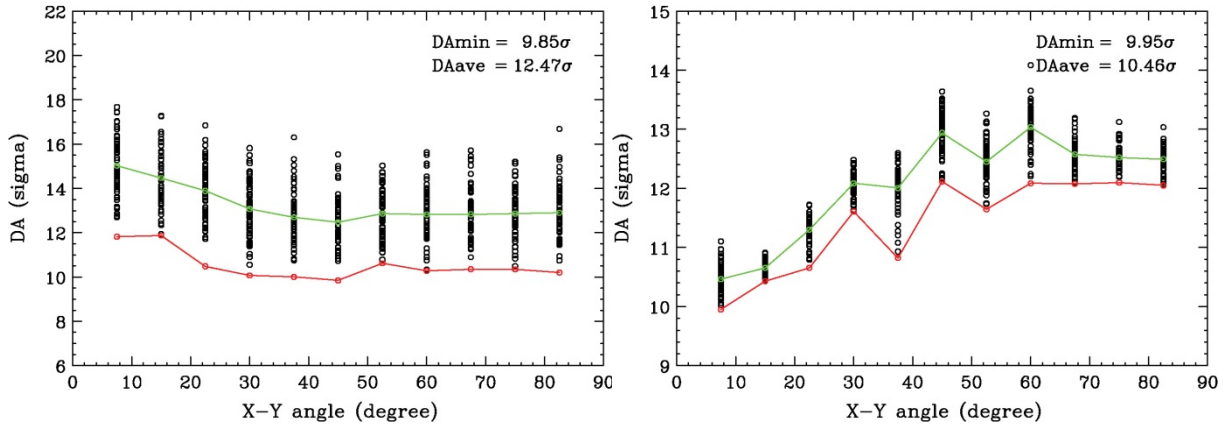
Figure 2-5: DA of HLHCV1.0. Left: DA at 7 TeV with adjusted estimated field quality of new magnets. Right: DA at 450 GeV with estimated field quality of new magnets. The r.m.s. beam size is that corresponding to a normalized emittance of 3.75 μm.

The β^* at injection for HLLHCV1.0 is 6.0 m, comparable to SLHCV3.1b. The impact of the field errors in the new magnets on the DA was verified and found insignificant (similar to SLHCV3.1b). The resulting DA with all errors ($DA_{min} = 9.9\sigma$ and $DA_{ave} = 10.5\sigma$) is acceptable, see Figure 2-5 (right).

Field quality and dynamic aperture studies will be pursued in the future along several lines, including:

- Dedicated studies to assess the impact of field quality of IT, D1, D2, Q4, Q5 on linear optics, knowing that the distortion of the optical parameters can stem from both the b_2 component and the feed-down from b_3 and a_3 via the crossing scheme bumps.

- Dedicated studies (on-going) to assess the maximum tolerable ripple in the power converters of the IT quadrupoles and magnets in the matching section [60].

- Specification of crab cavity field quality: preliminary results [61-64] seem to indicate that the estimated field quality should be good enough to prevent any impact on the DA.

- Assessment of the impact of fringe fields for the large aperture magnets, including the new IT quadrupoles and the separation dipoles.

Regarding fringe fields, the quadrupolar component has already been considered and found non-problematic in [65]. Preliminary analytical results [66] indicate that, albeit small, the detuning with amplitude induced by the fringe fields is not completely negligible, thus calling for a second level of study. This should include long term numerical simulations to study the non-linear effects generated. This opens the wide field of symplectic integration as in the presence of 3D magnetic fields the standard approach based on multipoles cannot be applied. Work is underway to study the best integration schemes and their implementation [67, 68], before starting the real numerical work.

2.4 Performance

2.4.1 Beam stability

The impedance in HL-LHC, shown in Figure 2-6 [69], is not dramatically higher than in the LHC. Molybdenum-coated secondary collimators could decrease the total impedance of more than a factor 2. However, special caution should be given to devices in high beta regions and unshielded elements.
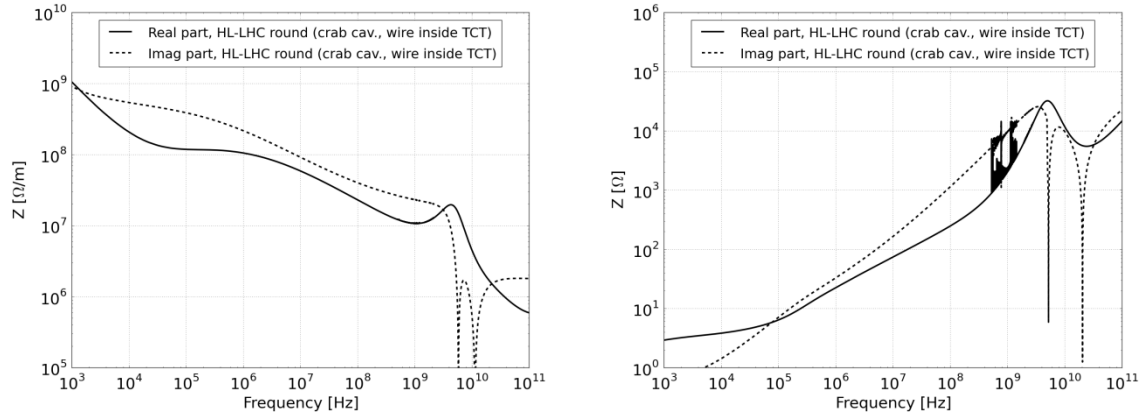
Figure 2-6: Left: First estimate of the horizontal dipolar impedance of HL-LHC, including both crab cavities and beam-beam wire compensators. The vertical dipolar impedance is similar to the horizontal. Right: longitudinal impedance.

Longitudinal instabilities are not expected to be an issue in HL-LHC [70]. Single bunch measurements in LHC at 4 TeV showed an intensity threshold at 1×10^{11} p/b, for an RF voltage of 12 MV and a longitudinal emittance of 1 eVs (4σ bunch length of 0.8 ns, scaled from the measurement of the full width at half maximum). Scaling to HL-LHC parameters (16 MV, 2.5 eVs) leads to an intensity threshold of $\sim 3.4\times10^{11}$ p/b. A double RF system is therefore not needed for beam stability in the longitudinal plane. However, a high harmonic RF system [71-77] in bunch shortening mode could provide additional margin for longitudinal stability; in bunch lengthening mode, by flattening the bunch

profile, a high harmonic RF system could reduce Intra-Beam Scattering (IBS) emittance growth rates, beam-induced heating and pile-up density. A preliminary cavity design for the 800 MHz RF system exists [78]. Recently, the use of a low harmonic RF system in the LHC (200 MHz) as the fundamental RF system has been suggested [79] since:

- it would allow to accept larger longitudinal emittance and therefore larger bunch population from the SPS after its upgrade;

- it could help to reduce IBS, beam-induced heating and e-cloud effects;

- together with the existing 400 MHz RF system, it could be used for luminosity and pile-up levelling;

- it also has a beneficial effect for ions and the momentum slip-stacking scheme in the SPS [80].

A new design has been proposed for a compact superconducting cavity [81]. The compatibility of this scheme with 400 MHz crab cavities or the possibility of installing 200 MHz crab cavities needs to be studied further if this scenario is considered. Finally, the expected benefits of a double RF system should be weighed against the impedance increase and the possible reduced reliability.

Transverse instabilities are a concern based on the experience of the LHC Run 1, during which a transverse instability at the end of the betatron squeeze could not be cured [70]. While Transvers Mode Coupling Instabilities (TMCI) thresholds well exceed the nominal HL-LHC bunch population both at injection and at high energy, to achieve transverse single-beam stability, the collimators will need to be coated with 5 μm of molybdenum [70] and the transverse damper must be able to damp coupled-bunch instabilities up to the maximum frequency (20 MHz). Figure 2-7 shows the expected HL-LHC single-beam stability limits for different scenarios with a transverse damper. If the instabilities observed in 2012 are mainly single-bunch (and therefore beyond the range of the damper), we will not be able to stabilize the HL-LHC beams in the case of the standard material collimators and RF dipole crab cavities. However, beam stability could be recovered with molybdenum-coated collimators. This assumes that the transverse damper can damp all coupled-bunch modes otherwise we will not be able to stabilize the HL-LHC beams for any scenario. It is thus clear that the operation of the transverse damper is vital for HL-LHC. The situation improves with the negative polarity of the Landau octupoles but the results are qualitatively the same.

In Figure 2-7, stability thresholds are plotted versus transverse emittance, assuming the fully squeezed ATS optics (with 15 cm β* in both planes) [25]. The high beta functions greatly enhance the impedance contribution from crab cavities compared to the un-squeezed flat top situation. The design of the crab cavities has to be carefully evaluated and optimized with regard to the High-Order Modes (HOMs), to minimize the contribution to the coupled-bunch instabilities. The coupled-bunch modes will have to be stabilized by the transverse damper; the damper specifications will therefore have to be finalized once the design of the crab cavities is more advanced (at present, the impedance model of the crab cavities is quite coarse and needs to be improved). During the squeeze, the tune spread (providing Landau damping) could be increased if the Achromatic Telescopic Squeeze can be implemented starting from β* = 2 m, thanks to the enhanced beta functions in the arcs. This effect would improve very significantly the situation in terms of stability. In reality the situation will be even less critical because of luminosity levelling, as the smallest β* will be reached only at a lower intensity. All these effects should be studied in more detail in the future.
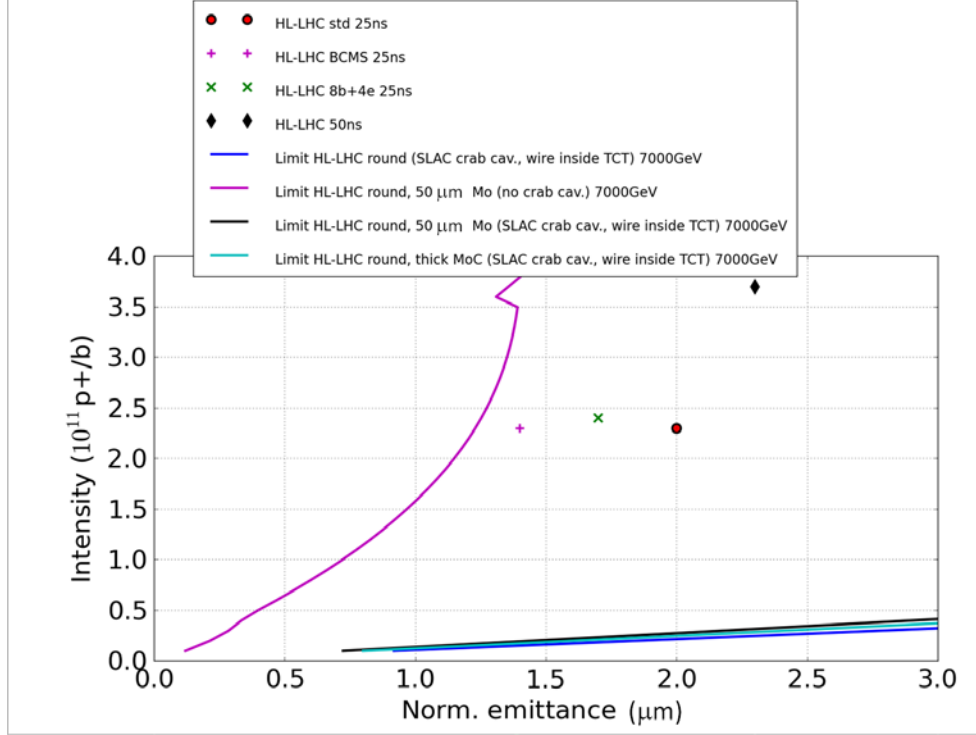
Figure 2-7: Single-beam (25 ns) intensity limit vs. transverse emittance with transverse damper (50-turn damping time) at top energy, for a chromaticity Q' ~ 15 for the two extreme cases (CFC collimators with ODU/SLAC crab cavities and Mo-coated collimators without crab cavities) and for positive polarity of the Landau octupoles.

With an additional 800 MHz RF system, the bunch-shortening mode should be preferred from the point of view of transverse beam stability, as even at low chromaticity beam stability could be reached [70]. However, the operating mode that has been envisaged up to now is bunch lengthening to create flat bunches; for that reason alternative scenarios (e.g. bunch flattening by band limited RF phase noise on the main 400 MHz system) should be studied.

The effect of electron cloud on beam stability still needs to be assessed. Induced heat loads from electron cloud are discussed in Section 2.4.3.

Based on experience from LHC Run 1, the interplay between impedance, Landau octupoles and beam-beam is expected to play an important role in defining the stability limits. A first estimate of the stability diagram for the fully squeezed optics ($\beta* = 15$ cm) in the presence of both octupoles and long-range beam-beam can be found in Ref. [82]. The stable region with octupoles only increases for $\beta*$ below 40 cm, and is about 2.5 times larger with the ATS compared to the nominal optics, due to the larger beta functions at the octupoles. As is the case for LHC, negative octupole polarity (negative amplitude detuning) is preferred for single-beam stability. On the other hand, compensation between negative amplitude detuning from the octupoles and positive amplitude detuning from long-range beam-beam leads to a reduction of the stable region during the squeeze [83]. Below a certain beam-beam separation, positive octupole polarity starts to give larger stable regions and is therefore preferred. Some details of the simulation still need to be checked. However, the proposed operational scenario for HL-LHC is first to bring the beams into collision, and then to squeeze. By taking advantage in this way as soon as possible of the large amount of Landau damping provided by head-on beam-beam interactions, this should remove possible instability issues arising from long-range beam-beam during the betatron squeeze, while keeping negative octupole polarity (which is better for single-beam stability).

2.4.2 Beam-beam effects

The beam-beam interaction is known to be an important factor limiting the performance reach of present particle colliders. Two of the most significant effects of beam-beam interactions are: (a) the induced particle losses that decrease the beam lifetime, create high background load for physics experiments and elevated heat and radiation load on the collimation system; and (b) the degradation of beam quality manifesting itself through the beam size blow-up that decreases the luminosity delivered to particle physics experiments.

Owing to the extensive theoretical and simulation campaign during the design of the LHC collider, the beam-beam effects in the present machine are well controlled [84]. However, the HL-LHC represents a quantitative as well as a qualitative leap into unknown territory with respect to beam-beam effects. The baseline configuration makes use of some novel concepts that have not so far been used to their full extent in hadron colliders, and thus require careful evaluation. The concepts related to beam-beam effects are: (a) luminosity levelling by variation of the beta function at the IPs; (b) tilting bunches in the main IPs with the use of RF crab cavities; (c) significantly high value of the head-on beam-beam tune shift.

Hence, the expected impact of beam-beam interactions on HL-LHC machine performance has been evaluated in order to provide insight into possible limitations. The studies were mostly performed with the use of the weak-strong approximation and employed the SixTrack and Lifetrack codes, which have been successfully used for the design and optimization of past and existing colliders [85, 86]. Both codes are capable of calculating the area of stable motion in phase space (the dynamic aperture), and hence a direct comparison of the results is possible. The performance reach for weak-strong codes is a few million turns, which is equivalent to a few minutes of machine time. Where necessary, strong-strong simulations with BeamBeam3D, COMBI and a code by K. Ohmi [87-99] were carried out.

In evaluation of the HL-LHC, the criteria used for establishing satisfactory beam dynamics behaviour were the same as in the LHC design study. In particular, the target value for the one-million turn DA was 6σ (for the nominal HL-LHC emittance of 2.5 μm) or more. The motivation for the choice of such a margin is explained in Ref. [85]. In short, the beam-beam driven diffusion at small amplitudes is quite slow, and the 10^6 turns of tracking typically does not represent the real long-term stability boundary. In the majority of studies, the 6σ DA corresponds to a true stability boundary of about 4σ with the appearance of chaotic spikes [85]. Benchmarking of the simulations with machine studies seem to indicate that losses and reduction of beam lifetime start to appear only at values of the crossing angle for which the simulated dynamic aperture is as low as 4σ [89, 90]. However, it must be noted that other studies indicate that the simulations of the dynamic aperture of the installed LHC overestimates the dynamic aperture by 20 to 30% [94].

In the baseline HL-LHC scenario (25 ns spacing), bunches will begin colliding with 2.2×10^{11} p/b and transverse normalized emittance 2.5 μm. The bunches will be tilted by crab cavities at each of the two main IPs to ensure head-on collisions despite the trajectories crossing at an angle. The luminosity will be levelled at the constant value of 5×10^{34} cm^{-2}s^{-1} by varying the beta function from ~69 cm at the beginning of the fill to 15 cm at the end, in the case of constant crossing angle of 590 μrad. Assuming negligible transverse emittance growth, the separation of beams at parasitic crossings will thus vary from 26σ at the beginning of the fill to 12.5σ at the end. Hence, from the point of view of beam-beam effects three stages can be distinguished over the course of a fill:

- Beginning of fill ($\beta^* = 69$ cm, $N = 2.2\times10^{11}$ p/b): weak long-range interactions (26σ separation) and strong head-on interactions, characterized by beam-beam tune shift $\xi = 0.031$ (assuming head-on collisions in LHCb), determined by beam brightness $B \sim N/\varepsilon$. Since optics with $\beta^* = 69$ cm were not readily available, simulations were performed with $\beta^* = 40$ cm, which, with the nominal initial intensity corresponds to a significantly enhanced beam-beam effect (worst-case scenario). The bunch intensity at the specified levelled luminosity is $N = 1.7\times10^{11}$ p/b.

- Middle of fill (β* = 33 cm, N = 1.5×10^{11} p/b): appreciably large long-range and head-on interactions.

- End of fill (β* = 15 cm, N = 1.1×10^{11} p/b): weak head-on (ξ = 0.015 due to the particle burn-off in collisions) and relatively strong long-range (12.5σ separation).

All simulations were performed with lattice version SLHCV3.1b. In addition to IR1 and IR5, the beams also collide with finite angle at IR8 (LHCb), which further enhances the negative impact of the head-on beam-beam effects on the dynamics. The long range effects are weaker thanks to the beneficial effects of the β* levelling [92]. Multipole errors in the IR magnets were included in the simulations as specified in [94]. A parametric study was performed to establish the robustness of the baseline HL-LHC scenario [93] and in order determine the optimal crossing angle. Figure 2-8 shows the dependence of the minimum DA value on the crossing angle at IP1 and IP5 for different bunch intensities. The dashed lines indicate the minimum target DA and the nominal crossing angle. For the operational cases described above, the DA is always largely above 6σ.
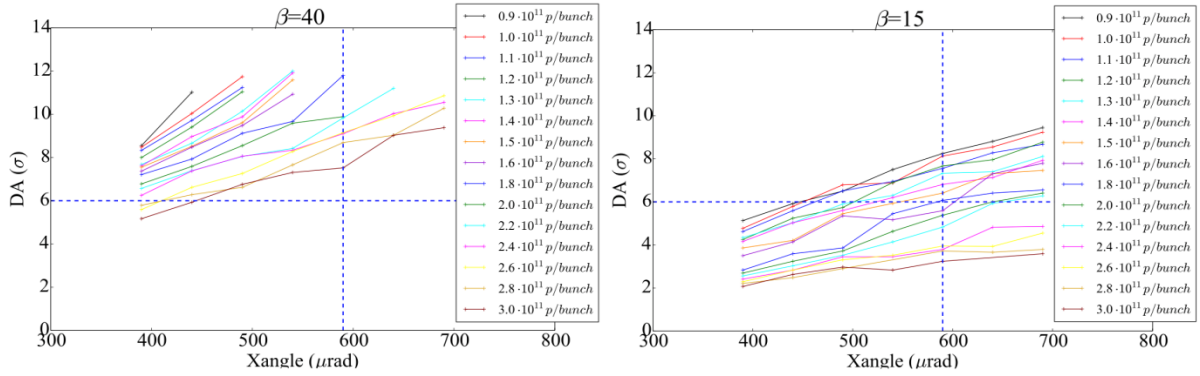
Figure 2-8: Minimum DA for β* = 40 cm optics (left) and β* = 15 cm optics (right) as a function of crossing angle for different bunch intensities. The r.m.s. beam size corresponds to a normalized emittance of 2.5 μm.

Pacman effects [95, 97] have been evaluated and shown not to have significant impact on DA and luminosity. The pacman effects are expected to be strongest at the end of the fill (β* = 15 cm), and will be weaker than the nominal LHC case due to a larger beam-beam separation (12.5σ compared to 9.5σ). With intensity N = 1.1×1011 p/b and long-range beam-beam separation of 12.5σ one expects a maximum offset at IP1 and IP5 of about 0.15σ. The spread over the bunch train is of the same order, 0.1 – 0.2σ. The long range variations at IP1 and IP5 result in a very small asymmetry in the tune footprint and no impact on long term tracking has been noticed [93].

The results of weak-strong simulations confirm the robustness of the baseline HL-LHC scenario with respect to beam lifetime and particle losses, and suggest that a significant margin exists that would allow to either decrease the crossing angle to approximately 450 µrad, or operate at higher values of levelled luminosity [95].

Beam-beam effects can induce beam emittance growth and related luminosity lifetime degradation via a variety of mechanisms. Weak-strong simulations of multi-particle bunches were used to evaluate the emittance growth due to beam-beam related betatron resonances. The results predict that the luminosity lifetime due to beam-beam effects will be more than 80 hours even in the worst case [98]. A more significant mechanism of emittance degradation can be related to the interplay between the nonlinearity of the beam-beam interaction and various sources of noise. In particular, the phase errors of crab cavities and the ripple of dipole magnet power supplies lead to fluctuations in the beam-beam separation. Strong-strong beam-beam simulations have been carried out for the HL-LHC parameters with large crossing angle and crab cavity compensation [99, 100]. A detailed damper model was included in the simulations. Both β* levelling and crab cavity levelling were simulated including crab

cavity noise and dipole power supply ripple [100]. For white random phase noise in the crab cavities, simulations suggest that the r.m.s. noise amplitude should be kept around the level of 3×10^{-5} rad in order to maintain a luminosity lifetime of 24 hours. This tolerance limit might over-estimate the crab cavity phase noise level since the real phase error will have some spectral distribution different from white noise. For the present studies the spectrum was sampled at a number of frequencies near the betatron frequency. Simulations suggest that strong emittance growth would occur with noise frequencies near the fractional tune of 0.30 and 0.31. The phase errors with those frequencies should be kept as small as possible. The 600 Hz dipole noise was found to have negligible effect on the beam emittance

2.4.3 Beam induced heat load on the cryogenic system

Both impedance and e-cloud induce heat loads on the cryogenic system [70]. The impedance-induced heat loads with the HL-LHC beam parameters [14] for several key systems are summarized in Table 2-9. In the analysis it is assumed that no forward physics detectors (e.g. ALFA and TOTEM) will be installed during the HL-LHC era. The impedance-induced heat loads for the different types of beam screens vs. temperature are summarized in Table 2-10

Electron cloud effects should be mitigated by beam-induced scrubbing in the arcs (experience from Run 2 will be vital in that respect) and by low Secondary Emission Yield (SEY) coatings and/or clearing electrodes in the new insertion regions, intended to keep the heat loads within the cooling capacity [70]. Similar actions will be required for the beam screen of the triplets/D1 in IR2 and IR8.

Figure 2-9 shows the heat load from e-cloud vs. bunch intensity for both an arc dipole and an arc quadrupole, for different SEYs. Provided that a low SEY is achieved, the increased bunch intensity should be acceptable for heat load, but the effect on the beam stability still needs to be assessed. The aim of the scrubbing run is to reach a SEY of ~ 1.3 in the arc main magnets: this applies for both LHC and HL-LHC, because the dependence of the SEY threshold on bunch intensity in the dipoles is weak. It is worth noting that the quadrupoles have a threshold below 1.1, which cannot be reached by scrubbing. The detrimental effects of the electron cloud in the LHC (heat load in cold regions and emittance blow-up) can be partly mitigated by using specially conceived filling patterns. The underlying idea is to use the flexibility of the injector complex to build bunch trains in LHC with long enough gaps interspersed, to prevent the build-up of an electron cloud along the beam. An alternative scenario (referred to as 8b+4e) based on beams with 25 ns spacing has been conceived to reduce the electron cloud effects in HL-LHC, if needed, in its initial phase of operation following the upgrade [101] and has been considered as part of the HL-LHC operational scenarios [3]. Operation with a 200 MHz main RF system would allow for longer bunches and would have a positive impact also on e-cloud [79]. The impact of the bunch length on e-cloud will be studied experimentally during the coming Run 2 (e.g. to reduce emittance blow-up at low energy).

Figure 2-10 shows the expected heat load along the triplet in IP1 and IP5 for different SEY values. The least efficient build-up (lower heat load) occurs at the locations of the long-range encounters (vertical dashed lines). Note that the values in the D1 dipole are comparable to or higher than the values in the quads. The comparison of the heat load from e-cloud for the current LHC and the future HL-LHC triplets shows that the larger bunch population and larger chamber size lead to a larger heat load by a factor ~ 3, for HL-LHC [69] (for the same SEY, similar energy of multipacting electrons and larger number of impacting electrons). For IP2 and IP8, scaling the results also leads to an increase of the heat load from e-cloud by a factor ~ 3, but detailed simulations remain to be done. Unlike IP1 and IP5, the cryostats in IP2 and IP8 already include D1 (about 10 m long).

Understanding e-cloud build-up in the matching section requires the study of a large number of configurations (beam screen shape and dimensions, magnetic field configuration, beam size, beam position, etc.). Parametric studies will be performed to assess which of these dependencies strongly impact the e-cloud build-up. Some preliminary simulations revealed that the beam size and the magnetic

field have small but non-negligible impact. The next step will be to try and disentangle these two effects. The effect of the beam position will then have to be studied in detail.

Table 2-9: Summary of the impedance-induced heat load computations for several key systems.

Element	Expected heat load [W]	Conclusion / comment
Equipment with RF fingers [102]	Negligible for conforming RF fingers.	Robust mechanical and quality control required during the installation phase.
Experimental beam pipes (resonant modes) [103-107]	ATLAS: no significant mode expected. ALICE: potentially* more than 1 kW. CMS: potentially* more than 350 W. LHCb: potentially* more than 250 W. (*if the longitudinal modes overlap with beam harmonic frequencies)	During Run 2, the temperature should be closely monitored in the large diameter regions of ALICE, CMS and LHCb. The impact of these potentially expected heat loads on hardware integrity and outgassing should be assessed.
All types of beam screens [104] and Table 2-10	See Table 2-10, where the power losses have been computed vs. temperature (between 20 K and 70 K).	The effects of the beam screen longitudinal weld, the two counter-rotating beams and the magneto-resistance have been taken into account. Decoupling of the cryogenics for the IR elements and the RF will provide more margin for acceptable heat load in the arcs.
Triplet Beam Position Monitors [109]	~ 0.2 W/m for the (most critical) 50 ns beam.	This assumes no interferences between the two beams electromagnetic fields (worst case) and copper coating.
New collimators with integrated BPMs and ferrites [110]	~ 100 W (of which ~ 5 to 7 W would be dissipated in the ferrites, and ~ 4 to 6 W in the RF fingers).	More thorough simulation studies as well as bench measurements are under way to confirm these results. This should be acceptable.
Injection kickers (MKIs) [111, 112]	Between ~ 125 W/m and ~ 191W/m (based on measurements of 9 MKIs upgraded to have the full complement of 24 screen conductors). For comparison, most of the MKIs before the Long Shutdown 1 (LS1) had a power deposition of ~ 70 W/m (which did not limit the LHC operation).	It is of the order of heat loads estimated with pre-LS1 parameters for the old MKI8D (i.e. before the 3rd Technical Stop of 2012) which had a 90° twist in the screen conductors and which had a power deposition of ~160 W/m, based on measurements of impedance during LS1. This required significant time to cool down after physics fills. For HL-LHC we are looking at: (i) further reducing the power deposition; (ii) improving the cooling; (iii) using high Curie point ferrites.
Crab cavities [113]	In the multi kW range if the longitudinal modes overlap with beam harmonic frequencies.	The design should allow detuning the longitudinal modes from multiples of 20 MHz by ~ 0.5 MHz.
Injection protection dump (TDI) [106]	The present design already suffers from beam induced heating (in the kW range for the injection settings) with nominal LHC parameters due to inefficient cooling.	The present design of the TDI is not compatible with the HL-LHC parameters and a new design is being studied, with installation foreseen for LS2.
Synchrotron Radiation Monitor (BSRT) [114]	The power deposited in the ferrite absorbers (heated at ~ 250-350°C according to simulations and measurements) during 2012 operation could not be efficiently transferred leading to damage.	A new design is being studied and installed during LS1. The usability of this design for HL-LHC will need to be assessed after LS1.

Table 2-10: Impedance-induced heat loads for the different types of beam screens (including the effects of the longitudinal weld, two counter-rotating beams and the magneto-resistance) vs. temperature: values are given for the 25 ns beam and for the 50 ns beam (in parentheses).

Power loss [W/m]	20 K	30 K	40 K	50 K	60 K	70 K
Q1 (49 mm, 6.9 T)	0.23 (0.28)	0.24 (0.31)	0.28 (0.35)	0.34 (0.43)	0.40 (0.51)	0.47 (0.59)
Q2-Q3 (59 mm, 8.3 T)	0.19 (0.24)	0.20 (0.26)	0.23 (0.29)	0.28 (0.35)	0.33 (0.42)	0.38 (0.49)
D1 (59 mm, 5.6 T)	0.17 (0.22)	0.19 (0.24)	0.22 (0.28)	0.27 (0.34)	0.32 (0.41)	0.38 (0.48)
D2 (42 mm, 4.5 T)	0.25 (0.32)	0.27 (0.34)	0.32 (0.40)	0.39 (0.50)	0.47 (0.59)	0.54 (0.69)
Q4 (32 mm, 3.7 T)	0.34 (0.43)	0.37 (0.47)	0.44 (0.56)	0.54 (0.68)	0.64 (0.81)	0.74 (0.94)
Q5 (22 mm, 4.4 T)	0.59 (0.74)	0.63 (0.80)	0.72 (0.91)	0.86 (1.09)	1.01 (1.28)	1.16 (1.46)
Q6 (17.7 mm, 3.5 T)	0.79 (0.99)	0.84 (1.06)	0.96 (1.22)	1.14 (1.44)	1.32 (1.68)	1.51 (1.91)
Q7 (17.2 mm, 3.4 T)	0.82 (1.03)	0.87 (1.11)	1.00 (1.26)	1.18 (1.49)	1.37 (1.74)	1.56 (1.98)
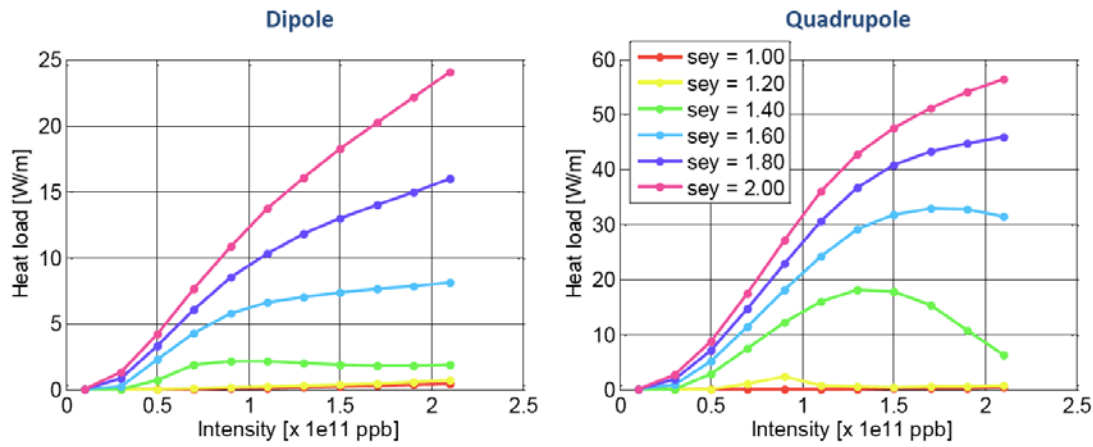
Figure 2-9: Heat load from e-cloud in the arc main magnets as a function of bunch intensity and SEY.
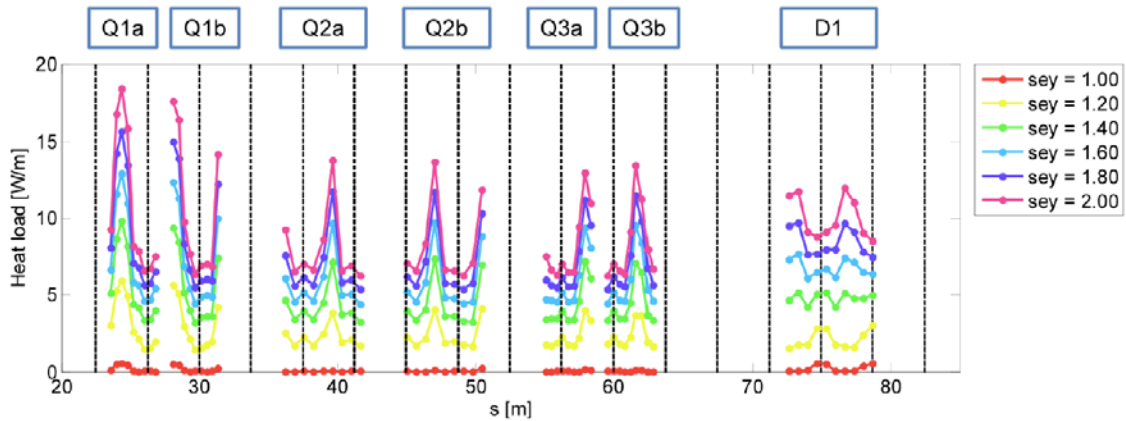
Figure 2-10: Heat load from e-cloud along the future HL-LHC triplets.

2.4.4 Luminosity performance

The peak performance at 7 TeV has been estimated in Table 2-1. The estimate of the integrated luminosity requires determining the luminosity evolution during a fill. The beam intensity evolution has been evaluated taking into account burn-off due to luminosity considering a total cross-section of 100 mb [115, 116], and an additional (unknown) source of intensity loss with a lifetime of 200 hours (based on 2012 experience [117]).

The emittance evolution has been determined including: intra-beam scattering (IBS) (based on Run 1 experience, no coupling has been assumed); radiation damping; an additional (unknown) source of vertical emittance blow-up with a lifetime of 40 hours (based on observations during Run 1). A finite difference method in steps of 5 minutes has been implemented to model the intensity evolution and the evolution of the IBS lifetime as a function of the bunch population. Figure 2-11, Figure 2-12 and Figure 2-13 show the evolution of the main parameters for two cases of levelling, corresponding to a pile-up of 140 and 210, for the standard filling scheme with parameters listed in Table 2-1. In the estimates the worst case scenario (with respect to the head on beam-beam tune spread) of β^* levelling in IP1, 5 and 8 has been considered. Full compensation of the crossing angle by crab cavities has been included for IP1 and IP5. The crossing angle is assumed to be constant during the fill. Alternative (or complementary) luminosity levelling scenarios include:

- crossing angle variation to increase the geometric reduction factor at the beginning of the fill;

- crab-cavity RF voltage variation to have a partial crossing angle compensation at the beginning of the fill;

- dynamic bunch length reduction;

- controlled variation of the transverse separation of the two colliding beams.

Options 1 and 2 have the disadvantage of increasing the line pile-up density at the start of the fill.

The performance estimates for the two cases considered (pile up 140 and 210) are listed in Table 2-11. The parameters used for the estimates of the HL-LHC integrated performance are listed in Table 2-12. The operation at the higher pile-up limit is appealing because it allows higher integrated luminosity while keeping the optimum fill length to values already obtained in 2012; however, in this case, the maximum pile-up density exceeds the target pile-up density limit of 1.3 events/mm/crossing. This could be reduced by increasing the bunch length. A more elegant solution could be provided by the "crab-kissing" scheme [16] and/or by the implementation of flat-beam optics with a smaller crossing angle (provided that long range effects can be kept under control, perhaps by the implementation of long range compensation schemes). These alternative scenarios will be described in the next section.

Table 2-11: Integrated performance estimate for levelling scenarios at pile-up levels of 140 (PU 140) and 210 (PU 210) events/crossing, respectively.

	Levelling time [h]	Optimum fill length [h]	Integrated Lumi [fb⁻¹/y] for η=50%, opt. fill length IP1-5/8/2	Maximum mean pile-up density [events/mm/xing] in IP1/5	Maximum mean pile-up [events/xing] in IP1/5
PU 140	8.1	9.4	261/8.9/0.105	1.25/140	140
PU 210	4.25	6	331/7.8/0.092	1.81/210	210

Table 2-12: Parameters assumed for HL-LHC performance estimate.

Scheduled physics time for p-p luminosity production/year (T_{phys}) [days]	160
Minimum turn-around time [h]	3
Performance efficiency – goal [%]	50
Pile-up limit IP1/5 [events/crossing]	140 / 200
Pile-up limit IP8 [events/crossing]	4.5
Pile-up density limit – IP1/5 [events/mm/crossing]	1.3
Visible cross-section IP1/2/5 [mb]	85
Visible cross-section IP8 [mb]	75 [118]
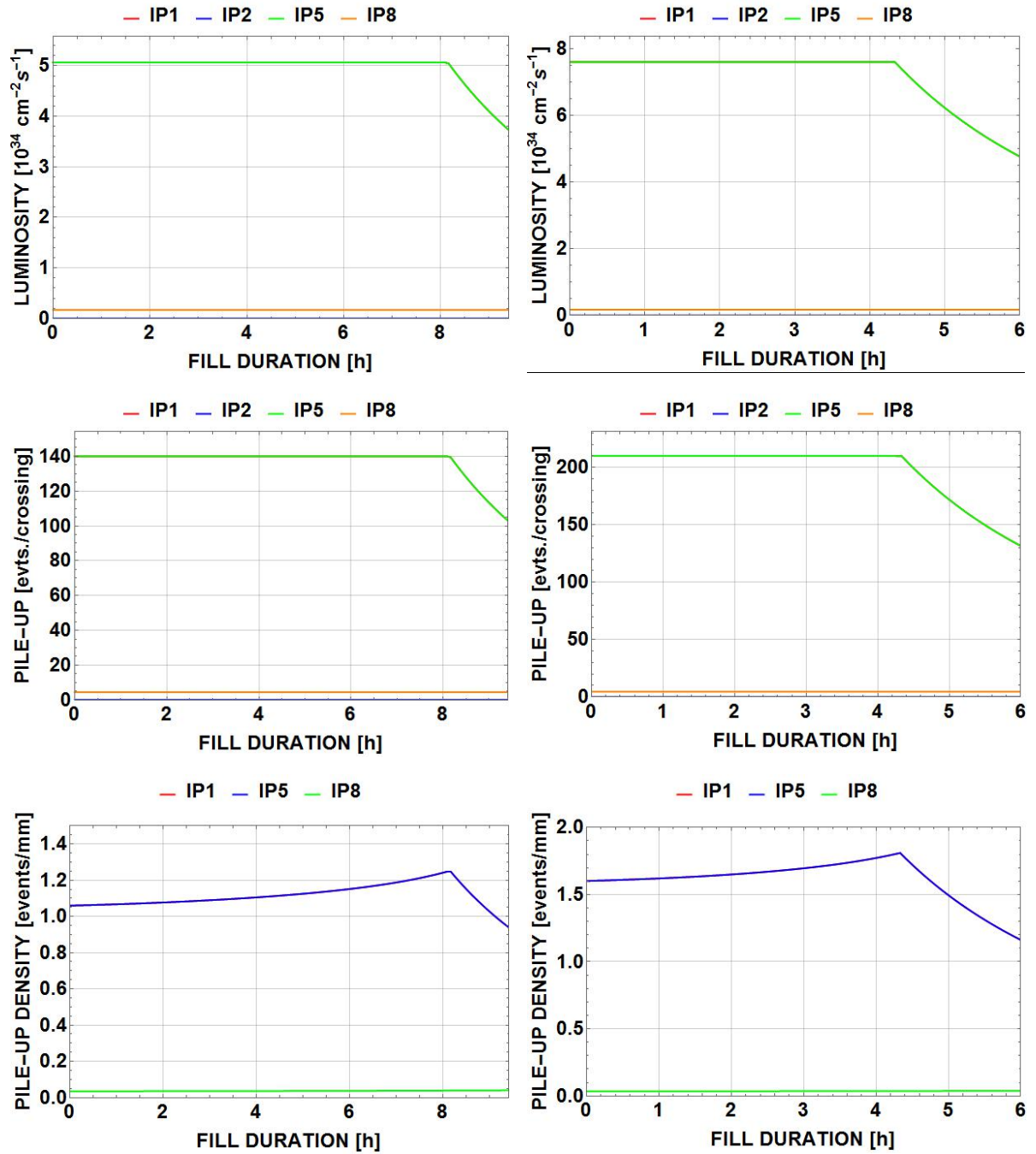
Figure 2-11: Evolution of Luminosity, pile-up and pile-up density assuming levelling at 140 events/crossing (left column) and 210 events/crossing (right column) in IP1 and 5. The small effects of RF curvature in the crab cavities is not included.
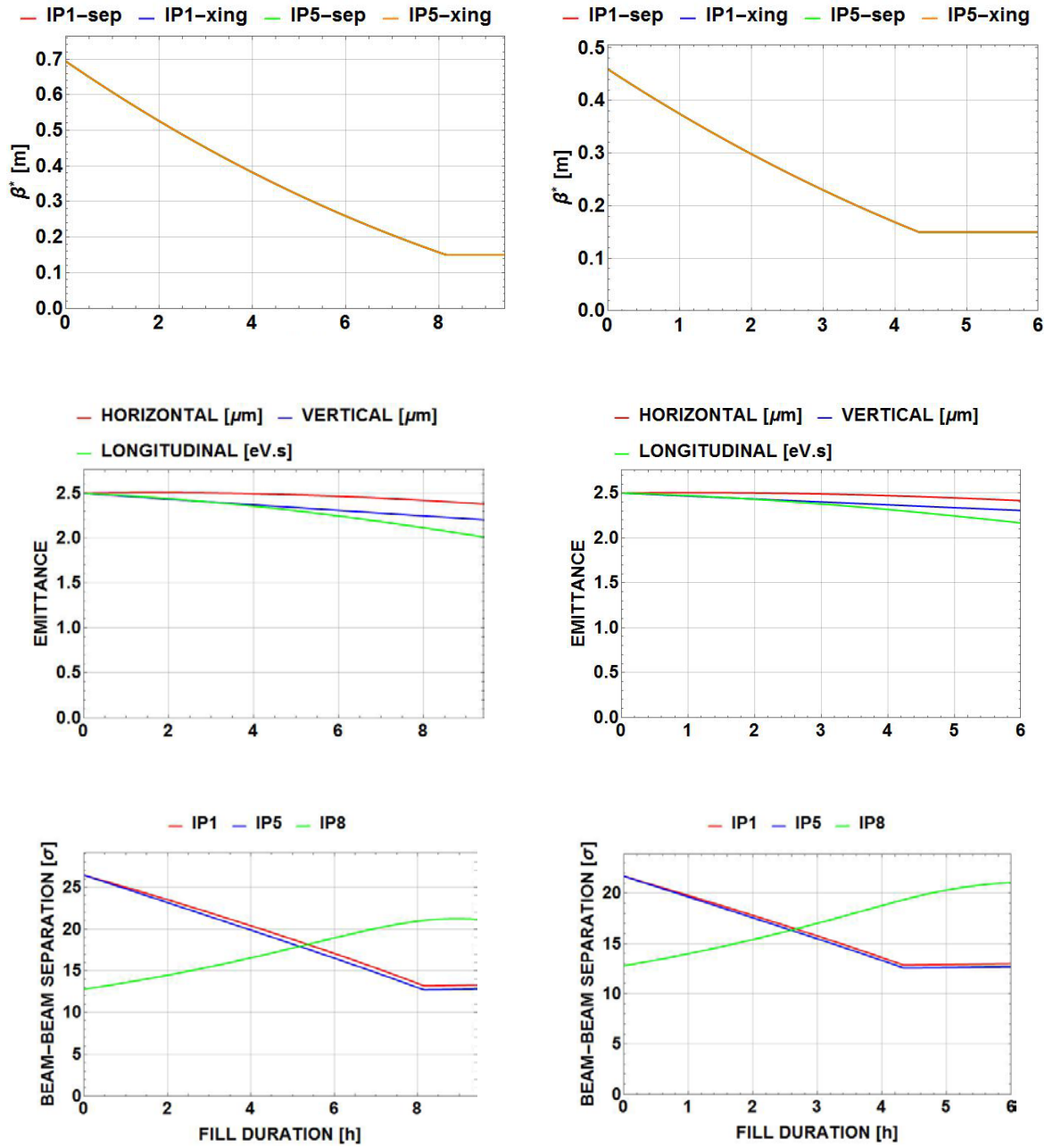
Figure 2-12: Evolution of β*, emittance and long range beam-beam normalized separation (d_bb) for levelling at 140 (left) and at 210 events/crossing (right) in IP1 and 5.
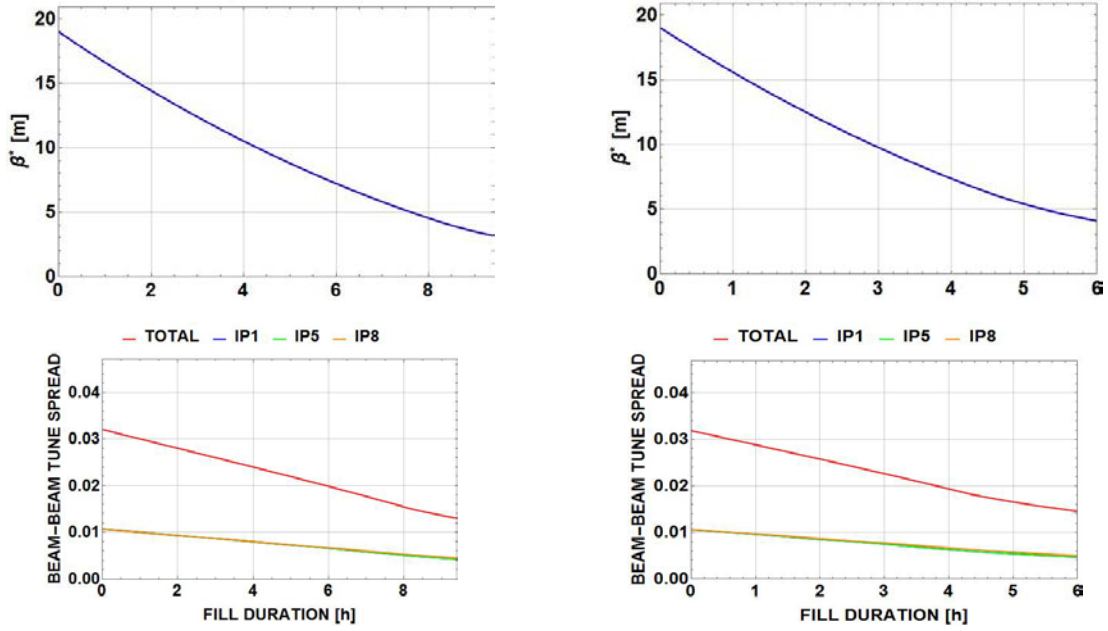
Figure 2-13: Evolution of β* in IP8, head-on beam-beam tune spread assuming levelling at 140 events/crossing (left column) and at 210 events/crossing (right column) in IP1 and 5.

2.5 Variants and Options

The HL-LHC project includes the study of various alternatives to the present baseline configuration with the aim either to improve the potential performance of the machine or to provide options for addressing possible limitations or changes in parameters (see Figure 2-14).

2.5.1 Pile-up density management

The "crab-kissing" scheme ([16, 119], and references therein) would allow either to improve the data taking quality by reducing the peak pile-up density at constant integrated luminosity, or to increase the integrated luminosity at constant total pile-up or levelled luminosity (see orange markers in Figure 2-14). At present, implementation of the crab-kissing scheme would require changes to the layout of the crab cavities, to allow bunch deflections in different planes. Also, a flat optics with beam-beam long range compensator would need to be implemented. These changes are not completely compatible with the nominal scheme because the crab cavity voltage is insufficient to provide the required deflections in both planes; however new optics solutions are being explored to keep the crab-kissing scheme and the nominal configuration mutually compatible.

In case crab kissing is not available it would still be possible to level peak pile-up density using β* with different total pile-up targets (see magenta markers in Figure 2-14). In this scenario a flat longitudinal profile is assumed to be reachable through use of a 2nd harmonic RF system or phase modulation as in the case of crab kissing. In absence of flat longitudinal profiles one could expect an increase of the peak pile-up by about 10%.

2.5.2 Alternative scenarios

A compact 200 MHz RF system could be installed ([79], and references therein) in the LHC, potentially allowing an increase in the injected intensity from the SPS, although further studies are needed to confirm what could be achieved. Such a system, together with a 400 MHz system, could offer the means

to increase the bunch length (e.g. 15 cm) to reduce electron cloud effects, reduce IBS growth rates, and provide flat longitudinal bunch charge density (see green markers in Figure 2-14).

In case e-cloud severely limits the beam current with 25 ns bunch spacing, the 8b+4e [79] filling scheme would allow comparable beam current at the cost of lower levelled luminosity with constant total pile-up. The 8b+4e scheme can provide about 2.3×10^{11} p/b with 1900 bunches [3], halfway between the corresponding 50 ns and 25 ns configurations, and therefore resulting in a performance reach between those two extremes (see blue markers in Figure 2-14).

In the absence of crab cavities, it may still be possible to implement some measures to limit the loss of performance [20]. By increasing $\beta*$ in the crossing plane and decreasing it in the separation plane, one could limit the impact of the geometric reduction factor thanks to the reduction of the necessary crossing angle (see rightmost black marker in Figure 2-14). However, a large crossing angle in units of σ is still needed (12σ for the lower $\beta* = 30$ cm) because of the partial loss of the IR1/5 long-range beam-beam (LRBB) interaction compensation (i.e. passive compensation from the non-symmetric alternating crossing between IP1 and IP5). However, a LRBB compensator could potentially allow 10σ separation, therefore restoring the luminosity compared to the nominal scenario at the cost of some increase in pile-up density (see leftmost black marker in Figure 2-14). Similarly, a staged upgrade scenario for which the replacement of the matching section is postponed (see [120, 47] and references therein) could still benefit from flat beam optics, although with a limited reach of $\beta*$ in the non-crossing plane (about 20 cm) but with the potential of reaching about 170 fb^{-1} per year (see dark yellow markers in Figure 2-14). In this context, a design for a movable TAXN that could be adapted to different $\beta*$ values would offer the best radiation protection for the downstream elements in all these scenarios, regardless of the chosen optics configurations.
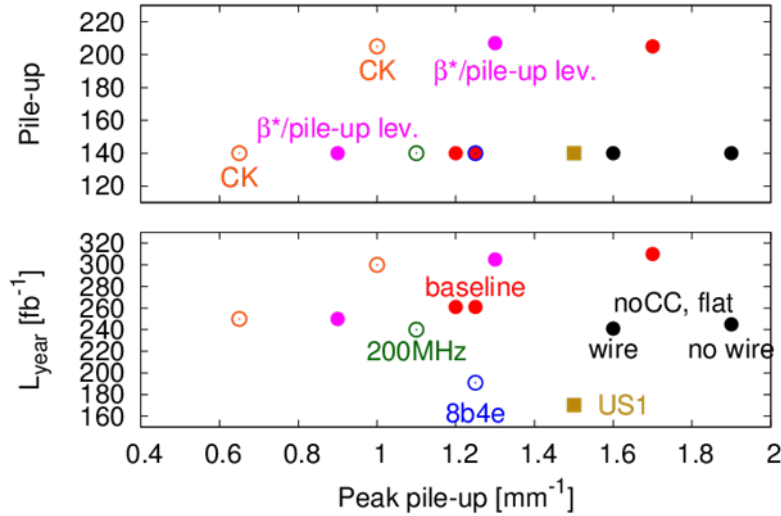
Figure 2-14: Performance expectation of different alternatives. The red markers represent the baseline scenarios (flat or round) for different target of total pile-up (140 and 200 event per crossing). In case crab cavities are absent (black marker) annual integrated luminosity could be recovered by using flat optics for an increase of the peak pile-up density that can be limited with long range compensators. The crab kissing scheme (magenta markers) on the other hand offers the target annual luminosity with means to control the pile-up density and to reduce it considerably with respect to the nominal scheme. Peak pile-up density can also be levelled with β*

(magenta markers). In case e-cloud effects needs to be mitigated, 200 MHz RF system or 8b+4e filling schemes (green and blue markers) could be deployed.

2.6   The HL-LHC as a Nucleus-Nucleus Collider

The LHC's second major physics programme provides nucleus-nucleus collisions to ALICE, CMS and ATLAS and proton-nucleus collisions to these three experiments with LHCb in addition. The overall goal of the programme is ultimately to accumulate 10 nb^{-1} of Pb-Pb luminosity during the whole LHC operating period after Run 2 [80, 121]. The p-Pb requirement will be for approximate equivalence in terms of integrated nucleon-pair luminosity [80, 122, 123]. The heavy-ion programme may also require short p-p runs at specific energies to provide reference data; the luminosity requirement will be similar (see 16.5.1). Nuclei other than $^{208}Pb^{82+}$ have not been requested by the experiments but remain as possible options with potential performance to be evaluated.

The heavy-ion luminosity upgrade aims at increasing integrated rather than peak luminosity and is therefore focused mainly on injecting the maximum beam current possible. With the expected upgrade to remove the event rate limit of the ALICE experiment, luminosity levelling will no longer be a necessity but may be employed to mitigate the rapid luminosity decay due to the large electromagnetic cross-sections [80, 124]. Low values of β* are required at three or four interaction points so the achromatic telescopic squeeze will not be used. The main elements of the heavy-ion luminosity upgrade should be in place a few years before those of the proton-proton part of the project.

Upgrades to the heavy-ion injector chain [125] would normally aim to increase the number of bunches and the intensity per bunch but these two quantities are not independent. Injecting long trains from the SPS lengthens the injection plateau in the SPS, subjecting some bunches to higher losses from the effects of intra-beam scattering, space charge and RF noise [126]. On the other hand, injecting a larger number of short trains from the SPS increases the average bunch intensity but leaves more gaps in the LHC bunch train and increases the LHC's injection time, reducing overall efficiency and subjecting some bunches to more emittance growth at LHC injection. In all cases, there is a broad distribution of bunch parameters in collision in the LHC. Optimisation of the injection and filling schemes has to take all these interdependencies into account [126] and will likely have to be done a new each year as a function of injector performance.

The present performance estimates are nevertheless based on an injection scheme which assumes that the maximum 12 PS batches of 4 bunches are assembled into a batch in the SPS, with a 50 ns bunch spacing achieved by slip-stacking. This is repeated 26 times to assemble a train of 1248 bunches in the LHC (practical filling scheme details will reduce this by some percent, depending on the experiment) and yielding a distribution of individual bunch-pair luminosities at the start of colliding beams as shown in Figure 2-15. Simulation of the evolution of these individual bunches, taking into account luminosity burn-off, IBS and radiation damping [126] leads to the total luminosity shown in Figure 2-16. Depending on the turn-around time (between beam dump and the next declaration of Stable Beams for physics), the fill length can be optimised to give the ideal average daily luminosity shown.

The rapid luminosity decay is due to the large cross-sections for electromagnetic processes in the collisions [126, 127]. The peak luminosity is expected to be substantially above the quench limit from losses due to the bound-free pair-production process and new collimators are foreseen in the dispersion suppressors to absorb these secondary beams emerging from the interaction points (see chapter 5.2). Intensity limitations may also arise from losses due to collimation inefficiency, which is higher for ion beams, due to the more complicated nuclear interactions with collimators [128, 129].

The 50 ns bunch spacing introduces close parasitic beam-beam encounters near to the ALICE experiment which may require the half-crossing angle to be increased beyond the 60 µrad limit imposed for optimum operation of the Zero-Degree Calorimeters. The minimum acceptable at the low Pb bunch

charge will be determined empirically [80]. The crossing angles for ATLAS and CMS are unrestricted and can be taken over from proton operation.

The principal beam parameters determining the luminosity are summarised in Table 2-13. Other parameters will be similar to those given in [130]. Further potential gains in luminosity may come from improved injector performance and, possibly, a cooling system [131] in the LHC.

Table 2-13: Average values of principal beam parameters at start of physics.

Number of bunches per beam	1248
Normalised transverse emittance (average)	1.6 µm
Optical function at interaction point	0.5 m
Crossing angle at ALICE experiment	60 µrad
Bunch population (average)	1.04×10^8
Bunch length	0.1 m
Peak luminosity	4.5×10^{27} cm-2s^{-1}
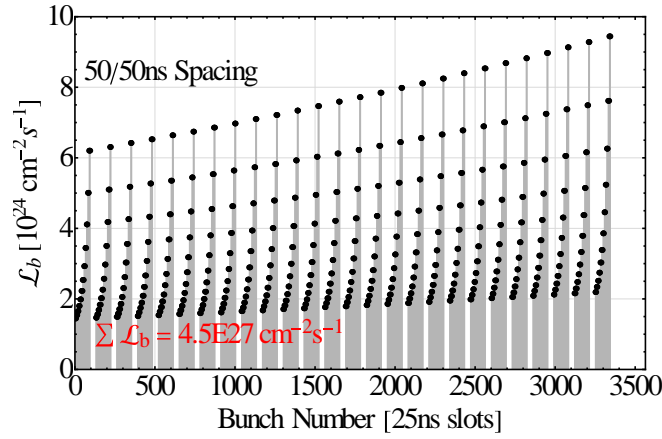
Figure 2-15: Initial luminosity for each colliding bunch pair along the full train in the LHC.
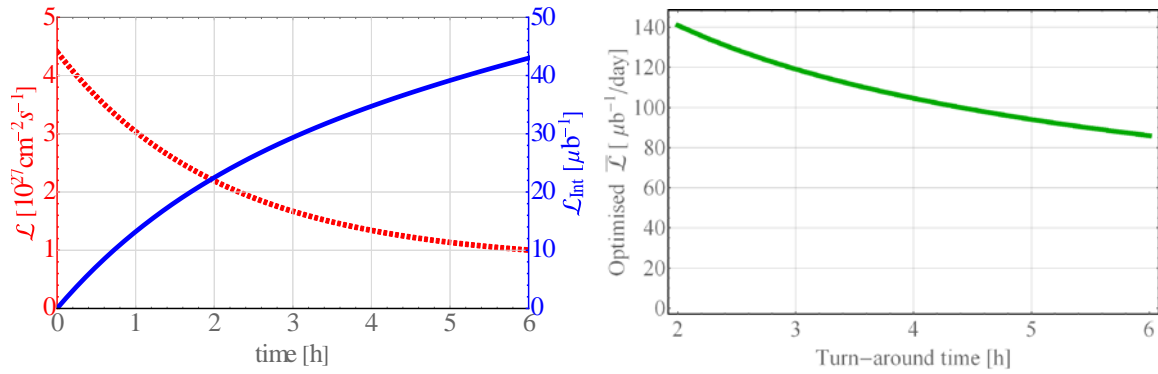
Figure 2-16: Left: Total luminosity (red) and integrated luminosity (blue) during a fill starting with the bunch-pair luminosities shown in Figure 2-15. Right: Average luminosity per day as a function of turn-around time (dump to next Stable Beams) when fill lengths are optimised, with lengths varying between 3 and 6 h, with the luminosity dependence shown in the left plot.

2.7 Acknowledgements

our gratitude to E. McIntosh for his continuous support for the numerical simulations and the SixTrack code.

2.8 References

[1] R. Jacobsson, "Future wishes and constraints from the experiments at the LHC for the proton-proton program", ICFA Mini-Workshop on Beam-Beam Effects in Hadron Colliders (BB2013), CERN, Geneva, Switzerland, 18 - 22 Mar 2013, W. Herr, G. Papotti, Eds., CERN-2014-004, p. 167-176.

[2] O.S. Brüning, F. Zimmermann, "Parameter Space for the LHC High Luminosity Upgrade", Proceedings of the 3rd International Particle Accelerator Conference, New Orleans, USA, 20-25 May 2012, C. Petit-Jean-Genaz, J. Corbett, eds., p. 127-129.

[3] G. Arduini, O. Brüning, R. De Maria, R. Garoby, S. Gilardoni, B. Goddard, B. Gorini, M. Meddahi, G. Rumolo, R. Tomás, "Beam parameters at LHC injection", CERN-ACC-2014-0006.

[4] O.S. Brüning, "HL-LHC Parameter Space and Scenarios", Proceedings of the Chamonix 2012 Workshop on LHC Performance, Chamonix, France, 6 - 10 Feb 2012, C. Carli ed., CERN-2012-006, p. 315-324.

[5] S. Fartoukh, F. Zimmermann, "The Accelerator Physics Challenges", to be published in International Journal of Modern Physics A and references therein.

[6] V. Kain, "Concerns with Low Emittance Beams Operation", LHC Performance Workshop (Chamonix 2014), Chamonix, France, 22 - 25 September 2014, http://indico.cern.ch/event/315665/session/5/contribution/22/material/slides/0.pdf

[7] V. Kain et al., "Injection Protection – Are we taking it seriously? How can we make it safer?", Proceedings of the 2nd Evian Workshop on LHC Beam Operation, Evian, France, 7-9 December 2010, B. Goddard, ed., p. 143-149.

[8] E. Métral, "Pushing the Limits: Beam", Proceedings of the Chamonix 2011 Workshop on LHC Performance - Chamonix 2011, Chamonix, France, 24 - 28 Jan 2011, C. Carli, ed., CERN-ATS-2011-005, p. 252-260.

[9] R.W. Assmann, "Implications of Higher Intensities in the LHC", Proceedings of the Chamonix 2011 Workshop on LHC Performance - Chamonix 2010, Chamonix, France, 25 - 29 Jan 2010, C. Carli, ed., CERN-ATS-2010-026, p. 328-333.

[10] X. Buffat, R. Giachino, W. Herr, G. Papotti, T. Pieloni, R. Calaga, S.M. White, "Observation of Coherent Beam-Beam Effects in the LHC", Proceedings of the 2nd International Particle Accelerator Conference, San Sebastian, Spain, 4 – 9 September 2011.

[11] R. Calaga, R. Tomas, F. Zimmermann, "LHC Crab-Cavity Aspects and Strategy", Proceedings of the 1st International Particle Accelerator Conference, Kyoto, Japan, 23 - 28 May 2010, A. Noda, C. Petit-Jean-Genaz, V. Schaa, T. Shirai, A. Shirakawa, eds., p. 1240-1242.

[12] E. Shaposhnikova, E. Ciapala, E. Montesinos, "Upgrade of the 200 MHz RF System in the CERN SPS", CERN-ATS-2011-042, Proceedings of the 2nd International Particle Accelerator Conference, S. Sebastian, Spain, 4 – 9 September 2011, C. Petit-Jean-Genaz, A. Blanco, I. Etxebarria, F. Perez, A. Wolski, V. Schaa, eds., p. 214-216.

[13] H. Bartosik, G. Iadarola, Y. Papaphilippou, G. Rumolo, E. Shaposhnikova, "Can we ever reach the HL-LHC requirements with the injectors?", Review of LHC and Injector Upgrade Plans Workshop, Archamps, 29-31 October 2013, https://indico.cern.ch/event/260492/session/4/contribution/18/material/paper/0.pdf

[14] HL-LHC Parameter and Layout Committee Parameter table v 4.1.0 (27/8/2014) https://espace.cern.ch/HiLumi/PLC/_layouts/xlviewer.aspx?id=/HiLumi/PLC/SiteAssets/Parameter%20Table.xlsx

[15] R. Bruce, A. Marsili, S. Redaelli, "Cleaning performance with 11 T dipoles and local dispersion suppressor collimation at the LHC", proceedings of IPAC14.

[16] S. Fartoukh, "Pile-Up Density Management at HL-LHC and the Crab-Kissing Scheme", HL-LHC brainstorming coordination meeting, July 2013. (http://indico.cern.ch/conferenceDisplay.py?confId=263083).

[17] S. Fartoukh, "Optics Challenges and Solutions for the LHC Insertion Upgrade Phase I", in Chamonix 2010 Workshop on LHC Performance, Chamonix, France, 25 - 29 January 2010, pp.262-290, CERN-sLHC-PROJECT-Report-0038.

[18] S. Fartoukh, "Layout and Optics Solution for the LHC Insertion Upgrade Phase I", IPAC10 Proceedings.

[19] S. Fartoukh, R. Tomás, J. Miles, "Specification of the closed orbit corrector magnets for the new LHC inner triplet", CERN-sLHC-PROJECT-Report-0030, 2009.

[20] S. Fartoukh, "Towards the LHC Upgrade using the LHC well-characterized technology", CERN-sLHC-PROJECT-Report-0049, 2010.

[21] S. Fartoukh, "Breaching the Phase I Optics Limitations for the HL-LHC", CERN-sLHC-PROJECT-Report-0053, 2011.

[22] S. Fartoukh, "An Achromatic Telescopic Squeezing (ATS) Scheme For The LHC Upgrade", IPAC11 Proceedings.

[23] S. Fartoukh, B. Goddard, W. Höfle, M. Lamont, R. de Maria, R. Miyamoto, G. Müller, L. Ponce, S. Redaelli, R. Steinhagen, M. Strzelczyk, R. Tomás, G. Vanbavinckhove, J. Wenninger, "The Achromatic Telescopic Squeezing Scheme: Basic Principles and First Demonstration at the LHC", IPAC12 Proceedings.

[24] S. Fartoukh, "Achromatic telescopic squeezing scheme and application to the LHC and its luminosity upgrade", Phys. Rev. Spec. Top. Accel. Beams 16 (2013) 111002.

[25] S. Fartoukh, G. Vanbavinckhove, M. C. Alabau Pons, R. Alemany Fernandez, R. Assmann, A. Butterworth, M. Giovannozzi, B. Goddard, P. Hagen, W. Höfle, D. Jacquet, R. de Maria, R. Miyamoto, G. Müller, S. Redaelli, R. Steinhagen, M. Strzelczyk, R. Suykerbuyk, E. Todesco, R. Tomás, W. Venturini, J. Wenninger, F. Zimmermann, "The Achromatic Telescopic Squeezing (ATS) MD part I", CERN-ATS-Note-2011-033 MD, 2011.

[26] S. Fartoukh, M. Lamont, R. De Maria, R. Miyamoto, G. Müller, L. Ponce, S. Redaelli, M. Strzelczyk, R. Tomás, G. Vanbavinckhove, J. Wenninger, M. Albert, R. Giachino, M. Giovannozzi, B. Goddard, P. Hagen, W. Höfle, V. Kain, A. Macpherson, L. Normann, G. Papotti, R. Steinhagen, D. Valuch, D. Wollman, "The Achromatic Telescopic Squeezing (ATS) MD part II", CERN-ATS-Note-2011-060 MD, 2011.

[27] S. Fartoukh, R. Tomás, B. Goddard, W. Höfle, D. Jacquet, G. Kruk, M. Lamont, R. de Maria, R. Miyamoto, G. Müller, M. Pojer, L. Ponce, S. Redaelli, N. Ryckx, R. Steinhagen, M. Strzelczyk, G. Vanbavinckhove, J. Wenninger, "The Achromatic Telescopic Squeezing (ATS) MD part III", CERN-ATS-Note-2011-132 MD, 2011.

[28] S. Fartoukh, V. Kain, Y. Levinsen, E. Maclean, R. de Maria, T. Persson, M. Pojer, L. Ponce, P. Skowronski, M. Solfaroli, R. Tomás, J. Wenninger, "The 10 cm beta* ATS MD", CERN-ATS-Note-2013-004 MD, 2013.

[29] S. Fartoukh, "First demonstration with beam of the Achromatic Telescopic Squeezing (ATS) scheme", in Chamonix 2012 Workshop on LHC Performance, Chamonix, France, 6 - 10 Feb 2012, pp.128-134.

[30] E. Todesco, H. Allain, G. Ambrosio, G. Arduini, F. Cerutti, R. De Maria, L. Esposito, S. Fartoukh, P. Ferracin, H. Felice, et al., "A First Baseline for the Magnets in the High Luminosity LHC Insertion Regions", CERN-ACC-2014-0036, 2014.

[31] S. Fartoukh, R. De Maria, "Database of Baseline Scenarios and Variants: Milestone: MS17", CERN-ACC-2014-0069, 2014.

[32] S. Fartoukh, R. De Maria, "Optics and Layout Solutions for HL-LHC with Large Aperture Nb$_3$Sn and Nb-Ti Inner Triplets", IPAC12 Proceedings.

[33] R. De Maria, S. Fartoukh, A. Bogomyagkov, M. Korostelev, "HLLHCV1.0: HL-LHC Layout and Optics Models for 150 mm Nb$_3$Sn Triplets and Local Crab-cavities", IPAC'13 Proceedings.

[34] R. Calaga, R. De Maria et al., 9th HL-LHC PLC meeting, https://indico.cern.ch/event/315418/

[35] M. Giovannozzi et al., "Optics and Layout Update", 3rd Joint HiLumi LHC– 22nd LARP Collaboration Meeting May 7-8, 2014, BNL, USA, https://indico.bnl.gov/conferenceDisplay.py?confId=730

[36] M. Giovannozzi, S. Fartoukh, R. De Maria, "Specification of a System of Correctors for the Triplets and Separation Dipoles of the LHC Upgrade", IPAC'13 Proceedings.

[37] M. Giovannozzi, S. Fartoukh, R. De Maria, "Initial models of correction systems", CERN-ACC-2014-0010, 2014.

[38] M. Fitterer, "Budget for HL-LHC Orbit Correctors", HSS meeting 14.04.2014, http://ab-dep-abp.web.cern.ch/ab-dep-abp/HSS/HSS_meetings/2014/20140414/HSSMeeting14042014.pdf

[39] M. Fitterer, R. De Maria, "IT BPM tolerances for HL-LHC orbit correction", HSS meeting 26.05.2014, http://ab-dep-abp.web.cern.ch/ab-dep-abp/HSS/HSS_meetings/2014/20140526/HSSMeeting26052014.pdf

[40] O. S. Brüning, P. Collier, P. Lebrun, S. Myers, R. Ostojic, J. Poole, P. Proudlock (eds.), "LHC Design Report, v.1: the LHC Main Ring", CERN-2004-003-V-1, 2012.

[41] J.-B. Jeanneret, "Geometrical Tolerances for the Qualification of LHC Magnets", LHC Project Report 1007 (2007).

[42] M. Korostelev, A. Wolski, R. De Maria, S. Fartoukh, "Optics Transition between Injection and Collision Optics for the HL-LHC Upgrade Project", IPAC13 Proceedings.

[43] M. Korostelev, "Transition between injection optics and collision optics (including ATS squeeze)", 3rd Joint HiLumi LHC-LARP Annual Meeting, 11-15 November 2013, https://indico.cern.ch/event/257368/session/11/contribution/31

[44] R. De Maria, "Parametric Study of Optics Options for the HL-LHC Project", IPAC12 Proceedings.

[45] B.J. Holzer, R. De Maria, S. Fartoukh, A. Chancé, B. Dalena, J. Payet, A. Bogomyagkov, R. B. Appleby, S. Kelly, M. B. Thomas, L. Thompson, M. Korostelev, K. M. Hock, A. Wolski, C. Milardi, A. Faus-Golfe, J. Resta Lopez, "Optics Design and Lattice Optimisation for the HL-LHC", IPAC13 Proceedings.

[46] B. Dalena, J. Payet and A. Chancè, R. De Maria, S. Fartoukh, "High Luminosity LHC matching section layout vs crab cavity voltage", IPAC13 Proceedings.

[47] M. Fitterer, R. Bruce, R. De Maria, S. Fartoukh, "Optics Considerations for PIC and US1 scenarios for HL-LHC in the framework of the RLIUP review", CERN-ACC-NOTE-2014-0031, 2014.

[48] B. Dalena, J. Payet, A. Chancé, R. De Maria, "Alternative high luminosity LHC matching section layout", IPAC14 Proceedings.

[49] M. Giovannozzi, et al., "LHC@Home: A Volunteer computing system for Massive Numerical Simulations of Beam Dynamics and High Energy Physics Events", IPAC12 Proceedings.

[50] S. Fartoukh, M. Giovannozzi, "Dynamic aperture computation for the as-built CERN Large Hadron Collider and impact of main dipoles sorting", Nucl. Instrum. Methods Phys. Res., A 671 (2012) 10-23.

[51] F. Schmidt, "SixTrack - Version 4.2.16 - Single Particle Tracking Code Treating Transverse Motion with Synchrotron Oscillations in a Symplectic Manner – Users' Reference Manual", CERN/SL/94-56 (AP) update (2012).

[52] SixTrack web site http://sixtrack-ng.web.cern.ch/sixtrack-ng/

[53] /afs/cern.ch/eng/lhc/optics/SLHCV3.1b/errors/

[54] /afs/cern.ch/eng/lhc/optics/HLLHCV1.0/errors/

[55] R. de Maria, S. Fartoukh, M. Giovannozzi, E. McIntosh, Y. Nosochkov, Y. Cai, M.-H. Wang, "HiLumi LHC Deliverable Report: Magnet Field Quality Specifications" (awaiting approval), 2014.

[56] Y. Nosochkov, Y. Cai, M.-H. Wang, R. de Maria, S. Fartoukh, M. Giovannozzi, E. McIntosh, "Optimization of Triplet Quadrupoles Field Quality for the LHC High Luminosity Lattice at Collision Energy", IPAC13 Proceedings.

[57] https://espace.cern.ch/HiLumi/WP3/SitePages/MBXF.aspx

[58] https://espace.cern.ch/HiLumi/WP3/SitePages/D2.aspx

[59] E. Todesco, private communication (2014).

[60] M. Fitterer, R. De Maria, M. Giovannozzi, "Powering requirements for HL-LHC triplet", WP2 task leader meeting
18.07.2014, https://indico.cern.ch/event/323862/contribution/2/material/slides/1.pdf

[61] Yi-Peng Sun, Ralph Assmann, Javier Barranco, Rogelio Tomás, Thomas Weiler, Frank Zimmermann, Rama Calaga, and Akio Morita , "Beam dynamics aspects of crab cavities in the CERN Large Hadron Collider", Phys. Rev. ST Accel. Beams 12, 101002, 2009.

[62] J. Barranco García, et al., "Study of Multipolar RF Kicks from the main deflecting mode in Compact Crab Cavities for LHC", IPAC12 Proceedings.

[63] D. R. Brett, et al., "Comparison of Taylor Maps with RF Multipoles in a Thin Lens 6D Tracking Code", IPAC13 Proceedings.

[64] R. Appleby, et al., "Modelling and Long Term Dynamics of Crab Cavities in the LHC", IPAC14 proceedings.

[65] S. Kelly, M.B. Thomas, R. Appleby, L. Thompson, B. Holzer, R. De Maria, S. Russenschuck, "Study of the Impact of Fringe Fields of the Large Aperture Triplets on the Linear Optics of the HL-LHC", IPAC13 Proceedings.

[66] A. Bogomyagkov, et al., "Analysis of the Non-linear Fringe Effects of Large Aperture Triplets for the HL LHC Project", IPAC13 Proceedings.

[67] B. Dalena, et al., "Fringe Fields Modelling for the High Luminosity LHC Large Aperture Quadrupoles", IPAC14 Proceedings.

[68] S. Jones, D. Newton, A. Wolski, "Initial estimate of fringe field effects in HL-LHC using frequency map analysis", IPAC14 Proceedings.

[69] E. Métral, "Initial Estimate of Machine Impedance", CERN-ACC-2014-0005 (2014).

[70] E. Métral, "Initial Estimates of Intensity Limitations", CERN-ACC-2014-0074 (2014).

[71] O. Bruning et al., "LHC Luminosity and Energy Upgrade: A Feasibility Study", LHC Project Report 626, 2002.

[72] F. Ruggiero and F. Zimmermann, "Luminosity Optimization near the Beam-Beam Limit by Increasing the Bunch Length or Crossing Angle", CERN-SL-2002-005-REV (AP), 2002.

[73] F. Ruggiero and F. Zimmermann, "Possible Scenario for an LHC Upgrade", CARE-Conf-05-002-HHH, Proc. of the HHH 2004 Workshop, Geneva, November 2004.

[74] T. Linnecar and E. Shaposhnikova, "An RF System for Landau Damping in the LHC", LHC Project Note 394, 2007.

[75] C. Bhat, "Bunch Shaping in the LHC: a Quick Look", CERN 97th LMC meeting, 22/06/2011.

[76] T. Mertens et al., "Emittance Growth, Debunching and Integrated Luminosity in the LHC with a Higher Harmonic RF System", CERN-AT-Note-2011-071 PERF.

[77] D. Shatilov and M. Zobov, "On the Possibility of Utilizing Flat Longitudinal Beam Profiles to Increase the Luminosity in Collisions with Large Piwinski Angle", 14 April 2012 (unpublished note: https://espace.cern.ch/HiLumi/WP2/task4/Shared%20Documents/flat_long_en.docx).

[78] L. Ficcadenti et al., "Summary of the 800 MHz RF Design", CERN meeting on High Harmonic RF system Review, 27/05/2013 (https://indico.cern.ch/event/254151/).

[79] R. Tomas et al., "HL-LHC: Exploring alternative ideas", Review of LHC and Injector Upgrade Plans Workshop (RLIUP), Archamps, France, 29-31 October 2013.

[80] J.M. Jowett et al., "Future Heavy-Ion Performance of the LHC", Review of LHC and Injector Upgrade Plans Workshop (RLIUP), Archamps, France, 29-31 October 2013.

[81] R. Calaga et al., "A Proposal for a Compact 200 MHz SC-RF System for the LHC", to be published.

[82] C. Tambasco et al., "Beam-Beam and Octupoles Stability Diagrams in the Betatron Squeeze for HL-LHC Optics", CERN beam-beam meeting, 21 August 2014.

[83] S. Fartoukh, "The Sign of the LHC Octupoles", CERN LMC meeting, 11 July 2012.

[84] W. Herr, "Observations of beam-beam effects in the LHC in 2011", Chamonix 2012 Workshop on LHC Performance (2012).

[85] Y. Luo and F. Schmidt, "Dynamic Aperture Studies for LHC Optics Version 6.2 at Collision", LHC Project Note 310 (2003).

[86] A. Valishev et al., "Simulation of Beam-Beam Effects and Tevatron Experience", JINST **7** P12002 (2012).

[87] J. Qiang et al., "A parallel particle-in-cell model for beam–beam interaction in high energy ring colliders", J. Comp. Phys., 198, p. 278 (2004).

[88] T. Pieloni, "A Study of Beam-Beam Effects in Hadron Colliders with a Large Number of Bunches", PhD thesis, EPFL (2008).

[89] W. Herr, X. Buffat, R. Calaga, R. Giachino, G. Papotti, T. Pieloni, D. Kaltchev, "Long Range Beam-Beam Effects in the LHC", CERN-2014-004, pp. 87-92 (2014).

[90] T. Pieloni, X. Buffat, D. Banfi, J. Barranco, G. Arduini, E. Mounet, N. Mounet, S.M. White, J. Qiang, "Two Beam Effects", Proceedings of the 5th EVIAN workshop, Evian, France, 2 – 4 June 2014.

[91] T. Pieloni, "Levelling Scenarios: present and future prospectives", LARP-HiLumi Meeting INFN Frascati 14-16 November 2012.

[92] X. Buffat, D. Banfi, G.R. Coombs, W. Herr, T. Pieloni, "Beam-Beam Effects in Different Luminosity Levelling Scenarios for the LHC", proceedings of IPAC'14, Dresden, Germany, 15-20 June 2014.

[93] D. Banfi, J. Barranco, T. Pieloni, A. Valishev, "Weak-Strong Beam-Beam Simulations for the HL-LHC", proceedings of IPAC'14, Dresden, Germany, 15-20 June 2014.

[94] M. Giovannozzi, "Dynamic Aperture: Simulations vs. Experiments and first DA results in the LHC", 14th HiLumi WP2 Task Leader Meeting, 27 August 2013, https://indico.cern.ch/getFile.py/access?contribId=2&resId=0&materialId=slides&confId=267840.

[95] T. Pieloni et al., "Beam-Beam Effects and Limitations in the HL-LHC", LARP-HiLUMI Collaboration Meeting, 7-9 May 2014, Brookhaven National Laboratory.

[96] M. Giovannozzi et al., "Dynamic aperture performance for different collision optics scenarios for the LHC luminosity upgrade", proceedings of IPAC'13, Shanghai, China, 12-17 May 2013.

[97] T. Pieloni et al., "Preliminary Studies of Beam-Beam Long-Range Effects: orbit, tune, chromaticity for HL-LHC", 35th HiLumi WP2 Task Leader Meeting, 10 October 2014.

[98] A. Valishev et al., "Preliminary estimates of beam-beam effects", HiLumi LHC Milestone Report, CERN-ACC-2014-0066 (2014).

[99] K. Ohmi, "Beam-Beam Effects under the Influence of External Noise", CERN-2014-004, pp. 69-74 (2014).

[100] J. Qiang et al., "Strong-strong beam-beam simulation for LHC upgrade", proceedings of IPAC'14, Dresden, Germany, 15-20 June 2014.

[101] H. Damerau, "LIU: Exploring Alternative Ideas", Review of LHC and Injector Upgrade Plans workshop (RLIUP), Archamps, France, 29-31 October 2013.

[102] E. Métral et al., "Lessons Learnt and Mitigation Measures for the CERN LHC Equipment with RF Fingers", Proc. of the IPAC'13 conference, Shanghai, China, 12-17 May, 2013.

[103] R. Veness et al, "Specification of New Vacuum Chambers for the LHC Experimental Interactions", Proc. of the IPAC'13 conference, Shanghai, China, 12-17 May, 2013.

[104] B. Salvant et al, "RF Analysis of ALICE, LHCb and AFP", 10th CERN LEB Technical Meeting, 15/06/2012.

[105] R. Wanzenberg and O. Zagorodnova, "Calculation of Wakefields and Higher Order Modes for the New Design of the Vacuum Chamber of the CMS Experiment for the HL-LHC", CERN-ATS-Note-2013-018 TECH, 10/04/2013.

[106] B. Salvant et al., "Heat Load from Impedance on Existing and New Hardware in the LHC Era", Joint HiLumi LHC-LARP Annual Meeting, Daresbury, UK, 11-15 November 2013.

[107] B. Salvant et al, "Impedance of New ALICE Beam Pipe", CERN internal TREX meeting, 31 July 2014.

[108] E. Métral and C. Zannini, "Temperature Effects on Image Current Losses in the HL-LHC Triplets – Part 2", 33rd HiLumi WP2 Task Leaders Meeting, CERN, 05 September 2014.

[109] N. Mounet et al., "Impedance Considerations for the Design of the Triplet / D1 Beam Screen", Technical Meeting on Vacuum for HL-LHC, CERN, 05 March 2014.

[110] E. Métral et al., "Expected Impedance and Heat Load of the Present Design of the HL- LHC BPMs", 28th HiLumi WP2 Task Leaders Meeting, CERN, 23 May 2014.

[111] H. Day et al., "TCTP Summary of Power Loss and Heat Load Calculations (with attention paid to the heat load of the ferrite damping material)", LHC collimation working group, 1 October 2012.

[112] H. Day, "Measurements and Simulations of Impedance Reduction Techniques in Particle Accelerators", Manchester university PhD thesis to be published (2013).

[113] B. Salvant et al., "Impedance Aspects of Crab Cavities", HiLumi-LHC/LARP Crab Cavity System External Review, BNL, USA, 05-06 May 2014.

[114] M. Wendt, "Wakefield Analysis of the LHC BSRT Mirror Holder", CERN Internal Impedance Meeting, 9 September 2013.

[115] G. Antchev et al., "Luminosity-independent measurements of total, elastic and inelastic cross sections at √s=7 TeV", CERN-PH-EP-2012-353.

[116] G. Antchev et al., "Luminosity-independent measurements of the proton-proton total cross section at √s=8 TeV", CERN-PH-EP-2012-354.

[117] G. Arduini et al., "PICS: what do we gain in beam performance", Review of LHC and Injector Upgrade Plans Workshop, Archamps, 29-31 October 2013, https://indico.cern.ch/event/260492/session/3/contribution/16/material/slides/7.pdf

[118] R. Jacobsson, private communication (2014).

[119] S. Fartoukh, "Pile up management at the High Luminosity LHC and introduction to the crab-kissing concept", CERN-ACC-2014-0076, (2014).

[120] O. Brüning et al., "HL-LHC: How to achieve Upgrade Scenario 1 goals in the LHC?" Proceedings of the Review of LHC and Injectors Upgrade Plans Workshop, (Archamps, France, 2013).

[121] J.M. Jowett, R. Alemany-Fernandez, R. Assmann, P. Baudrenghien, G. Bellodi, S. Hancock, M. Lamont, D. Manglunki, S. Redaelli, M. Sapinski, M. Schaumann, M. Solfaroli, R. Versteegen, J. Wenninger, and D. Wollmann, "Heavy Ions in 2012 and the Programme up to 2022", Proc. of the Chamonix 2012 Workshop on LHC Performance, CERN-2012-006 (2012).

[122] C.A. Salgado, J. Alvarez-Muniz, F. Arleo, N. Armesto, M. Botje, et al., "Proton-nucleus collisions at the LHC: scientific opportunities and requirements", J. Phys. G39, 015010 (2012).

[123] J.M. Jowett, R. Alemany-Fernandez, P. Baudrenghien, D. Jacquet, M. Lamont, D. Manglunki, S. Redaelli, M. Sapinski, M. Schaumann, M. Solfaroli, Camillocci, R. Tomas, J. Uythoven, D. Valuch, R. Versteegen, and J. Wenninger, "Proton nucleus collisions in the LHC", IPAC 2013, Shanghai (2013), pp. 49-51.

[124] R. Bruce, D. Bocian, S. Gilardoni, and J.M. Jowett, "Beam losses from ultraperipheral nuclear collisions between $^{208}Pb^{82+}$ ions in the large hadron collider and their alleviation", Phys. Rev.ST Accel. Beams **12**, 071002 (2009).

[125] M. Bodendorfer, "Ions: Baseline, Studies Plan and Strategy for Pending Options", LHC Performance Workshop (Chamonix 2014), Chamonix, France, 22 - 25 September 2014, http://indico.cern.ch/event/315665/session/5/contribution/24/material/slides/4.pptx

[126] M. Schaumann, "Semi-empirical model for optimising future heavy-ion luminosity of the LHC", IPAC 2014, Dresden (2014) 1033-1035.

[127] J.M. Jowett, H.-H. Braun, M.I. Gresham, E. Mahner, A.N. Nicholson, et al. "Limits to the performance of the LHC with ion beams", EPAC 2004, Lucerne (2004), pp. 578-580.

[128] H.-H. Braun, R.W. Assmann, A. Ferrari, J.-B. Jeanneret, J.M. Jowett, and I.A. Pshenichnov, "Collimation of heavy ion beams in LHC", EPAC 2004, Lucerne (2004), pp. 551-553.

[129] H.-H. Braun, A. Fassò, A. Ferrari, J.M. Jowett, P.R. Sala, and G.I. Smirnov, "Hadronic and electromagnetic fragmentation of ultrarelativistic heavy ions at LHC", Phys. Rev. ST Accel. Beams 17, 021006 (2014).

[130] Ibid. [40], Chapter 21.

[131] M. Schaumann et al., "Potential of stochastic cooling of heavy ions in the LHC", IPAC 2014, Dresden (2014), pp. 76-78.

Chapter 3

Insertion magnets

G. Ambrosio [10], M. Anerella [3], R. Bossert [10], D. Cheng [17], G. Chlachidze [10], D. Dietderich [17], D Duarte Ramos [5], P. Fabbricatore [13], S. Farinon [13], H. Felice [17], P. Ferracin [5], P. Fessia [5], J. Garcia Matos [7], A. Ghosh [3], P. Hagen [5], S. Izquierdo Bermudez [5], M. Juchno [5], S. Krave [10], M. Marchevsky [17], T., Nakamoto [16], T. Ogitsu [16], J.C. Perez [5], H. Prin [5], J.M. Rifflet [4], G.L. Sabbi [17], K. Sasaki [16], J. Schmalzle [3], M. Segreti [4], M. Sugano [16], E. Todesco [5], F. Toral [7], G. Volpini [14], P. Wanderer [3], X. Wang [17], R.V. Weelderen [5], Q. Xu [16], M. Yu [10]

[3]BNL, Brookhaven National Laboratory, Upton, NY 11973, USA
[4]CEA/SACLAY, DSM/Irfu/SACM - 91191 Gif-sur-Yvette - France
[5]CERN, Accelerator & Technology Sector, CH-1211, Geneva, Switzerland
[7]CIEMAT, Madrid, Spain
[10]FNAL, Fermi National Accelerator Laboratory, Batavia, P.O. Box 500, IL, USA
[13]INFN, Sezione di Genova, I-16146 Genova, Italy
[14]INFN-LASA, Milan, Italy
[16]KEK, Oho, Tsukuba, 305-0801, Japan
[17]LBNL, Lawrence Berkeley National Laboratory, Berkeley, CA 94720, USA

3   Insertion magnets

3.1   Overview

The layout of the HL-LHC insertion magnets is shown in Figure 3-1 and compared to the LHC case in Figure 3-2 . The main technical choices can be summarized as follows [1,2]:

- Maintain a distance of the first magnet to the collision point of ~23 m. This allows to preserve the most critical interfaces with the detectors.

- Increase the triplet coil aperture from 70 to 150 mm to allow a smaller β*. The technology of Nb$_3$Sn has been selected for the quadrupoles [3], allowing an increase in the aperture while keeping the magnet length at acceptable values. The choice of a large coil width (about 36 mm, arranged in two layers of 18-mm-wide cable) aims at reaching the maximum performance in terms of gradient [1,4]. At the same time, the operational current is set at 80% of the loadline, which is a good compromise between risk and performance [5,6]. In these conditions, Nb$_3$Sn can generate 140 T/m operational field [7], corresponding to a triplet length of ~35 m, compared to ~25 m in the LHC with an operational gradient of 200 T/m.

- To recover the 10 m of additional space allocated to the triplet, and further gain space to insert the crab cavities (see Chapters 2 and 4), three steps are taken:

    o We increase the strength of the separation/recombination dipoles from 26 T·m to 35 T·m, thus reducing the D1-D2 distance to 70 m and recovering 15 m.

    o We replace the 20-m-long normal conducting magnet D1 operating at 1.28 T, with a superconducting 6.27-m-long magnet, operating at 5.5 T [8], thus recovering ~14 m;

- o The power feeding of the triplet and D1 is not done through a module placed between D1 and the triplet as in the LHC (indicated by DFB in the Figure 3-2), but through a service module on the D2 side of D1 (not shown in Figure 3-1). This allows to shift D2 towards the IP by a few meters, at the price of having the powering through the D1 to feed the triplet and corrector magnets.
- The Q4 is also shifted by ~5 m away from the Interaction Point (IP)
- The apertures of the magnets between the triplet and the dispersion suppressor have to be increased: D1 from 60 mm to 150 mm, D2 from 80 mm to 105 mm, Q4 from 70 mm to 90 mm, Q5 from 56 mm to 70 mm. For all these magnets, Nb-Ti technology is chosen [1,2], since the potential performance improvement given by Nb_3Sn is not sufficient to justify the additional cost and complexity. Since the size of the magnet is limited by the cryostat, and the aperture is enlarged, for D1, D2 and Q4 we select a small coil width (15 mm) to have enough space for an appropriate iron yoke. We opted to reuse the LHC cable in a single layer configuration to reduce risks (cable properties are well known), ease schedule (lengths are already available), simplify the protection (quench heaters can be replaced by a dump resistor), at the price of a larger operational current.
- All magnets are operating at 1.9 K to have the maximum superconductor performance. This is an important change with respect to the LHC, where D2, Q4, Q5 and Q6 operational temperature is 4.5 K.
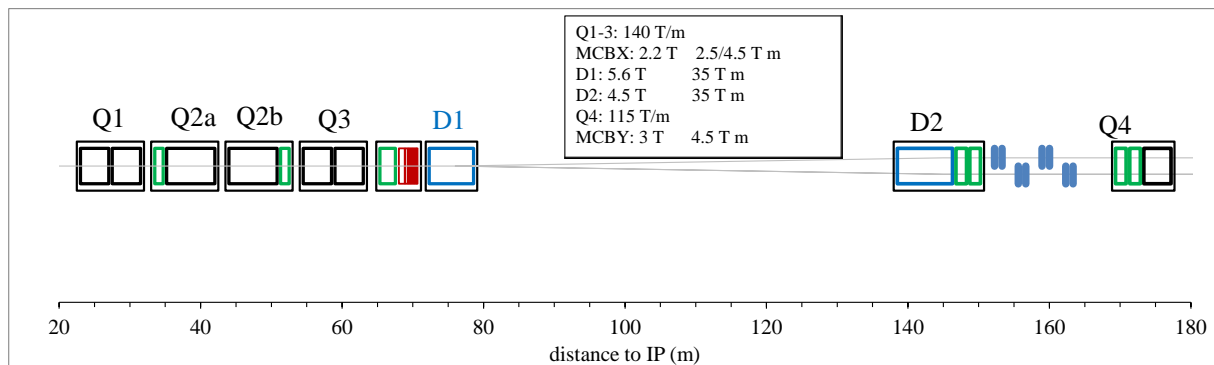
Figure 3-1: **Conceptual layout of the IR region of HL-LHC– thick boxes are magnets, thin boxes are cryostats**
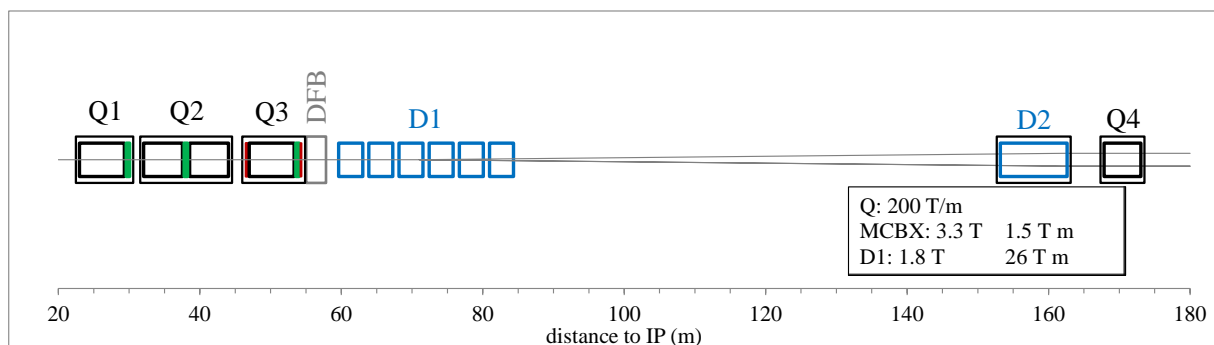
Figure 3-2: **Schematic layout of the IR region of present LHC – thick boxes are magnets, thin boxes are cryostats**

- Three orbit correctors are required in the triplet. The strength is increased from 1.5 T·m (LHC value) to 2.5 T·m for the correctors close to Q2a/b, and to 4.5 T·m for the corrector close to Q3. The position is the same as in the LHC layout, with the exception of the corrector between Q2a and Q2b which is moved between Q2b and Q3.

- A skew quadrupole is used to correct the triplet tilt as in the LHC. Non-linear correctors of order 3, 4, 5, and 6 are required, both normal and skew. With respect to the LHC layout, normal and skew decapole correctors and a skew dodecapole corrector are added. Experience with LHC operation and field quality of the triplet short models will confirm whether these correctors are needed.
- With a nominal luminosity 5 times larger than the nominal design goal of the LHC, a newly designed absorber, using thick tungsten (W) shielding attached to the outer surface of the beam screen (Figure 3-3) is foreseen to reduce the effect of collision debris. The W shielding will limit the radiation damage over the HL-LHC accumulated luminosity of 3000 fb^{-1} to a maximum of 30 MGy and the peak energy deposition to a maximum of 4 mW/cm^3 [9]. These values are similar to the expected heat load and radiation doses for the nominal LHC [10]. The cryogenic system from the triplet to D1 has to absorb 1.2 kW steady state at the nominal luminosity of 5×10^{34} cm^{-2} s^{-1}, half of it is intercepted by the cold mass at 1.9 K and half by the beam screen, where heat is removed at 40-60 K. Note that the system has to be able to remove 50% larger load, corresponding to the ultimate peak luminosity of 7.5×10^{34} cm^{-2} s^{-1}.
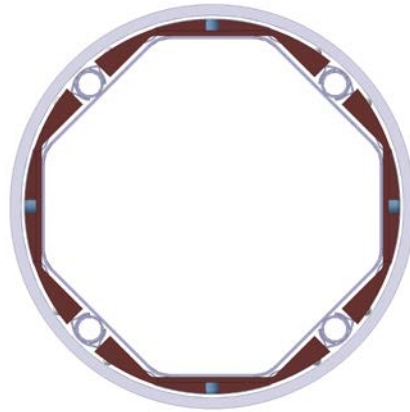
Figure 3-3: Beam screen (grey) with tungsten shielding (dark brown) and cooling tubes in Q1 (left) and in Q2-D1 (right)

The main parameters of the magnets are listed in Table 3-1. In the table, the following conventions have been adopted:
- [1]aperture is the coil inner diameter at room temperature, excluding ground insulation, cold bore and beam screen; distance between apertures is given at 1.9 K;
- [2]magnetic length is given at 1.9 K;
- [3]strand/cable dimensions are given at room temperature, before reaction for the Nb3Sn case;
- [4]insulation dimensions are given at room temperature;
- [5]filling factor is defined as the fraction of superconductor in the insulated cable;
- [6]peak field in the coil is given including the contribution of the strand where the peak is located (what is usually called self-field correction);
- [7]overall current density is average over the whole cross-section of the insulated cable at 1.9 K (i.e. including voids or impregnation and insulation, but not copper wedges);
- [8]loadline fraction is the ratio between the operational current and the short sample current on the load line;

Table 3-1: Overview of the main parameters of the insertion magnets – see text for definitions of footnotes

		Triplet Q1/Q3	Triplet Q2a/b	Short orbit corrector MCBXB	Long orbit corrector MCBXA	Separation dipole D1	Recomb. dipole D2	Large ap. 2-in-1 Q Q4	Orbit corrector MCBRD
Aperture[1]	(mm)	150	150	150	150	150	105	90	100
Field	(T)			2.10	2.10	5.58	4.50		3.00
Gradient	(T/m)	140	140					115	
Magnetic length[2]	(m)	4.00	6.80	1.20	2.20	6.27	7.78	3.83	1.50
Int field	(T m)			2.5	4.5	35.0	35.0		4.5
Int gradient	(T)	560	952					440	
Number of apertures		1	1	1	1	1	2	2	2
Distance between apertures[1]	(mm)						188	194	188
Number of circuits		4	4	16	8	4	4	8	32
Units needed		16	8	8	4	4	4	4	16
Spares		4	2	2	2	2	2	2	2
Cable data									
Material		Nb_3Sn	Nb_3Sn	Nb-Ti	Nb-Ti	Nb-Ti	Nb-Ti	Nb-Ti	Nb-Ti
Cable thick. in.[3]	(mm)	1.438	1.438	0.819	0.819	1.362	1.362	1.362	0.819
Cable thick. ou.[3]	(mm)	1.612	1.612	0.871	0.871	1.598	1.598	1.598	0.871
Cable width[3]	(mm)	18.15	18.15	4.37	4.37	15.10	15.10	15.10	4.37
Ins. thick radial[4]	(mm)	0.150	0.150	0.105	0.105	0.155	0.150	0.160	0.105
Ins. thick azimuth.[4]	(mm)	0.150	0.150	0.105	0.105	0.135	0.130	0.145	0.105
No. strands		40	40	18	18	36	36	36	18
Strand diameter[3]	(mm)	0.850	0.850	0.480	0.480	0.825	0.825	0.825	0.480
Cu/NonCu		1.20	1.20	1.75	1.75	1.95	1.95	1.95	1.75
Filling factor[5]		0.31	0.31	0.25	0.25	0.24	0.24	0.24	0.25
Coil design									
N. layers		2	2	1+1	1+1	1	1	1	1
N. turns/pole		50	50	74/88	74/88	44	31	14	52
Cable length/pole	(m)	430	710	220/240	380/430	600	500	110	310
Operational parameters									
Peak field[6]	(T)	12.1	12.1	4.32	3.5	6.6	5.1	6.0	3.8
Temperature	(K)	1.9	1.9	1.9	1.9	1.9	1.9	1.9	1.9
Current	(kA)	17.46	17.46	2.42 / 2.14	2.42 / 2.14	11.80	12.00	15.65	3.20
j overall[7]	(A/mm^2)	486	486	501 / 443	501 / 443	438	448	573	662
Loadline fraction[8]	(adim)	0.80	0.80	0.60	0.60	0.75	0.65	0.80	0.50
Temperature margin	(K)	4.2	4.2	3.5	3.5	2.5	3.0	2.0	
Stored energy/m	(MJ/m)	1.32	1.32	0.100	0.100	0.342	0.284	0.190	0.174
Inductance/m	(mH/m)	8.22	8.22	15.2 / 24.2	15.2 / 24.2	4.01	3.51	0.77	
Stored energy[9]	MJ	5.28	8.98	0.122	0.223	2.15	2.21	0.73	
Mechanical structure									
Forces x	(MN/m)	2.74	2.74	0.322	0.322	1.53	0.64	0.33	
Forces y	(MN/m)	-3.91	-3.91	0.402	0.402	-0.64	-0.40	-0.47	
F_{mag} stress[10]	(MPa)	130	130	135	135	100	50	35	
Protection									
Circuit inductance[11]	(mH)	132	112	18.3 / 29.1	33.5 / 53.2	25	27	2.9	
Coil energy density[12]	(J/mm^3)	0.092	0.092	0.026 / 0.032	0.026 / 0.032	0.072	0.043	0.062	
Dump resistor[13]	(mΩ)	50	50	300	300	70	70	50	250
Heater circuits[14]		12	12	0	0	4 or 0	4 or 0	0	0
Dose and heat load given by collision debris									
Coil peak power[15]	(mW/cm^3)	1.1/2.5	2.0/2.5	1.1/2.5	1.1	1.3	1.8	0.3	0.6
Heat load cold mass[16]	(W)	110/160	105/130		70	100	50	6	10
Heat load beam screen[16]	(W)	150/60	50/70		45	50	<5	<1	<1
Peak dose[17]	(MGy)	11/33.	22/32	28	44	15	36	8	20

- [9]stored energy is given for the whole magnet: in case of independently powered apertures or of nested magnets, stored energy is given for both circuits powered with maximum nominal current;
- [10]stress is an estimate given by the accumulation of the azimuthal Lorentz forces at nominal current divided by the coil radial width – the impact of the structure, preload and bending is not considered;
- [11]circuit inductance is the differential inductance of the circuit at maximum nominal current;
- [12]energy density is given over the coil volume at 1.9 K, including insulation but not coil parts such as copper wedges and pole pieces;
- [13]dump resistor is estimated using a maximum voltage target of ~750 V;
- [14]the number of heater circuits is the number of independent circuits for each magnet;
- [15]peak power is the maximum deposited power in the coil for nominal luminosity 5×10^{34} cm^{-2} s^{-1} (details on the binning and simulations are given in Chapter 10);
- [16]heat load is given for nominal luminosity 5×10^{34} cm^{-2} s^{-1}, separated between cold mass (this portion is absorbed at 1.9 K) and beam screen (where it is absorbed at 40-60 K); values for the short orbit correctors and for Q2a and Q2b are given together, in the Q2a Q2b column; the load on the interconnections is given in the text. For ultimate performance these values are 50% larger;
- [17]peak dose is as the maximum dose in the magnet (for details on the binning and simulations see Chapter 10).

3.2 Triplet Q1-Q3

Function and operational modes: The triplet ramps with the energy of the LHC, with a nominal gradient of 9 T/m at 450 GeV, and of 140 T/m at 7 TeV. During squeeze, its gradient is constant or decreases of not more than 10%. Q1 and Q3 will be operated in series, and the same for Q2a and Q2b. A 2 kA powering trim is acting on Q3: this is needed for special beam measurements requiring a different powering between Q1 and Q3. The quadrupoles of the triplet are developed by U.S. LARP and CERN.

Cable: A Nb$_3$Sn cable based on 40 strands, with 0.85 mm diameter, has been chosen [7]. Main specifications are:

- the minimum non-copper critical current density of 1400 A/mm2 at 15 T and 4.2 K,

- a strand RRR larger than 150, and (iii) a Cu/no Cu ratio of 1.2 (54.5% of copper in the strand). The cable has a S2 glass braided insulation, whose thickness is 150µm at 5 MPa before reaction. The cable contains a 12-mm-wide, 25-µm-thick stainless steel core to control and reduce the dynamic effects.

Coil, current density and margin: with two layers one can reach the operational gradient of 140 T/m at 0.80 of the short sample limit on the loadline (i.e 20% of loadline margin). Each layer has a copper wedge to tune field quality.

Lengths and transverse size: the triplet is made of Q1 and Q3, each unit requiring magnetic length of 8 m, plus two units Q2a and Q2b each one with a 6.8 m long magnetic length. The U.S.LARP collaboration, in charge of the Q1 and Q3 construction, has proposed to split both Q1 and Q3 in two parts each resulting in 4-m-long magnets separated by 0.5 m. The Q1, Q2 and Q3 cross-sections are the identical, and make use of the same design, technologies and components. The magnet cross-section has a 630 mm diameter, i.e. 60 mm more than the LHC dipoles, including the stainless steel vessel.
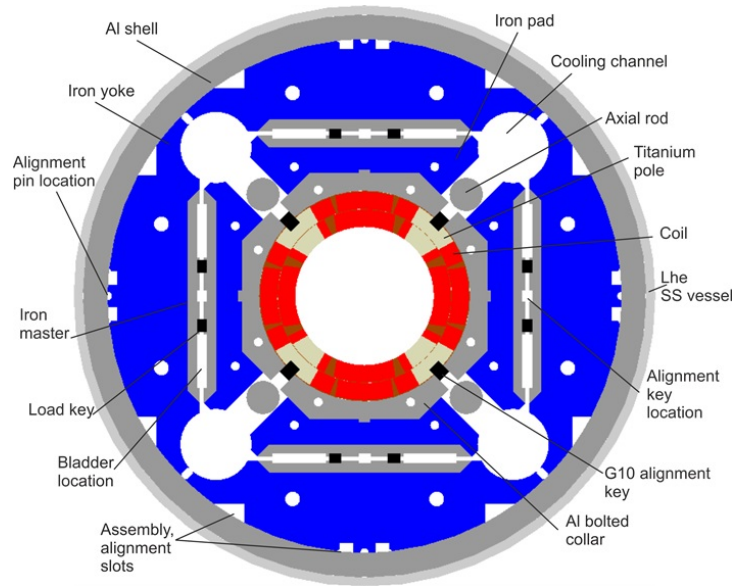
Figure 3-4 Sketch of triplet cross-section

Mechanical structure: the quadrupole makes use of a shell based structure developed at LBNL and within the LARP collaboration [11]. The structure scale up to 3.4 m length was demonstrated in the LARP LR and LQ quadrupole models [12], and features to assure alignment in operative conditions have been included in the 120-mm-aperture quadrupole HQ [13]. The QXF cross-section is a scale up of the HQ design. Coils are mainly prestressed by the Al shell during the cool-down, acting as the structure to contain the Lorentz forces during powering. The level of stress is fine-tuned during the loading of the coil, which is done at room temperature using water-pressurized bladders and interference keys. Typically one has ~70 MPa at room temperature of azimuthal coil compression, which becomes ~150 MPa at 1.9 K thanks to the interplay of the thermal contractions of the different components. The structure keeps the coil under compression up to the ultimate current, corresponding to 150 T/m (7% above nominal).

Protection: The energy density in the coil is ~0.1 mJ/mm3, about twice the Nb-Ti LHC magnets [14]. This makes quench protection particularly challenging. Since the circuit inductance is of the order of 100 mH, only a small fraction of the energy can be extracted on a dump resistor. Therefore we have to rely on quench heaters on the outer layer of the coil, i.e. 25 µm stainless steel strips with a 50 µm polyamide layer to ensure proper insulation. The heaters will have heating stations of 40 mm length, separated by 120 mm section with lower resistance thanks to a 10 µm copper cladding (see Figure 3-5, left). Since the width of the heating stations is 20 mm, two strips independently powered will cover the two blocks of the outer layer; a 6.8-m-long magnet will have ~40 heating stations. The typical time needed to quench the coil is of the order of 15-20 ms following heater firing [15]. Assuming 5 ms for the detection time, a validation window of 10 ms and a few ms for the switch opening, this brings the hotspot temperature at ~350 K [16]. To reduce this value and ensure some redundancy, we plan to have also heaters on the inner layer, and/or use the CLIQ system [17], recently developed at CERN, based on coil heating induced by fast current discharge in the magnet. For the inner layer, heating stations are also needed, with a more complex geometry since a ~50% of the surface must be left free for heat removal. A single strip slaloms between the two blocks, with 25 mm long heating stations and 40 mm long cladding (see Figure 3-5, right). The CLIQ system has the interesting feature of acting rapidly on the inner layer, and therefore is complementary to the outer layer quench heaters. It requires an additional lead to bring the current between coil poles: the viability of this protection system in case of more complex circuits (two magnets in series, with an additional trim) is to be carefully studied.

Figure 3-5: Sketch of quench heaters for the outer layer (left) and a design for the inner layer (right); stainless steel (SS) in grey and copper cladding in red

Field quality: Allowed field harmonics (b6, b10) are optimized at high field, and will be below one unit in absolute value. Contributions of the coil ends have to be taken into account and optimized and/or compensated through the straight part [18]. Fine tuning of b6 can be done in the short model phase through small changes to the coil cross-section. Random components are estimated for a 25 µm random error in the block positioning for non-allowed, and 100 µm for the allowed (see Table 3-2); most critical components are low order harmonics (b3, a3, b4, a4). To minimize these components we opted for a strategy similar to what used in RHIC magnets [19], with magnetic shims to be inserted in the bladder location [20]. This allows correcting (i) ±5 units of b3, (ii) ±5 units of a3, (iii) ±3 units of b4, (iv) ±1 units of a4, for a maximum of two harmonics at the same time, through an asymmetric magnetic shimming.

Table 3-2: Expected systematic harmonics (left) and random components (right) in the triplet

	Geometric	Saturation	Persistent	Injection	High field
b_6	4.20	-3.80	-20.00	-15.80	0.40
b_{10}	-0.37	-0.02	4.00	3.63	-0.39
b_{14}	-0.60	-0.07	0.00	-0.60	-0.67

Order	Normal	Skew
0	Normal	Skew
3	0.82	0.80
4	0.57	0.65
5	0.42	0.43
6	1.10	0.31
7	0.19	0.19
8	0.13	0.11
9	0.07	0.08

Cooling: The magnet is in a static bath of pressurized HeII, with a welded stainless steel shell placed outside the Al structure acting as a helium vessel. Cooling is ensured via two heat exchangers in which saturated HeII circulates, of 68-mm-inner-diameter, housed in the 77-mm-diameter holes of the iron located in the upper part, see Figure 3-4 [21]. This circuit cools the triplet and the short orbit correctors, with the separation dipole and corrector package on a different circuit (see the cooling section for more details). With this design, one can remove comfortably ~800 W, and ultimately ~1000 W, of heat load on the triplet, i.e. 500 W on the cold mass given by debris (see Table 3-1), plus a 100 W budget for other loads (among them the 25 W load on interconnections), with a 50% margin. For the Nb-Ti coils in the LHC, the peak heat deposition target was set at 4 mW/cm3; this has a factor three safety on the 12 mW/cm3 which were considered to be the hard limit. Later experience showed that the hard limit is a factor two larger. In the HL-LHC, thanks to the W shielding, we are always below the 4 mW/cm3 target. Considering that Nb3Sn conductor is expected to have three times larger margin, peak power in HL-LHC will not be critical.

The heat loads from the coils and the beam-pipe area can only evacuate to the two heat exchangers by means of the pressurized HeII. To this end the cold mass design shall incorporate the necessary helium passages: 1.5 mm annular spacing between cold bore and inner coil-block, and free passage through the coil pole and subsequent G10-alignment key. The free passage needed through the coil pole and G10-alignment key in the transverse direction is estimated to be at least 4% (equivalent to 8 mm diameters holes repeated every 40 mm).

Cryostat: Independent cryostats are used for each one of Q1, Q2a, Q2b and Q3. The Q1 and Q3 cryostats contain two 4-m-long magnets. The Q2a and Q2b cryostats contain the 6.8-m-long magnet plus the orbit correctors described in the next section. The cryostat size should be able to accommodate the cold mass, the shielding and the cooling pipes. First estimates show that the standard size of 980 mm (including flanges) is very tight to fit all these components. Two options are being considered [22]: a 1050-mm-diameter cryostat, and an elliptic cryostat (see Figure 3-6).
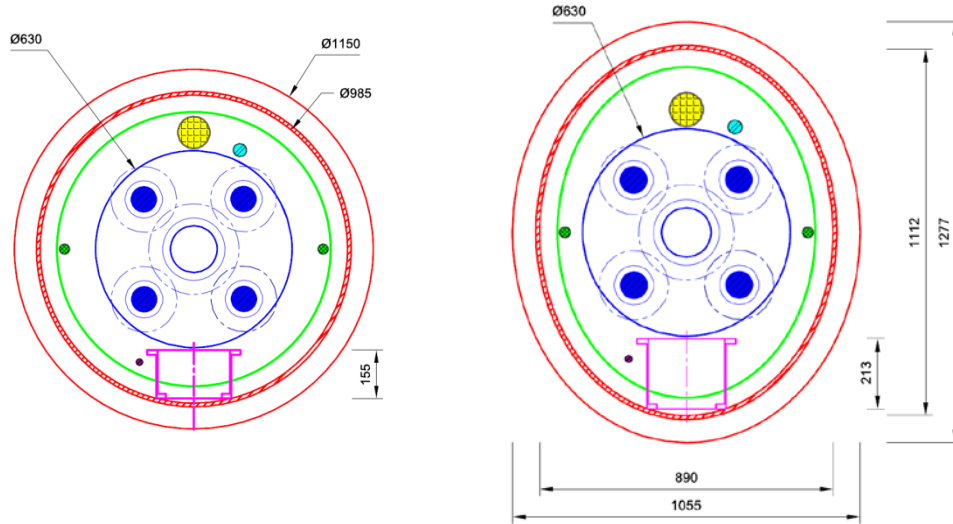
Figure 3-6: Possible cross-sections of the cryostat: larger diameter (left) and elliptical solution (right)

3.3 Orbit correctors

Function and operational modes: The orbit correctors are single aperture magnets. Two versions are required, providing 2.5 T·m and 4.5 T·m integrated field respectively. To have a more compact layout, a nested design has been adopted, with horizontal and vertical dipole coil in the same cross-section (see Figure 3-7). The field in each plane has been limited to 2.1 T, giving a maximum combined field of 3 T. Powering will be allowed in a square in the H/V plane, with both positive and negative currents. These magnets are used to create the crossing angle and partially to correct quadrupole misalignment. Orbit correctors are being developed by CIEMAT [23].

Cable: The 4.5-mm-wide Nb-Ti cable developed for the S-LHC corrector [24] is adopted. This is based on a 0.48-mm-diameter strand, arranged in a Rutherford cable with 18 strands.

Coil, current density and margin: With one layer per dipole direction, it can reach the operational field of 2.1 T simultaneously in both planes at 60% of the loadline.

Lengths and transverse size: The magnetic length is 1.2 m for the short version (MCBXB) and 2.2 m for the long one (MCBXA). The magnet cross-section has a 570 mm diameter, including the stainless steel vessel, i.e. as the LHC dipoles and D1. Cooling channels are shared with the quadrupoles for MCBXB, so the iron has 77-mm-diameter holes at 45°. MCBXA will share cooling channels with D1, thus the iron has 60-mm-diameter holes as in D1 (i.e., at 90° and 270º).

Mechanical structure: The magnet makes use of iron and shell support and collars. An aluminium shell is used to increase the rigidity of the assembly, applying a pre-stress through the iron that will increase during cool-down. Approximately 20-mm-thick collars are used for keeping the inner coil, and the same for the outer coil. Due to the nested option, a complex collaring based on two steps

(first the inner, then the outer) is needed. The inner collars are closed with 2 round pins, meanwhile the outer ones will be kept in place by 4 prismatic keys. A difficulty is that when both H and V coils are powered, Lorentz forces push the inner coil towards the centre of the aperture: this requires a structure between the inner coil and the cold bore to prevent movements. A titanium tube has been proposed as a solution, given that its contraction coefficient is lower than those of the rest of materials. All these issues are being addressed at the moment of writing.
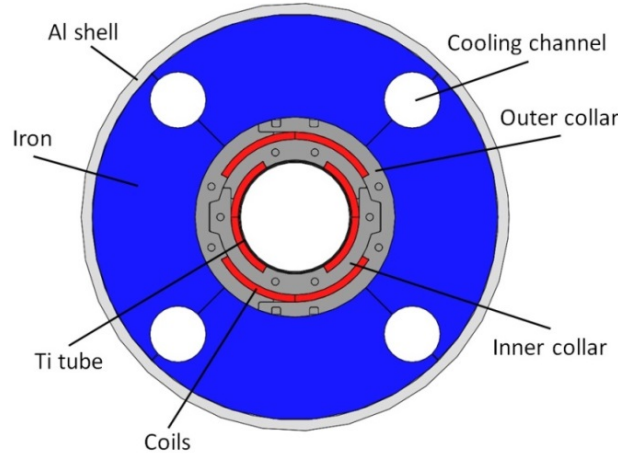
Figure 3-7: Sketch of orbit corrector cross-section (short version MCBXB, in the cold mass of the triplet magnets Q2a and Q2b)

3.4 High order correctors

Function, design and operational modes: The high order correctors (skew quadrupole, normal and skew sextupole, octupole, decapole and dodecapole) are specified on the expected field quality and alignment errors (see Chapter 2), with a safety factor 2 on the quadrupole, sextupole and octupole, and 1.5 on the decapole and dodecapole. The magnets shall operate with settings based on the measured field errors of the triplet and separation dipole. To ease operation a non-nested layout (see Figure 3-8) has been adopted, with a superferric technology, already developed for the S-LHC [25]. Nb-Ti racetrack coils provide the ampere-turns, with iron giving the required field shape. The aperture is 150 mm as the triplet and D1 (see Figure 3-9). The high order correctors are being developed by INFN-Milano.
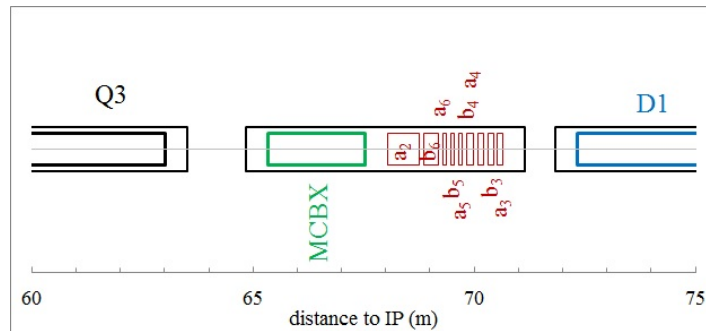
Figure 3-8: **Layout of the corrector region (left), and sketch of skew quadrupole cross-section (right)**
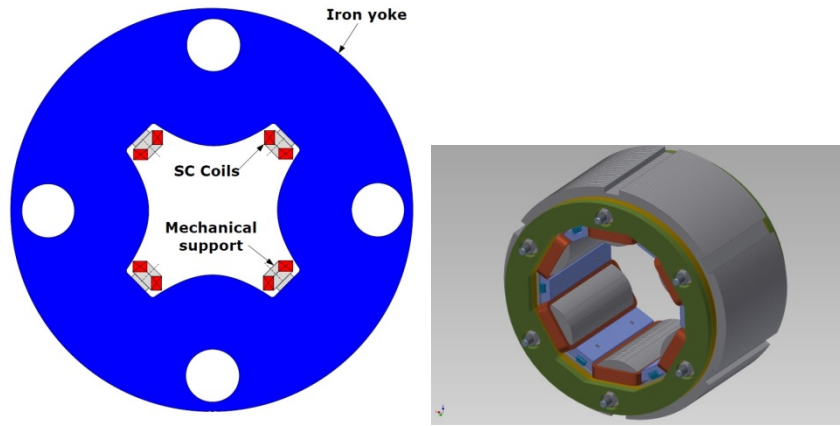
Figure 3-9: **Cross-section of the skew quadrupole (left) and 3 D view for a sextupole (right)**
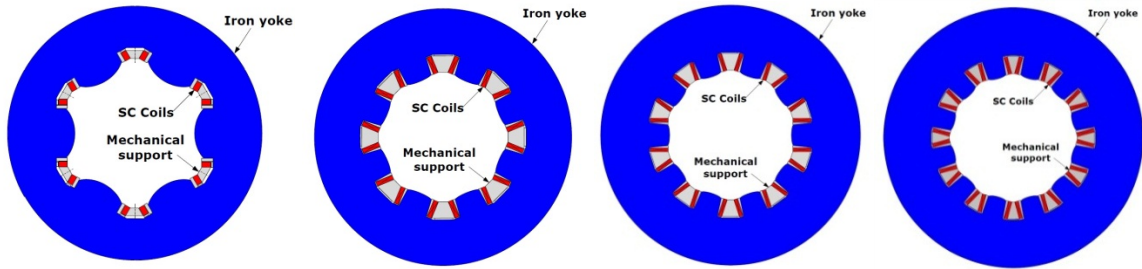
Figure 3-10: Sketch of nonlinear corrector cross-sections for normal sextupole, octupole, decapole and dodecapole correctors, and 3 D view for a sextupole

Cable: It is a single Nb-Ti strand, with 0.7 mm (for the quadrupole) and 0.5 mm diameter (for the higher orders). Insulation is done with a 0.07-mm-thick S2 glass. Further ground insulation is added on the external side of the coil.

Coil, current density and margin: We chose to operate at 60% on the loadline. The optimization [26] provides a current density of the order of 300 A/mm2, with peak fields on the coil in the range 2.0-2.3 T for the nonlinear correctors, and 3.0 T for the skew quadrupole (see Table 3-3). Coils are impregnated with CTD-101.

Lengths and transverse size: The magnet coil lengths are ~0.1 m for sextupole, octupole, decapole and skew dodecapole (see Table 3-3). The normal dodecapole and the skew sextupole require larger strengths, giving a coil length of ~0.45 m and ~0.84 m respectively. For the skew quadrupole one needs a 460 mm diameter iron that has to include the cooling holes for the heat exchanger of D1 and orbit corrector. The nonlinear correctors can have an iron diameter of 320 mm, which fits inside the cooling holes. Spacers are required to match the transverse size of the correctors to the same value of the orbit correctors MCBXA, and to align in the cold mass. Heat exchangers will go through these spacers to cool the whole cold mass.

Mechanical structure: The mechanical support for the correctors coils are under study. The forces are of the order of 60 kN/m for the quadrupole, and 10-30 kN/m for the other magnets.

The main parameters of the correctors are given in Table 3-3, where the following conventions are adopted:

[1]Integrated strength is defined as the field at the 50 mm reference radius times the magnetic length;

[2]Coil length refers to the physical coil length, and not to magnetic length;

[3]The overall current density includes 0.07-mm-thick strand insulation and the coil ground insulation.

Table 3-3: **Overview of the main parameters of the triplet corrector magnets**

		MCQSX	MCSX/MCSSX	MCOX/MCOSX	MCDX/MCDSX	MCTX	MCTSX
Order		2	3	4	5	6	6
Aperture	(mm)	150	150	150	150	150	150
Integrated strength[1]	(T m)	1	0.06	0.04	0.03	0.086	0.017
Coil length[2]	(mm)	841	123	99	107	449	102
Gradient	(T/m^{n-1})	25	11	3690	50600	640000	613000
Number of apertures		1	1	1	1	1	1
Number of circuits		1	2	2	2	1	1
Units needed		4	8	8	8	4	4
Spares		2	2	2	2	2	2
Cable data							
Strand diameter	(mm)	0.700	0.500	0.500	0.500	0.500	0.500
Insulation thickness	(mm)	0.070	0.070	0.070	0.070	0.070	0.070
Cu/No_Cu		2.3	2.3	2.3	2.3	2.3	2.3
Coil design							
Material		Nb-Ti	Nb-Ti	Nb-Ti	Nb-Ti	Nb-Ti	Nb-Ti
N. turns/pole		320	214	344	256	154	172
Cable length/pole	(m)	604	79	88	67	144	42
Operational parameters							
Coil peak field	(T)	2.97	2.33	2.41	2.34	2.04	2.01
Temperature	(K)	1.9	1.9	1.9	1.9	1.9	1.9
Current	(A)	182	132	120	139	167	157
j overall[3]	(A/mm^2)	303	353	314	360	259	284
Loadline fraction		0.60	0.60	0.60	0.60	0.60	0.60
Differential inductance	(mH)	1247	118	152	107	229	52
Stored energy	(kJ)	24.6	1.24	1.41	1.39	4.35	0.92
Dose and heat load							
Heat load cold mass	(W)			70			
Heat load beam screen	(W)			45			
Peak dose	(MGy)			44			

3.5   Separation dipole D1

Function and operational modes: the separation dipole is ramped with the energy of the LHC, and is constant during squeeze. Each magnet is independently powered. The separation dipole is being developed by KEK.

Cable: The 15-mm-wide Nb-Ti cable used for the outer layer of the main LHC dipole is adopted (see Figure 3-11). The required unit length is smaller than the main LHC dipole outer cable unit length (780 m).

Coil, current density and margin: In the initial choice of 70% operational level, the magnet length was slightly longer than the KEK test station [8,27]. We therefore fixed the operational current at 75% of the loadline. This allows reaching an operational field of 5.58 T and a magnetic length of 6.27 m, fitting the vertical test station without significantly increasing the risk related to the lower margin.

Lengths and transverse size: The magnet cross-section has a 570 mm diameter, including the stainless steel vessel, i.e. as the LHC dipoles. A larger diameter has been excluded to be able to reuse the yoking tooling used for J-PARC in KEK.

Mechanical structure: forces are kept by the iron, with thin spacers between the iron and the coil, as the J-PARC [28], RHIC magnets [29], and LHC Q1/Q3 [30]. Here the prestress is given by the iron laminations, horizontally split, that are locked through keys (see Figure 3-10). A thin stainless steel collar acts as a spacer between the coil and the iron. An average prestress of 90 MPa is given at room temperature during the so-called yoking. During cool down the prestress lowers to 70 MPa, enough to counteract the Lorentz forces during powering.

Protection: The large cable and operational current of 12 kA (see Table 3-1) will probably allow to safely operate with an energy extraction on a dump, and without quench heaters. Simulations show that with a 75 mΩ resistor the hotspot temperature in the adiabatic approximation is 220 K for the nominal current of 12 kA. Quench heaters or CLIQ [17] are still being considered to add margin and redundancy.

Field quality: The main issue here is the saturation component [8], which is optimized via the iron shaping (see Table 3-4). Following the analysis given in [31,32], the random components are estimated through random positioning of the coil block with different amplitudes for each family of harmonics, namely 40 µm for the allowed b_{2n+1}, 30 µm for the even skew a_{2n}, 15 µm for the odd skew a_{2n+1} and 10 µm for the even normal multipoles b_{2n}.

Cooling: The magnet is in a static bath of pressurized HeII, with a stainless steel shell acting as a helium vessel. Cooling is ensured via two heat exchangers, of 49 mm inner diameter, housed in the 60 mm diameter holes of the iron.

Cryostat: The cryostat has the same geometry of the triplet cryostat (see Figure 3-6).
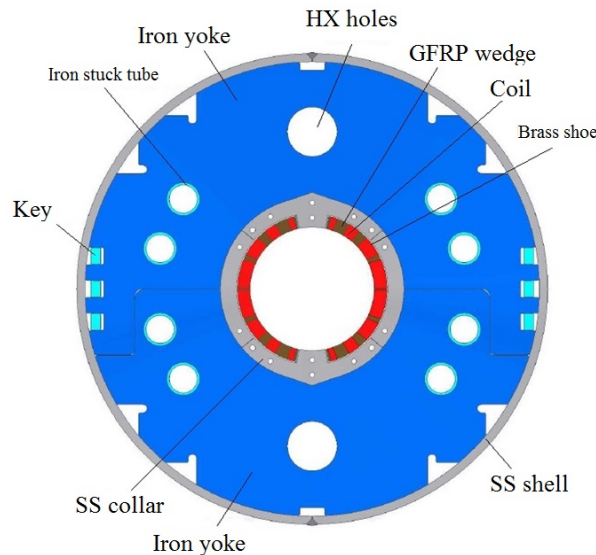
Figure 3-11: Sketch of separation dipole cross-section

Table 3-4: Expected systematic harmonics (left) and random components (right) of the D1

	Geometric	Saturation	Persistent	Injection	High field
b_3	-1.80	0.90	-14.20	-16.00	-0.90
b_5	0.50	-0.50	-1.00	-0.50	0.00
b_7	1.60	-1.20	-0.70	0.90	0.40
b_9	-0.68	0.09	0.02	-0.66	-0.59
b_{11}	0.44	0.03	0.00	0.44	0.47

Order	Normal	Skew
2	0.20	0.68
3	0.73	0.28
4	0.13	0.44
5	0.36	0.15
6	0.06	0.18
7	0.16	0.06
8	0.03	0.06
9	0.06	0.02
10	0.01	0.03
11	0.02	0.01

3.6   Recombination dipole D2

Function and operational modes: the recombination dipole is ramped with the energy of the LHC, and is constant during squeeze. Each magnet is independently powered, and the two apertures are in series. The fields point in the same direction in both apertures; this makes field quality control much more challenging than in the LHC dipole, where the field points in opposite directions. The design of the recombination dipole is being studied by INFN-Genova.

Cable: The 15-mm-wide Nb-Ti cable used for the outer layer of the main LHC dipole is adopted. The required unit length is not larger than the LHC main dipole outer layer unit length (780 m).

Coil, current density and margin: We selected a conservative margin, operating at 65% of the loadline with a single layer 15-mm-width coil, and an operational field of 4.5 T. In these conditions, the approach used in the current D2, using iron to magnetically decouple the two apertures, leads to large saturation effects. An alternative approach using left-right asymmetric coils was therefore adopted [33] to compensate for the cross-talk between the two apertures (see Figure 3-12). A very careful optimization is needed to find the best solution. After some iteration, it has been found a cross-section where the left-right asymmetry is only given by the angles of the blocks, but the number of cable per block is the same [34]. This allows much simpler coil heads.

Lengths and transverse size: The magnetic length is 7.78 m. The magnet requires an adequate iron thickness to reduce the fringe field. An elliptical iron is proposed, with 570 mm vertical size and 630 mm horizontal size.

Mechanical structure: The square design of the central aperture in the iron is imposed by the field quality optimization, namely the reduction of the field harmonics due to saturation. The accumulation of Lorentz forces correspond to a pressure in the midplane of about 40 MPa. A self-supporting stainless steel twin collar, where the iron acts only as alignment, is shown to be viable, with a peak stress during collaring of the order of 100 MPa [35]. The alternative structure with separated stainless collars, allowing more flexibility in the production, is also being considered.

Protection: Protection will be probably based on quench heaters; studies are in progress at the moment of writing.

Field quality: is the main issue in this magnet. The cross-talk is optimized via the asymmetric cross-section, and the saturation through an iron shaping. Field quality tables are still in progress at the time of writing.

Cooling: The magnet is in a static bath of pressurized HeII. Cooling is ensured via two heat exchangers, of 51 mm diameter, housed in the 60 mm diameter hole of the iron located in the upper part.
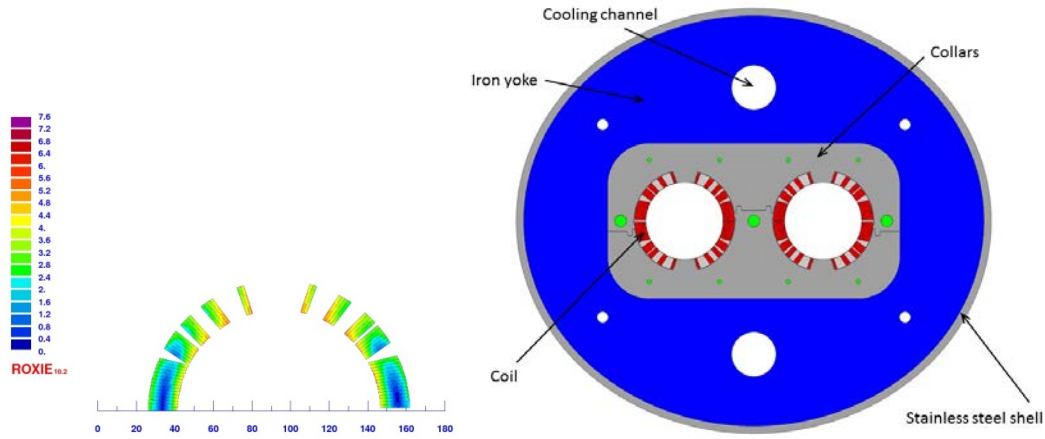
Figure 3-12: Sketch of recombination dipole cross-section: asymmetric coil (left) and magnet cross-section (right)

3.7   D2 and Q4 correctors

Function and operational modes: both D2 and Q4 need orbit correctors for each beam and each plane (H and V), with an integrated strength of 4.5 T·m. An aperture of 100 mm is required. In the preliminary layout, a field of 3 T for a magnetic length of 1.5 m has been allocated. These correctors are used to open the crossing angle and to correct the closed orbit, and therefore they should be powered in any configuration.

Cable: The 4.5-mm-wide Nb-Ti cable used for the single aperture orbit corrector is considered.

Coil, current density and margin: With one layer, one can reach the operational field of 3 T with a comfortable margin (~40%) on the loadline.

Field quality: the challenge in these magnets is the cross-talk between the apertures. Since the beam distance is at 194 mm, and the aperture is 100 mm, little space is left for the iron to decouple the two apertures [36]. No optimization can be made through iron or coil cross-section as in the case of D2 since these magnets have to be powered with any combination of currents. The solution is to keep the coil width as small as possible and to have thin collars to maximize the iron thickness. Requirements on field quality are stringent, especially on b3 where the tolerance is of the order of 1.5 units. Given these constraints, the operational field will probably have to be lowered to reduce the cross-talk. Special ferromagnetic laminations are also considered as an option to further decrease the coupling between the apertures.

Mechanical structure: 15-mm-thick collars would provide a self-supporting structure, allowing to use the iron to align the two modules, and to shield the fields.

Cooling: The magnets will share the cooling with D2 and Q4, so will have the heat exchangers in the same position.

3.8   Large aperture two-in-one quadrupole Q4

Function and operational modes: the Q4 quadrupole (MQYY) is ramped with the energy of the LHC. During the squeeze the gradient is lowered and a minimum operational current of 3% of nominal is required, to allow flexibility to the optics. The two apertures are independently powered, with a possible current unbalance up to 50%. The gradients shall have the same sign in both apertures, resulting in a focusing effect for one beam and defocusing for the other one. A Q4 short model, however of single aperture only, is being developed by CEA-Saclay.

Cable: The 15-mm-wide Nb-Ti cable used for the outer layer of the main LHC dipole is adopted. The required unit length is much smaller than the LHC unit length (780 m), so short lengths of the production that could not be used in the dipoles can be employed, at zero cost and not affecting the LHC dipole spares. Insulation is based on the enhanced scheme proposed in [37], allowing a direct path from the cooling bath to the strand.

Coil, current density and margin: With one layer, can reach the operational gradient of 115 T/m at 80% of the loadline [38].

Lengths and transverse size: The magnetic length is 3.83 m. The magnet cross-section has a 497.5 mm nominal diameter, including the stainless steel vessel, i.e. as the LHC main quadrupoles.

Mechanical structure: the quadrupole makes use of self-standing collars, as the main LHC quadrupoles [39] or MQXC [40]. Here the prestress is given by the 25-mm-thick thick collars, which are locked through keys. An average prestress of 80 MPa is given at room temperature after the so-called yoking. Then, 30% of prestress is lost due to cable insulation creep, leading to 55 MPa. During cool down the prestress lowers to 40 MPa, enough to counteract the Lorentz forces during powering. The iron is used to separate magnetically the two apertures, close the flux lines and provide alignment. The shells will be probably welded with the quadrupole and the correctors, since an inertia tube would become too long (8 m) for the vertical assembly.

Protection: The large cable and operational current will allow to safely operate with energy extraction on a dump. Simulations show that with a 50 mΩ resistor the hotspot temperature in the adiabatic case is below 200 K.

Field quality: The coil has three blocks, allowing to have b6 and b10 within 1 unit and b14 within 2 units (see Table 3-5). Shimming on the pole and in the midplane is foreseen to allow steering b6 in the model/prototype phase. An estimate of the random component is given in Table 3-5.

Cooling: The magnet is in a static bath of HeII, with a stainless steel inertia tube acting as a helium vessel. Cooling is ensured via one heat exchangers of 51 mm diameter, housed in the 60 mm diameter holes of the iron located in the upper part.

Cryostat: The cryostat will include the quadrupole plus two orbit correctors (see previous section), for a total length of about 8 m.
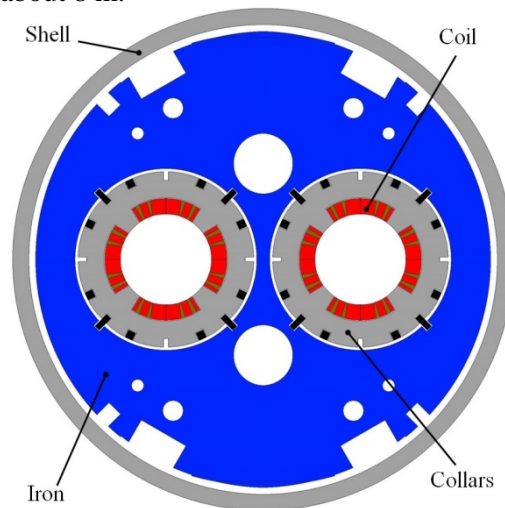
Figure 3-13: Sketch of Q4 cross-section

Table 3-5: **Expected systematic harmonics (left) and random components (right)**

	Geometric	Saturation	Persistent	Injection	High field
b_6	-0.45	0.40	-11.00	-11.45	-0.05
b_{10}	0.00	0.00	1.00	1.00	0.00
b_{14}	1.50	0.00	0.00	1.50	1.50

Order	Normal	Skew
3	1.79	1.79
4	1.16	1.16
5	0.75	0.75
6	1.93	0.48
7	0.31	0.31
8	0.20	0.20
9	0.13	0.13
10	0.34	0.08

3.9 Q5

For the Q5 magnet, the present baseline is to replace it with a 70-mm-aperture MQY [41] (today the Q4 around IP1 and IP5), operated at 1.9 K. With an operational current of 4510 A, it reaches an operational gradient of 200 T/m. As for Q4, apertures are independently powered. There are seven available spares, plus four MQY that will be recovered from IP1 and IP5 in the Q4 position. An alternative option, requiring a larger aperture, is also under consideration. In this case the 90 mm aperture Q4 would be also used as Q5, in a longer length or with two units.

3.10 Powering

The baseline of the powering scheme of the triplet-corrector-separation dipole is shown in Figure 3-14. The powering is from the D2-side of D1, allowing a more compact layout with respect to the LHC, where this is done through a distribution feedbox taking few meters between the triplet and D1. This choice improves performance at the price of having triplet and corrector cables going through (or along) the separation dipole. The second important choice is that magnets are fed by a superconducting link: therefore the transition from superconducting to resistive leads is shifted from the neighbourhood of the beam line. For the triplet, the baseline option is to have Q1 and Q3 in series, and Q2a and Q2b in series, with two 20 kA independent power converters, plus a 2 kA trim on Q3. This configuration provides a good compromise between cost and operation. Other options are under considerations at the moment of writing

-   Power in series Q1 and Q2a, and Q2b and Q3; this configuration allows to have a compensation of the power converter ripple between couple of focusing/defocusing quadrupoles, at the price of a smaller flexibility in the optics.
-   All four magnets in series, with a single 20 kA power converter. In this case a 2 kA trim is needed on Q1 and a second trim on Q3. This configuration minimizes the cost of the hardware, but is the more complex from the point of view of operation. It also provides the largest inductance per circuit, increasing the challenges related to the busbar and magnet protection.
-   Four independent circuits for Q1, Q2a, Q2b, and Q3, with four 20 kA power converters. This solution provides the best flexibility for optics and operation at the higher hardware cost. It also provides the lowest inductance per circuit, easing protection of the busbar and of the magnet.

Besides the triplet, one has one 13 kA circuit for the D1, and six 3 kA circuits for the orbit correctors, plus the nine correctors rated at 200-300 A. In the baseline case, with 20 kA circuits for the triplet, one has a total of ~70 kA of current to bring in and out of the triplet-D1 area through the link (see chapter 6). For the busbar the baseline is to place it inside the magnet (as in the LHC main cell), through the iron holes which are not used by the heat exchangers; two options are also under study:

-   Busbar inside the cryostat, but outside the cold mass, in a separate line (as the M line in the LHC cell, carrying some correctors busbars).

- Busbar outside the cryostat in a separate cryostat; in this case each magnet is fed by a bypass of the busbar cryostat.

The matching section is fed by a second superconducting link, bringing current to the recombination dipole D2, the Q4, and the orbit correctors. Here we have one 13 kA circuit for D2, two 20 kA circuits for Q4, and four 3 kA circuit for the orbit correctors, for a total of 65 kA.
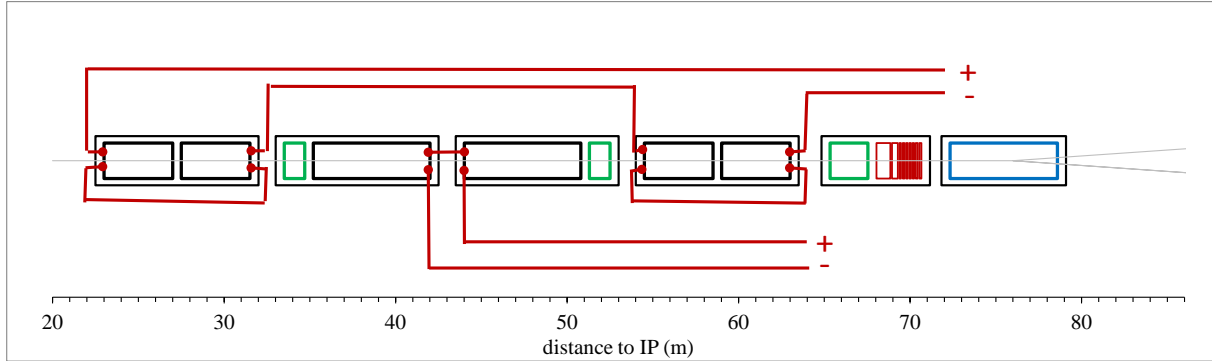
Figure 3-14: **Sketch of baseline for triplet powering (trims not shown)**

3.11 Cooling

The static heat load on the cold mass is mainly due to collision debris: 500 W on the triplet, and 70 W on the separation dipole. A factor 1.5 has to be applied to these estimates to be compatible with the ultimate luminosity of 7.5×10^{34} cm^{-2} s^{-1}. The heat load on the triplet is removed via two 68-mm-inner-diameter heat exchangers providing ability to remove up to 1000 W ultimately (see Figure 3-15). To cope with these high heat loads, an additional low pressure pumping is added between Q2a and Q2b to keep the two-phase vapour flow velocity below 7 m/s, above which the HX's would not function correctly anymore. These heat exchangers also cool the 1.2-m-long orbit corrector. Simulations show that a solution with one (or more) heat exchangers cooling the whole string triplet-D1 is not viable. Therefore, a second system of heat exchangers is used to cool the corrector package and D1, which receive 50 and 70 W respectively at nominal luminosity. Here the baseline is to have two heat exchangers of 49 mm inner diameter, able to remove 250 W. One heat exchanger would provide only 125 W, barely enough to remove the 120 W due to collision debris, without the required 50% margin. An additional low pressure pumping is added between Q2a and Q2b.

The beam screen receives ~500 W in the triplet-correctors-D1 region (see Table 3-1, including 80 W from the interconnections). Given a 50% margin to reach ultimate peak luminosity, and a 150 W budget for the residual effect of electron cloud, one has to remove ~975 W over 55 m, i.e. ~17 W/m. Heat is removed at 40-60 K [42]. The cooling tubes inner diameter is kept ~7 mm thanks to an increase of the pressure of the helium to 18 bar. This choice is more challenging for the piping system but allows minimizing the space taken by the cooling pipes, which reduces the aperture available to the beam.
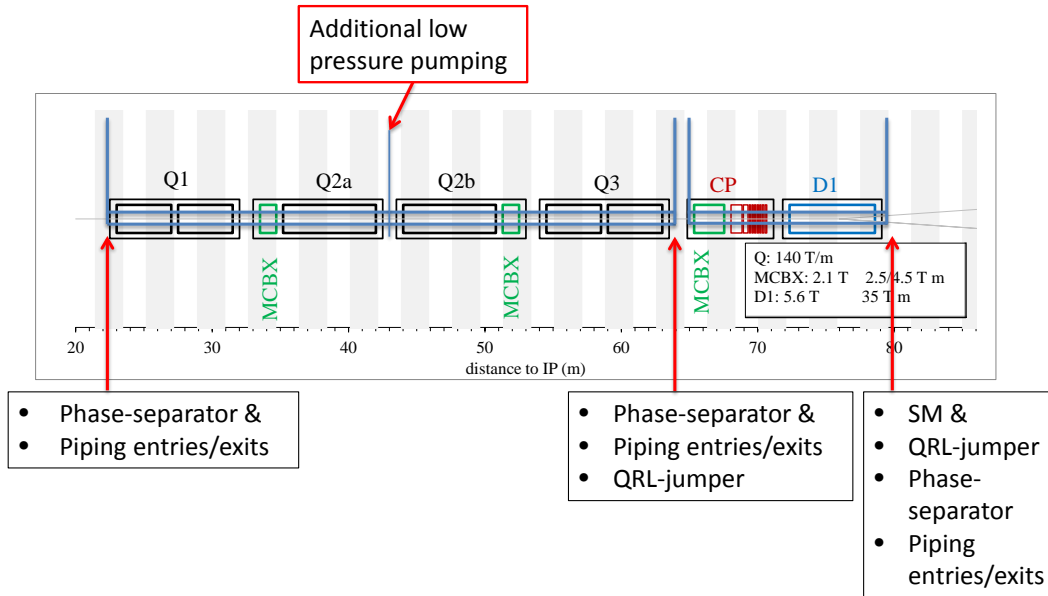
Figure 3-15: **Sketch of the cooling**

For the stand-alone magnets, the jumper is located on the upper part of the slope, and the symmetry of the cryostat with respect to the interaction point is lost. This means that the left and right cryostats are not interchangeable, but the piping needed for the cooling system is simpler. This choice cannot be taken for the triplet, where there is no space for a jumper between the quadrupole and the interaction point. So the jumper is on the D1 side, requiring an additional return pipe.

3.12 Instrumentation

We give here a short summary of the instrumentation foreseen for the IR magnets.
- Quench protection requires voltage taps; for dipoles and quadrupoles we foresee possibility of monitoring the voltage on each coil. Quench detection is therefore based on the analysis of the difference between signals of different coils, thus allowing to cancel the inductive voltage.
- Beam loss monitors will be located inside the triplet cold mass to have the possibility of monitoring beam losses closer to the beam pipe and to the coil. It is foreseen to install special beam loss monitors in one of the iron holes not used by the heat exchangers or by the busbars.
- Temperature sensors: one per cold mass, plus a spare, as in the LHC.
- Strain gauges: all quadrupoles, based on the bladder and key structure will have strain gauges on the Al shell. Gauges will be installed also on the coil (winding pole) in the model and prototype phase, and possibly during production. One could consider having these signals extracted from the cryostat to have them available during operation. In the case of the LHC dipoles, strain gauges were used in the initial prototyping phase only.
- Beam position monitors will be placed in the interconnections between Q1 and Q2a, Q2b and Q3, Q3 and the corrector package, and between the corrector package and D1. Moreover they will be present close to D2, Q4 and Q5.

3.13 Test

In general, magnets will be tested individually in a vertical test station, and then horizontally in the final cold mass assembly within the final cryostat. In some cases the first test will be possible in laboratories collaborating with CERN (for instance FNAL for the Q1/Q3, and KEK for the D1). The second one will be carried out at CERN. A string including the magnets from Q1 to D1 will be assembled in the CERN test facility (SM18) by 2019-2020. Magnetic measurements at 1.9 K with the rotating coil technique

will be carried for all main magnets and for all the low order (dipole and quadrupole) correctors. For the high order corrector the magnetic measurement strategy is still to be defined.

3.14 References

[1] Hilumi Book

[2] E. Todesco, et al., "A first baseline for the magnets in the high luminosity LHC insertion regions", *IEEE Trans. Appl. Supercond.* **24** (2014) 4003305.

[3] G. Sabbi, "Nb$_3$Sn IR Quadrupoles for the High Luminosity LHC", *IEEE Trans. Appl. Supercond.* **23** (2013) 4000707.

[4] L. Rossi, E. Todesco, `Electromagnetic design of superconducting quadrupoles', *Phys. Rev. STAB* **9** 102401 (2006).

[5] A. Tollestrup, et al., "The development of superconducting magnets for use in particle accelerators: from Tevatron to the LHC', *Rev. Sci. Accel. Tech.* **1** (2008) 185-210.

[6] P. Ferracin, et al., "Limits to high field magnets for particle accelerators", *IEEE Trans. Appl. Supercond.* **22** (2012) 4003106.

[7] P. Ferracin, et al., "Magnet design of the 150 mm aperture low-beta quadrupoles for the high luminosity LHC", *IEEE Trans. Appl. Supercond.* **24** (2014) 4002306.

[8] Q. Xu, et al., "Design optimization of the new D1 dipole for HL-LHC upgrade", *IEEE Trans. Appl. Supercond.* **24** (2014) 4000104.

[9] L. Esposito, et al., "Fluka energy deposition studies for the HL-LHC, IPAC (2013) 1379-1381.

[10] N. Mokhov, et al., "Protecting LHC IP1/IP5 component against radiation resulting from colliding beam interactions", LHC project report 633 (2003) 55 p

[11] S. Caspi, et al., "Test Results of LARP Nb$_3$Sn Quadrupole Magnets Using a Shell-based Support Structure (TQS)" *IEEE Trans. Appl. Supercond.,* **19** (2) pp. 1221-1225, June 2009.

[12] G, Ambrosio, et al., "Test Results of the First 3.7 m Long Nb$_3$Sn Quadrupole by LARP and Future Plans", *IEEE Appl. Supercond.* 21 (3), pp. 1858-1862, March 2011

[13] H. Felice, et al., "Design of HQ – A High Field, Large Bore *IEEE Trans. Appl. Supercond.* 19 (3), pp. 1235-1239, June 2009

[14] E. Todesco, "Quench limits in the next generation of magnets", CERN Yellow Report 2013-006 (2013) 10-16.

[15] T. Salmi, et al., "Modeling heat transfer from quench protection heaters to superconducting cables in Nb$_3$Sn magnets", *CERN Yellow Report* **2013-006** (2013) 30-37.

[16] V. Marinozzi, et al., "Study of quench protection for the low β quadrupole for the LHC luminosity upgrade", submitted to *IEEE Trans. Appl. Supercond.*, presented at ASC 2014.

[17] E. Ravaioli, et al., "New coupling loss induced quench protection system for superconducting accelerator magnets", *IEEE Trans. Appl. Supercond.* **24** (2014) 0500905.

[18] S. Izquierdo Bermudez, et al., "Coil end optimization of the low β quadrupole for the high luminosity LHC", submitted to *IEEE Trans. Appl. Supercond.*, presented at ASC 2014.

[19] R. Gupta, "Tuning shims for high field quality in superconducting magnets", *IEEE Trans. Magn.* **32** (1996) 2069-2073.

[20] P. Hagen, "Study of magnetic shimming in triplet magnets", Milestone Report 36 of HiLumi project, available at http://www.cern.ch/hilumi/wp3

[21] R. Van Weelderen, "Superfluid helium cooling", Milestone Report 42 of HiLumi project, available at http://www.cern.ch/hilumi/wp3

[22] D. Duarte Ramos, et al., talk given at WP3 meeting on 28 January 2014, available at https://espace.cern.ch/HiLumi/WP3/SitePages/Minutes%20and%20Presentations.aspx

[23] J. Garcia Matos, et al., talk given at WP3 meeting on 17 July 2014, available at https://espace.cern.ch/HiLumi/WP3/SitePages/Minutes%20and%20Presentations.aspx

[24] M. Karppinen, "Corrector magnets for the LHC upgrade phase-1", CERN EDMS doc. N. 1039976, and R. Ostojic, et al., "Conceptual design of the LHC interaction region upgrade: phase I", LHC Project Report **1163** (2008) 42 p.

[25] F. Toral, et al., "Development of radiation resistant superconducting corrector magnets for the LHC upgrade", *IEEE Trans. Appl. Supercond.* **23** (2013) 4101204.

[26] G. Volpini, et al., "Nb-Ti superferric corrector magnets for the LHC luminosity upgrade", submitted to *IEEE Trans. Appl. Supercond.*, presented at ASC 2014.

[27] T. Nakamoto, et al., "Model magnet development of D1 beam separation dipole for the HL-LHC upgrade", submitted to *IEEE Trans. Appl. Supercond.*, presented at ASC 2014.

[28] T. Nakamoto, et al., "Construction of superconducting magnet system for the j-PARC neutrino beam line", *IEEE Trans. Appl. Supercond.* **20** (2010) 208-213.

[29] M. Anerella, et al., "The RHIC magnet system", Nucl. Instrum. Meths. A 499 (2003) 280-315.

[30] Y. Ajima, et al., "The MQXA quadrupoles for the LHC low-beta insertions, Nucl. Instrum. Meths. A 550 (2005) 499-513.

[31] B. Bellesia, J. P. Koutchouk, E. Todesco, `Field quality in low-beta superconducting quadrupoles and impact on the beam dynamics for the Large Hadron Collider', *Phys. Rev. STAB* **10** (2007) 062401.

[32] B. Bellesia, C. Santoni, E. Todesco, `Random errors in superconducting dipoles', *Tenth European Particle Accelerator Conference* (2006) 2601-3.

[33] G. Sabbi, et al., "Conceptual Design Study of the High Luminosity LHC Recombination Dipole", Proceedings of the 5th International Particle Accelerator Conference, June 2014. http://accelconf.web.cern.ch/AccelConf/IPAC2014/papers/wepri094.pdf

[34] P. Fabbricatore, et al., talk given at WP3 meeting on 17 September 2014, available at https://espace.cern.ch/HiLumi/WP3/SitePages/Minutes%20and%20Presentations.aspx

[35] S. Farinon, et al., talk given at WP3 meeting on 17 September 2014, available at https://espace.cern.ch/HiLumi/WP3/SitePages/Minutes%20and%20Presentations.aspx

[36] J. Rysti, et al., talk given at WP3 meeting on 17 September 2014, available at https://espace.cern.ch/HiLumi/WP3/SitePages/Minutes%20and%20Presentations.aspx

[37] P. P. Granieri, et al., "Thermally enhanced cable insulation for the Nb-Ti high luminosity LHC inner triplet model", *IEEE Trans. Appl. Supercond.* **22** (2012) 7700404.

[38] M. Segreti, et al., "A Nb-Ti 90 mm double aperture quadrupole for the high luminosity LHC upgrade", submitted to *IEEE Trans. Appl. Supercond.*, presented at ASC 2014.

[39] T. Tortschanoff, et al., "The LHC main quadrupoles during series fabrication", *IEEE Trans. Appl. Supercond.* **16** (2006) 281.

[40] G. Kirby, et al., "LHC IR upgrade Nb-Ti, 120 mm aperture model quadrupole test results at 1.8 K", *IEEE Trans. Appl. Supercond.* **24** (2014) 4002405.

[41] G. Kirby, et al., "Performance of the 1-m model of the 70 mm twin aperture superconducting quadrupole for the LHC insertions", *IEEE Trans. Appl. Supercond.* **11** (2001) 1641.

[42] V. Baglin, et al., "Cryogenic beam screens for high energy particle accelerators", presented at *International Cryogenic Engineering Conference*, CERN ATS-2013-006.

Chapter 4

RF Systems

P. Baudrenghien[5], G. Burt[22], R. Calaga[5], O. Capatina[5], W. Hofle[5], E. Jensen[5], A. Macpherson[5], E. Montesinos[5], A. Ratti[10], E. Shaposhnikova[5]

[5]CERN, Accelerator & Technology Sector, CH-1211, Geneva, Switzerland
[10]FNAL, Fermi National Accelerator Laboratory, Batavia, P.O. Box 500, IL, USA
[22]University of Lancaster, Lancaster, UK and Cockcroft Institute Sci-Tech Daresbury, Warrington UK

4   RF systems

4.1   Introduction

The HL-LHC upgrade to enhance the integrated luminosity by a factor 10 per year will need the following RF systems:

-   Deflecting (or crab) cavities for compensation of the effective geometric crossing angle at the IP to recover the luminosity loss due to increased crossing angle

-   Harmonic RF system for bunch manipulation and increased stability

-   A transverse damper upgrade for higher power, bandwidth and low noise

The above RF systems are described in with relevant technical details in the following sections. The beam and machine parameters from Annex A.1 are used to design the RF systems.

4.2   Crab cavities

The LHC uses a 60 m common focusing channel plus 21 m common drift space and 20 m common dipole channel on each side of the interaction region (IR) where the two counter-rotating beams have to be separated transversely to avoid parasitic collisions. The separation is accomplished by introducing a crossing angle at the interaction point (IP) which need to increase with the inverse of the transverse beam size at the collision point in order to maintain a constant normalized beam separation. The non-zero crossing angle implies an inefficient overlap of the colliding bunches. The luminosity reduction compared to that of a zero crossing angle, assuming a Gaussian distribution, can be conveniently expressed by a reduction factor,

$$R_\Phi = \frac{1}{\sqrt{1+\Phi^2}},$$ (4-1)

where $\Phi = \sigma_z \phi / \sigma_x$ is the aspect ratio of the longitudinal (σ_z) to the transverse (σ_x) beam sizes multiplied by the half crossing angle ϕ or is also known as the Piwinski angle [1]. The reduction can be alternatively viewed as an increase in the transverse beam size at the collision point to effective beam size given by $\sigma_{eff} = \sqrt{\sigma_x^2 + \sigma_z^2 \phi^2}$. For HL-LHC beam parameters, the reduction compared to the case of a head-on collision can be 70% or larger. Therefore, the effective gain in luminosity by simply reducing the beam size at the collision point diminishes rapidly.

To recover the loss, an elegant scheme using RF deflectors (also known as crab cavities) on either side of the collision point was first proposed and used for electrons [2, 3]. The time dependent transverse kick from an RF deflecting cavity is used to perform a bunch rotation, in the $x - z$ plane or y-z plane depending on the crossing angle orientation, about the barycentre of the bunch (see Figure 4-1). The kick is transformed to a relative displacement of the head and the tail of the bunch at the IP to impose a head-on collision while maintaining the required beam separation to minimize parasitic collisions. The upstream RF deflector is used to reverse the kick to confine the bunch rotation to within the IR. The crab crossing scheme in a global compensation using only a single cavity per beam was successfully implemented at the e⁺e⁻ collider at KEKB in Japan to achieve record luminosity performance [4].

Figure 4-1: Bunches colliding with a crossing angle without (left) and with (right) the crab crossing

Since, the luminosity gain is substantial, the crab crossing scheme is adopted as a baseline of the HL-LHC upgrade. The time dependent transverse kick can equally be used to regulate the crossing angle at the IP and therefore allows for a natural knob to control the total number of events per crossing (luminosity levelling), a feature highly desired by the experiments. Levelling by means of collision offsets is already used at LHCb and ALICE. More sophisticated means of levelling to control the density of the events along the luminous region by means of crab cavities is under investigation [5].

4.2.1 Beam and RF System Parameters

The HL-LHC upgrade lattice requires crab cavities to provide a total voltage of 12-13 MV per beam per side of each collision point at a frequency of 400.79 MHz. Since the crossing plane in the two experiments is different, a local crab cavity system is a pre-requisite. The nominal configuration will use a two-cavity cryomodule as a basic unit. Four such modules per IP side at P1 and P5 are required to perform the bunch rotation resulting in 16 modules (total 32 cavities). Four spare modules (8 cavities) are required. Two are designed for horizontal crossing and the other two for vertical crossing to perform crab crossing for P5 and P1 respectively. The low frequency is required to minimize the RF curvature for the long LHC bunches (see Annex A.1). The machine constraints near the interaction region require cavities with a transverse dimension compatible with the location of the adjacent beam pipe. The RF and machine parameters directly relevant to the crab cavities are shown in Table 4-1.

Table 4-1: Relevant RF parameters for HL-LHC crab cavities

Characteristics	Units	Value
Resonance frequency	MHz	400.79
Bunch Length	ns	1.0 (4σ)
Maximum cavity radius	mm	≤ 145
Nominal kick voltage	MV	3.4
R/Q (assumed, linac convention)	Ω	400
Q_0		$\geq 1 \cdot 10^{10}$
Q_{ext} (Fixed coupling range)		$3 \cdot 10^5 \cdots 5 \cdot 10^5$
RF Power	kW	80
Power coupler OD (50Ω)	mm	62
LLRF Loop Delay	µs	≈ 1
Cavity detuning	kHz	≈ 1.0

The operating temperature of 2 K is chosen as a baseline. A pressure stability on the cavity surface should be minimized to less than 1 mbar. The static and dynamic heat load is expected to be approximately 30 W to the 2 K bath for a two-cavity module. A cavity vacuum level to better than 10^{-10} mbar is required to assure stable performance.

The input RF power of 80 kW is available to power each of the 8 cavities to their nominal voltage with sufficient margin to cope with beam loading caused by beam offset. The Low Level RF (LLRF) will include a regulation loop around the tetrode (to reduce the RF amplitude and phase noise in a band extending to few tens of kHz), plus an RF feedback to control the vector sum precisely on the two sides of the interaction region. Longitudinal PUs located close to the crab cavities (one per IP-side per beam) are used to regulate the slow drifts of the deflecting voltage with respect to the average bunch centre. To stay within the specified RF power limits, an orbit stability including mechanical tolerances must not exceed 1 mm with stable beams at flattop. The cavity is kept on tune at all times. The resonant frequency should be precisely controlled by a tuning system to a level well below 0.5 kHz to be compatible with the RF power limits.

4.2.2 RF cavity design

In order to sustain the surface fields at the required kick gradient of 3.4 MV/cavity for LHC crab crossing superconducting technology is essential; space restrictions, voltage requirements and impedance considerations strongly rule out a normal-conducting option. "Conventional" superconducting elliptical cavities, which have already been used at KEK, pose significant integration problems at the operating frequency of 400 MHz in the LHC due to their transverse size.

This led to the concept of "compact" cavities. These cavities have unconventional geometries not widely used in superconducting technology. A few concepts with complex shapes exist primarily in the field of heavy ion acceleration. Such structures fit within the LHC constraints in the existing tunnel and reveal significantly better surface field characteristics than the conventional cavities for beam deflection. As a result of an intense R&D program within the EuCARD and LARP programs and with other external collaborators during the past 4 years, three compact designs at 400 MHz have emerged as potential candidates. Their topologies are shown in Figure 4-2. The three proposed designs are at least 4 times smaller in the plane of crossing compared to an elliptical cavity with a ratio of the kick gradient to the peak surface fields lower by a factor of 2.
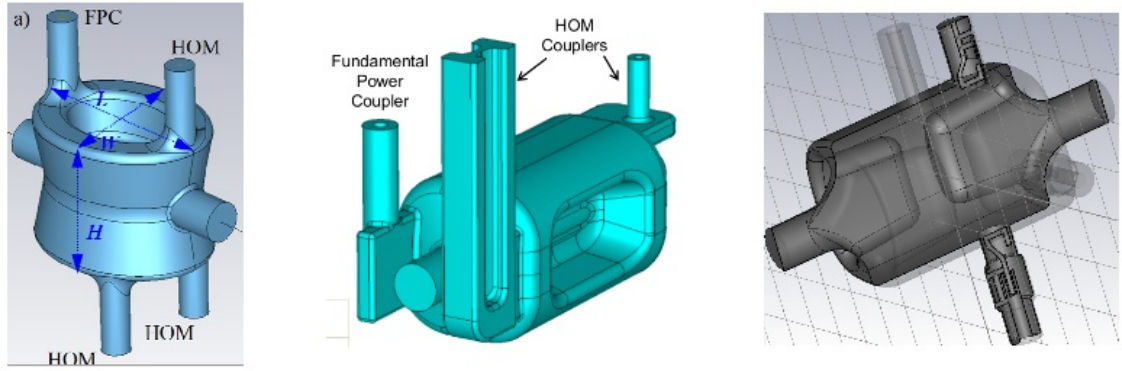
Figure 4-2: Compact cavities: a): Double quarter wave cavity (DQW) b): RF dipole cavity (RFD) c): 4-Rod Cavity (Courtesy Brookhaven National Lab, Old Dominion University and Lancaster University).

As a part of the R&D phase, it was determined to prototype full-scale cavities for all the three designs for a field validation at the nominal kick voltage. Following the recommendation by the Crab Cavity Advisory Panel a prototype module in a two-cavity configuration will be tested with beam in the SPS machine with LHC type beams [6]. These tests will help validate the cavity performance and operation with beam and understand the effects on protons as well as relevant machine protection aspects. The three cavities were fabricated in 2012-13 and their performance validated at or beyond the nominal kick voltage [7,8,9]. The cavity designs including the fundamental power coupler and higher order mode couplers have evolved significantly from the prototype to meet the impedance requirements of the LHC. Following the recommendation of the May 2014 technical review [10], only two cavity designs are considered towards the SPS tests (DQW & RFD).

The development of a two-cavity cryomodule for the SPS tests in 2017 is at an advanced stage. An overview of the Crab Cavity Planning spanning approximately 10 years until the full installation in the LHC is shown in Table 4-2. A more detailed planning both the SPS and the LHC including the pre-series and series production can be found in [35].

Table 4-2: Overview of Crab Cavity Planning from R&D to installation in the LHC.

2013-2014	2015-2016	2017-18	2019-2023	2023-24
Cavity Testing & Prototype Cryomodule	SPS Cryomodule Fabrication	SPS Tests & LHC Pre-Series Module	LHC Cryomodule Construction & Testing	LHC Installation

4.2.3 Beam loading and RF Power

In deflecting cavities operated in the crabbing mode, the RF phase and the RF component of the beam current are in quadrature ($\phi_s = 0$, synchrotron convention). For a beam transversely centred, there is no beam loading: the RF generator does not pass power to the beam. With a superconducting cavity (negligible surface losses) the needed RF power to maintain the cavity voltage decreases monotonically with Q_L. Therefore, with a perfectly centred beam, the choice of Q_L only requires sufficient bandwidth for unavoidable frequency transients due to external perturbations (see section- frequency tuning).

The situation is different for a beam circulating at an offset Δx. The beam induced voltage due to an orbit offset is given by

$$\Delta V = I_B \cdot \frac{R_T}{Q_0} \cdot Q_L \cdot \Delta x \qquad \qquad \textbf{4-2}$$

where, I_b is the average beam current, $\frac{R_T}{Q_0} \cdot Q_L$ is the transverse shunt impedance in Ω and the Δx is the offset. A sufficient bandwidth and the corresponding RF power are required to compensate for the

unavoidable orbit offsets. Figure 4-3 shows the required forward power as a function of the Q_L for a beam that is centred (red) and off-centred by 1 mm (green) and 2 mm (blue). It is expected that the orbit will be kept within 0.5 mm for the entire energy cycle of the LHC; another 0.5 mm should be added for mechanical tolerances.
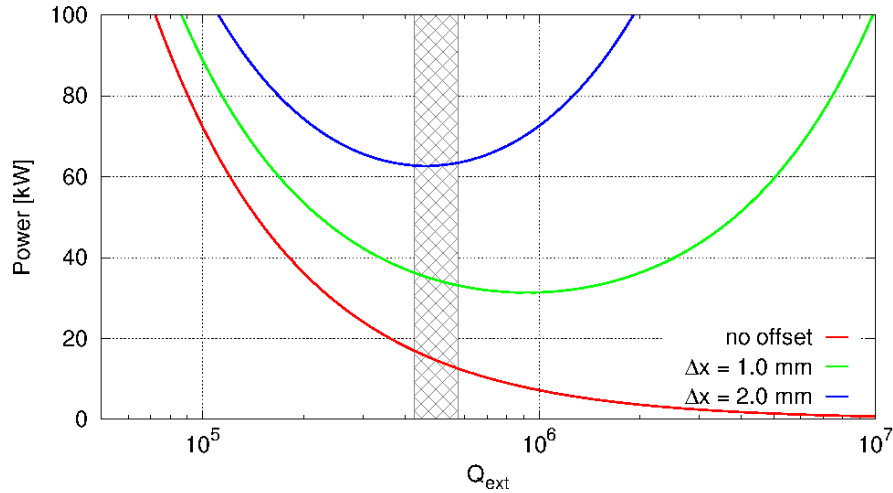
Figure 4-3: Forward power vs. cavity Q_L for centered (red) and 1 mm offset (green) and 2 mm offset (blue) beams. Assumed $R/Q = 400 \, \Omega$, $3.4 \, MV \, RF$, $1.1 \, A \, DC$.

The required RF power has a broad minimum (≤ 40 kW) from a Q_L of about $3 \cdot 10^5$ to $1.5 \cdot 10^6$ for an offset specification of 1mm. Selection of an optimal Q_L value in the broad minimum is a compromise between the feasible tuning precision and the minimization of the field fluctuations from the amplifier electronic. For larger bandwidth (leading to more stability), lower Q_L values are favoured – the hashed area in Figure 4-3 was chosen as a compromise. A lower Q_L is also favourable for the tuning system as it relaxes the precision needed by a mechanical system and the power needed to compensate for fast frequency changes.

4.2.4 RF power coupler

The RF power coupler was designed in view of the HL-LHC requirements; additional constraints (common platform) were introduced to limit the variances between the alternative designs in view of the SPS tests.

The crab cavity power coupler adopted will use a single coaxial disk window type to separate the cavity vacuum and the air side. The antenna shape is specific to each cavity as the coupling mechanisms to the different cavities are not identical. However, a common platform starting from the cavity flange followed by the ceramic and double wall tube is imposed. To respect the common platform, the inner antenna is dimensioned to 27 mm diameter with the outer coaxial line of 62 mm diameter for a maximum power capability of approximately 200 kW. The inner line is made of a copper tube and the outer line is Stainless Steel 316LN with inner surface coated with copper. The vacuum to air separation is achieved with a coaxial ceramic window (Al_2O_3) with the outer flange made of titanium. The rest of the items are built from massive OFE 3D forged copper blocks. The coupler body is made of a conical line to increase the near the ceramic region to limit arcing with the primary aim to enlarge the air side to the maximum while keeping the 62/27 mm dimensions for the input antenna in the vacuum side. A coaxial to waveguide transition is performed with a WR2300 half-height without a doorknob (see Figure 4-4).

The air side of the coupler will be air-cooled while the antenna itself will be water-cooled. The waveguide design includes the possibility of a DC polarisation in order to avoid multipacting effects. Each coupler is equipped with three ports for a vacuum gauge, electron monitoring and arc detection devices. The vacuum gauge, mandatory to protect the window during conditioning as well as in

operation, will be oriented along the air line in order to minimize the cryomodule flange size. Special test boxes to condition the couplers are also designed (see Figure 4-4). The Coupler ports are designed to come out on the top of the cryomodule, perpendicular to the beam axis for ease of integration with the WR2300 waveguide transition. The cavity Helium vessel is designed to withstand the weight of the couplers and the waveguide (approx. 35 kg). The alternating crossing angle scheme will require that the orientation of a coupler assembly be robust for horizontal and vertical deflections.
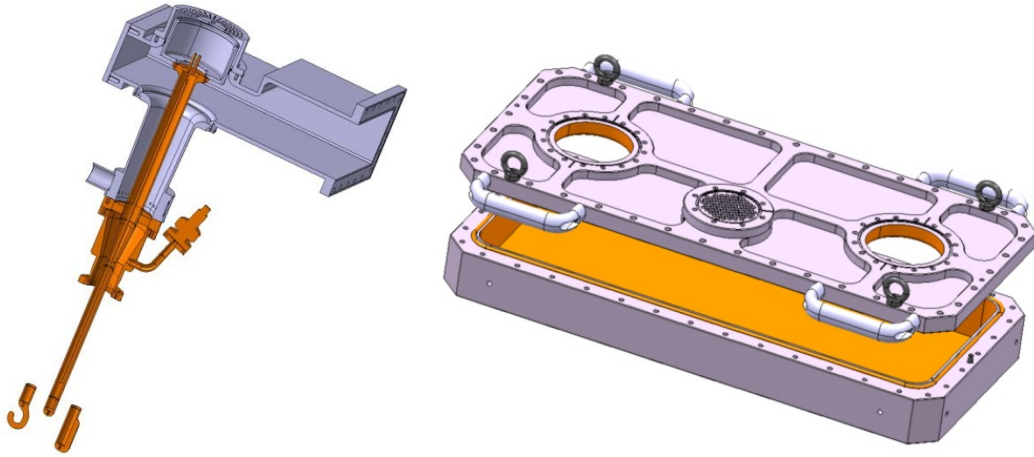
Figure 4-4: Input coupler assembly (left) and the test box for RF conditioning.

4.2.5 Coupled bunch instabilities

The crab cavities must cope with the various modes of the collider cycle: filling, ramping and physics. During filling of the 2808 bunches into the LHC, ramping or operation without crab cavities (crabbing off), the cavity can be detuned, but a small field should be kept for the active tuning system. This is referred to as "parking". Parking the cavity half distance between two revolution frequency sidebands would be ideal for stability. Another possibility to operate with "crabbing off" is possible since more than one cavity is used, namely counter-phasing to make the effective kick voltage zero while always keeping accurate control of the cavity field. This counter-phasing ensures both zero effective voltage and beam stability on tune – in fact it is found that this is the preferred scenario [11].

If detuning is used with a positive non-integer tune ($Q_h = 64.3$), the cavity should be tuned above the RF frequency to make the mode $l = -64$ stabilizing (see Ref. [11]). Though RF feedback is not mandatory for stability with a detuned cavity, it is preferred for accurate knowledge and control of the cavity resonance frequency and field. Active feedback will also keep the beam induced voltage zero if the beam is off-centred. The additional RF power is used as a measurement of beam loading to guide the beam centring. The RF signal picked up through the HOM couplers, might also be used.

On the flattop detuning can be reduced (but keeping the total kick voltage at zero initially). The RF feedback keeps the cavity impedance small (beam stability) and compensates for the beam loading as the cavity moves to resonance. Once the cavity detuning is reduced to zero, we drive counter-phasing to zero and use the functions to synchronously change the voltage in all crab cavities as desired (crabbing on). In physics run, with the crabbing on, the active RF feedback will continue to provide precise control of the cavity field. The RF feedback reduces the peak cavity impedance and transforms the high Q resonator to an effective impedance that covers several revolution frequency lines. The actual cavity tune has no big importance for stability anymore. The growth rates and damping rates are much reduced, and we have no more dominant mode as shown in Figure 4-5.
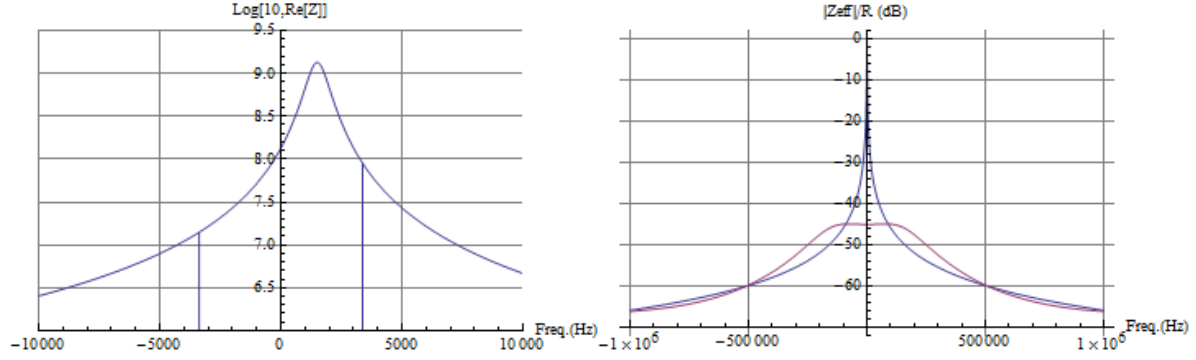
Figure 4-5: Left: Real part of the deflecting mode impedance with a detuning of 1.5 kHz from from 400 MHz. The vertical lines represent the difference in $\Re\{Z\}$ evaluated at $\pm 0.3\, f_{rev}$ for the computation of damping rate (mode l=-64). Right: Modulus of the cavity impedance seen by the beam with the RF feedback on (red) and off (blue) normalized to the cavity impedance at the fundamental mode.

4.2.6 Impedance budget

On resonance, the large impedance of the fundamental deflecting (dipole) mode is cancelled between the positive and negative sideband frequencies, which are symmetric around ω_{RF}. The active feedback will reduce the growth rates by a large factor.

For higher order modes (HOMs), both narrowband and broadband impedance should be minimized during the entire machine cycle as LHC will accelerate and store beams of currents exceeding 1.1 A (DC). Tolerances are set from impedance thresholds estimated from Ref. [12]

The longitudinal impedance has approximately a quadratic behaviour vs. f in the region of interest with the minimum threshold value at $(300 - 600)$ MHz. The total maximum allowed impedance from each HOM, summing over all cavities in one beam, assuming that the HOM falls exactly on a beam harmonic, is set at < 200 kΩ, so if all 16 cavities have identical HOM frequencies, the longitudinal impedance must not exceed 12.5 kΩ per cavity. For frequencies higher than 600 MHz, the threshold is higher ($\propto f^{5/3}$), but the same threshold was imposed. Modes with frequencies above 2 GHz are expected to be Landau-damped due to natural frequency spread and synchrotron oscillations.

In the transverse plane, the impedance threshold is set by the bunch-by-bunch feedback system with a damping time of $\tau_D = 5$ ms [12]. Assuming the pessimistic case that the HOM frequency coincides with the beam harmonic, the maximum impedance is set to be <4.8 MΩ/m. Again, assuming 16 cavities per beam, the maximum allowed impedance per cavity is 0.3 MΩ/m. Analogous to the longitudinal modes, frequencies above 2 GHz are expected to be Landau-damped due to natural frequency spread, chromaticity and Landau octupoles. It should be noted that there are nominally only 8 cavities per each transverse plane, so the threshold per cavity is higher, but the 0.3 MΩ/m is given assuming that the crossing plane between the experiments could become the same as a worst case scenario.

Due to the very tight impedance thresholds, the distribution of the HOM frequencies due to manufacturing errors can help relax the tolerances. The beam power deposited in the longitudinal HOMs can become significant when the frequencies coincide with bunch harmonics. The HOM couplers were dimensioned to accept a maximum of 1 kW to be able to cope with HL-LHC beams [13].

4.2.7 HOM Couplers

The first design goal of the HOM filter is to block the transmission of the main deflecting mode, while transmitting all remaining HOMs. Several HOM coupler designs were developed and optimized for

113

different cavity geometries. Two high-pass filter designs, incorporating a notch filter at the fundamental frequency are shown in Figure 4-6 with both HOMs using hook-like antennas to couple to the HOMs.

Simulations show that the HOM coupler must have a superconductive surface due to the high fields of the fundamental mode. A second design constraint requires the HOM couplers to be able to efficiently remove the power in the HOMs (up to 1 kW) and the heat dissipated by the fundamental mode in the inner part of the HOM coupler from the cavity. High purity bulk niobium with sufficient cooling can ensure this. The required cooling may be possible by conduction, but the possibility to actively cool with superfluid liquid helium or immersion in a small He tank is also under study.
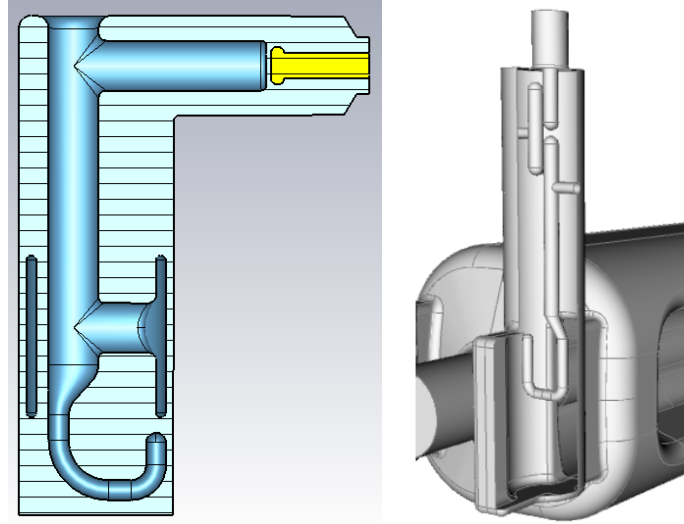
Figure 4-6: HOM filter for the DQW (left) and RFD (right).

4.2.8 RF Multipoles

The crab cavity designs presently considered are such that they lack axial symmetry. Therefore, they can potentially exhibit all higher order components of the main deflecting field. Due to the placement of the cavities at high beta-function locations, the higher order components of the main deflecting mode can affect long term particle stability. RF multipole components b_n of the RF deflecting field can be approximated and hence expressed in a similar fashion to magnets[8] [14]. The quadrupolar component b_2 is zero in case of perfect symmetry; due to fabrication errors and ancillary components it is non-zero – it must be smaller than 10 units leading to a tune shift in the order of $\Delta Q \approx 10^{-4}$. The first systematic multipole is the sextupolar component, b_3. Long term simulations with the optical functions of the HL-LHC indicate that the b_3 component should be limited to approximately $1000 \pm 10\%$ units which results in an acceptable degradation of the dynamic aperture below 1σ for orbit offsets of 1.5 mm [1]. No specifications are provided for higher order terms yet, but it is expected that they be controlled to smaller values than the neighbouring D2 dipole magnet.

For $n \geq 4$, assuming a very approximate scaling of the additional kick from an orbit offset via b_n, the b_n must be kept $< \mathcal{O}(10^n)$. Better estimates are pending; results from long-term tracking are needed.

---

[8] Definition of b_n: $b_n = \int_0^L \frac{1}{qc} F_\perp^n \, dz$ in units of T m^{2-n}.

4.2.9 Lorentz Force Detuning & Multipacting

When the cavity contains RF fields there is a Lorentz force on the cavity surface resulting from the high radiation pressure on the cavity walls. This results in a detuning of the cavity frequency. The Lorentz force detuning is kept small (≤ 0.6 kHz) at the nominal field.

Another common problem in complex RF structures is multipactor. This is a resonant electron phenomenon where an electron follows a regular trajectory in the RF fields where it strikes the surface with energy such that the number of secondaries produced is statistically likely to be greater than one. If these secondaries follow the same trajectory then the process will repeat causing an exponential growth in the number of secondaries. The electrons will absorb RF power limiting the field to a finite level and depositing additional heat load in the walls. Initially the cavity surface may have an oxidised layer which will increase the secondary emission yield (SEY). However multipactor also conditions the surface removing this layer. If the multipactor disappears after processing or if sufficient power is available to overcome the multipactor it is termed a "soft" barrier, otherwise it is termed a "hard" barrier.

Multipactor was modelled in all cavities and couplers using two codes using different methodologies to identify multipactor. CST Particle Studio uses particle tracking with accurate secondary emission models to simulate the growth in electrons with time, while Track3P tracks a single particle in the RF fields and looks for resonant trajectories.

In CST three SEY models were used to look at the effect of surface cleanliness. The models were for wet treated, baked and processed niobium surfaces. While multipactor in all cavities was found for the wet-treated and baked models, no multipacting trajectories were found for the processed surface, suggesting that any multipactor would be soft and easily processed through. Similarly Track3P found multipactor at low field. This is in good agreement with the results from the prototype tests, where multipactor was observed and could be processed away easily.

4.2.10 Cryomodule and Integration

4.2.10.1 Temperature choice

The BCS resistance of Niobium at 4.5 K and 400 MHz is around 50 nΩ, which is more than 10 times larger than the value at 2 K. The complex shapes of the cavities may also be susceptible to microphonics caused by Liquid He boil-off, hence operation below the lambda point of He is preferred. For these reasons operation at 2 K is baseline. This will require the provision of Liquid He at 2 K to the crab cavity location in LHC. The current heat load limits for LHC are currently not known, but are likely to be around 3 W of dynamic load per cavity at 2 K.

4.2.10.2 Cavity Interfaces and Cold Mass

Following the recommendation of the May 2014 technical review [10], only two cavity designs are considered for the engineering design towards the SPS tests (DQW & RFD). The mechanical design of the cavities ensures their safe use under maximum loading condition during its entire life-cycle. The cavity was dimensioned to cope with several mechanical constraints: ensure elastic deformation during maximum pressure as well as during all transport and handling conditions; maximise tuning range; minimise sensitivity to pressure fluctuation; avoid buckling due to external pressure; maximise the frequency of the first mechanical natural mode. The final mechanical design of the cavities including all external interfaces is shown in Figure 4-7.

Figure 4-7: Schematic view of the cavity with interfaces (left: DQW & Right: RFD).

The superconducting resonators are fabricated from bulk niobium sheets by electron-beam welding of deep-drawn parts. A final thickness of 4 mm was calculated to be acceptable in order to cope with all the mechanical constraints as well as minimizing the cost of the cavity production. The cavities are bath-cooled by saturated super-fluid helium at 2 K. Each cavity is equipped with: a helium tank, a tuning system, a fundamental RF power coupler, a field probe and two or three HOM couplers. A functional specification including all tolerances for the cavity with its interfaces to develop manufacturing drawings for the DQW and the RFD are shown in Figure 4-8 and Figure 4-9 respectively.

Figure 4-8: Dimensional plot with tolerances of the DQW cavity

Figure 4-9: Dimensional plot with tolerances of the RFD cavity

4.2.10.3 Helium Vessel & Dressed Cavity Unit

The helium tank will contain saturated superfluid helium at 2 K, cooling the cavity and allowing the extraction of the heat dissipated in the cavity and adjacent cold components. Superfluid helium is an excellent thermal conductor for small heat flux. Above a critical heat flux, the temperature increases drastically and eventually superfluidity is lost. The geometry of the helium tank has been determined to allow this maximum heat extraction while optimising the quantity of the helium to be used.

Two choices of material have been studied for the helium tank: stainless steel and titanium. The titanium has the advantage of the same thermal contraction as niobium (in the order of 1.5 mm/m from ambient temperature to 2 K), while the thermal contraction of stainless steel is twice as large leading to larger thermal stresses. The advantage of stainless steel is the manufacturability and thus the cost. However, for the unconventional geometries of the crab cavities, titanium grade 2 was chosen as the optimum material for the helium tank, allowing for rigid connections of cavity ports to the helium vessel.

The helium tank has a structural role and its rigid connection to the cavity ports ensures optimum boundary conditions for the cavity during mechanical loading, in particular during maximum pressure loading and tuning. The helium tank geometry was chosen to limit the maximum stress on the cavity to tolerable values [12]. Figure 4-10 shows a qualitative stress distribution in the cavity wall during maximum pressure. The red colour indicates only small areas of high stress, which is tolerable. This distribution as well as the maximum values is directly influenced not only by the cavity geometry but also by the helium tank configuration.
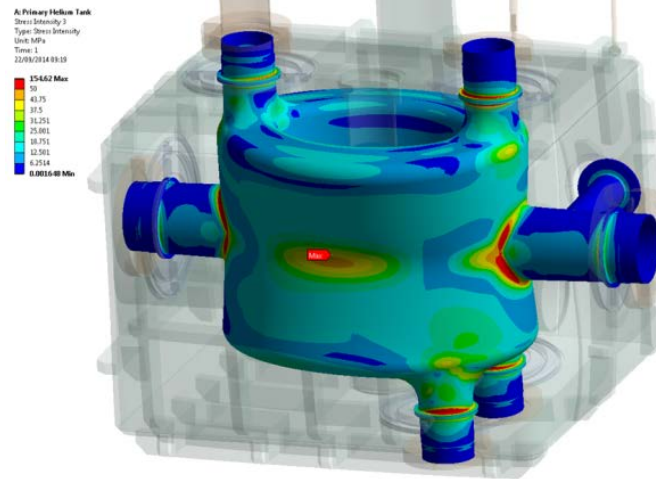
Figure 4-10: Mechanical stress induced by maximum pressure on the DQW cavity inside its helium tank. Red indicates regions with highest stress, which can be tolerated if confined to small areas.

A major concern for the mechanical design were the transitions from the helium tank to all the adjacent components, in particular the main coupler, HOM couplers, the flanges for connection to the beam pipes and helium pipes. All flange connections are stainless steel to stainless steel connections. Due to its proximity, the second beam pipe had to be integrated inside the helium vessel and consequently will be at 2 K; it is proposed to use a niobium beam pipe. A schematic view of the DQW and RFD cavities inside their helium tanks and equipped with the required ancillary equipment are shown in Figure 4-11 and Figure 4-12.
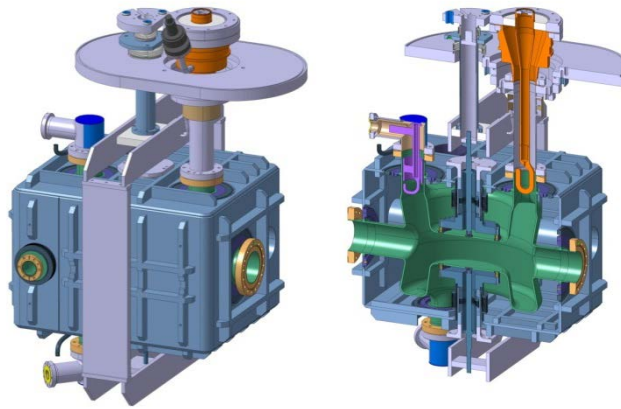
Figure 4-11: Left: The DQW cavity inside its helium tank with the field probe port (front), beam port (right) and tuner frame around. Right: sectional view of the DQW cavity inside its helium tank with the power coupler (top right, orange), HOM coupler (left, top and bottom) and tuner (centre, top and bottom).
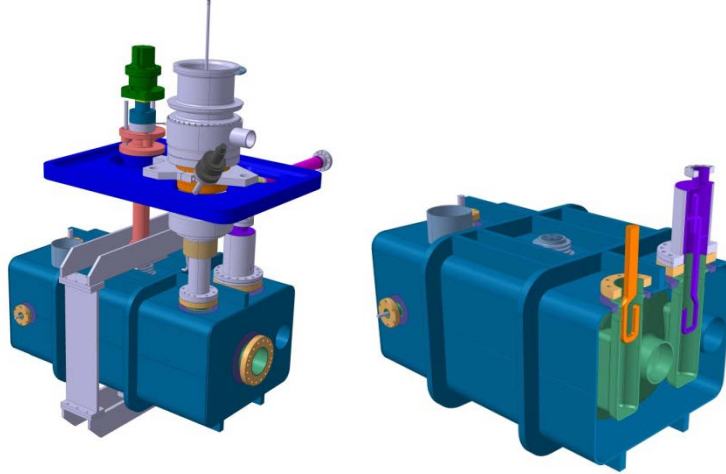
Figure 4-12: Left: The RFD cavity inside its helium tank with the field probe port (centre left), beam port (centre right), tuner frame around helium vessel and tuner actuation (top centre). Right: Schematic sectional view of the RFD cavity inside its helium tank with the power coupler (orange) and HOM coupler (violet).

4.2.10.4 Frequency Tuning

The final resonance frequency of the cavity will depend on a number of fabrication and handling steps and cool-down (hundreds of kHz). A "slow" mechanical tuning system is required to compensate for the uncertainties of the above steps by altering the cavity shape – this will dominate the tuner requirement. At 2 K, it must be possible to tune the cavity to $f_{res} = f_{operation} \pm \Delta f_{LFD}$, where Δf_{LFD} denotes Lorentz force detuning occurring during cavity filling. The operating frequency can vary by additional 60 kHz (cf. 4.1.1.18.4 below). Despite the large resulting tuning range ($\approx \pm 200$ kHz) the resolution of the tuner should allow at least 4 steps inside the cavity bandwidth (≈ 800 Hz); backlash and hysteresis must be small.

The tuning system, similar for both cavities (DQW and RFD), is shown in Figure 4-11 and Figure 4-12. It consists of an actuation system that is placed outside the cryomodule, is operated at room temperature and at atmospheric pressure, which makes it accessible and thus maintainable. The actuation system consists of a stepper motor, a harmonic gearbox, a roller screw and linear guide bearings. The concept is based on a design developed and already in use at JLAB. The detail of the prototype actuation system is shown in Figure 4-13. Since the cavity will be operated in CW mode and frequency variations are expected to be small, active tuning with piezoelectric actuators may not be needed in the final design. A piezo is however foreseen for the first cavity tests to validate this assumption.

The actuation induces a relative movement between two titanium cylinders. The inner one is directly connected to the top of the cavity, the outer one to the bottom via a titanium frame. A symmetric deformation is thus applied simultaneously to the cavity top and bottom.
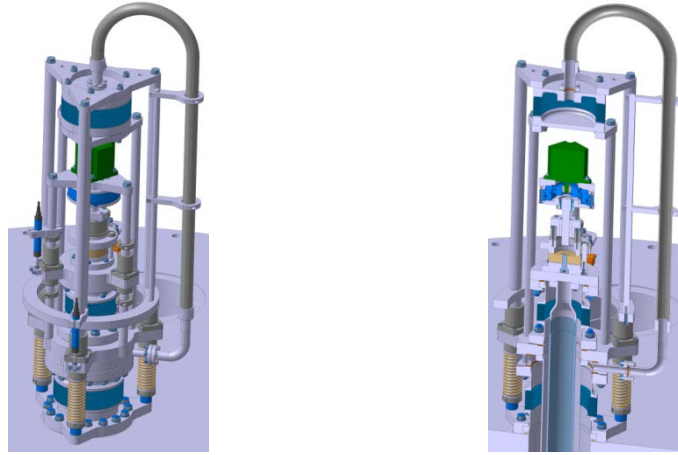
Figure 4-13: Actuation system of the prototype tuning system for both DQW and RFD cavities.

The estimated mechanical resolution of the tuning at the connection to the cavity is estimated to be in the order of 0.1 μm, which is equivalent to few tens of Hz for both cavities, allowing for at least 10 micro-steps inside the cavity RF frequency bandwidth.

Low frequency mechanical resonances (below 150 Hz) should be avoided to minimize the cavity perturbation due to both helium pressure fluctuations $\mathcal{O}(1\,\text{mbar})$ and external noise sources. Resonances above 150 Hz are considered benign. If fast-acting tuners (piezos) are deemed necessary, they should be able to compensate deformations of $\leq (10 \div 20)$ μm to reduce the RF power overhead (see Figure 4-14).
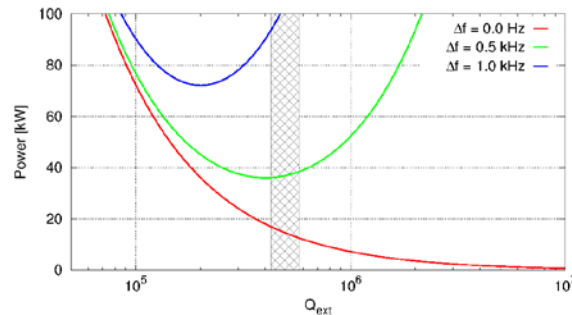
Figure 4-14: Forward power required a function of Q_{ext} for different detuning of the cavity. The hatched area indicates the nominal range of Q_{ext}.

4.2.10.5 Space, Modularity and Second Vacuum Chamber

Machine architecture and integration studies for LHC led to the choice of housing two individual cavities in standalone cryomodules, individually connected to a cryogenic distribution line cryostat running in parallel to the main line. The nominal configuration will use a two-cavity cryomodule as a basic unit. As a consequence, a total of 8 cold-to-warm transitions for the beam tube and 4 connections to the cryogenic distribution line are required for one side of an LHC interaction region (Figure 4-15).

The length of the cryomodule depends on the cavity type, and with the longest cavity results in a total of 13.4 m for 8 cavities (4 cryomodules) per side of the LHC interaction region for both beams including gate valves from interconnection plane, as shown in Figure 4-15. For each two-cavity module, two gate valves inside the cryomodule vacuum (see Figure 4-16) and two valves outside at ambient temperature are foreseen.
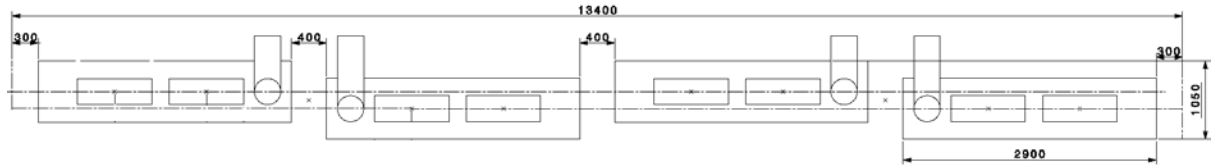
Figure 4-15: Cryomodule layout for one side of the interaction region in the LHC.

A detailed view of the cryomodule containing two DQW and RFD cavities is illustrated in Figure 4-16. The fixed RF coaxial coupler, with a single ceramic window, providing 80 kW average power, is mounted onto the cavity via a ConFlat[TM] flange assembly equipped with a specific vacuum/RF seal designed at CERN and widely used elsewhere.
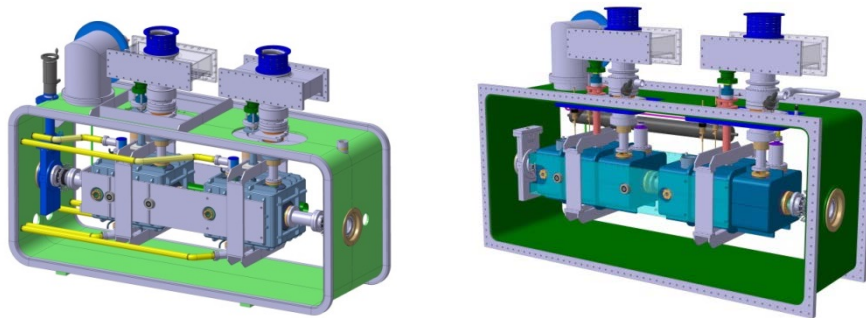
Figure 4-16: Cryomodules for the DQW (left) and RFD (right) cavities respectively.

The RF coupler is mounted on the cavity in the clean-room, constraining the assembly of subsequent components of the cryomodule due to its size. The vacuum vessel was designed in three parts and uses a lateral assembly procedure of the cavity string inside the vessel [16]. This allows the possibility of cavity alignment with optical devices (laser trackers for example) while making fine adjustments through the adjustable supports before closing the cryomodule lateral covers.

The cavity supporting concept uses the external conductor of the RF coupler as the main mechanical support of the dressed cavities. An additional supporting point to keep cavity alignment stability within requirements is obtained by the inter-cavity support. In the RFD cavity, the power coupler is transversely offset from the cavity axis, which requires additional vertical support, as shown in Figure 4-16 (right).

For the LHC cryomodule, two options are considered. The baseline consists of four cryomodules per side per IP, each with two cavities similar to the SPS test prototype cryomodule. This would have the advantage of a topology similar to that having been tested in the SPS. The overall design would probably become simpler than for the SPS test prototype cryomodule. As a second option, a single eight-cavity cryomodule could be considered, optimised for LHC operation requiring less access and minimizing cold-to-warm transitions.

Currently only the SPS test cryomodule exists with full technical specifications. The cryomodules are designed to have a rectangular outer vacuum vessel with removable side panels such that the dressed cavities are side-loaded into the vessel [16]. All external connections except the beam pipes are on the top of the cryomodule. The cavities are supported by the power couplers. This allows easy access as required for a prototype. This design requires several stiffening ribs to keep the stress within reasonable limits when placed under vacuum pressure and during cool-down. The designs for both cavity variants are kept as similar as possible.

4.2.10.6 Magnetic and Thermal Shielding

Assuming a cavity geometric factor of $G \approx 100 \ \Omega$, the additional surface resistance due to trapped flux R_{mag} is required to be below $(1 \div 2) \ n\Omega$ to stay in the shadow of the total surface resistance specification of $10 \ n\Omega$. To achieve this, magnetic shielding in the cryostat should reduce the external magnetic field on the outer surface of the cavity by at least a factor 100 (reaching $< 1 \ \mu T$ assuming the earth magnetic field).

The external warm magnetic shield is made of 3 mm thick mu-metal and will be directly attached to the vacuum vessel. Due to the large apertures in the shielding for couplers and beam pipes this layer on its own is not sufficient to completely shield the earth's magnetic field to the required level with sufficient safety margin. Figure 4-17 shows the magnetic field amplitude inside a 2-cavity CM without an internal shield for an applied external shield of $60 \ \mu T$ in the longitudinal direction. To meet the magnetic field requirements a 2nd shield is required close to the cavity. In order to reduce the size of the holes in the internal shield the cold magnetic shielding will be integrated inside the helium vessel as presented in Figure 4-17. The internal shield is 1 mm thick and will be made from Cryoperm or Aperam Cryophy. Magnetization of both materials is adversely affected due to stresses. Hence degradation of the shielding material during assembly and handling should be carefully studied and monitored. Effects of weight and thermal stresses were modelled in ANSYS, as shown in Figure 4-17. The simulations indicate that while the maximum stress is 439 MPa in the Ti supports, the stress on the shield is kept to less than 150 MPa. It is possible that this may affect the magnetization locally, but the effect is comparable to that of a small hole in the shield. Simulation results from OPERA, assuming the worst case field orientation show that the use of the proposed two-layer shielding solution to achieve magnetic fields well below $1 \ \mu T$ is feasible, as shown in Figure 4-17 [17].
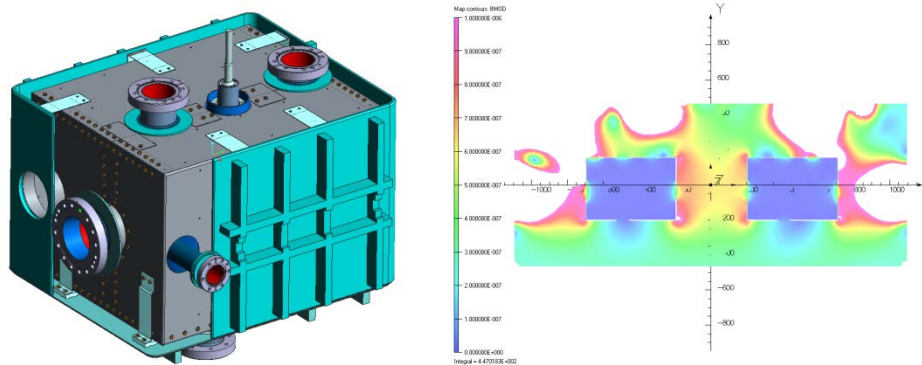
Figure 4-17: Cold magnetic shielding inside the helium vessel (left), magnetic field amplitude inside the 2-cavity CM without the 2nd internal cold magnetic shield, scale 0 to 1 μT (right). An external field of 60 μT in the direction parallel to X (longitudinal) is used.

The thermal shield is made of rolled aluminium sheets. The shield is suspended to the vacuum vessel via flexible guides made in titanium alloy which also cope, by angular movements, with its thermal contractions. The absence of mechanical contact between the shield and the string of cavities eliminates the risk of interference with the alignment of the cavities induced by differential contractions and cooling transients. The cryomodule contains a single thermal shield, actively cooled in the LHC at about 50 K by a cryogenic cooling line containing pressurized helium gas. For the SPS tests, this active cooling will be done with pressurized liquid nitrogen. A 30-layer prefabricated MLI blanket protects the thermal shield whereas a 10-layer blanket is mounted around each helium vessel.

4.2.11 RF powering & control architecture

The overall architecture and approximate volume of the RF infrastructure is schematically shown in Figure 4-18. Near Point 1 and 5, the existing caverns closest to the cavity (RR caverns) are

approximately 80 m away while requiring large space in the tunnel to pass the RF transmission lines along this distance. Radiation concerns rule out the installation of highly sensitive RF electronics in those caverns. Therefore, two remaining options are under study:

- RF gallery near crab cavities: The longitudinal range would be approximately at 155 m from IP1 and IP5 on either side in a gallery parallel to the LHC tunnel. Access to the gallery is required with RF ON and field in the cavity but without circulating beam.

- Surface Option: The longitudinal range is similar as above, preferably above the crab cavity locations on the surface on either side of IP1 and IP5. To minimize the high power RF transmission line dimensions, the circulator and load is assumed to be in an extended tunnel alcove close to the cavity.

An independent powering system using LEP-type 400 MHz tetrodes (or an equivalent IOT) of (40…80) kW is assumed. Recent advances in solid state technology could eventually lead to power sources in the required power range and may provide a cheaper and more robust platform. The tetrodes provide adequate power overhead in a compact footprint. This scheme also would allow for a fast and independent control of the cavity set point voltage and phase to ensure accurate control of the closed orbit and the crossing angle in the multi-cavity scheme. Most importantly, the fast control of the cavity fields will minimize the risk to the LHC during an abrupt failure of one of the cavities to ensure machine protection before the beams can be safely extracted. For such a fast and active feedback, a short overall loop delay between the RF system and the cavity is required [11].
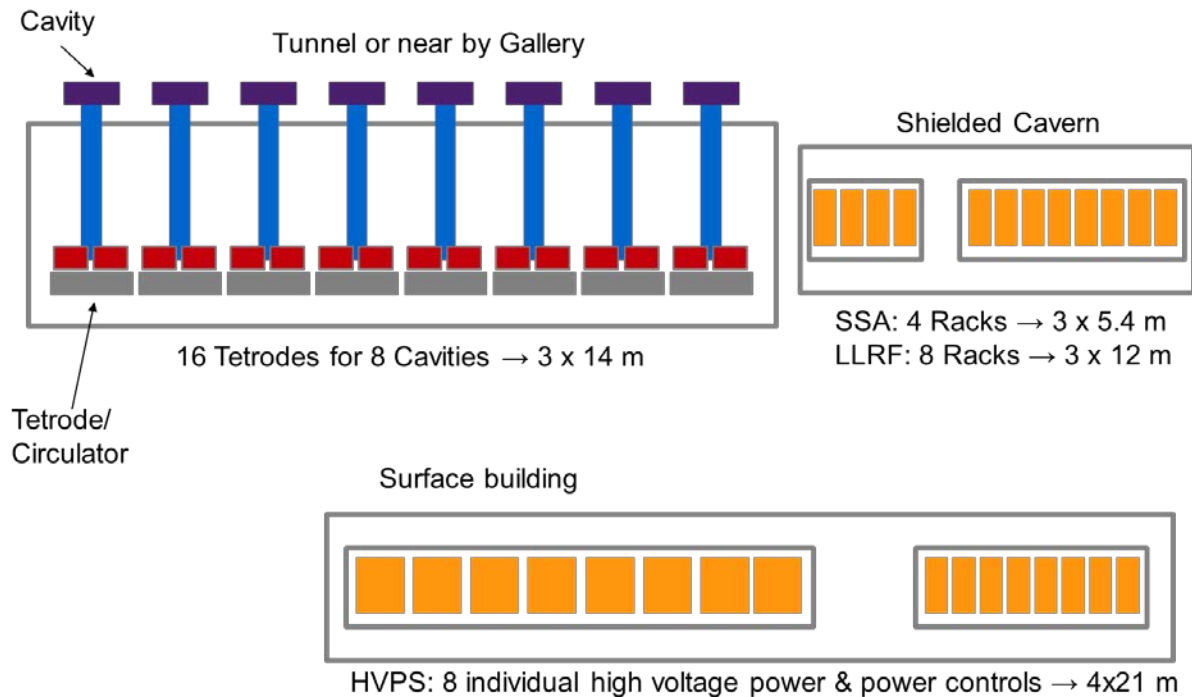
Figure 4-18: Schematic of the RF system layout in the LHC tunnel and the electronics racks required close to the cavities and on the surface building. Note that these are only estimated values of space requirements.

To provide a strong feedback, the low level RF system requires the total loop delay to be approximately $1 - 2$ µs. This includes the group delay of the driver, amplifier, circulator and cable delays. Therefore, a distance less than 100 m is desired for the separation between the amplifier, electronics and the cavity in the tunnel. Such a short delay is already in place for the ACS main RF system in Point 4 (650 ns loop delay) with a service gallery running parallel to the tunnel.

The controls and driver electronics are required to be located in a radiation minimized zone. Assuming two tetrode amplifiers per cavity to provide the 80 kW and electronic racks required for drivers, PLC, LLRF and fast interlocks for 8 cavities per IP side, an area of approximately 100 m² is needed near the cavities. The high-voltage power supplies and the power controls would need an additional 85 m² which will nominally be placed on the surface. If all high and low power RF and controls are placed on the surface, an equivalent of 185 m² will be required there. The proximity of the circulator and RF loads to the cavity will allow for smaller RF transmission lines from the surface to the tunnel.
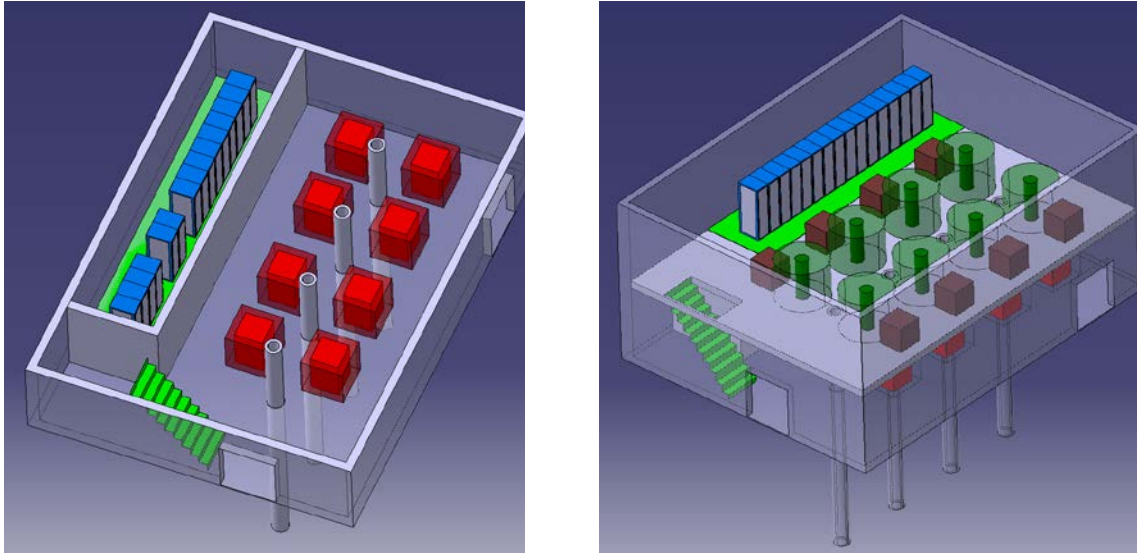
Figure 4-19: Preliminary sketch of a high-power RF, controls and LLRF layout in a surface building, distributed over two levels. Lower level containing pumps and general services (left), upper level containing RF amplifiers and equipment racks (right), courtesy C. Magnier, P. Fessia.

A total height of approx. 6 m is estimated for the high power RF, controls and services, distributed over two levels. This allows a minimum space of 3 m for the equipment racks, amplifiers etc. while leaving 3 m height directly underneath cooling pumps, cabling and services, see Figure 4-19. Alternatively, additional volume adjacent to the building to accommodate the pumps, ventilation and other required units for high power amplifiers can be envisioned to limit the height. All "surface" buildings could actually be underground and would not occupy any surface area. The required electrical interfaces are specified in Ref. [18]. A study is ongoing to determine the feasibility of the civil engineering with minimal perturbation to the LHC running [19].

4.2.12 LLRF Architecture and Operational Scenarios

The RF control system, also commonly referred as the low level RF system (LLRF) includes several functionalities. First, a tuning control is required to keep the cavity resonant frequency on-tune with the beam during the crabbing operation. If required, the LLRF also has to ensure that the cavity is safely parked at an optimal detuned position during filling, ramping and collisions without crabbing. This system also synchronizes the phase of the RF kicks with the exact passage of the bunches for both beams. The LLRF includes a regulation loop around the amplifier (to reduce the RF amplitude noise and phase noise in a band extending to few tens of kHz), plus an RF feedback to control the cavity field precisely. The feedback loop consists of both a local loop around the cavity-amplifier and a global loop regulating the vector sum of voltages on the two sides of the interactions region. The global loop will reduce beam perturbation following a single cavity trip, by quickly reducing the field in the companion

cavities to track the uncontrolled voltage in the faulty cavity. The beam dump system has a 3-turns (270 µs) response delay.

For each ring, the eight accelerating cavities (ACS) are driven from a single reference generated in a surface building above IP4. These two signals must be sent over phase-compensated links to IP1 (ATLAS) and IP5 (CMS). The eight crab cavities of a given ring at each IP are coupled with a 8-IN, 8-OUT multi-cavity feedback (MFB). Figure 4-20 shows the proposed architecture.
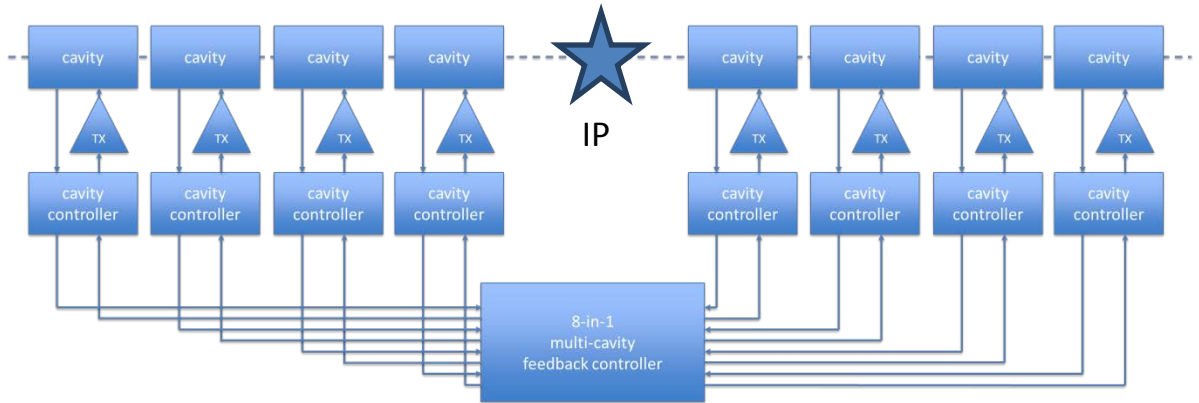
Figure 4-20: Proposed LLRF architecture for one ring at one IP.

Per ring and IP, a central controller receives measurements from all relevant cavities and makes corrections to the drive of all individual TX. If the field starts changing in a cavity, the MFB will adjust the field in the other cavities on both sides of the IP, such that the orbit distortions remain local. As described in 4.2.5 on flat-top, counter-phasing is nulled while keeping the voltage set point small. The RF feedback keeps the cavity impedance small (beam stability) and compensates for the beam loading as the cavity moves to resonance. The voltage set points are ramped to synchronously change the voltage in all crab cavities as desired. Any levelling scheme is possible. With a circulator between amplifier and cavity, the TX response is not affected by the cavity tune.

At present the spacing between LHC bunches within a batch is strictly constant along the ring. A large amount of RF power is used in the ACS system to fully compensate the transient beam loading caused by the 3 µs long abort gap and the smaller gaps required for the injection kicker ("half detuning"). This scheme cannot be extended into the HL-LHC era as it would require excessive RF power. The power required is minimized by optimally detuning the cavity ("full detuning") and adapting the cavity set-point phases bunch by bunch. It results in bunch arrival time modulation of up to ± 42 ps [20]. This may be acceptable given the 1 ns bunch length. There is no effect on the luminosity as the modulation is identical in both beams, only vertex position is modulated around the nominal vertex by a maximum of 1 µm over 1-turn. The bunch to bunch variation within a batch is at least an order of magnitude smaller. If not, the LLRF must synchronize the bunch-by-bunch crabbing field with the actual phase modulation.

4.2.13 Cavity Failure Scenarios

Crab cavity failures can lead to a fast voltage and/or phase change with a fast time constant. This can lead to large, global head-tail oscillations or coherent betatron oscillations with a change in transverse beam trajectories of 1.7 σ for a single cavity failure; the effect is cumulative with the number of failing cavities. These failures can be broadly classified into two categories

- Fast failures, single or few turns. For example a sudden cavity quench or breakdown.

- Slow failures, several tens of turns or greater (caused by vacuum degradation, voltage and phase drifts or similar).

Due to the relatively high quality factor in the superconducting cavity, the stored energy inside the cavity can typically only be extracted with a time constant determined by Q_L, which results from the strong coupling to the cavity via the power coupler. The stored energy will decay with a time constant $\tau = 2Q_L/\omega_0$. For a $Q_L = 5 \cdot 10^5$, the time constant is approximately 400 μs. The three turn delay time (267 μs) for a beam dump trigger is an important consideration during a RF source failure, where the cavity field decays to roughly half its value before the beam can be safely aborted. In the case of a quench, the time constant of field decay may be dominated by the quench dynamics rather than Q_L. The situation is similar due to strong and sudden electron loading due to multipacting or other phenomena.

The cavity quench mechanism described above and measurements from KEKB crab cavities [21] indicate that a quench typically is a slow thermal process (typically of the order of several milliseconds). Once the temperature on a sufficiently large area exceeds the critical temperature of Niobium, the quench can propagate very fast to completely quench or cause RF breakdown. However, any change in cavity quality factor already well before reaching a critical temperature limit could be easily detected from the requested forward power (fast) or changes in the cavity temperature bath (slow). An interlock on the forward power, except due to induced orbit excursion, can cut the RF to slow down or stop the quench propagation. A beam abort if required can be triggered simultaneously (a few μs) for machine protection.

4.2.14 Failure Scenarios Mitigation

The choice of low operation temperature (2 K) and moderate surface field levels allows operation with ample margin from quench temperature and field limits. The significantly better thermal conductivity of superfluid Helium should also improve the thermal performance and stability of the cavity. Additional measures in the cryomodule design are being considered to dimension the Helium enclosures with sufficient margin for heat flux. The cavity thermal and RF stability will be thoroughly tested in the SM18 test facility and during the SPS beam tests.

To minimize the perturbation on the beam during a cavity failure, the MFB will adjust the field in the other cavities on both sides of the IP, such that the orbit distortion remains local. Figure 4-21 shows the cavity control of two cavities across the IP with one cavity failure and the RF controller to adjust the second cavity to follow. The rapid change in field will also result in a detuning of the cavity, however, the mechanical tuning system is -unable to adjust the tune within 400 μs. Since a rapid breakdown of a failed cavity may become unpredictable, it is probably safest to ramp down the cavities synchronously. However, small and slow changes in one of the cavities can be adjusted without aborting the beam.
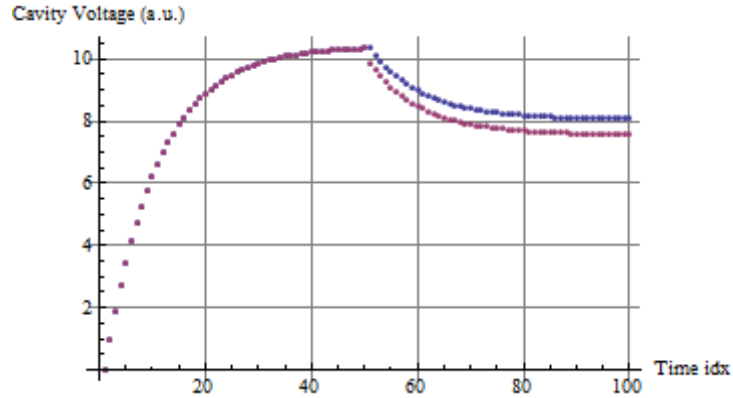
Figure 4-21: Voltage response with strongly coupled cavities across the IP as a function of time [μs]. At 50 μs, one cavity trips (red trace) and the other one is forced by the RF controller to follow (blue trace).

The cavities can be equipped with fast tuning system such as a piezo mechanism. If the speed of such tuning devices is sufficient, it could compensate for Lorentz force detuning during transients and thus keeping the tune within the bandwidth of the feedback system.

An additional mitigation to avoid large beam losses (and hence deposited energy) in case of single or multiple cavity failure is a robust measurement and interlocking of the tail population and eventual head-tail oscillations. This could be achieved with new equipment such as a hollow electron lens for cleaning of the bunch tails and interlocking with improved diagnostics like fast head-tail monitors and/or fast beam loss monitors (diamond, e.g.).

4.2.15 Heat loads and Cryogenics

The cavities are housed in individual titanium helium tanks connected by a 100 mm diameter two-phase He pipe placed above the cavities. This pipe ensures liquid feeding to the cavities by gravity, and is also used as a pumping line for gaseous helium. A saturated helium bath maintains the cavities operating temperature at 2 K. Liquid helium is supplied to the two-phase pipe through a capillary. It is proposed to fill from one single point at one extremity of the bi-phase pipe, and control the He level in the phase separator only. The static plus dynamic heat load is expected to be approximately 30 W to the 2 K bath for a two-cavity module. The cryogenic limits in the LHC are not precisely known at this time. However, the 15 W per cavity heat load at 2 K is small compared to the LHC heat load capacity; the total heat load of the LHC crab cavity systems is estimated at 0.5 kW at 2 K.

4.2.16 Vacuum System

The crab cavity system has three independent types of vacuum systems: the cavity vacuum, the adjacent beam pipe and the cryostat. The two-cavity common vacuum is pumped at room temperature with two ion pumps mounted at each end of the modules. However, at 2 K, the cryogenic pumping of the cavity walls is dominating feature with a pumping speed of 10000 l/s. The background pressure, without RF is expected to much better than 10^{-10} mbar and likely limited by the measurement devices such as penning gauges. Pressure signals provided for RF control are a hardware interlock from the ion pumps to cut the high voltage and readout from the Penning gauges, one per coupler, to limit the RF power. The cavity vacuum can be isolated by two all-metal valves at the ends of each module, to maintain vacuum during transport and installation.

The second beam pipe for the counter-rotating beam has to pass through the cavity Helium vessel due to its proximity. It is presently foreseen to be made of Niobium and will remain superconducting at close to 2 K to preserve the same surface conditions as in the cavity. The use of carbon coating in the

warm regions near the crab cavities to reduce the pressure and to avoid electron cloud effects is presently not considered; it would risk contamination of the cavities.

The insulation vacuum is less demanding in terms of pressure, the modules being pumped to 10^{-5} mbar before being cooled down. When cold, the insulation vacuum also benefits from the cryogenic pumping of the cold surfaces and the operating pressure will decrease to 10^{-7} mbar. Turbo molecular pumps are used and pressures are measured using Penning gauges. Intense gamma radiation could be produced during cavity RF conditioning and operation of high fields.

4.2.17 Interlocks for Machine Protection

Due to the immense stored energy (> 700 MJ), the transient behaviour of the crab cavities is of concern. The crab cavity system will be equipped with several levels of interlocks both for machine protection and to protect the RF system itself. Slow and fast interlocks, including specific RF interlocks (reflected power, signal levels, arc detections, etc.) will ensure safe operation under all conditions and cope with transients; the interlock system will be fully embedded in the overall machine interlock system. All RF systems, including amplifiers, circulators and loads are designed to withstand full reflection in case of a malfunction in the RF chain.

4.2.18 SM18 and SPS Beam Tests

The addition of crab cavities to the LHC should ensure a robust functioning through the entire sequence of the LHC physics cycle. Since crab cavities of such type have yet to be realized and used with hadrons, beam tests with a prototype two-cavity cryomodule is a pre-requisite to identify potential risks of the technology for a safe and reliable operation of the LHC. Therefore, an essential milestone for a crab cavity in the SPS is to demonstrate the machine protection and cavity transparency. All RF manipulations and cavity-beam interactions will be first validated and commissioned in the SPS with the prototype module. The beam tests are planned as machine development studies during the run 2017-18. Successful validation of the crab cavities in the SPS is a prerequisite for installation in LHC.

4.2.18.1 Tests before Installation

The two cavity cryomodule will be assembled in SM18 with the cold masses (cavities, helium vessels, HOMs and tuner) provided by the USLARP collaboration. The cold masses are tested and qualified in the U.S. to its final specification and delivered under vacuum to the SM18 facility. Only the assembly of the power coupler is foreseen in SM18 due to the risk associated of its damage during transport.

The assembled SPS cryomodule in its final stage along with the all the major components will be tested for vacuum integrity, RF performance and operational reliability in the SM18 horizontal bunker to its nominal specification prior to its installation in the SPS. The RF control and interlock system will also be validated in SM18.

4.2.18.2 SPS Environment

The SPS ring is equipped in LSS4 (presently used for the COLDEX experiment) with a special bypass (Y-chamber) with mechanical bellows that allow horizontal displacement. This allows for a test module to be moved out of the beam line during the regular operation of the SPS and only moved in the beam line during the dedicated periods to study the crab cavity test module with beam. This setup is essential both due to aperture limitations of the crab cavities and the risk associated with leaving the cavities in the beam line with different modes of operation in the SPS. The cryomodule is placed on a movable table which can be moved sideways by 510 mm (see Figure 4-22). A special working group (crab cavity technical coordination) has been set up to follow up the various integration issues including the RF and cryogenic systems.
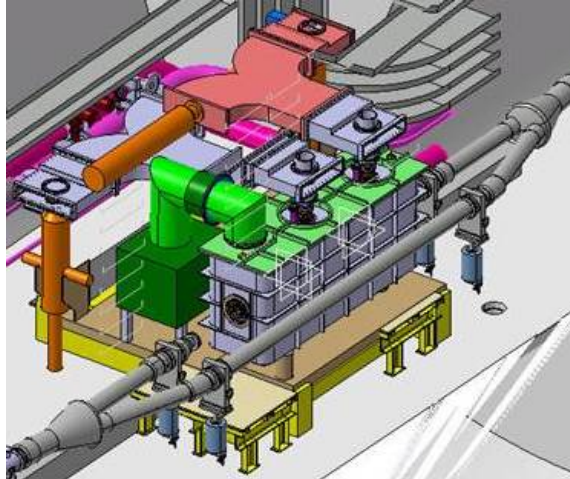
Figure 4-22: 3D integration of the cryomodule, RF assembly and the cryogenics in the SPS.

The relevant cryomodule envelope dimensions for the SPS tests is given in Table 4-3. In general, the SPS constraints are tighter than those of the LHC.

Table 4-3: Cryomodule envelope dimensions

Description	Distance [mm]
Cryomodule-length (gate-valve to gate-valve)	3000
Horizontal distance cavity axis to inner edge of cryomodule volume	420
Vertical distance floor to cavity axis	1200
Maximum height above cavity axis	1200
Inner diameter of cavity beam pipe	84
Horizontal distance cavity axis to bypass beam pipe axis	510

4.2.18.3 SPS RF System and Operation

Specially designed WR2300 will feed the RF power from the Tetrode amplifiers to the respective cavity (see Figure 4-23). Placement of the amplifiers on the movable table will depend on the full integration of the cryomodule, transmission lines and circulator. An LHC type circulator, although over-dimensioned, is preferred for reasons of maintenance and spare policy. A 3D integration of the cryomodule and the RF assembly in the LSS4 region is shown in Figure 4-22
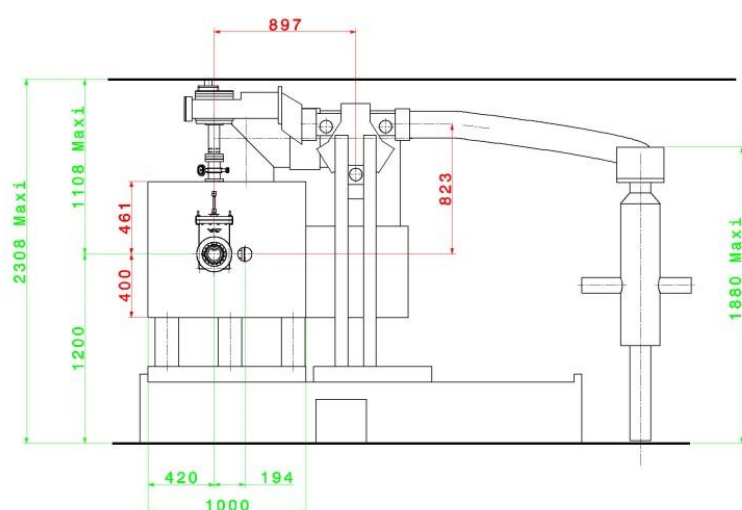
Figure 4-23: Cryomodule and RF system layout in the LSS44 cavern (left) and a 400 MHz Tetrode amplifier under test (right).

In the LHC, the 4 cavities per IP side are always powered on tune, initially with a small voltage (10-15% of the nominal) and counter-phased with active feedback to guarantee maximum beam stability during the entire cycle. Therefore, beam injection with counter-phased cavities with low voltage requires testing in the SPS. Other issues related to beam loading and transient effects with and without RF feedback & slow orbit control will be studied to evaluate the stability and tolerances required from the feedback systems. Induced RF trips and their effects on the beam will be studied in detail to guarantee machine protection and to devise appropriate interlocks. Long term effects with crab cavities on coasting beams at various energies will also be tested.

4.2.18.4 SPS Requirements on cryogenics

At present, the SPS-LSS4 region is equipped with the TCF20 cryogenic box. It was originally planned to upgrade the existing cold box to deliver 2 K Helium for the operation of the crab cavities [15]. Due to the very limited capacity available in the SPS TCF20 refrigerator, the total losses (static and dynamic) are limited to a maximum of 25 W (at 2 K). The heat load of the two-cavity cryomodule, however conservative, is at least 15% higher than the TCF20 capacity. A replacement for the TCF20 to increase the capacity to approximately 40 W is planned to be put in place for the SPS tests [15]. Despite the plan to increase the capacity, a strong effort is put in place to minimize the heat load of all cavity elements and cryomodule interfaces to ensure a successful beam test in the SPS prior to any installation in the SPS.

4.2.18.5 SPS Requirements on Tuning

For beam tests in the SPS a slow mechanical tuner system is required to bring the cavity on resonance in the energy range of the SPS $\left(\begin{smallmatrix} 0 \\ -60 \end{smallmatrix} \text{ kHz}\right)$. In addition the tuner must allow detuning of the cavity to its parking position and has to be precise enough to work together with the RF feedback. Table 4-4 summarizes the potential energies at which SPS can be operated for crab cavity tests and their corresponding RF frequencies compared to that of the LHC operation.

Table 4-4: Detuning ranges for the LHC and SPS

Parameter	Unit	LHC	SPS		
Energy	GeV	450…7000	120	270	450
Frequency	MHz	400.79	400.73	400.78	400.79
ΔF_0	kHz	0	-58.2	12.2	-2.4
Bandwidth	kHz	0.4…4	0.4…4	0.4…4	0.4…4
Detuning	Hz	±5.5		±21.7	

The detuning required to tune the cavity in its parking position (between betatron lines) is approximately ±21.7 kHz in the SPS. The detuning requires a resolution of at least ¼ of the final cavity bandwidth due to available power limits. Additional studies have to be carried out to verify if a tuning speed higher than that possible with the mechanical tuner is required if limitations arise from feedback and/or orbit control.

4.2.18.6 SPS Test Objectives

The test program objectives in the SPS are as below:

- Demonstration of cavity deflecting field with proton beam including injection, energy ramp and coast at energies ranging from 26-450 GeV.

- Verification and control of cavity field (amplitude and phase), frequency, tuning sensitivity, input coupling, power overhead and HOM signals. Establish and test operational cycle with crab cavities.

- Demonstrate the possibility to operate w/o crab cavity action (make them invisible) by both counter-phasing the two cavities or by appropriate detuning (to parking position) at energies ranging from 26-450 GeV.

- Measurements of beam orbit centering, crab dispersive orbit and bunch rotation with available instrumentation such as BPMs and head-tail monitors.

- Demonstrate MFB operation.

- Demonstrate non-correlated operation of two cavities in a common cryomodule – trigger quench in one cavity without inducing quench in the other.

- Define and implement interlock hierarchy. Verification of machine protection aspects and functioning of slow and fast interlocks.

- Test HOM coupler operation with high beam currents, different filling schemes and associated power levels. Measurement of impedance and instability thresholds for nominal mode and HOMs.

- Measure emittance growth induced by the crab cavities as far as possible.

4.2.18.7 Outline of an SPS Test Program

- Initial RF commissioning with CM in out-of-beam position (no dedicated MD required).

- RF commissioning with low intensity beam, single to few bunches. Establish the proper RF parameters, including cavity tune, operating frequency, amplitude and phase. Verify both, crab cavity active and invisible.

- High intensity single bunches to trains of bunches to investigate the effect of cavity performance, impedance, machine protection and characterize the transient behaviour of the crab cavity system

as a function of beam current. Verify cavity stability over many hours (as relevant for LHC physics fill).

- Long term behaviour of coasting beams in the SPS with relatively low intensity to study the effects of emittance growth and possibly non-linear effects such as RF multipoles

4.3 Harmonic Systems

The harmonic cavity systems are presently not part of the HL-LHC baseline. Two categories of harmonic systems are proposed [20], [22]:

- A higher harmonic (800 MHz) system can be used either for changing the bunch profile (in bunch lengthening mode, BL) or for increasing the synchrotron frequency spread (in BL or shortening mode, BS). Depending on the mode of operation, this RF system can help to reduce the beam induced heating, effect intra-beam scattering, improve longitudinal beam stability and in some scenarios can increase or level luminosity.

- A sub-harmonic (200 MHz) system could either completely replace the existing main RF system or work jointly with the 400 MHz RF system, which in this case will act as the 2nd harmonic. The lower harmonic RF system will improve the capture efficiency for longer SPS bunches with very high intensity. The benefits of the combined 200 MHz and 400 MHz system are similar to the above double-harmonic system but with the primary aim of luminosity improvement.

For the higher harmonic system (800 MHz), a maximum of 8 MV longitudinal voltage can be provided from approximately 4-10 cavities depending on the mode of operation [20]. Relevant RF parameters are listed in Table 4-5. This is a maximum of 300 kW input power assumed feasible [23]. The BS mode, with the full-detuning scheme in the fundamental 400 MHz cavities, requires significantly lower RF power. Therefore, a 4-cavity system is more than adequate to provide the required 8 MV with a maximum power of 300 kW per cavity. In the BL mode, the required RF power at 1 MV already exceeds 300 kW. Therefore, approximately 10 cavities are needed to provide for the required 8 MV to stay below the RF power limit

Table 4-5: Relevant RF parameters for 800MHz RF cavities

Characteristics	Units	Value
Resonance frequency	MHz	801.58
Total accelerating voltage	MV	8
Number of Cavities		4 (BS) to $\approx$ 10 (BL)
Residual resistance R_s	nΩ	$\approx$ 250
R/Q	Ω	$\approx$ 45
Q_0		$\geq 1 \cdot 10^9$
Q_{ext}	-	N/A
RF Power per cavity	kW	10^5 (BS), $\approx 10^4$ (BL)
Operating Temperature	K	4.5

Replacing the existing acceleration system with a sub-harmonic system (200 MHz) will require a minimum of 3 MV of longitudinal voltage to capture, accelerate and store the HL-LHC beams [24]. This can be provided from 2-4 compact quarter wave cavities where the number of cavities also depends on power requirements and technology constraints [20]. Some relevant RF parameters for the 200 MHz cavities are listed in Table 4-6.

Table 4-6: Relevant RF parameters for 200 MHzc RF cavities

Characteristics	Units	Value
Resonance frequency	MHz	200.4
Total accelerating voltage	MV	3-6
Residual resistance R_s	nΩ	≤ 10
R/Q	Ω	≈ 50
Q_0		$\geq 1 \cdot 10^{10}$
Q_{ext}	-	N/A
RF Power (assumed)	kW	500
Operating Temperature	K	4.5

The total static and dynamic heat load for either system has to be evaluated in detail during the engineering phase of the cryomodule. A cryogenic sectorization of two cavities per cryomodule is assumed for modularity, maintenance and reliability. For 200 MHz, a preliminary estimate of 120 W for a two-cavity module at 4.5 K can be assumed where each cavity operates at 3 MV. The cavity technology (bulk Niobium or Nb coated copper cavities) can play a role in the final quality factor of the cavity and hence the heat loads at the operating gradient.

For the 800 MHz system, the frequency dependence of the surface resistance gives 250 nΩ leading to approximately 50 W at 4.5 K due to dynamic RF losses. It is only 1 W at 2 K. A geometric factor of 230Ω and a cavity voltage of 2 MV are assumed. Therefore, it is preferable to operate the 800 MHz at 2K to both take advantage of the lower surface resistance and superior properties of superfluid Helium. Assuming the baseline of 4.5 K, approximately 200 W can be assumed as an upper limit for a two-cavity module.

4.4 Transverse Damper (ADT) Upgrade

The LHC requires a transverse feedback to damp injection oscillations and provide stability for impedance driven transverse instabilities thus guaranteeing preservation of beam intensity and emittance [25]. The existing coupled bunch feedback system ADT, installed in point 4 of the LHC was fully commissioned in 2010 [26]. It damps transverse instabilities within a bandwidth of 20 MHz, correcting the oscillations of the centre of gravity of the individual bunches about their orbit.

As upgrades of the ADT system three possible routes have been identified in the past [27]: increase of kick strength, reduction of noise, increase of bandwidth. A space reservation of apriximately 5 m on each side was made in the original design of the LHC to install more kickers adjacent to the existing ADTs in Point 4 [28].

Following the experience of the LHC Run 1, priority was given to an upgrade of the pick-up and signal processing systems aimed at reducing the noise floor, one of the options already foreseen in 2006. This includes new electronics and doubling the number of pick-ups from two to four per beam and plane with commissioning foreseen after LS1 [29]. The experience of run 1 has also shown that an increase in kick strength may not be required, as injection errors are on average more than a factor four smaller than originally assumed, and fast damping times of less than 20 turns for the injection errors can be achieved with the existing system. During Run 1 improvements in the signal processing of ADT were tested to address single bunch oscillations observed, which were different in nature from the coupled bunch oscillations typically driven by the resistive wall impedance, which falls off in frequency towards 20 MHz. The nature of some of these observed instabilities was not entirely unravelled during Run 1 and new diagnostics such as the Multiband-Instability-Monitor (MIM) added in LHC to better characterise these instabilities [30]. Improvements in the ADT signal processing tested during Run 1 permit to run with a flat frequency response of up to 20 MHz, approximately [31]. Beyond 20 MHz, the kicker and power amplifier system of ADT cannot be used.

For HL-LHC, a transverse kicker system with a larger bandwidth than 20 MHz would be an asset in view of the high bunch intensity.

In the SPS a development was started in 2008 to design a High Bandwidth Transverse Feedback System [32], [33] that aims at damping intra-bunch motion. The system consists of pick-ups, kickers, power amplifiers and signal processing. Both slot-line and strip-line kickers are studied for this system, slot-line kickers could offer broadband response up to 1.2 GHz [34]. The system can be used to also damp and attenuate intra-bunch motion caused by electron could, impedance driven instabilities or other perturbations driven e.g. by beam-beam effects or crab cavities. With its generic approach the results of the SPS development are relevant to other accelerators, including LHC or other large colliders.

At 1 GHz four slotlines as developed for the SPS LIU project [34] with 2 kW amplifier power per coupling port can develop a transverse voltage of 37 kV. Consequently the beam can be kicked by 82 nrad at 450 GeV and 5 nrad at 7 TeV. Assuming a reference beta function value of 180 m, at pick-up and kicker, the kick strength corresponds to removing 15 μm of oscillation at 450 GeV and 0.9 μm at 7 TeV, within a single turn. As a feedback system with a gain corresponding to 500 turns damping time, saturation would occur at 3.7 mm at 450 GeV and 225 μm at 7 TeV.

4.5   References

[1]   A. Piwinski, Nucl. Instr. and Meth. 81, 199 (1970).

[2]   R. Palmer, Energy scaling, crab crossing and the pair problem SLAC-PUB-4707, 1988.

[3]   K. Oide, K. Yokoya, The crab crossing scheme for storage-ring colliders, SLAC-PUB-4832.

[4]   Y. Funakoshi, Operational Experience with Crab Cavities at KEKB, http://arxiv.org/pdf/1410.4036

[5]   S. Fartoukh, Pile up management at the High Luminosity LHC and introduction to the crab kissing concept, CERN-ACC-2014-0076 (2014).

[6]   G. Arduini et al., Summary of the LHC-CC11 Crab Cavity Workshop, CERN-ATS-2012-055, 2011.

[7]   S . De Silva et al., in the proceedings of IPAC13, Shanghai, 2013.

[8]   B. Hall et al., in the proceedings of IPAC12, New Orleans, 2012; G. Burt et al., in the proceedings of IPAC13, Shanghai, 2013.

[9]   R. Calaga et al., in the proceedings of IPAC13, Shanghai, 2013; Q. Wu et al., in the proceedings of IPAC13, Shanghai, 2013.

[10]   A. Yamamoto et al., Crab cavity system external review report, CERN-ACC-2014-0093, 2014.

[11]   P. Baudrenghien, presented at the 2nd HiLumi Meeting, Frascati, 2012.

[12]   P. Baudrenghien et al., Functional specification of the LHC prototype crab cavity system, CERN-ACC-Note-2013-003, 2013.

[13]   R. Calaga, B. Salvant, Comments on crab cavity HOM power, (unpublished).

[14]   M. Navarro-Tapia, R. Calaga, A. Grudiev, RF mulipoles from crab cavities, IPAC13, Shanghai, 2013.

[15]   K. Brodrinski, S. Claudet, Private communication.

[16]   S. Pattalwar et al., Key Design features of the Crab-Cavity cryomodule for HI-LUMI LHC, in the proceedings of IPAC14, Dresden, 2014.

[17]   T. Jones et al., Crab cavity manufacturing readiness meeting, CERN, 2014.

[18]   L. Arnaudon et al., Conceptual specification of the crab cavity RF system, EDMS 1363181.

[19]   P. Fessia et al., Private communication.

[20]   R. Calaga, Chamonix 2014, in the proceedings of Chamonix 2014 (to be published).

[21]   K. Nakanishi et al., in the proceedings of IPAC10, Kyoto, 2010.

[22]   R. Calaga et al., Conceptual specification of the LHC RF harmonic system, EDMS 1363179.

[23]   E. Montesinos, Private communication.

[24]   E. Shaposhnikova, presented 4th HiLumi Meeting, KEK, 2014.

[25]   O. Bruning et al. (ed.), LHC Design Report, CERN-2004-003, CERN, Geneva (2004), p. 140-142.

[26]   W. Hofle , D. Valuch, Transverse Feedback: high intensity operation, AGC, IGC, lessons for 2012, LHC Beam Operation Workshop, Evian, December 2011, CERN-ATS-2012-083, CERN, Geneva (2012), p. 97-100.

[27]   W. Hofle, Transverse Feedback Systems in LHC and its Injectors: Projected Performance and Upgrade Paths, 3rd CARE-HHH-APD Workshop, LHC-Lumi-06, Valencia, 16-20 October 2006, CERN-2007-002, CERN Geneva (2007), p. 177-179.

[28]   CERN CDD Drawing LHCLJ4GA0007 AH, March 2007

[29]   W. Hofle, G. Kotzian,T. Levens, D. Valuch, Transverse Feedback, 5th Evian Workshop, 2-4 June 2014, CERN Geneva (2014).

[30]   R. J. Steinhagen, M. J. Boland, T. G. Lucas, A Multiband-Instability-Monitor for High-Frequency Intra-Bunch Beam Diagnostics, Proc. IBIC 2013, Oxford UK (2013), 327-330.

[31]   W. Hofle, F. Dubouchet, G. Kotzian, D. Valuch, Performance of the LHC Transverse Damper with Bunch Trains, Proc. IPAC 2013, Shanghai (2013), p. 3022-3024.

[32]   J. R. Thompson et al., Initial Simulation of Damping System for Electron Cloud Driven Instabilities in the CERN SPS, Proc. PAC 2009, Vancouver (2009), p. 4713-4715.

[33]   J.D. Fox et al., First Results and Analysis of the Performance of a 4 GS/s Intra-Bunch Vertical Feedback System at the SPS, Proc. IPAC 2013, Shanghai (2013), p. 3070-3072.

[34]   J. M. Cesaratto et al., SPS Wideband Transverse Feedback Kicker: Design Report, SLAC-R-1037, SLAC (2013);. M. Cesaratto et al., A Wideband Slotted Kicker Design for the SPS Transverse Intra-Bunch Feedback, Proc. IPAC 2013, Shanghai (2013), p. 3073-3075.

[35] R. Calaga, A. Ratti, Presented at the 4th HiLumi Meeting, KEK, 2014.

Chapter 5

Collimation system

R.B. Appleby [21], R. Barlow [20], A. Bertarelli [5], R. Bruce [5], F. Carra [5], F. Cerutti [5], L. Esposito [5], A. Faus-Golfe [11], H. Garcia Morales [26], L. Gentini [5], S. M. Gibson [26], P. Gradassi [5], J.M. Jowett [5], R. Kwee-Hinzmann [26], L. Lari [12], A. Lechner [5], T. Markiewicz [19], A. Marsili [5], J. Molson [21], L. J. Nevay [26], E. Quaranta [5], H. Rafique [20], S. Redaelli [5], M. Serluca [21], E. Skordis [5], G. Stancari [10], G. Steele [5], A. Toader [20]

[5]CERN, Accelerator & Technology Sector, CH-1211, Geneva, Switzerland
[11]IFIC, Instituto de Fısica Corpuscular, CSIC,E-46071 Valencia, Spain
[12]IFIC, Instituto de Fısica Corpuscular, CSIC,E-46071 Valencia, Spain (now at ESS)
[19]SLAC National Accelerator Laboratory, 2575 Sand Hill Road, Menlo Park California 94025 USA
[20]UHUD, University of Huddersfield, United Kingdom
[21]UMAN, The University of Manchester and the Cockcroft Institute, United Kingdom
[26]URHL, Royal Holloway, United Kingdom

5 Collimation system

5.1 LHC multi-stage collimation system

5.1.1 Motivation

A variety of processes can cause unavoidable beam losses during normal and abnormal operation. Because of the high stored energy of above 700 MJ, the beams are highly destructive. Even a local beam loss of a tiny fraction of the full beam in a superconducting magnet could cause a quench, and large beam losses could cause damage to accelerator components. Therefore, all beam losses must be tightly controlled. For this purpose, a multistage collimation system has been installed [1–8] to safely dispose of beam losses. Unlike other high-energy colliders, where the main purpose of collimation is to reduce experimental background, the LHC and HL-LHC require collimation during all stages of operation to protect its elements.

The HL-LHC imposes increased challenges for the collimation system. For the same collimation cleaning and primary beam loss conditions as in the LHC, the factor ~2 increase in total stored beam energy foreseen by the HL-LHC parameters requires a corresponding improvement of cleaning performance to achieve the same losses in cold magnets. Total losses might also exceed the robustness limit of collimators. The LHC system was designed to withstand without damage lifetime drops down to 0.2 h during 10 s, corresponding to peak losses up to 500 kW. The collimation system must be upgraded to cope with this higher loss levels. The larger stored energy also imposes more severe challenges for the collimator robustness against design loss scenarios for cleaning. In case of single-turn beam failures, brighter beams impose higher demands on the collimator materials and designs. The higher peak luminosity challenges entail the definition of new concepts for physics debris cleaning and an overall redesign of the IR collimation layouts. For example, in the present LHC layout, the inner triplet represents the IR aperture bottleneck and is protected by two dedicated tertiary collimators per

plane per beam. Future optics scenarios might add critical aperture restrictions at magnets further away from the IP, requiring additional cleaning and protection.

To meet the new challenges, the HL-LHC collimation system therefore builds on the existing LHC collimation system, with the addition of several upgrades.

5.1.2 Collimation system inherited from LHC

The backbone of the HL-LHC collimation system will remain, as for the present LHC, the betatron (IR7) and momentum (IR3) cleaning systems installed in two separated warm insertions [1]. A very efficient halo cleaning, as required to operate the LHC with unprecedented stored beam energies in a superconducting collider, is achieved by placing very precisely blocks of materials close to the circulating beams, while respecting a pre-defined collimator hierarchy that ensures optimum cleaning in a multi-stage collimation process. This is illustrated schematically in Figure 5-1. Most collimators consist of two movable blocks referred to as "jaws", typically placed symmetrically around the circulating beams. The present system deployed for the LHC operation between 2010 and 2013 provided a cleaning efficiency above 99.99 % [2], i.e. it ensured that less than 10^{-4} of the beam losses is lost in superconducting magnets.

The LHC collimators are built as high precision devices in order to ensure the correct hierarchy of devices along the 27 km ring with beam sizes as small as 200 microns. Details of the collimator design can be found in [20]. Key features of the design are (1) a jaw flatness of about 40 microns along the 1 m-long active jaw surface, (2) a surface roughness below 2 microns, (3) a 5 micron positioning resolution (mechanical, controls), (4) an overall setting reproducibility below 20 microns [21], (5) a minimal gap of 0.5 mm, and (6) evacuated heat loads of up to 7 kW in steady-state regime (1 h beam lifetime) and of up to 30 kW in transient conditions (0.2 h beam lifetime). Two photographs of the present LHC collimator are given in Figure 5-3, where a horizontal and a 45 degree tilted collimator are shown. An example of the tunnel installation layout for a IR7 collimator is given in Figure 5-4. The complete list of collimators, including injection protection collimators in the transfer lines, is given in Table 5-1. For completeness, the injection protection TDI blocks and the one-side beam dump collimator TCDQ (considered part of the beam transfer rather than of the LHC collimation system, but designed with similar concept) are also listed (see Chapter 14). The full system comprises 118 collimators, 108 of which are movable.

Since the collimator jaws are close to the beam (e.g., the minimum collimator gap in 2012 was 2.1 mm, i.e. jaws were 1.05 mm apart from the circulating beam), the collimation system has also a critical role in the passive machine protection in case of beam failures that cannot be counteracted by active systems. Primary and secondary collimators in IR7 are the closest to the beam; their jaws are mainly made of robust Carbon-fibre Carbon composites (CFC), and are designed to withstand without significant permanent damage beam impacts for the worst failure cases such as impacts of a full injection batch of $288 \times 1.15 \times 10^{11}$ protons at 450 GeV and of up to $8 \times 1.15 \times 10^{11}$ protons at 7 TeV [22]. However they contribute significantly to the machine impedance, critical in particular at top energy, because of the low electrical conductivity of the CFC. Impedance constraints determine the smallest gaps that can be used in IR3 and IR7 and hence the minimum β* in the experiment [3]. Other absorbers and tertiary collimators are positioned at larger gaps in units of the local beam size. They can be less robust, in term of resistance to impact of the beam, than primary and secondary collimators because they are less exposed to beam losses. Thus, metal-based jaws can be used which are more effective in absorbing particles.

The initial collimator design has been improved by adding 2 beam position monitors (BPMs, nicknamed as "buttons") on both extremity of each jaw [23].18 collimators (16 TCTP and 2 TCSP) have been already upgraded with this new design during LS1. This concept allows a fast collimator alignment as well as a continuous monitoring of the beam orbit at the collimator, while the BLM-based alignment can only be performed during dedicated low-intensity commissioning fills. The BPM buttons will

improve significantly the collimation performance in terms of operational flexibility and β* reach [3]. The BPM collimator design is considered as the baseline for future collimation upgrades and the BPM design is equally applicable to all collimators regardless of the jaw material. The concept has been tested extensively at the CERN SPS with a collimator prototype with BPMs [24, 25, 26]. An example of a CFC jaw prototype with in-jaw BPMs is shown in Figure 5-4
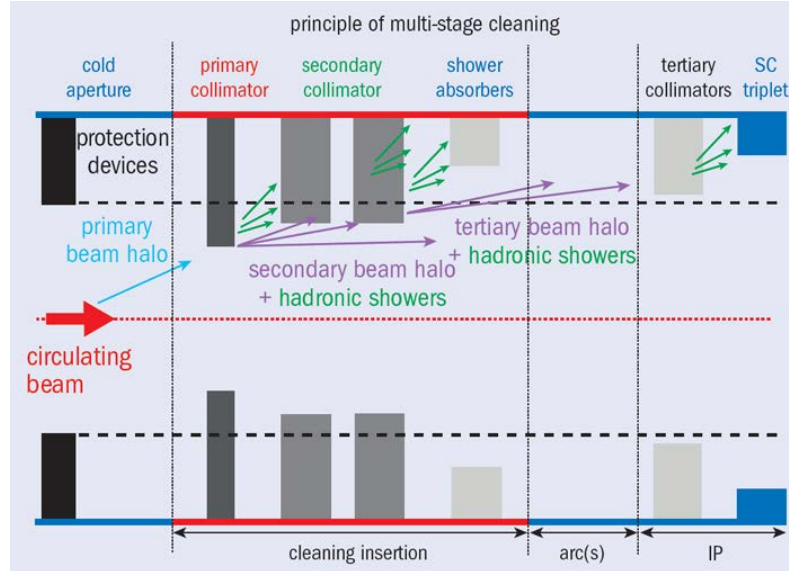
Figure 5-1: Schematic illustration of the multi-stage collimation cleaning at the LHC. Primary and secondary collimators (darkest grey) are the devices closest to the circulating beam and are made of robust carbon-fibre composites. Shower absorbers and tertiary collimators (lighter grey) sit at larger apertures and are made of a Tungsten alloy to improve absorption. Collimators of different families are ordered in a pre-defined collimation hierarchy that must be respected in order to ensure the required system functionalities. The collimator hierarchy is ensured by defining collimator settings in units of local beam size at the collimator location.
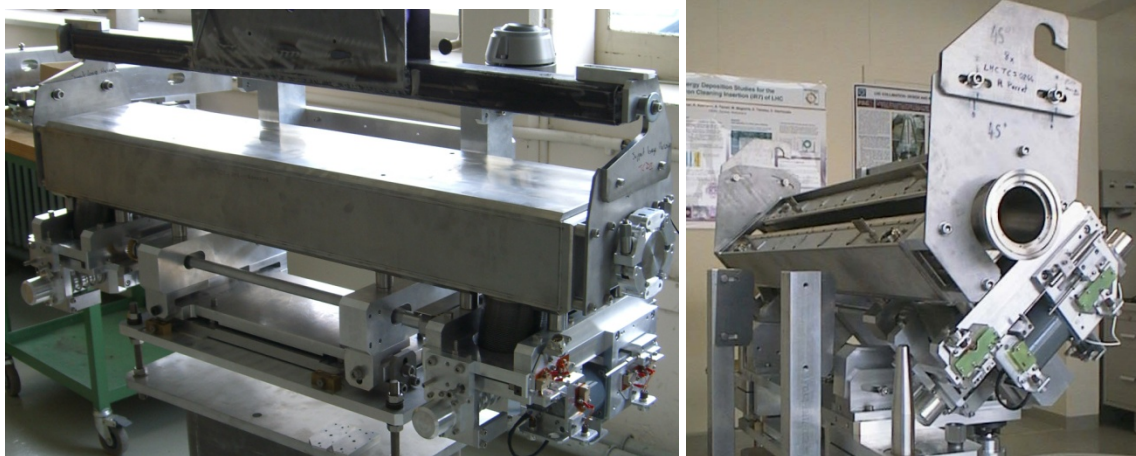
Figure 5-2: Photograph of a horizontal (left) and a skew (right) LHC collimator. The latter has the vacuum tank open to show the two movable CFC jaws.

Figure 5-3: Photograph of the active absorber TCLA.B6R7.B1 as installed in the betatron cleaning insertion.
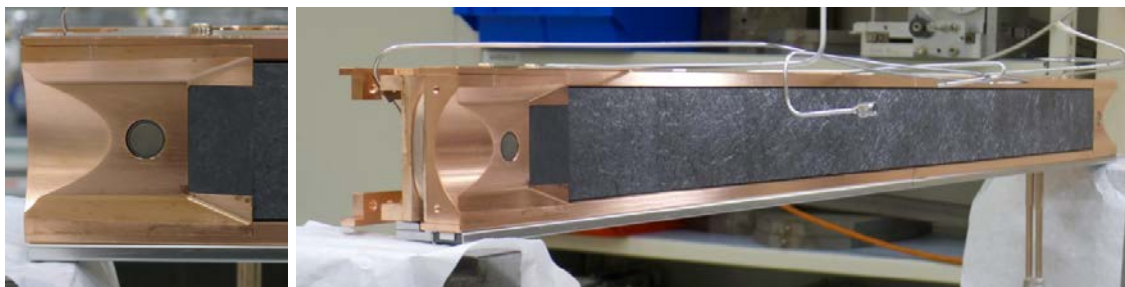
Figure 5-4: New Carbon/Carbon collimator jaw with integrated BPMs at each extremity ("buttons") to be installed as secondary collimator in the dump insertion IR6. A detail of the BPM is given on the left side. A variant of this design, made with a Glidcop support and Tungsten inserts on the active jaw part, will be used for the tertiary collimators in all IRs.

In addition to the beam halo cleaning, the collimation system has also other important roles:

- Passive machine protection: the collimators are the closest elements to the circulating beam and represent the first line of defense in case of various normal and abnormal loss cases. Due to the damage potential of the LHC beams, this functionality has become one of the most critical aspects for the LHC operation and commissioning. In particular, it must be ensured that the triplet magnets in the experiments are protected during the betatron squeeze [3].

- Active cleaning of collision debris products: this is achieved with dedicated (TCL) collimators located on the outgoing beams of each high-luminosity experiment that catch the debris produced by the collisions. These collimators keep losses below the quench limit of the superconducting magnets in the matching sections and dispersion suppressors close to the interaction points.

- Experiment background optimization: this is one of the classical roles of collimation systems in previous colliders like the ISR, the SppS and the Tevatron. For the LHC, the contribution to background from beam halo has always been expected to be small, due to effective IR7 collimation cleaning that induces only limited losses close to the experiments. The initial run confirmed this expectation [4].

- Concentration of radiation losses: for high power machines, it is becoming increasingly important to be able to localize beam losses in confined and optimized "hot" areas rather than having a distributed activation of equipment along the machine. This is an essential functionality to allow easy access for maintenance in the largest fraction of machine.

- Local protection of equipment and improvement of lifetime: dedicated movable or fixed collimators are used to shield equipment. For example, eight passive absorbers are used in the collimation insertions in order to reduce the total dose to warm dipoles and quadrupoles that otherwise would have a short lifetime in the high-radiation environment foreseen during the nominal LHC operation.

- Beam halo scraping and halo diagnostics: collimator scans in association to the very sensitive LHC beam loss monitoring system proved to be a powerful way to probe the population of beam tails [5, 6], otherwise too small compared to the beam core to be measured by conventional emittance measurements. Thanks to their robustness, the present primary collimators can also be efficiently used to scrape and shape the beams, as in [7].

In order to fulfil all these functionalities, the LHC collimation system features an unprecedented complexity compared to previous state-of-the-art in particle accelerators. The Run 1 system required managing about 400 degrees of freedom for collimator movements [8]. As a comparison, the Tevatron collimation system had less than 30 degrees of freedom. For this reason, the possibility to operate reliably the collimation system has always been considered as a major concern for the LHC performance. Upgrade scenarios must address improved operational aspects as the HL-LHC goal relies on machine availability.

Table 5-1: Collimators for the LHC Run 2, starting in 2015. For each type, acronyms, rotation plane (horizontal, vertical or skew), material and number of devices, summed over the two beams, are given. For completeness, movable injection and dump protection devices are also listed. In addition, the collimation system comprises 10 fixed-aperture absorbers in IR3 and IR7 to reduce total doses to worm magnets of the cleaning insertions.

Functional type	Name	Plane	Number	Material
Primary IR3	TCP	H	2	CFC
Secondary IR3	TCSG	H	8	CFC
Absorber IR3	TCLA	H,V	8	Inermet180
Primary IR7	TCP	H,V,S	6	CFC
Secondary IR7	TCSG	H,V,S	22	CFC
Absorber IR7	TCLA	H,V,S	10	Inermet 180
Tertiary IR1/2/5/8	TCTP	H,V	16	Inermet 180
Physics debris absorbers IR1/5	TCL	H	12	Cu, Inermet180
Dump protection IR6	TCDQ	H	2	CFC
	TCSP	H	2	CFC
Injection protection (transfer lines)	TCDI	H,V	13	C
Injection protection IR2/8	TDI	V	2	hBN,Al, Cu/Be
	TCLI	V	4	C, CFC
	TCDD	V	1	Copper

5.2   Baseline upgrades to the LHC collimation system

To cope with the increased challenges in HL-LHC, the LHC collimation system must be upgraded in several of its functionalities. We discuss how to improve the cleaning performance, the impedance, and the collimation in the experimental IRs.

5.2.1 Upgrades for cleaning improvement

5.2.1.1   Upgrades of the IR7 system

Protons and ions interacting with the collimators in IR7 emerge from the IR with a modified magnetic rigidity. This represents a source of local heat deposition in the cold dispersion suppressor (DS) magnets downstream of IR7, where the dispersion starts to increase (see [62] and references): these losses are the highest cold losses around the ring. This may pose a certain risk for inducing magnet quenches, in particular in view of the higher intensities expected for HL-LHC.

A possible solution to this problem is to add local collimators in the dispersion suppressors, which is only feasible with a major change of the cold layout at the locations where the dispersion start rising. Indeed, the present system's multi-stage cleaning is not efficient at catching these dispersive losses. Clearly, the need for local collimation depends on the absolute level of losses achieved in operation and the quench limit of superconducting magnets. In this design phase where the quench limits and the operational performance are not yet known accurately enough at beam energies close to 7 TeV, it is important to take appropriate margins to minimize the risk of being limited in the future (LHC operation at beam intensity above nominal design, and even more in the HL-LHC era).

A strategy to eliminate any risk of quench is the installation of DS collimators (Target Collimator Long Dispersion suppressor or TCLDs). As shown below, two collimators per side of IR7, one per beam per each side, would be sufficient to effectively intercept the protons or ions that would otherwise hit the DS magnets. In order to make space for the new collimators, it is envisaged to replace, for each TCLD, an existing main dipole by two shorter 11T dipoles with the TCLD in between as schematically shown in Figure 5-5 and Figure 5-5 bis. This is a modular solution that can actually be applied to any dipole without additional changes to the adjacent superconducting magnets or other cold elements, would in future a space in the continuous cryostat be needed for any reason. [37].

Extensive tracking and energy deposition simulations have been performed to assess the effect of the TCLDs [39, 40, 63, 64, 65], based on the assumption that the dipoles MB.B8R7 and MB.B10R7 are substituted for the B1 cleaning, and MB.B8L7 and MB.B10L7 for the B2 cleaning. This layout makes room for two TCLDs per beam. For example, the simulated energy deposition profile of the DS magnets for the case of 0.2 h lifetime in the nominal LHC beam is illustrated in Figure 5-6. It is seen that the presence of local DS collimators reduces the peak energy deposition by about a factor 10 compared to the present layout with standard dipoles.
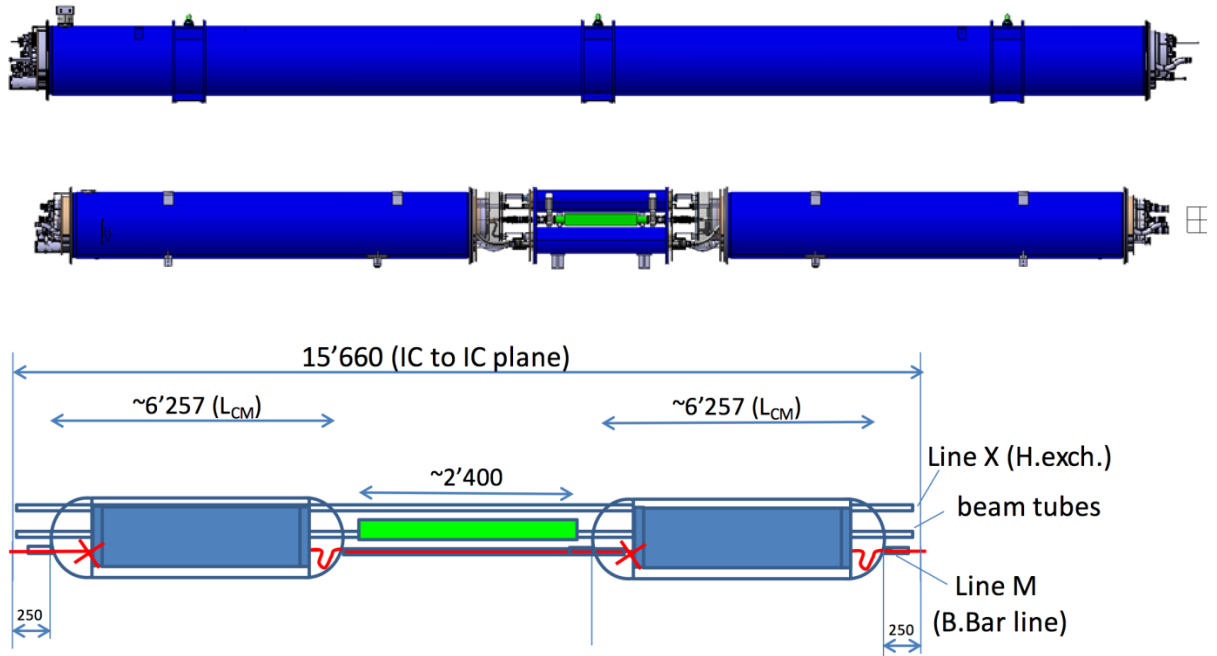
Figure 5-5: Schematic view of the assembly of two shorter 11 T dipoles with a collimator in between, which can replace one standard main dipole. Courtesy of V. Parma.
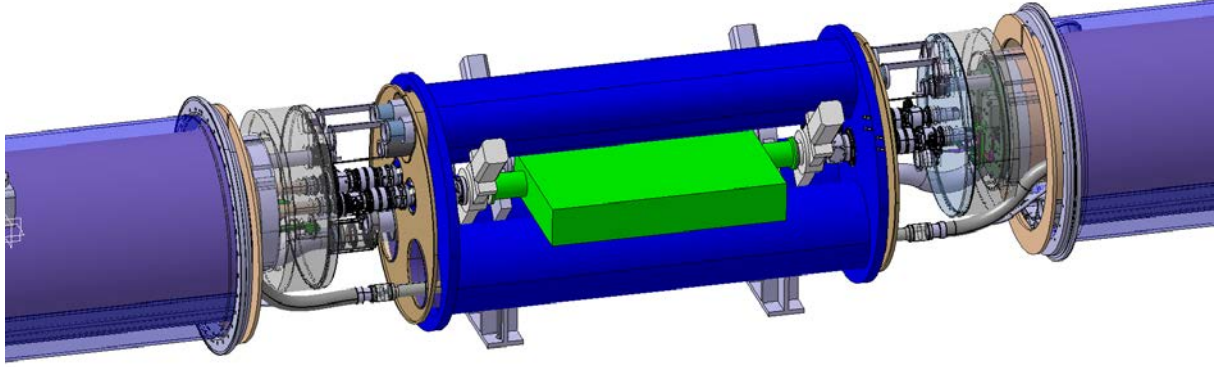
Figure 5-5 bis: preliminary 3D model of a TCLD assembly showing the collimator (in green), the two short dipole cryostats and the connection cryostat. Note the very tight space constraints for the collimator unit.
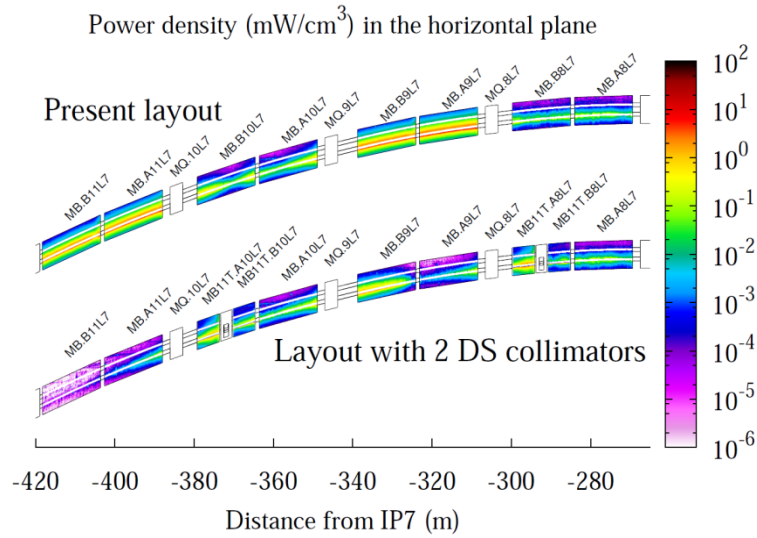
Figure 5-6: Simulated power density map in the horizontal plane of DS dipoles for nominal 7 TeV operation and a beam lifetime of 0.2h (4.5e11 protons lost per second). Comparison of the present layout and a layout with 2 TCLDs. Results correspond to relaxed collimator settings. Beam direction is from the right to the left. From [40].

TCLD collimators also make the cleaning performance more robust against various errors of the collimation system, of the optics, and of the orbit [65], as they remove the off-momentum particles at the first high dispersion location downstream of IR7. This is of particular concern for the ATS optics that requires modified optics in the cold arcs. Indeed, for the HL baseline optics, this solution almost eliminates losses around the ring coming from the telescopic squeeze. Should the total intensity be limited by collimation cleaning, the factor 10 quoted above would translate into the same gain factor for the total stored beam energy.

Furthermore, the improvement in cleaning could be very beneficial for the LHC operation even if not limited by the collimation losses. For example, a better cleaning performance might allow relaxing the opening of some secondary collimators with a subsequent reduction of the machine impedance. It should be noted also that the DS collimation solution might also mitigate issues related to radiation damage of cold magnets protected by the TCLD collimators and the activation of near-by components.

The real need for this gain can only be addressed after having accumulated beam experience at higher energies during the post-LS1 operation (including beam tests of quench limits at energies close to 7 TeV). On the other hand, a recent collimation project review recommended to pursue with high priority the preparation of DS collimation in IR7 [59].

Even if the full performance improvement provided by the DS collimation solution in IR7 relies on 2 TCLD collimators per side, alternative solutions based on one single unit are being considered as possible "staged" deployment in IR7, in case of performance limitations during high intensity proton operation were made apparent by the post-LS1 operation experience.

The TCLD collimators design is derived from one of the standard LHC collimators [66], in particular it incorporates the latest design improvements, such as in-jaw BPMs. TCLD collimators require a reduced set of controls cables because each jaw will be moved with one single motor but still require cooling water and baking equipment. The key parameters are listed in Table 5-2. Although some design features are less demanding, also due to lower losses compared to other collimators, integration design aspects are much more complicated due to their location between cold elements.

The new baseline that relies on shorter 11 T dipoles has been reviewed from the integration point of view [12]. The space is tight and the length of all components and transitions must be carefully optimized. The present baseline is that the TCLD will have an active jaw length of 80 cm that proved to be sufficient to improve the cleaning in all relevant cases. Tungsten heavy alloy is assumed for the material because the TCLD will rarely be exposed to large beam load, so there is no need at this stage to consider advanced materials. From the RF view point, designs with transverse RF finger (as in the present system) as well as with ferrite blocks to absorb high order modes (as in the collimators with BPMs) are being comparatively assessed. A possible design is shown in Figure 5-7, where a detail of the collimator jaw extremity is given.

Table 5-2: Key parameters of TCLD collimators

Characteristics	Units	Value
Jaw active length	mm	80
Jaw material	--	Inermet 180
Flange-to-flange distance	mm	TBD
Number of jaws	--	2
Orientation	--	Horizontal
Dipole replaced by 11 T dipole/TCLD	--	MB.B10
Number of BPMs per jaw	--	2
RF damping	--	RF fingers or ferrite
Cooling of the jaw	--	Yes
Cooling of the vacuum tank	--	No
Minimum gap	mm	< 2
Maximum gap	mm	> 45
Stroke across zero	mm	> 4
Number of motors per jaw	--	1
Angular adjustment	--	No
Transverse jaw movement (5th axis)	--	No
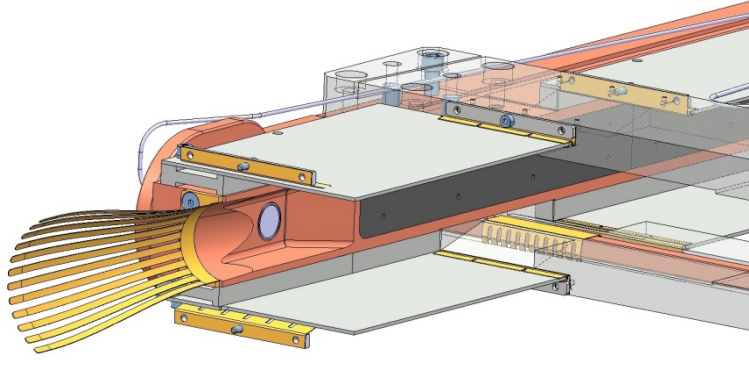
Figure 5-7: Detail of one corner of the TCLD collimator to be installed in the DS between two new 11 T dipoles. The present design foresees an 80 cm long jaw made of tungsten (the first of 4, 20 cm tungsten tiles is shown) and will have 2 jaws. Designs with transverse RF fingers or ferrite tiles are being comparatively assessed to reduce the detrimental effects of trapped RF modes.

5.2.1.2 Upgrades for improved cleaning of physics debris close to experiments

Collision products emerging from the interaction points might be lost in the matching sections and the dispersion suppressors (DSs) around the experiments. In particular, protons that changed their magnetic rigidity represent a source of local heat deposition in the first DS cells where the dispersion function starts rising. These physics debris losses may pose a certain risk of inducing magnet quenches.

Mechanisms with similar effects occur also during heavy-ion operation [52, 53, 54, 12]. Secondary ion beams with a changed magnetic rigidity are created when ions undergo ultra-peripheral interactions at the collisions. The dominating processes are bound-free pair production (BFPP), where electron-positron pairs are created and an electron is caught in a bound state by one (BFPP1) or both (BFPP2) nuclei, thus changing their charge, and 1- or 2-neutron electromagnetic dissociation (EMD1 and EMD2) where one of the colliding ions emits one or 2 neutrons, respectively, thus changing mass. Further photo-induced processes also take place, but the four ones mentioned here have the higher cross sections. An example of ion beams produced in collisions of $^{208}Pb^{82+}$ nuclei in IR2 is given in Figure 5-8.
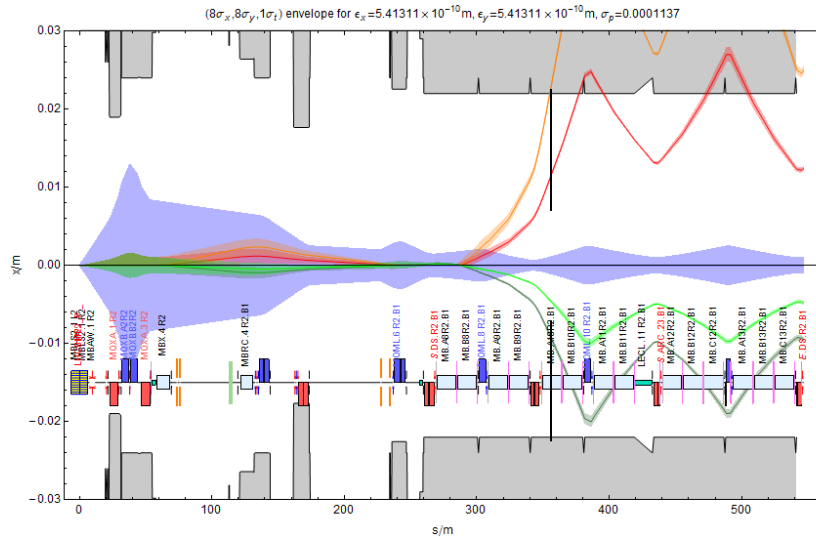
Figure 5-8: **1-σ envelope of the main Pb^{82+} beam (violet) together with the dispersive trajectories of ions undergone BFPP1 (red), BFPP2 (orange), EMD1 (light green) and EMD2 (dark green) coming out of the ALICE experiment in nominal optics. The DS collimator appears as a black**

line. Varying its opening allows different secondary beams to be intercepted (note that the orange BFPP2 beam carries energies well below the quench limit).

As can be seen, these secondary beams are lost very locally due to the big and sudden change of magnetic rigidity and may pose a risk of inducing magnet quenches [54,62]. For the LS2 ALICE upgrade, aiming at a peak luminosity of 6 x 10^{27}cm^{-2}s^{-1} (about 6 times higher than the nominal one), the dominant Bound-Free Pair Production (BFPP1) beam can carry about 150W, resulting in a power load in the coils of the MB.B10 dipole of about 50 mW/cm^3 [67], in the DS regions on both sides of ALICE. This is about a factor 2 above the quench limit according to figures presented at a recent collimation review [59]. Similar losses occur also in the DS regions around ATLAS and CMS during ion operation.

A strategy to eliminate any risk of quenches in the experimental IRs, both for proton and heavy-ion runs, is the installation of TCLD collimators in the DS to catch ions beams before they reach the magnets, as schematically shown in Figure 5-8. For heavy-ion operation, one collimator per side of the experiment would be sufficient to effectively intercept the secondary beams from the most dominant processes in a location where these ions are well separated from the main beam.

Extensive energy deposition simulations in the DS around ALICE, where MB.A10 is substituted by a pair of 11 T magnets and a TCLD collimator, confirm this assumption [62, 67]. The proposed TCLD collimator installation, with a jaw based on 80 cm of a tungsten heavy alloy, is expected to reduce by more than a factor 100 the peak power density in the new 11 T dipoles compared to the power density in cold dipoles with the present layout with old dipoles and no TCLD collimators [67]. DS collimation around IR2 is therefore considered necessary for the full exploitation of the ALICE detector upgrade.

Different jaw lengths and materials have been comparatively addressed for the specific case of ions in IR2 by using as a figure of merit the reduction factor of losses in the DS dipoles [67]. Simulations show that 50 cm of Copper would suffice (see for example the results presented at the collimation review [59]). However, in order to minimize design effort and production works both for the collimator and for the design of the cryo by-pass, the same length of 80 cm adopted for the TCLD in IR7 (see Table 5-2) is also used as a baseline for the TCLD collimators in the experimental IRs. For the jaw material, the tungsten alloy Inermet 180 is used as baseline for IR7. Should the Cu design be easier/less costly, it could be considered for the implementation around P2.

For high-intensity proton operation, the losses observed around IR1 and IR5 can be reduced with 2 TCLD collimators per IR side. The need for such implementation depends on the dipole quench limits and on the effectiveness of the physics debris collimation with TCL collimators. Layouts based on TCL collimators only (positioned in the straight section of IR1 and IR5 where the local dispersion from the collision point is low) might be sufficient but this requires further studies with the latest HL-LHC layouts that will estimate the peak energy deposited in the DS magnets. The TCLDs would then complement if needed the present system with TCLs.

5.2.2 Upgrades for impedance improvement

The LHC impedance budget is largely dominated by the contribution of the LHC collimators. For this reason, the present collimation system has been conceived in a way that it can be easily upgraded to reduce the impedance [55]: every secondary collimator slot in IR3 and IR7 features a companion slot for the future installation of a low-impedance secondary collimator. A total of 22 slots (IR7) and 8 slots (IR3) are already cabled for a quick installation of new collimators – referred to as TCSMP in the present database naming convention – that can either replace the present TCSGs or be used together with them. Partial preparation of these slots is on-going in LS1.

The importance of minimizing the machine impedance for the HL-LHC has been emphasized in [56, 57, 58] and also in a recent LHC collimation review [59]. We therefore foresee that, by the time of the full HL-LHC implementation (LS3), some or all the available TCSMP slots might be equipped with advanced collimators using new materials, and possibly coating, to reduce the impedance. A staged

installation using the various technical stops and shutdowns after LS1 is possible according to actual needs.

Secondary collimators in the betatron cleaning insertion (IR7) also have a crucial role in the LHC machine protection and might be exposed to large beam losses. Therefore, new material choices and designs must be robust also against beam failure (at least the ones exposed to horizontal losses). The driving requirements for the development of new materials are thus (1) low resistive-wall impedance to avoid beam instabilities, (2) high cleaning efficiency, (3) high geometrical stability to maintain the extreme precision of the collimator jaw during operation despite temperature changes and (4) high structural robustness in case of accidental events like single-turn losses.

The present baseline for the upgraded secondary collimators relies thus on a Molybdenum Carbide- Graphite (MoGr) composites, possibly coated with pure Mo. Other lower Z refractory coatings are presently under study. The Mo coating considered now would reduce the surface resistivity by about a factor 10 to 20 compared to Mo-Gr and by more than a factor 100 compared to CFC. The benefit on the impedance budget of the collimation system would be significant: in the relevant frequency range, impedance would be reduced to 10 % of the one of the CFC jaws [60], as illustrated in Figure 5-10.

On the other hand, the new design and materials [61] must be validated for operation. Material properties and the coating options have to be validated for the operation in the LHC. For this purposes, a rich program of validation is in progress, involving:

- tests at HiRadMat, covering both material samples as well as full jaw validation;
- mechanical engineering prototyping;
- beam tests at the LHC, planned for 2016 (collimation installation in the 2015 shutdown).

In addition to the impedance improvements, the new TCSPM also feature a number of improvements in the mechanical design (Figure 5-11) [61]. They incorporate the BPM button design. The key hardware parameters are listed in Table 5-3.
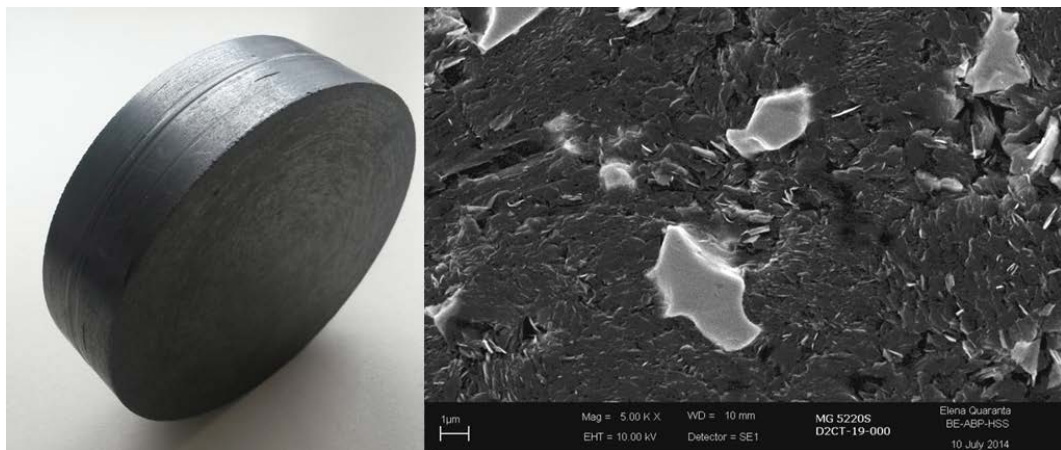
Figure 5-9: MoGr plate recently produced by Brevetti Bizz, Italy (left). Dimensions of the plate: 90mm diameter and 24.3mm thickness. It is a massive piece prepared in view of the production of the LHC collimator jaw inserts. A detail of the microstructure is shown on the right side, where the graphite flakes matrix well sintered with the carbon fibers is visible together with few molybdenum carbide "islands" of about 5μm length.
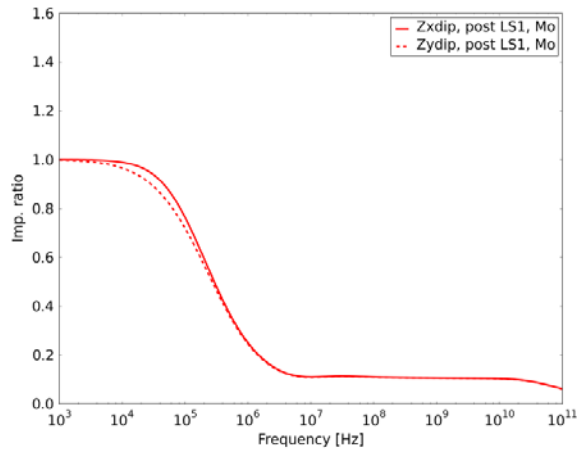
Figure 5-10: Collimation impedance versus frequency: impedance ratio between Mo coating on Mo-Gr (50 μm layer) and present CFC jaw for the real (solid) and imaginary (dotted) parts. A secondary collimator is considered. Courtesy of N. Mounet.
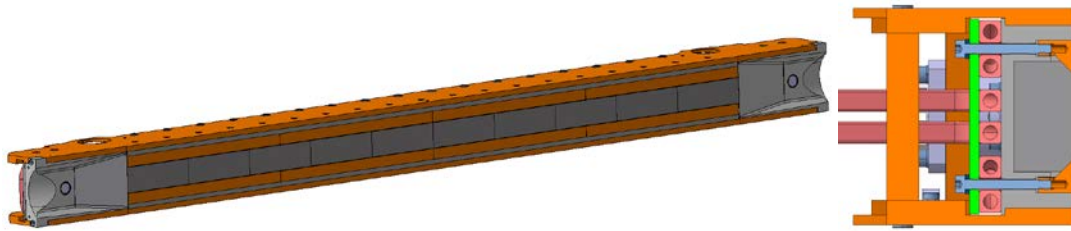
Figure 5-11: Preliminary design of the TCSMP jaw. This features 10 MoGr blocks. Also note lengthened jaw taperings, futher reducing contribution to HOM RF instabilities in the geometrical transition zones.

Table 5-3: Parameters of TCSMP collimators

Characteristics	Units	Value
Jaw active length	mm	1000
Jaw material	--	MoGr (TBD)
Flange-to-flange distance	mm	1480
Number of jaws	--	2
Orientation	--	Horiz., vert., skew
Number of motors per jaw	--	2
Number of BPMs per jaw	--	2
RF damping	--	Fingers
Cooling of the jaw	--	Yes
Cooling of the vacuum tank	--	Yes
Minimum gap	mm	< 1
Maximum gap	mm	> 60
Stroke across zero	mm	> 5
Angular adjustment	--	Yes
Jaw coating	--	Mo (TBC)
Transverse jaw movement (5th axis)	mm	+/- 10

5.2.3 Upgrades to the collimation of the incoming beam in the experimental IRs

The LHC Run 1 operation period has shown that protection of the IR superconducting magnets and experiments is a key asset for the machine performance: the available aperture, to be protected in all operational phases, determines the collimation hierarchy. The present tertiary collimators (TCTP, Target Collimator Tertiary with Pickup) are located at positions that protect the triplet and are made of a heavy tungsten alloy (Inermet 180). They effectively protect the elements downstream but are not robust against high beam losses, in particular during very fast beam failures which might occur if the beam dumping system does not trigger synchronously with the abort gap (an asynchronous beam dump). Setting margins are added to the collimator hierarchy to minimise the risk of exposure of these collimators to beam losses in case of such failures [3]. A design with improved robustness would allow reducing these margins and, as a result, pushing further the β* performance of the LHC, in particular for the HL optics baseline (ATS) that features an unfavourable phase between dump kickers and triplet magnets.

In addition to improvements from increased robustness, the HL-LHC layout puts additional aperture constraints [2, 3] because the aperture of the magnets up to the Q5 is now smaller than in the present layout. Thus, up to 4 more tertiary collimators might be required in IR1/5 to protect the Q4 and Q5 quadrupole magnets, in addition to those installed to protect the triplet (2 TCTP collimators – one horizontal and one vertical). The present baseline under study includes also a pair of new collimators in front of the Q5. On-going studies are addressing (1) the need for additional Q4 protection and (2) the need to keep tertiary collimators at the present locations in case additional tertiaries are added upstream.

A new design of tertiary collimators, referred to as TCTPM (Target Collimator Tertiary with Pick-up Metallic), is under study to address the new challenges. This design will be based on novel materials to improve the collimator robustness while ensuring adequate absorption, adequate cleaning and protection of the elements downstream. The TCTPM design and material choice must also take impedance constraints under consideration to keep the collimator impedance under control. A summary of the technical key parameters are given in Table 5-4.

The experimental experience of beam impacts on collimator material samples at HiRadMat [4, 5] indicates that a Molybdenum-Graphite (MoGr) composite can improve the TCTP robustness by a factor of several hundreds. Note that the present Inermet design is expected to undergo severe damage requiring a collimator replacement if hit by one single LHC nominal bunch of 10^{11} proton at 7 TeV. Other advanced materials are being studied as possible alternatives to further improve the robustness. The HL beam parameters with bigger charge and smaller emittance pose additional challenges in terms of beam damage potential.

Despite being less critical because of the larger β^* values, upgraded TCTP's are under consideration also for IR2/8 because various luminosity scenarios in there IRs require the usage of tertiary collimators, although at relaxed settings compared to IR1 and IR5.

Table 5-4: Equipment parameters of the TCTPM

Characteristics	Units	Value
Jaw active length	mm	1000
Jaw material	--	MoGr (TBD)
Flange-to-flange distance	mm	1480 (to be reviewed)
Number of jaws	--	2
Orientation	--	Horiz., vert.
Number of motors per jaw	--	2
Number of BPMs per jaw	--	2
RF damping	--	Fingers
Cooling of the jaw	--	Yes

Cooling of the vacuum tank	--	Yes
Minimum gap	mm	< 1
Maximum gap	mm	> 60 (to be reviewed)
Stroke across zero	mm	> 5
Angular adjustment	--	Yes
Jaw coating	--	No
Transverse jaw movement (5th axis)	mm	+/- 10 mm (at least)

5.3   Advanced collimation concepts

In this section we discuss new, more advanced, collimation concepts that still require R&D and therefore are not in the baseline. However, depending on the results of Run 2, some of these concepts may become an important asset for LHC and HL-LHC.

5.3.1 Halo diffusion control techniques

The 2012 operational experience indicates that the LHC collimation would profit from halo control mechanisms. These mechanisms were used in other machines like HERA and Tevatron. The idea is that, by controlling the diffusion speed of halo particles, one can act on the time profile of the losses, for example by reducing rates of losses that otherwise would take place in short time, or simply by controlling the static population of halo particles in a certain aperture range. These aspects were recently discussed at a collimation review on the possible usage of the hollow e-lens collimation concept at the LHC [41], where it was concluded that hollow e-lenses could be used at the LHC for this purpose. In this case, a hollow electron beam, runs parallel to the proton or ion beam that is on the axis of the cylindrical layer of electron. This hollow beam produces an electromagnetic field affecting only halo particles above a given transverse amplitude and can change their transverse speed. The conceptual working principle is illustrated in the left part of Figure 5-12. A solid experimental basis achieved at the Tevatron indicates this solution is promising for the LHC ([42] and reference therein).
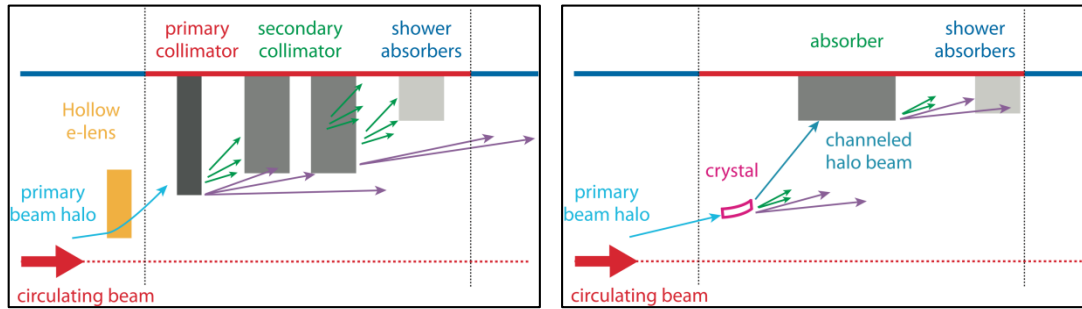
Figure 5-12: Illustrative view of the collimation system with integrated hollow e-lens or equivalent halo diffusion mechanism (left) and of an ideal crystal-based collimation (right). A reduced collimator layout than the one in Figure 5-1is adopted to show the betatron cleaning functionality only (one side only). Halo control technics are used to globally change the diffusion speed of halo particles and rely on the full collimation system remaining in place. Crystals entail a change of concept where the whole beam losses are concentrated, ideally, in one single beam absorber per plane.

The potential advantages of the electron lens collimation are several:

- Control of the primary loss rates, with potential mitigation of peak loss rates in the cold magnets, for a given collimation cleaning. Peak power losses on the collimators themselves can be optimized as well.

- Controlled depletion of beam tails, with beneficial effects in case of fast failures.

151

- Reduction of tails population and therefore peak loss rates in case of orbit drifts.

- Beam scraping at very low amplitudes (>3σ) without damage risk as for bulk scrapers.

- Tuning of the impact parameters on the primary collimators with possible improvement in cleaning efficiency.

Since the main beam core is not affected, the HEB (Hollow Electron Beam) operation should in theory be transparent for the luminosity performance if this technique works as designed. This was demonstrated at the Tevatron for DC powering of the electron beams.

The usage of HEB requires the collimation system in place in order to dispose of the tail particles expelled in a controlled way. No losses occur at the HEB location and the tail control mechanism can be put in place in any ring location. Larger beam size locations are favourable as they entail reduced alignment accuracy for the hollow beam. The IR4 is considered as a best candidate for two HEB devices due to larger than standard inter-beam distance (which ease integration of the device on the beam) cryogenics availability, low-radiation environment, and quasi-round beam.

While the functionality of HEB will provide clear benefits for the LHC operation, the real need for such scheme at the LHC and HL-LHC has to be addressed after gaining sufficient operational experience at energies close to 7 TeV on quench limits, beam lifetime and loss rates during the operational cycle, and collimation cleaning. Fast failure scenarios of the crab cavities require a low tail population above about 4 beam sigma: HEB is the only technique solidly validated experimentally in other machines that could ensure a safe operation in this case.

The HEB is targeted at enabling active control of beam tails above 3 beam sigma, with tail depletion efficiencies of the order of 90 % over times of tens of seconds, in all phases of the operational cycle, specifically before and after beams are put in collision.

The HEB implementation should ensure (1) the possibility to pulse the current turn-by-turn (as required to drive resonances in the linear machine before beams are in collision); (2) a train-by-train selective excitation (leaving "witness" trains with populated halos for diagnostics and machine protection purposes).

The main systems/components of a HEB can be summarized as:

- Electron beam generation and disposal: electron gun and collector, with the required powering.

- Several superconducting and resistive magnets: solenoids, dipoles and correctors to stabilize and steer the electron beam.

- Beam instrumentation for the optimization of the electron beam.

The parameters listed here are extracted from the conceptual design document [68] compiled by the colleagues from FNAL who worked on this topics within the US-LARP collaboration. A detail engineering design is now on-going at CERN. The first goal will be to define the volumes for a full integration into the LHC.

Table 5-5: Equipment parameters of the HEB from [68]

Parameter	Value or range
Beam and lattice	
Proton kinetic energy, T_p [TeV]	7
Proton emittance (rms, normalized), ε_p [μm]	3.75
Amplitude function at electron lens, $\beta_{x,y}$ [m]	200
Dispersion at electron lens, $D_{x,y}$ [m]	≤ 1
Proton beam size at electron lens, σ_p [mm]	0.32
Geometry	
Length of the interaction region, L [m]	3
Desired range of scraping positions, r_{mi} [σ_p]	4–8
Magnetic fields	
Gun solenoid (resistive), B_g [T]	0.2–0.4
Main solenoid (superconducting), B_m [T]	2–6
Collector solenoid (resistive), B_c [T]	0.2–0.4
Compression factor, $k \equiv \sqrt{B_m/B_g}$	2.2–5.5
Electron gun	
Inner cathode radius, r_{gi} [mm]	6.75
Outer cathode radius, r_{go} [mm]	12.7
Gun perveance, P [μperv]	5
Peak yield at 10 kV, I_e [A]	5
High-voltage modulator	
Cathode-anode voltage, V_{ca} [kV]	10
Rise time (10%–90%), τ_{mod} [ns]	200
Repetition rate, f_{mod} [kHz]	35

At the collimation review [41], it became clear that, if loss spikes were limiting the LHC performance after LS1, the hollow e-lens solution would not be viable because it could only be implemented in a next long shutdown at the earliest (driven by time for the integration into the cryogenics system). It is therefore crucial to work on viable alternatives that, if needed, might be implemented on an appropriate time scale. Two alternatives are presently being considered:

- Tune modulation through a ripple in the current of lattice quadrupoles;

- Narrow-band excitation of halo particles with the transverse damper system.

Though very different from the hardware point of view, both these techniques rely on exciting tail particles through resonances induced in the tune space by appropriate excitations. This works in the assumption of a presence of a well-known and stable correlation between halo particles with large amplitudes and corresponding tune shift in tune space (de-tuning with amplitude). Clearly, both methods require a solid experimental verification in a very low noise machine like the LHC, in particular to demonstrate that this type of excitations do not perturb the beam core emittance. Unlike hollow e-lenses, that act directly in the transverse plane by affecting particles at an amplitudes above the inner radius of the hollow beam, resonance excitation methods required a good knowledge of the beam core tune even in dynamic phases of the operational cycle, so the possibility to use these techniques at the LHC remains to be demonstrated. For this purpose, simulation efforts are on-going with the aim of defining the required hardware interventions during LS1 that might enable beam tests of these two halo control methods early on in 2015. Ideally, these measurements would profit from appropriate halo diagnostic

tools. However we are confident that conclusive measurements could be achieved already in Run 2 with the techniques describe for example in [5].

5.3.2 Crystal collimation

Highly pure bent crystal can be used to steer high-energy particles that get trapped by the potential of parallel lattice planes. Equivalent bending fields up to hundreds of Tesla can be achieved in crystals with a length of only 3-4 mm, which allows in principle to steer halo particles to a well-defined point. As opposed to a standard collimation system based on amorphous materials, requiring several secondary collimators and absorbers to catch the products developed through the interaction with matter (Figure 5-1), one single absorber per collimation plane is in theory sufficient in a crystal-based collimation system [43]. This is shown in the scheme in Figure 5-12 (right). Indeed, nuclear interactions with well-aligned crystals are much reduced compared to a primary collimator, provided that high channelling efficiencies of halo particles can be achieved (particles impinging on the crystal to be channelled within a few turns). This is expected to reduce significantly the dispersive beam losses in the DS of the betatron cleaning insertion (IR7) compared to the present system that is limited by the leakage of particles from the primary collimators. Simulations indicate a possible gain between 5 and 10 [44] even for a layout without an optimized absorber design. The crystal collimation option is particularly interesting for collimating heavy-ion beams thanks to the reduced probability of ion dissociation and fragmentation compared to the present primary collimators. SPS test results are promising [45].

Another potential of crystal collimation is a strong reduction of the machine impedance due to the facts that (1) only a small number of collimator absorbers is required and that (2) the absorbers can be set at much larger gaps thanks to the large bending angle from the crystal (40-50 μrad instead of a few μrad from the multiple-Coulomb scattering in the primary collimator). On the other hand, an appropriate absorber design must be conceived in order to handle the peak loss rates in case of beam instabilities: the absorber must withstand continuous losses up to 1 MW during 10 s while ensuring the correct collimation functionality. This is a change of paradigm compared to the present system where such losses are distributed among several collimators. Other potential issues concern the machine protection aspects of this system (such as the implications of a crystal not properly aligned and therefore channelling an large fraction of the total stored energy to the wrong place) and the operability of the system that requires mechanical angular stability in the sub-μrad range to be ensured through the operational cycle of the LHC (injection, ramp, squeeze and collision).

Promising results have been achieved in dedicated crystal collimation tests at SPS performed from 2009 within the UA9 experiment [45, 46, 47]. On the other hand, some outstanding issues about the feasibility of the crystal collimation concept for the LHC can only be addressed by dedicated beam tests at high energy in the LHC. For this purpose, a study at the LHC has been proposed [48]: two goniometers housing crystals have been installed in IR7 during LS1 for horizontal and vertical crystal collimation tests. The main purpose of beam tests at the LHC is to demonstrate the feasibility of the crystal-collimation concept in the LHC environment, in particular to demonstrate that such a system can provide a better cleaning of the present high-performance system throughout the operational cycle. Until a solid demonstration is achieved, crystal collimation schemes cannot be considered for future HL-LHC baseline scenarios.

5.3.3 Improved optics scenarios for the collimation insertions

Alternative optics concepts in IR7 can be conceived in order to improve some present collimation limitations without major hardware changes. For example, non-linear optics schemes derived from the linear collider experience [49] were considered for IR7. The idea is that one can create a "non-linear bump" that deforms the trajectories of halo particles and effectively increases their transverse amplitudes in a way that allows opening the gaps of primary and secondary collimators. These studies are well advanced from the optics point of view but for the moment it was not easily possible to find a

layout solution providing the same cleaning as the present system [50]. These studies, and other aimed at increasing the beta functions at the collimators, are on-going.

5.3.4 Rotatory collimator design

The rotatory collimator design developed at SLAC under the US-LARP effort proposes a "consumable collimator" concept based on 2 round jaws with 20 flat facets that can be rotated to offer to the beam a fresh collimator material in case a facet is damaged [27]. This design features a low-impedance and is based on standard non-exotic materials. It is conceived for a high-power operation, with a performing 12 kW active cooling system to withstand the extreme power loads experienced by the secondary collimators in IR7. A photograph of this device before closing the vacuum tank is given in Figure 5-13, where the rotatory glidcop (a copper alloy) jaws are visible. The first full-scale prototype of this advanced collimator concept has recently been delivered to CERN [28] and is being tested in preparation of beam tests. The ultimate goal is to validate the rotation mechanism after high-intensity shock impacts at the HiRadMat facility, aimed at demonstrating that the concept of consumable collimator surface can indeed work for the LHC beam load scenarios. The precision accuracy of this prototype and the impedance are also being tested together with its vacuum performance. The vacuum measurements indicated that the SLAC prototype is suitable for installation in the SPS or even LHC. Optimum strategy for beam tests is being established based on these new results.
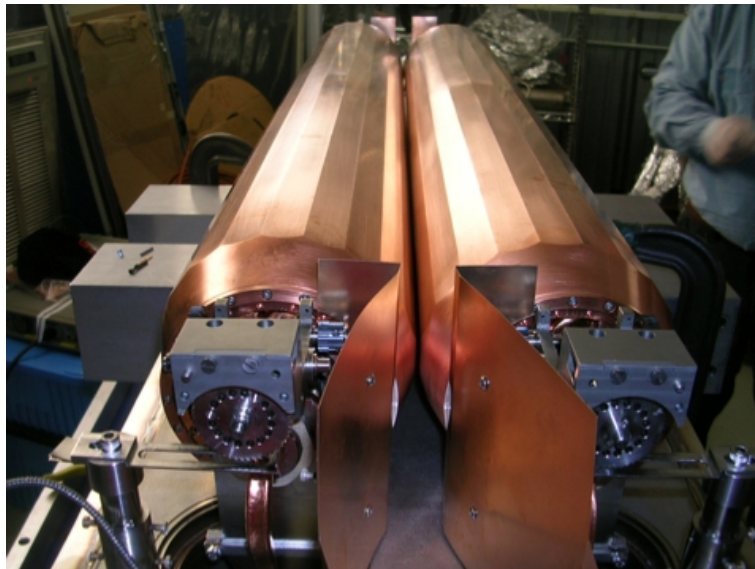
Figure 5-13: Photograph of the SLAC rotatory collimator prototype jaws before assembly in the vacuum tank. Courtesy of T. Markiewicz (SLAC, US-LARP).

5.4 Other collimators of the present system required in HL-LHC

It is important to realize that more than 60 % of the LHC collimators, which are not to be modified or replaced in the present collimation upgrade baseline described above, must remain reliably operational for the HL-LHC era. Even devices whose design is deemed adequate for the HL-LHC parameters, can hardly survive for the lifetime of the LHC machine without appropriate maintenance, substitution or revamping. A long-term strategy must be put in place order to ensure that the LHC collimation system can meet the performance and availability challenges of the HL-LHC project. In this section, the present LHC collimators that will also be needed for HL-LHC, possibly with improved design and features, are described.

5.4.1 IR3 and IR7 primary collimators (TCP, TCPP)

Carbon-based primary collimators (TCP, Target Collimator Primary) are used in the LHC to define the primary beam halo cut in the momentum (IR3) and betatron (IR7) cleaning insertion. One TCP collimator per beam is used in IR3 (horizontal orientation) whereas 3 collimators per beam are used in IR7 (horizontal, vertical and skew orientations) for a total of 8 primary collimators in the LHC. Since these collimators are the closest ones to the circulating beams, their jaws are built with a robust Carbon-Fibre Composite (CFC) that is designed to withstand the design LHC failure scenarios at injection (full injection train of 288 bunches impacting on one jaw) and at 7 TeV (up to 8 bunches impacting on one jaw in case of an asynchronous dump) [1]. The need to improve the TCP collimator design in view of the updated beam parameters for the HL-LHC design is being assessed.

The LHC primary collimator might needed to be upgraded for HL-LHC if the present design:

- proves not to be adequate to cope with the design LHC failure scenarios updated for the upgraded HL-LHC beam parameters (larger bunch intensity and smaller emittances);

- proves not to be adequate for standard operational losses with a larger stored beam energy in HL-LHC: for the same assumed minimum beam lifetime in operation, the total loss rates expected on the collimators might be up to a factor 2 larger for HL-LHC than for LHC;

- can be improved in a way that HL-LHC could profit from; e.g. improving materials or alignment features (integrated BPMs) for a more efficient operation.

The primary collimators are a fundamental element of the LHC multi-stage collimation hierarchy and are required in all operational conditions with beam in the machine. These are therefore high-reliability devices that must be compatible with operation in very high radiation environments and withstand standard operational losses and relevant failure cases without permanent damage that can jeopardize their functionality.

Note that presently a design with BPM-integrated jaw for primary collimators is being studied. This design, referred to as TCPP (TCP with Pick-up) uses for the moment the same CFC materials for the jaw but provides greatly improved operational features in terms of alignment speed and beam position monitoring. This design is considered also for HL upgrades.

5.4.2 IR3 and IR7 secondary collimators (TCSG)

Carbon-based secondary collimators (TCSG, Target Collimator Secondary Graphite) are used in the LHC as secondary stage of the beam halo cut in the momentum (IR3) and betatron (IR7) cleaning insertion. Four secondary collimators per beam are used in IR3 whereas 11 collimators are used in IR7 for a total of 30 TCSG collimators in the LHC. Horizontal, vertical and skew orientations are used in different locations. Since these collimators are among the closest ones to the circulating beams, their jaws are built with a robust Carbon-Fibre Composite (CFC) that is designed to withstand the same design LHC failure scenarios at injection and at 7 TeV as the primary collimators.

The present baseline for HL-LHC is that new secondary collimators, TCSPM, based on advanced robust and low-impedance materials will be added in IR3 and IR7, using existing TCSM slots [2]. In this scenario, the need to maintain the operability of the present CFC secondary collimators remains to be assessed. This depends for example on whether the new TCSPM collimators will be able to withstand the injection failure scenario. These aspects are presently under study.

5.4.3 IR3 and IR7 active shower absorbers collimators (TCLA)

Tungsten-based shower absorbers collimators (TCLA, Target Collimator Long Absorber) are used in the LHC as third or fourth stage of cleaning of beam halos in the momentum (IR3) and betatron (IR7) cleaning insertion. Four TCLA collimators per beam are used in IR3 whereas five collimators are used in IR7 for a total of 18 TCLA collimators in the LHC. Horizontal and vertical orientations are used

depending on the location. Operationally, these collimators are not supposed to intercept primary or secondary beam losses. They are therefore built using a heavy tungsten alloy that maximises efficiency in cleaning but that it is not robust with respect to beam impact with considerable power. The need to improve the TCLA collimator design in view of the updated beam parameters for the HL-LHC design is being assessed.

As for the previous case, the upgrade of the LHC shower absorber collimators might be needed for HL-LHC if the present design proved not to be adequate for the standard operational losses with a larger stored beam energy in HL-LHC and/or if it can be improved in a way that HL-LHC could profit from (improved materials, BPM features).

The TCLA collimators are an important element of the LHC multi-stage collimation hierarchy and are required in all operational conditions with beam in the machine. Operation might continue temporarily in case of isolated TCLA failures but we assumed here that HL operation for physics without TCLA collimators will not be possible. These are therefore high-reliability devices that must be compatible with operation in very high radiation environments and withstand standard operational losses and relevant failure cases without permanent damage that can jeopardize their functionality.

A joint study of collimation team with the beam dump team, has indicated the addition of two TCLA collimators per beam in IR6 in order to improve the protection of the Q4 and Q5 magnets immediately downstream of the dump protection devices [69]. The results indicate that this improvement was not necessary for the post-LS1 operation. The requirements for HL will be reviewed in 2015.

5.4.4 IR6 secondary collimators with pick-up (TCSP)

Carbon-based secondary collimators with pick-up buttons (TCSP, Target Collimator Secondary with Pick-up) are used in the LHC IR6 insertion as a part of the LHC protection system. Two collimators are used in the LHC, one per beam, as auxiliary dump protection device in the horizontal plane. In LS1, the TCSG design without integrated beam position monitors (BPMs) was replaced with the new one with BPMs for improved alignment and local orbit monitoring. Since these collimators are among the closest ones to the circulating beams, and are expected to be heavily exposed to beam losses in case of asynchronous dumps, their jaws are built with a robust Carbon-Fibre Composite (CFC) that is designed to withstand the design LHC failure scenarios at injection (full injection train of 288 bunches impacting on one jaw) and at 7 TeV (up to 8 bunches impacting on one jaw in case of an asynchronous dump). The need to improve the IR6 TCSP collimator design in view of the updated beam parameters for the HL-LHC design is being assessed.

5.4.5 Passive absorbers in IR3 and IR7 (TCAPA, TCAPB, TCAPC, TCAPD)

Tungsten-based passive shower absorbers collimators (TCAP, Target Collimator Absorber Passive) are used in the LHC as fixed-aperture collimators in the momentum (IR3) and betatron (IR7) cleaning insertion to reduce radiation doses to the warm quadrupole and dipoles in these insertions. Two TCAP collimators per beam are used in IR3 whereas three collimators are used in IR7 for a total of 10 TCAP collimators in the LHC. Four variants of these collimators exist to match the dimensions and orientations of the aperture of the adjacent warm magnets: TCAPA, TCAPB, TCAPC, TCAPD. Operationally, these collimators are not supposed to intercept primary or secondary beam losses but rather to absorb shower products generated by halo particles impinging on primary and secondary collimators. They are built using a heavy tungsten alloy that maximizes shower absorption, surrounded by copper. The need to improve the TCAP collimator design in view of the updated beam parameters for the HL-LHC design is being assessed.

The TCAP collimators ensure that doses on warm magnets in the cleaning insertions are minimized. Doses are determined by the integrated luminosity and therefore the possibility to improve

the warm magnet protection must be envisaged for the HL-LHC luminosity goal. The upgrade of the passive absorber collimators might be needed for HL-LHC if the present design proved not to be adequate for HL-LHC operational loss cases and/or if it can be improved by increasing the lifetime of warm magnets due to radiation wear (e.g., new materials or improved layouts/designs).

5.4.6 Tertiary collimators with pick-up in the experimental regions (TCTP)

As discussed above, tungsten-based tertiary collimators with pick-up buttons (TCTP, Target Collimator Tertiary with Pick-up) are used in the LHC to protect the superconducting triplets and the experiments in each experimental insertion against horizontal (TCTPH) and vertical (TCTPV) beam losses. A complete re-design of IR1 and IR5 collimation is imposed by the layout changes foreseen in HL-LHC for LS3. The need to improve the present TCTP collimators in IR1/5 in view of the updated beam parameters for the HL-LHC design is also being assessed. In particular, it is considered the possibility to replace the TCTP's with most robust ones based on novel materials, at least in the horizontal plane affected by beam dump failures.

5.4.7 Physics debris collimators in the experimental regions (TCL)

Physics debris absorbers are used in IR1 and IR5 to protect the matching sections and the dispersion suppressor from beam losses caused by collision product. The LHC IR layouts as of 2015 feature 3 horizontal TCL collimators per beam and per IR, for a total of 12 TCL collimators, installed in cells 4, 5 and 6. Their jaws are made of Copper (TCLs in cells 4 and 5) and Inermet 180 (cell6), as the latter were installed by recuperating tertiary collimators replaced in LS1 with the new TCTPs. The present baseline foresees to change all TCLs for HL by adding the BPM feature. If it is proven that this new feature is not mandatory, the present TCL collimators might be re-used for HL-LHC by being moved to the new layout positions. Mechanical and radiation ware should be studies for this scenario.

5.5 References

[1]   O. Brüning (Ed.) et al., LHC Design Report Vol. 1, CERN-2004-003-V-1.

[2]   R. Assman et al., "The final collimation system for the LHC", proceedings of EPAC2006, Edinburgh (UK), 2006. Also as CERN-LHC-PROJECT-REPORT-919 (2006).

[3]   R. Bruce et al., "LHC beta* reach in 2012", LHC Operation Workshop, EVIAN2011, Evian (FR), 2011. http://indico.cern.ch/event/155520

[4]   R. Bruce et al., "Sources of machine-induced background in the ATLAS and CMS detectors at the CERN Large Hadron Collider", Nuclear Instruments and Methods in Physics Research A 729 (2013) 825–840 .

[5]   G. Valentino et al., "Beam diffusion measurements using collimator scans at the LHC", Phys. Rev. Spec. Top. Accel. Beams 16 (2013) 021003.

[6]   K.H. Mess and M. Seidel, "Collimators as diagnostic tools in the proton machine of HERA", Nucl. Instrum. Meth. A351 (1994) 279-285.

[7]   H. Burkhardt, S. Redaelli, B. Salvachua, G. Valentino, "Collimation down to 2 sigmas in special physics runs in the LHC", proceedings of IPAC2013, Shanghai (China). Also as CERN-ACC-2013-0144 (2013).

[8]   S. Redaelli et al., "LHC collimator controls for a safe LHC operation", proc. of ICALEPSC2011, Grenoble (FR), 2011. http://accelconf.web.cern.ch/AccelConf/icalepcs2011/papers/wepmu020.pdf

[9]   B. Salvachua et al., "Cleaning Performance of the LHC Collimation System up to 4 TeV", proc. of IPAC2013, Shanghai (China). https://cds.cern.ch/record/1574583?ln=en

[10]   B. Salvachua et al., "Lifetime analysis at high intensity colliders applied to the LHC," proc. of IPAC2013, Shanghai (China). http://cds.cern.ch/record/1574586/files/CERN-ACC-2013-0072.pdf

[11]   N. Mounet et al., "Beam stability with separated beams at 6.5 TeV," proc. of LHC Operations Workshop, EVIAN2012, Evian (Fr). https://indico.cern.ch/getFile.py/access?contribId=18&sessionId=10&resId=0&materialId=paper&confId=211614

[12]   2013 Collimation Project Review, http://indico.cern.ch/event/251588

[13]   S. Redaelli et al., "Quench Tests at the Large Hadron Collider with Collimation Losses at 3.5 Z TeV," proc. of HB2012, Beijing (CH). http://accelconf.web.cern.ch/AccelConf/HB2012/papers/mop245.pdf

[14]   Recommendation from the external review panel of the 2013 collimation review. Available here.

[15]   A. Marsili et al., "Simulations and measurements of physics debris losses at the 4 TeV LHC," proceedings of IPAC2013, Shanghai (China).

[16]   CERN EDMS document 1283867 (2013), also available at http://lhc-collimation-project.web.cern.ch/lhc-collimation-project/LS1/default.php.

[17]   CERN EDMS document 1283826 (2013), also available at http://lhc-collimation-project.web.cern.ch/lhc-collimation-project/LS1/default.php.

[18]   L. Esposito, presentation at the 2nd HiLumi Annual meeting, Frascati (I), 2012. http://indico.cern.ch/event/183635

[19]   L. Esposito, presentation at the 3rd HiLumi Annual meeting, Daresbury (UK), 2012. http://indico.cern.ch/event/257368

[20]   A. Bertarelli et al., "The mechanical design for the LHC collimators," proceedings of EPAC2004, Lucern (CH), EPAC-2004-MOPLT008.

[21]   S. Redaelli et al., "Final implementation and performance of the LHC collimator control system," proceedings of PAC09, Vancouver (CA).

[22]   A. Bertarelli et al., "Mechanical design for robustness of the LHC collimators," proc. of PAC2005, Knoxville (USA). http://accelconf.web.cern.ch/AccelConf/p05/PAPERS/TPAP004.PDF

[23]   F. Carra et al., "LHC collimators with embedded beam position monitors: a new advanced mechanical design," proc. of IPAC2011, San Sebastian (E), IPAC-2011-TUPS035.

[24]   D. Wollmann et al., "First beam results for a collimator with in-jaw beam position monitors," proc. of IPAC2011, http://accelconf.web.cern.ch/AccelConf/IPAC2011/papers/thpz027.pdf

[25]   D. Wollmann et al., "Experimental verification for a collimator with in-jaw beam position monitors," proc. of HB2012, http://accelconf.web.cern.ch/AccelConf/HB2012/papers/mop242.pdf

[26]   G. Valentino et al., "Successive approximation algorithm for BPM-based LHC collimator alignment," submitted to PRST-AB (2013).

[27]   J. Smith et al., "Design of a rotatable copper collimator for the LHC phase II collimation upgrade," EPAC2008, Genova (I). http://accelconf.web.cern.ch/AccelConf/e08/papers/mopc096.pdf

[28]   T. Markiewiz, "Status of SLAC RC," presentation at the 3rd HiLumi annual meeting, Daresbury (UK), 2013. http://indico.cern.ch/event/257368

[29]   A. Bertarelli et al., "First results of an experiment on advanced collimator materials at CERN HiRadMat facility," proc. of IPAC2013, Shanghai (China). https://cds.cern.ch/record/1635957/files/CERN-ACC-2013-0268.pdf

[30] A. Bertarelli et al., "An experiment to test advanced materials impacted by intense proton pulses at CERN HiRadMat facility", Nucl. Instr. Meth. B (2013) http://dx.doi.org/10.1016/j.nimb.2013.05.007

[31] M. Cauchi et al., "High energy beam impact tests on a LHC tertiary collimator at CERN HiRadMat facility," submitted to PRST-AB (2013).

[32] S. Redaelli, "The LHC collimation baseline for HL-LHC," presentation at the 3rd HiLumi annual meeting, Daresbury (UK), 2013. http://indico.cern.ch/event/257368

[33] A. Marsili, "Simulations of collimation cleaning performance for HL-LHC optics," proc. of IPAC2013, Shanghai (China).

[34] R. Assmann et al., "Accelerator physics concept for upgraded LHC collimator performance," PAC2009, Vancouver (CA). https://cds.cern.ch/record/1307562/files/EuCARD-CON-2009-047.pdf

[35] S. Redaelli et al., "Do we really need a collimation upgrade?" LHC Performance Workshop, Chamonix2012, https://indico.cern.ch/event/164089

[36] 2011 Collimation Project review, https://indico.cern.ch/event/139719

[37] Review of 11 T dipoles and cold collimation, https://indico.cern.ch/event/155408

[38] HiLumi-WP5 (collimation) section at the 3rd Joint HiLumi LHC-LARP Annual Meeting, Daresbury (UK), 2013. http://indico.cern.ch/event/257368

[39] A. Marsili, "Simulated cleaning for HL-LHC layouts with errors", presentation at the 3rd Joint HiLumi LHC-LARP Annual Meeting, Daresbury (UK), 2013. http://indico.cern.ch/event/257368

[40] A. Lechner, "Energy deposition with cryo-collimators in IR2 (ions) and IR7", presentation at the 3rd Joint HiLumi LHC-LARP Annual Meeting, Daresbury (UK), 2013. http://indico.cern.ch/event/257368

[41] Review of hollow e-lens for the LHC collimation, https://indico.cern.ch/event/213752

[42] G. Stancari, "Progress towards the conceptual design of a hollow electron lens for the LHC", presentation at the 3rd Joint HiLumi LHC-LARP Annual Meeting, Daresbury (UK), 2013. http://indico.cern.ch/event/257368

[43] W. Scandale, "Crystal-based collimation in modern hadron colliders," Int.J.Mod.Phys. A25S1 (2010) 70-85

[44] D. Mirarchi et al., "Layouts for crystal collimation tests at the LHC," proc. of IPAC2013, Shanghai (China) https://cds.cern.ch/record/1573725?ln=en

[45] W. Scandale et al., "Comparative results on collimation of the SPS beam of protons and Pb ions with bent crystals," Phys.Lett. B703 (2011) 547-551

[46] W. Scandale et al., "Optimization of the crystal-assisted collimation of the SPS beam," Phys. Lett. B726 (2013) 182-186

[47] W. Scandale et al., "Strong reduction of the off-momentum halo in crystal assisted collimation of the SPS beam," Phys.Lett. B714 (2012) 231-236

[48] CERN EDMS document 1329235, LHC-TEC-EC-0001 (2013).

[49] A. Faus-Golfe et al., "Non-linear collimation in linear and circular colliders," proc. of EPAC2006, Edinbourgh (UK). http://accelconf.web.cern.ch/AccelConf/e06/PAPERS/WEXFI03.PDF

[50] L. Lari et al., "Studies for an alternative LHC non-linear collimation system," proc. of IPAC2012 . http://accelconf.web.cern.ch/AccelConf/IPAC2012/papers/moppd077.pdf

[51] H.-H. Braun et al, "Collimation of Heavy Ion Beams in LHC", proceedings of EPAC 2004, Lucerne, http://accelconf.web.cern.ch/AccelConf/e04/PAPERS/MOPLT010.PDF (2004).

[52] LHC Collimation Review 2009, http://indico.cern.ch/conferenceDisplay.py?confId=55195

[53] J.M. Jowett et al, "Heavy Ion Beams in the LHC", proceedings of PAC 2003, Portland (2003), http://accelconf.web.cern.ch/AccelConf/p03/PAPERS/TPPB029.PDF

[54] R. Bruce et al, "Beam losses from ultraperipheral nuclear collisions between 208Pb82+ ions in the Large Hadron Collider and their alleviation", Phys. Rev. ST Accel. Beams 12, 071002 (2009).

[55] R. Assmann et al., Collimation chapter of the LHC Design Report, edited by O. Brüning et al., http://ab-div.web.cern.ch/ab-div/Publications/LHC-DesignReport.html

[56] HiLumi WP2 deliverable document D2.1, https://cds.cern.ch/record/1557082/files/CERN-ACC-2013-009.pdf

[57] HiLumi WP2 milestone document M29, "Initial estimate of machine impedance", https://cds.cern.ch/record/1644770/files/CERN-ACC-2014-0005.pdf

[58] HiLumi WP2 milestone document M31, "Preliminary estimates of beam-beam effect", http://cds.cern.ch/record/1709432/files/CERN-ACC-2014-0066.pdf

[59] Recommendation of 2013 Collimation Project review panel, https://indico.cern.ch/event/251588/

[60] N. Mounet, "Trensverse impedance in the HL-LHC era", presentation at the 3rd HiLumi Annual meeting, Daresbury, UK (2013), https://indico.cern.ch/event/257368/

[61] F. Carra et al., "Mechanical engineering and design of novel collimators for HL-LHC," IPAC2014, Dresden, GE (2014). http://accelconf.web.cern.ch/AccelConf/IPAC2014/papers/mopro116.pdf

[62] HiLumi-WP5 deliverable document 5.4, available on the HiLumi web page: http://hilumilhc.web.cern.ch/HiLumiLHC/results/deliverables/

[63] R. Bruce, A. Marsili, S. Redaelli, "Cleaning performance with 11 T dipoles and local dispersion suppressor collimation at the LHC", IPAC2014, Dresden, GE (2014). http://accelconf.web.cern.ch/AccelConf/IPAC2014/papers/mopro042.pdf

[64] A. Lechner et al., "Power deposition in LHC magnets with and without dispersion suppressor collimators downstream of the betatron cleaning insertion", IPAC2014, Dresden, GE (2014). http://accelconf.web.cern.ch/AccelConf/IPAC2014/papers/mopro021.pdf

[65] A. Marsili, R. Bruce, S. Redaelli, "Collimation cleaning for HL-LHC optics with error models," IPAC2014, Dresden, GE (2014). http://accelconf.web.cern.ch/AccelConf/IPAC2014/papers/mopro040.pdf

[66] L. Gentini, presentation at the 30th meeting of the Collimation Upgrade Specification working group, http://indico.cern.ch/event/278104/

[67] G. Steele et al., "Heat load scenarios and protection levels for ions", presentation at the 2013 LHC Collimation Project review, http://indico.cern.ch/event/251588

[68] G. Stancari et al., "Conceptual design of hollow electron lenses for beam halo control in the Large Hadron Collider," FNAL note FERMILAB-TM-2572-APC (2014) and CERN ATS note to be published.

[69] Collimation Working group meeting, https://indico.cern.ch/event/244412/

Chapter 6

Cold Powering

A. Ballarino[5], J.P. Burnet[5], D. Ramos[5], U. Wagner[5],S.Weisz[5], Y. Yang[25]
[5]CERN, Accelerator & Technology Sector, CH-1211, Geneva, Switzerland
[25]University of Southampton, Southampton SO17 1BJ, UK

6   Cold Powering

6.1   Overview

The electrical feed of the approximately 1700 Large Hadron Collider (LHC) superconducting (SC) circuits requires the transmission of more than ± 1.5 MA of current from the power converters to the magnets. This is done via conventional copper cables for the room temperature path between power converters and current leads, and High Temperature Superconducting (HTS) and resistive currents leads for the transfer to the 4.5 K liquid helium bath. Nb-Ti bus-bars operated in liquid helium at 4.5 K or in superfluid helium at 1.9 K provide the connection to the SC magnets. In the present LHC configuration, the power converters and the current leads are both located in underground areas, the former mainly in alcoves situated adjacent to the machine tunnel, and the latter in cryostats that are near the LHC interaction points and in line with the SC magnets. The 60 A power converters for the dipole orbit correctors are located in the tunnel, underneath the main dipole magnets. From each of the eight interaction points, power converters and current leads feed the magnets occupying half of the two adjacent machine sectors. Some equipment in the tunnel is exposed to significant levels of radiation.

For the HL-LHC upgrade novel superconducting lines (hereafter called "links") are being developed to supply current to the magnets from remote locations [1]. The new electrical layout envisages the location of the power converters and current leads either in surface buildings or in underground areas, some hundred meters away from the tunnel. The transmission of the current to the magnets is performed via SC links containing tens of cables feeding different circuits. Each link would transfer all together up to about 150 kA. The benefits of this remote powering via SC links are several and can be summarized as follows:

-   Access of personnel for maintenance, tests and interventions on power converters, current leads and associated equipment in radiation free areas, in accordance with the principle of radiation protection that optimizes doses to personnel exposed to radiation by keeping them As Low As Reasonably Achievable (ALARA);

-   Removal of the current leads and associated cryostats from the accelerator ring, thus making space available for other accelerator components. In the baseline hardware layout of the HL-LHC Interaction Regions (IR) around P1 and P5, no space is available for current leads and cryostats in line with the magnets. Also, there is no space in the existing underground alcoves for locating the power converters feeding the HL-LHC circuits;

-   Location of the power converters in radiation free areas.

The on-going programme focuses on the development of SC links to be integrated at the LHC interaction point 1 (P1), point 5 (P5) and point 7 (P7).

6.1.1 Cold Powering Systems at LHC P7, P1 and P5

The Cold Powering System consists of:

- Power converters;

- Current leads, located as near as possible to the power converters in a radiation free zone at some hundred meters distance from the LHC tunnel. The leads are connected to the power converters via room temperature conventional cables;

- A dedicated cryostat (DFH), where the cold terminations of the leads are electrically connected to the cables in the link;

- A link, made of superconducting cables housed in a semi-flexible cryostat (DSH). The link electrically connects the leads to the magnet bus-bar;

- A cryostat (DF) in line with the magnets at the location where the link terminates in the LHC tunnel. In the DF cryostat, each cable of the link is connected to the Nb-Ti bus-bar feeding a magnet circuit. The helium cryogen required for the cooling of the Cold Powering System is supplied from this cryostat;

- Cryogenic instrumentation required for control, monitoring and interlock functions as well as electrical instrumentation needed for protection of superconducting components and current leads.

The Cold Powering System relies on cooling with helium gas, and the superconducting part of the system spans the temperature range from 4.2 K up to 35 K - 50 K. The use of MgB_2 and HTS materials enables safe operation of the superconducting components, for which a temperature margin, intended as the increase of temperature that generates a resistive transition, of at least 10 K is guaranteed

In the tunnel, vapour generated in the DF cryostat from a two-phase helium bath is conveyed inside the superconducting link cold mass [2]. The gas cools the SC cables in the link and warms up to about 17 K while absorbing the static heat load of the cryostat. The DSH cryostat includes a thermal shield actively cooled by forced flow of He gas taken from the tunnel at about 20 K. For the Cold Powering Systems at LHC P1 and P5, the two helium flows are mixed at the level of the DFH to produce the flow of He gas, at about 30 K, required for the cooling of the current leads. The system at LHC P7 does not need mixing - the helium flow in the superconducting link cold mass is sufficient for the cooling of the leads. The design of the current leads is such that the gas is recovered at room temperature at their warm end.

The development of the Cold Powering System for LHC P7 [9]is well advanced to date:

- Concepts [3] and prototype [4] SC cables have been developed and tested,

- Dedicated cabling machines conceived for production of long unit lengths of novel HTS or MgB_2 cables have been designed, assembled and operated [5],

- A prototype Cold Powering System has been developed and tested [6],

- Integration studies in the LHC have been performed [7],

---

[9] The SC link in the P7 has recently been removed from the HL-LHC baseline; see LMC199 of 17 December 2014. However, the PDR refers to the baseline of October-November 2104, therefore we prefer to keep the description of P7 SC link in this text. In addition this assure consistency with the first version of PDR delivered to the FP7 office on 30 November 2014, and also to avoid a revision of other parts of the PDR referring to November 2014 baseline,

- New concepts of current leads and DFH cryostats optimized for easy transport and integration in the LHC underground areas have been elaborated. Detailed drawing activity for production of prototypes is being launched.

The design of the Cold Powering Systems is such as to minimize the work done in the tunnel during installation of components. It also takes into account boundary conditions imposed by transport in the LHC underground areas. In particular, volumes of individual components have been minimized according to transport requirements, and the main components (SC link, i.e. DSH cryostat with the SC cables inside, current leads, DFH and DF cryostats) are integrated as complete and pre-tested assemblies. Activities after integration are limited to splicing between current leads and link and closure of the DFH cryostat, splicing between SC link and Nb-Ti bus-bar and closure of the DF cryostat, and connection of the conventional room temperature cables to current leads and power converters.

6.1.2 Superconducting Link

The superconducting link is a semi-flexible transfer line, of a total length of up to about 500 m, which houses the SC cables connecting the cold end of the current leads to the Nb-Ti bus-bar of the magnet [1]. The transfer line consists of four corrugated concentric pipes that define the SC link cold mass, the actively cooled thermal shield and the external vacuum insulation wall.

The number of SC cables contained inside the link and their operating current vary for the different Cold Powering Systems that are to date under study. Inside the cold mass of each link there are tens of cables rated at different DC currents ranging from a minimum of 120 A up to a maximum of 20 kA. The cables are grouped in the form of compact cable assemblies with a total current capability of up to about |150| kA.

The links presently under study are proposed for integration at LHC P1, P5 and P7.

At LHC P1 and P5, six superconducting links, three right and three left of each interaction point, are being considered for integration in the LHC machine:

- Two SC links for the powering of the HL-LHC Insertions (low-β quadrupoles, D1 and corrector magnets),

- Two SC links for the powering of the HL-LHC Matching Sections,

- Two SC links for the powering of the LHC magnets in the arc[10].

The associated Cold Powering Systems replace the LHC cryogenic feedboxes (DFBX, DFBL and DFBA). New current leads and cryostats (DFHX, DFHM and DFHA), connected to the link in a radiation free area away from the tunnel, are being developed.

Work until now has been focused on the systems for the HL-LHC upgrade, but the development is directly applicable to the Cold Powering Systems aiming at replacing the DFBA. The present baseline electrical layout envisages the installation of the power converters and current leads in surface buildings. This calls for development of superconducting links, about 300 m long, including a vertical section of about 80 m.

At LHC P7 it is proposed to move power converters and current leads in an underground radiation-free gallery, which serves as access to the LHC ring (TZ76 gallery). Two superconducting links, each of them about 500 m long, are needed to connect the DF cryostat in the tunnel, to the DFH in the TZ76 (see section 6.1). The SC link will contain all cables feeding the LHC 600 A circuits today

---

[10] SC links for the LHC magnet in the arc (change of DFBA) has been removed from HL-LHC baseline (see LMC199 of 17 December 2104). However, for reason of coherence with November 2014 baseline that is the reference of the present PDR (see previous footnote), the text has not bene modified. The change will recorded in the next version of the Technical Design Report foreseen at end of 2015.

powered via the DFBA and DFBM at P7. The cable assembly in the SC link cold mass requires forty-eight cables rated at 600 A, for a total current-carrying capability of about |29| kA.

The need of the Cold Powering Systems for the LHC circuits that are not part of the HL-LHC upgrade, i.e. those feeding either the magnets in the arc at LHC P1 and P5 or the magnets at P7, is driven by Radiation To Electronics (R2E) requirements of power converters. Their integration in the LHC machine will be decided at a later stage of the project.

The present baseline proposal envisages using MgB_2 conductor in the longest part of the SC links (from 4.2 K to 20 K), and HTS material (YBCO or Bi-2223) in temperature range from 20 K up to 35 K – 50 K. The potential low cost of MgB_2 conductor and the possibility of cooling the superconducting link cold mass with He gas enable the development of Cold Powering Systems with improved performance. There is higher temperature margin, at the benefit of a safer operation and lower total exergetic cost of the refrigeration, with no extra cost with respect to the conventional Nb-Ti solution. Figure 6-2 shows the cross section of the superconducting cable assembly proposed for the SC links powering the HL-LHC Insertions at LHC P1 and P5. The total current transferred by these forty-four cables is 165 kA. Six 20 kA cables are required for powering the low-β insertion Nb3Sn quadrupole magnets and the Nb-Ti separation dipole, while the other cables feed corrector and trim circuits. Details of the cable assemblies developed for other Cold Powering Systems are presented elsewhere [1].
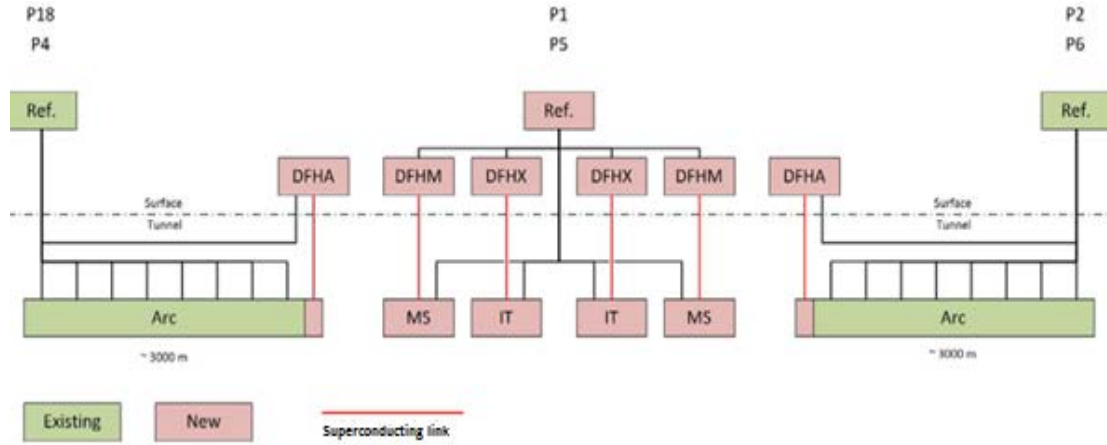
Figure 6-1: Superconducting links at LHC P1 and P5
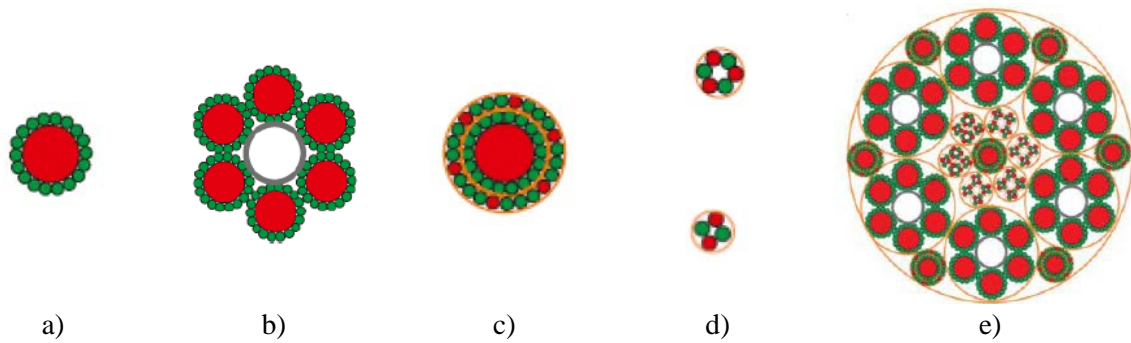
Figure 6-2: Cable assemblies for superconducting links at LHC P1 and P5. From left: a) Sub-unit of 20 kA cable, Φ~6.5 mm; b) 20 kA cable, Φ~19.5 mm; c) concentric 2×3 kA cable, Φ~8.5 mm; d) 0.4 kA cable (top) and 0.12 kA cable (bottom), Φ<3 mm ; e) 165 kA cable assembly for LHC P1 and P5 (6×20 kA, 7×2×3 kA, 4×0.4 kA, 18×0.12 kA), Φ~65 mm. The cables are made of copper stabilizer (red) and MgB_2 wire (green)

The cable (Twisted-Pair of superconducting tapes or wires) and cable assemblies developed for LHC P7 are optimized for transport of 1 kA range current. Details of the cable concepts and results from

tests performed in nominal operating conditions are presented elsewhere [4]. The cable assemblies are incorporated in a semi-flexible cryostat of the CRYOFLEX® type. The present baseline, which is to be confirmed through on-going integration studies and tests, envisages integration in the LHC tunnel of the cryostat with the cable assemblies already pulled in at the surface. To limit the risks associated with high-current resistive joints operated in helium gas environment, the cables are planned to be assembled in one single unit length with no splices between cables inside the link.

The main achievements to date are:

- the development of a the first MgB$_2$ Powder In Tube (PIT) round wire with electrical and mechanical performance that permit its use in high-current cables - work done in collaboration between CERN and Columbus Superconductors, Genova,

- the test of a 3 m long superconducting link of the type needed at LHC P7 [6],

- the design of a Cold Powering System optimized for integration at LHC P7 [6],

- the successful development and test of the first 2×20 m long cable made from MgB$_2$ round wire operated successfully up to 20 kA at 24 K [8].

Figure 6-3 shows the test station designed and successfully operated at CERN for the test of up to 20 m long superconducting links. As in the final configuration, the cables are cooled by forced flow of helium gas operating at any temperature from about 5 K to 35 K. Temperatures of up to 70 K can be achieved, enabling appraisal of cables made from different types of conductor.
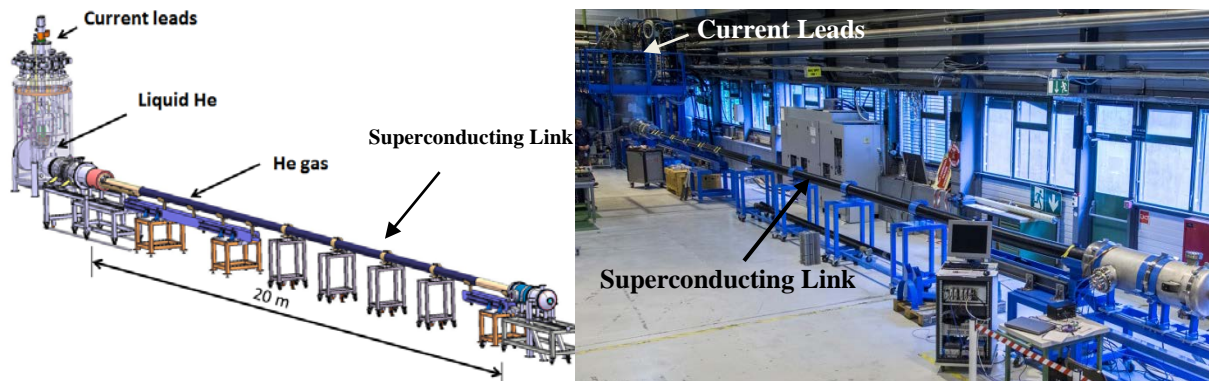
Figure 6-3: Test station designed and operated at CERN for the test of up to 20 m long superconducting links. The cables are cooled by forced flow of helium gas operating at any temperature from about 5 K to 35 K. Temperatures of up to 70 K can be achieved, enabling appraisal of cables made from different types of conductor

6.2   Cold Powering System design

In essence the Cold Powering System for the powering of the LHC magnets by superconducting links is a semi-flexible cryostat extended over a few hundred metres. The novel design has to face several challenges never encountered previously.

6.2.1 Cryostat for the superconducting link

The superconducting link cryostat (DSH) must maintain a stable and well defined cryogenic environment within which the superconducting cables are cooled by forced flow of helium gas. Unlike the liquid helium cooled superconducting bus-bars in the LHC machine, the cryogenic stability of the superconducting cables depends more critically on the cooling efficiency in helium gas environment within the superconducting link cold mass. The basic cryostat structure consists of an inner vessel

surrounded by an actively cooled thermal shield and enclosed by an outer vessel as room temperature vacuum envelope. At present the reference design of the cryostat is analogous to the Nexan's 4-Tube Coaxial CRYOFLEX® transfer line, which can be manufactured and delivered in one continuous length compatible to the cold powering requirements. It is essential to minimise the number of splices between cables inside the SC link cold mass due to their multiple circuit complexity and cooling challenges for high current resistive joints cooled by gaseous helium. While the cryostat flexibility is a crucial design aspect, it is recognised that the mechanical support to the vertical section at LHC P1 and P5 requires additional consideration. As part of the HL-LHC design studies, pre-prototype cryostats in 5 m and 20 m lengths have been procured from Nexans and tested at CERN [8] and at the University of Southampton [6]. The working experiences have been positive so far and a 60 m long cryostat will be procured in the coming months for integration tests in configurations similar to those in the LHC underground areas and for horizontal and vertical evaluation.

The gaseous helium in the cold mass of the SC link provides cooling for (a) steady-state heat load of the radial heat in-leak (conduction and radiation) from the surrounding thermal shield and heat conduction along the link and the inner vessel wall from the warmer end at 20 K and (b) transient heat load due to local disturbances in the link and/or thermal/vacuum instability in the cryostat. Under nominal operating conditions, the radial heat in-leak is dominant, estimated conservatively at below 0.2 W/m for a thermal shield temperature of ~ 60 K without multilayer insulation. The thermal shield will be actively cooled by flowing helium gas with an inlet temperature at 20 K. Further discussions on the cooling requirement can be found in [2].

6.3   Interfaces to the superconducting link

The SC link has a colder (4.2 K) interface to the LHC machine at one end and a warmer (20 K) interface to the current leads at the level of the DFH cryostat. The two interfaces are an integral part of the Cold Powering System due to electrical continuity and synergy in the cooling arrangements.

The present LHC current leads consist of a self-cooled HTS section and a 20 K helium gas cooled resistive copper section [9]. The former is connected to the Nb-Ti bus-bar in helium and the latter extends from the warm end of the HTS at 50 K to room temperature. The Cold Powering System design seeks the integration of the different helium gas flows at the interface of the superconducting link and current leads.

6.3.1   Electrical interface between the superconducting link and the current leads

Each of the multiple cables inside the superconducting link is spliced and connected to its corresponding current lead inside the DFH interconnection cryostat. The cryostat must allow easy access for making the electrical connections after the deployment of the superconducting link cable assembly in the semi-flexible DSH cryostat. The primary design focus is the reliable and secure handling of the SC cables via robust tooling and procedures. In addition, the design ensures in-situ completion of low resistance joints between the SC cables in the link and the current leads. Effective cooling of the resistive joints via the helium gas inside the link also requires integrated heat transfer features.

There are additional considerations to address specific circumstances for the systems at P1, P5 and P7. For example, the SC link at P7 terminates in the underground TZ76 gallery. The present configuration of TZ76 imposes stringent space restrictions for component transportation and installation. These constraints have been satisfied in the present baseline design where a stand-alone interconnection cryostat is connected to twelve discrete units of 4x600A current lead assemblies via HTS cables housed in twelve slim transfer-line type cryostats. A prototype of the Cold Powering System at LHC P7 will be manufactured and tested in the SM-18 in 2015. The existing test station incorporating the 20 m CRYOFLEX® line (see Figure 6-3) will be used for this purpose.

6.3.2 Cryogenic interface between the superconducting link and the current leads

The interface between the superconducting link and the current leads involves several cryogenic aspects. First of all, the continuation of the helium gas from the superconducting link into the current leads and its mixing with additional cooling gas if necessary shall be assured. The present cooling proposal for the systems at P1 and P5 [2] uses the warm exit of the helium gas cooling the SC link thermal shield as the supplementary coolant for the current leads. Since the exit temperature of the shield cooling gas always exceeds the warm boundary condition of 20 K for the SC cable in the link, this option implicitly imposes the hydraulic separation of the helium spaces of the link and the leads. This is likely to be the scenario for P1 and P5, where the superconducting link cold mass requires ~1 g/s while the current leads require ~10 g/s for a total transfer of about 150 kA.

The cooling requirements for the SC link and current leads at P7 are well matched, with 1.5 g/s for the DSH cold mass and 1.4 g/s for the DFH. Therefore there is a compelling case for using only the helium gas from the SC link cold mass for cooling the current leads. The elimination of hydraulic separation/re-mixing is an attractive proposition for aspects of both assembly and installation.

It is envisaged that the superconducting link cryostat (DSH) and current leads share a common vacuum space. A Paschen scenario will be avoided by ensuring that all the high tension side is surrounded by helium cooling gas at about 1 bar.

6.3.3 Control

The stable operation of the Cold Powering System relies on maintaining two temperature boundary conditions, i.e. 20 K at the splice terminations between the superconducting link and the current leads and about 35 K to 50 K at the cold end of the resistive section of the current leads. The former is controlled by a heater to generate the required helium boil-off from the DF cryostat in the LHC tunnel while the latter is controlled by a valve at the helium warm exit of each current lead. If a single helium flow is adopted for P7, then appropriate override should be devised for the two controllers to work correctly in tandem. Specifically, in case more flow is required by the current leads, the boil-off heater must allow the temperature in the DF to drift below the set value of 20 K. Conversely, in case higher boil-off is necessary for the cooling of the interconnections, a pressure controlled cold bleed will be used to discharge the excess in order to avoid over-cooling of the current leads.

6.4 Interface to the LHC machine

6.4.1 General

The DF cryostat interfacing the superconducting link to the magnets cold mass performs the role of electrical, cryogenic and mechanical interface. It includes:

- The required connections to the LHC cryogenic distribution line (QRL),

- A saturated liquid helium bath for the electrical splices between the cables in the link and the Nb-Ti cables,

- A hydraulic separation with respect to the superfluid helium bath cooling the magnets,

- The instrumentation required for cryogenic process control.

Different variants of DF cryostats are necessary for the Cold Powering Systems under study. The DF cryostats are vacuum insulated and equipped with an actively cooled thermal shield wrapped in multilayer insulation. Vacuum barriers are foreseen to separate the insulation vacuum of the DF cryostat from that of the link, in order to allow interventions on either equipment without the need for vacuum conditioning of the full system.

6.4.2 Interface cryostat for the HL-LHC Insertions

A continuous cryostat of approximately 60 m in length is foreseen to house the magnets from Q1 to D1 in a common insulation vacuum, with the interface cryostat to the link (DFX) located at its non-IP extremity, after D1. This being the most suitable location from the machine optics point of view, it implies on the other hand that the DFX vacuum vessel and respective supports must be designed to withstand an axial force, of up to 10 tonnes, induced by the unbalanced atmospheric pressure. The DFX will include a jumper to the QRL with helium piping for the supply of both the superconducting link and part of the continuous cryostat.

The DFX may either be designed as an independent cryostat or as service module integrated in the D1 cryostat. The choice between these two configurations will be made not only on the basis of integration and engineering considerations, but most importantly taking into account the need for minimizing the residual radiation doses to personnel during specific interventions that may occur in the lifetime of the HL-LHC machine, such as exchange of a magnet.

6.4.3 Interface cryostat for the Matching Sections

The most compact solution for the Cold powering System of the Matching Sections is to include the connection to the link in the service module of the magnet cryostat (QQS). From there, a first link cooled by supercritical helium is routed up to the DFM cryostat that replaces the present LHC DFL feedbox. All cables are then gathered inside the DFM into a main link, this one connecting the DFM to the current leads at the surface. The supercritical helium arriving from the link in the tunnel is expanded inside the DFM in order to generate liquid for the splices and gas for the cooling of the SC link joining the surface. As such, this concept does not require a connection to the QRL at the level of the DFM.

6.4.4 Interface cryostat for the Arcs

The DFBA LHC feedboxes comprise the so-called current modules, housing the current leads, and a shuffling module that serves as an interface to the Q7; all being supported in a stiff beam which spreads the axial force from atmospheric pressure to the tunnel floor. The most cost effective approach consists in exchanging the existing current module with a new DFA cryostat, profiting from the existing interfaces to the arc cryostat and the QRL. In this way, no interventions are required on the shuffling module and on the support beam. The DFA includes the connection to the QRL and provides the helium supply for the link. The DFA also contains two 13 kA current leads, used for energy extraction of the main dipole circuit, which will remain in their current location. Because they require a precise control of the liquid helium level, these leads will be cooled by a separate helium bath. In the particular case of LHC P7, a supercritical helium cooled link connects the Q6 to the DFA.

6.5 Integration of the Cold Powering Systems in the LHC machine

The constraints for integration of the Cold Powering Systems at LHC P7, P1 and P5 are very different and each of these cases requires a specific analysis:

- P7 is below the border between France and Switzerland, near the Lycée International of Ferney Voltaire, and surface buildings cannot be envisaged in this environment;

- P1 is equipped with a large service shaft and the LHC tunnel is enlarged in the corresponding straight section;

- P5 underground conditions are very restrictive, with a service shaft that is small and off centre, and with standard LHC tunnel around the collision region.

The following sections summarise the solutions presently retained for installing the Cold Powering Systems in these different areas.

6.5.1 Integration of the Cold Powering Systems at LHC P7

The insertion at P7 houses the betatron collimation system where a large fraction of the beam losses is intercepted. This induces a radiation level that is a long standing issue regarding single event upset in the electronic devices installed in the area. Additional shielding to protect the RR was installed in 2008 [10]. The Uninterruptible Powering System (UPS) was also relocated in 2008 [11]. All sensitive elements were relocated out of UJ76 during the Long Shutdown 1 (LS1) [12]. The power converters located in the RR73 and RR77 are the next source of concern as both the energy and intensity of the circulating beam will increase in the future. The solutions envisaged require either to increase the radiation tolerance or to relocate these power converters, and the Cold Powering System provides a practical solution for the second option.

As already mentioned, the geographical situation of P7 strongly constrains the installation of surface buildings and this is the reason why the access shaft, which dates from the LEP construction era, is located about 400 m from the machine tunnel. Figure 6-4 gives an overview of the corresponding underground premises. The long gallery TZ76, that was already used to relocate equipment originally installed in the UJ76 cavern, provides a radiation free area to install the power converters after their removal from RR73 and RR77. The red and yellow lines in Figure 6-4 indicate the routing of the Cold Powering Systems associated respectively with the arc 6-7 and arc 7-8. The total length of each line is about 500 m, with 250 m along the beam line in the LHC tunnel. The following section presents the integration of the Cold Powering System along the different portions of these routings, starting from the RR toward the service gallery TZ.

The RR73/77 alcoves contain the LHC DFBAM/N feedboxes that provide the warm to cold transition via the current leads. These DFBs will be replaced by the DFAM/N interfaces between the SC link and the Nb-Ti bus-bar of the magnets.

The SC links and the helium gas warm recovery lines can be installed close to the ceiling of the LHC tunnel in the long straight sections R74 and R771.

The passage of the SC links from the LHC tunnel to the TZ76 service gallery is the most delicate area regarding the installation of the Cold Powering Systems at LHC P7. Two alternatives are presently under consideration. The first involves a large number of rather sharp bends of the SC link to comply with the geometry of the UJ76 junction area (see Figure 6-5). The second relies on the drilling of two long ducts (each ~19 m long) to simplify the routing of the SC link (see Figure 6-6). A 60 m long cryostat should become available in spring 2015 to test the handling and installation of a SC link in order to decide between these two options.

The two SC links and the two He return lines can be installed on the upper part of the TZ76 service gallery as shown on Figure 6-7 (right). The routing in this configuration would be about 500 m until one reaches an equipment free area where the current leads and the relocated power converters can be installed. Figure 6-7 (left) gives a schematic view. The precise dimension and shape of the DFH cryostats are being defined. Space has been allocated for the power converters and their associated cooling units.
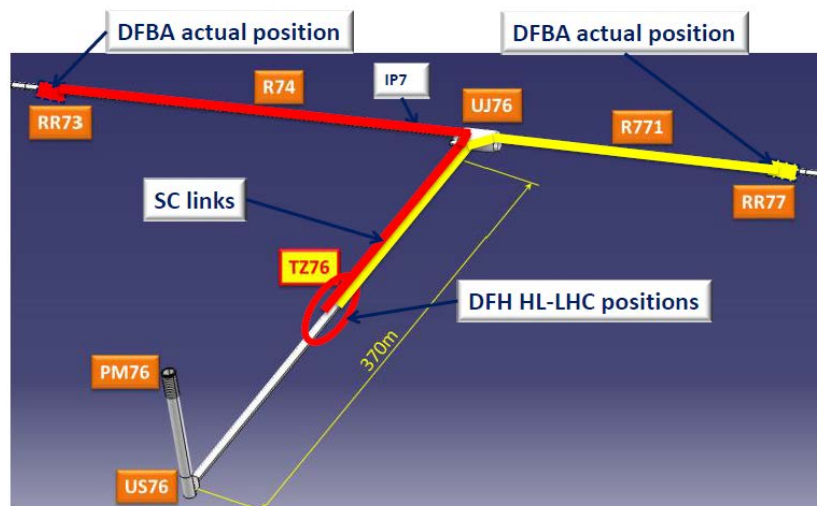
Figure 6-4: Underground layout at LHC P7
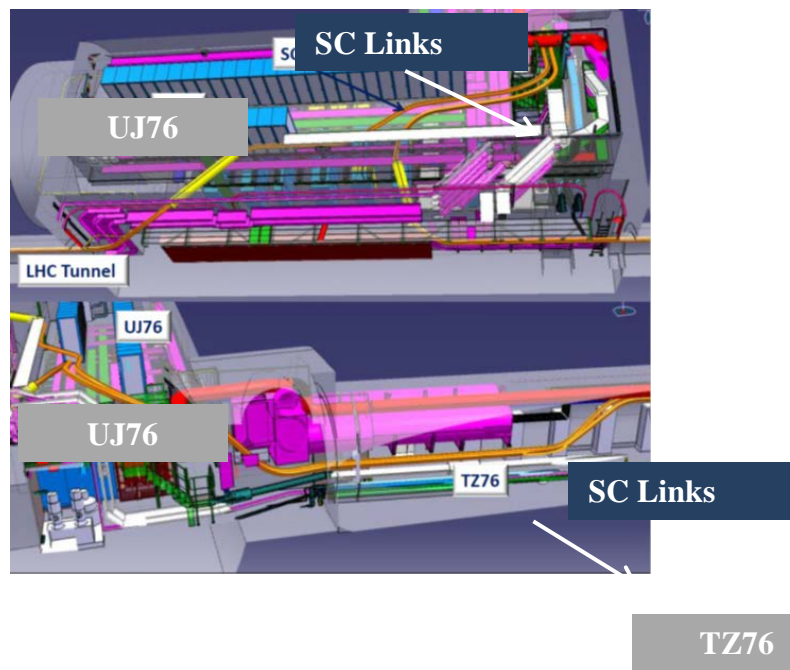
Figure 6-5: Passage through UJ76 with routing of the SC links in the UJ76 area
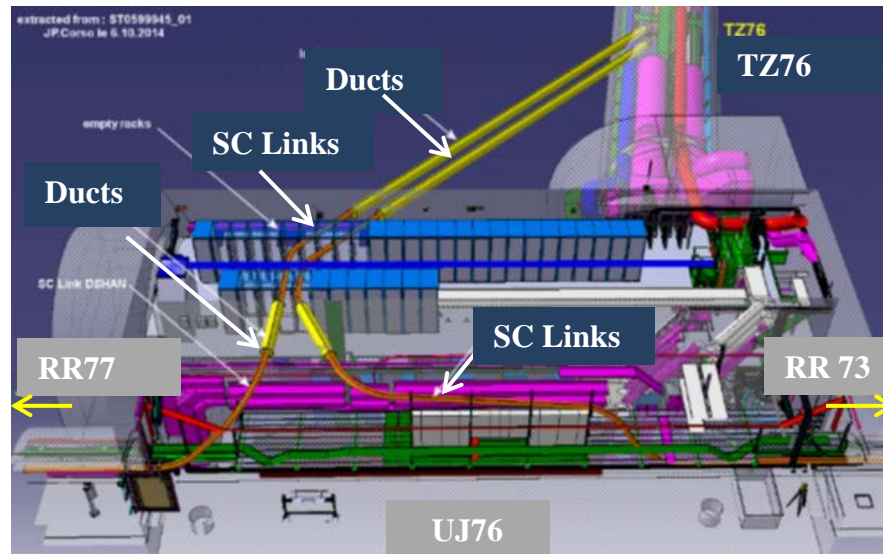
Figure 6-6: Passage of SC links through UJ76 with additional ducts
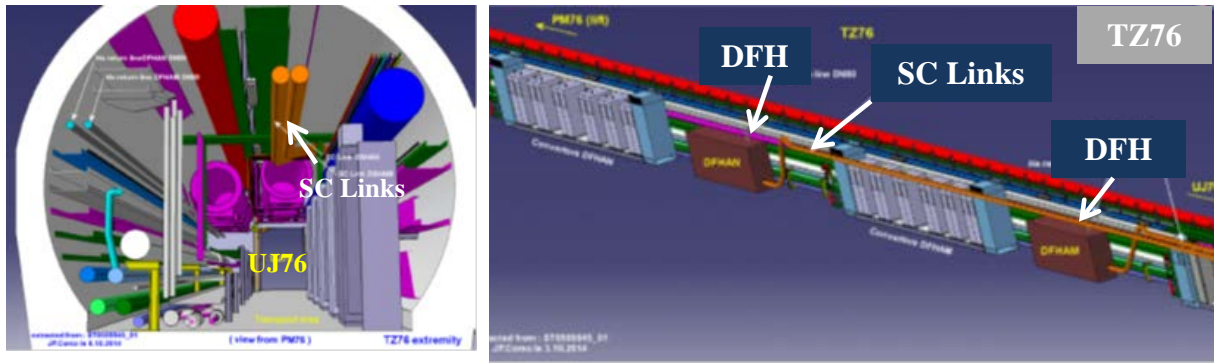
Figure 6-7: Routing of the two SC links and the two He return lines in the service gallery (left). Installation of the DFH and of the power converters in TZ76 (right)

6.5.2 Integration of the Cold Powering Systems at LHC P1

Point 1 houses high luminosity insertions that are totally redesigned to meet the HL-LHC performance requirements. The Inner Triplet quadrupoles, the D1-D2 separation dipoles and the Matching Sections will be replaced. Much higher current will be required to power the new magnets. The present underground premises at P1 do not provide enough space for the corresponding power converters and the objective of the Cold Powering System is to allow the installation of these new power converters at the surface. There is a large service shaft (PM15) at P1 that can be used to route several SC links, and those powering the new low-β triplets and D1 have a quite simple path as shown on Figure 6-8.

The D2 separation dipole and the stand alone quadrupoles of the Matching Section are presently powered through a Nb-Ti superconducting link with distribution feedboxes (DFBLA and DFBLB) and power converters located in the alcoves located at about 250 m distance from the tunnel on both sides of IP1 (RR13 and RR17). The new Cold Powering Systems include DFM cryostats between the Nb-Ti magnet bus-bars and the MgB_2 cables that would be installed in place of the present DFBLA and DFBLB. The SC links will then be routed along the beam lines in the long straight sections until reaching the junction caverns (UJ13 and UJ17 respectively left and right of IP1) and then running to the surface as sketched in Figure 6-8. The precise position of the SC links in the long straight section is not defined yet as they will need to pass across the crab-cavities area that is still being designed. However, as the LHC tunnel is enlarged to a 4.4 m diameter around P1, no space difficulties are expected there.

The RR13 and RR17 also house feedboxes (DFBAA and DFBAB) and power converters for the arcs 8-1 and 1-2 respectively. Radiation levels in these areas will increase with luminosity and may become an issue. Moreover, HL-LHC involves new equipment in the high-luminosity insertions which in turn will require additional space. While the impact of the radiation level and the need for shielding are being assessed, there are clear incentives to relocate as many as possible of the present power converters from RR13/RR17 to the surface. If this is the case, the removal of the DFBAs would free space to install new DFA cryostats in a similar way as described in section 4.1 for P7, with the current leads for energy extraction of the main dipole circuit and the connections to the QRL remaining at their current locations. The SC links would then follow the same path to the surface as those discussed above for D2 and Matching Section quadrupoles.

The detailed integration of the power converters in a surface building is not yet available, but it will involve an extension of the SD15 building at the top of PM15 with a total size that has to account for the total number of relocated power converters and for other additional HL-LHC related equipment.

174
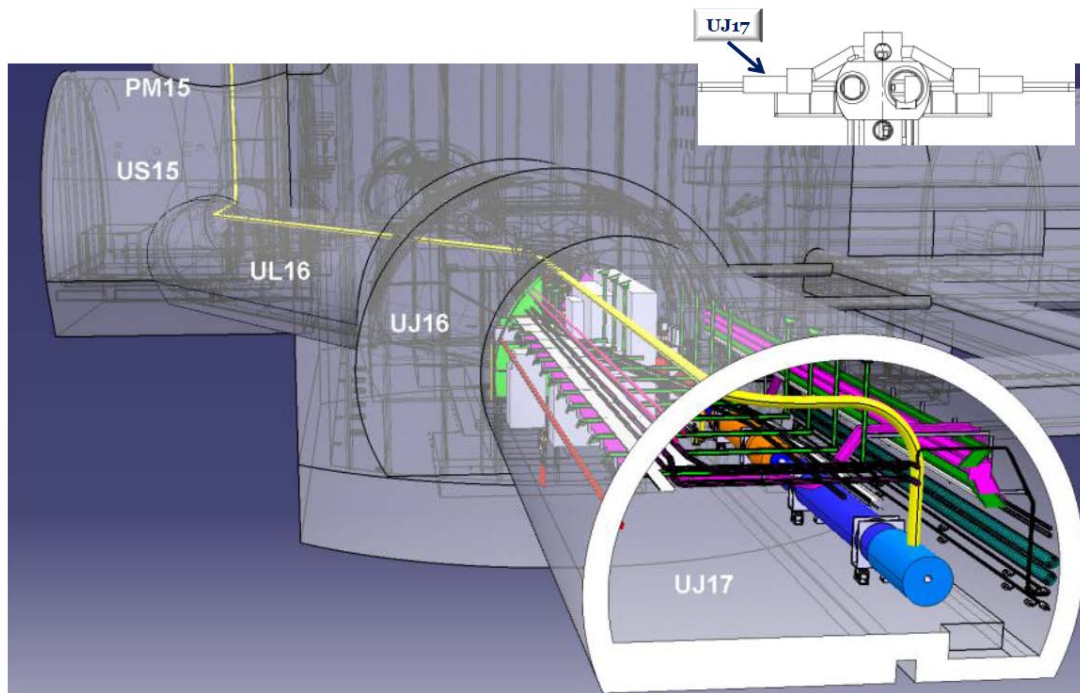
Figure 6-8: Routing of the SC links to surface for the low-β triplet right of LHC P1

6.5.3 Integration of the Cold Powering Systems at LHC P5

The elements of the Cold Powering Systems to be installed for HL-LHC at P5 are the same as those for P1. However, the environment at P5 is different. The tunnel diameter in the straight sections is 3.8 m, and nearly all the space is already allocated. The service shaft (PM56), located right of P5, is a small shaft dedicated to personnel access only. Therefore, a totally different routing to the surface must be envisaged for the SC links compared with the solution retained for P1.

Vertical shafts would allow routing the SC links from the LHC machine to the surface. They can be done with a standard excavation method (so called Auger Drilling) providing a 0.4 m internal diameter duct that is sufficient for housing one SC link and its supporting system. As it is a top-down drilling technique, there is a precision of about 0.5 m on the position of the shaft when it reaches the LHC level some 90 m below ground. This would be problematic if the target is the narrow machine tunnel, but it is acceptable if the shaft has to reach enlarged areas as the RRs or UJs, which are respectively 10.40 m and 8.40 m wide. The position of these enlarged areas at P5 is indicated in Figure 6-9. Vertical shafts above the UJ53 and the UJ57 would be allocated to the SC links for the new low-β triplets and D1 separation dipoles. Those above the RR53 and the RR57 would be allocated to the SC links for the stand-alone magnets of the Matching Sections. If the power converters for the arcs will also relocated to the surface, shafts would be drilled above the RR53 and the RR57 for the corresponding SC links.

New surface buildings will be required to house the power converters. The optimisation process between small local buildings or larger ones, connected through trenches to regroup the power converters, has yet to be done. A global optimisation should take account of all new equipment required for HL-LHC. The crab cavity system is facing a similar problem and it should be mentioned that a study is on-going for new underground premises to cope with the space requirements of the cryogenics cold boxes, the crab cavities and the powering equipment.

175
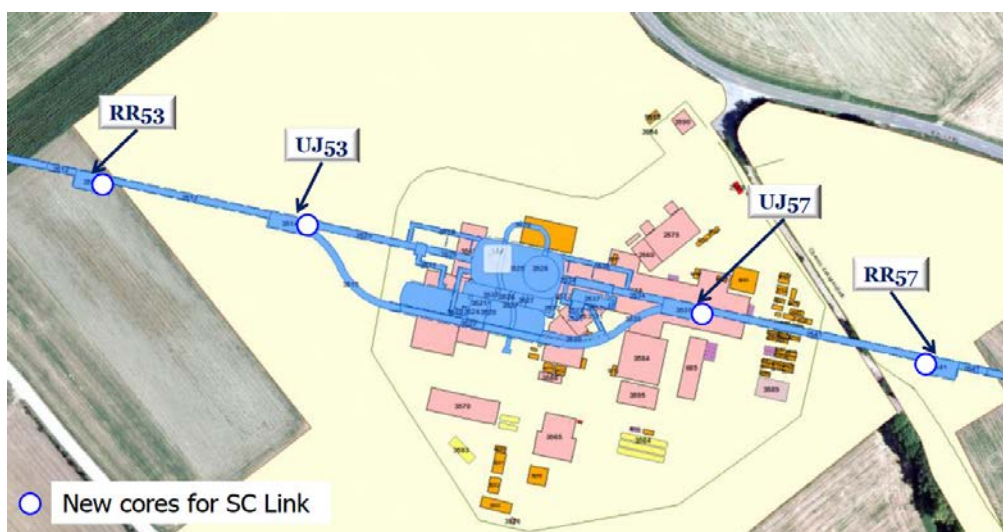
Figure 6-9: Layout of underground premises and of surface buildings at P5

6.6 Powering layout

Figure 6-10 shows the powering layout of the present LHC Inner Triplets. This powering scheme consists of a nested circuit with three power converters and free-wheeling protection circuits [13].

It requires a dedicated control system to decouple the control of the power converters [14]. At the beginning of the LHC operation, this specificity generated longer down-times with respect to the other electrical circuits. Today, thanks to the gained experience and to the development of diagnostic tools, the system has reached a good level of reliability. It should be noted that the ramp down time of these circuits, which defines the minimum time before a beam injection, had to be slowed down with respect to that obtained with the free-wheeling process. This was done in order to avoid trips of the power converters generated by the nested configuration.

The baseline powering layout of the HL-LHC Inner Triplets is shown in Figure 6-11. The low-β quadrupole (Q1, Q2 and Q3) are powered via two main circuits, each equipped with one trim power converter. The two Q2 units are powered in series with a 200 A trim converter on Q2b. Q1 and Q3 are powered in series with a 2 kA trim converter on Q3. The separation dipole (D1) and the corrector magnets are individually powered. This layout a) provides maximum flexibility for beam optics, b) simplifies the powering scheme with respect to the layout in Figure 6-10 at the advantage of a reduction of the Mean Time To Repair for interventions on the power converters. It should be noted that the total current transferred for feeding each triplet increases from about 40 kA in the present LHC scheme to above 150 kA for the HL-LHC configuration.

The possibility of powering all low-β quadrupoles in series, with dedicated trims, was considered. However, the layout in Figure 6-11 was preferred because of the smaller inductance per circuit and therefore reduced challenges for magnet quench protection. The powering of each low-β quadrupole magnet via a separate circuit was also not retained because of the related higher cost of the powering equipment – power converters and Cold Powering System.
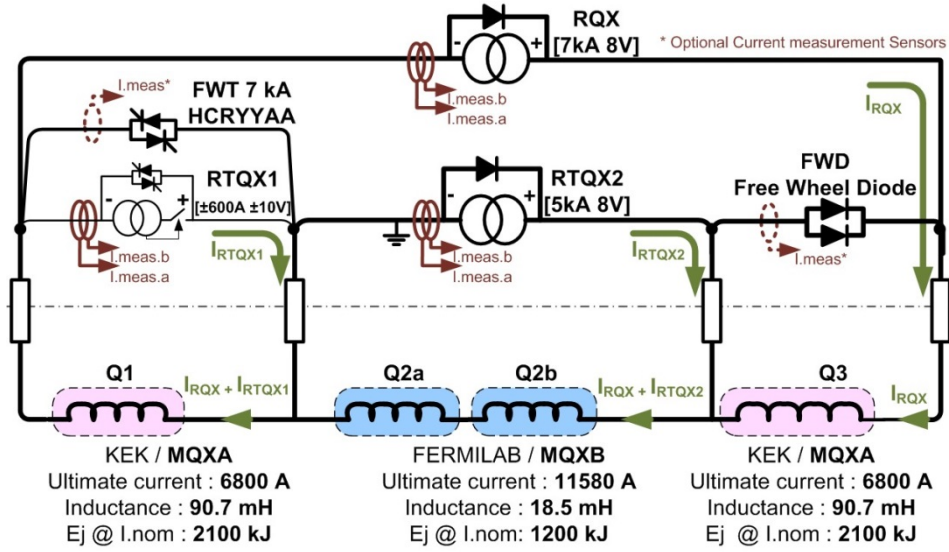
Figure 6-10: Powering layout of the present LHC Inner Triplets
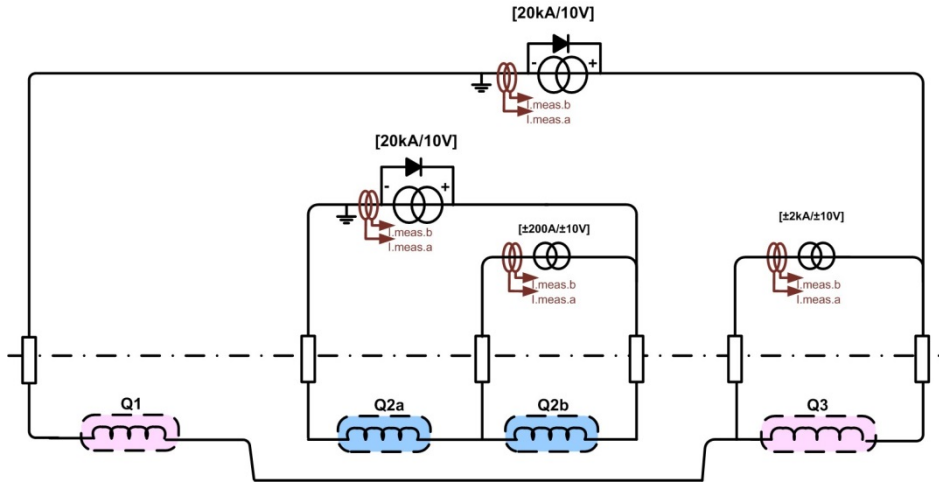
Figure 6-11: Powering layout of the HL-LHC Inner Triplets

The powering layout of the HL-LHC Matching Sections has also been reviewed. In the present LHC Matching Sections, the quadrupole magnets of beam 1 and beam 2 have a common return current lead. This choice was made in order to reduce the number of current leads from four- for individually powered magnets - to three. This electrical coupling puts constraints on the current settings of both circuits with the consequence of reducing the flexibility for different beam optics configurations. For this reason, in the HL-LHC Matching Sections the quadrupoles Q4, Q5 and Q6 are proposed to be individually powered with two current leads per circuit.

In the present LHC Matching Sections one-quadrant power converters are used for all the quadrupoles. The decrease of the magnet current is done with a free-wheeling process, and the ramp rate depends on the time constant of the circuit, which in turn is defined mainly by the inductance of the circuit. With the present configuration, the beam squeeze process takes up to 20 minutes – and for the HL-LHC, the squeeze process would be even longer due to the wider range of β*. The use of two-quadrant power converters (with bipolar voltage) is being considered for Q5. This would allow a faster decrease of the quadrupole current and therefore a reduced time of the beam squeeze process.

6.7 Power converters

The LHC was built with modular power converters to facilitate maintenance and integrate the redundancy principle [15] - redundancy was included in all LHC power converters rated at currents above 600 A. This has proven to be a real asset during operation. The N+1 redundancy allows running the power converters even with one module in fault. The advantages are the following: a) in case of fault, only one sub-converter is not operational and, in most of the cases, the fault does not generate a beam dump; b) the LHC can run with some faulty sub-converters in the machine and all interventions for repair can be performed during a machine technical stop. With the exception of dipole magnets, switch-mode technology was chosen for the LHC power converters in order to minimize their size and assure low output voltage ripple. All LHC power converters rated at currents above 120 A are water-cooled, with the advantage of a reduced size of the hardware. All these design principles will be maintained for the new power converters of the HL-LHC magnets.

6.7.1 Performance of the power converters

The HL-LHC power converters will be regulated in a closed current loop. Those for Q1, Q2 and Q3 will be of the highest precision class, like the LHC main dipole circuits. The stability of the low-β power converters will be at the level of 1 ppm (10^{-6} of nominal current) - with an uncertainty of ± 1 ppm [16]. The stability of the other power converters will be of the order of 10 ppm. The achievement of this level of stability does not require new developments. All hardware developed for the LHC power converters will be re-used, e.g. for the 20 kA DCCT and 22 bits $\Sigma\Delta$ ADC.

For the control of the power converters, the powerful FGC (Function Generator and Controller) system, which allows controlling all LHC power converters with the same hardware and software [17], is proposed. Its limitation is within the WORLDFIP bus, which has a speed limited at 2.5 Mbits/s. The replacement of this bus by an ETHERNET type bus is being considered.

6.7.2 Location of the power converters

The present LHC power converters are installed in underground areas. Of the 1710 total units, 1065 are exposed to radiation. During machine operation up to 2013, the power converters generated a number of beam dumps due to SEE (Single Event Effect). The faults due to SEE represented about 20% of the total power converter faults. A R2E (Radiations To Electronics) program was launched in 2010 to mitigate radiation issues for the whole LHC machine. In this framework, all power converters connected to the present DFBX were relocated to reduce their exposition to radiation. More shielding was added inside the RR alcoves to reduce particles fluences. A new radiation tolerant version of the FGC system, called FGClite, was developed for integration in the machine in 2016. The 600 A, the 4 kA, 6 kA and 8 kA power converters are being redesigned to be radiation tolerant. After the full deployment of this program - presently foreseen in 2018 - all power converters will able to operate in the RR alcoves and withstand the radiation levels foreseen for HL-LHC.

According to the present baseline, the power converters for the powering of HL-LHC magnets will be installed in surface buildings. The on-going development of radiation tolerant power converters aims at operating the power converters of the circuits fed via the DFBA in the RR alcoves, where they are presently located.

6.7.3 Power converters for HL-LHC

The list of magnets and corresponding power converters needed for HL-LHC is reported in Table 6-1.

Table 6-1: Magnets at each side of LHC P1 and P5

Optics	Magnet	Operating current [kA]	Inductance [mH]	Power converters [kA]	Uncertainty ppm of max current with weekly calibration	1/2 hour stability ppm of max current
MQXF Q1-Q3	MQXF	17.46	170	20	±1ppm	±1ppm
Q3	trim Q3	±2	85	±3.2	±10ppm	±5ppm
Q2a-Q2b	MQXF	17.46	145	20	±1ppm	±1ppm
Q2b	trim Q2	±0.3	72.5	±0.8	±100ppm	±10ppm
CP	MCBX	±2.42	25	±3.2	±10ppm	±5ppm
CP	MQSXF	0.182	1600	±0.2	±100ppm	±10ppm
CP	MCTXF	0.167	600	±0.2	±100ppm	±10ppm
CP	MCTSXF	0.157	150	±0.2	±100ppm	±10ppm
CP	MCDXF	0.139	300	±0.2	±100ppm	±10ppm
CP	MCDSXF	0.139	300	±0.2	±100ppm	±10ppm
CP	MCOXF	0.12	400	±0.2	±100ppm	±10ppm
CP	MCOSXF	0.12	400	±0.2	±100ppm	±10ppm
CP	MCSXF	0.132	180	±0.2	±100ppm	±10ppm
CP	MCSSXF	0.132	180	±0.2	±100ppm	±10ppm
D1	MBXF	11.8	36	14	±10ppm	±5ppm
D2	MBRD	12	37	14	±10ppm	±5ppm
	MCBRD	±3.2	12	±4	±10ppm	±5ppm
Q4	MQYY	15.65	6	18	±10ppm	±5ppm
	MCBYY	±3	12	±4	±10ppm	±5ppm
Q5	MQY	4.51	74	8	±10ppm	±5ppm
	MCBY	0.088		±0.12	±100ppm	±10ppm
Q6	MQML	5.39	21	8	±10ppm	±5ppm
	MCBC	0.1		±0.12	±100ppm	±10ppm

The list of power converters for HL-LHC is reported in Table 6-2.

Table 6-2: List of new power converters for Inner triplet and Matching Section magnets

Power converter	Current	Voltage	Quadrant	Quantity per IP side	Spare	total quantity
Type 1	20kA	<20V	1	4	2	18
Type 2	18kA	<20V	1	2	2	10
Type 3	14kA	<20V	1	2	2	10
Type 4	8kA	<±10V	2	4	2	18
Type 5	±4kA	<±10V	4	15	6	66
Type 6	±600A	<±10V	4	1	2	6
Type 8	±200A	<±10V	4	9	6	42
Type 9	±120A	<±10V	4	8	6	38
Total				45		208

In the present LHC machine, 8kA, 600A and 120A power converters are already in operation.

HL-LHC will require the development of two types of new power converters: a) the 1-quadrant converter 20 kA/10 V, which will be based on an extension of the 8 kA LHC power converter family; b) the 4-quadrant converter ±4kA/±10V, which will be based on the present topology of 600 A LHC power converters.

HL-LHC could require new topologies of 2-quadrant power converters rated at 8kA/±10V. This development is mandatory if the squeeze time process needs to be reduced.

Also, by replacing the present 13kA/18V power converters of the main quadrupole circuits with 2-quadrant power converters 13kA/±18V, the ramp down of the machine can be reduced by about 30 minutes. This upgrade would increase the global availability of the machine by about 4%.

6.8 Radiation tolerant power converters

The power converters today in the RR alcoves will be replaced with radiation tolerant converters. This development concerns the 600 A and the 4 kA, 6 kA and 8 kA families. The replacement is planned to take place during the Long Shutdown 2 (LS2). The new power converters will be able to withstand the doses and the fluences expected after the HL-LHC upgrade.

The present 60 A converters will not withstand the doses estimated during HL-LHC operation. They were designed for tolerating a maximum total dose of about 50 Gy, and the power converters placed in or close to the Matching Sections will receive a dose of up to 32 Gy/year. These converters will be replaced with new ones designed for withstanding a total dose of 200 Gy. This target corresponds to the maximum dose that can be tolerated by a design based on COTS (commercial component). A rotation between highly exposed and less exposed power converters is also foreseen. Development of 120 A radiation hard power converters is also required.

6.5 Power converters and LHC machine availability

The global machine availability is affected by the pre-cycle needed to degauss the magnets and by the magnets ramp-down time. In the present LHC, the most limiting circuits are those of the Inner Triplet quadrupoles and of the main quadrupoles. All these circuits are powered via 1-quadrant converters, which are the cause for the long ramp down time. Two upgrades can be envisaged if machine availability needs to be improved: a) replacement of these power converters with 2-quadrant converter types; b) use of external dump resistors to accelerate the discharge. As an illustration, by replacing the present 13kA/18V power converters of the main quadrupole circuits with 2-quadrant power converter 13kA/±18V, the ramp down of the machine can be reduced by 30 minutes. As mentioned in section 6.3, it is estimated that the replacement of both power converters powering the Inner Triplet quadrupole and main quadrupole circuits will increase the global availability of the machine by about 4 %.

6.9 Reference

[1] A. Ballarino, Development of Superconducting Links for the LHC Machine, Superconductor Science and Technology, vol. 27, 044024 (2014)

[2] U. Wagner, A. Ballarino, Y. Yang, Cryogenic Scenarios for the Cold Powering System, HiLumi LHC Milestone Report, FP7 High Luminosity Large Hadron Collider Design Study, CERN-ACC-2014-0065 (2014)

[3] A. Ballarino, Alternative Design Concepts for Multi-Circuit HTS Link Systems, IEEE Trans. Appl. Supercond., vol. 21, 980-984 (2011)

[4] A. Ballarino, J. Fleiter, J. Hurte, M. Sitko, G. Willering, First tests of twisted-pair HTS 1 kA range cables for use in superconducting links, Physics Procedia, vol. 36 (2012)

[5] A. Ballarino, M7.5.1: Final design report HTS link, EuCARD-REP-2012-017 (2012)

[6] Y. Yang, E. A. Young, W. O. S. Bailey, C. Beduz, A. Ballarino, Development of superconducting links for the Large Hadron Collider machine, Supercond. Sci. Technol., vol. 27 (2014)

[7] J. P. Corso, HL-LHC Integration SC links Point 7, CERN Engineering and Equipment Data Management Service, EDMS N. 1419773 (2014)

[8] http://phys.org/news/2014-04-cern-world-record-current-superconductor.html

[9] A. Ballarino, Large capacity current leads, Physica C 468 2143–2148 (2008)

[10] S. Weisz, Mobile shielding for RR73/77, LHC-LC-EC-0021, CERN Engineering and Equipment Data Management Service, EDMS N° 985313

[11] S. Weisz, Protection of equipment located in UJ76, LHC-LJ-EC-0019, CERN Engineering and Equipment Data Management Service, EDMS N° 977085

[12] A-L. Perrot, Protection of equipment located in UJ76, LHC-LJ-EC-0030, CERN Engineering and Equipment Data Management Service, EDMS N° 1260765

[13] F. Bordry, H. Thiesen, LHC Inner Triplet Powering Strategy, Proceedings of the 2001 Particle Accelerator Conference, Chicago (2001)

[14] F. Bordry, D. Nisbet, H. Thiesen, J. Thomsen, Powering and Control Strategy for the Main Quadrupole Magnets of the LHC Inner Triplet System, Presented at the 13th European Conference on Power Electronics and Applications (EPE'2009), Barcelona, CERN/ATS 2010-022 (2009)

[15] F. Bordry, V. Montabonnet, H. Thiesen, Soft switching (ZVZCS) high current, low voltage modular power converter (13 kA, 16 V), presented at EPE'01 (2001)

[16] H. Thiesen, M. Cerqueira-Bastos, G. Hudson, Q. King, V. Montabonnet, D. Nisbet, S. Page, High precision current control for the LHC main power converters, Proceedings of IPAC'10, Kyoto, Japan (2010)

[17] I. Barnett, D. Hundzinger, Q. King, J.G.Pett, Developments in the high precision control of magnet currents for LHC, PAC'99 (1999)

Chapter 7

Machine protection, interlocks and availability

A. Apollonio[5], T. Baer[5], K. Dahlerup-Petersen[5], R. Denz[5], I. Romera Ramirez[5], R. Schmidt[5], A. Siemko[5], J. Wenninger[5], D. Wollmann[5],M. Zerlauth[5]
[5]CERN, Accelerator & Technology Sector, CH-1211, Geneva, Switzerland

7   Machine protection, interlocks and availability

7.1   Machine Protection with a 700MJ Beam

The combination of high intensity and high energy that characterizes the nominal beam in the LHC leads to a stored energy of 362 MJ in each of the two beams. This energy is more than two orders of magnitude larger than in any previous accelerator. For HL-LHC it will increase by another factor of two as shown in the comparisons of Figure 7-1. With intensities expected to increase up to 2.3×10^{11} p/bunch with 25 ns bunch spacing, respectively to 3.7×10^{11} p/bunch with 50 ns bunch spacing [1], an uncontrolled beam loss at the LHC could cause even more severe damage to accelerator equipment than for today's nominal beam parameters. Recent simulations that couple energy-deposition and hydro-dynamic simulation codes show that already the nominal LHC beam can penetrate fully through a 20 m long block of copper, in case the entire beam is deflected accidentally. Such an accident could happen if the beam extraction kickers deflect the beam by a wrong angle. Hence, it becomes necessary to revisit many of the damage studies in light of the new beam parameters [2]. In addition, new failure scenarios will have to be considered following the proposed optics changes and the installation of new accelerator components such as crab cavities and hollow electron beam lenses. Special care is required to find a trade-off between equipment protection and machine availability in view of the reduced operational margins (e.g. decreasing quench limits and beam loss thresholds versus increased beam intensity and tighter collimator settings, UFOs at higher energies and reduced bunch spacing…).
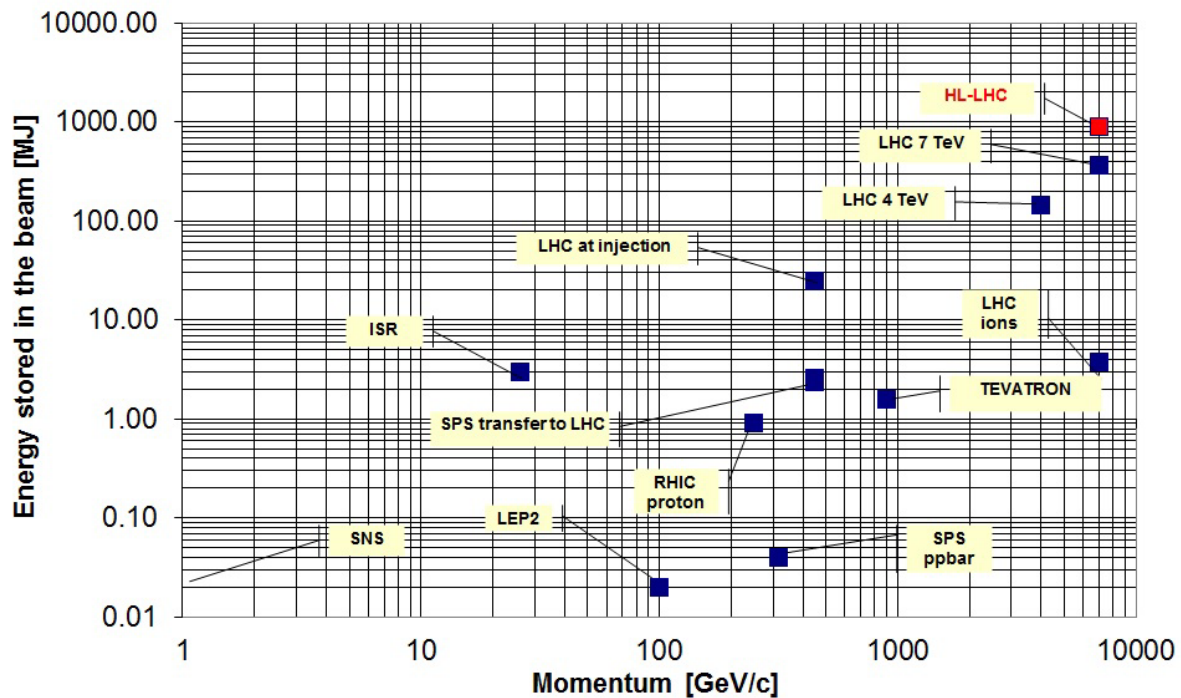
Figure 7-1: Stored beam energy as a function of beam momentum of HL-LHC in comparison with other particle accelerators.

Safe operation of the LHC currently relies on a complex system of equipment protection. The machine protection system (MPS) is designed for preventing the uncontrolled release of energy stored in the magnet system and damage due to beam losses with very high reliability. An essential element of the active MPS system is the early detection of failures within the equipment. In addition the beam parameters are monitored with fast and reliable beam instrumentation. This is required throughout the entire cycle, from injection to collisions. Once a failure is detected by any of the protection systems, the information is transmitted to the beam interlock system (BIS), which triggers the extraction of the particle beams via the LHC beam dumping system (LBDS). It is essential that the beams are always properly extracted from the accelerator via 700 m long transfer lines into large graphite dump blocks. These are the only elements of the LHC that can withstand the impact of the full beams.

The current machine protection architecture is based on the assumption of three types of failure scenarios [3], namely
- Ultra-Fast failures: failures within less than three turns, e.g. during beam transfer from the SPS to the LHC, beam extraction into the LHC beam dump channel or the effect of missing beam-beam deflection during beam extraction (1 LHC turn = 88.9 μs). In case of these failures passive protection elements need to intercept the beams and protect the accelerator equipment from damage as no active protection is possible.
- Fast failures: timescale of several LHC turns (less than few milliseconds) as a result of equipment failures with fast effect on particle trajectories. The active extraction of the beams is completed within up to 3 turns after the detection of the failure and hence provides protection against such failures.
- Slow failures: multi-turn failures on timescales equal to or more than few milliseconds, e.g. powering failures, magnet quenches, RF failures, ...

7.2 Protection against un-controlled beam losses

Equipment failures or beam instabilities appearing on the timescale of multiple turns allow for dedicated protection systems to mitigate their effects on the circulating beams. Figure 7-2 shows a comparison of the failure detection times of different protection systems. Therein the LHC Beam Loss Monitoring system (BLM) has the fastest detection time of 40 μs. The BLM system is complemented with fast interlocks on the beam position in IR6, Fast Magnet Current Change Monitors (FMCM) and a beam lifetime monitor (currently under development by the beam instrumentation group at CERN). All of these systems feature similar failure detection times in the 100 μs – 1 ms range, providing diverse redundancy to the BLM system.
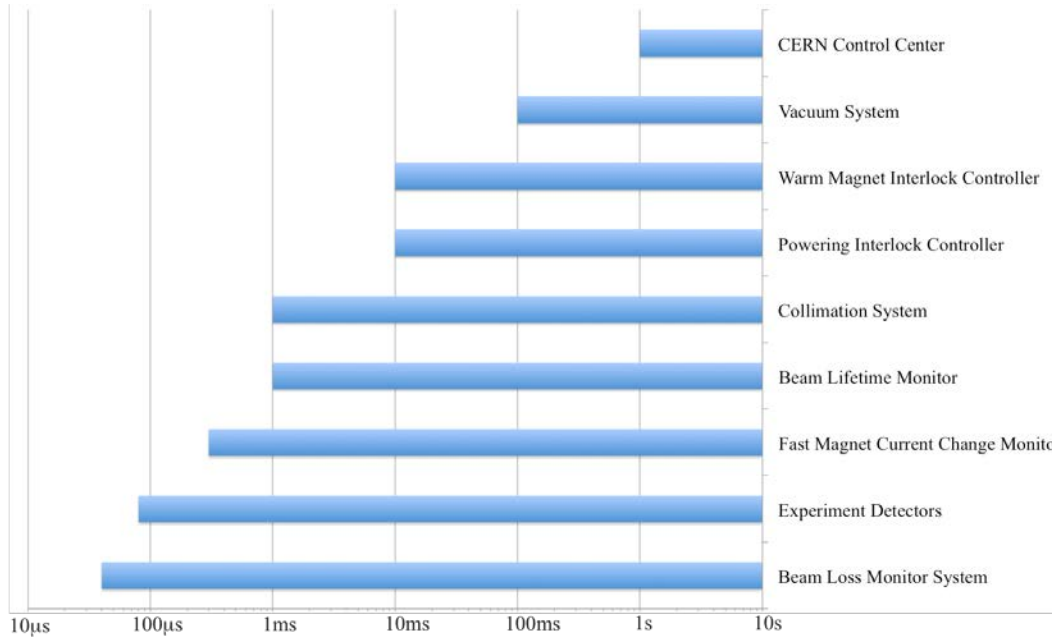
Figure 7-2: Some failure detection times at the LHC. The shortest failure detection time is currently assured by the BLM system, with a fastest integration time of 40 μs, which is equivalent to half a LHC turn.

Adding the additional time required to transmit the detected failure through the LHC Beam Interlock system, the time required to synchronize the firing of the beam dump kickers with the abort gap as well as the time needed to completely extract the beam from the LHC leads to an equivalent worst case MPS response time of three LHC turns after the failure detection as depicted in Figure 7-3.
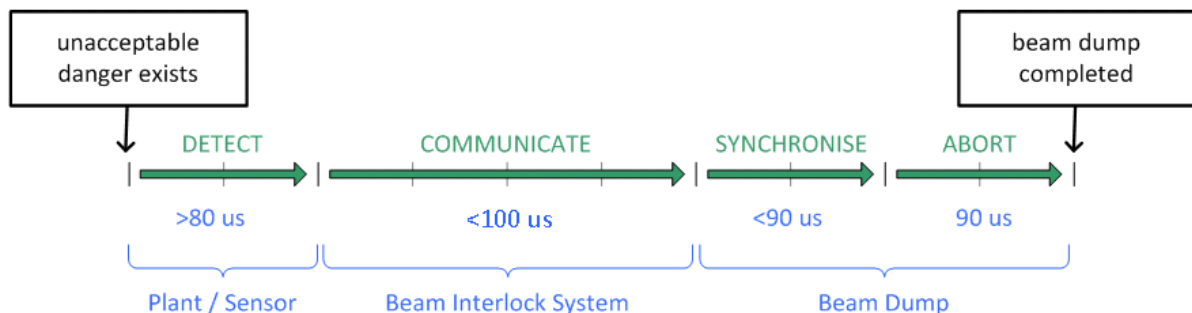
Figure 7-3: Current MPS response time from failure detection to completion of beam dump.

This reaction time is sufficient in the absence of failures occurring on timescales below 10 LHC turns. A failure of the normal conducting separation dipole D1 in IP1 and 5 is currently considered the

fastest possible failure with circulating beam. Therefore, it was the basis for the design of the current MPS system. Due to their location in areas with high beta functions and the fast decay of magnet current in case of a magnet powering failure, these normal conducting magnets can induce fast changes of the particle trajectory. These changes lead to rapidly increasing beam losses in the LHC betatron cleaning insertion (IR7), which define the smallest aperture in the LHC. At nominal energy and intensity the losses after that special failure can reach the damage level of collimators within ten turns only. Therefore, a dedicated protection system – the so called Fast Magnet Current Change Monitors (FMCM) – has been very successfully deployed on critical magnets in the LHC and its transfer lines in 2006 [8].

With the HL-LHC upgrade, the optics in the insertion regions will significantly change. For certain types of ATS optics the β-function at the D1 separation dipole magnets in IR1 and IR5 will increase up to ~ 17000 m, which will enhance its effect on the beam trajectory. The replacement of the D1 separation dipole magnets by a superconducting magnet would significantly increase the time constants of these circuits, practically mitigating the potential of fast failures originating from these magnets.

For HL-LHC operation, the use of crab cavities will introduce failures that can affect the particle beams on timescales well below the fastest failures considered so far [9]. Studies of different failure scenarios are still underway. These studies require considering details of the design finally to be adopted for the crab cavity and the corresponding low-level RF system. Both have a significant impact on the effect on the circulating beams following e.g. cavity quenches or trips of the RF power generator. In addition detailed measurements of the quench and failure behaviour of the chosen design have to be conducted. First experience with similar devices at KEK however shows that certain failures can happen within very few turns only as depicted in Figure 7-4.
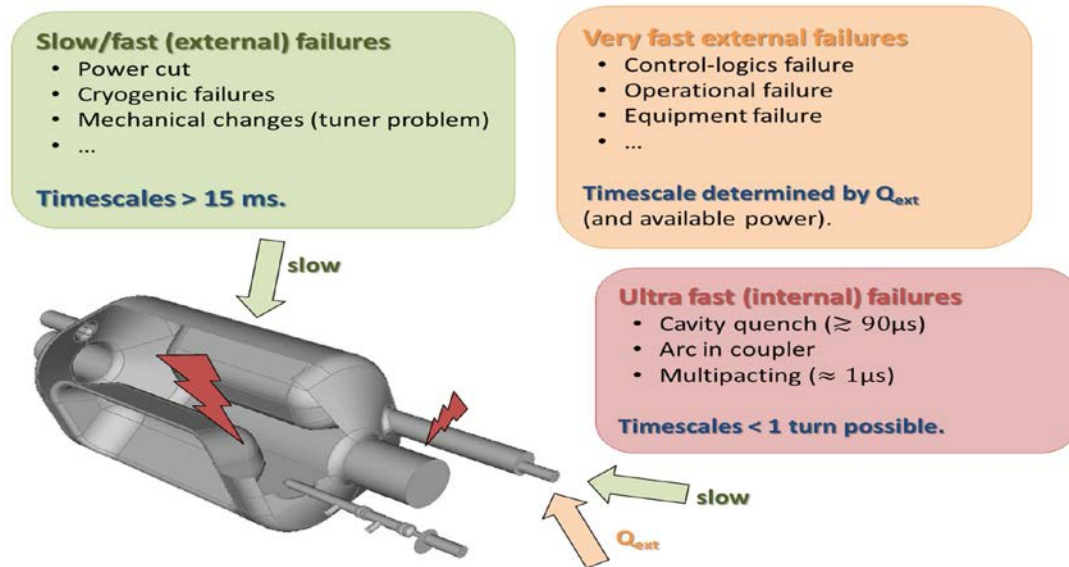
Figure 7-4: Schematic overview of crab cavity failure categories [9]

While the protection against failures with time constants >15ms is not expected to be of fundamental concern, voltage and/or phase changes of the crab cavities will happen with a time constant τ which is proportional to the Q_{ext}. For a 400 MHz cavity with a $Q_{ext}=1E^6$ this will result in a time constant as low as 800 μs. The situation becomes even more critical for cavity quenches, where the energy stored in the cavity can be dissipated in the cavity walls on ultra-fast timescales. Failures believed to be quenches observed in cavities at KEKB show a complete decay of the cavity voltage within 100 μs, accompanied by an oscillation of the phase by 50 degrees in only 50 μs. Such crab cavity failures can imply large global betatron oscillations, which could lead to critical beam losses for amplitudes above about 1 $\sigma_{nom.}$ Highly overpopulated transverse tails compared with Gaussian beams were

measured in the LHC. Based on these observations the energy stored in the tails beyond 4 σ are expected to correspond to ~30 MJ for HL-LHC parameters. These levels are significantly beyond the specification of the collimation system, capable to absorb up to 1 MJ for very fast accidental beam losses.

Therefore, mitigation techniques have to include a fast, dependable and redundant detection and interlocking of a crab cavity failure on these timescales as well as taking appropriate measures when designing the cavity and associated RF control to increase as much as possible the failure time constants, namely:

- Avoid correlated failures of multiple cavities (on one side of an IP) through mechanical and cryogenic separation of the individual modules and appropriate design of the low-level RF [10];

- Investigate the use of fast failure detection mechanisms such as RF field monitor probes, diamond beam loss detectors, power transmission through input coupler and head-tail monitors;

- Ensure the partial depletion of the transverse beam tails to reduce the energy stored in the beam halo, which would potentially be deflected onto the collimation system beyond the design value of 1 MJ. For the current baseline this would correspond to an area of 1.7 σnom (before reaching the closest primary collimator) as the possible transverse beam trajectory perturbation following an ultra-fast failure of a single crab cavity. It is important to note that the partial depletion of the beam halo may have a negative effect on the available time to detect a failure with other machine protection systems like BLMs. The consequences of this need to be studied carefully.

- Decrease the reaction time of the MP system for such ultra-fast failures by e.g. increasing the number of abort gaps, accepting to trigger asynchronous beam dumps with potential local damage, add direct links to the beam dumping system in IR6 and consider the installation of disposable absorbers.

7.2.1 Beam Interlock System

The Beam Interlock System (BIS) is a highly dependable fast interlock system and a key element of the accelerator machine protection. It is today used in the LHC, SPS and parts of the injector chain at CERN. Its primary objective is to provide a highly reliable link between the users requesting a beam abort and the beam dumping system. The hardware implementation of the system is based on custom made electronics, as industrial solutions have been found not being adequate for the specific requirements of the system, e.g. in terms of reaction time combined with the geographical distribution of the system. Due to obsolescence of electronic components and potential problems with the optical links the present system will need to be upgraded. To fulfil the requirements of HL-LHC, the system will be equipped with additional input channels to connect more user interfaces and to provide more flexibility in the configuration of the various user inputs. The number of required channels is subject to a future functional specification to be provided by the SPS and LHC Machine Protection Panel (MPP). The possibility to implement very fast interlock channels and direct links between the crab cavities and the LHC beam dumping system will be studied but the feasibility cannot be confirmed, yet. The new system will be equipped with advanced diagnostic features for all optical links allowing pre-emptive maintenance e.g. in case of a degraded performance due to the enhanced radiation load in some underground areas.

7.2.1.1 Equipment performance objective

The upgraded system is supposed to reach the same performance level in terms of reliability as the present system, which corresponds to safety integrity level (SIL) 3. The safety critical part of the BIS hardware architecture will be based on well-proven principles and solutions but adapted to state of the art electronic components and assemblies. Hereby it is probably possible to reuse a major part of the safety critical code, which is very well tested and fully validated. Considering the system complexity, dimension and the experience gained so far, it is expected that the system performance will hardly affect the LHC availability, e.g. not producing more than one spurious beam abort per year.

The new BIS could be equipped with a new hardware controls interface, replacing obsolete architectures for communication busses and simplifying maintenance and potential upgrades. The BIS hardware will as well feature advanced diagnostic tools for the system hardware and the optical links.

All the proposed changes will require a major revision of the high level supervision and controls software and be adapted to the accelerator controls environment then in place.

7.2.2 Fast Magnet Current Change Monitor

The main task of the Fast Magnet Current Change Monitors (FMCM) is to monitor fast current changes in electrical circuits with normal conducting magnets. A fast current change can be caused by sudden powering failures or perturbations on the supply network, which change the particle trajectories leading to fast beam losses. These monitors are required for electrical circuits with a short decay time constant and magnets installed in regions with high beta functions. Each monitor delivers a permit signal to the Beam Interlock System to request the extraction of the particle beams before losses occur. Therefore, the FMCM provides a redundant protection to the Beam Loss Monitors (BLM). A total of 26 monitors are presently installed to protect the LHC and SPS-LHC transfer lines.

7.2.2.1 Objective for the HL-LHC machine performance

The installation of FMCMs is required to ensure machine protection against powering failures in critical magnetic elements during all operational phases. 12 monitors are currently installed in the LHC, namely for dump septa magnets in IR6, collimation insertion regions in IR3/IR7, Alice compensator circuits in IR2 and main separation dipoles D1 in IR1 and IR5 [10]. Additional input from WP3 (Magnets) and WP2 (Accelerator Physics) is required to clarify the necessity of additional FMCM units for the protection of the new magnet powering in the high luminosity insertion regions IR1 and IR5 and the HL-LHC optics. In addition, new failure modes derived from the introduction of new elements (such as crab cavities) need to be studied to understand the machine protection requirements and to estimate the number of monitors required to protect the accelerator equipment in the HL-LHC.

7.2.2.2 Equipment performance objective

FMCMs have successfully operated in the LHC and the SPS-LHC transfer lines for many years and no missed dump has been identified since the start of operation. For the protection of the electrical circuits in the HL-LHC the use of the same design is recommended. However, a review of the system needs in view of HL-LHC followed by a corresponding reproduction of additional units will be required. The review and potential redesign of the hardware is a mandatory step due to the aging and obsolescence of electronic parts used in the current system.

The aim of the upgrade of the FMCM will be to improve the maintainability of the system and to comply with the requirements of the HL-LHC.

7.3 Magnet powering protection

During operation at 7TeV the energy stored in the main dipole circuits of each sector reaches ~1GJ. This illustrates that the LHC magnet system needs to be protected against damage due to failures in the magnet powering or quenches.

Therefore the superconducting circuits, the bus bars and future superconducting links must be equipped with a quench protection system (QPS), which detects changes in the superconducting state and activates quench heaters and/or the energy extraction systems (EE) to safely extract the magnetic energy stored in the circuit.

Furthermore, the correct powering conditions have to be ensured for each circuit by a powering interlock system (PIC), which will interlock the powering of the circuit via the power converter in case

of problems and potentially request a beam dump. Therefore, the PIC is interfacing the quench protection systems, power converters, cryogenic systems and technical services such as uninterruptable power supplies (UPS), emergency stop buttons (AUG) and controls.

The protection of the normal conducting magnets in the LHC and its injector complex is ensured by the warm magnet interlock system (WIC), which collects signals from thermo switches installed on the magnets and status signals from the associated power converters.

As a failure in the magnet system will also impact the stored particle beam, these systems have to interface the magnet powering systems with the beam interlock system (BIS) and initiate a beam dump in case of a failure.

7.3.1 Quench Protection System

The HL-LHC will incorporate new superconducting elements requiring dedicated protection systems. The upgrade of the QPS will provide this functionality, including the related data acquisition systems, monitoring the state of the protection systems and the protected elements.

The enhanced luminosity of the HL-LHC will increase the radiation levels in certain underground areas like the dispersion suppressors to levels no longer compatible with the operation of radiation tolerant electronics based on components off the shelf (COTS) installed at present in those areas. Based on the progress in electronics, it is probably feasible to re-locate a major part of the protection electronics to low radiation zones or eventually to surface buildings and use long instrumentation cables or optical fibres to link to the protected elements.

The proposed upgrade will also include new communication links for supervision and data acquisition (DAQ) superseding the then obsolete classical fieldbus networks. At the same time, advanced tools for remote diagnostics and maintenance will be provided.

7.3.1.1 Equipment performance objective

The QPS is a highly complex system incorporating a large amount of electronic components and assemblies. As for the existing system, a particular design effort will be necessary to achieve the very demanding level of system dependability required for successful LHC operation. The number of accesses to LHC underground areas needs to be minimized for personnel protection and machine availability.

The protection parameter settings will be subject to a functional specification to be issued by the LHC Magnet circuits, Powering and Performance Panel (MP3) based on the input of equipment specialists.

The request for very fast magnet protection systems with reaction times in the order of some milliseconds will be addressed in a feasibility study but a potential implementation will rely strongly on the proper instrumentation of the protected element (magnet, sc. link) and the respectively adapted reaction time of other protection systems such as energy extraction systems and the powering interlock system.

The hardware capabilities of the DAQ and related communication links will be enhanced to allow higher data transmission rates and advanced maintenance. All the proposed changes will require a major revision of the high-level supervision and controls software, which also needs to be adapted to the accelerator controls environment then in place.

7.3.2 Energy Extraction System

Energy extraction systems (EE) are an integrated part of the safety-critical quench protection systems, widely used in the existing LHC machine with a total of 234 installed facilities (202 for the 600A corrector circuits and 32 13kA systems for the main dipole and quadruple circuits). The systems are

strongly circuit specific, tailor-made for a particular set of requirements and adapted to the local infrastructure.

The current mechanical energy extraction switches will have to be replaced for the HL-LHC era. To allow for faster reaction times, which may be required by future superconducting magnets, the development of fast switches based on semiconductors (IGCTs, IGBTs) is currently on-going. Alternatively also slower (~20ms) hybrid systems, where an electro-mechanical switch is connected in parallel to a semiconductor switch are under study. Furthermore, for slow switching times, classical mechanical switches in combination with large snubber-capacitor banks could be used.

The new design of the extraction resistors (DQR) will be significantly different from those developed and built for the present LHC main circuits. The pursued characteristics and properties of these new energy absorbers are very fast recovery (cooling) times, compact design (minimized volume) and easily changeable resistance values.

7.3.2.1 Equipment performance objectives

The new energy extraction equipment for the HL-LHC will use a new generation of switches, incorporate the newest technology for high-current transmission, benefit from built-in features for facilitating diagnostics and maintenance, offer systems which will minimize intervention time for accessing all parts of the facilities and profit from the experience gained with the operation of the existing LHC EE facilities.

7.3.3 Powering Interlock System

The powering interlock system (PIC) ensures the correct powering conditions of the different electrical circuits with superconducting magnets in the LHC. At the same time, it guarantees the protection of the magnet equipment by interfacing quench protection systems, power converters, cryogenics and technical services such as uninterruptable power supplies (UPS), emergency stop buttons (AUG) and controls. The PIC is a distributed system currently consisting of 36 individual powering interlock controllers, which manage the powering of each of the 28 powering subsectors [11].

7.3.3.1 Objective for the HL-LHC machine performance

Magnet interlocks are required to guarantee safe magnet powering during all phases of operation from injection to collisions. In order to achieve this protection while maintaining the time constraints required for equipment protection, interlock electronics is usually installed close to the main clients (QPS and power converters) such as the UA, UJ and RR alcoves. At the design luminosity for HL-LHC ($5x10^{34}$ $cm^{-2}s^{-1}$) the thermal neutron and high-energy hadron fluencies in the areas close to the tunnel will increase considerably with respect to the values for which the existing PIC has been designed. Additional changes and requirements from the new quench protection system will have to be reflected in the upgraded interlock system to assure the dependability of the system during the HL-LHC era. For these reasons, a new design of the distributed I/O modules is required to cope with the increment of particle flux in the most sensitive areas. In addition, an upgrade of the used industrial components will very likely become necessary due to the change of the low-level I/O components used.

7.3.3.2 Equipment performance objectives

The PIC was installed as of 2006 and has been operating since the start of the LHC in 2008. By the time the HL-LHC will start operation the system will have been running for more than 15 years. Therefore, some of the electronic components will reach their end of life expectancy, which can have an impact on the availability of the system. In addition, obsolescence of electronic parts needs to be addressed since some of the critical components of the system cannot be purchased on the market anymore, affecting its

maintainability. Furthermore, the increased radiation dose in certain areas will affect the most sensitive components of the PIC.

The upgrade of the PIC will address the issues mentioned above to adapt to HL-LHC requirements. In addition, the system will be reviewed to provide enhanced diagnostics of the safety critical hardwired loops in line with the upgrades foreseen for the quench protection system. The implementation of triple redundancy in combination with a 2-out-of-3 voting is considered for the quench loop.

7.3.4 Warm Magnet Interlock System (WIC)

The warm magnet interlock system (WIC) is assuring the protection of normal conducting magnets in the LHC and its injector complex. It collects signals from thermo switches installed on the magnets and status signals from the associated power converters. Based on these input signals a programmable logic controller (PLC) calculates and transmits fast abort signals to interlock the power converter of a given electrical circuit in case of powering failures. In addition, it initiates a beam dump in case a circuit relevant for beam operation of the given machine is not operating in nominal conditions [12].

7.3.4.1 Objective for the HL-LHC machine performance

Magnet interlocks are required to guarantee safe magnet powering during all phases of operation from injection to collisions and to abort beam operation avoiding inevitable beam losses in case of powering failures. In addition, interlock systems provide remote diagnostic features to allow an efficient and precise identification of the faulty equipment. As normal conducting magnets in the LHC are concentrated around the IPs, a single industrial controller installed in a radiation free area is required to manage the protection of powering equipment in a given IR. The main objective for the HL-LHC era is a consolidation of the existing system, along with an upgrade to accommodate for the changes and new requirements of the magnet powering system in the different insertion regions.

7.3.4.2 Equipment performance objectives

The WIC - consisting of eight industrial controllers and several I/O crates - has been installed in the LHC since 2006 and has been continuously operating since the start of the LHC in 2008. No failures have been observed in the WIC system throughout the whole run 1. Nevertheless, by the time the HL-LHC will start operation the WIC system will have been running for more than 15 years, requiring an upgrade of the used electronic and industrial components to assure the current dependability throughout the full HL-LHC period. Furthermore, the increased radiation dose in certain areas will affect the most sensitive components of the WIC (mostly the magnet and remote test interconnection boxes) for which a new design and production has to be envisaged.

7.4 Availability requirements to achieve HL-LHC goals for integrated luminosity

The challenging goals in terms of integrated luminosity require a high level of accelerator availability and operational efficiency. In this paragraph the estimated integrated luminosity as a function of machine availability is analysed. There are three important figures to be considered when evaluating LHC availability:
- the stable beams time: the time for beam collisions. This quantity must be optimized by operators as a function of the observed distributions of turnaround time and fault time. Stable beams optimization will be particularly relevant for leveled operation.
- the turnaround time: the time to go from a beam dump at the end of stable beams to the next stable beams, when no faults occur. This quantity has a minimum value imposed by the injection process and the ramp time of superconducting magnets. Efforts must be devoted to reaching this lower value. Parallelizing/combining machine modes (e.g. collide and squeeze) is one possibility to optimize the turnaround time.

- the fault time: the time to clear machine faults and recover operational conditions for beam injection. It includes the time for expert diagnostics and intervention, eventually requiring access to the LHC tunnel.

For the following extrapolations, the 2012 LHC run is taken as a reference, being the most stable and reproducible year of the first LHC run [13]. In 2012 the average turnaround time was 5.5h, but the energy was limited to 4 TeV, requiring current ramps of only 13 min. For HL-LHC operation, the reference energy will be 7 TeV, resulting in an increased average turnaround time, estimated to be 6.2h. Making predictions on the fault time distribution for HL-LHC operation is not trivial, as many factors will play a role in this respect. The increased energies and intensities will result in higher radiation levels, which could have a direct impact on the observed number of single event effects (SEE) per year and on long-term effects on components due to the total integrated dose (TID). Mitigations to these effects have been deployed during LS1, with major relocation of sensitive equipment in protected areas of the LHC tunnel. Nevertheless future radiation levels will have to be measured for a final assessment of the expected increase of beam dumps due to radiation effects in electronic components (R2E). It is already foreseen that a new generation of electronic systems will be designed before the HL-LHC era. New designs should cope with such radiation levels. The increased energy and intensities will also have a direct impact on the observed UFO-induced beam dumps due to localised losses. Current extrapolations assume a significant increase of UFO events which are large enough to provoke a beam dump, if 2012-like BLM thresholds will be kept. A balance between the tolerated number of UFO-dumps and the possibility of having beam-induced quenches should be found, by the definition of suitable threshold and, eventually, BLM relocation. On the equipment side, components will operate closer to design limits and partially reach the end-of-life.

A Monte Carlo model [14, 15] of LHC availability was used to qualitatively assess the combined impact of all these factors. A sensitivity analysis has been carried out with respect to the average fault time and machine failure rate, defined as the ratio between fills to stable beams followed by failures and the total number of physics fills. The results are presented in Figure 7-5, for 200 days of HL-LHC operation. Nominal HL-LHC parameters (5×10^{34} s^{-1}cm^{-2} levelled luminosity, 2.19×10^{35} s^{-1}cm^{-2} virtual peak luminosity, 4.5 h average luminosity lifetime, 7 TeV) and the same duration of intensity ramp-up as 2012 were assumed.

The results show that assuming 2012 figures for average fault duration (6.9 h) and machine failure rate (70 %), 260 fb^{-1} could be produced in 200 days of HL-LHC operation. To reach the goal of 300 fb^{-1} per year, a reduction of 10 % of the machine failure rate, combined with a reduction of the average fault time of around 25 %, are necessary (HL1). As an alternative to reach 300 fb^{-1}, the sensitivity analysis shows that a further reduction of the machine failure rate to 50%, would allow keeping the same average system fault time as observed in 2012 (HL2). These requirements need to be considered in particular during the design of future electronics equipment.
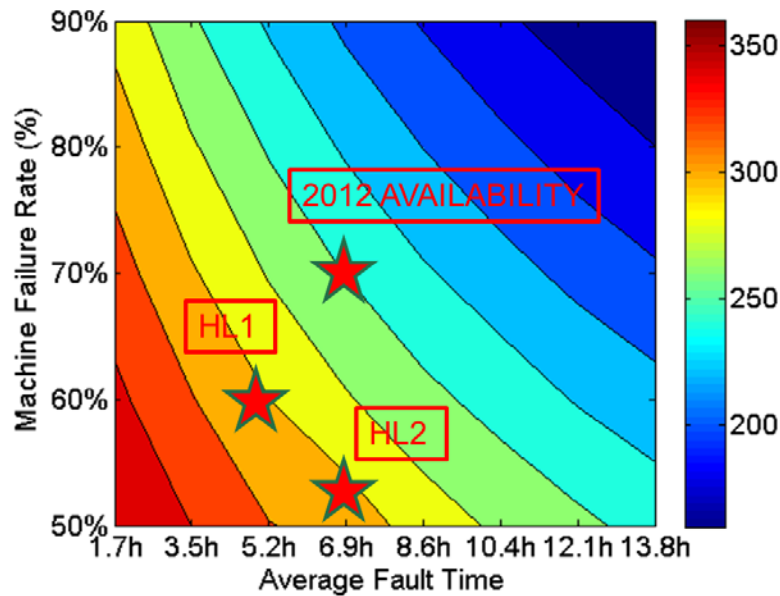
Figure 7-5: Sensitivity analysis of integrated luminosity to the machine failure rate and average fault time.

7.5 References

1. O.S. Bruning, "HL-LHC Parameter Space and Scenarios", Proceedings of Chamonix 2012 workshop on LHC Performance, CERN-2012-006, p.315.

2. N.A. Tahir, J.B. Sancho, A.Shutov, R.Schmidt and A.R. Piriz, "Impact of high energy high intensity proton beams on targets: Case studies for Super Proton Synchrotron and Large Hadron Collider", Phys. Rev. ST ACcel. Beams, vol. 15, p051003, May 2012.

3. R.Filippini, B.Goddard, M.Gyr, V.Kain, R.Schmidt, J.Uythoven and J.Wenninger, "Possible Causes and Consequences of Serious Failures of the LHC Machine Protection Systems" in 9th European Particle Accelerator Conference, Lucerne, Switzerland, 5-9 July 2004, pp620, 2004.

4. T.Baer, "Very Fast Losses of the Circulating LHC Beam, their Mitigation and Machine Protection" PhD Thesis, CERN, University of Hamburg, 2013

5. G. Stancari et al., "Collimation with Hollow Electron Beams", Phys. Rev. Lett., vol. 107, p. 084802, Aug. 2011.

6. S. Redaelli et al., "Proceedings of Internal Review of Tevatron Hollow E-Lens Usage at CERN", Nov. 2012

7. V.Kain and R.Schmidt, "Machine Protection and Beam Quality during the LHC Injection Process", Ph.D. dissertation, Technical University Vienna/ CERN, Oct. 2005, CERN-THESIS-2005-047.

8. M. Werner, "Einrichtung zur Bestimmung der Starke des Magnetfeldes eines Elektromagneten", Patent DE102005045537B3 28.12.2006, Sep. 2005.

9. T. Baer et al., "Very Fast Crab Cavity Failures and their Mitigation", in Proceedings of IPAC'12, May 2012, pp. 121-123, MOPPC003.

10. M.Werner, M.Zerlauth, A.Dinius, B.Puccio: 'Requirements for the Fast Manget Current Change Monitors (FMCM) in the LHC and SPS-LHC transfer lines', LHC-CIW-ES-0002, EDMS Doc Nr. 678140

11.   R.Schmidt, B.Puccio, M.Zerlauth: 'The Hardware Interfaces between the powering interlock system, power converters and quench protection system', LHC-D-ES-0003, EDMS Doc.Nr.: 368927

12.   P.Dahlen, R.Harrison, R.Schmidt, M.Zerlauth: 'The Warm Magnet Interlock System for the LHC ring', LHC-CIW-ES-0003, EDMS Doc.Nr.: 653548

[13] B. Todd et al. "The Workshop on Machine Availability and Dependability for Post-LS1 LHC", proceedings of the workshop, CERN, 2013.

[14] A. Apollonio et al., "HL-LHC: Integrated Luminosity and availability", TUPFI012, proceedings of IPAC'13.

[15] A. Apollonio et al., "Update on predictions for yearly integrated luminosity for HL-LHC based on expected machine availability", TUPRO015, proceedings of IPAC'14, Dresden, Germany.

Chapter 8

Interface with Experiments

H. Burkhardt[5], I. Efthymiopoulos[5]
[5]CERN, Accelerator & Technology Sector, CH-1211, Geneva, Switzerland

8   Interface with experiments

8.1   Introduction

The machine upgrade for high luminosity requires major changes on the machine side. Key ingredients for the luminosity increase are larger apertures in the focusing sections around the experiments and higher beam intensities. The experiments are upgraded for reduced inner beam pipes with more powerful vertex detectors. This is important for physics and essential for the increased pile-up.

Other key design considerations for the upgraded LHC detectors include longevity at increased radiation levels and minimisation of activation. The definition of the Machine-Experiment Interface issues and its timeline is described in the M18 document. [1]

8.2   Interaction regions

Figure 8-1 shows the schematic layout of the LHC with its four interaction regions.
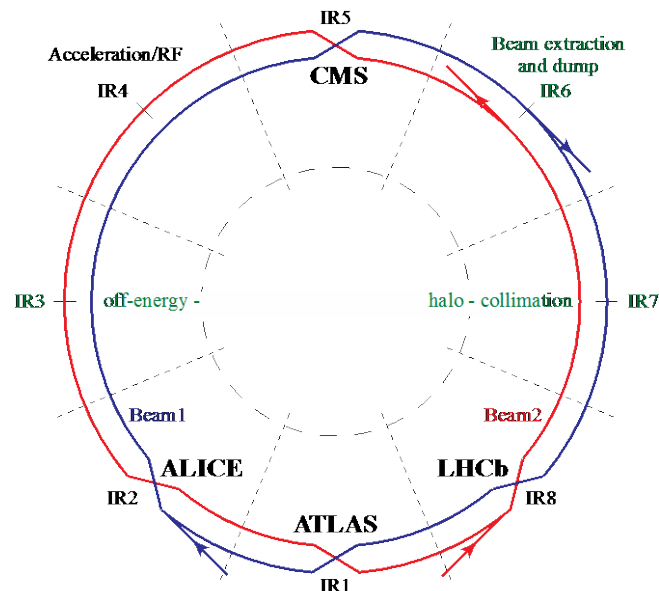
Figure 8-1: Schematic layout of the LHC with the four interaction regions that house the ALICE, ATLAS, CMS and LHCb experiments.

The HL-LHC design is for four experiments: the two high-luminosity experiments ATLAS and CMS at IR1 and IR5 respectively; ALICE at IR2; and LHCb at IR8.

Table 8-1 shows the target luminosities for the experiments in proton-proton operation for the original LHC design and for the high-luminosity upgrade. Operation at so called 'ultimate' conditions with peak luminosity of 7.5×10^{34} cm^{-2} s^{-1} is considered. With levelling, this would lead to around 4000 fb^{-1} in 12 years of operation.

Table 8-1 Target luminosities for p-p operation for the HL-LHC. The luminosities for the LHC Run 2 are also included for comparison. Total target integrated luminosity in CMS and ATLAS is 3000 fb-1after 12 years of operation.

Peak levelled Luminosity [cm^{-2} s^{-1}]			
Experiment	**HL-LHC**	**LHC**	**IP**
ATLAS	5×10^{34}	2×10^{34}	1
CMS	5×10^{34}	2×10^{34}	5
ALICE	1×10^{31}	1×10^{31}	2
LHCb	2×10^{33}	4×10^{32}	8

The main luminosity upgrade is for the interaction regions IR1 and IR5 and will be implemented in the long shutdown LS3. The ALICE and LHCb experiments installed in IR2 and IR8 will have their most significant detector upgrades during LS2 scheduled for 2018/2019 and will continue to run after LS3. LHCb has requested a luminosity increase up to 2×10^{33} cm^{-2} s^{-1}. This is possible without changes to the magnet layout in IR8 and the required detector and vacuum beam pipe upgrades can be implemented in the long shutdown LS2. It should be accompanied by an improved shielding (including a minimal TAN upstream of D2), to minimize the impact of the increase in radiation and heating of cold machine elements. The low target luminosity for ALICE in p-p operation will require collisions with large transverse offsets.

The experimental programs of other smaller experiments (LHCf, TOTEM) do not extend beyond LS3 at present. Should these or other experimental proposals appear in the future, they will need to adapt to the HL-LHC beam conditions and installed hardware planned for the straight sections. The HL-LHC will be more constrained towards high-luminosity/low β operation than the present LHC. Very high β* running will have to end with LS3. The upper limit for β* for physics at top energy is expected to be reduced to about 30 m.

For HL-LHC operation, the machine layout in IR1 and IR5 will change significantly. The most relevant machine modification for the experiments will be the installation of the new large aperture triplet magnets Q1-Q3 in IR1 and IR5. Details are described in Chapter 3. What is important for the layout of the interface with the experiments is that the distance of the first quadrupole magnet (Q1) from the IP will remain the same (23 m) as before the upgrade. As a result no modifications to the forward shielding of the experiments need to be implemented to accommodate changes in the accelerator layout. The inner coil diameter of the triplet magnets however will increase by roughly a factor of two from 70 mm to 150 mm. This implies that the inner beam pipe radius will have to increase between the triplet and the experiment. In particular, the passive absorbers (TAS) installed at 19 m from the interaction points will have to be replaced by a new larger aperture absorber (TAXS).

8.3   Experimental beam-pipes

A key upgrade of the ATLAS and CMS experiments for HL-LHC operation is that of the inner tracker detectors. The change to a smaller radius beam pipe was already done during LS1 [3]. This is important for the detectors to deal with high pile-up and will be kept for the HL-LHC operation. The ALICE and LHCb experiments also plan modifications to their experimental beam pipe to a reduced inner radius. The present and foreseen experimental beam apertures are summarized in Table 8-2.

The LHCb VELO is movable. It is only closed in stable physics to the value shown in the table, and retracted to 30 mm otherwise.

Table 8-2: Original and reduced inner beam pipe radii at the IPs.

IP	Original r_{min} mm	Reduced r_{min} mm	Experiment	When
1	29	23.5	ATLAS	LS1
2	29	18.2	ALICE	LS2
5	29	21.7	CMS	LS1
8	5	3.5	LHCb, VELO	LS2

8.4   The passive forward Absorbers

The high-luminosity regions of LHC at IP1/ATLAS and IP5/CMS are equipped with passive absorbers for charged (TAS) [4] and neutral (TAN) [5] particles. The TAS is installed on either side of the interaction region at the transition of the experimental caverns to the LHC tunnel. The TAS and TAN's primary function is to protect the superconducting quadrupoles in the straight section from the collision debris coming from the interaction region. The TAS shields primarily the inner triplet quadrupoles Q1-Q3; the TAN the D2 and Q4 quadrupoles. In parallel the TAS completes the forward shielding of the experiments and both the TAS and TAN participate in the reduction of background to the experiments.

For HL-LHC operation the following modifications are foreseen:

- New TAS and TAN absorbers on either side of **IP1** and **IP5**, called **TAXS** and **TAXN** respectively should replace the existing ones. The protection must be extended to D1 magnets that in HL-LHC will be superconducting (they are normal conducting in the present LHC). The new absorbers must have an aperture adapted to the HL-LHC beam optics and operation and should be designed to cope with the increased energy deposition.

- A new **TAXN** absorber is planned for **IP8** designed to operate at the foreseen 5 times higher luminosity operation. The installation of a TAXS absorber around IP8 is not required.

- The new absorbers will be designed to operate at the ultimate luminosity conditions during HL-LHC as defined above.

8.4.1 The charged particle passive absorber - TAXS

The TAXS absorber is located at approx. 19 m from the interaction point on either side of IP1 or IP5. Its core is a 0.5 m diameter and 1.8 m long copper cylinder traversed on axis by a constant aperture beam pipe. The design of the new TAXS absorbers for HL-LHC for IP1 and IP5 is based on that of the presently installed TAS absorbers, with the following modifications and improvements:

- The beam pipe aperture increases to 54 mm in diameter from the present 34 mm.

- The cooling power increases to dissipate the approx. 780 W deposited in the TAXS during ultimate beam operation conditions of HL-LHC including a safety margin.

- The overall design of the TAXS remains compatible with the mechanical and envelope constraints from the surrounding shielding of the experiments.

Improvements in the alignment mechanism and vacuum exchange should be incorporated in the new design in view of the need for optimized maintenance operations and exposure to radiation. The change from the TAS to TAXS is to happen during LS3 after a few months (at least) of cool-down. The overall procedure must be optimized such to minimize the exposure of personnel to radiation in

compliance with the ALARA principle and the overall planning of the activities in the LHC tunnel and experimental caverns.

8.4.2 The neutral particle passive absorber – TAXN

The TAXN absorber is designed to absorb the flux of forward high-energy neutral particles produced at the interaction region of IP1 and IP5. There is a TAXN absorber installed in either side of IP1 and IP5 located between the separation/recombination dipole pair D1 and D2 and contains the transition from the single common beam pipe to the two separate pipes for the incoming/outgoing beams.

The design of the new TAXN absorbers for IP1 and IP5 is based on that of the presently installed TAN, with the following modifications and improvements:

- The position of the TAXN is different by few meters (towards IP) with respect to the present.

- The overall design and layout is to be adapted to the available space constraints while maintaining the correct shielding efficiency.

- The vacuum chamber layout is adapted to the new geometry protection efficiently for the adjacent quadrupoles and optimization for the background conditions to the experiment. The TAXN vacuum pipes have a fixed aperture, that combined with a specially designed TCL collimator with movable jaws just downstream towards D2 provides the maximum protection efficiency at all beam optics scenarios for HL-LHC.

- Active water cooling will be required to dissipate the approx. 1.5 kW of power from the beam, expected during the ultimate operation during HL-LHC.

Improvements in the mechanical design of the absorber should be incorporated in the design to allow optimized installation and maintenance activities. The locations for beam instrumentation for luminosity monitoring and experimental detectors will be maintained unless they impose important constraints in the TAXN design and maintenance.

In IP8 new TAXN absorbers should be installed in either side of the interaction region in available slots upstream of D2.

8.5 References

[1] Interface Machine-Experiments: Definition and Time Plan, M18 document.

[2] High-Luminosity Project Book Chapter 5

[3] M. Gallilee, CMS Central chamber diameter reduction, LHC-VC5-EC-0001, EDMS No: 1230176.

   M. Galilee, Reduction of ATLAS VI Diameter, LHC-VC1I-EC-0001, EDMS No:1230222.

[4] E. Hoyer et al., Interface Specification LHC IP1/IP5, Front Quadrupole Absorbers (TAS), LHC-TAS-ES-0003, EDMS No 111998.

   E. Hoyer et al., Functional Specification LHC IP1/IP5 Front Quadrupole Absorbers (TAS), LHC-TAS-ES-0001, EDMS No 101559.

[5] E. Hoyer et al., LHC IP1/IP5 Neutral Beam Absorbers (TAN), LHC-TAN-ES-0100, EDMS No: 108093.

Chapter 9

Cryogenics for HL-LHC

S. Claudet[5], L. Tavian[5]
[5]CERN, Accelerator & Technology Sector, CH-1211, Geneva, Switzerland

9   Cryogenics for HL-LHC

9.1   Introduction

The upgrade of the cryogenics for HL-LHC will consist of:

- The design and installation of two new 1.9 K cryogenic plants at Point 1 (P1) and 5 (P5) for the high luminosity insertions. This upgrade will be based on a new sectorization scheme aiming at separating the cooling of the magnets in these insertion regions from the magnets of the arcs, as well as on a new cryogenic architecture based on electrical feed boxes located at ground level and vertical superconducting links.

- The design and installation of a new 4.2 K cryogenic plant at Point 4 (P4) for the SRF cryo-modules and other future possible cryogenic equipment (e-lens, RF harmonic system).

- The design of new cryogenic circuits at Point 7 for the HTS links and displaced current feed boxes.

- Cryogenic design support for cryo-collimators and 11 T dipoles.

  Figure 9-1 shows the overall LHC cryogenic layout including the upgraded infrastructure.
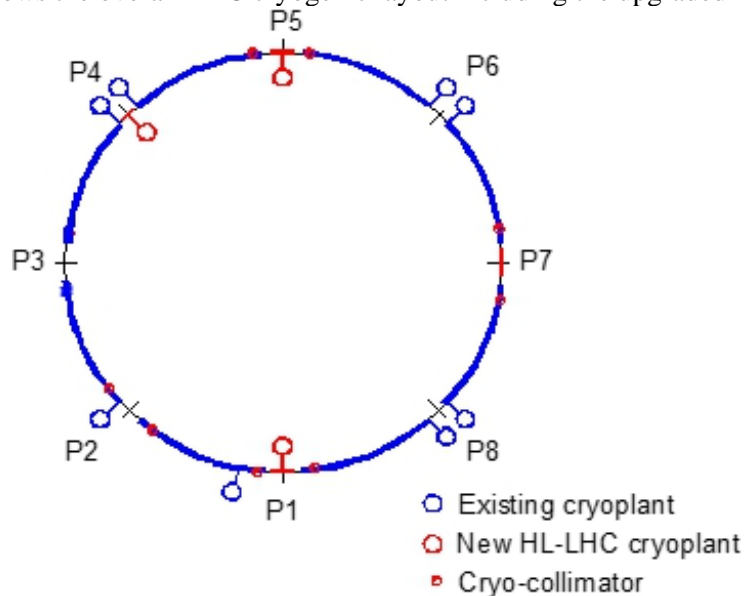
Figure 9-1: Overall LHC cryogenic layout including the upgraded infrastructure

9.2 LHC machine upgrades

9.2.1 Upgraded beam parameters and constraints

The main parameters impacting on the cryogenic system are given in Table 9-1. With respect to the nominal beam parameters, the beam bunch population will double and the luminosity in the detectors of the high-luminosity insertions at P1 and P5 will be multiplied by a factor 5.

Table 9-1: LHC upgraded beam parameters for 25ns bunch spacing

Parameter		Nominal	Upgrade
Beam energy, E	[TeV]	7	7
Bunch population, Nb	[protons/bunch]	$1.15 \cdot 10^{11}$	$2.2 \cdot 10^{11}$
Number of bunches per beam, nb	[-]	2808	2748
Luminosity, L	[$cm^{-2} s^{-1}$]	10^{34}	$5 \cdot 10^{34}$
Bunch length	[ns]	1.04	1.04

These upgraded beam parameters will introduce new constraints to the cryogenic system:

- The collimation scheme must be upgraded by adding collimators in the continuous cryostat close to Points 2 (P2) and Point 7 (P7), and possibly also P1 and P5. The corresponding integration space must be created by developing shorter but stronger 11 T cryo-dipoles. As the new collimators will work at room temperature, cryogenic bypasses are required to guarantee the continuity of the cryogenic and electrical distribution. Figure 9-2 shows the nominal and upgraded layouts of the continuous cryostat. Halo control for HL-LHC may require the installation of hollow electron lenses at P4, making use of a superconducting solenoid. While not yet in the HL-LHC baseline, this device may be the best option for controlling particle diffusion by depopulating the halo of the high-power hadron beams, thereby avoiding uncontrolled losses during critical operations such as the squeeze. Figure 9-3 shows the nominal and upgraded layouts of the P4 insertion region, anticipating the installation of an e-lens and a new SRF system.

- The increase of the level of radiation to electronics could possibly require relocating power convertors and related current feed boxes in an access gallery at Point 7 and at ground level at Points 1 and 5. New superconducting links will be required to connect the displaced current feed boxes to the magnets. Figure 9-4 and Figure 9-5 show the nominal and upgraded layouts of the insertion regions at Points 1, 5 and 7.

- To better control the bunch longitudinal profile, reduce heating and improve the pile-up density, new cryo-modules of 800 MHz RF cavities could be added to the existing 400 MHz cryo-modules at P4 creating a high-harmonic RF system (see Figure 9-3). Actually, discussions are underway to see if a better scheme would be the installation of a new 200 MHz SRF system, rather than the 800 MHz. From the cryogenic point of view the requests are similar, so we will consider below the 800 MHz system that is in an advanced phase of study.

- To improve the luminosity performance by addressing the geometric luminosity reduction factor and possibly allowing the levelling of the luminosity, cryo-modules of crab-cavities (CC) will be added at P1 and P5 (see Figure 9-5).

- Finally, the matching and final focusing of the beams will require completely new insertion cryoassemblies at P1 and P5 (see Figure 9-5)
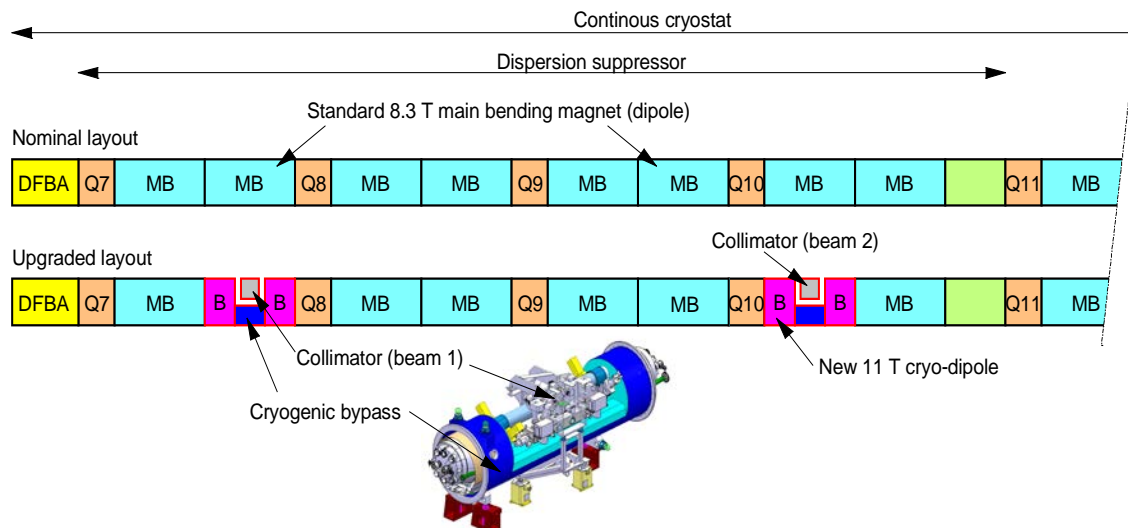
Figure 9-2: Upgraded layout of the continuous cryostat at Point 2 (as well at Points 1, 5 and 7)
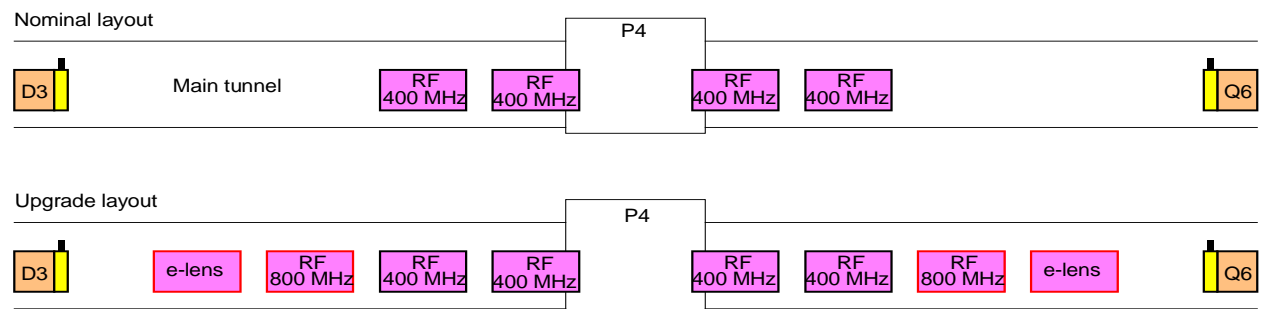
Figure 9-3: Possible upgraded layout of Point 4 insertion region
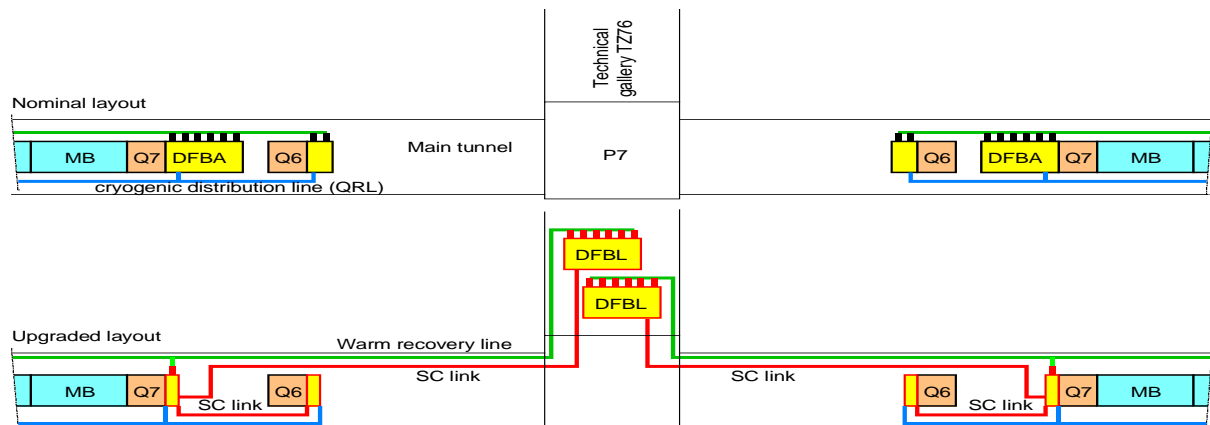
Figure 9-4: Upgraded layout of Point 7 insertion region.
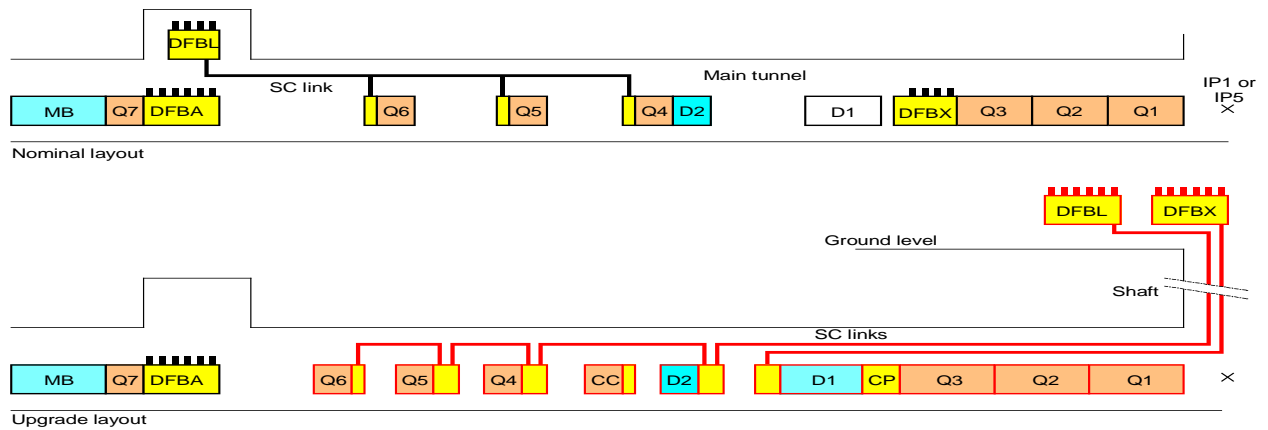
Figure 9-5: Upgraded layout of Point 1/5 insertion region (half insertion).

9.3 Temperature level and heat loads

Heat loads to the cryogenic system have various origins and uncertainties. As done for the LHC and clearly described in the design report, two categories of heat loads are considered: static heat loads (Q_{static}) to be compensated just to reach the desired temperature level, and dynamic heat loads ($Q_{dynamic}$) due to energising or circulating beams. These heat loads are primarily considered without contingency to avoid piling-up margins. However, the cooling capacity to be installed has to include margins that vary for the static and dynamic heat loads to properly allow the nominal beam scenario. This margin vanishes for the ultimate beam scenario.

In Table 9-2 the static heat in-leaks are reported, for different temperature levels. For new equipment, the thermal performance of supporting systems, radiative insulation and thermal shields is considered identical to that of existing LHC equipment.

Table 9-2: Static heat in-leaks of HL-LHC machine (w/o contingency)

			Nominal	Upgrade
4.6-20 K	Beam screen circuit (arc + DS)	[mW/m]	140	
	Beam screen circuit (IT)	[mW/m]	125	
	Beam screen circuit (MS)	[mW/m]	578	
1.9 K	Cold mass (arc + DS)	[mW/m]	170	
	Cold mass (IT)	[mW/m]	1250	
	Crab-cavities	[W per module]	0	25
4.5 K	Cold mass (MS)	[mW/m]	3556	
	400 MHz RF module	[W per module]	200	
	800 MHz RF module	[W per module]	0	120
	Electron-lens	[W per module]	0	12
20-300 K	Current lead	[g/s per kA]	0.035	

) beam scrubbing is considered.

Table 9-3 gives the dynamic heat loads expected for the HL-LHC. The main concern is the electron-cloud impingement on the beam screens, which can only be reduced by efficient beam scrubbing (dipole off) of the beam screens. This remains to be demonstrated. Without efficient beam scrubbing (dipole on), the e-cloud activity will remain high (more than 4 W per meter and per beam) in the arcs and dispersion suppressors (DS). This heat deposition corresponds to about twice the local cooling limitation given by the hydraulic impedance of the beam screen cooling circuits. In addition, the corresponding integrated power over a sector (more than 25 kW) is not compatible with the installed capacity of the sector cryogenic plants. For e-cloud deposition in the arcs and dispersion suppressors, efficient (dipole off) or inefficient (dipole on) beam scrubbing is considered.

Table 9-3: Dynamic heat loads on HL-LHC machine (w/o contingency)

			Nominal	Upgrade
4.6-20 K	Synchrotron radiation (arc + DS)	[mW/m per beam]	165	310
	Image current (arc + DS + MS)	[mW/m per beam]	145	522
	Image current (IT low-luminosity)	[mW/m]	475	1698
	Image current (IT high-luminosity)	[mW/m]	166	596
	E-clouds (arc + DS) (dipole off)	[mW/m per beam]	271	41
	E-clouds (arc + DS) (dipole on)	[mW/m per beam]	4264	4097
	E-clouds (IT high luminosity)	[mW/m]	5500	9455
	E-clouds (IT low-luminosity)	[mW/m]	5500	5500
	E-clouds (MS)	[mW/m per beam]	2550	383
	Secondaries (IT beam screen P1 andP5)	[W per IT]	0	650
1.9 K	Beam gas scattering	[mW/m per beam]	24	45
	Resistive heating in splices	[mW/m]	56	56
	Secondaries (IT cold mass P1 and P5)	[W per IT]	155	630
	Secondaries (DS cold mass P1 and P5)	[W per DS]	37	185
	SCRF crab-cavities	[W per module]	0	24
4.5 K	SCRF 400 MHz	[W per module]	101	366
	SCRF 800 MHz	[W per module]	0	183
	E-lens	[W per module]	0	2
20-300 K	Current lead	[g/s per kA]	0.035	

The beam screens of the new inner triplets at Point 1 and 5 will be protected by tungsten shielding which will be able to absorb about half of the energy deposited by collision debris escaping the high-luminosity detectors. For simplicity at this stage, beam screen loads were considered to be between 4.6 K and 20 K as for present LHC. However, the large dynamic power to be extracted could force consideration of the next possible temperature range compatible with beam vacuum requirements i.e. the range 40 K to 60 K. Despite of this thick W-shielding, the 1.9 K load, i.e. the energy that collision debris deposited onto the magnet coil and cold mass, increases by four times with respect to the nominal LHC case. The W-shielding, in any case, reduces the overall refrigeration cost and increases the lifetime of the inner-triplet coils.

9.4   Impact on existing sector cryogenic plants

With new cryogenic plants dedicated to the cooling of cryogenic equipment in the P1, P4 and P5, the cooling duty of the existing sector cryogenic plants will be reduced and more equally distributed. Figure 9-6 shows the required cooling capacities for the different temperature levels and compares them to the nominal cooling requirements and to the installed capacities. The low-load sectors equipped with upgraded ex-LEP cryogenic plants have lower installed capacity than the 4 cryogenic plants especially ordered for LHC for the high-load sectors. For HL-LHC, sufficient capacity margin still exists providing that the beam scrubbing of dipole beam-screens is efficient (dipole off).
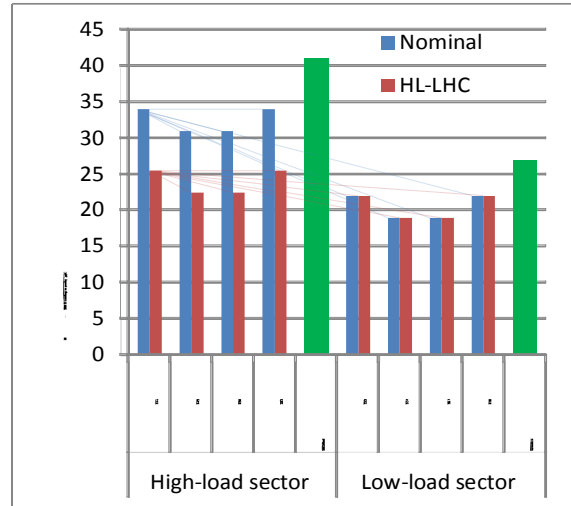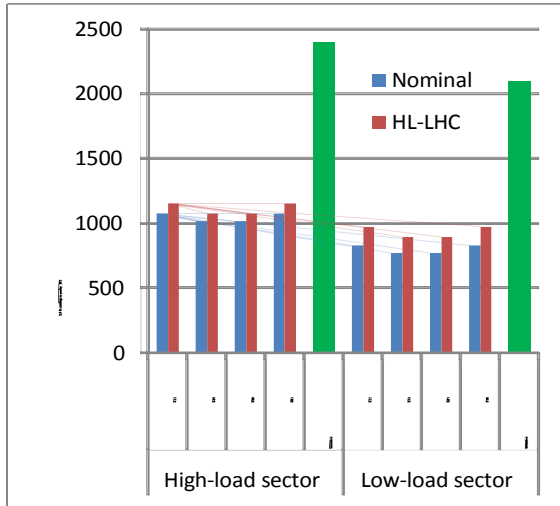
Cold mass

Current leads

Thermal shield
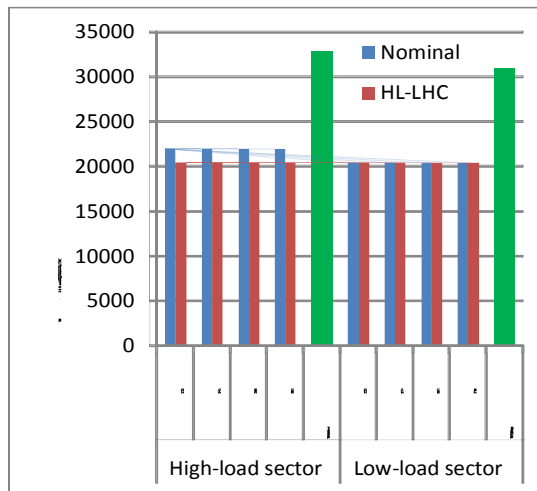
Beam screen (dipole off)

Beam screen (dipole on)
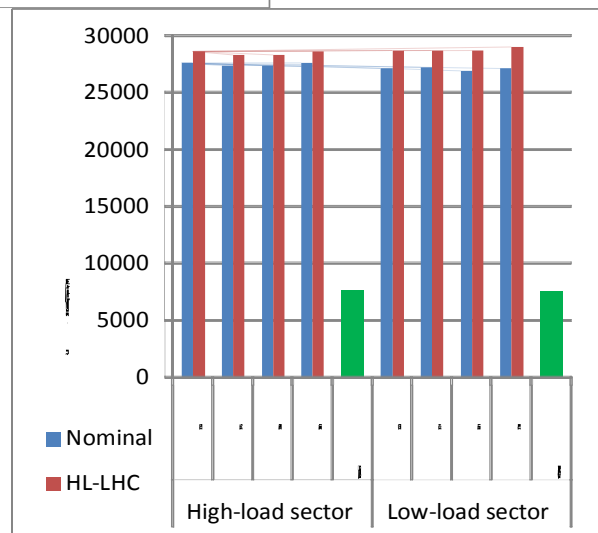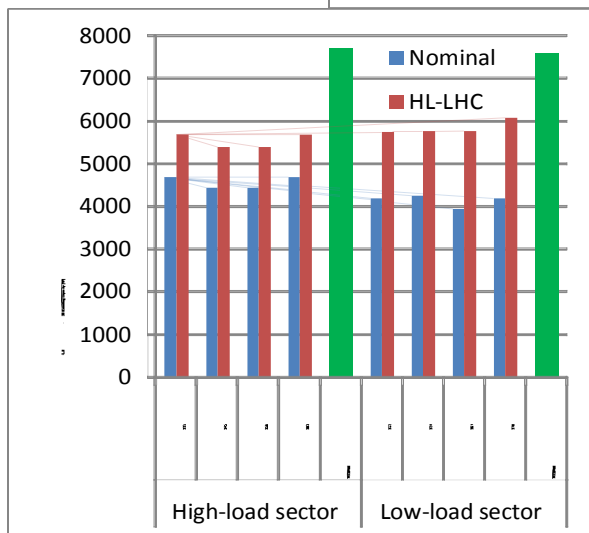
Figure 9-6: Cooling capacity requirement of sector cryogenic plants

9.5 New cryogenics for Point 4 insertion

Figure 9-7 shows the cryogenic architecture of the upgraded Point 4 insertion consisting of:

- a warm compressor station (WCS) located in a noise-insulated surface building and connected to a helium buffer storage;

- a lower cold box (LCB) located in the UX45 cavern and connected to a cryogenic distribution valve box (DVB) as well located in the UX45 cavern;

- main cryogenic distribution lines connecting the cryo-modules to the distribution valve box;

- auxiliary cryogenic distribution lines interconnecting the new infrastructure with the existing QRL service modules (SM) and allowing redundancy cooling with adjacent-sector cryogenic plants;

- a warm-helium recovery line network.

Concerning the planned installed capacity ($Q_{installed}$) of the new cryogenic plant, some uncertainty (f_u) and overcapacity (f_o) margins have to be introduced as shown in the following equation:

$$Q_{installed} = f_o \text{ x } (Q_{static} \text{ x } f_u + Q_{dynamic}) \text{ with } f_o = 1.5 \text{ and } f_u = 1.5 \qquad (9\text{-}1)$$

Table 9-4 gives the installed capacity of the Point 4 cryogenic plant required at the different temperature levels. The Point 4 cryogenic plant will require an equivalent capacity of about 6 kW at 4.5 K.

This is considered as the present baseline, with the evaluation of an alternative scenario for the refrigeration part. The alternative scenario would consist of an upgrade of one of the existing refrigerator of Point 4 to fulfil the required cooling capacity of existing SRF modules with sufficient margin, while keeping the baseline new distribution scenario. This modular and staged approach would allow the installation at a later stage of a new and dedicated refrigerator adapted to the loads presently under definition.
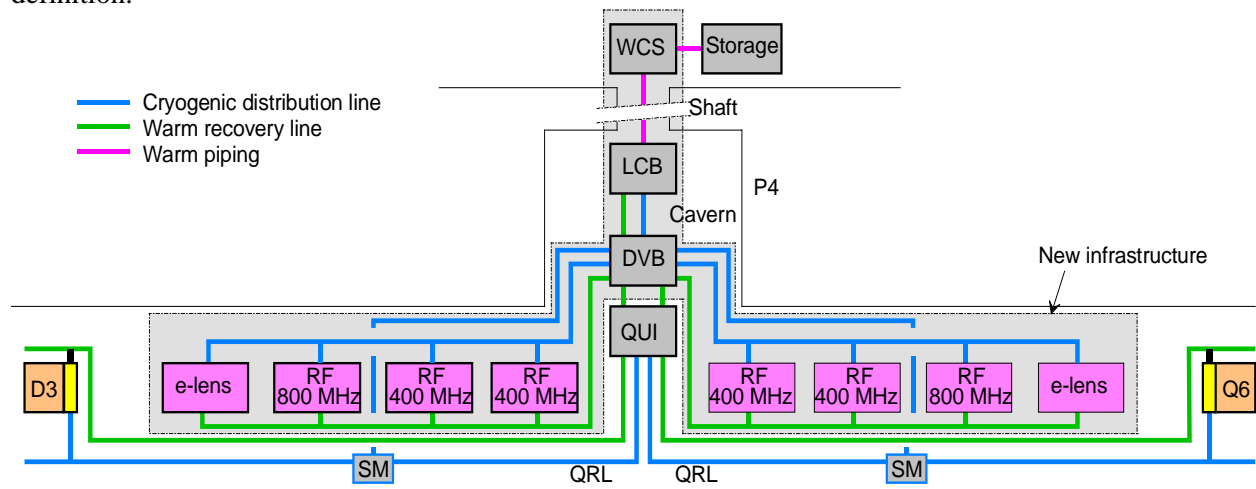
Figure 9-7: Upgraded cryogenic architecture at Point 4

Table 9-4: Installed capacity requirements of the new cryogenic plant at Point 4

Temperature level		Static	Dynamic	Installed	Equivalent installed capacity @ 4.5 K [kW]	
4.5 K	[W]	1144	1736	5223	5.6	5.8
50-75 K	[W]	1000	0	2250	0.2	

9.6   New cryogenics for high-luminosity insertions at Point 1 and Point 5

Figure 9-8 shows the proposed cryogenic architecture of the Point 1 and 5 high-luminosity insertions consisting of:

- a warm compressor station (WCS) located in a noise-insulated surface building and connected to a helium buffer storage;

- an upper cold box (UCB) located in a ground level building;

- a quench buffer (QV) located at ground level;

- 1 or 2 cold compressor boxes (CCB) in underground cavern;

- 2 main cryogenic distribution lines (one per half-insertion);

- 2 interconnection valve boxes with existing QRL cryogenic line allowing redundancy with the cryogenic plants of adjacent sectors.
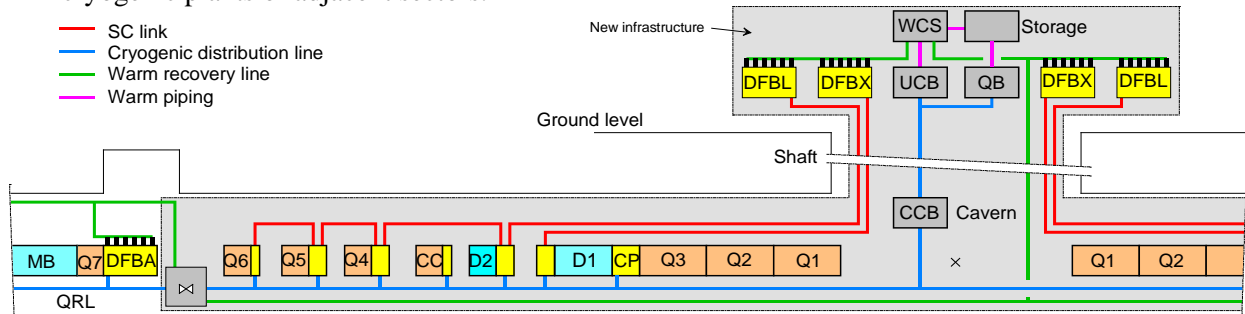
Figure 9-8: Upgraded cryogenic architecture at Point 1 and Point 5

Table 9-5 gives the installed capacity of the proposed Point 1 and 5 cryogenic plants required at the different temperature levels and using the same uncertainty and overcapacity margins as those used for Point 4. The cryogenic plants will require an equivalent capacity of about 18 kW at 4.5 K, including 3 kW at 1.8 K.

Table 9-5: Installed capacity requirements of the new cryogenic plants at Point 1 and 5

Temperature level		Static	Dynamic	Installed	Equivalent installed capacity @ 4.5 K [kW]	
1.9 K	[W]	433	1380	3045	12	
4.5 K	[W]	196	8	452	0.5	
4.6-20 K	[W]	154	2668	4348	2.4	18
50-75 K	[W]	4900	0	7350	0.5	
20-300 K	[g/s]	16	16	59	2.6	

At P1 and P5, the superconducting magnets of the ATLAS and CMS detectors are cooled with dedicated cryogenic plants. A possible redundancy with detector cryogenic plants could be interesting in case of major breakdown of the detector cryogenic plants. The corresponding power requirements are about 1.5 kW at 4.5 K for CMS and 3 kW at 4.5 K for ATLAS.

The cooling capacity of 3 kW at 1.8 K is higher than the 2.4 kW installed capacity of a LHC sector, which corresponds to the present state-of-the-art for the cold compressor size. Consequently:

- larger cold compressors have to be studied and developed;

- or parallel cold compressor trains have to be implemented (one 1.5 kW train per half insertion);

- or duplication of the first stage of cold compression to keep the machine within the available size.

9.7   Building and general service requirement

Table 9-6 gives the buildings and general services at P1, P4 and P5 required by the cryogenic infrastructure. At P4, the required surface and volume for the warm compression station and for the cold box are respectively available in the existing SUH4 building and in the UX45 cavern.

Table 9-6: Building and general service requirement

Cryogenic system			P1 and P5	P4
Warm compressor building	Surface	[m^2]	700	400
	Crane	[t]	20	20
	Electrical power	[MW]	4.6	2.0
	Cooling water	[m^3/h]	540	227
	Compressed air	[Nm^3/h]	30	20
	Ventilation	[kW]	250	100
	Type	[-]	Noise-insulated (~108 dB_A)	
Surface "SD" building	Surface	[m^2]	30x10	N/A
	Height	[m]	12	N/A
	Crane	[t]	5	N/A
	Electrical power	[kW]	50	N/A
	Cooling water	[m^3/h]	15	N/A
	Compressed air	[Nm^3/h]	90	N/A
Cavern	Volume	[m^3]	200	300
	Local handling	[t]	2	2
	Electrical power	[kW]	100	20
	Cooling water	[m^3/h]	20	20
	Compressed air	[Nm^3/h]	40	30

9.8   Conclusion

The HL-LHC project will require a major cryogenic upgrade. The main challenges will be:

- Cooling circuits for large heat deposition:

  o up to 13 W/m on 1.9 K cold masses for heat extraction from SC cables and sufficient quench energy margin. Accurate heat flow calculation in coil and yoke cross section must be developed.

  o up to 23 W/m on inner-triplet beam-screens with possibly a different operating range (40-60 K) and with a large dynamic range which will require specific cryogenic-plant adaptation studies.

- Cooling of HTS SC links and current feed boxes.

- Cooling and pressure relief of crab-cavities.

- Validation tests on SC link, crab-cavities, magnets, beam screens…

- Reactivation of the Heat Load Working Group.

- Quench containment and recovery.

- Larger 1.8 K refrigeration capacities beyond the present state-of-the-art.

- Large capacity (1500/3000 W) sub-cooling heat exchangers.

- Larger turndown capacity factor (up to 10) on the 1.8 K refrigeration cycle.

Chapter 10

Energy deposition and radiation to electronics

A. Bignami[14], F. Broggi[14], M. Brugger[5], F. Cerutti[5], L.S. Esposito[5], A. Lechner[5], N.V. Mokhov[10], I.L. Rakhno[10], C. Santini[18], E. Skordis[5], I.S. Tropin[10]
[5]CERN, Accelerator & Technology Sector, CH-1211, Geneva, Switzerland
[10]FNAL, Fermi National Accelerator Laboratory, Batavia, P.O. Box 500, IL, USA
[14]INFN-LASA, Milan, Italy
[18]Politecnico of Milan, Italy

10   Energy deposition and radiation to electronic

10.1   Characterization of the radiation source

Proton-proton inelastic collisions taking place in the LHC inside its four detectors generate a large number of secondary particles with average multiplicities of approximately 100 (120) per single proton-proton interaction with 3.5 (7) TeV beams, but with very substantial fluctuations over different events. Moving away from the interaction point (IP), this multiform population evolves, even before touching the surrounding material, because of the decay of unstable particles (in particular neutral pions decaying into photon pairs). Figure 10-1 illustrates the composition of the debris at 5 mm from the point of a 14 TeV center of mass collision, featuring a $\sim$ 30% increase in number of particles, due to aforementioned decays, and a clear prevalence of photons (almost one half) and charged pions ($\sim$ 35%).

Most of these particles are intercepted by the detector and its forward region shielding releasing their energy within the experimental cavern. However, the most energetic ones, emitted at small angles with respect to the beam direction, travel farther in the vacuum and reach the accelerator elements, causing a significant impact on the magnets along the Insertion Regions (IRs), in particular the final focusing quadrupoles and the separation dipoles. Figure 10-1 shows also the breakdown of the debris components going through the aperture of the TAS (Target Absorber Secondaries) absorber, a protection element consisting of a 1.8-m long copper core located at 20 m from the IP and representing the interface between the detector and the accelerator. The TAS absorbers are installed only at each side of the high-luminosity detectors, ATLAS in P1 and CMS in P5, since their protection role, in fact limited to the first quadrupole, is not needed for luminosities up to 0.2×10^{34} cm^{-2} s^{-1} [1].

Despite the fact that the number of particles per collision leaving the TAS aperture is more than one order of magnitude lower than the total number of debris particles, they carry about 80% of the total energy, implying that 40% of the released energy at the IP exits on each side of the experiments. At the nominal HL-LHC luminosity (5×10^{34} cm^{-2} s^{-1}), this represents about 3800 W per side that is inevitably impacting the LHC elements and consequently dissipated in the machine and in the nearby equipment (e.g. electronics, racks,...) and in the tunnels walls.

It is fundamental to study how these particles are lost in order to implement the necessary protections for shielding sensitive parts of the LHC magnets and the machine. For these purposes, Monte

Carlo simulations of the particle interactions with matter play an essential role, relying on a detailed implementation of physics models and an accurate 3D-description of the region of interest.
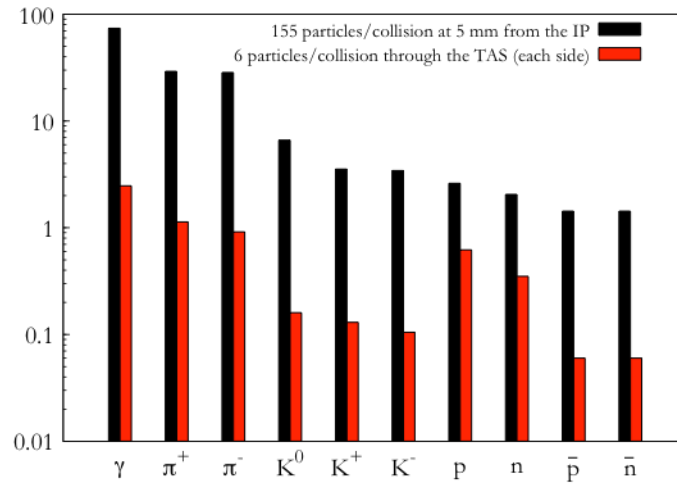
Figure 10-1: Number of debris particles per single proton-proton inelastic interaction at 5 mm from the interaction point (black histogram) and at the exit of each 60-mm TAS aperture (red).

In addition to the luminosity debris, which dominates energy deposition in the vicinity of the collision points, regular and accidental beam losses represent other relevant sources of radiation. In particular, beam halo particles caught in the collimators (see Chapter 5) initiate hadronic and electromagnetic showers, mainly in the betatron and momentum cleaning IRs. The same happens with injection and dumping protection devices (see Chapter 14). Moreover, secondary particle showers are also originated by beam interactions with the residual gas inside the vacuum chamber all along the accelerator, as well as with dust fragments falling into the beam path.

10.2 Power and dose evaluations concerning the triplet-D1 region

The LHC upgrade includes replacement of the inner triplet (IT) 70-mm NbTi quadrupoles in Point 1 (P1) and Point 5 (P5) with the 150-mm coil aperture Nb_3Sn quadrupoles along with the new 150-mm coil aperture NbTi dipole magnet and orbit correctors. Moreover, a corrector package (CP) that includes a skew quadrupole and eight high-order magnets (from sextupole to dodecapole, normal and skew, based on the NbTi technology) will be located between the triplet and the D1.

As the first studies of radiation loads in the LHC upgrades have shown [2,3], one could provide the operational stability and adequate lifetime of the IR superconducting magnets by using Tungsten-based inner absorbers in the magnets. The goals are: (1) reduce the peak power density in the inner Nb_3Sn cable to below the quench limit with a safety margin; (2) keep the 3000 fb^{-1} lifetime peak dose in the innermost layers of insulation and radiation loads on inorganic materials in the hottest spots of the coils below the known radiation damage limits; (3) keep the dynamic heat load to the cold mass at a manageable level.

10.2.1 FLUKA – MARS Modeling

To design such a system in a consistent and confident way, coherent investigations have been undertaken with two independent Monte-Carlo codes benchmarked in the TeV energy region and regularly used in such applications: FLUKA at CERN [4-7] and MARS15(2014) at Fermilab [8-10]. The studies were done for 7+7 TeV pp-collisions with a 295-µrad half-angle vertical crossing in IP1 (which was found earlier to be the worst case) using DPMJET-III as the event generator.

The identical, very detailed geometry model was created and used in both the codes with same materials and magnetic field distributions in each of the components of the 80-m region from IP through the D1 dipole. An octagonal stainless steel beam screen, equipped with 6-mm Tungsten absorbers on the mid-planes, is placed inside the cold bore along the triplet, the CP and the D1, except in Q1 where the Tungsten thickness is increased to 16 mm, compatible with the relaxed aperture requirements. The absorbers are in between the beam screen and the 1.9-K beam pipe: they are supported by the beam screen, and thermally connected to it, whereas they have negligible contact with the cold mass. Therefore, from the point of view of energy deposition, the beam screen function is two-fold:

- It shields the coils from the debris by reducing the energy deposited in there,

- It removes a sizable part of the heat load from the 1.9 K cooling system, intercepting it at higher temperature.

The present HL-LHC layout foresees six cryostats on each side of the IP: four for the triplet quadrupoles (Q1, Q2A, Q2B and Q3), one for the CP and the last for the D1. The distance between the magnets in the interconnections is 1.5 - 1.7 m and an interruption of the beam screen is necessary therein. As a reasonable baseline, we assume here a 500-mm interruption of the Tungsten absorbers in the middle of interconnects. Figure 10-2 and Figure 10-3 show a 3D view of the model and details in the inner parts of the quadrupoles and orbit correctors.
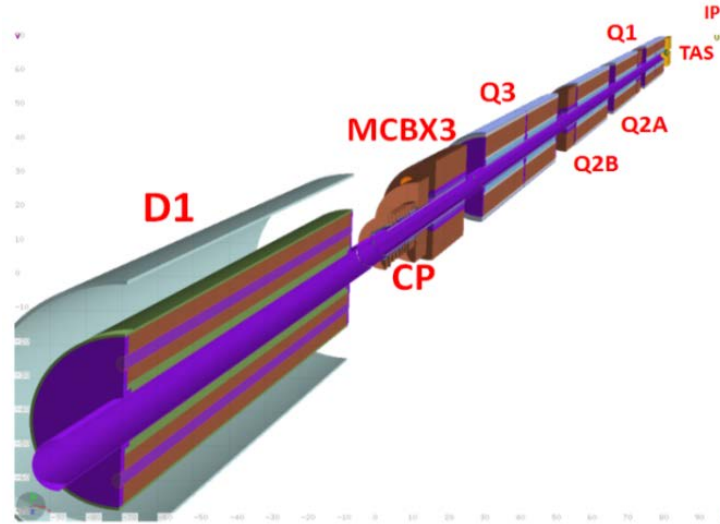
Figure 10-2: Computer model of HL-LHC inner triplet with MCBX/CP correctors and D1 dipole.

Fine-mesh distributions of power density as well as of absorbed dose, neutron fluence and Displacements-Per-Atom (DPA) along with dynamic heat load in every IT component were calculated with FLUKA and MARS in high-statistics runs. The power density and dynamic heat load results are normalized to the luminosity of 5×10^{34} cm^{-2}s^{-1}, while all other ones to 3000 fb^{-1} integrated luminosity corresponding to ~10-12 years of the HL-LHC operation. Longitudinal scoring bins are 10 cm, and azimuthal ones are 2°. Radially, power density is averaged over the superconducting cable width, while dose, fluence and DPA are scored within the innermost layer equal to 3-mm or its thickness, whatever is thinner.
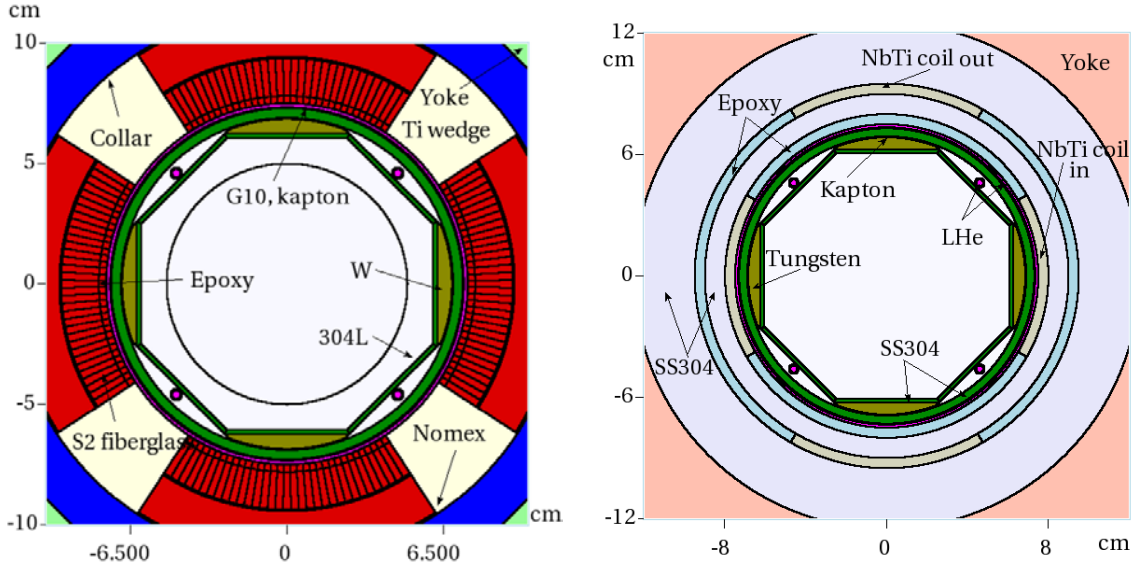
Figure 10-3: Details of the FLUKA-MARS model in the innermost regions of the Q2-Q3 quadrupoles (left) and MCBX orbit correctors (right).

10.2.2 Operational Radiation Loads

Power density isocontours at the IP end of the cold mass of the Q2A quadrupole are shown in Figure 10-4 (left). The longitudinal peak power density profile on the inner coils of the IT magnets at the azimuthal maxima is presented in Figure 10-4 (right). Results from FLUKA and MARS are in an excellent agreement, being observable discrepancies – which are naturally related to the use of fully independent tracking and scoring algorithms and physics models – largely within the safety margin to be recommended at the design stage. The peak value of 2 mW/cm^3 in the quadrupoles is 20 times less than the assumed quench limit of 40 mW/cm^3 in Nb$_3$Sn coils [2]. The peak value of ~1.5 mW/cm^3 in the NbTi based coils of the correctors and D1 dipole is almost ten times less of the known quench limit of 13 mW/cm^3 in such coils [11].
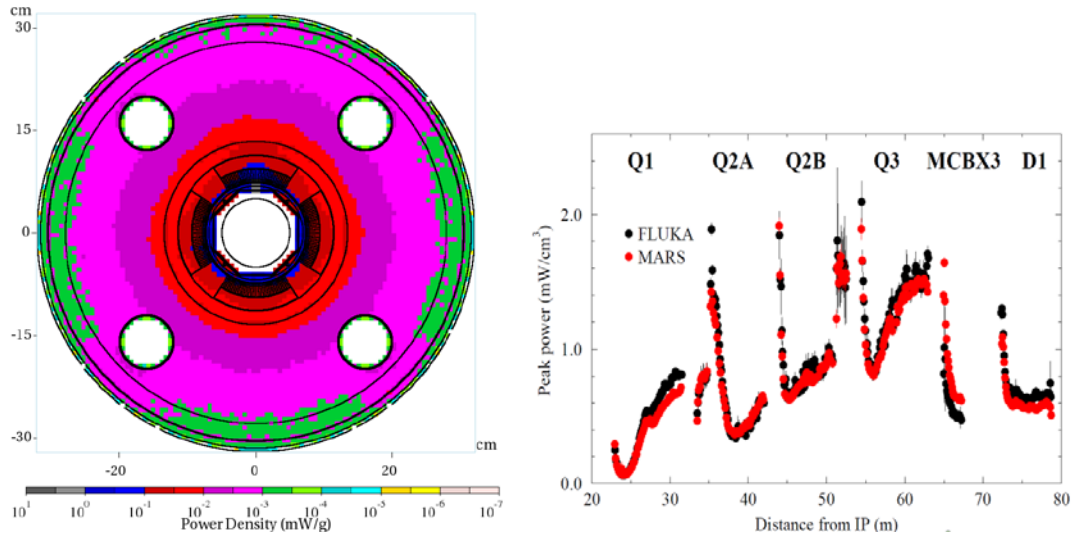
Figure 10-4: Power density isocontours at the IP end of Q2A (left) and longitudinal peak power density profile on the inner coils of the IT magnets (right).

The total power dissipation in the Inner Triplet IT region from the IP1 collision debris splits roughly 50-50 between the cold mass and the beam screen with Tungsten absorber: 630 W and 615 W,

respectively, from the FLUKA calculations. MARS predicts about 2% lower values. For the 45-m effective length of the cold mass, the average dynamic heat load on it is ~14 W/m.

10.2.3 Lifetime Radiation Loads

The peak dose and DPA – the quantities that define radiation damage and lifetime of insulators and non-organic materials of the IT magnets, respectively – are calculated at the azimuthal maxima in the innermost tiny layers of each the IT component shown in Figure 10-2.

The longitudinal peak dose profiles on the inner coils and insulating materials are presented in Figure 10-5 (left). The values in the MCBX orbit correctors (located in the Q1-Q2A, Q2B-Q3 and Q3-D1 regions) are given for the epoxy layer (FLUKA) and kapton layer (MARS); see Figure 10-3 for details. Results from FLUKA and MARS are again in a good agreement. The larger aperture IT magnets and the simulated implementation of Tungsten absorbers perform very well, reducing the peak values of both power density and absorbed dose in the HL-LHC IR to the levels which correspond to the LHC nominal luminosity.
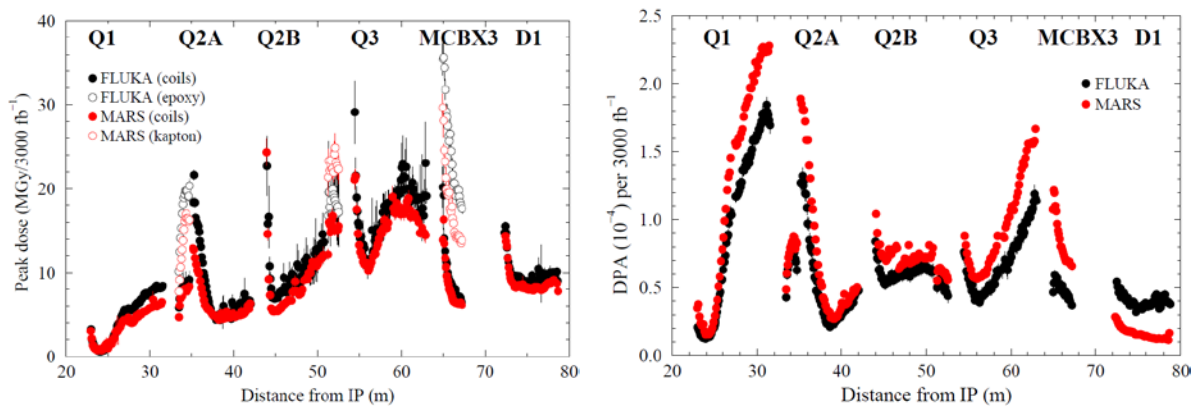
Figure 10-5: Longitudinal distributions of peak dose on inner coils and nearby insulators (left) and of peak DPA on inner coils (right).

The maximum peak dose in the coils is about 25 MGy for quadrupoles and ~15 MGy for the D1 dipole. The integrated peak dose in the IT magnet insulation reaches 30-36 MGy in the MCBX3 corrector, 28-30 MGy in the quadrupoles and ~22 MGy in the D1 dipole. This is at or slightly above the common limits for kapton (25-35 MGy) and CTD-101K epoxy (25 MGy).

Degradation of the critical properties of inorganic materials of the IT magnets – Nb_3Sn and NbTi superconductors, copper stabilizer and mechanical structures – is usually characterized not by absorbed dose but by integrated neutron fluence and by DPA accumulated in the hottest spots over the expected magnet lifetime. DPA is the most universal way to characterize the impact of irradiation on inorganic materials. In both FLUKA and MARS, all products of elastic and inelastic nuclear interactions as well as Coulomb elastic scattering (NIEL) of transported charged particles (hadrons, electrons, muons and heavy ions) from ~1 keV to TeV energies contribute to DPA using Lindhard partition function and energy-dependent displacement efficiency. For neutrons at <20 MeV (FLUKA) and <150 MeV (MARS), the ENDF-VII database with NJOY99 processing is used in both the codes.

The longitudinal peak DPA profiles on the IT magnet coils are presented in Figure 10-5 (right). The peaks are generally observed at the inner coils; therefore, the data is given there. With the vertical crossing in IP1, the MCBX3 orbit corrector is the exception with the peak in the outer coil in the vertical plane (see Figure 10-5). To see this effect, the MARS data in Figure 10-5 (right) for MCBX3 is given for the outer coil, while FLUKA shows results for the inner coil as in all other magnets. Contrary to the power density and dose distributions driven by electromagnetic showers initiated by photons from π^0 decays, DPA peaks at the non-IP end of the Q1B quadrupole. At that location, about 70% of DPA is

from neutrons with E < 20 MeV, ~25% from transported nuclear recoils above 0.25 keV/A, and the rest is due to other transported particles and non-transported recoils. The thicker Q1 shielding, while assuring a very effective dose reduction, plays a clear role in enhancing neutron production.

The peak in the Q1B inner coil is about 2×10^{-4} DPA per 3000 fb^{-1} integrated luminosity. In other IT components it is about $(1\pm0.5)\times10^{-4}$. These numbers should be acceptable for the superconductors and copper stabilizer provided periodic annealing during the collider shutdowns. Taking into account a good correlation of DPA with neutron fluence in the coils, one can also compare the latter with known limits. In the quadrupole coils, the peak fluence is $\sim2\times10^{17}$ cm^{-2} which is substantially lower than the 3×10^{18} cm^{-2} limit used for the Nb$_3$Sn superconductor. In the orbit corrector and D1 dipole coils, the peak fluence is $\sim5\times10^{16}$ cm^{-2} which is again lower than the 10^{18} cm^{-2} limit used for the NbTi superconductor. The integrated DPA in the magnet mechanical structures are 0.003 to 0.01 in the steel beam screen and Tungsten absorber, $\sim10^{-4}$ in the collar and yoke, and noticeably less outside. These are to be compared to a ~10 DPA limit for mechanical properties of these materials. Neutron fluences in the IT mechanical structures range from 3×10^{16} cm^{-2} to 3×10^{17} cm^{-2} compared to the 10^{21} cm^{-2} to 7×10^{22} cm^{-2} limits.

Peak dose on the beam screen was found to be of the order of several hundred MGy after 3000 fb^{-1} integrated luminosity (up to 700 MGy in the D1), mostly carried by electromagnetic particles. Its impact on carbon coating has to be considered.

10.3 Critical dependencies

The beam screen equipped with Tungsten absorbers represents the backbone element for the protection of the IR magnets. Therefore, the details of its design play a crucial role in determining its actual effectiveness.

After the preliminary studies described in the previous section, new estimates were necessary to include:

- the real absorber material, INERMET 180 that has a density of 18 g cm^{-3}, about 8% less than pure Tungsten, implying a reduced shielding performance,

- the first prototype taking into account the machinability of INERMET and the required size of the cooling tubes as dictated by preliminary cryogenics estimates,

- the reduction of the beam screen thickness (from 2 to 1 mm) necessary to let the structure respond elastically to possible deformations occurring during a quench.

Figure 10-6 (left) shows the transverse section of the beam screen model (BS#2) embedding the aforementioned modifications. It can be compared to the model (BS#1) used in the calculations reported in the previous section (see Figure 10-3). The longitudinal peak dose profile on the inner coils of the IR magnets is presented in Figure 10-7 for the case of BS#1 (black points) and of BS#2 (red points). In the latter case, the accumulated peak dose turns out to be systematically higher all along the IR magnets, almost doubling its value in the Q3 and reaching about 55 MGy in the MCBX3 corrector. Along the Q2, most of the impacting debris, positively charged, is pushed by the magnetic field from the crossing angle side to the opposite one, i.e. from top to bottom in the assumed crossing scheme, where the outgoing beam points upwards. This moves the energy deposition peak through different azimuthal regions, which in the revised design (BS#2) are no longer shielded by the beam screen absorbers, hence yielding the resulting substantial increase. To fix this problem, we considered a third version of the beam screen (BS#3), where the INERMET absorbers were extended as much as possible to cover the coils towards the poles (see Figure 10-6, right). The estimated peak dose distribution (green points in Figure 10-7, left) shows a significant improvement in the Q3-CP region, when compared to the BS#2 case. It should also be noticed that, mainly due to the reduced absorber density, the sharing of the total deposited power between cold mass and beam screen gets unbalanced, moving to 55-45 and making the heat released in the cold mass approach 700W (at 5×10^{34} cm^{-2}s^{-1}).
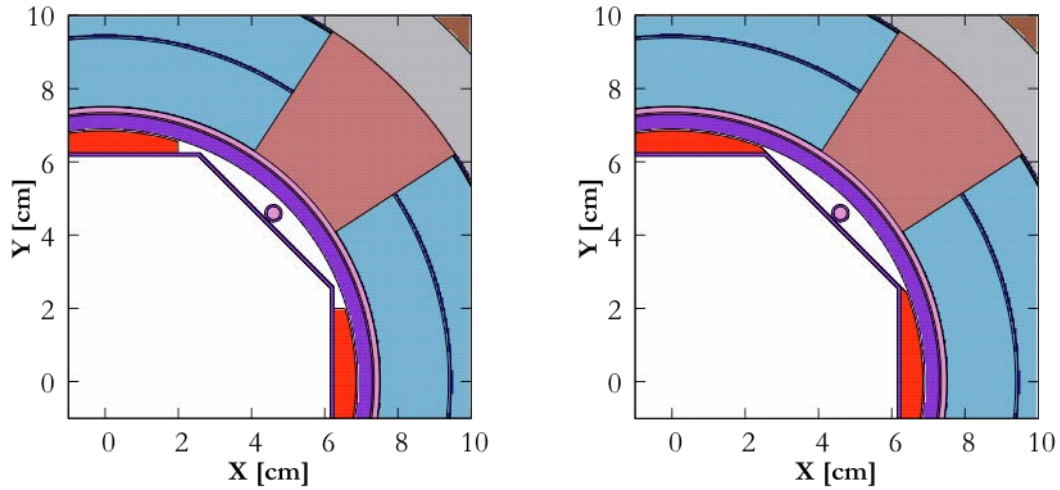
Figure 10-6: Left: beam screen model as per the first conceptual design developed by WP12 (BS#2). Right: beam screen model with the modification of the absorbers driven by energy deposition considerations (BS#3).

Another crucial aspect is the longitudinal interruption of the beam screen and its absorbers, which is necessary between two consecutive cryostats in order to host a bellow and a BPM. As mentioned in the previous section, we initially assumed a 500-mm gap. Shorter gaps are possible if the BPMs are going to be equipped with absorber layers like the ones in the beam screen (see Chapter 12). To mimic this case, we looked at the effect of a 100-mm gap, which should be considered as the most optimistic case. The peak dose dependence on the gap length is presented in Figure 10-7 (left) where the improvement achieved downstream the Q2A-Q2B, Q2B-Q3 and especially Q3-CP interconnects is visible, with a reduction from 55 to 35 MGy in the MCBX3 for the BS#2 design.
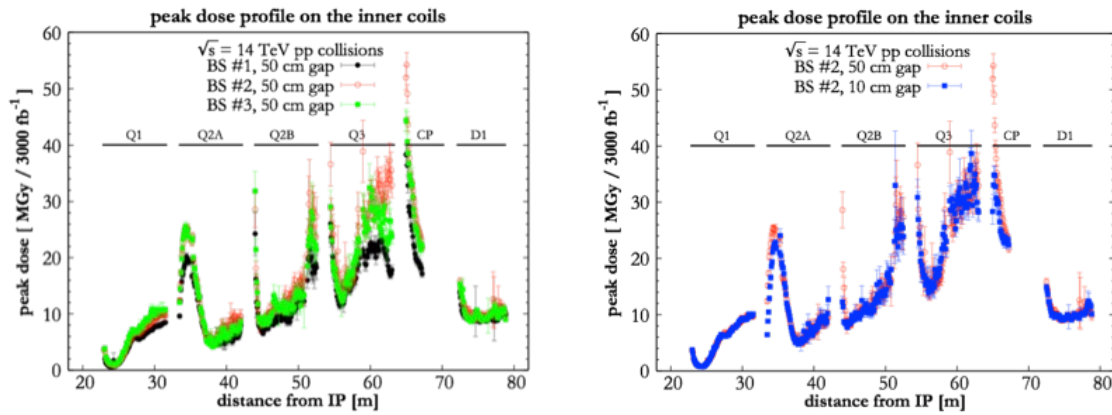
 Figure 10-7: Longitudinal distributions of peak dose on the inner coils of the IR magnets referring to different beam screen designs (left) and to different lengths of the beam screen gap in the interconnects (right).

Therefore, the actual implementation of the absorber layers in the design of both the beam screen and the relevant BPMs considerably affects the maximum dose expected in the IT coils.

10.4 Impact on the matching section and protection strategy

The HL upgrade foresees changes in the IR1 and IR5 Matching Section, implying a new TAN (Target Absorber Neutral) absorber with larger apertures, a new recombination dipole D2 and Q4 (both with larger twin apertures, together with their respective correctors). The present baseline foresees also the

Q5 replacement by the present Q4 (providing a larger aperture) and the installation of Crab Cavities. From Q6 onwards, no hardware modifications are expected inside the IRs.

With respect to the present LHC, the variation of three ingredients mainly impacts the energy deposition in the Matching Section elements. They are:

- the distance between the separation/recombination dipoles (reduced from 86 m to 67 m),

- the aperture of the upstream magnets (IT quadrupoles, CP correctors, and the D1), and (3)

- the TAN design, which has to comply with larger beam separation and sizes.

As a consequence, the number of debris particles entering the Matching Section per primary collision is much larger than in the case of the current machine. This is illustrated in Figure 10-8 where the debris particle distributions at the exit of the TAN outgoing beam pipe are shown for the LHC (left) and the HL-LHC (right). The number of protons is increased by about 30% (from 0.12 to 0.16 protons/collision), while the number of photons and neutrons is about 7 times higher (from 0.06 to 0.41 particles/collision). Note that in the case of the HL-LHC optics the beam size at this location is about twice as large as the one of the LHC optics. Therefore, a collimator set at the same aperture in beam sigma's turns out to be less effective in intercepting debris particles, as clearly revealed in the figure by the amount of particles left inside the beam envelope.
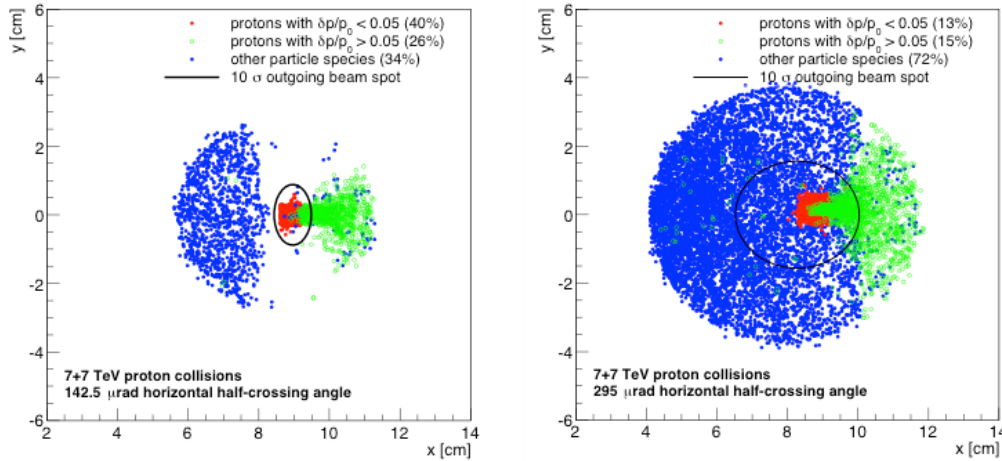
Figure 10-8: Debris particle distribution at the exit of the outgoing beam pipe of the TAN for the LHC (left) and the HL-LHC (right). Red points indicate protons with magnetic rigidity within 5% with respect to beam protons and green points indicate protons with lower magnetic rigidity. Blue points indicate neutral particles (photons and neutrons). The same number of collision is simulated in both cases. The black ellipse shows the 10σ outgoing beam spot.

In the present LHC machine, a network of TCL (Target Collimator Long physics debris) collimators secures the protection of the cold magnets in the Matching Section. There is one copper TCL in front of the D2 (TCL4, installed during LS1), one copper TCL in front of the Q5 (TCL5, the only one already present and operated during Run 1) and one Tungsten TCL in front of the Q6 (TCL6, whose installation during LS1 was triggered by specific Roman Pot operation scenarios). However, at nominal luminosity not all TCLs are necessary to keep the heat load below the quench level. It was shown that the single TCL4 set at 15σ is sufficient to maintain the peak power density below 0.3 mW/cm^3 in all magnets of the Matching Section [12].

Conversely, in the HL-LHC case, all these TCLs are indispensable for magnet protection. For the purposes of the estimates presented here, the jaws of all the collimators are assumed to be made of Tungsten (INERMET 180) because of its greater absorption efficiency (higher density and atomic number than copper). Moreover, additional fixed TCLM (Target Collimator Long Mask) masks are

required in order to further shield the magnet aperture. The masks are supposed to be placed between the magnet cryostat and the TCL collimator (where present). Since the hottest spot is typically located on the IP-side of each magnet, a shielding strategy based on a beam screen equipped with thick absorbers, as in the IT region, does not pay here. On the other hand, the masks, which have the same shape and aperture as the beam screen of the protected magnet and a radial thickness sufficient to shadow the downstream coils, can assure an effective interception of the shower coming from the upstream elements. The sensitivity to the mask presence and length has been investigated, aiming to comply also with integration issues that are particularly challenging in the TAN-D2 region.
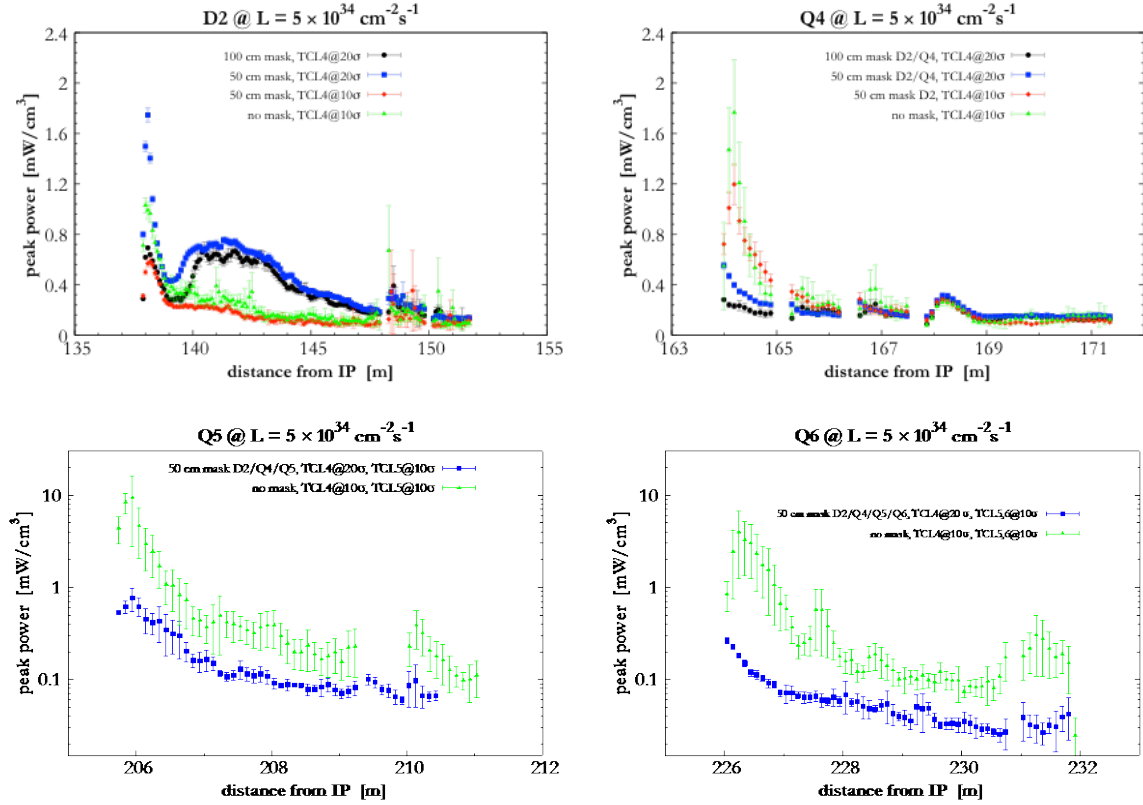
Figure 10-9: Longitudinal profile of peak power density along the D2 (top left), Q4 (top right), Q5 (bottom left, log scale) and Q6 (bottom right, log scale) at the HL-LHC target luminosity of 5×10^{34} cm^{-2}s^{-1}. Different layouts and settings are compared. Error bars indicate statistical uncertainties.

Preliminary longitudinal profiles of the peak power density along the D2, Q4, Q5 and Q6 are shown in Figure 10-9. All the TCLs are set to 10σ, but for TCL4 also the 20σ aperture is explored. Dedicated masks turn out to be necessary for the Q5 and Q6, while their need is less obvious for the D2 and Q4, for which further studies are being carried out taking into account refined specifications concerning the TAN and TCL4 aperture and position. Considering lifetime issues, the installation of 50 cm masks in front of Q5 and Q6 keeps the respective peak dose values within 20 MGy after 3000 fb^{-1}.

The heat load due to collision debris on the most exposed Crab Cavity (the first one on the outgoing beam) was estimated to be about 0.2 W. The maximum power density is located on the cavity internal plate and is about 0.4 mW/cm^3. It corresponds to ~3 MGy after the target HL-LHC integrated luminosity. The contribution from beam-gas interactions is expected to be 10 times smaller, for a conservative residual gas density of 10^{15} H$_2$-equivalent molecules/m^3.

10.5 Exposure of the Superconducting Links

Cold Powering of the HL-LHC magnets foresees moving of the power converters on to the surface [13]. The consequences of this new configuration are:

- a safer long-term operation of powering equipment (power converters, current leads and associate auxiliary devices), being located in a radiation-free environment;

- a safer access of personnel to equipment for maintenance, repair, diagnostic and routine tests interventions;

- a reduced time of interventions on power converters, current leads;

- more free space in the beam areas which becomes available for other equipment.

The connecting lines will be made of MgB_2. The Link cold mass contains superconducting (SC) cables which are connected at one end, in the tunnel, to the NbTi magnet bus-bar operated in liquid helium and the other end to the bottom end of the Current Leads maintained at a maximum temperature (T_{CL}) of about 20 K in helium gas environment, see Figure 10-10 [14].
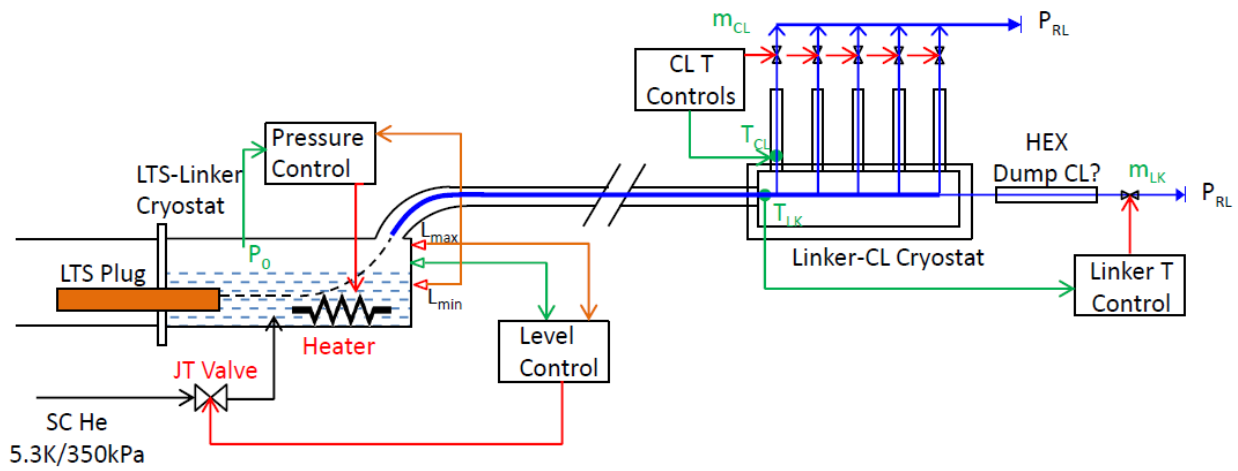
Figure 10-10: Cooling scheme of Cold Powering System. Left: Low Temperature (LT) side, where there are the connections with the SC magnet cable. Right: connection with the Current Leads (CL).

The radiation impact on the MgB_2 SC Links is evaluated from different points of view. The Boron consumption by thermal neutrons is not a concern. The total amount of neutrons escaping from the first quadrupole of the new triplet is of the order of 10^{21}, over an integrated luminosity of 3000 fb^{-1}. Considering the amount of ^{10}B in the Links, the consumption can be estimated as much less than 0.01%.
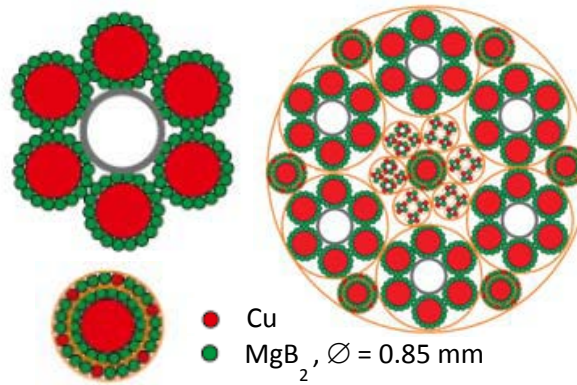
Figure 10-11: Left: 20 kA MgB$_2$ cable, $\varnothing$=19.5 mm (top), two MgB$_2$ concentric cables for 3kA total current, $\varnothing$ =8.2 mm (bottom). Middle: 150 kA cable assembly for LHC P1 and P5 (6x20 kA, 7x3 kA, 4x0.4 kA, 20x0.12 kA), $\varnothing$ =65 mm. Right: The FLUKA model of the cable.

The Links in P1 and P5 consist of a multi-cable assembly as shown in Figure 10-11 (left). Its model as implemented in the FLUKA geometry is also shown in Figure 10-11 (right).

The calculated dose maps for the horizontal and vertical routing of the SC Link inside the shuffling module in P1 are shown in Figure 10-12. The obtained values (up to about 1 MGy) are not expected to affect the Link operation (provided that the chosen insulator is radiation resistant). The maximum DPA induced in the Links is of the order of 10^{-6}. Preliminary simulations for P5 indicate the same outcome as for P1.
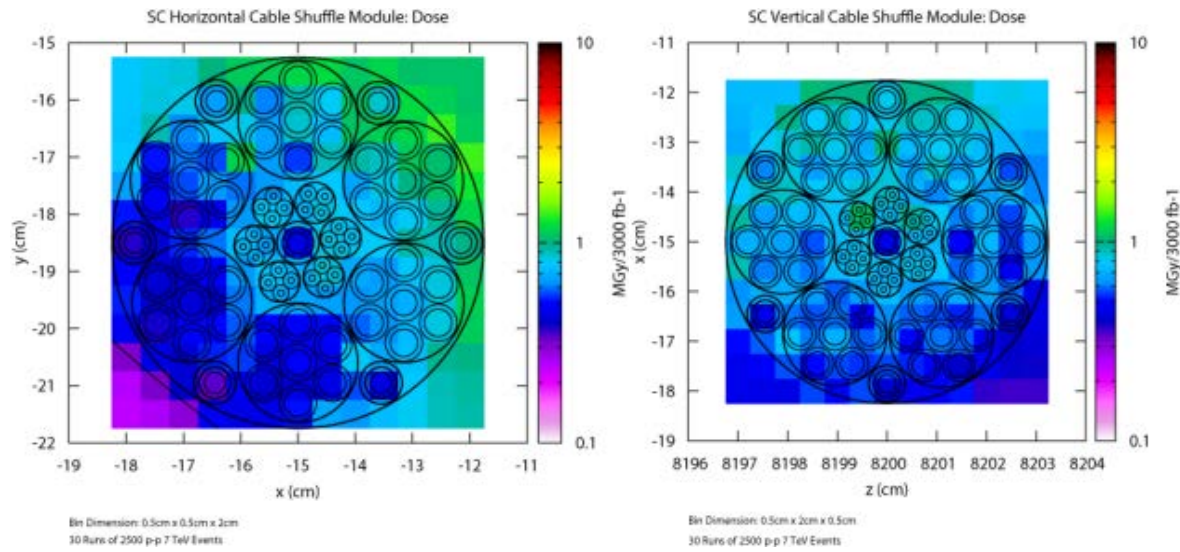
Figure 10-12: Maps of dose released in the SC Link in the P1 shuffling module. Values (in MGy) are normalized to 3000 fb^{-1}.

The modelling of the cable in P7 is in progress, so, as a first approximation, the same cable as in P1 and P5 has been used in order to evaluate its level of exposure to radiation. In this case, the latter is originated by beam losses in the collimators, from which energetic particle showers develop. The Link routing has been implemented at about 1 m above the beam. The hottest region is downstream the primary collimators, close to the passive absorber that shields the warm dipoles. Assuming that the ratio between yearly losses in the collimators and accumulated luminosity does not get significantly worse than what was achieved with the present machine, the resulting maximum dose and DPA are again not of concern for the Link operation and long-term integrity.

10.6 Radiation To Electronics

A specific problem is represented by the electronics sensitivity to radiation. The above described particle debris emerging from the IP, together with the additional loss contribution from beam-gas interactions, will impact equipment present in the areas adjacent to the LHC tunnel (UJs, RRs). Installed (present or future) control systems are either fully commercial or based on so-called COTS (Commercial-Off-The-Shelf) components, both possibly affected by radiation. This includes the immediate risk of so-called Single Event Effects (SEE) and a possible direct impact on beam operation, as well as in the long-term cumulative dose effects (impacting the component/system lifetime) which additionally have to be considered.

For the tunnel equipment in the existing LHC, radiation was only partially taken into account as a design criteria prior to construction, and most of the equipment placed in adjacent and partly shielded areas was not conceived nor tested for their actual radiation environment. Therefore, given the large amount of electronics being installed in these areas, during the past years a CERN wide project called R2E (Radiation To Electronics) [15] has been initiated to quantify the danger of radiation-induced failures and to mitigate the risk for nominal beams and beyond to below one failure a week. The respective mitigation process included a detailed analysis of involved radiation fields, intensities and related Monte-Carlo calculations; radiation monitoring and benchmarking; the behaviour of commercial equipment/systems and their use in the LHC radiation fields; as well as radiation tests with dedicated test areas and facilities [15, 16].

In parallel, radiation induced failures were analysed in detail in order to confirm early predictions of failure rates, as well as to study the effectiveness of implemented mitigation measures. Figure 10-13 shows the actual number of Single-Event-Effects (SEE) failures measured during 2011 and 2012 operation, the achieved improvement (please note that the failure rate measured during 2011 already benefitted from mitigation measures implemented during 2009 and 2010), as well as the goal for operation after LS1 and during HL-LHC.

Aiming for annual luminosities of up to 300 fb^{-1}, it is clear that machine availability has to be maximized during the HL-LHC period in order to successfully achieve the physics goal. This implies that existing electronic control systems are either installed in fully safe areas, sufficiently protected by shielding or adequately radiation tolerant.

The last statement implies that existing equipment, as well as any future equipment to be possibly installed in R2E critical areas, must be conceived in a specific way.

Radiation damage to electronics is often considered in space applications. However, it is important to note that the radiation environment encountered at the LHC, the high number of electronic systems and components partly exposed to radiation, as well as the actual impact of radiation induced failures strongly differ from the context of space applications. While for the latter application design, test and monitoring standards are already well defined, additional constraints, but in some cases also simplifications, have to be considered for accelerator environment.

The mixed particle type and energy field encountered in the relevant LHC areas is composed of charged and neutral hadrons (protons, pions, kaons and neutrons), photons, electrons and muons ranging from thermal energies up to the GeV range. This complex field has been extensively simulated by the FLUKA Monte Carlo code and benchmarked in detail for radiation damage issues at the LHC [17,18]. As previously discussed in this chapter, the observed radiation is due to particles generated by proton-proton (or ion-ion) collisions in the LHC experimental areas, distributed beam losses (protons, ions) around the machine, and to beam interacting with the residual gas inside the beam pipe. The proportion of the different particle species in the field depends on the distance and on the angle with respect to the original loss point, as well as on the amount (if any) of installed shielding material. In this environment, electronic components and systems exposed to a mixed radiation field will experience three different types of radiation damages: displacement damage, damage from the Total Ionising Dose (TID) and so-

called Single-Event-Effects (SEEs). The latter ones range from single or multiple bit upsets (SEUs or MBUs), transients (SETs) up to possible destructive latch-ups (SELs), destructive gate ruptures or burn-outs (SEGRs and SEBs).
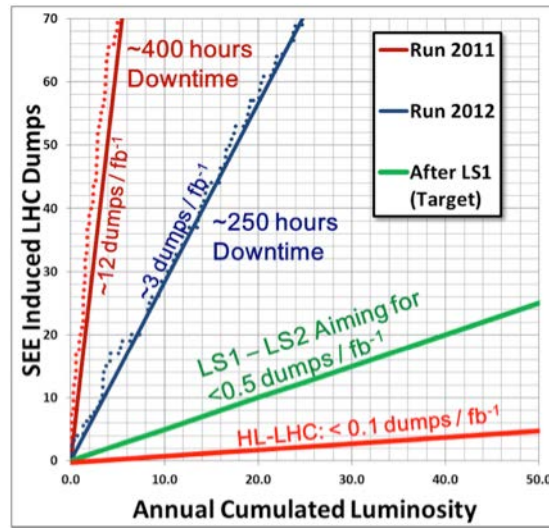
Figure 10-13: LHC beam dumps due to single-event effects against beam luminosity. Dots (2011 and 2012) refer to measurements, whereas lines show annual averages for both, past and future operation.

The first two groups are of cumulative nature and are measured through TID and non-ionizing energy deposition (NIEL[11], generally quantified through accumulated 1-MeV neutron equivalent fluence), where the steady accumulation of defects cause measurable effects which can ultimately lead to device failure. As for stochastic SEE failures, they form an entirely different group, since they are due to the direct ionization by a single particle, able to deposit sufficient energy through ionization processes in order to perturb the operation of the device. They can only be characterized in terms of their probability of occurring as a function of accumulated High Energy ($> 5 \div 20$ MeV) Hadron (HEH) fluence. The probability of failure will strongly depend on the device as well as on the flux and nature of the particles. In the context of HL-LHC, several tunnel areas close to the LHC tunnel, and partly not sufficiently shielded, are or are supposed to be equipped with commercial or not specifically designed electronics which are mostly affected by the risk of SEEs, whereas electronics installed in the LHC tunnel will also suffer from accumulated damage in the long-term [19].

Three distinct areas are to be distinguished:

- The accelerator between the inner triplet and Q6: in this area no active electronics is installed and any future installation should clearly be avoided as radiation levels clearly exceed the usability domain of commercial components and also pose significant constraints to custom designs, including Application Specific Integrated Circuits (ASICs).

- The adjacent (shielded) areas: where the shielding has been maximized before and during LS1 and where radiation levels become acceptable for characterized and qualified custom electronics. The equipment and selected electronic components have to be qualified for both SEEs and TID. For the first, it is important that radiation tests are carried out in a representative radiation environment, or adequate safety margins have to be added. Fully commercial systems (COTS based) are still to be avoided in these areas. In case they are required, their failure impact and respective mitigation has to be studied in the context of accelerator operation.

---

[11] Non-Ionizing Energy Losses.

- The dispersion suppressor area: given the fact that the magnets have to be protected against quenches, it is likely that the leakage into this area must not increase significantly with respect to nominal LHC operation. A detailed quantification is however needed in order to coherently design the required control electronics, again both for SEE effects as well for their lifetime (TID) in order to comply with the stringent availability requirement as shown in Figure 10-13.

During the first years of LHC operation, the radiation levels in the LHC tunnel and in the (partly) shielded areas have been measured by using the CERN RadMon system [20] dedicated to the analysis of radiation levels possibly impacting installed electronic equipment. Table 10-1 summarizes the level of accumulated HEH fluence measured during 2012 for the most critical LHC areas where electronic equipment is installed and which are relevant for the HL-LHC project, together with the expected annual radiation levels for nominal LHC performance (50 fb^{-1}/y). The HEH fluence measurements are based on the RadMon reading of the Single Event Upsets (SEU) of SRAM memories whose sensitivity was extensively calibrated in various facilities [21]. The results obtained during 2012 LHC proton operation show that the measurements compare very well with previously performed FLUKA calculations and observed differences can actually be attributed to changes of operational parameters not considered in the calculations [22]. In a first approximation, the measured radiation levels can also be used to extrapolate towards HL-LHC by purely scaling with annual luminosity (see last two columns of Table 10-1), however keeping in mind that operational and layout parameters (beam energy, crossing angle, TAN design, absorbers, etc.) can have a non-negligible impact on the final values, especially for the RRs close to the Matching Section. The resulting values clearly indicate that any equipment installed in the LHC tunnel will not only suffer SEE failures, but will also be heavily impacted by the TID effects thus limiting the respective equipment lifetime.

Table 10-1: **Predicted and measured annual HEH fluence in critical shielded areas for a cumulated ATLAS/CMS luminosity of 15 fb^{-1} during 2012 operation, then extrapolated based on the measurement to the expected nominal and HL-LHC performance (50 fb^{-1}/y for nominal and 300 fb^{-1}/y for HL-LHC performance, except for P8 where 2012 can already be considered as almost nominal and HL-LHC refers to a 5-fold increase). For HL-LHC an estimate for corresponding annual TID levels is also given.**

LHC area	Prediction (HEH/cm^2)	Measured (HEH/cm^2)	Nominal (HEH/cm^2)	HL-LHC (HEH/cm^2)	HL-LHC (Dose/Gy)
UJ14/16	1.4×10^8	1.6×10^8	5×10^8	3×10^9	6
RR13/17	2.0×10^8	2.5×10^8	8×10^8	5×10^9	10
UJ56	1.6×10^8	1.5×10^8	5×10^8	3×10^9	6
RR53/57	2.0×10^8	2.5×10^8	8×10^8	5×10^9	10
UJ76	2.1×10^7	6.0×10^7	2×10^8	1×10^9	2
RR73/77	2.9×10^7	5.0×10^7	2×10^8	1×10^9	2
UX85B	4.3×10^8	3.5×10^8	4×10^8	2×10^9	4
US85	1.3×10^8	8.8×10^7	9×10^7	4×10^8	1

A first calculation aimed to assess the radiation levels in the UJ/UL/UP areas close the new IT during the HL-LHC operation, was carried out, implementing the dedicated shielding presently in place. Figure 10-14 shows the expected annual HEH fluence, which confirms the order of magnitude of the respective extrapolation reported on the first row of Table 10-1.

Concerning the radiation in the RR area adjacent to the Matching Section, HL-LHC simulations are at this stage still premature due to the optics and layout unknowns. Nevertheless, specific studies were performed for the present LHC, evaluating the contribution of the relevant source terms, which in this

case include both the collision debris and the beam interactions with the residual gas, as shown in Figure 10-15. A significant effect in increasing the fluence levels – to be re-evaluated for the HL-LHC machine – is played here by the TCL6 collimator, due to its position.
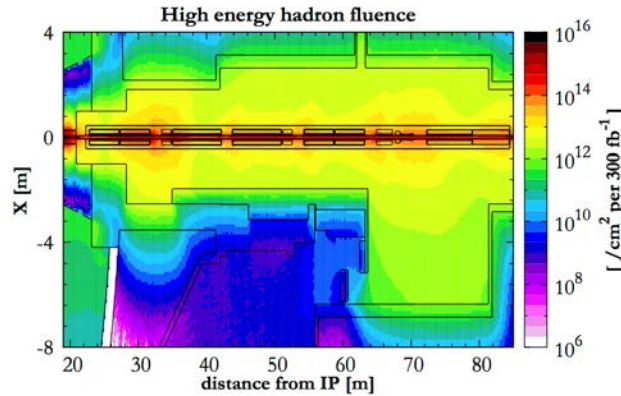
Figure 10-14: Annual HEH fluence expected in the IT region and in the adjacent UJ/UL/UP areas at Point 1 during the HL-LHC era (normalized to 300 fb^{-1}).
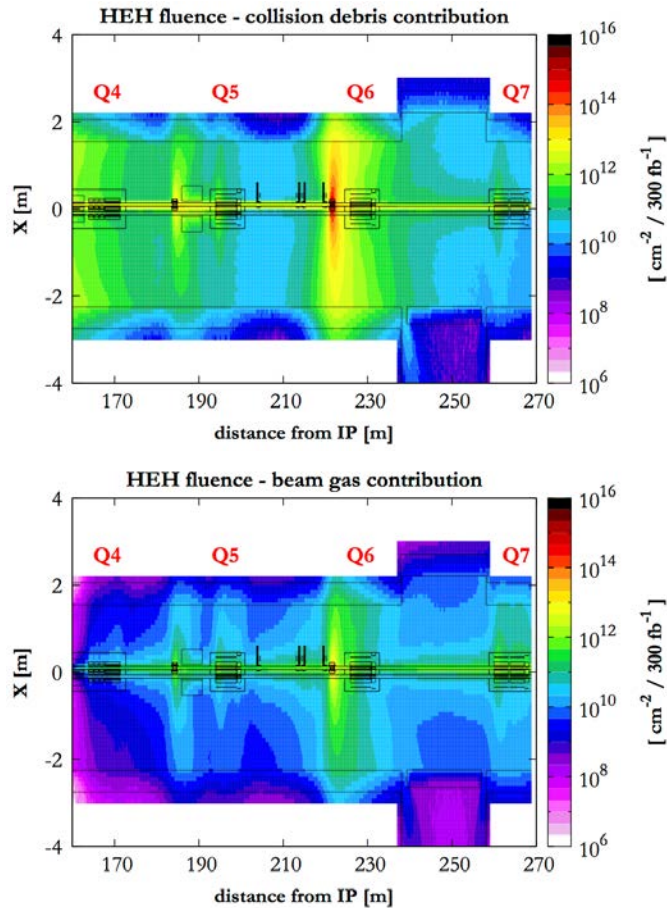
Figure 10-15: Cumulated HEH fluence expected in the Matching Section region and in the adjacent RR area at Point 5 for the operation of the present LHC at 7 TeV beam energy. Top: contribution from the collision debris normalized to 300 fb^{-1}. Bottom: contribution from interactions of the outgoing beam (Beam 1) with the residual gas, normalized to nominal current over $3 \cdot 10^7$ s (i.e. the time needed to accumulate 300 fb^{-1} at nominal luminosity) and to a gas density

of 10^{15} H$_2$-equivalent molecules/m^3. TCL collimator settings: 15 σ (TCL4), 35 σ (TCL5), 10 σ (TCL6).

Any control equipment (commercial or based on commercial components) to be installed in these areas, clearly has to be proven to be sufficiently radiation tolerant. For comparison, as mentioned earlier, during the last years of operation we already observed a number of radiation induced failures on commercial equipment for radiation levels corresponding to $10^8 \div 10^9$ cm^{-2}/y (which is about 1000 ÷ 10000 more than what one would get at surface due to cosmic radiation).

The analysis of the performed radiation tests, as well as the experience acquired during LHC Run-1 operation allowed the deduction of an acceptable limit of 10^7 cm^{-2} y^{-1} annual radiation level, leading to the definition of so-called protected areas (in terms of overall risk of radiation induced failures). Therefore, for HL-LHC any installation of non-tested (and not specifically designed) electronic equipment in the UJs, part of the ULs and RRs is clearly to be avoided or subject to a detailed analysis process before an exceptional installation can be granted under the following conditions:

- the equipment is not linked to any safety system,

- the failure of the equipment will not lead to a beam dump,

- the failure of the equipment does not require quick access (thus lead to downtime),

- there is no any other operational impact (loss of important data, etc.).

In all other cases requiring installation in critical areas, a respective radiation tolerant electronics development must be considered from the very early stage onward. Related expertise exists at CERN within the equipment groups, the R2E project and a dedicated working group [23].

In a first approximation and limiting the total number of exposed systems, the above mentioned annual radiation design level of 10^7 cm^{-2} y^{-1} can also be chosen as acceptable aiming to achieve an overall performance of less than one radiation induced failure per one or two weeks of HL-LHC operation.

For operation critical equipment, the HL-LHC project foresees respective radiation tolerant developments already at an early stage of the design phase, taking into account that:

- for the LHC-tunnel: in addition to SEEs also cumulative damage has to be considered for both existing and future equipment,

- for partly shielded areas (UJs, RRs, ULs): cumulative damage should be carefully analyzed but can most likely be mitigated by preventive maintenance (detailed monitoring mandatory), however radiation tolerant design is mandatory in order to limit SEE induced failures,

- the knowledge of radiation induced failures and radiation tolerant development within the equipment groups and in the overall accelerator and technology sector has to be maintained and further strengthened,

- the access and availability of radiation test facilities (both inside CERN and outside) has to be ensured, providing efficient support to equipment groups,

- building on the experience obtained during the LHC R2E project and in view of the HL-LHC time-scale, it is important that the expertise of and support to radiation tolerant developments (currently available through the Radiation Working Group [23]) is maintained and ensured from the early project stage onwards.

10.7 References

[1] L.S. Esposito et al., Power load from collision debris on the LHC Point 8 insertion magnets implied by the LHCb luminosity increase, IPAC2013, TUPFI022, p. 1382.

[2] N.V. Mokhov, I. L. Rakhno, Mitigating radiation loads in Nb3Sn quadrupoles for the CERN Large Hadron Collider upgrades, Phys. Rev. ST Accel. Beams **9**, 101001 (2006).

[3] L.S. Esposito, F. Cerutti, E. Todesco, IPAC2013, TUPFI021, p. 1379.

[4] G. Battistoni et al., The FLUKA code: Description and benchmarking, in AIP Conf.Proc. 896 (2007) 31-49.

[5] A. Ferrari et al., FLUKA: A multi-particle transport code (Program version 2005), CERN-2005-010; http://www.fluka.org

[6] V. Vlachoudis, FLAIR: A Powerful But User Friendly Graphical Interface For FLUKA, Proc. Int. Conf. on Mathematics, Computational Methods & Reactor Physics, Saratoga Springs, New York, (2009).

[7] A. Mereghetti et al., The FLUKA LineBuilder and Element DataBase: Tools for Building Complex Models of Accelerator Beam Lines, IPAC2012, WEPPD071, p. 2687.

[8] N.V. Mokhov, C. James, The MARS Code System User's Guide, http://www-ap.fnal.gov/MARS

[9] N.V. Mokhov, S.I. Striganov, MARS15 Overview, in Proc. of Hadronic Shower Simulation Workshop, Fermilab, AIP Conf. Proc. **896** (2007) pp. 50-60.

[10] N.V. Mokhov et al., Progress in Nuclear Science and Technology, vol. **4** (2014) pp. 496-501.

[11] N.V. Mokhov et al., Protecting LHC IP1/IP5 Components Against Radiation Resulting from Colliding Beam Interactions, CERN-LHC-Project-Report-633.

[12] L.S. Esposito, F. Cerutti, FLUKA simulations of collision debris with TCL6, presentation at LHC Collimation Working Group #163, http://indico.cern.ch/event/267815/contribution/1/material/slides/0.pdf

[13] A. Ballarino, Development of Superconducting Links for the LHC Machine, EEE/CSC & ESAS SUPERCONDUCTIVITY NEWS FORUM (global edition), October 2013.

[14] A. Ballarino, Preliminary report on cooling options for the cold powering system, June 2013, http://cds.cern.ch/record/1557215/files/CERN-ACC-2013-010.pdf

[15] R2E website, www.cern.ch/r2e

[16] M. Brugger et al., R2E Experience and Outlook for 2012, Proceedings of LHC Performance workshop, Chamonix 2012.

[17] K. Roed et al., FLUKA simulations for SEE studies of critical LHC underground areas, Nuclear Science, IEEE Transactions on, vol. 58, no. 3, p. 932, (2011).

[18] M. Brugger et al., FLUKA capabilities and CERN applications for the study of radiation damage to electronics at high-energy hadron accelerators, Progress in Nuclear Science and Technology, PNST10184-R1 (2010).

[19] K. Roed, M. Brugger, G. Spiezia, An overview of the radiation environment at the LHC in light of R2E irradiation test activities, CERN publication, CERN-ATS-Note-2011-077 TECH, (2011).

[20] G. Spiezia et al., The LHC accelerator Radiation Monitoring System - RadMON, in Proceedings of Science, 2011.

[21] D. Kramer et al., LHC RadMon SRAM Detectors Used at Different Voltages to Determine the Thermal Neutron to High Energy Hadron Fluence Ratio, IEEE Trans. Nucl. Sci., vol. 58, no. 3, p. 1117, 2011.

[22] G. Spiezia et al., R2E Experience and Outlook, LHC Beam Operation Workshop, Evian, (2012).

[23] CERN Radiation Working Group (RadWG), www.cern.ch/radwg

Chapter 11

11T Dipole for the Dispersion suppressor Collimators

M. Karppinen[1], S. Izquierdo Bermudez[1], A. Nobrega[2], H. Prin[1], D. Ramos[1], S. Redaelli[1], F. Savary[1], D. Smekens[1] and A. Zlobin[2]
1 CERN, Accelerator & Technology Sector, CH-1211, Geneva, Switzerland
2 FNAL, Fermi National Accelerator Laboratory, Batavia, P.O. Box 500, IL, USA

11   11T Dipole for the Dispersion suppressor Collimators

11.1   Introduction

A pair of 11T dipoles will replace some of the main dipoles (MB) in the dispersion suppressor (DS) regions of LHC to create space for additional collimators, which are necessary to cope with beam intensities that are larger than nominal, such as in the High Luminosity LHC (HL LHC) Project [1].

A joint research and development (R&D) programme was initiated in October 2010 at Fermi National Laboratory (FNAL) in the United States and in the middle of 2011 at CERN with the goal of developing the necessary technology for the fabrication of a full-length two-in-one aperture Nb_3Sn dipole prototype suitable for installation in the LHC [2]. After the design, fabrication and test of a number of short models of 1 and 2 m lengths, FNAL is now slowing down, when CERN is gradually ramping up with the fabrication of 2-m long models and the preparation of the tooling for full-length prototypes. The design of the 11T dipole described in this preliminary design report features the solutions developed in the framework of the CERN programme. Except for the pole loading concept, for the cable insulation scheme and for features specific to full-length magnets, the solutions used at CERN are vastly based on the results of the R&D programme conducted at FNAL.

11.2   The cryo-assembly

11.2.1 Description

An MB cryoassembly will be replaced by a string of three independently installed and aligned cryoassemblies: two of them housing each a 6.252 m long 11T dipole, hereinafter referred to as the MBH, plus a by-pass cryostat installed in-between. The by-pass cryostat ensures the continuity of the cryogenic and electrical circuits and comprises cold to warm transitions on the beam lines in order to create a room temperature vacuum sector for the collimator.

Figure 11-1 shows a schematic layout of the string of cryostats composing the 11T cryo-assembly, which will replace an MB cryostat.
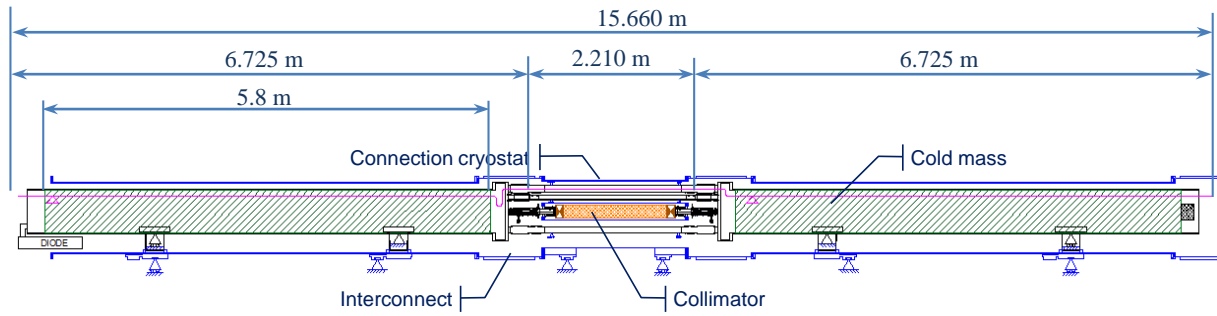
Figure 11-1: Longitudinal section of the 11T cryo-assembly showing also the collimator and the cold-warm transitions

The cryostat for the MBH shall follow the same design and fabrication principles as the other arc cryostats; it shall comply with the static heat loads specified by the Heat Load Working Group [3]. Standard LHC cryostat performance in terms of alignment tolerances and geometrical stability shall be ensured.

The design of the by-pass cryostat shall be compatible with the integration of the collimator and also RF-shielded gate valves at the extremity of the cold to warm transitions. All cryogenic lines and powering bus bars shall have their continuity ensured across the by-pass cryostat.

In the present concept, independent installation and alignment of the three cryostats is foreseen. In addition, the TCLD collimator shall be supported directly to the tunnel floor in order to not be affected by deformations of the cryostat vacuum vessels due to alignment or pressure induced forces.

11.2.2 Equipment parameters

The main parameters of the 11T cryo-assembly are given in Table 11-1. The lengths are, for the moment, provisional and may vary depending on the detail design of the MBH and on the collimator integration details. The dimensions of the cryogenic pipes are equivalent to those of a standard LHC arc continuous cryostat.

Table 11-1: **Main parameters of the 11T cryo-assembly**

Characteristics	Unit	Value
Total length including interconnects	mm	15660
Upstream cryostat length between interconnect planes	mm	6725
Downstream cryostat length between interconnect planes	mm	6725
By-pass cryostat length between interconnect planes	mm	2210
Beam line cold bore diameter (inner)	mm	50
Length of room temperature beam vacuum sector measured between cold to warm transition flanges	mm	1550

The preliminary design of the 11T cryo-assembly is based on the following assumptions:

- The interface between the cold beam lines of the MBH cryostats and the beam vacuum sector of the collimator requires sectorization by RF-shielded gate valves;

- As opposed to other collimators in the machine, residual radiation to personnel is assumed to be compatible with the removal and installation of the TCLD collimator without remote handling equipment. Given the integration constraints in the LHC dispersion suppressors, the design of a collimator compatible with remote handling is most likely not achievable;

- Radiation doses on the cryostat throughout the HL-LHC lifetime are compatible with the usage of LHC standard cryostat materials;

- Magnetic shielding is not required on the by-pass cryostat. It is assumed that the magnetic field created by the bus bar currents will not be detrimental to the accuracy of the TCLD instrumentation and controls.

11.3 The 11T Dipole

The design of the MBH is based on the two-in-one concept, i.e. the cold mass comprises two apertures in a common yoke and shell assembly. The MBH cold mass assembly has a length of 6.252 m between the datum planes "C" and "L" that are materialized on the end covers, see Figure 11-2. The coils have a length of 5.415 m without the outermost end spacers called saddles, and 5.573 mm with the saddles, see Figure 11-3. A pair of MBHs is needed to produce an integrated field of 119 Tm at 11.85 kA, which corresponds to the bending strength of the MB. The MBHs need to be compatible with the LHC lattice and its main systems. They will be connected in series with the MBs.
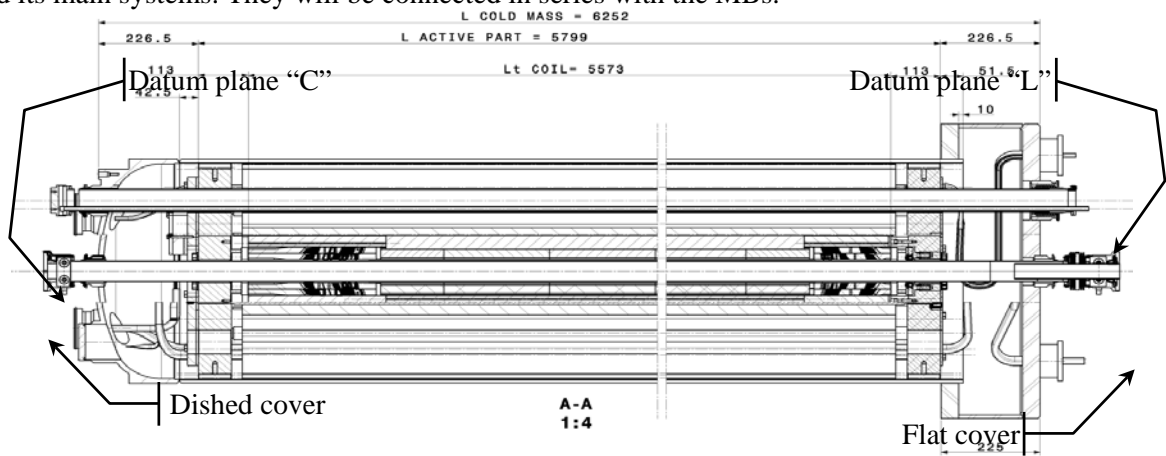
Figure 11-2: Longitudinal section of the cold mass assembly of the MBH
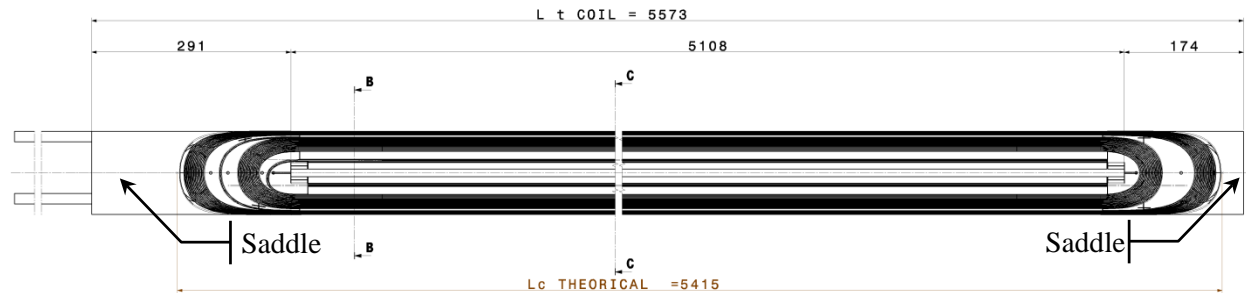
Figure 11-3: Longitudinal section of the coil

11.3.1 Description

The coils of the MBH are made of 2 layers and 6 blocks with Nb_3Sn keystoned Rutherford type cable as shown in Figure 11-4 . Each coil comprises 56 turns, of which 22 in the inner layer and 34 in the outer layer. There is no splice at the layer jump, i.e. the 2 layers are wound from the same cable unit length. The cable is made of 40 strands of 0.7 mm diameter. Two manufacturing routes are considered for the strand: the restacked rod process (RRP) and the powder-in-tube process (PIT).

The mechanical structure comprises separate austenitic steel collars for each aperture to balance the electromagnetic forces, and a vertically split iron yoke surrounded by a welded stainless steel shrinking cylinder, which contributes to the overall rigidity of the assembly. The axial component of the electromagnetic forces is also transferred to the shrinking cylinder via thick end plates, which are welded

to it, and bolts in contact with the saddles. The bolts are screwed in the end plates. The cold mass envelope is closed in the ends by a dished cover on the side of the assembly facing the existing MBs and by a flat cover of larger diameter on the side of the assembly facing the collimator, see Figure 11-1. A larger diameter is needed on that side to allow the routing of the bus bars across the by-pass cryostat within the limits of the radial and longitudinal space available.

The cross-section of the MBH is shown in Figure 11-4, without the bus bars, heat exchanger tube, support pads, and line N. The key parts of the collared coil are also shown in Figure 11-4.
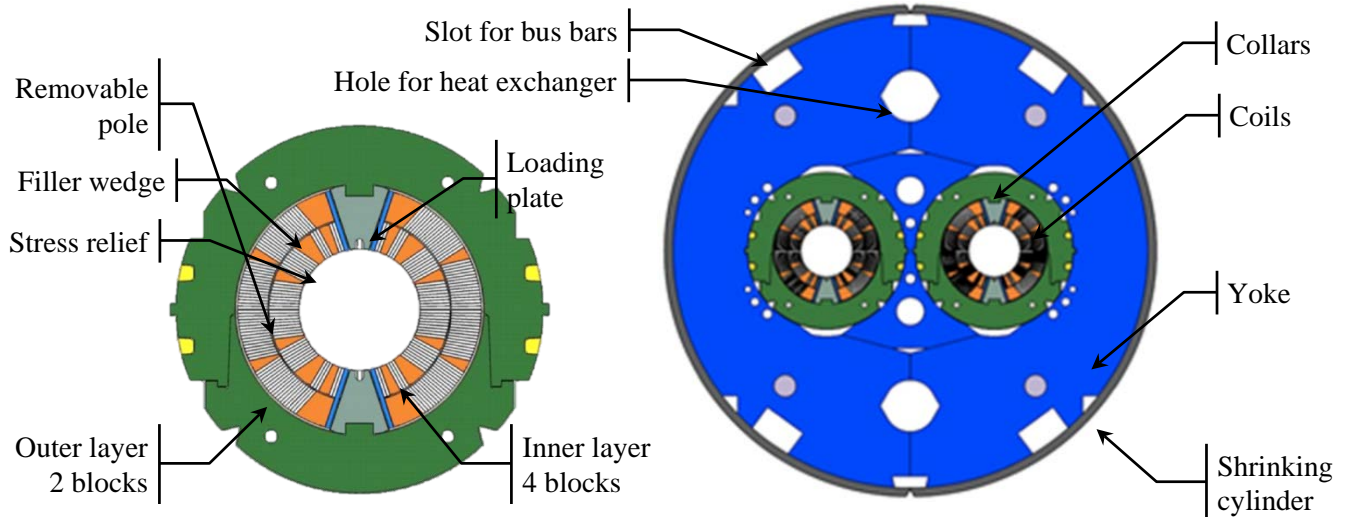
Figure 11-4: Cross-section of the 11T dipole collared coil (left) and cold mass assembly (right)

To avoid deformation of the beam closed orbit, the integrated transfer function of a pair of MBHs shall be identical to that of the MB. However, this is not possible in the entire range of current during ramping up to nominal, as shown in Figure 11-5. The design is such that a pair of MBHs provides the same integrated field of 119 Tm as a standard MB at the nominal current of 11.85 kA.
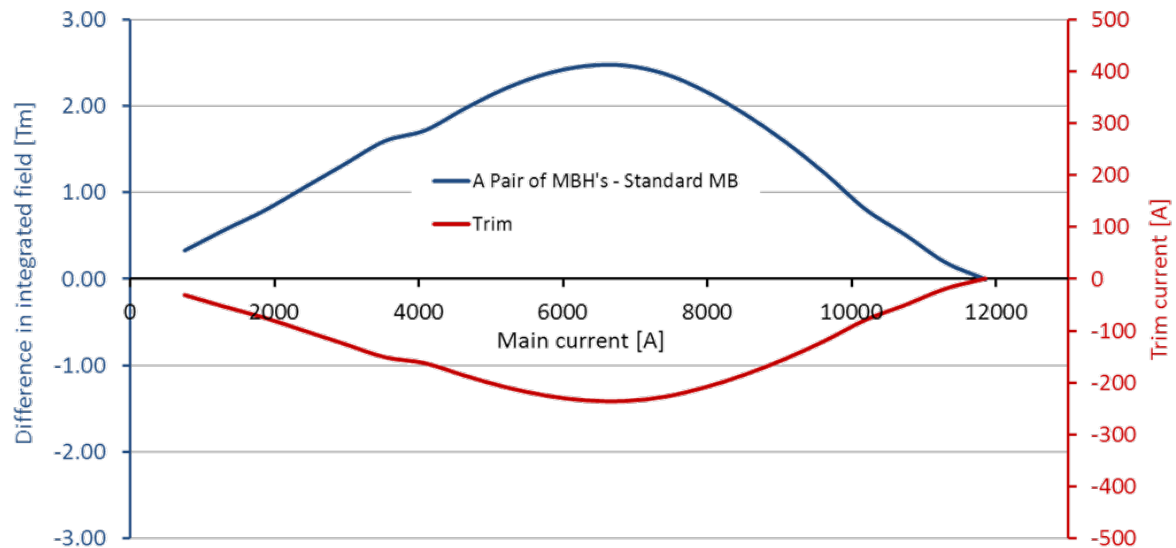
Figure 11-5: The blue line shows the difference in integrated field between a pair of MBHs and an MB, both delivering 119 Tm at 11.85 kA. The red line shows the trim current needed to correct the difference at currents below 11.85 kA

The MBH is stronger at lower currents (it has more turns) with a peak difference in integrated field around 6.5 kA. This can be mitigated by adding a dedicated trim power converter. In absence of

trim current, the resulting orbit distortion could be mitigated by means of the standard orbit correctors in the LHC lattice. However, a fully validated solution is not available at the moment, including machine protection, reliability, and availability (for example, the operation of LHC would be compromised in case of failure of an orbit corrector). The correction of the transfer function with a trim current is the preferred option as it would allow simpler and more transparent operation.

Unlike the MB, which is curved in the horizontal plane, the MBH will be straight because of the brittleness of Nb_3Sn after reaction. Also, it will be equipped with the same cold bore tube and beam screen as the present curved MB to facilitate integration. To mitigate the corresponding reduction of mechanical aperture, the two MBHs of a cryo-assembly will be assembled with an angle of 2.55 mrad relative to each other, and shifted by 0.8 mm towards the centre of the machine.

Depending on the location, the MB to be replaced may be of type A or type B, i.e. it will have, respectively, both magnet corrector sextupole (MCS) on the lyre side (i.e. downstream) and nested magnet corrector decapole/octupole (MCDO) on the connection side (i.e. upstream), or only MCS on the lyre side. The MBH, which is on the right side of the collimator for an observer looking at the machine from its centre, will have only the MCS on the lyre side. In the current stage of the project, it is also planned to install the MCDO on the connection side of the MBH that is installed on the left side of the collimator. The MCDO may be connected, or not, depending on the installation location of the cryo-assembly.

11.3.2 Equipment parameters

A pair of MBHs will provide an integrated field of 119 Tm at the nominal operation current of the MBs, 11.85 kA. This corresponds to a nominal magnetic flux density of 11.23 T at the centre of the bore. This goal shall be obtained with a margin of ~20% on the magnet load line [4].

The geometric field quality will be optimized to keep the low-order field errors below 1 unit. The different contributions to the field errors are given in Table 1. These include the contributions of the coil ends, cryostat, persistent currents and eddy currents effects. The field errors shall be confirmed by magnetic measurements. The main parameters of the MBH are listed in Table 11-3.

Table 11-2: **Field errors - Rref = 17 mm**

Normal	Systematic					Uncertainty		Random	
	Geometric	**Saturation**	**Persistent**	**Injection**	**High field**	**Injection**	**High field**	**Injection**	**High field**
2	0.000	-12.200	1.010	1.010	-12.200	1.930	1.930	1.9300	1.930
3	7.459	-0.279	-1.299	6.160	7.180	1.240	1.240	1.2400	1.240
4	0.000	-0.400	0.070	0.070	-0.400	0.600	0.600	0.6000	0.600
5	-0.014	0.514	6.594	6.580	0.500	0.310	0.310	0.3100	0.310
6	0.000	-0.020	0.000	0.000	-0.020	0.180	0.180	0.1800	0.180
7	-0.093	0.062	-0.688	-0.780	-0.030	0.110	0.110	0.1100	0.110
8	0.000	0.000	0.000	0.000	0.000	0.060	0.060	0.0600	0.060
9	0.912	0.028	1.024	1.936	0.940	0.030	0.030	0.0300	0.030
10	0.000	0.000	0.000	0.000	0.000	0.010	0.010	0.0100	0.010
11	0.450	0.000	-0.090	0.360	0.450	0.010	0.010	0.0100	0.010
12	0.000	0.000	0.000	0.000	0.000	0.000	0.000	0.000	0.000
13	-0.115	-0.006	-0.028	-0.143	-0.121	0.000	0.000	0.000	0.000
14	0.000	0.000	0.000	0.000	0.000	0.000	0.000	0.000	0.000
15	-0.032	-0.002	-0.008	-0.040	-0.034	0.000	0.000	0.000	0.000
Skew	**Geometric**	**Saturation**	**Persistent**	**Injection**	**High field**	**Injection**	**High field**	**Injection**	**High field**
2	0.000	-0.261	0.000	0.000	-0.261	1.660	1.660	1.660	1.660
3	-0.130	0.050	0.000	-0.130	-0.080	1.000	1.000	1.000	1.000
4	0.000	-0.010	0.000	0.000	-0.010	0.640	0.640	0.640	0.640
5	0.080	0.000	0.000	0.080	0.080	0.380	0.380	0.380	0.380
6	0.000	0.000	0.000	0.000	0.000	0.200	0.200	0.200	0.200
7	0.030	0.000	0.000	0.030	0.030	0.090	0.090	0.090	0.090
8	0.000	0.000	0.000	0.000	0.000	0.050	0.050	0.050	0.050
9	0.000	0.000	0.000	0.000	0.000	0.030	0.030	0.030	0.030
10	0.000	0.000	0.000	0.000	0.000	0.020	0.020	0.020	0.020
11	0.000	0.000	0.000	0.000	0.000	0.010	0.010	0.010	0.010
12	0.000	0.000	0.000	0.000	0.000	0.000	0.000	0.000	0.000
13	0.000	0.000	0.000	0.000	0.000	0.000	0.000	0.000	0.000
14	0.000	0.000	0.000	0.000	0.000	0.000	0.000	0.000	0.000
15	0.000	0.000	0.000	0.000	0.000	0.000	0.000	0.000	0.000

Table 11-3: **Main parameters of the MBH**

Characteristics	Unit	Value
Aperture	mm	60
Number of apertures	-	2
Distance between apertures @ RT/1.9 K	mm	194.52/194.00
Cold mass outer diameter	mm	580
Magnetic length	m	5.307
Coil physical length, as per magnetic design	m	5.415
Magnet physical length: active part (in between the end plates)	m	5.799
Magnet physical length: cold mass (in between the datum planes "C" and "L")	m	6.252
Cold mass weight	tonne	~ 8
Nominal operation current	kA	11.85
Bore field @ nominal current	T	11.23
Peak field @ nominal current (without strand self-field correction)	T	11.59
Operating temperature	K	1.9
Load line margin	(%)	19
Stored energy per meter @ Inom.	MJ/m	0.9663
Differential inductance per meter @ Inom.	mH/m	11.97
Number of layers	-	2
Number of turns (inner/outer layer)	-	56 (22/34)
Superconductor	-	Nb_3Sn
Cable bare width before reaction	mm	14.7
Cable bare mid-thickness before reaction	mm	1.25
Keystone angle	degree	0.79
Cable unit length for the two layers (no layer jump splice)	m	~ 600
Strand diameter	mm	0.700 ± 0.003
Number of strands per cable	-	40
Cu to Non-Cu ratio	-	1.15 ± 0.10
RRR, after reaction	-	>100
Minimum strand critical current, I_c, without self-field correction (12 T, 4.222 K)	A	438
Minimum strand current density, J_c, at 12 T, 4.222 K	A/mm^2	2560
Cable insulation thickness per side azimuthal, before/after reaction	mm	0.155/0.110
Heat exchanger hole diameter	mm	60
Heat exchanger distance from centre (same position as in the MB)	mm	180
Cold Bore Tube inner diameter/thickness (assuming the current CBT is used)	mm	50/1.5
Gap CBT to coil (assuming the current CBT and ground insulation are used)	mm	3

11.3.3 Protection

The MBH will be protected with quench heaters and a by-pass diode operating at cold, integrated to the cold mass assembly. In the current stage of the development, it is foreseen to use one by-pass diode for the two MBHs of a cryo-assembly. However, this needs to be validated.

11.3.4 Radiation

The MBH will, inevitably, see a shower of particles from the collimator. The worst case being at the moment with ion operation at IP2 for which the peak dose in the coils is estimated around 1 MGy [5]. The 11 T dipole cold mass will be designed with reasonable margin, for 5 MGy.

11.3.5 Installation and dismantling

The cold mass of the MBH will be equipped with standard features in the ends facing the existing MBs in the tunnel to facilitate the installation and connection, e.g. M-flanges and bellows, preparation of the bus bar extremities in view of the splicing, end flanges on the X/V lines, … The ends facing the collimator need to be specific; however, standard elements will be used as much as possible.

11.4 Inventory of units to be installed and spare policy

Two full-length MBH prototypes will be fabricated to validate the design, the overall performance in nominal operation conditions (to be checked on horizontal test benches in building SM18 at CERN), and the different interfaces with the neighbour systems.

The cryo-assemblies to be installed in LHC are listed here after.

For LS2, around IP2, 2 cryo-assemblies to replace 2 main dipoles MB.A10L2 and MB.A10R2, i.e. 4 MBH's and 2 by-pass cryostats.

For LS3, around IP7, 4 cryo-assemblies to replace 4 main dipoles MB.B8L7, MB.B10L7, MB.B8R7, and MB.B10R7, i.e. 8 MBH's and 4 by-pass cryostats.

For LS3, to be confirmed, around IP1 and IP5, up to a maximum of 8 cryo-assemblies to replace 8 main dipoles, location to be defined.

It is planned to fabricate at least two spare MBHs and one spare by-pass cryostat. The prototypes may be used as spares, should they conform fully to the functional requirements.

11.5 References

[1] L. Rossi, "LHC Upgrade Plans: Options and Strategy", IPAC2011

[2] F. Savary et al., "Status of the 11 T Nb$_3$Sn Dipole Project for the LHC"

[3] Heat Load Working Group, http://lhc-mgt-hlwg.web.cern.ch/lhc-mgt-hlwg/default.htm

[4] M. Karppinen et al., "Design of 11 T Twin-Aperture Nb$_3$Sn Dipole Demonstrator Magnet for LHC Upgrades", CERN-ATS-2013-025

[5] Private communication A. Lechner 28 Aug. 2014, and G. Steel et al., "Limits on collimator settings and reach in β*", LHC Collimation Review 2013

Chapter 12

Vacuum System

V. Baglin[5], P. Chiggiato[5], P. Cruikshank[5], M. Gallilee[5], Garion[5], R. Kersevan,
[5]CERN, Accelerator & Technology Sector, CH-1211, Geneva, Switzerland

12   Vacuum system

12.1   Overview

The luminosity upgrade program (HL-LHC) requires modifications of the present LHC's vacuum system, in particular in the triplets and experimental areas. Such modifications must follow guidelines, similar to those followed for the present machine. The increased stored current implies a higher thermal power in the beam screen from the image current moving along with the stored particles and stronger synchrotron radiation (SR) and electron cloud (EC) effects, which in turn translate into higher degassing rates.

One of the main tasks of the Vacuum HL-LHC work package is to define the geometry of the vacuum equipment in the new superconducting (SC) triplet and D1 magnets. It is also necessary to define a strategy for assembling and inserting high-density shielding material into the SC IR magnets. This is mandatory for protecting the magnets from collision debris coming from the experiments' interaction points (IPs). A balance between cold bore size and vacuum pumping system will be defined based on experience gained with the present machine, and recent advances on new materials. A number of new ideas have emerged recently - for example the amorphous carbon coating whose validation is ongoing.

The change of the aperture of the triplets at IR1 and IR5 implies that the experimental vacuum chambers of CMS and ATLAS will require a review of aperture, impedance, and vacuum (dynamic and static) values. From preliminary analyses, the forward regions of CMS and ATLAS will need to be adapted to cope with the new beam geometry in IR1 and IR5. New materials will likely be needed to mitigate the additional activation from the increased luminosity. New access procedures will be needed to allow the minimization of the integrated dose to personnel. With the HL-LHC, less flexibility will be available for the optics of LHCb and ALICE; therefore, the vacuum chambers at IR2 and IR8 must be validated for ultimate running conditions to ensure that these chambers do not impose a limitation. Positions of mechanical supports, pumps, and gauges must be analyzed to ensure that layouts are optimized for the new machine configuration. Bake-out equipment will be redefined depending on activation and specific needs. All experimental chambers must be treated (NEG coated or equivalent) to minimize secondary electron yield (SEY), thus reducing electron cloud effects.

12.2   Beam vacuum requirements

The HL-LHC beam vacuum system must be designed to ensure the required performance when beams with HL-LHC nominal parameters circulate. The system must be designed for HL-LHC ultimate parameters, without margin.

The vacuum system must be designed to avoid pressure runaway induced by ion stimulated desorption. It must also be designed to take into account the effects of synchrotron radiation, electron cloud and ion stimulated desorption from the walls. Heat load onto the beam vacuum chamber walls or flanges and beam impedance effects must also be taken into account [1].

The system must be compatible with the global LHC impedance budget and the machine aperture.

The average gas density along the IR must satisfy the level defined by the 100 h vacuum life time due to nuclear scattering, i.e. less than $1.2 \cdot 10^{15}$ H_2 molecules m^{-3} in the LHC [2]. This limit decreases proportionally to the inverse of the beam current. Table 12-1 gives the molecular gas densities yielding a 100 h vacuum lifetime in LHC and HL-LHC assuming the presence of a single gas in the vacuum system. The average gas density along the IR 1, 2, 5 and 8 must also ensure that the background to the LHC experiments is minimum [3, 4]. In absence of specified values from the LHC experiments themselves, the LHC design value will be scaled to HL-LHC parameters.

Table 12-1: **Single gas species molecular gas density (m^{-3}) to satisfy 100 h vacuum lifetime in LHC and HL-LHC [2].**

Machine	I (A)	H_2	CH_4	H_2O	CO	CO_2
LHC	0.58	$1.2 \cdot 10^{15}$	$1.8 \cdot 10^{14}$	$1.8 \cdot 10^{14}$	$1.2 \cdot 10^{14}$	$7.9 \cdot 10^{13}$
HL-LHC	1.09	$6.4 \cdot 10^{14}$	$9.6 \cdot 10^{13}$	$9.6 \cdot 10^{13}$	$6.4 \cdot 10^{13}$	$4.2 \cdot 10^{13}$

12.3 Vacuum layout requirements

The vacuum layout must ensure the vacuum requirements when beams with HL-LHC nominal parameters circulate. The system must be designed for the HL-LHC ultimate luminosity (i.e., 7.5×10^{34} $cm^{-2}s^{-1}$), without margin.

- All beam vacuum elements must be leak tight (leak rate less than 10^{-11} mbar-l/s He equivalent) clean according to CERN vacuum standards and free of contamination.

- According to the LHC baseline [2], the vacuum system in the LSS must be sectorised with gated valves. The vacuum sectorization is delimited by cold-warm transitions, length of vacuum sectors, or specificity of components (fragility, maintenance …) [5].

- Vacuum sector valves must be installed at each cold-warm transition in order to decouple the room temperature and cryogenic temperature vacuum systems during bake-out and cool down phases.

- The distance between the vacuum sector valve and the cold-warm transition must be minimised in order to reduce the length of the beamline that is not baked-out in situ.

- Dedicated vacuum instrumentation must be provided close to and either side of each sector valve and along each vacuum sector.

- Sector valves must be remote controlled and interlocked in order to dump the circulating beam in case of malfunctioning. The LHC and HL-LHC vacuum sectorizations delimit two types of vacuum system:

  o Room temperature vacuum system.

  o Cryogenic temperature vacuum system.

- The vacuum system shall be integrated in the tunnel and cavern volumes with the permanent /mobile bake-out system, bake-out racks, quick flanges collars, mobile pumping systems, and diagnostics systems. The corresponding space must be reserved into the tunnel integration to allow a proper access and operation of the vacuum system.

- Integration studies must be also performed for installation and uninstallation phases of equipment to identify potential conflicts.

- Integration and installation drawings must be circulated and validated before installation in the tunnel and caverns.

- The vacuum chamber aperture is defined by the beam optics system and by machine protection and background to experiments considerations. The aperture of the vacuum chamber must not be the limiting aperture.

- All components to be installed into the vacuum systems must be approved and their vacuum performance validated before installation.

- A maximum of LHC beam vacuum components will be reused for HL-LHC upgrade.

- High radiation areas along the LSS must be clearly identified at an early stage of the design, in particular to highlight positions where remote handling / tooling might be preferred and positions where instrumentations must be radiation resistant.

- When needed, irradiation tests of specific components (instruments, bake-out jackets, cables, electronics, o-rings...) must be conducted to meet the radiation dose specifications.

- The spare policy will follow the general A&T sector policy. A spare policy must be made available from the early time of procurement to benefit from large quantity orders, in particular for highly specialized equipment such as beam screens, modules etc.

- Cryogenic elements must be installed first; then room temperature vacuum sector valves followed by completion of the room temperature vacuum sectors.

- Time, resources and space to allow the temporary storage of LHC vacuum components, which need to be dismounted to allow HL-LHC infrastructure modifications and equipment installation will be evaluated in the next phase of the project.

12.3.1 Room temperature vacuum system requirements

Standard vacuum chambers and vacuum modules connect the machine components.

In order to accommodate thermal expansion during bake-out and sustain "vacuum forces" due to the differential pressure, each component containing a beampipe must have a single fixed point. Other supporting points, if any, must be sliding.

All machine components operating at room temperature must be bakeable. The required bakeout temperature is 230 °C +/- 20 °C for NEG coated vacuum chambers and 300 °C +/- 20 °C for uncoated stainless steel beampipes. To optimise the bakeout duration while minimising the mechanical strength and radiation to personnel, the applied heating rate during bakeout is 50 °C/h.

The vacuum system layout must be designed to fulfil the stated requirements throughout a full run. In particular, the impact of the outgassing rate of specific components, *e.g.* collimators, must be taken into account during the layout definition phase. No NEG coating re-activation can be foreseen during short stops to recover loss of pumping performance.

A vacuum module equipped with bellow must be inserted between each machine component and vacuum chamber, and between vacuum chambers themselves.

These vacuum modules must be screened by an RF bridge for impedance reasons.

For the sake of cost, reliability, spare policy and standardisation, the maximum number of vacuum module variants must be reduced with respect to the LHC baseline.

The warm vacuum chambers must be circular and bakeable. The current LHC variants are ID 80, 100, 130 and 212 mm: the further variants needed for HL-LHC will be kept to a minimum necessary.

Special chambers may be designed if needed but the quantity must be kept to a minimum. A typical case is the one of the recombination chambers installed into the TAN absorber which is not circular by definition.

Vacuum chamber transitions (VCT), which gives offsets and adaptation between pipe apertures, must be integrated at the early design stage by the equipment owners themselves into the concerned equipment, *e.g.* BTV, ACS, TCDQ etc in agreement with the vacuum group.

The vacuum chambers are aligned by TE-VSC within +/- 3 mm accuracy. Better tolerance will required the installation of survey targets. Alignment of other equipment is the responsibility of the survey group.

The choice of the vacuum chamber material between Cu alloy and stainless steel (either Cu coated or bare) is dictated by beam impedance constraints. Aluminium alloys are preferred in high-radiation areas

Connection between equipment must be done by Conflat bolt technology unless radiation issues and / or remote handling require the use of quick release flanges with, for example, chain clamps.

The vacuum system must be integrated in the tunnel with the permanent or mobile bakeout system, bakeout racks, quick flanges collars, mobile pumping systems and diagnostics systems. The corresponding space must be reserved into the tunnel integration studies to allow a proper operation of the vacuum system.

12.3.2 Cryogenic temperature beam vacuum system requirements

The cryogenic beam vacuum system must be tightly decoupled by sector valves from the room temperature vacuum system. Dedicated instruments must be provided close to the sector valves to allow roughing, monitoring, and safety of the vessel.

A cold-warm transition must be integrated into the cryogenic beam vacuum sector at each extremity of the cryogenic system.

A continuous cold bore, *i.e.* without penetrating welds between the beam vacuum and helium enclosure, ensures the leak tightness between the superfluid helium and beam vacuum along the cryogenic beam vacuum sector. The LHC nominal cold bore temperature is 1.9 K in the arcs.

A beam screen must be inserted into the cold bore to extract the beam induced heat load at a higher temperature than 1.9 K. The beam screen must be perforated with slots (4% transparency) to allow pumping onto the cold bore [2]. The LHC beam screen operates from 5 to 20 K. The HL-LHC beam screens of the IT+D1 will probably need to run at a higher temperature (between 40 and 60 K) due to a much higher heat load. In-situ heating of the beam screen up to 90 K, with cold bore < 3 K, is required to flush the condensed gas present on the beam screen inner surfaces towards the cold bore. This heating cycle may be required after a long technical stop or even between physics fills. The HL-LHC beam screen perforation percentage will be scaled to HL-LHC parameters and therefore increased as compared to the LHC.

When a cold bore operates at 4.5 K, cryoabsorbers are installed outside the beam screen in order to provide hydrogen pumping speed and capacity.

In the LHC, the maximum length without beam screen is less than 1 m. This LHC design value will be scaled to HL-LHC parameters and therefore reduced.

For the HL-LHC, the beam screen aperture will be derived from beam optics and magnet aperture inputs.

12.4 Insulation vacuum requirements

The insulation vacuum system ensures the required performance of the cryogenic system by eliminating the heat losses due to gas convection. The insulation vacuum systems under the responsibility of TE-VSC include the QRL and cryogenic machine components, but exclude transfer lines outside the LHC tunnel or those of the experimental cavern.

The requirements of the insulation vacuum system for HL-LHC can be summarised as follow:

- The pressure must be below 10^{-5} mbar,

- The helium leak rate, at the component level, must be below 10^{-10} mbar.l/s

- It must be compatible with the LHC insulation vacuum system [2].

- It must be built with the same standards used for the LHC insulation vacuum system.

The cryogenic distribution line (QRL) and the magnet cryostats are connected via jumpers. However, their insulation vacuum are separated through vacuum barriers. The QRL and continuous cryostat are sectorised through vacuum barriers. There is no sectorization of the QRL in the LSS of the LHC. Sectorization of the HL-LHC cryostats shall ensure longitudinal leak location techniques can be employed. Connection to cryoplant or transfer lines outside the LHC tunnel, shall be delimited by vacuum barriers.

The insulation vacuum relies on cryopumping in normal operation. Fixed turbo molecular pumping groups are used for pumping before cool down. This system also mitigates the impact of helium leaks during operation. Such pumps are used also for detection of helium or air leaks. Dedicated pumping ports are used for rough pumping groups, pressure gauges, pressure relief valves, longitudinal leak localisation techniques and additional pump placement in case of operational leaks. A by-pass equipped with isolation valves is installed between subsectors. The standard for pumping ports is the ISO-K DN 100 flange. Each insulation vacuum volume has to be equipped with pressure relief valves. Elastomer seals (Viton, NBR) are used where system demountability is necessary (interconnections, instrumentations, etc). The layout detailed design, testing and final acceptance of HL-LHC cryostat are subject to TE-VSC approval.

For the HL-LHC project, in the areas of expected high irradiation, specific seals (metals or hard-rad polymers) have to be installed on new equipment and to replace standard seals on any retained equipment.

Regular preventive maintenance will be carried out on turbomolecular pumping groups during technical stops.

12.5 Experimental vacuum system requirements

The experimental vacuum system is located between Q1L and Q1R of each interaction point. Similarly to the LSS, the vacuum layout of each experimental vacuum system must ensure the vacuum requirements when beams with HL-LHC nominal parameters circulate. The system shall be designed for HL-LHC ultimate parameters, without margin. Therefore, all constraints and requirements defined in section 3 and 3.1 apply in this section.

During long beam stops (> 10 days), neon venting is needed to protect the fragile experimental vacuum chambers from deformations caused by mechanical shocks. The baseline is no work in the vicinity of the vacuum chambers whilst they are under vacuum.

The vacuum chamber supporting system must be compatible with standard activities performed in the experimental cavern during short stops (e.g. winter technical stops). In particular, no personnel is allowed in the vicinity of the beampipe (< 2 m radius) during these phases.

A vacuum sector valve is installed at each Q1 extremity. This vacuum sector valve, installed just after the cold-warm transition, ensures decoupling of the room temperature and cryogenic temperature vacuum systems during bakeout and cryogenic temperature transients. The Q1 sector valves are interlocked to the circulating beam.

A second vacuum sector valve is installed between Q1 and TAS on the left and right side of the ATLAS and CMS experiments. On the left and right side of the ALICE and LHCb experiments a sector valve is installed between Q1 and the cavern shielding. Such vacuum valves allow the decoupling of two delicate and complex beam vacuum sectors *i.e.* the inner triplets vacuum sector and the experimental vacuum sector, in areas that can be radioactive. They are blocked open during operation *i.e.* they are out of the interlock chain.

A rupture disk is installed in the buffer zones in order to protect the experimental vacuum chambers in case of liquid helium inrush. Therefore, the Q1 sector valve located at the cold-warm transition position must be interlocked against possible helium inrush in case of a cryogenic accident inside the inner triplets.

As for the present LSS vacuum system, all machine components operating at room temperature must be bakeable and NEG coated.

Scheduled or accidental air venting in air for repair or maintenance of any of the vacuum sectors of the experimental vacuum system implies a complete NEG recommissionning of the beampipes *i.e.* two bakeout cycles, the first for the bakeout of the metallic part, the second for the NEG activation.

An ultra-pure neon venting system is installed in the buffer zone (for ATLAS, CMS and ALICE) or in the detector itself (i.e. the Vertex Locator, VELO) to allow remote venting of the experimental vacuum system during long stops (> 10 days).

12.5.1 High luminosity experiments: ATLAS and CMS

ATLAS and CMS vacuum layout drawings are described in [6, 7].

On both sides of ATLAS and CMS, a pumping system is installed in the buffer zone to allow pump-down and vacuum commissioning during NEG activation of the ATLAS and CMS experiment.

In the Q1-TAS areas instrumentation must be minimised. The Q1 sector valve must remain in the interlock chain in order to protect the experimental area from gas contamination or liquid helium inrush.

To avoid personnel intervention in a high radiation area:

- A pumping and neon systems must be installed in the buffer zone on the right side of ATLAS to complement the left side.

- Remote tooling must be foreseen to avoid personnel intervention. Quick type flanges are mandatory. Welds are preferred to flanges.

- Installed components must be robust, in particular, sliding fingers in RF bridges are forbidden.

- The bakeout system must be permanent and fully integrated from the design phase with the other systems.

- Detector modifications shall be designed taking into account movement and intervention of personnel. They shall also take into account the beampipe system and flanges for detector movements. It must be ensured that standard interventions during technical stops and chamber replacements are thoroughly studied in the design phase with the aim to minimise radiation dose to personnel during the detector and chamber lifecycle.

ATLAS is equipped with a permanent bakeout system while CMS is not. However, HL-LHC might require the use of permanent bakeout systems for both detectors due to radiation issues. In CMS,

a specific design of the jackets, thermocouple and cable layouts must also comply with the radiation requirements.

The vacuum modules are not screened by sliding RF finger for access and space constraints, radiation protection reasons, and potential risk of aperture loss.

The alignment of the vacuum chambers shall be performed remotely with appropriate hardware.

The choice of the vacuum chamber material between Cu alloy and stainless steel (either Cu coated or bare) is dictated by beam impedance requirements. Al alloys are preferred in high-radiation areas.

The connection between equipment shall be done by Conflat bolted technology unless there are radiation issues and/or remote handling which require the use of quick release flanges.

It is assumed that the ATLAS central beampipe inner diameter, as installed during LS1, remains the same until at least LS3 [8].

According to [8], it is assumed that:

-   the CMS central beampipe inner diameter, as installed during LS1 remains the same until at least LS3.

-   "End cap, HF, CT2 and forwards pipes" of the CMS vacuum system must be upgraded to Al bulk material during LS2. No mechanical intervention between TAS L and TAS R is therefore expected during LS3.

Any new chamber to be installed in the future must be compatible with remote tooling *e.g.* equipped with a "quick flange" type system.

Since the TAS needs to be replaced during LS3, the vacuum system located inside the experimental cavern needs to be recommissioned, *i.e.* NEG activation even if no changes of the vacuum system inside the cavern are foreseen.

12.5.2 ALICE and LHCb experiments

On the right side of ALICE, a pumping system is installed in the buffer zone to allow pumpdown and commissioning during NEG activation of the beampipes.

In the ALICE cavern, a manual valve, located on the left side of the beryllium central beampipe, allows the isolation of the detector vacuum sector from the RB 24 vacuum sector. Consequently, the vacuum chambers in the RB24 area can be dismounted during long shutdowns if needed.

ALICE vacuum layout drawing is described in [10].

The ALICE central beryllium beampipe is not equipped with a permanent bakeout system. The beampipes located ion the RB26 area of the ALICE cavern (*i.e.* the right side of the IP) are equipped with a permanent bakeout system. From the left of the central beampipe to the end of RB26 the vacuum modules are not screened by sliding RF fingers because of: access and space constraints; radiation issues; and the potential risk of aperture loss.

In LHCb, the Vertex Locator (VELO) detectors are installed into a secondary vacuum system, which is isolated from the beam vacuum system by a thin RF shield. The RF shield mechanical integrity is protected during pumping and venting phase by an automatic gas balance system to maintain the pressure difference within a mechanically stable range.

At the VELO, an automatic pumping system is installed to allow the pumpdown and commissioning during NEG activation while protecting the VELO RF shield.

At the VELO, an ultra-pure neon venting system is installed to allow remote venting of the LHCb with an automatic gas balance system while protecting the VELO RF shield during long stops (> 10 days).

The LHCb beampipes are not equipped with a permanent bakeout system. However, part of the UX85/3 vacuum chamber in the region of the calorimeter is foreseen to be equipped with permanent bakeout for LS2 [13].

The VELO beampipe must be baked at least 180 °C for 48 h to suppress electron cloud.

From the right side of the VELO beampipe to the end of UX85, the vacuum modules are not screened by sliding RF fingers because of: access and space constraints; radiation issues; and the potential risk of aperture loss.

Wake-field suppressors are installed at the VELO beampipe extremities for impedance reasons.

The LHCb vacuum layout drawing is described in [11].

According to [12], it is assumed that the ALICE central beampipe inner diameter will be changed during LS2 and remains unchanged afterward.

According to [13], it is assumed that:

– the LHCb VELO beampipe will be changed during LS2 and remains in the ring afterward [3].

– the 2-m long Cu-alloy vacuum chamber, VCDBV, located on the right side of the VELO will be replaced by an Al-alloy beampipe. This change will take place during LS2. No modification is expected afterward.

– Part of the UX85/3 vacuum chamber in the calorimeter region will be equipped with permanent bakeout jackets during LS2. It is also assumed that there will be no more installation of permanent bakeout jackets after LS2.

12.6 Beam screen requirements

Beam screens are inserted into cryogenic cold bores in order to guarantee the vacuum performance. They are part of the LHC vacuum system baseline [1]. The requirements of the HL-LHC beam screen can be summarised as follow:

– The system lifetime must be longer than the HL-LHC lifetime, namely 40 years of operation and 50 quenches.

– The system must fulfil the required vacuum performance in terms of vacuum stability, vacuum lifetime, and background to the experiments.

– The shielded beam screen must be perforated (or be shadowing) in order to fulfill the vacuum performance in a way to allow pumping of the molecules onto the cold bore.

– The cold bore temperature must be held below 3 K to allow cryosorption of all molecules with the exception of helium.

– The shielded beam screen must be heatable to allow a transfer of the gas onto the shielded beam screen towards the cold bore during machine stops.

– The shielded beam screen must withstand the Lorentz forces induced by Eddy current during a quench.

– The temperature of the shielded beam screen must be actively controlled in a given temperature range.

- To minimise the heat load on the shielded beam screen due to electron cloud, a coating *e.g.* amorphous carbon or a clearing electrode system must be studied, validated and implemented. The e-cloud mitigation measures must be applied not only to the new high luminosity insertion regions that will renovated, IP1 and IP5. They will be applied also to the interaction regions of IP2 and IP8. These are indeed low luminosity insertions, however the beam pattern will be the same as in the high luminosity insertions. This point is quite recent and mitigation measures are currently under investigation.

- The system must be compatible with impedance budget.

- The system must be compatible with the machine aperture.

- The surface of the beam screen must withstand a dose of several hundred MGy during its lifetime.

In order to operate properly, the beam vacuum system must be evacuated for, at least, 5 consecutive weeks prior to cooldown to allow the outgassing rate of adsorbed water to reduce to acceptable levels.

During cool down of a cryogenic system, the cold bore must be cooled first in order to minimise gas condensation onto the beam screen.

In the case that gas is condensed onto the beam screen during operation, *e.g.* after a magnet quench, a transfer of this gas towards the cold bore via beam screen heating is needed. This procedure should be carried out in a couple of days.

The HL-LHC beam screen must be inserted during cryostating phase prior to tunnel installation. The surface of the beam screens must be kept clean during the assembly. This implies that the beam screen is installed at the last stage of cryostating. Without specific tooling and procedures, no probe or device can be inserted into the vacuum system once the beam screens are installed.

The cooling tubes must be dimensioned to allow a proper cooling of the system during operation within the limits defined above.

According to vacuum standards, full penetrating welds are forbidden in the vessel wall separating the beam vacuum and helium enclosures. However, given the limited number and length of new vacuum elements to be installed, this general rule might be revised in case of compelling reasons, if compensated by adequate measures of risk mitigation.

Depending on the location, two types of beam screens may exist: shielded beam screens and non-shielded beam screens. The shielded beams screens intercept part of the debris produced at the high luminosity IPs thereby protecting the cold masses from radiation induced damaged.

Amorphous carbon (a-C) coating is at resent the baseline for inner surface of HL-LHC shielded and non-shielded beam screens. Due to the a-C properties, strong electron cloud suppression in these HL-LHC components is expected. a-C coating will be applied on HL-LHC beam screens if needed for heat load to cryogenic system reduction and / or background to experiment reduction and / or beam physics requirements.

A demonstration of the electron cloud suppression must be performed with a dedicated set up such as COLDEX in SPS LSS4. Studies will be held during SPS scrubbing runs and dedicated machine developments. Experimental results must be supported by theoretical expectations derived from simulations codes such as Ecloud or PyCloud.

a-C coating should be the last step of the beam vacuum preparation before lowering the magnet into the tunnel, avoiding any insertion of tooling or other devices inside the beam vacuum line afterwards.

For IP2 and IP8 *in-situ* coating of the present beam screen (or alternatively the placement of a clear electrode) must be studied and conducted during the long shutdown (LS2 or LS3). In the case the

in-situ coating would not be possible, removal of the magnet cryostat will be considered to allow the beam screen exchange.

If needed, a sawtooth structure can be produced on the beam screen walls (dipoles and quadrupoles). The sawtooth must be designed to intercept the synchrotron radiation at perpendicular incidence and to reduce the forward scattering of the light.

12.6.1 Shielded beam screen

HL-LHC shielded beam screens are to be inserted into HL-LHC D1 and IT of LSS1 and LSS5. Such beam screens ensure the vacuum requirements, the shielding of the cold mass from physics debris, and the screening of the 1.9 K cold bore cryogenic system from beam induced heating.

As a base line, the shielded beam screen is assumed to fulfil the vacuum requirements with a-C coating operating at 40-60 K.

The shielded beam screen is estimated to operate in the 40-60 K +/- 10 K temperature range. The operating temperature range will be defined by the available cooling power, the expected beam induced heat load, and the compatibility with the vacuum requirements.

The selected shielding material is Inermet, a tungsten alloy. It is made of 40 cm long blocks, which must be accommodated onto the beam screen structure [14].

12.6.2 Non-shielded beam screen

HL-LHC non-shielded beam screens are to be inserted into HL-LHC D2, Q4, Q5, Q6 of LSS1 and LSS5 and, if needed, in D1, DFBX and IT of LSS2 and LSS8. Such beam screens ensure the vacuum requirements together with screening of the 1.9 K cold bore from beam induced heating.

As a base line, the amorphous carbon (a-C) beam screen is assumed to fulfil its vacuum requirements with a-C coating operating at 5-20 K.

In LSS 1 and LSS5, the a-C beam screen is part of the new D2, Q4, Q5, Q6 system for HL-LHC which will replace the present ones.

In LSS 2 and 8LSS, the a-C coated beam screens will replace the part of the present beam screens. The dismounting of the D1, DFBX and IT of LSS 2 and LSS8 is needed unless the cryogenic system can be upgraded.

The a-C coated beam screen is estimated to operate in the 5-20 K +/- 3 K temperature range. The operating temperature range will be defined by the available cooling power, the expected beam induced heat load and the compatibility with the vacuum requirements.

The selected a-C coated beam screen material is P506 non-magnetic stainless steel. It is similar to the one used for the present beam screens. Cu will be co-laminated for impedance reasons. The proposed thickness of the Cu layer is 60 μm.

12.6.3 Vacuum beam line interconnection

HL-LHC shielded beam screens are to be inserted into HL-LHC D1 and IT of LSS1 and LSS5. Beam vacuum interconnections ensure the continuity of the beam vacuum envelope, a smooth transition between adjacent beam screens, and the electrical continuity for the image current. The beam screens are fixed on one side to the cold mass; on the other side, a compensation bellow between the beam screen extremity and the cold mass has to be integrated to cope with the differential thermal displacements between the beam screens and the cold mass.

The HL-LHC beam screens rely on larger-than-present cooling tubes. The routing of these cooling tubes, in and out of the cold bore, requires exit pieces with significant longitudinal space.

Trough-wall welds on helium circuit are forbidden in the beam vacuum. Automatic welds have to be used in the insulation vacuum.

A bellow between two adjacent beam screens has to be integrated to allow thermal contraction as well as to compensate the mechanical and alignment tolerances. In the transitions, collisions debris shielding with circular aperture and non-sliding RF fingers are foreseen and are being studied.

The vacuum beamline interconnections in the triplets integrate BPM as well. They define the interconnection length. Therefore, iteration and optimisation of the different elements are required to complete machine integration.

12.7 References

[1] O. Grobner, Overview of the LHC vacuum system. Vacuum 60 (2001) 25-34.

[2] LHC Design Report, CERN-2004-003 (2004).

[3] A. Rossi, CERN LHC Project Report 783, 2004.

[4] A. Rossi, Residual Gas Density Estimations of the LHC Experimental Interaction Regions. CERN LHC Project Report 674, 2003. EDMS 410413, 2003-11-19.

[5] Model of LSS LayoutLHCLJV_L0011

[6] ATLAS Vacuum Layout Q1/Q1. LHCVC1__0007

[7] CMS Vacuum Layout Q1/Q1. LHCVC5__0006

[8] M. Gallilee, TE-VSC & ATLAS Work Packages Consolidation and Upgrade of the Beam Vacuum Systems. 1065775, 2013-4-24.

[9] M. Gallilee, TE-VSC & CMS Work Packages Consolidation and Upgrade of the Beam Vacuum Systems. 1065775, 2013-4-24.

[10] ALICE Vacuum Layout Q1/Q1. LHCVC2__0001.

[11] LHCb Vacuum Layout Q1/Q1. LHCVC8B_0151.

[12] M. Gallilee, TE-VSC & ALICE Work Packages Consolidation and Upgrade of the Beam Vacuum Systems. EDMS 1065775, 2013-4-11.

[13] M. Gallilee, TE-VSC & LHCb Work Packages Consolidation and Upgrade of the Beam Vacuum Systems. EDMS 1065775, 2013-4-11.

[14] R. Kersevan *et al*. 3rd Joint HiLumi LHC-LARP Annual meeting, 11-15 November 2013, Daresbury.

Chapter 13

Beam Instrumentation and Long-Range Beam-Beam Compensation

E. Bravin[5], B. Dehning[5], R. Jones[5], T. Lefevre[5], H. Schmickler[5].
[5]CERN, Accelerator & Technology Sector, CH-1211, Geneva, Switzerland.

13   Beam Instrumentation and Long-Range Beam-Beam Compensation

13.1   Introduction

The extensive array of beam instrumentation with which the LHC is equipped, has played a major role in its commissioning, rapid intensity ramp-up, and safe and reliable operation. In addition to all of this existing diagnostics HL-LHC brings a number of new challenges in terms of instrumentation that are currently being addressed.

The beam loss system, designed to protect the LHC from losses that could cause damage or quench a superconducting magnet, will need a significant upgrade in order to be able to cope with the new demands of HL-LHC. In particular cryogenic beam loss monitors are under investigation for deployment in the new inner triplet magnets to distinguish between collision debris and primary beam losses. Radiation tolerant integrated circuits are also under development to allow the front-end electronics to sit much closer to the detector, so minimising the cable length required and reducing the influence of noise.

The use of crab cavities and possible use of long-range beam-beam compensators and hollow-electron lenses also implies new instrumentation in order to allow for optimisation of their performance. Several additional diagnostic systems will therefore be considered. Very high bandwidth pick-ups and a streak camera installation to perform intra-bunch transverse position measurements are being investigated, along with new techniques for transverse beam size measurements such as a beam gas vertex detector.

An upgrade to several existing systems is also envisaged, including the beam position measurement system in the interaction regions and the addition of a halo measurement capability to synchrotron light diagnostics.

13.2   Beam Loss Measurement

Monitoring of beam losses is essential for the safe and reliable operation of the LHC. The beam loss monitoring (BLM) system provides knowledge of the location and intensity of such losses, allowing an estimation to be made of the energy dissipated in the equipment along the accelerator. The information is used for machine protection, to qualify the collimation hierarchy, to optimise beam conditions and to track the radiation dose to which equipment has been exposed. This is currently done using nearly 4000 ionisation monitors distributed around the machine and located at all probable loss locations, with the majority mounted on the outside of the quadrupole magnets, including those in the inner triplet regions. Around one third of the arc monitors have recently been relocated in order to optimise the system for

protection against fast beam losses believed to be caused by dust particles falling into the vacuum pipe. While the existing system is believed to meet the needs of the HL-LHC for the arcs, this will no longer be the case for the high luminosity interaction points.

In the HL-LHC high luminosity insertions the magnets will be subjected to a greatly enhanced continuous radiation level due to the increase in collision debris resulting from the higher luminosity. With the presently installed configuration of ionisation chambers in this region the additional signal from any dangerous accidental losses would be completely masked by that coming from collision debris. This is a critical issue for LHC machine protection and therefore R&D has started to investigate possible options for placing radiation detectors inside the cryostat of the triplet magnets as close as possible to the superconducting coils. The dose measured by such detectors would then correspond much more precisely to the dose deposited in the coils, allowing the system to be used once again to prevent a quench or damage.

The quench level signals estimated for 7 TeV running are, for some detectors, very close to the noise level of the acquisition system. This is mainly determined by the length of cable required to bring the signal from the radiation hard detector to the more radiation sensitive front-end electronics. Although qualified for use in the low radiation environments of the LHC arcs, the current electronics cannot be located close to the detectors in the higher radiation insertion regions. Development has thus started to implement this electronics in a radiation hard Application Specific Integrated Circuit (ASIC).

13.2.1 Beam Loss Monitors for the HL-LHC Triplet Magnets

Three detectors are currently under investigation as candidates for operation at cryogenic temperatures inside the cryostat of the triplet magnets [1]:

- Single crystal chemical vapor deposition (CVD) Diamond with a thickness of 500 μm, an active area of 22 mm2 and gold as the electrode material.

- p+-n-n+ silicon wafers with a thickness of 280 μm, an active area of 23 mm2 and aluminum as the electrode material.

- Liquid helium ionisation chambers.

Experiments have already been performed to observe the behaviour of such detectors in a cryogenic environment and on the radiation effects at such temperatures for silicon and single crystal diamond. Irradiation up to 2 MGy (0.8×10^{14} protons/cm^2) showed degradation in the charge collection efficiency for CVD diamond by a factor of 15 and for Si by a factor of 25 (see Figure 13-1). The major downside of silicon compared to diamond, its much higher leakage current when irradiated, has been observed to disappear at liquid helium temperatures, with the leakage current remaining below 100 pA at 400 V, even under forward bias for an irradiated diode. Further experiments combining irradiation with cryogenic temperatures will be necessary to optimise the final detector design. These experiments will be accompanied by tests of detectors mounted inside the cryostats of existing LHC magnets with the aim of gaining experience with the long term performance of such detectors under operational conditions. The technology chosen will need to able to withstand irradiation up to 20 MGy at 4.5K.

Up to 6 detectors will be installed inside the cold mass of each main triplet quadrupole magnet, which leads to a baseline procurement of 100 detectors (96 installed and 4 spares). If the option of equipping the 11 T dipole and all the spare triplet magnet assemblies is also taken into account, then a total procurement of 150 detectors would be required. They are foreseen to be housed in existing holes of the iron yoke within the cold mass of the magnet. Each detector will be equipped with a single semi-rigid coaxial cable that will provide the necessary high voltage (up to 1000V) and extract the loss signal from each detector. Feedthroughs allowing a total of 6 coaxial cable connections will need to be integrated into each of the main triplet quadrupole cryostats with the location of the feedthrough chosen such as to minimise the cable length required.
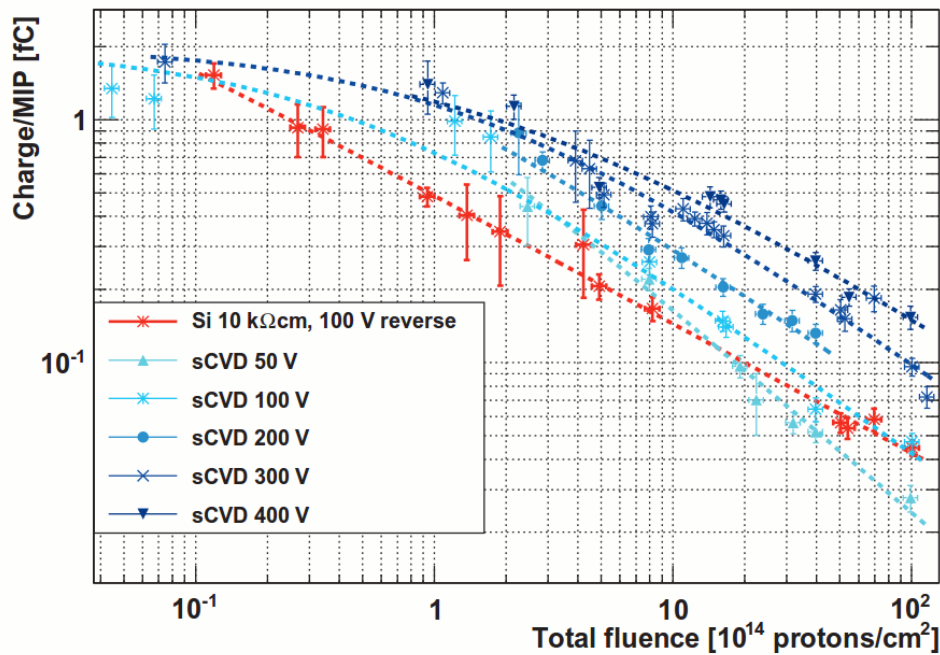
Figure 13-1: Charge collection efficiency for silicon and diamond detectors with increasing radiation fluence in a cryogenic environment.

As part of the machine protection system these components need to be highly reliable and maintenance free. In the event that some of these monitors stop functioning the existing external BLM system should still provide adequate protection against damage due to excessive beam loss, but will probably not be able to distinguish quench provoking losses from the experimental background.

13.2.2 A Radiation Tolerant ASIC for the HL-LHC Beam Loss Monitoring System

The current front-end electronics for the LHC BLM system, while providing a 40 μs integration time, is limited in the dynamic range it can handle and is only radiation tolerant up to ~500 Gy. The latter implies the use of long cables in the higher radiation LSS regions, which further limits the dynamic range and in some cases brings the noise floor close to the quench level signal at 7 TeV. Instead of the discrete component currently used, an optimised ASIC is therefore under development. This is still based on the current to frequency conversion used in the existing system, but packaged in a compact, radiation-tolerant form with an increased dynamic range. The technique employed allows the digitisation of bipolar charge over a 120 dB dynamic range (corresponding to an electric charge range of 40 fC – 42 nC) with a 40 μs integration time and a conversion reference provided by an adjustable, temperature-compensated current reference [2].

Figure 13-2 shows the block diagram of the integrated circuit. It is composed of a bipolar, fully-differential integrator that converts the charge received from the detector into a voltage input for a synchronous comparator system. A three-level Digital-to-Analogue Converter (DAC) drives the discharge current for the integrator and is connected in a feedback loop to the comparator output. A first logic block is used to select the gain in the integrator, the current step in the DAC and the threshold in the comparators, while a second logic block encodes the output signal from the comparators. The results of both of these are used by a third block to assemble the final, correctly weighted output word.
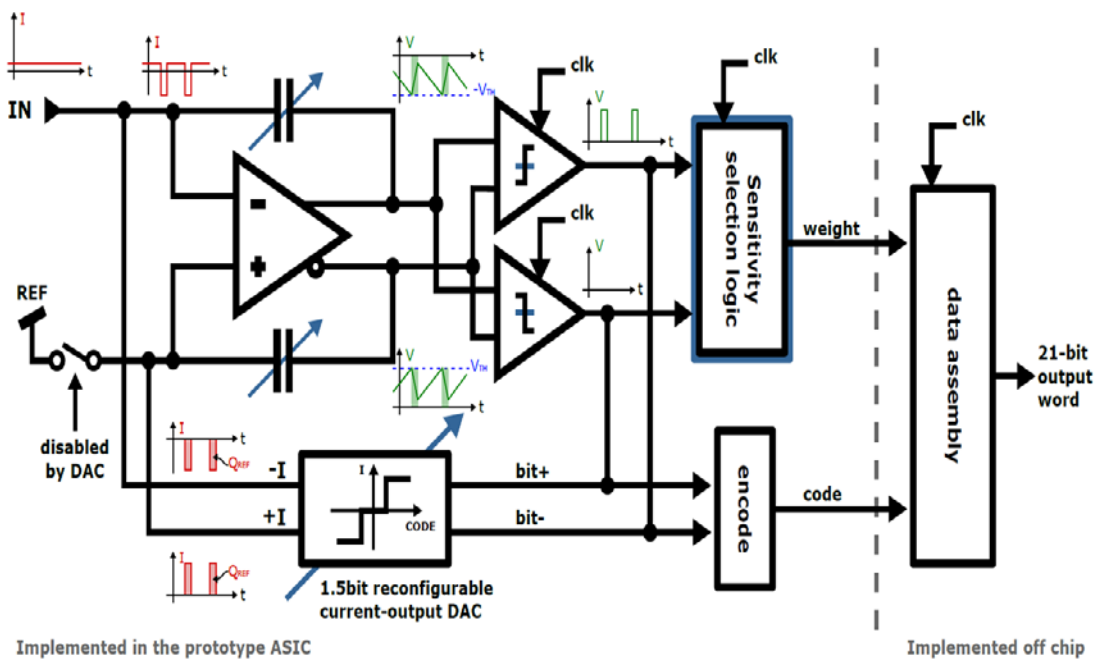
Figure 13-2: Schematic representation of the ASIC implementation currently under development.

The prototype ASIC is designed in commercial CMOS technology and has two Analogue-to-Digital (A/D) channels and a sensitivity selection logic that can be disabled to implement the circuitry externally. This strategy has been useful for testing the device and improving the algorithm. Its measured characteristics are listed in Table 13-1.

Table 13-1: Characteristics of the prototype HL-LHC BLM system ASIC.

A/D converter

Integration time	$40\,\mu s$	Linearity error	$< \pm 5\%$
Input current range	$-1.05\,mA$ to $1.05\,mA$	Peak S/N ratio	$53\,dB$
Input charge range	$-42\,nC$ to $42\,nC$	SFDR at 999Hz, 1mA	$50\,dB$
Offset	$< 40\,aC$, $40\,\mu s$ integration	Total ionizing dose	$10\,Mrad(Si)$
	$< 1\,pA$	Supply voltage	$2.5\,V$
Default LSB step	$50\,fC \pm 20\%$, adjustable	Clock	$12.8\,MHz$
Dynamic range	$120\,dB$	Power	$40\,mW$

Reference charge

Drift with TID	3% at $10\,Mrad(Si)$	Drift with temperature	< 600 ppm/°C

The measured linearity is limited by transistor matching imperfections in the DAC, introducing an error at the transition between the sensitivities. However, overall the error is less than 5% and well inside specification (<10%).

Total Ionizing Dose (TID) effects on the ASIC have been investigated using an X-ray beam with 20 keV peak energy. The characteristics of the device were measured up to 100 kGy (Si), followed by a 1-week annealing cycle at 100 °C. From the beginning to the end of the irradiation cycles, the functionality was always preserved, with the conversion offset remaining below 1 Least Significant Bit (LSB) and the value of the full scale charge drifting by less than 3%. Development will now continue

to address the issues found using the prototype and to implement more advanced logic blocks within the ASIC.

A total of some 300 detectors, mainly located in the LSS regions, are foreseen to be equipped with such a front-end ASIC.

13.3 Beam Position Monitoring

With its 1070 monitors, the LHC Beam Position Monitor (BPM) system is the largest BPM system in the world [3]. Based on the Wide Band Time Normalizer (WBTN) principle, it provides bunch-by-bunch beam position over a wide dynamic range (~50 dB). Despite its size and complexity (3820 electronic cards in the accelerator tunnel and 1070 digital post-processing cards in surface buildings) the performance of the system during the last three years has been excellent, with greater than 97% overall availability.

13.3.1 Current performance and limitations

The position resolution of the LHC arc BPMs has been measured to be better than 150 μm when measuring a single bunch on a single turn and better than 10 μm for the average position of all bunches. The main limitation on the accuracy of the BPM system is linked to temperature dependent effects in the acquisition electronics, which can generate offsets of up to a millimetre over a timescale of hours. On-line compensation was introduced to limit this effect during operation and temperature controlled racks are currently being installed with the hope of eliminating this limitation from the Run 2 start-up in 2015.

The non-linearity of the BPMs located near the interaction points has also proven to be problematic, in particular for accurate measurements during the beta-squeeze and during machine development periods. A new correction algorithm has therefore been developed, based on exhaustive electro-magnetic simulations, with the aim of bringing down the residual error to below 20 μm over most of the useable BPM area [4]. Developed to be able to distinguish between the positions of two counter propagating beams in the same beam pipe, these BPMs also suffer from non-optimal decoupling between the beams, which is something that will need to be addressed for HL-LHC.

13.3.2 A high resolution orbit measurement system for the HL-LHC

Originally developed to process signals from BPM buttons embedded in LHC collimator jaws, orbit measurement using a compensated diode detector scheme [5], has already been demonstrated to be simple and robust, and to provide a position resolution down to the nanometre level. A comparison of the orbit measured on a single BPM during a van der Meer scan by the current orbit system and the new diode orbit system is presented in Figure 13-3, where the resolution of the new system can be seen to be over 50 times better. All new LHC collimators will have BPMs using this acquisition system installed with them, with plans to also equip the BPMs in all four LHC interaction regions. It is important to note, however, that the new system does not provide the bunch-by-bunch measurement capability of the existing system.

At the start of the HL-LHC era the existing BPM system will have been operational for over 15 years, using components that are over 20 years old. It is therefore likely that a completely new system will need to be installed during HL-LHC operation. One candidate would be to extend the new diode orbit system to the whole machine for accurate global orbit measurements, and complement this with a system capable of providing the high-resolution bunch-by-bunch, turn-by-turn measurements required in particular for optics studies and the many other accelerator physics experiments that will be needed to understand and optimise HL-LHC performance.

With the higher bunch intensities foreseen, the dynamic range of the BPM system for HL-LHC will need to be increased accordingly. The present system implements two sensitivity ranges, optimised

for pilot and nominal bunch intensities. Issues have been observed in the first 3 years of operation with BPMs providing large errors when reaching the limit of their dynamic range. For the interlock BPMs located in Point 6, this can trigger false beam dumps, which clearly has an impact on machine availability. Although improvements have already been made to this interlock system for Run 2, any consolidation of the LHC BPM system should include developing dedicated electronics to this system, optimised for both high reliability and availability.
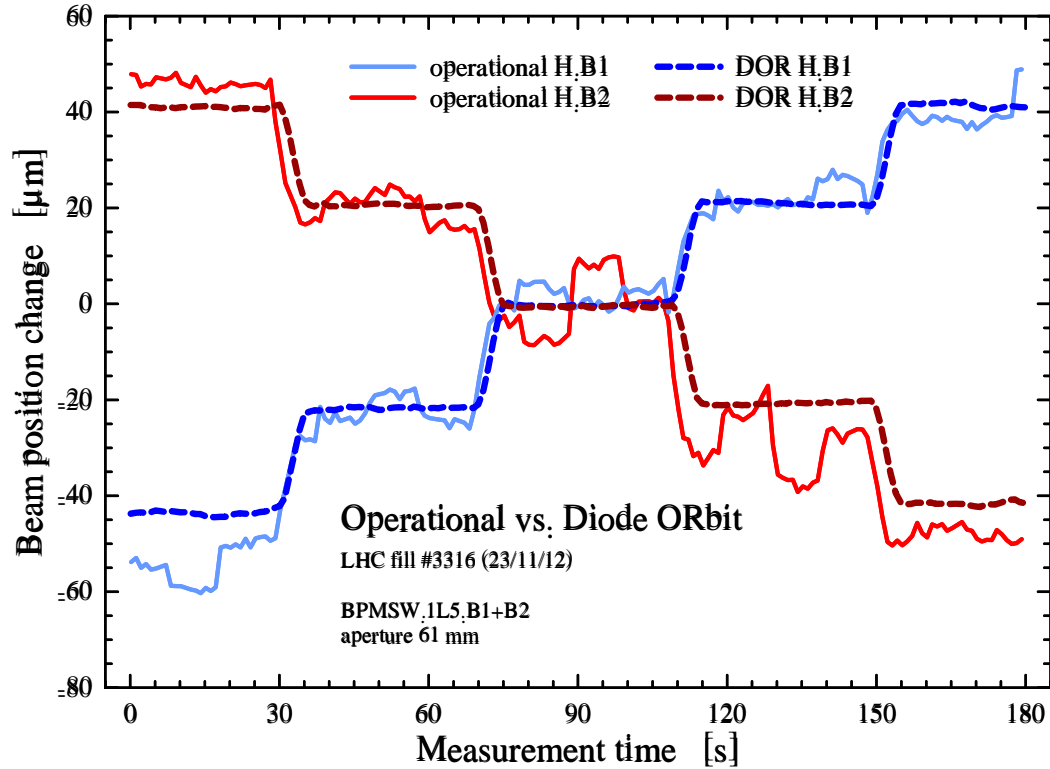
Figure 13-3: Comparison of the new LHC orbit system electronics with the existing system during a Van der Meer scan.

13.3.3 High directivity strip-line pick-ups for the HL-LHC Insertion Regions

In the BPMs close to the interaction regions, the two beams circulate in the same vacuum chamber. Directional strip-line pick-ups are therefore used to distinguish between the positions of both beams. When the two beams pass through the BPM at nearly the same time, the two signals interfere due to the limited directivity of the strip-line which, in the present design, only gives a factor of 10 isolation between the wanted signal and that coming from the other beam. This effect can be minimised by installing the BPMs at a location where the two beams do not overlap temporally. This is a constraint included in both the present and future layout, but which cannot be satisfied for all BPM locations. The ideal longitudinal location corresponds to $(1.87 + N \times 3.743)$ m from the IP where N is an integer. Any deviation from this will diminish the possibility of the system to distinguish one beam from the other.

For the HL-LHC BPMs in front of the Q2a, Q3 magnets and the triplet corrector magnet package, there is the additional constraint that tungsten shielding is required in the cold bore to minimise the heat deposition in these magnets. A mechanical re-design coupled with extensive electro-magnetic simulations is therefore necessary to optimise the directivity under these constraints.

As part of the beam position system of the LHC these components need to be highly reliable and maintenance free, while the system should be able to measure the beam position for each beam with a resolution of 1 μm and a medium term (fill to fill) reproducibility of 10 μm.

13.3.3.1 Cold Stripline BPMs

The HL-LHC high luminosity insertion regions will be equipped with two types of cold stripline BPMs, measuring simultaneously the position of both beams in both planes.

The beam position monitors located in the interconnect in front of the Q2b and Q3 magnets and the triplet corrector magnet package, will be cold stripline BPMs, rotated by 45° to allow the insertion of tungsten shielding in the median planes of both horizontal and vertical axes.

The beam position monitors located in front of the Q2a and before and after the D1 magnet will be cold, stripline BPMs with orthogonally positioned electrodes and without tungsten shielding

The signal from all of these BPMs will be extracted using 8 semi-rigid, radiation resistant coaxial cables per BPM. Two feedthroughs with 4 coaxial cable connections will be integrated into the Q2a, Q2b and Q3 cryostats and into the cryostat of the triplet corrector magnet package, with four such feedthroughs integrated into the D1 cryostat. The outputs on these feedthroughs will be connected to standard ½" coaxial cables taking the signal to the electronics in the UA/UJ.

A total of 12 stripline BPMs of each type will be installed with 3 spares foreseen per type of BPM assembly.

13.3.3.2 Warm Stripline BPMs

The beam position monitor in front of the Q1a will be a warm stripline BPM simultaneously measuring the position of both beams in both planes. The signal will be extracted using 8 semi-rigid, radiation resistant coaxial cables, to a patch panel located in a lower radiation area on the tunnel wall, where they will connect to eight standard ½" coaxial cables taking the signal to the electronics in the UA/UJ.

A total of 4 such BPMs will be installed with 2 spares foreseen for this type of BPM assembly.

13.3.4 Collimator BPMs

All next generation collimators in the LHC will have button electrodes embedded in their jaws for on-line measurement of the jaw to beam position [6]. This is expected to provide a fast and direct way of positioning the collimator-jaws and subsequently allow constant verification of the beam position at the collimator location, improving the reliability of the collimation system as a whole. The design of such a BPM was intensively simulated using both electro-magnetic (EM) and thermo-mechanical simulation codes. In order to provide the best accuracy, the BPM readings must be corrected for the non-linearity coming from the varying geometry of the collimator jaws as they are closed and opened, for which a 2D polynomial correction has been obtained from EM-simulations and qualified with beam tests using a prototype system installed in the CERN-SPS.

The collimator BPM hardware, i.e. the button electrode located in the jaw, the cable connecting the electrode to the electrical feed-through mounted on the vacuum enclosure and the feedthrough itself have been chosen to withstand the radiation dose of 20 MGy expected during the lifetime of the collimator.

13.4 Beam Profile Measurements

The LHC is currently fitted with a host of beam size measurement systems used to determine the beam emittance. These different monitors are required in order to overcome the specific limitation of each individual system. Wirescanners are used as the absolute calibration reference, but can only be operated with a low number of bunches in the machine due to intensity limitations linked to wire breakage. A

cross-calibrated synchrotron light monitor is therefore used to provide beam size measurements, both average and bunch-by-bunch, during nominal operation. However, the small beam sizes achieved at 7 TeV, the multiple sources of synchrotron radiation (undulator, D3 edge radiation, central D3 radiation), and the long optical path required to extract the light imply that the correction needed to extract an absolute value is of the same order of magnitude as the value itself. This requires an excellent knowledge of the error sources to obtain meaningful results. The third system installed is an ionisation profile monitor, which is foreseen to provide beam size information for lead ions at injection, when there is insufficient synchrotron light. The monitor has also been used for protons, but suffers from significant space charge effects at energies above 2 TeV.

Whilst efforts are ongoing to improve the performance of all the above systems, alternative techniques to measure the transverse beam size and profile are also under study for the HL-LHC.

13.4.1 Fast Wirescanners

The currently installed LHC linear wirescanners have a maximum scan speed of 1 ms^{-1}. This gives a limit on the total intensity that can be scanned at injection of ~2.7×10^{13} protons for an emittance of ~2µm, or some 200 nominal bunches. Scanning at 20 ms-1 would allow systematic, average beam size measurements to be performed on the full physics beam at injection. A new fast, rotational wirescanner concept is therefore being explored to reach such speeds whilst achieving an accuracy of 5 µm on the beam width determination, i.e. an error of 5% or less for nominal emittance beams.

The mechanics will be based on the design currently being developed for the injector complex as part of the LHC Injector Upgrade project [7]. It eliminates the need for mechanical bellows by placing all moveable parts of the rotational scanner in the beam vacuum. These bellows have a limited lifetime which, due to their intensive use in the LHC, can be reached within a matter of years. The use of a magnetically coupled motor without the need for moving vacuum parts should significantly increase the MTBF of the mechanics. In addition, the current shower detection acquisition will be replaced with a diamond based sensor connected to high dynamic range acquisition electronics, which should considerably improve the operational ease-of-use of these devices.

Plans to install 2 horizontal and 2 vertical scanners for Beam 1 next to the existing scanners in 5R4 and 2 horizontal and 2 vertical scanners for Beam 2 next to the existing scanners in 5L4 are foreseen. One spare horizontal and one spare vertical unit will also be manufactured.

13.4.2 A Beam Gas Vertex Profile Monitor (BGV)

The VELO detector of the LHCb experiment has shown how beam-gas interactions can be used to reconstruct the transverse beam profile of the circulating beams in the LHC [8]. The new concept under study is to see whether a simplified version of such a particle physics tracking detector can be used to monitor the beams throughout the LHC acceleration cycle. This concept has, up to now, never been applied to the field of beam instrumentation, mainly because of the high level of data treatment required. However, the advantages compared to the standard beam profile measurement methods listed above are impressive: high resolution profile reconstruction, single bunch measurements in three dimensions, quasi non-destructive, no detector equipment required in the beam vacuum, high radiation tolerance of the particle detectors and accompanying acquisition electronics.

Such a beam shape measurement technique is based on the reconstruction of beam gas interaction vertices, where the charged particles produced in inelastic beam gas interactions are detected with high-precision tracking detectors. Using the tracks left in the detectors, the vertex of the particle-gas interaction can be reconstructed so, with enough statistics, building up a complete 2-dimensional transverse beam profile (Figure 13-4). The longitudinal profile could also be re-constructed in this way if relative arrival time information is additionally acquired by the system, something which is not currently planned.
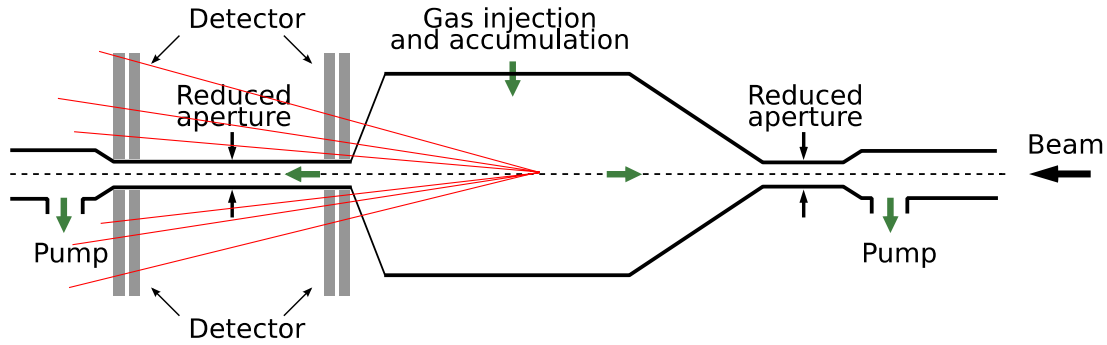
Figure 13-4: A sketch demonstrating the beam gas vertex measurement concept.

Unlike LHCb, where the detector is placed very close to the beam and can therefore only be used during Stable Beams, the aim with the BGV detector is to design a robust instrument that can be used for beam size measurements throughout the LHC cycle. Its final specifications are to provide:

- transverse bunch size measurements with a 5% resolution within 1 minute.

- average transverse beam size measurements with an absolute accuracy of 2% within 1 minute.
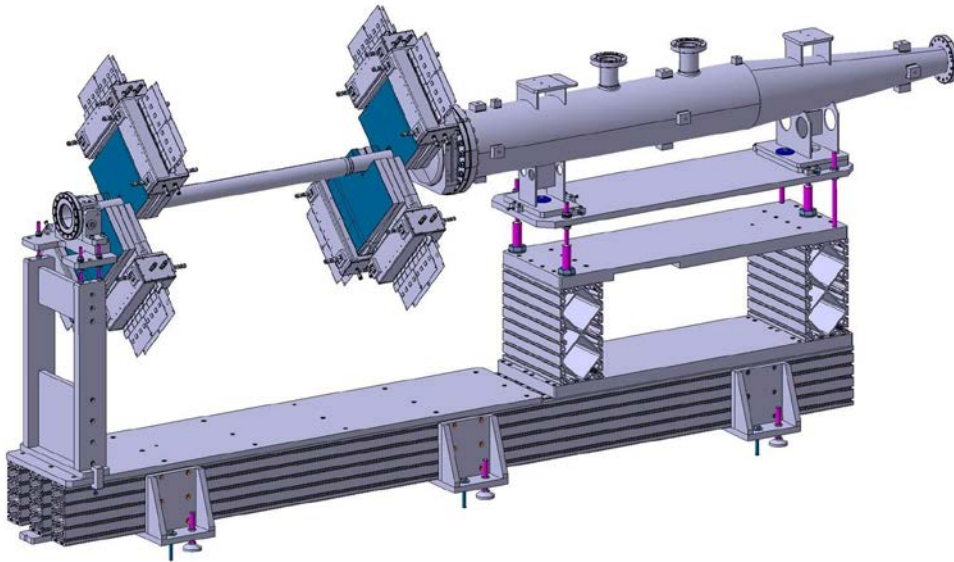
Figure 13-5: The demonstrator Beam Gas Vertex detector installed in the LHC during LS1.

The main subsystems are: a neon gas target at a pressure of 6×10^{-8} mbar, a thin aluminium exit window, tracking detector based on scintillating fibre modules read out by silicon photomultipliers, hardware and software triggers, and a readout and data acquisition system based on that used for LHCb. As the tracking detector is external to the vacuum chamber, no movable parts are needed. The final design of the prototype is shown in Figure 13-5.

A proof-of-principle demonstrator is foreseen for installation on the left side of LHC IP4 on Beam 2 during LS1, with a second system for Beam 1 installed on the right side of IP4 in LS2. A full upgrade of these systems, to include a third detector layer and upgraded electronics, may be required in LS3 to reach the full design goals outlined above. This upgrade is currently not part of the HL-LHC baseline.

13.5 Diagnostics for Crab Cavities

The crab cavities for the HL-LHC are proposed to counter the geometric reduction factor and so to enhance luminosity. These cavities will be installed around the high luminosity interaction points (IP1 and IP5) and used to create a transverse bunch rotation at the IP. The head and tail of each bunch is kicked in opposite directions by the crab cavities such that the incoming bunches will cross parallel to each other at the interaction point. These intra-bunch bumps are closed by crab-cavities acting in the other direction on the outgoing side of the interaction region. If the bumps are not perfectly closed the head and tail of the bunch will follow different orbits along the ring. Monitors capable of measuring the closure of the head-tail bump and any head-tail rotation/oscillation outside of the interaction regions are therefore required.

13.5.1 Bunch shape monitoring using electromagnetic pick-ups

Electromagnetic monitors for intra-bunch diagnostics are already installed in the LHC. These so-called "Head-Tail" monitors mainly provide information on instabilities and have a bandwidth of some 2 GHz. To go to a higher resolution within the bunch a bandwidth of 10 GHz or more is desirable. This will be important to better understand instabilities in HL-LHC and to help with the tuning of the crab-cavities, with several of these systems foreseen for installation around the interaction points. In addition to studies aimed at improving the existing electromagnetic pick-ups, which include optimisation of the pick-up design and the testing of faster acquisition systems, pick-ups based on electro-optical crystals in combination with laser pulses are also being considered [9]. Such pick-ups have already demonstrated fast time response in the picosecond range [10]. Developed mainly for linear accelerators, this technology is now also being considered for circular machines, with a design for a prototype to be tested on the CERN-SPS recently initiated.

13.5.2 Bunch shape monitoring using streak cameras

The use of synchrotron light combined with a streak camera may be an easier alternative to electromagnetic or electro-optical pick-ups for high resolution temporal imaging. Using an optical system to re-image the synchrotron light at the entrance of a streak camera allows the transverse profile of the beam to be captured in one direction (X or Y) with a very fast time resolution (below the picosecond level). Only one transverse axis can be acquired with a given setup, while the other is used for the streaking. Using a sophisticated optical setup it is however possible to monitor both axes at the same time, as was performed in LEP [11].

Streak cameras can be used to observe a number of parameters simultaneously: bunch length, transverse profiles along the bunch, longitudinal coherent motion, head-tail motion etc. The main limitation of the streak camera is the repetition rate of the acquisition, typically < 50 Hz, and the limited length of the recorded sample, given by the CCD size. Double scan streak cameras exist that allow an increase in the record length. By using a CCD with 1000×1000 pixels working at 50 Hz and adjusting the optical magnification and scan speed such that the image of each bunch covers an area of about 100×100 pixels one can record a maximum of 100 bunch images per 20 ms i.e. 5000 bunches per second. This is clearly just an optimistic upper limit with other factors likely to reduce this value.

The longitudinal resolution of around 50 ps required for HL-LHC is rather easy to achieve using streak cameras, where measurements down to the sub-picosecond are now possible. In terms of transverse resolution two distinctions have to be made.

- Measurement of the beam width is affected by diffraction due to the large relativistic gamma of the beam, with the diffraction disk of the same order as the beam size. This will significantly reduce the resolution for such measurements.

- The centroid motion (i.e. the center of gravity) is not directly affected by the diffraction, which produces a symmetrical blur, and therefore the resolution for this type of measurement will be much better.

For determining crab cavity non-closure only the average position along the bunch is of importance and not changes to the beam size. The streak camera should therefore be able to achieve a resolution of a few percent of the beam sigma for this measurement.

Streak cameras are expensive and delicate devices not designed for the harsh environment inside an accelerator. Radiation dose studies are therefore required in order to verify if a streak camera can be installed directly in the tunnel or if, which seems more likely, it has to be housed in a dedicated, shielded, hutch. The latter would imply an optical line to transport the synchrotron light from the machine to the camera, something for which an integration study will be initiated.

Another point to consider is the synchrotron light source. At the moment two synchrotron light telescopes are installed in the LHC, one per beam. These telescopes already share their light amongst three different instruments, the synchrotron light monitor, the abort gap monitor and the longitudinal density monitor, and in the future will also have to accommodate halo diagnostics (see next section). It will therefore be difficult to integrate yet another optical beam line for the streak camera. The installation of additional light extraction mirrors will therefore be necessary to provide the light for the streak cameras. Since the crab cavities are only needed at high energy, dipole magnets can be used as the source of the visible synchrotron radiation for the streak cameras, with no need for the installation of additional undulators which are only required at injection energy, where the dipole radiation is in the infra-red. The best location and corresponding light extraction system for such an additional synchrotron radiation source is currently under study.

13.6   Halo Diagnostics

Population of the beam "halo", i.e. particles in between the beam core and the limits set by the primary collimators, can lead to important loss spikes through orbit jitter at the collimator locations. Measurement of the beam halo distribution is therefore important for understanding and controlling this mechanism. Such measurements are also important to determine the effectiveness of equipment that influences the beam halo, such as hollow electron lenses or long-range beam-beam compensators. Moreover, in the HL-LHC, any failure of a crab cavity module could result in the loss of the halo in a single turn. If the halo population is too high this could cause serious damage to the collimation system or to other components of the machine. In order to fulfil all of these diagnostic requirements for halo observation in the HL-LHC, the final system should be capable of measuring halo populations at the level of 10^{-5} relative to that of the core.

Three techniques are currently being considered for halo monitoring in the HL-LHC:

- the use of high dynamic range cameras combined with apodisation;

- core masking followed by acquisition using standard cameras;

- use of the beam gas vertex detector.

The first two techniques make use of synchrotron light and, as for the streak cameras, may require an additional light source for the final HL-LHC configuration.

13.7   Luminosity Measurement

The measurement of the collision rate at the luminous interaction points is very important for the optimization of the machine. The LHC experiments can certainly provide accurate information about the instantaneous luminosity, but this information is often not available until stable collisions have been established, and is often missing altogether during machine development periods. For this reason simple and reliable collision rate monitors, similar to those now used in LHC, are also needed for HL-LHC.

This measurement is currently obtained by measuring the flux of forward neutral particles generated in the collisions using fast ionization chambers installed at the point where the two beams are separated into individual vacuum chambers. The detectors (BRAN) are installed inside the neutral shower absorber (TAN) whose role is to avoid that the neutral collision debris, and the secondary showers these induce, reach and damage downstream machine components. The luminosity monitors therefore already operate in a very high radiation area, which for HL-LHC is anticipated be a further ten times the nominal LHC value. For this reason the technology chosen for HL-LHC is likely to be based on the radiation hard LHC design [12], with the geometry adapted to the new TAN design. In order to further increase the radiation resistance some current features, such as their bunch-to-bunch capability, may need to be sacrificed and redundancy added.

13.8   Long Range Beam-Beam Compensation

The simulated strong effect of the LHC long-range interactions inspired a proposed long-range beam-beam compensation for the LHC based on current-carrying wires [13]. In order to correct all non-linear effects the correction must be made individually in each high luminosity interaction point, with the wire generating the same integrated transverse force as the opposing beam at the parasitic long-range encounters.
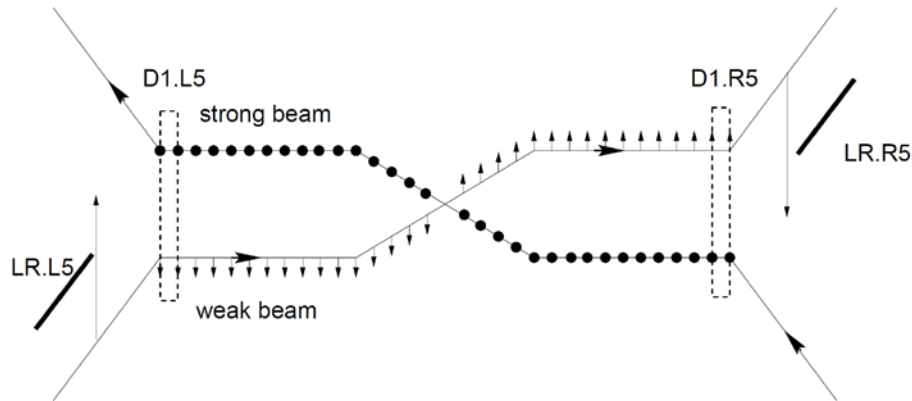
Figure 13-6: Illustration of the compensation principle [13]

The ideal location for compensation of the long-range beam-beam tune-spread is found where the beta functions are equal, there is little phase advance difference with respect to the one between the long-range encounters and the IP, and where the beams are sufficiently well separated. Hence for HL-LHC the proposed layout features compensators placed after the D1 separation dipole in IP1 and IP5 (Figure 13-6). In order to get the compensation correct for all multipoles the transverse location of a wire compensator must be on the inside of the compensated beam, i.e. between the two circulating beams, at a distance equivalent to the average long-range beam-beam separation. This poses significant technical constraints since at the ideal longitudinal position the transverse separation of the beams is only a few centimetres in a region with a high flux of secondary neutrons, and the transverse wire position is only a few mm from the beam. Placing and aligning a "wire" at these locations, in particular in between the two counter-rotating proton beams, will be very difficult. An alternative is to replace the "wire" with an electron beam produced in a manner similar to that of well-established electron coolers (Figure 13-7).
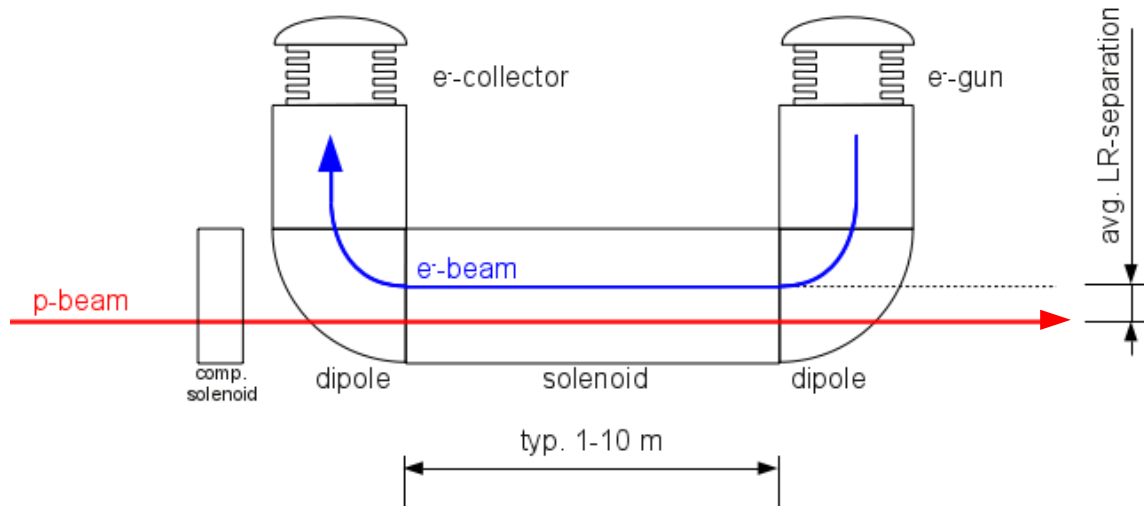
Figure 13-7: Sketch of an electron cooler type layout for long-range beam-beam compensation.

Although such systems have been used for head-on beam-beam compensation at both the Tevatron (FNAL, USA) [14] and RHIC (BNL, USA) [15], the implementation required for HL-LHC is beyond what has been achieved so far. Assuming an effective length of 6m on both sides of the IP an electron beam current of about 15-20 A would be needed, significantly higher than for previous implementations. Compensation with one system per beam in both IR1 and IR5 is also possible, and would reduce the necessary infrastructure by a factor two, but imply electron currents of up to 40 A, almost an order of magnitude larger than what has been achieved so far.

Preliminary simulations and integration studies started to look into the feasibility of such an implementation in the LHC. However, it is clear that such infrastructure could only be installed at the same time as the upgrade of the interaction regions for the HL-LHC, ruling out the possibility to test such a long-range beam-beam compensator beforehand. Since long-range beam-beam compensation has, so far, never been demonstrated at a long-range beam-beam limited machine, it was deemed essential to install a prototype in the LHC as soon as possible. With a test of the electron beam solution ruled out in the short term, a fall-back solution relying on wires will be pursued, with a view to installing a demonstrator in the 2015/2016 end of year technical stop.

13.8.1 Long-Range Beam-Beam Demonstrator

The only solid objects that can approach the beam accurately to within 10σ or less are the LHC collimators. By embedding a wire in such a collimator it would be possible to use the collimator as a host for a demonstrator version of a long-range beam-beam compensator. The best compensation effect in this scenario is obtained by a wire in the tertiary collimators (TCT) located just in front of the D2 magnet. A 1 m long wire at this location would require a DC current of some 180 A at a distance of 9.5σ to the beam or over 200 A at a distance of 11σ. These values correspond to a symmetric layout with one compensator left of the IP and another on the right side, a set-up which will probably be necessary since the ratio of the horizontal and vertical beta functions are not equal at the TCT locations.

Integration of DC powered wires into collimator jaws seems the only possibility to make realistic beam tests before embarking on a final implementation of the wires for the LHC high luminosity operation. This integration itself requires the solution of many important technical issues:

- no interference of the wires with the nominal operation of the collimators;

- transfer of 1 kW resistive heat loss in the wire by heat conduction to the water cooled collimator jaw;

- shielding of the wire from the beam through a thin metallic layer for impedance reasons.

The design of such a wire-in-jaw tertiary collimator is well advanced (Figure 13-8) and the production of 4 such collimators is foreseen to start before the end of 2014. The necessary DC cables and power converted infrastructure has been installed during LHC Long Shutdown 1.

Embedded wire

Cable carrying DC compensation current
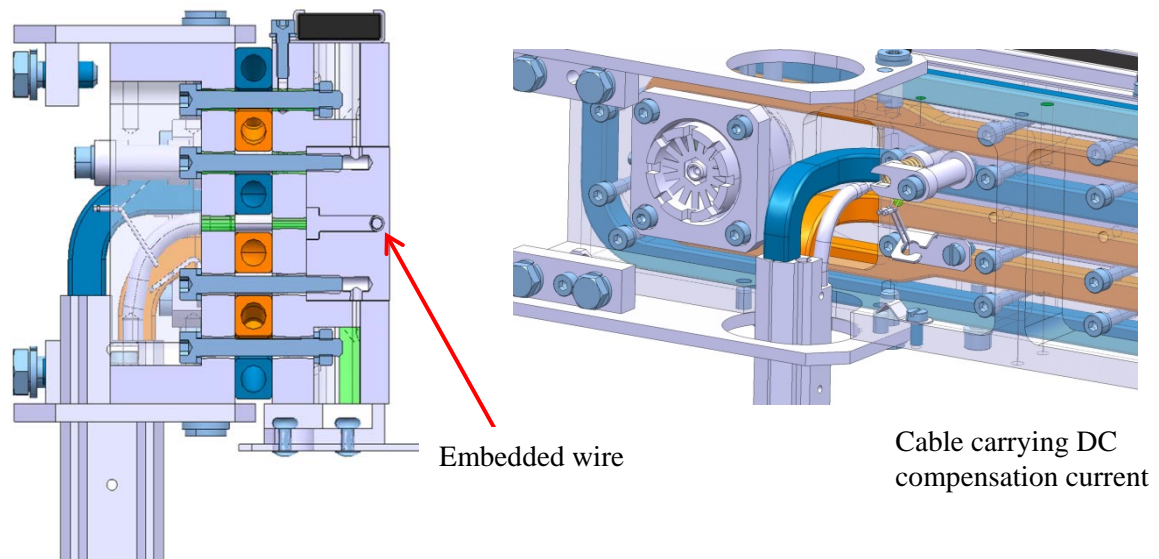
Figure 13-8: Technical drawing of the wire-in-jaw collimator design.

The earliest date at which such collimators equipped with a long-range beam-beam compensation wire can be installed in the LHC is the end of year technical stop 2015/2016. Machine experiments are then planned to validate the coherence of predictions by simulation.

13.9 References

[1] C. Kurfuerst et al. "Radiation Tolerance of Cryogenic Beam Loss Monitor Detectors", 4th International Particle Accelerator Conference, Shanghai, China, 12 - 17 May 2013J.M. Raby, Biophysical aspects of radiation quality, IAEA, Technical Reports Series No. 58 (1966). (

[2] G. Venturini, F. Anghinolfi, B. Dehning, M. Kayal "Characterization of a wide dynamic-range, radiation-tolerant charge-digitizer ASIC for monitoring of Beam losses", Proceedings of IBIC12, Tsukuba, Japan, 2012.

[3] E. Calvo et al, "The LHC Orbit and Trajectory System", Proceeding of DIPAC03, Mainz, Germany, 2003, 187.

[4] A. Nosych et al, "Electromagnetic Simulations of an Embedded BPM in Collimator Jaws", Proceeding of DIPAC11, Hamburg, Germany, 2011, 71.

[5] M. Gasior, J. Olexa, R.J. Steinhagen, "BPM electronics based on compensated diode detectors - results from development systems", CERN-ATS-2012-247. Proceeding of BIW12, Newport News, Virginia, USA, 2012.

[6] A. Nosych et al, "Electromagnetic Simulations of an Embedded BPM in Collimator Jaws", Proceeding of DIPAC, Hamburg, Germany, 2011, 71.

[7] B. Dehning et al, "Vacuum Actuator and Controller Design for a Fast Wire Scanner", Proceedings of IBIC12, Tsukuba, Japan, 2012.

[8] LHCb Collaboration, "Absolute luminosity measurements with the LHCb detector at the LHC", J. Instrum. 7 (2012) P01010, IOP and SISSA.

[9] M.A. Brubaker et al, "Electro-Optic Beam Position and Pulsed Power Monitors for the Second Axis of DARHT", Proceedings of PAC01, Chicago, USA 2001, 534.

[10] Y. Okayasu et al, "The First Electron Bunch Measurement by Means of Organic EO Crystals", Proceedings of IBIC12, Tsukuba, Japan, 2012.

[11] E. Rossa, "Real time single shot three-dimensional measurement of picosecond photon bunches", 6th Beam Instrumentation workshop, Vancouver, British Columbia (Canada), 3−6 Oct 1994

[12] J.F. Beche, A. Ratti, et. al, "Rad hard luminosity monitoring for the LHC", Proc. EPAC06, Edinburgh, Scotland, June 2006.

[13] J.-P. Koutchouk, "Principle of a Correction of the Long-Range Beam-Beam Effect in LHC using Electromagnetic Lenses," LHC Project Note 223 (2000).

[14] F. Zimmermann, P. Lebrun, T. Sen, V. Shiltsev, X.L. Zhang, "Using the Tevatron Electron Lens as a Wire and Other TEL Studies at FNAL," CERN AB-Note-2004-041 (2004).

[15] W. Fischer, R. Calaga, U. Dorda, J.-P. Koutchouk, F. Zimmermann, V. Ranjbar, T. Sen, J. Shi, J. Qiang, A. Kabel, "Observation of Long-Range Beam-Beam Effect in RHIC and Plans for Compensation," EPAC'06 Edinburgh (2006).

Chapter 14

Injection and Dumping Systems

B.Goddard[5], A.Lechner[5], J.Uythoven[5]
[5]CERN, Accelerator & Technology Sector, CH-1211, Geneva, Switzerland

14   Injection and Dumping Systems

14.1   Injection and dumping systems overview

The beam transfer into the LHC is achieved by the two long transfer lines TI 2 and TI 8, together with the septum and injection kicker systems, plus associated machine protection systems to ensure protection of the LHC elements in case of mis-steered beam. The LHC is filled by approximately 10 injections per beam. The MKI kicker pulse length consists of an 8 μs flat top, with a rise time of 0.9 μs and a fall time of 2.5 μs. Filling each ring takes 8 minutes with the SPS supplying interleaved beams to other facilities. The foreseen increase in injected intensity and brightness for the HL-LHC means that the protection functionality of the beam-intercepting devices needs upgrading, see Ref. [1]. In addition the higher beam current significantly increases the beam induced power deposited in many elements, including the injection kicker magnets in the LHC ring.

The beam dumping system is also based on DC septa and fast kickers, with various beam intercepting protection devices including the beam dump block. Again, the significant change in the beam parameters for the HL-LHC implies redesign of several of the dump system devices, because of the increased energy deposition in the case of direct impact, but also because of increased radiation background which could affect the reliability of this key machine protection system [1].

In the following sections the changes planned in the light of the HL-LHC for the different LHC beam transfer systems are described.

14.2   Injection systems

The high injected beam intensity and energy mean that precautions must be taken against damage and quenches, by means of collimators placed close to the beam in the injection regions. The layout of the injection region and associated protection devices is shown schematically in Figure 14-1. The beam to be injected passes through 5 horizontally deflecting steel septum magnets (MSI) with a total deflection of 12 mrad, and 4 vertically deflecting kickers (MKI) with a nominal total kick strength of 0.85 mrad. Uncontrolled beam loss resulting from errors (missing, partial, badly synchronised or wrong kick strength) in the MKI could result in serious damage of downstream equipment in the LHC injection regions, in particular the superconducting separation dipole D1, the triplet quadrupole magnets near the ALICE or LHCb experiments, or in the arcs of the LHC machine itself. Damaging detector components, in particular those close to the beam pipe, with excessive showers generated by lost protons is also possible.
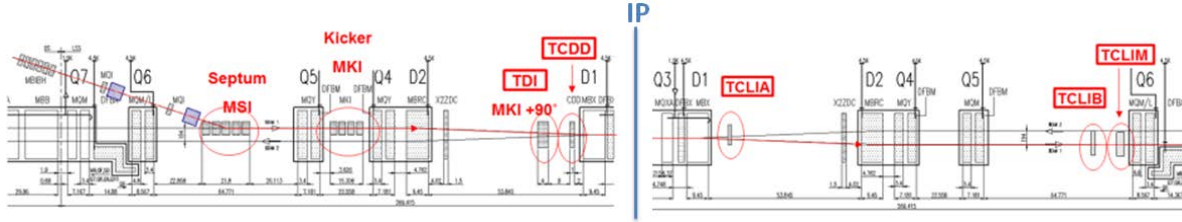
Figure 14-1: Overview of the present injection system into the LHC and the associated protection devices (Beam 1, IR2). The beam is injected from the left hand side.

14.2.1 Injection absorber [TDIS]

The TDI is a movable two-sided absorber. Its purpose is to protect machine elements in case of MKI malfunctions and to intercept low intensity bunches during set-up or commissioning of the injection system. The present TDI, see Ref. [2], needs to be adapted to HL-LHC and LIU beam parameters. This implies a change of the absorber materials but no significant change to the total absorber length. In addition, problems with the present design have become apparent during the first years of LHC operation. Instead of having one long jaw (4.185 m) as in the present TDI, the new TDIS (where the S stands for Segmented) is foreseen to comprise shorter absorbers accommodated in separate tanks, which would imply an increase in the total length.

The above stated protection objective concerns both mis-deflections of the injected beam due to MKI faults as well as accidental kicks of the stored beam due to MKI timing errors. In the first of these cases, too little or zero kick strength causes the incoming beam to impact the upper TDIS jaws. In the second case, the mis-kicked stored beam impacts the lower TDIS jaws. The protection objectives should be met for any impact condition, including cases where beams are swept over the aperture (mis-fires during MKI rise-time) or where a full batch is grazing the TDIS jaws due to a non-nominal MKI kick strength. The maximum possible impact parameter (vertical distance between equilibrium orbit and impact position) on the absorber front face is estimated to be 3 cm. The largest energy deposition in downstream magnets and the highest stresses in the jaw itself are expected for small impact parameters (around 1-2σ, which is about 1 mm from the absorber edge) which could occur in the case of a magnet breakdown. New low-Z absorber materials, replacing the boron nitride (BN5000, 1.93 g/cm^3) used for the present TDI, are under study.

If the above stated protections objectives cannot be met for a full injected beam of 288 bunches, the total number of injected bunches will need to be decreased accordingly. This has to be done in conjunction with a reduction of the MKI pulse length in order to limit the number of circulating bunches that could be mis-kicked onto the TDIS in case of a timing error.

Apart from the aperture requirements for circulating and injected beams that are identical to the present TDI, see Ref. [2], there are additional aperture requirements coming from the ALICE ZDC, Ref [3].

The jaw positioning requirements are listed in Table 14-1. Jaws at fully closed positions will be required during optimisation of the injection systems. A fully open position is important to reduce beam impedance, and thus reduce heating when not injecting beam. The positions given are relative to the closed orbit, which nominally includes the separation and crossing bumps.

Table 14-1: **TDIS position relative to the orbit.**

Characteristics	Units	Value
Position fully closed	mm	1.0
Typical position during injection	mm	± 3.8
Position when no injection	mm	± 55.0

The beam impedance should be minimised during the injection process (absorber blocks close to the beam) and when injection is finished and the jaws are retracted (absorber blocks in parking position). The resulting beam impedance should be acceptable from the beam stability perspective and in terms of the deposited power in the TDIS. If necessary water cooling of the absorbers, will need to be installed.

The correct positioning of the TDIS is a vital element of the machine protection system during injection. Redundant position measurement of the blocks is required with redundant interlock channels going to the beam interlock system (BIS). Both LVDT and laser interferometric position measurements are foreseen. A Beam Energy Tracking System (BETS) to guarantee the correct position at injection energy is foreseen and will use the laser interferometric position readings. For a multi-module TDIS system the correct alignment with beam between the different modules will be very important, as is illustrated by Figure 14-2.

The new TDISs will be approximately at the same position as the present TDIs, as they need to be at 90° betatron phase advance relative to the MKIs. The extension of the TDIs is to take place in the upstream direction, keeping the distance between the downstream end of the TDI and D1 unchanged. For IP2 this means that the large 800 mm chamber upstream of the TDI needs to be shortened. This has been discussed with the ALICE experiment and is acceptable as long as a minimum opening position is guaranteed when jaws are retracted.
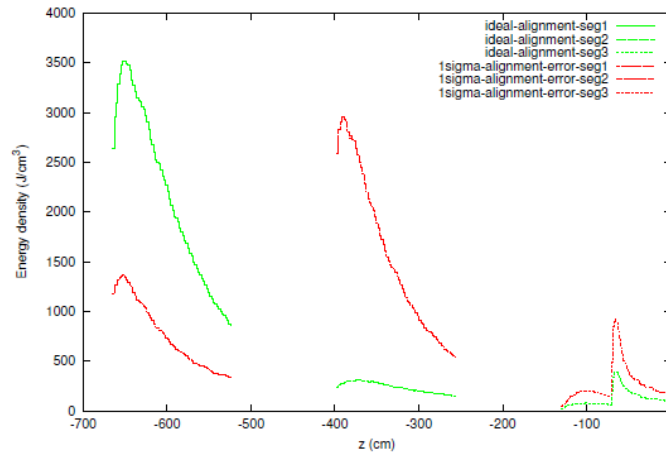
Figure 14-2: Energy deposition in a TDIS consisting of three modules (graphite, graphite and aluminium / copper) for grazing beam impact and showing the effect of a 1σ alignment difference between the first and second module (courtesy N. Shetty).

14.2.2 Auxiliary injection protection collimator [TCLIA]

The TDIS will be complemented by two auxiliary collimators TCLIA and TCLIB, which are located on the other side of the IP, at phase advances which are designed to be ± 20° (modulo 180°) relative to the TDI. The position of these auxiliary absorbers is shown in Figure 14-1. The TCLIA is a two-sided auxiliary injection protection collimator located between the separation dipoles in IR2 (right side) and IR8 (left side). Owing to its position close to the D1, the TCLIA also hosts the other circulating beam. Together with another auxiliary collimator (TCLIB) it complements the primary injection protection

absorber TDIS in case of injection kicker (MKI) failures. The present TCLIA consists of low-Z absorber blocks (graphite R4550, 1.83 g/cm^3) with a total active length of 1 m. It is being evaluated if the present TCLIA design, in particular the absorber material, can be retained for the HL-LHC era or if a new design is required due to the increased beam brightness. In addition, it is to be determined if the present TCLIA design is compatible with aperture requirements imposed by the ALICE ZDC (Ref. [3]) operation during heavy ion physics runs. If the present aperture is found to be incompatible, a new design with a larger stroke for the open position will be required.

In case of beam impact on the TCLIA, no damage must occur to downstream machine elements, in particular to the superconducting separation dipole D2. However a quench of magnets can not be excluded for all MKI failure scenarios. In all cases, the TCLIA itself must not sustain damage during injection failures.

The TDI and TCLI elements need to protect the LHC arc aperture from mis-steered beams. Tracking studies showed that settings of 6.8 σ for the TDI and TCLI systems adequately protect the LHC arc aperture against MKI flashovers, see Ref. [4]. This result depends on the injected intensity, and it may be necessary to reduce the 6.8 σ settings slightly for injection of higher intensity beams - this needs to be analysed in the context of the beam cleaning collimation system settings for injection. Auxiliary injection protection collimator [TCLIB]

The TCLIB is a two-sided auxiliary injection protection collimator located between the matching section quadrupoles Q5 and Q6 in IR2 (right side) and IR8 (left side). Together with the already described auxiliary collimator TCLIA it complements the primary injection protection absorber TDIS in case of injection kicker failures. The present TCLIB accommodates low-Z absorber blocks (CfC AC150, 1.67 g/cm^3) with a total active length of 1 m. It is complemented by a mask in front of Q6 (TCLIM) which is required to absorb secondary showers from the TCLIB such that damage to the Q6 and other downstream equipment is prevented. It is to be evaluated if the present TCLIB design, in particular the absorber material, can be retained for the HL-LHC era or if a new design is required due to the increased beam brightness.

Depending on the injection kicker strength, badly injected beam will be absorbed by the TDIS, TCLIA or TCLIB. It is shown in Figure 14-3 that TCLIB intercepts up to 28 % of the 5 σ area of single particle emittance for injection kicker failures with ± 10 % kick nominal strength, which corresponds to a grazing incidence of the beam on the TDIS.
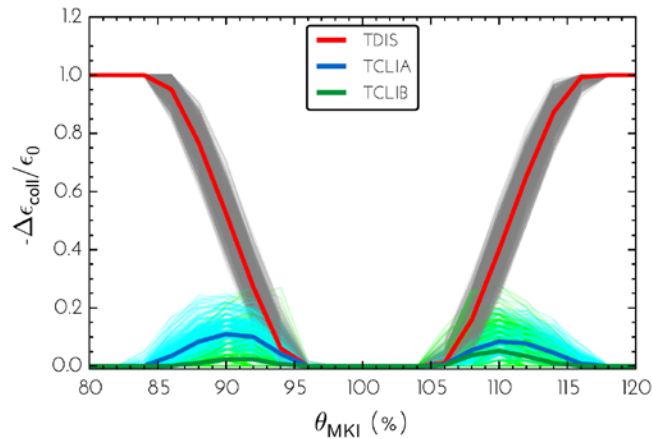
Figure 14-3: Fraction of five sigma single particle emittance absorbed by the different injection protection absorbers TDIS, TCLIA or TCLIB for different injection kicker amplitudes (courtesy F.M. Velotti).

14.2.3 Injection protection masks [TCDD] & [TCDDM]

The TCDD and TCDDM are masks upstream of the superconducting D1 in IR2 (left) and IR8 (right), which complement the primary injection protection absorber TDIS in case of injection kicker malfunctions, see Figure 14-1. The masks are 1 m long Cu blocks, which in IR2 are required to open for ALICE ZDC data-taking during ion runs. The TCDD/TCDDM is required to sufficiently absorb secondary showers or scattered protons from the TDIS such that it prevents damage to the D1 and other equipment for any possible TDIS impact conditions and for all HL-LHC and LIU beam parameters. In IR2, any new design or new mask position must account for ALICE ZDC aperture requirements. The aperture of the present TCDD/TCDDM might need to be further minimised to protect the D1 against particle showers from the high intensity beams grazing the TDIS absorber. The aperture requirements for the circulating beam and damage limits of the D1 separation dipole are important parameters to be taken into account.

14.2.4 Injection protection mask [TCLIM]

The TCLIM is a fixed mask upstream of the superconducting matching section quadrupole Q6 in IR2 (right side) and IR8 (left side). It presently consists of 1 m active length made of stainless steel. In case of injection kicker malfunctions leading to beam impact on the auxiliary injection protection collimator TCLIB, the mask is required to absorb secondary showers from the TCLIB such that it prevents damage to the Q6 and other downstream equipment. The protection has to be ensured for all HL-LHC and LIU beam parameters. It is to be evaluated if the present TCLIM design can be retained or if a new design is required, possibly with a different length and material.

14.2.5 Injection kicker magnet [MKI]

The injection kicker magnets MKI installed in IR2 and IR8, see Figure 14-1, deflect the injected beam onto the LHC closed orbits. During Run 1 of the LHC a number of issues have been encountered with the MKI magnets installed prior to LS1 these include beam induced heating of the ferrite yoke; inefficient cooling of the ferrite yoke; electrical flashovers; beam losses due to macro particles falling into the beam; and electron cloud [5, 6].

If the ferrites of the injection kicker magnets reach a temperature above their Curie temperature their magnetic properties are compromised and the beam cannot be injected. Reducing beam induced heating, additional cooling and/or ferrites with a higher Curie temperature avoids waiting periods without beam before the beam can be injected into the LHC. A reduced magnetic field of the injection kickers is also a machine protection issue, possibly leading to quenches of downstream magnets. The beam impedance of the MKI magnets has been reduced in LS1 by completing the number of beam screen conductors to 24, see Figure 14-4. However it cannot be guaranteed that this will sufficiently reduce beam induced heating for HL-LHC operation. Operational experience during Run 1 has shown that a beam power deposition of about 160 W/m occasionally limited the ability to inject beam. The present power deposition estimate for HL-LHC beams is 190 W/m, assuming the improved beam screen as installed in LS1. For this reason a proto-type MKI magnet with additional cooling and different ferrite types will be developed for testing in the LHC. A ferrite such as CMD10, which has a higher Curie temperature than the CMD5005 or 8C11 presently used for the MKI yoke, would permit high-intensity beam operation with better availability. However, operating at higher yoke temperatures will result in higher pressure in the vacuum tank, which may result in an increased electrical breakdown and surface flashover rate. Further optimisation of the capacitively coupled end of the beam screen are being made to further reduce the electric field strength and so the likelihood of surface flashovers.

The exchange of an MKI during the third technical stop (TS3) of 2012, and its subsequent operation in the LHC, demonstrated that electron cloud in the ceramic tube can limit the beam intensity until conditioning had occurred (~250 hours of beam). Electron cloud in the ceramic tube results in a pressure increase and therefore can prevent operation of the injection kickers. A low SEY coating would

eliminate multipactoring, and thus the related pressure rise, permitting more reliable operation of the injection kickers. Thus research and development of special coatings for the inner surface of theceramic tube is being carried out and it is planned to include a coating on the tube of the prototype MKI.

After a comprehensive study program in 2011, the macro particles causing beam losses around the MKIs were identified as fragments originating from the ceramic tube inside the MKI magnets [7]. Thus the ceramic tube of MKI8D installed during TS3 was subject to improved cleaning, which included iterations of flushing of the inside of the tube with N_2 at 10 bar and dust sampling, until no significant further reduction of macro particles was noted. Before TS3, MKI8D exhibited the highest rate of beam-dust particle interactions of all MKIs in P8; the replacement MKI8D, in operation after TS3, exhibited the lowest rate. Extensive additional cleaning was carried out on the ceramic tubes installed during LS1.

The modification of the series of MKI magnets is not part of the HL-LHC baseline. The necessity of the described changes for the series of magnets depends on the performance of the magnets installed in LS1 and the final beam parameters to be used for the HL-LHC beams (especially the bunch length). The installation of a proto-type magnet to test the developed technologies is foreseen.
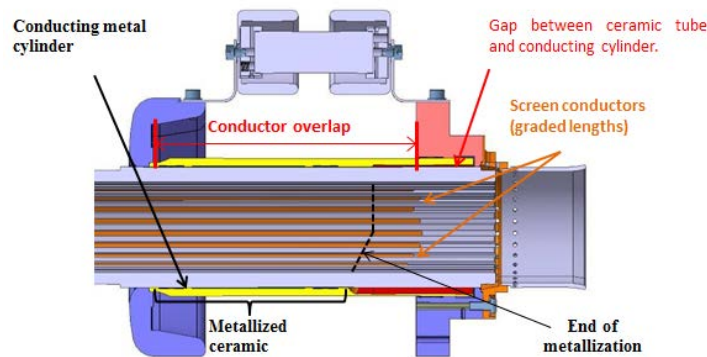
Figure 14-4: View of the capacitively coupled extremity of the MKI beam screen supporting the 24 screen conductors and the conductor overlap (courtesy M.J. Barnes).

14.3 Beam dumping system

The beam in the LHC is aborted or dumped by a dedicated system based on pulsed extraction kickers and DC septum magnets located in the dedicated insertion in Point 6, followed by a dilution kicker system MKB, a long drift chamber and a graphite beam dump absorber block (TDE) kept under N_2 gas at atmospheric pressure. The 3 μs rise time of the extraction kicker field is synchronized by a highly reliable timing system to a beam-free abort gap in the circulating bunch pattern. The horizontal and vertical dilution kickers are powered with anti-phase sinusoidal currents in order to paint the bunches onto the TDE with an elliptical shape, see Figure 14-5.
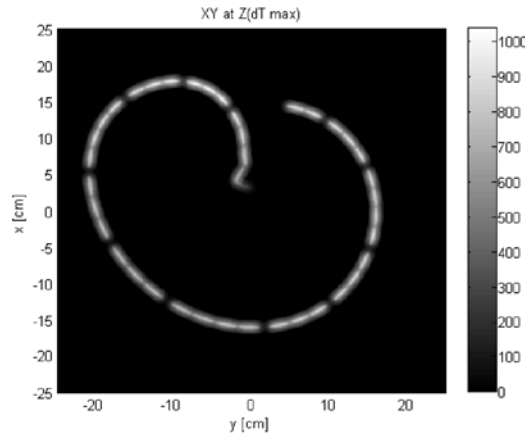
Figure 14-5: Sweep form of 25 ns spacing LHC beam on TDE dump block with a bunch intensity of 1.7×10^{11} protons per bunch and the resulting temperature rise.

14.3.1 Beam dumping system limitations

The LHC beam dump block TDE and its entrance window [8, 9] will need to withstand the high intensity HL-LHC beams. Simulations are foreseen to verify if the present system can withstand the repeated beam impact of these beams. Concerns are the temperature rise of TDE block which could lead to a venting of the overpressure of nitrogen within the TDE. Another concern is the entrance window of the TDE. As a possible solution it could be required to install additional dilution kicker magnets on the beam dump lines TD62 and TD68.

As the performance mentioned above can possibly be met by the existing system, any modifications are not part of the present baseline.

14.3.2 Beam dumping system absorber [TCDS]

Several failure modes exist in the synchronization system and in the kicker switches which could lead to an asynchronous dump, in which the full beam intensity would be swept across the LHC aperture by the rising kicker field. Without dedicated protection devices this would lead to massive damage of the LHC magnets in LSS6 and the downstream arcs 5-6 and 6-7, and depending on the operational configuration a number of collimators and possibly experimental triplet magnets. The protection devices against asynchronous beam dumps are shown in Figure 14-6: the TCDS is a fixed absorber which protects the downstream extraction septum MSD and the TCDQ is a movable absorber which together with the secondary collimator TCS protects the superconducting quadrupole Q4 and further downstream elements, including the arc. The increased beam intensity and brightness for HL-LHC requires a redesign of the TCDS and TCDQ absorbers.

An upgraded TCDQ will already be installed before LHC Run 2. The new design, which is described in detail in Ref. [10], includes an extension of the absorber length from 6 to 9 m, and the replacement of the higher density graphite absorber material by different grades (1.4 and 1.8 g/cm^3) of carbon fibre composites (CfC). The energy deposition and induced thermal stresses then remain acceptable during an asynchronous abort and the protection of the Q4 and downstream elements remain sufficient, with a maximum energy density in the magnet coils of around 20 J/cm^3. The TCS collimators will be upgraded with integrated button BPMs in the jaws, which should allow faster and more accurate setup.

A similar level of redesign will be needed for the TCDS absorber. There is one TCDS system, presently consisting of two units, per beam. The robustness of the present TCDS and the protection of the MSD magnets in the case of an asynchronous beam dump with full intensity HL-LHC beams need

to be verified and the absorber material and/or length need to be adapted if necessary. Any additional length will reduce slightly the aperture for the circulating or extracted beams, by a small fraction of a sigma, which should be acceptable.

A further upgrade of the TCDQ is not part of the HL-LHC baseline, an upgrade of the TCDS is.
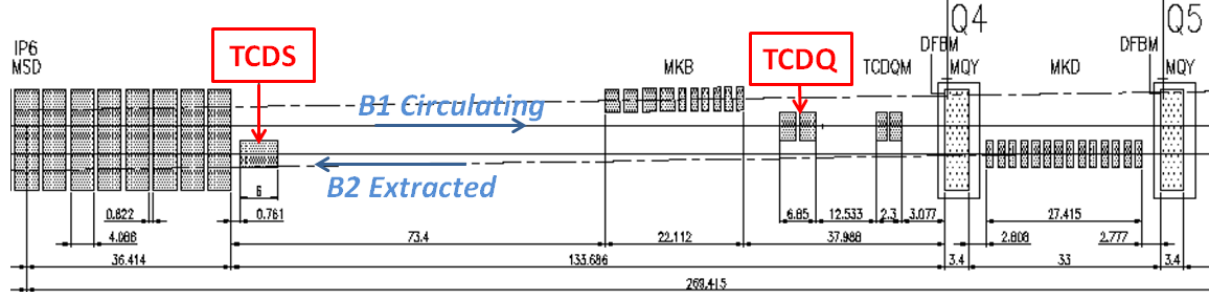
Figure 14-6: Schematic layout of the beam dump area right of Point 6 as used during LHC Run 1, showing the extraction absorber element TCDS on Beam 2 and the TCDQ on Beam 1.

14.4   References

[1] J.Uythoven et al., Upgrades to the injection and beam dumping systems for the HL-LHC project, proc. Of IPAC14, MOPRO032, http://www.JACoW.org, 2014.

[2] B.Goddard, V.Kain, M.Lamont, Function and operating conditions of the TDI Beam Absorber, Functional Specification, 25-11-2004, edms no. 508735, 2004.

[3] ALICE collaboration, The zero degree calorimeters for the ALICE experiment, CERN-ALICE-PUB-99-17, 1999.

[4] V.Kain et al., The expected performance of the LHC injection protection system, EPAC'04; 9th European Particle Accelerator Conference 2004.

[5] M.J.Barnes et al., Upgrade of the LHC Injection Kicker Magnets, proc. Of IPAC13, MOPWA030, http://www.JACoW.org, 2013.

[6] T. Baer et al., UFOs: Observations, Statistics and Extrapolations, Proc. LHC Beam Operation workshop, Evian, 17-20 December 2012.

[7] B.Goddard et al., Transient beam losses in the LHC injection kickers from micron scale dust particles, IPAC'12, TUPPR092, http://www.JACoW.org, 2012.

[8] J.Zazula and S.Peraire, LHC beam dump desing study: 1, simulation of energy deposition by particle cascades; implications for the dump core and beam sweeping system, CERN-LHC-Project_Report-80, 1996.

[9] B.Goddard et. al., A large diameter entrance window for the LHC beam dump line, LHC Project Report 823, 2005.

[10] R.Versaci, B.Goddard, V.Vlachoudis, LHC asynchronous beam dump: study of new TCDQ model and effects on downstream magnets, CERN-ATS-Note-2012-084-MD, 2012.

Chapter 15

Integration & (De-)installation

P. Fessia[5] , S. Weisz[5]
[5]CERN, Accelerator & Technology Sector, CH-1211, Geneva, Switzerland

15   Integration & (De-)installation

15.1   HL-LHC the geographical distribution of the upgrade interventions

HL-LHC will require modifying the machine and infrastructure installations of the LHC in several points along the ring. In particular:

- Point 4

- Point 7

- Point 2

- Point 6

- Point 1

- Point 5

While the equipment in Point 1, Point 5 and Point 6 are meant to be installed during LS3 (Long Shutdown 3), the modifications and improvement in Point 4, Point 7 (as far as the superconducting links are concerned) and Point 2 shall be completed during the LS2 and be operational for the LHC Run III. Below we list the activities required Point by Point according to the presently foreseen chronological order. Point 8 will have minor modification during LS2, not considered here.

15.2   Point 4
In Point 4 will be equipped with a new cryogenic plant dedicated to the RF systems (and other cryogenic equipment that might be installed in IR4) [Paragraph 9.5]. The installation will require:

- Surface: installation of the warm compressors systems in the SU4

- Junction surface to the underground cavern via the PX46

- Underground: installation of the cold box in the TX46. See Figure 15-1

- Connection between the cold box and the QRL via the UX45

- QRL modification between -25 m to +25 m around IP4
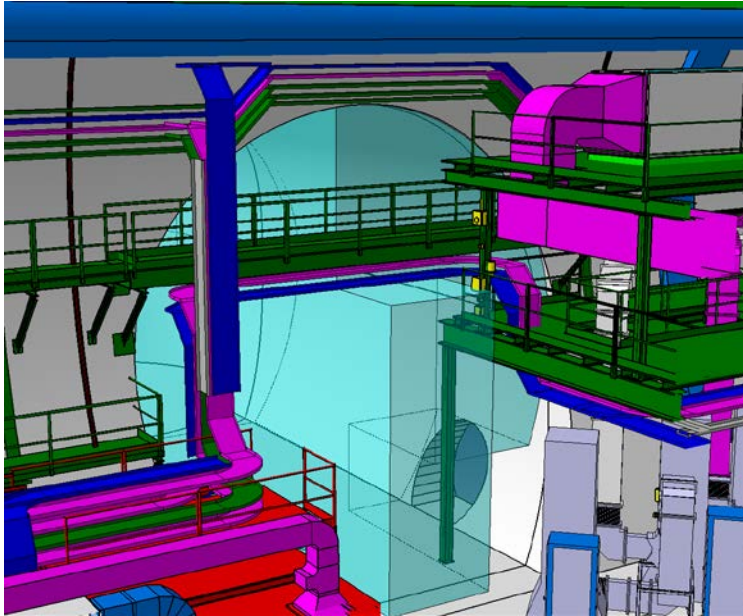
Figure 15-1: **Volume reserved for the installation of the new cold box unit dedicated to RF system cooling. In light blue**

The solutions presently adopted make the maximum use of existing volumes, requiring very limited civil engineering work, mainly devoted to the routing of the piping from the SU4 to the SX4 and to the vertical wall of the PX46.

The whole system installation shall be completed for the end of LS2.

Figure 15-2 provides a schematic of the Point 4 buildings
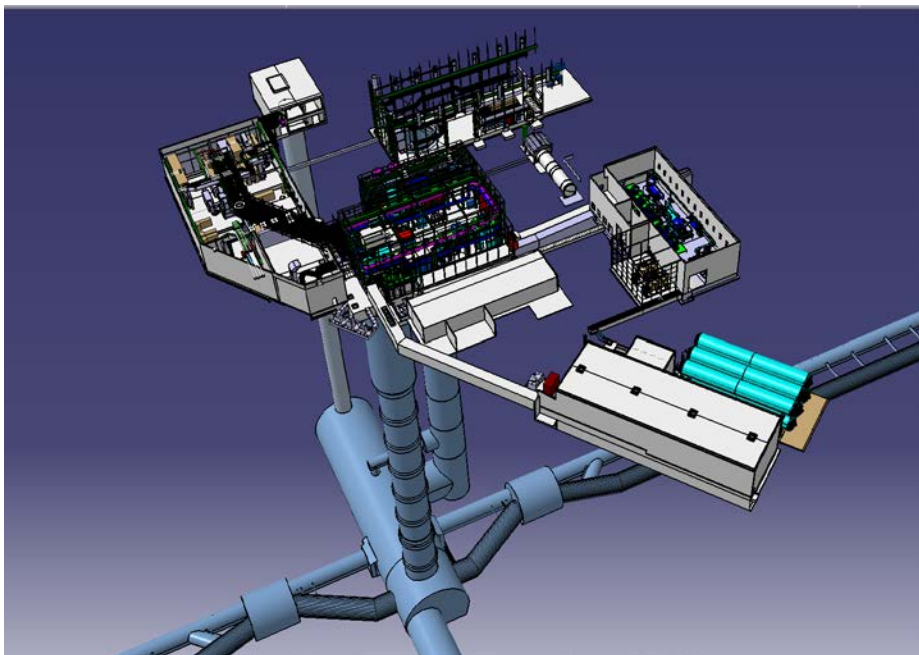
Figure 15-2: **View of the LHC civil works at Point 4**

15.3 Point 7

15.3.1 The Horizontal Superconducting Links

In Point 7 two horizontal SC links will be installed in order to electrically feed the 600 A circuits connected to the 2 DFBAs (DFBAM and DFBAN). The related power converters will be installed in the TZ76 and via short warm cables will be connected to the superconducting link. The two superconducting links will then run for about 220 meters in the TZ76 and then enter into the LHC machine tunnel via the UJ76. They will then be routed for about 250 m in the LHC tunnel in order to be connected to the DFBAM and DFBAN (Figure 15-3). The whole installation shall take place during the LS2; no long access is available before. Possibilities to advance part of the interventions in the EYETS shall be evaluated and the radiological cooling time shall be accounted for the preparation of the interventions in the LHC tunnel. Some preparatory work has been performed already during LS, in particular the removal of the chill water pipes. This system was not of use in Point 7 and its dismantling has made available space to be used for the SC link installation.

In order to perform the installation of the SC links in the LHC tunnel the need of de-installing part of the present equipment (for sake of precaution to avoid possible damages) still needs to be fully assessed.
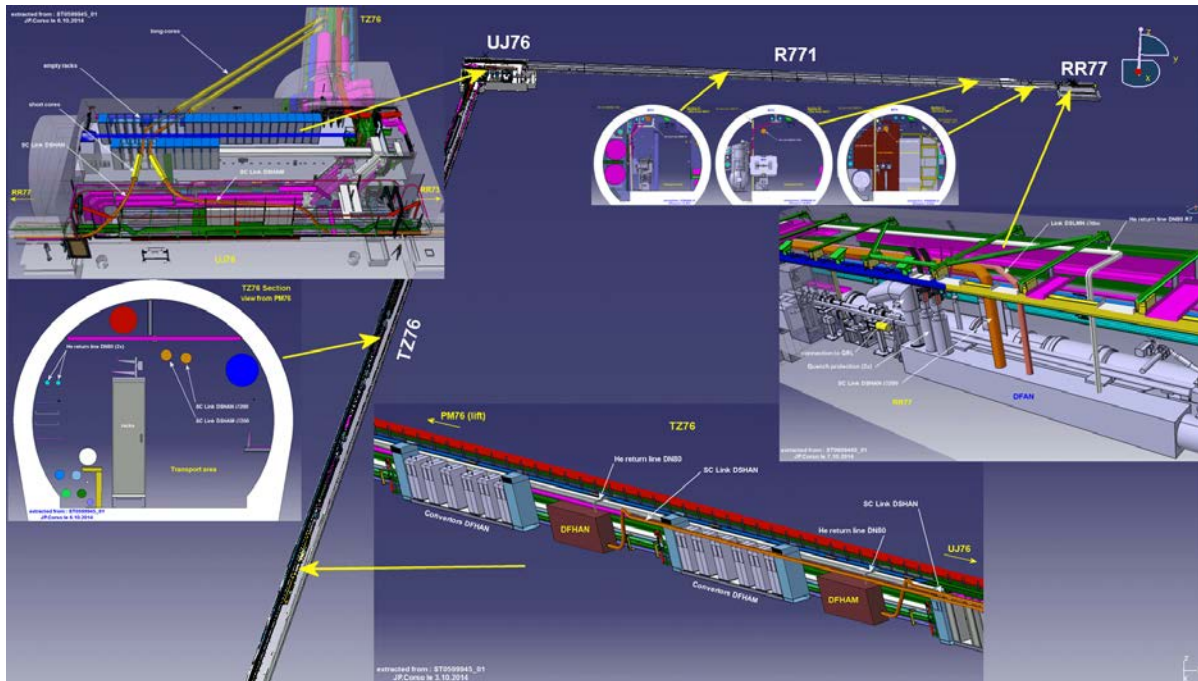
Figure 15-3: View of the foreseen installation of the Superconducting link system at point 7. Power Converters in the TZ76, routing of the link from the TZ76, via the UJ76 till the RR 77

15.3.2 New collimators in the Dispersion Suppressor

In order to protect the superconducting magnets (excess heat deposition) from off-momentum proton leakage from the main collimator system itself, some special collimators must be installed in the Dispersion Suppression region, i.e. in the continuous cryostat. The evaluation of the real need of this modification will be completed on the base of the first results of the LHC Run II. Unless RunII shows dramatic and unexpected, results, the installation will eventually take place during the LS3.

In order to cope with the proton losses in the Dispersion Suppressor area it has been decided to install two collimators on each side of the IP. In order to do so it will be necessary to

- De-install the MB.B8L7 plus the MB.B10L7 and the symmetric MB.B8L7 plus the MB. B10L7

- Substitute each removed dipole by a unit composed of two 11 T dipoles [Chapter 11] separated by a cryogenic by-pass.

- Install on the top of the cryogenic by-pass the collimator [Paragraph 5.2.2]

The magnet installation will probably require also a new dedicated quench protection system and a trim circuit with its own power converter. The location and the installation approach for this equipment are still under evaluation, but very probably it will be located in the nearby RR

15.4 Point 2

In order to limit the heat deposition from collision debris in the superconducting magnets during the ion run, collimators in the dispersion suppressor will also be installed in Point 2 [Paragraph 5.2.1 and 5.9]. In this case the installation will take place only in one slot on each side of the IP replacing the MB.A10L2 and MB.A10R2. This equipment is necessary for the LHC Run III with ions, to allow Alice to fully profit of the upgrade carried out during LS2. Therefore the installation of the unit composed by the 11 T dipoles and the cryo-bypass needs to be completed during LS2. The collimator itself can be assembled at the same time or later in a short technical stop or in a YETS (Year End Technical Stop). All the other issues listed in Paragraph 15.3.2 are applicable, but the proximity services will be probably installed in the UAs.

15.5 Point 6

In Point 6 the two magnet quadrupoles Q5 will be modified in order to fulfil the needs of the new HL-LHC ATS optics. Two options are presently under evaluation leading either to the exchange of the present Q5 with a new Q5 or the installation of Q5-bis near the currently operated Q5. Both options will require the local reshuffling of the vacuum lay-out and possible modifications of the QRL.

The intervention in Point 6 is required to be completed in LS3, but options to anticipate it in LS2, both to limit the amount of work during LS3 and to reduce personnel exposure to radiation due to the proximity to the bam dump line, are under study.

15.6 Point 1 and Point 5

The largest part of the new equipment, required by the HL-LHC performance objectives, will be installed in Point 1 and Point 5. The items to be installed and actions to be carried out are listed below and are applicable to both points if not otherwise specified. The list is organised by geographical areas.

15.6.1 LHC machine tunnel

- De-installation:
  o All the machine equipment from the interface with the experimental cavern (TAS included) till the DFBA (included) need to be removed.

  o The present QRL will be removed in the same area. A new return module will be installed in the ex-DFBA area in order to allow separating the flows of the coolant coming from the LHC QRL and the one of the new HL-LHC QRL that will feed the part of the machine from the Q1 to the Q6. This return module should also provide the possibility, in case of need, to connect the LHC QRL with the newly installed one, ensuring an increased level of redundancy in the system.

  o Services linked to the above de-installed equipment will be removed and new ones shall be installed

    − Preparation for re-installation

- o Minor works could be necessary in order to prepare the tunnel floor and wall to receive the installation of the new equipment (for larger and dedicated civil engineering works as described later).

- Installation

  - o Installation of the new equipment probably in the following sequence:

    - TAXS

    - Services

    - QRL with related valve and service modules

    - Horizontal superconducting links from the DFM to the magnets to be fed

    - Magnets and crab cavity support system

    - Magnets and crab cavity

    - Distribution feed boxes for the Q1 to D1 magnet system (DFX) and for the D2 to Q6 magnet system (DFM)

The sequence of installation of the vertical superconducting links to be connected to the DFX and DFM still need to be assessed according to the options retained for its routing.

In addition to the interventions described above, it may be necessary to strengthen the collimation system with new collimators in the dispersion suppressor as it has been described for Point 7 in 15.3.2.

15.6.2 Existing LHC tunnel service areas

The RRs on both sides of Point 1 and Point 5 will need to be re-organised and in particular it will be necessary to:

- De-install the power converter and other related systems (i.e. quench detection system) linked to the powering of the removed LHC matching section

- Re-organise the remaining equipment in order to have the most efficient space occupation, increase if necessary the radiation shielding and place the most radioactive sensitive equipment in the most protected areas. Possible equipment replacement with new radiation-hard elements can be envisaged.

At present no civil work interventions are foreseen in the RRs areas

15.6.3 New HL-LHC tunnel service areas

The installation of the new cryogenic plant in Point 1 and Point 5 will have two objectives:

- Provide independent and redundant cooling capacity to feed the final focus and matching sections left and right of each of the two High Luminosity insertions of the LHC.

- Provide redundancy to the cryogenic plant installed to cool the experimental systems.

The cold box shall be installed in underground areas. Presently the required volume does not exist. Therefore conceptual studies have started in order to identify the best options for building new underground caverns to install this equipment and the related service and control system]. Figure 15-4, Figure 15-5 and Figure 15-6 correspond to solutions with magnet power converters on surface (baseline), while Figure 15-7 corresponds to a solution with power converters in the underground areas.
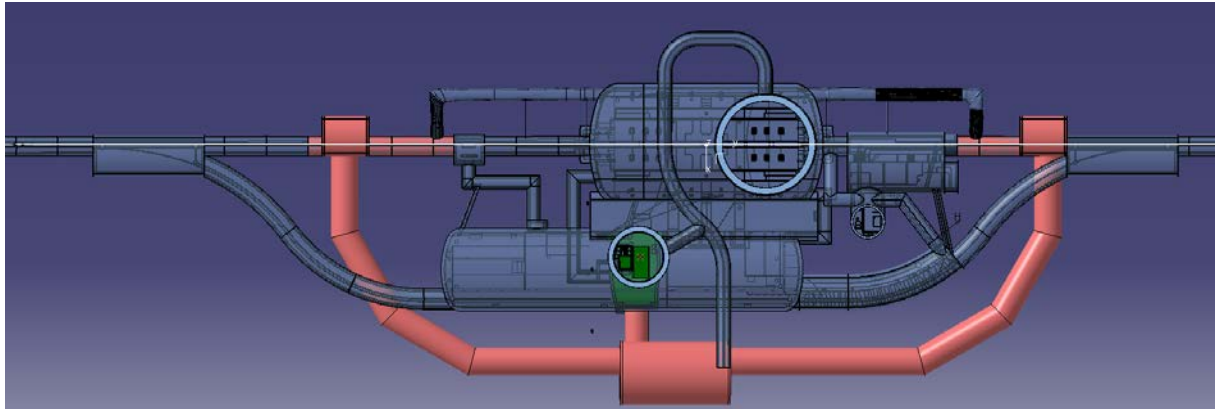
Figure 15-4: Possible option for underground work at Point 5 including links to the LHC tunnel. Solution without independent shaft to access to the surface. New structures in light red, zones of the LHC tunnel to be impacted by construction the new structures in green.
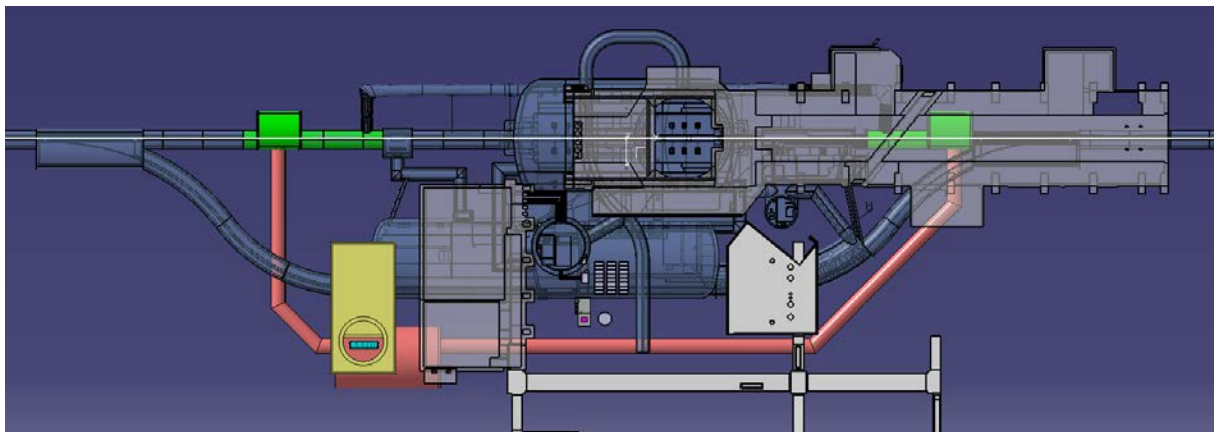
Figure 15-5: **Possible option for underground work at Point 5 including links to the LHC tunnel. Solution with independent shaft to access to the surface. New structures in light red and yellow, zones of the LHC tunnel to be impacted by construction the new structures in green.**
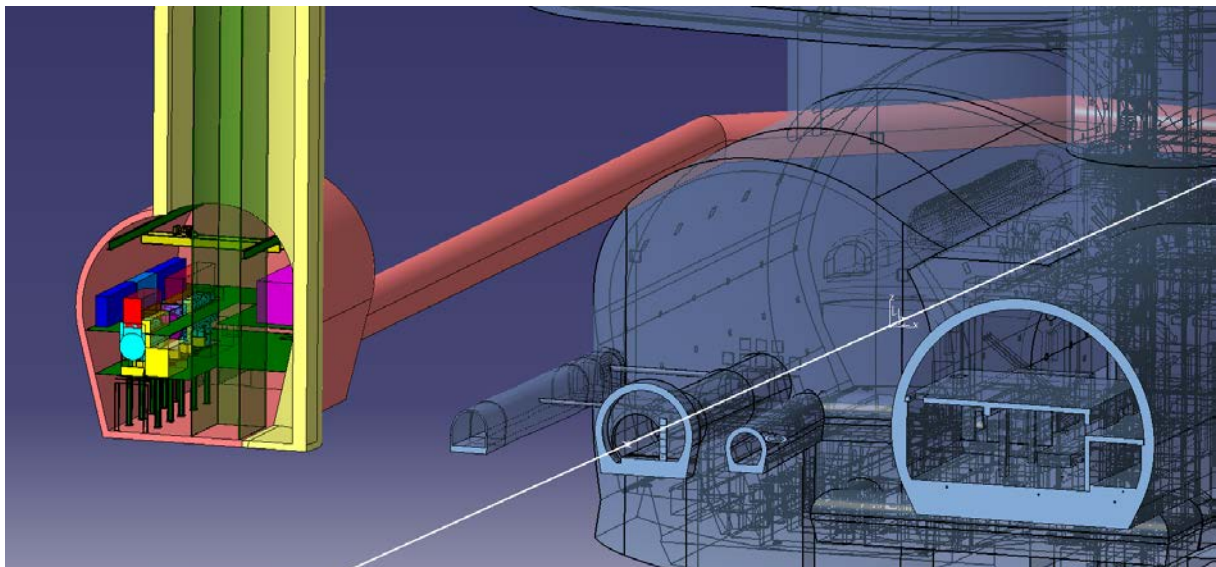
Figure 15-6: Possible option for underground work at Point 5 including links to the LHC tunnel. Solution with independent shaft to access to the surface, cross section of the cryogenic equipment arrangement. New structures in light red and yellow.
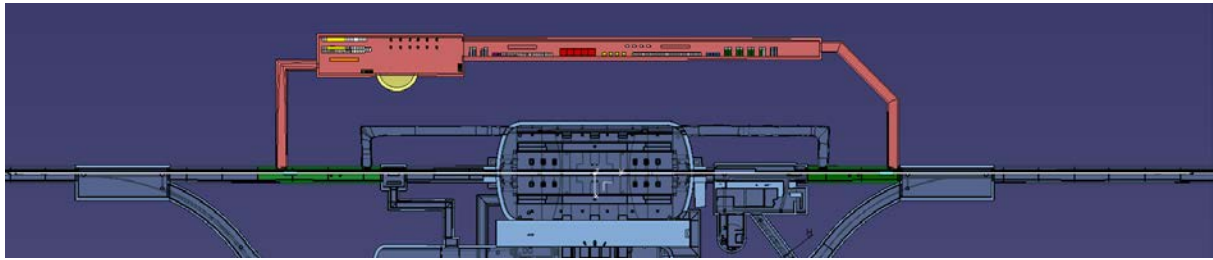
Figure 15-7: Possible option for underground work at Point 5 including links to the LHC tunnel. Solution with independent shaft to access to the surface, and larger connection tunnel for possible Power Converter underground installation. New structures in light red and yellow, zones of the LHC tunnel to be impacted by construction the new structures in green.

15.6.4 New connection from the LHC tunnel and HL-LHC service areas to the surface

The following connections between the surface and the underground installation shall be made available:

- LHC tunnel, crab cavity area, to the surface. The crab cavities need to be connected to the dedicated RF power system and their control system. The present preferred choice is to install these services in dedicated surface buildings (see later). The underground to surface connection will need to house eight RF coaxial cables (about 300 mm in diameter each), plus the required control cables. Two options are under study

  o The construction of 8 ducts over each crab module, linking directly the tunnel vault with the surface crab service building

  o The construction of a shaft where all the previously listed cables can be hosted together. In this case a local enlargement of the LHC tunnel will be necessary. Alternatively there will be a need for the construction of a separate small cavern where the shaft will send. The extra underground work is necessary taking into account that the minimum shaft dimension is larger compared to the LHC tunnel diameter

- New HL-LHC service area to the surface. These connections are necessary to link the surface part of the cryogenic plant with the cold box installed in the new underground HL-LHC service areas.

- Vertical routing of the superconducting links. In each point at least four superconducting links will need to be routed from the surface to the underground areas. Three options are possible and they are listed from the more convenient to the less one:

  o Installation of the superconducting links in the same vertical duct linking the cryogenic plant to the surface

  o Installation of the superconducting links in the same vertical duct linking the crab cavity to the surface

  o Installation of the superconducting links in new dedicated vertical ducts

15.6.5 New surface installation

The following installations shall find space on surface in Point 1 and Point 5 and in their proximities:

- Crab cavity RF power and services hosted in two ad hoc surface buildings (Yellow boxes in 8). They shall be positioned on the surface, vertically directly above the tunnel position where the

crab cavities will be installed. There will be two surface buildings for each point, one on the left part of the machine and one on the right part. The surface extremities of the ducts/shaft for the crab cavity coax or shaft shall be housed inside this building. The part of the building with controls shall be electromagnetic shielded

- Cryogenic installation. On surface the warm compressors and the other part of the cryogenic plant shall be installed.

Figure 15-8: **Surface position of the two new Crab cavity service buildings (in yellow) at Point 5.**

- Power converters, upper extremities of the superconducting links, protection systems and energy extraction system related to the circuits fed via the superconducting link. This area shall be possibly located near the surface part of the cryogenic plant and in any case on the top of the surface extremity of the routing of the vertical superconducting link

Presently it looks very difficult to find the required surfaces in existing buildings; therefore the construction of new structures to host the above listed systems is probably necessary (Figure 15-9).
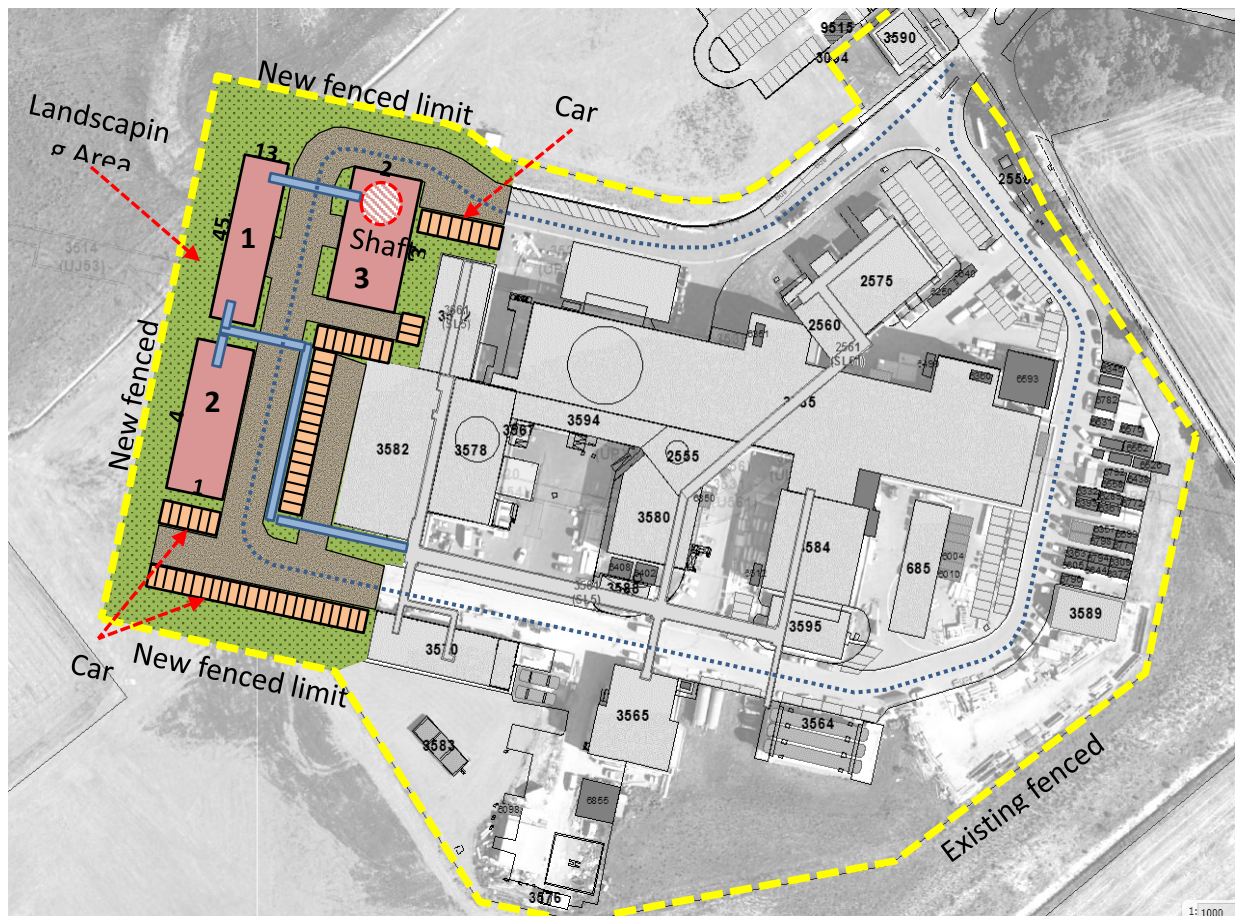
Figure 15-9: **Preliminary study of building foot print in LHC Point 5. Building 1: Power Converters and SC links terminals, Building 2 cryogenic surface equipment, Building 3 access to shaft. In light blue possible technical galleries**

In addition to the above mentioned options, a solution, where also the power convertors and the crab cavity ancillaries would be installed underground, is under study. Such option would lead to underground structure of much larger volume, but this increase in cost could be partially balanced by the reduction of the number of cores from the surface to the tunnel, the reduction of the numbers of surface structures to be built and the simplification of the surface worksite.

15.6.6 Activity sequence considerations

While the sequence of intervention on the underground LHC installed equipment (machine and RR) is quite clear and linked to the end of the LHC Run III, for what concerns the other installation and civil work activities the sequence is still under evaluation. The worksite organisation will depend a lot on the options chosen and that is why, in the evaluation of the selection of the final solutions for the underground caverns, the connection tunnel to surface and the surface building, three main parameters shall be taken into account: cost, possibility of performing the work in advance respect to the LS3 start date and the easiness of installation and connection since some options could lead to very complex and cross connected installation worksites making LS3 unacceptably long.

Chapter 16

Commissioning and operation

M. Lamont, M. Pojer, J. M. Jowett
CERN, Geneva, Switzerland

16   Commissioning and operation

16.1   Commissioning and operation

Come the commissioning and subsequent operation of the HL-LHC, the LHC itself will have been operational for over 10 years and a wealth of knowledge and experience will have been built up. The key operational procedures and tools will have been well established. The understanding of beam dynamics will be profound and refined by relevant measurement and correction techniques. Key beam related systems will have been thoroughly optimized and functionality sufficiently enhanced to deal with most challenges up to that point. Availability will have been optimized significantly across all systems. This collected experience will form the initial operational basis following the upgrade.

However the HL-LHC will pose significant additional challenges. The target integrated luminosity will make considerable demands on machine availability and operational efficiency. The planned beam characteristics will push beam dynamics to new limits. In the following discussion the operational cycle is revisited in light of the key HL-LHC challenges. The expectations and issues relating to availability in the HL-LHC are then outlined.

The planned bunch intensity, β*, and compensation of the geometrical reduction factor lead to a potential bunch luminosity well above the acceptable maximum in terms of pile-up for the experiments. Thus, as discussed in Chapter 2, an obligatory operational principle of the HL-LHC will be luminosity levelling. The aim is to reduce a potential peak or virtual luminosity to a more manageable levelled value by some luminosity reduction technique. As the number of particles in the beam falls with time, appropriate adjustments keep the luminosity at the levelled value. The options include: the use of transverse offsets; crab cavities; variation of the crossing angle; and dynamic change of the β*. Some combination (e.g. dynamic change of beta* and crab cavities) will be deployed. The longitudinal pile-up density is another critical parameter for the experiments, which must be taken into account during the levelling process.

16.1.1 The nominal cycle

The nominal operation cycle provides the framework underpinning luminosity production. Given the higher than ever stored beam energy of the HL-LHC era, the nominal cycle must be fully mastered for effective, safe operation. As of 2012, the nominal operational cycle is well established for 50 ns and bunch population exceeding nominal. A brief outline of the phases of the nominal cycle follows.

- **Pre-cycle** Following extensive experience during Run 1, it is known that the magnetic state of machine can be re-established before every fill by rigorous application of either: a combined ramp-

down/pre-cycle of the main circuits and a "de-Gauss" of the corrector circuits; or, following an access, by a full cycle of all circuits.

- **Set-up** The machine settings are verified with the injection of a limited number of bunches which have a reduced population (pilot, one bunch) or nominal population (intermediate, 12 bunches).

- **Injection** The two LHC rings are progressively filled with trains of bunches transferred from the SPS to the LHC. The injection process should be well optimized by the time of the upgrade. However high bunch intensities will have to be anticipated and all necessary mechanisms to minimize particle loss and emittance blow-up, and maximize reproducibility should be deployed.

- **Ramp** Once the machine is filled with the required number of bunches, the beams are accelerated to top momentum (up to 7 TeV/c). The ramp should hold no surprises. The characteristics of snap-back and correction of associated parameter swings can be taken as given. The 10 A/s ramp rate of main dipole power converters will still hold. Transverse feedback and tune feedback and their healthy cohabitation should be anticipated. Orbit feedback will be mandatory. Controlled longitudinal blow-up will be required.

- **Squeeze** The mechanics of the squeeze including feedbacks will have to have been fully mastered. Issues of beam instabilities should have been resolved and might include squeezing with colliding beams. Again this should have been made operational before the HL-LHC era. The possibility of combining the part of the squeeze process in the ramp is being considered to reduce the time required for the squeeze process.

- **Adjust** At the end of the squeeze the beams are brought in collision at the interaction points. There is some flexibility in sequencing the order in which the beams are collided in the different interaction points. The process is relatively fast and will be well established.

- **Stable Beams** Once all the above procedures are completed and no abnormal conditions are detected the conditions are met for safely switching on the detectors and the start of data taking. In general, this phase is expected to be stable with sufficient Landau damping from beam-beam, and small movements in beam overlap thanks to good orbit stability. Emittance growth and losses to the collimation regions must be anticipated.

The principal challenges during the cycle involve the injection, and transmission through the cycle of high bunch and high beam current while preserving emittance. Given the experience of LHC operations thus far, the following potential issues may be identified:

- electron cloud;

- UFOs;

- localized beam induced heating of specific hardware or vacuum assembly non-conformities – this can result in outgassing and bad vacuum as a result;

- cryogenic heat load;

- excessive beam loss in the cleaning sections.

High bunch population implies the need for very good parameter control and the need to properly control beam loss through the cycle. Beam instabilities will have to be fully under control using a variety of measures. Low β^* implies strong non-linearities from the inner triplets and the need for associated correction. On the positive side, the HL-LHC should be able to count on excellent magnetic reproducibility and good stability. Hardware systems such as power converters, RF and transverse dampers have already demonstrated impressive performance.

16.1.2 Availability and operational efficiency
The terms relevant to the year long operational view are first defined.

- **Scheduled proton physics time (SPT)** is the time scheduled in a given year for high luminosity proton physics. It does not include initial re-commissioning, special physics runs, ions, machine development (MD), and technical stops. It does include the intensity ramp-up following re-commissioning at the start of the year. It does not include special physics runs, operation with ions, and MD. Note that high luminosity running involves a number of challenges not present in other modes of operation and different machine availability can be expected.

- **Availability** is the scheduled proton physics time minus the time assigned to faults and fault recovery. It is normally expressed as a percentage of the SPT. Edge effects (e.g. recovery from access, the pre-cycle) should be fully included in the assigned fault time.

- The **turnaround time** is defined as time taken to go from Stable Beam mode back to Stable Beam mode in the absence of significant interruptions due to fault diagnosis and resolution.

- **Physics efficiency** is the fraction of the scheduled physics time spent in Stable Beams.

16.1.2.1 Standard year of operation

The longer-term operational planning consists of a series of long years (see Table 16-1) of operation interspersed with long shutdowns of order of a year or more. The long shutdowns are foreseen for essential plant maintenance, experiment upgrades and so forth. It is estimated that required length of a standard long shutdown in the HL-LHC era will alternate between 16 and 20 months. The approximate breakdown of a generic long year is:

- 13 weeks Christmas technical stop including 2 weeks hardware commissioning (this would account for 3 weeks at the end of a year and for 10 weeks at the start of the following year);

- around 160 days proton-proton operation;

- three technical stops of 5 days duration during the year;

- a 4 week ion run (the working assumption is that the ion program continues into the HL-LHC era, this is not to say that the HL-LHC will operate with ions for its total period of operation);

- and dedicated time for special physics and machine development.

A more detailed breakdown is shown in Table 16-1.

Table 16-1: Potential breakdown of a standard HL-LHC year

Activity	Time assigned [days]
Christmas technical stop including HWC	91
Commissioning with beam	21
Machine development	22
Scrubbing	7 (to 14)
Technical stops	15
Technical stop recovery	6
Proton physics including intensity ramp-up	160
Special physics runs	8
Ion run setup	4
Ion physics	24
Contingency	7

16.1.2.2 Availability and operation efficiency

The HL-LHC will place challenging demands on availability and operational efficiency if the ambitious integrated luminosity goals are to be met. Given that the requisite high intensity beam can be injected,

ramped, squeezed, collided, and the luminosity levelled, the principle operational challenges will be assuring high availability and maximizing physics efficiency.

16.1.2.2.1 Faults

Faults cover an enormous range from a simple front-end computer reboot to the loss of a cold compressor with corresponding loss of time to operations ranging from 10 minutes to potentially days. The impact of a typical fault requiring tunnel access shows the following sequence of steps from the occurrence of the original fault through to full recovery.

- Premature beam dump in Stable Beams.
- Original diagnosis of fault by control room operator - contact expert.
- Remote diagnosis by expert.
- Access required and prepared.
- Travel of expert to site. Travel of radiation protection piquet to site.
- Intervention, on-site diagnosis and repair by expert.
- Recovery from access.
- Recovery from the impact of the fault (for example, cool-down following quench).
- Re-establish machine state: pre-cycle, injection etc.

It can be seen that besides the cost to fix a fault, there are also significant additional overheads. Faults often dump the beam with the cost of at least a full turnaround to re-establish the state of the machine. The cost in time of turnaround and the fault recovery component is now examined in more detail.

16.1.2.3 Turnaround time

A breakdown of the foreseen HL-LHC turnaround time is shown below.

Table 16-2: Breakdown of turnaround and estimated minimum time for each phase

Phase	Time [minutes]
Ramp-down/pre-cycle	60
Pre-injection set-up	15
Set-up with beam	15
Nominal injection	20
Prepare ramp	5
Ramp	25
Flat-top	5
Squeeze	25
Adjust/collide	10
TOTAL	180

From Table 16-2, one can see that realistically a three-hour minimum turn around time may be assumed in the HL-LHC era. The main components are the ramp-down from top energy; the injection of beam from the SPS; the ramp to high energy; and the squeeze. The ramp-down, the ramp, and the squeeze duration are given by the current rate limitations of the power converters. Of note is the 10 A/s limit up and down for the main dipoles, the need to respect the natural decay constants of the main quadrupoles, the individually powered quadrupoles and the triplets during the ramp-down and the squeeze. These quadrupoles are powered by single quadrant power converters and it takes a considerable time to come for the current to fall to the required level. A faster pre-cycle via upgrades to the power converters might be anticipated. Two quadrant power converters for the inner triplets, for example, would remove them as a ramp-down bottleneck.

In practice, the turnaround has to contend with a number of issues which could involve lengthy beam based set-up and optimization. Typical beam based optimization might include: the need to re-steer the transfer lines; occasional energy matching between the SPS and LHC; the need for the SPS to adjust scraping during the injection process. Injector and LHC tuning and optimization are accounted for in the average turn around time.

16.1.2.4 Lost fills and fill length

Another important consideration directly impacting operational efficiency are the overheads of losing a fill (in the ramp, in the squeeze, in physics). In 2012, for example, 70% of all fills were terminated by a fault with costs ranging from a full turnaround plus fault recovery time to curtailed Stable Beam time. In 2012, having made it into Stable Beams, operations experienced a lot of short unproductive fills because of premature dumps. The cost of the short fills is a corresponding number of extra turnarounds which fold directly into lost time for physics. All means must be used (?) during Run 2 and Run 3 to target all causes of premature dumps and in the HL-LHC era make a choice of robust operating parameters must be made to avoid losing fills to high beam loss and instabilities during the cycle.

16.1.3 Discussion

A number of studies have been made that model the potential integrated luminosity that can be delivered by the HL-LHC at a levelled luminosity of 5×10^{34} cm^{-2}s^{-1}. All conclude that it will be challenging to deliver 250 fb^{-1} per year. Every attempt must therefore be made to target high availability, shorter turn around times, and a low number of premature dumps. Some of the main areas that might be targeted in the interest of improved availability and operational efficiency have been identified.

Reduce the number of faults (hardware and software) – this is the natural target for improved availability. It requires targeted improvements and consolidation across all systems.

Reduce time to fix faults, reduce intervention times, and reduce the number of tunnel interventions (for example by universal remote reset functionality or improved remote diagnostics or increase redundancy).

Reduce number of beam-induced faults (R2E, beam induced heating, vacuum issues).

Reduce the mean turnaround time. Here one could imagine targeting routine optimization, test runs, and the nominal cycle.

Choose a robust set of beam parameters to avoid unnecessary dumps from beam related issues.

16.2 Hardware commissioning

16.2.1 Commissioning of the superconducting circuits

16.2.1.1 Test of the superconducting links in short circuit configuration

All superconducting links [1] will be individually (cryogenically and electrically) tested in the SM18 magnet test facility prior to installation in the tunnel [2]. As it is the case for all superconducting elements installed in the machine, these links will have to be further tested in situ to assess that no degradation occurred during transport and installation.

A test similar to those presently performed on the warm part of all superconducting circuits, is suggested, with one extremity in short-circuit configuration: the electrical connections to the power converters are the nominal ones; the conductor at the other extremity of the link are not connected to the magnets, but short-circuited, in a configuration which allows the powering up to the nominal current of all bus bar pairs. The link will have to be cooled down to its nominal temperature; thus the configuration and the precise place of short-circuit installation will be decided in accordance with the

final design of the connection boxes (DFMs and DFXs), also taking into account the planning constraints.

Once the short-circuit is installed and the nominal cryogenic conditions established, a high voltage qualification (ElQA) of all lines will be performed in order to validate the galvanic insulation versus ground and the capacity of all lines to withstand the mutual high voltages developed during fast change of current in the different circuits (typically during a fast abort or quench). The values of voltages to be applied and the maximum acceptable leakage current values will be defined at a later stage; document [3] will have to be updated correspondingly.

After the ElQA validation, all lines can be powered. The powering will consist of several phases, each of them to be analysed and approved by the experts, before progressing to the next phase. At each phase the cryogenics team will have to verify the correct behaviour of the cryogenic system and cooling loop. Each circuit should be powered to increasing current levels (e.g. minimum operational current, 25% of nominal, 50% of nominal and nominal current). At each current level, the powering, protection and cryogenic systems will be qualified. The detailed steps and qualification criteria will be identical to those prepared for SM18 and will have to include the simultaneous powering of different circuits, and stress tests such as the fast discharge of a line with all the others powered at nominal current in order to study the cross talk between them.

16.2.2 Electrical Quality Assurance tests

As stated in [3], the objective of the ELQA tests is to release each individual superconducting circuit for powering, to gather all the necessary electrical parameters for operation, and to track all the data acquired and to manage the related non-conformities.

16.2.2.1 ElQA at warm

At the end of the installation and connection of all magnets, resistance measurements and a high voltage qualification of all circuits will be performed: to check whether the circuit is closed; determine a reference resistance value at warm; and to validate the galvanic insulation versus ground. The values of voltages to be applied and the maximum acceptable leakage current values will be defined at a later stage.

16.2.2.2 ElQA at cold

Similar tests will be performed at cold, with larger test voltages applied. The circuits and the corresponding link will be cooled down to their nominal temperature. For the high voltage qualification of all lines, this will be performed to validate the galvanic insulation versus ground and the capacity of all lines to withstand the mutual high voltages developed during fast change of current in the different circuits (typically during a fast abort or quench).

The high voltage qualification also includes testing of all the elements that are electrically connected to the tested circuit. Such elements are:

- the instrumentation and feed-through systems,
- the magnet protection units,
- the temperature sensors with the related tunnel cabling and electronics,
- the tunnel cabling for routing the voltage taps used for the protection of the superconducting circuits.

In addition, transfer function measurements will be performed, with the aim of determining the impedance as a function of the frequency. The results of these measurements are used to spot possible inter-turn shorts, and by the power converter group to adjust the power converter regulation.

The values of voltages to be applied and the maximum acceptable leakage current values will be defined in a later stage and document [3] will be updated accordingly.

16.2.3 Powering tests

The HL-LHC magnets present several peculiarities [4] that have to be kept in mind for their commissioning. The most relevant are: the fact that all magnets will be cooled down to 1.9 K (instead of 4.5 K of all present matching section magnets); that Nb_3Sn will be used for the first time; that the current of the Inner Triplet and the Q4 magnet will be the highest in the machine (close to 20 kA); and importantly that some of the high current magnets will be protected only via energy extraction in a dump resistor without quench heaters. In addition, the powering scheme of the Inner Triplet will be different from the present one, with Q1 in series with Q3 and Q2a and Q2b in series in a separate circuit: this is important in case of quench of one of the magnets.

The powering of all circuits up to nominal current will be done in steps. At the end of each step, online and offline analysis are performed by equipment owners and protection experts to assess the performance of all hardware in the circuit. In particular, for the powering of individual circuits, several cycles at different current levels will be performed to study the performance of the magnets, the efficiency of the protection mechanisms (by provoking fast aborts and even quenches) and to checks all functionalities of the powering interlocks and of the power converters (via provoked powering failures).

A typical series of tests includes:

- at minimum operational current, test of the full interlock chain, with the verification of cryogenic signals, power permit, powering failure, circuit quench transmission and fast power abort requests;

- at low current, check of the power converter performance and verification of all protection functionalities, by means of provoked slow and fast power aborts, with energy extraction;

- repetition of a series of power aborts and possibly simulation of quenches from progressively higher current levels, with more and more energy stored (e.g. 25%, 50% and 100% of the nominal current).

Before starting a new powering test, all previous tests must have been validated. The validation includes approval by power converter and powering interlock experts, magnet owners and protection expert. Cryogenics experts should also confirm the correct operation of their installations and instrumentations. The criteria for approval, the parameters and the relevant information to be stored will be discussed in due time. The first time they will be applied is in 2019-20, when the test of a full string of magnets (reproducing from Q1 to D1) is foreseen, powered by a superconducting link. All valuable data extracted from the test on the string will be translated in powering procedures steps and criteria.

After the individual test of all circuits up to the design current, the common powering of a set of circuits will be done for magnets that are in the same cryogenic envelope and are powered from the same link (usually referred to as powering of group of circuits). The objective of this simultaneous powering is to validate operation of all magnets in nominal conditions; current cycles similar to those applied in normal operation should be used for the powering of group of circuits. Important at this stage is the behaviour with combined powering in critical conditions, such as the fast power abort on a circuit when the others are at full current. For the inner triplets, in particular, quenching in a triplet quadrupole might induce the quench in a nearby quadrupole or corrector if the current in this related circuit is not extracted fast enough. These tests should be performed on all the magnets and could well trigger the change of detection thresholds and protection configurations. Once more, all tests should be approved by a group of experts and recorded for future reference.

Particular attention has to be also paid to those circuits that are not equipped with heaters and are protected by energy extraction on a dump resistor. For such circuits, precise estimate of the energy deposited during a quench has to be performed, not only in the case of bench tests, but also in the more severe conditions of combined powering in the tunnel. Eventually, the protection threshold should be adapted to reduce energy deposition and improve magnet safety during powering.

It is important to observe that the first commissioning campaign will already take place in long shutdown 2 (LS2 in 2018-19), when the 11 T Nb_3Sn magnets in the dispersion suppression region around Point 2 will be installed. The superconducting link at Point 7 will be installed in the same period to power the circuits presently powered from power converters installed in RR73 and 77. All powering procedures and commissioning steps will then need to be ready by then.

16.3 Hardware commissioning of HL collimation system

The collimator settings, controls and operational sequences should be intensively tested during hardware commissioning phase [5]. A dedicated test to address the reproducibility of the collimator movements during critical operational sequences (such as the Ramp) will be performed. At this stage the collimators should have been fully installed and the local collimator controls in the tunnel fully validated.

Before beam is injected in the machine, the machine protection (MP) functionality of the collimation system must be guaranteed. Each collimator is connected to the beam interlock system (BIS) and has more than 20 interlocks that will need to be verified. The jaw positions and collimator gaps are monitored via 6 LVDT (Linear Variable Differential Transformer) sensors. These signals are interlocked with INNER and OUTER limit values, making a total of 12 interlocks per collimator. In addition, there are a total of 6 energy-dependent and beta-star-dependent limit functions and an interlock to protect from "local" mode collimation control. The temperature of the collimators is also monitored and interlocked with minimum and maximum adjustable thresholds independently for 5 sensors per collimator. After successful result of these tests, the system will be ready to allow beam in the machine.

The main upgrade of the collimation system for HL-LHC [6] will ensure cleaning of beam halo and will keep losses in high luminosity experimental regions at an appropriate level. For this, the project foresees the installation of local collimation in the dispersion suppressors (DS). The design of a collimator to be installed between two short 11 T dipoles (TCLD) is on-going. These collimators will feature the latest design improvements, including embedded BPMs for fast alignment. Altogether, between 10 to 14 TCLDs are foreseen for the HL-LHC in addition to 8 new tertiary collimators and some additional secondary collimators. Depending on the final update program, one should expect about 30 more collimators with respect to the present LHC system. Unlike other hardware commissioning tests (such as the magnets), most of collimation commissioning can be done parasitically, the main exception being the testing of the interlock system where the BIS needs to be available.

16.4 Commissioning of the cryogenic systems

The HL-LHC foresees numerous modifications of the cryogenic system [7]. Among them:

- the new cooling system for the superconducting links;
- the modifications to cool the previously 4.5 K elements to 1.9 K;
- the independent RF cooling system;
- plus the cooling loop for the crab cavities and much more.

The operation of all of them, together with the time needed to qualify and tune the systems, will be detailed once the design is definitive. Provisionally, an approximate time of three weeks is considered as mandatory to commission the scheme for the superconducting magnets.

16.5 Commissioning of the Crab Cavities

As for all elements in the LHC, the crab cavities will be first tested on the surface to nominal specification prior to installation in the tunnel. In addition, some modules will be installed in the SPS for a complete qualification of the standard 2-cavity module with LHC type beams. This is presently planned for the 2017 run after the extended year-end technical stop.

The test of the cavities can be differentiated into: the commissioning of the RF cavities and associated ancillary systems (cryogenics, vacuum); and the RF commissioning with beam. The need in terms of time and manpower will be assessed later.

Concerning the commissioning of the cryogenics, the correct operation of the cooling loop and the capacity will be verified, together with the expected behaviour of the instrumentation; proper verification criteria and sequence will be defined at later time with input from the qualification of the cryogenic-module on the surface tests. The vacuum integrity and the vacuum interlocks will be tested as well, which should cut the RF power in case of issues and during cavity conditioning.

The conditioning of the cavities will first be performed on the surface in the nominal configuration, but the commissioning of the low level RF system (the tuning control, the regulation loop around the amplifier plus the RF feedback) will have to be validated in the SPS for the first time in its nominal configuration. A detailed procedure for the verification of all functionalities will be prepared well in advance. The information and issues arising from these tests will directly help in efficiently commissioning the system in the LHC.

All possible RF manipulations foreseen for the LHC operation cycle will first be performed without beam. An important verification concerns the efficiency of the fast feedback of the cavity field. The delay loops in the SPS between the two cavities will be arranged to mimic the cavity setup in the LHC to both ensure the fast and independent control of the cavity set point voltage and phase and the slower loop to regulate the cavities on either side of the IP. This is essential to ensure the machine protection in case of an abrupt failure of one of the cavities.

16.6 Commissioning with beam

One is fully able to draw on past experience in outlining a commissioning plan for initial operation following LS3. A skeleton plan is shown in Table 16-3.

Table 16-3: Outline of initial commissioning following LS3

Phase	Key objectives
Injection and first turn	Injection region aperture, injection kicker timing
Circulating beam	RF capture, beam instrumentation, initial parameter checks
450 GeV initial commissioning	Transfer line and injection set-up, orbit,
450 GeV measurements and setup	Beam instrumentation, optics, aperture, collimation, LBDS
450 GeV two beam operation	Separation bump checks, beam instrumentation
Ramp	Snapback, chromaticity control, orbit and tune feedbacks
Flat top checks	Collimation, optics, orbit, decay
Squeeze	Optics, collimation set-up
Validation	Loss maps, asynchronous dumps
Collide	First stable beam with a low number of bunches

The initial commissioning phase should evolve through initial set-up; system commissioning through the nominal cycle; standard measurement and correction; set-up of protection devices; and validation. It is a relatively complex phase with necessary interplay between the various teams to allow beam-based commissioning of systems such as tune and orbit feedbacks, transverse dampers, RF etc. under appropriate conditions at the various phases of the operational cycle.

The aims of the initial commissioning phase are as follows.

- Establish nominal cycle with a robust set of operating parameters. This will include commissioning of the squeeze to an appropriate β* with measurement and correction of the optics and key beam parameters at each stage. One should not expect to probe the limits of the HL-LHC parameter space at this stage.

- Measure and correct the optics. Measure the aperture.

- Set-up injection, beam dump, collimation and validate set-up with beam.

- Commission beam based systems: transverse feedback, RF, injection, beam dump systems, beam instrumentation, orbit and tune feedbacks.

- Commission and test machine protection backbone with beam.

- Check the understanding of: magnet model; higher order optics.

The initial commissioning phase is performed with low intensity, low number of bunches, and generally safe beam. The output of this phase is taken to be first collisions in Stable Beams with a small number of bunches. Following this, pilot physics can be delivered with up to the order of one hundred widely space bunches. Scrubbing will then be required before entering the intensity ramp-up phase. Scrubbing could well following the two-stage approach deployed following LS1. This approach is outlined below.

- Initial scrubbing with 50 and 25 ns beam following initial commissioning opening the way for a period of 50 ns operation.

- Intensity ramp-up with 50 ns is then foreseen. During this stage system commissioning with higher intensity continues (instrumentation, RF, TFB, injection, beam dumps, machine protection, vacuum...). Variables at this stage include: bunch intensity, batch structure, number of bunches, and emittance. Physics fills can be kept reasonably short. The intensity ramp-up is performed in a number of clearly defined steps with associated machine protection and other checks.

- Following the 50 ns intensity ramp-up a reasonably short period of 50 ns operation is envisaged. This will be used to characterize vacuum, heat load, electron cloud, losses, instabilities, UFOs, and impedance.

- Thereafter a further scrubbing period with 25 ns and the doublet beam will be required for 25 ns operation.

- This followed by an intensity ramp up with 25 ns dictated by electron cloud conditions with further scrubbing as required.

Important beam related characteristics such as lifetime, beam loss through the cycle, stability, quench levels, UFO rates will only become accessible with an increase in bunch intensity and number of bunches during the intensity ramp-up phase.

16.6.1 Operation with heavy ions

In a typical LHC operating year, one month is reserved for the nuclear collision programme.

16.6.1.1 Pb-Pb operation

Collisions of fully stripped $^{208}Pb^{82+}$ nuclei are requested by the ATLAS, ALICE and CMS experiments. These heavy-ion runs will generally be scheduled following an extended period of p-p operation. The reduced activation of the LHC and injectors will allow interventions to start promptly in the subsequent shutdown periods. The runs will be short, typically one month in total, and there is a high premium on rapid commissioning of collision conditions with full luminosity within a few days.

To minimise commissioning time, the heavy-ion magnetic cycle will generally exploit the magnetic reproducibility of the LHC and equal magnetic rigidity of the beams to use as much as possible of the cycle previously established for proton beams. Due care must nevertheless be taken to reproduce the same orbits in the higher-sensitivity mode of the beam-position monitors and to adjust the RF frequencies to capture the ion beams [7]. However the collision optics will always be different and a new squeeze process will have to be established to provide a low β^*=0.5–0.6 m at the ALICE experiment with similar values (generally not as low as for protons) at ATLAS and CMS. Crossing angles will also be changed, with that of ALICE carefully minimised for the benefit of its Zero-Degree Calorimeter. With the 50 ns bunch spacing, the minimum acceptable separations at parasitic encounters will be established empirically [9][10]. In all cases, the validation of the collimation configuration and machine protection will be an essential step in the set-up of heavy-ion physics conditions. During each run, a reversal of the ALICE spectrometer magnet polarity and flipping of the crossing angle should be foreseen [9].

Controlled blow-up of the longitudinal emittance, using RF noise with a spectrum focussed on the core of the bunch, will play an important role in minimising transverse emittance blow-up due to intra-beam scattering at injection [10] and, very likely, also during Stable Beams.

Because of the very rapid luminosity burn-off (halving in about 2 hours with 3 experiments active), the fills will be short and frequent refilling and recycling of the machine will be required, typically 4 times per day. Although the experiments will be able to handle the highest peak luminosity foreseen, it may nevertheless be useful to briefly level the luminosity with separation at the start of fills to reduce the intensity burn-off during the initial set-up of collision conditions. This will have negligible impact on average daily luminosity.

Secondary beams created in the collisions [124][10] will impinge on the beam pipe in the dispersion suppressors on either side of each collision point. The power in these beams is expected to be sufficient to quench superconducting magnet, and counter-measures will have to be applied immediately when the beams are put into collision. The most effective are expected to be the dispersion suppressor collimators [10] which will be positioned during the squeeze process. Initially these will be installed in IR2 for the ALICE experiment. The attainable peak luminosity for ATLAS and CMS will be maximised using an orbit bump technique that will spread the losses over a larger area. If necessary, similar collimators may be installed in IR1 and IR5 later. In any case, the dump thresholds for the beam-loss monitors in the dispersion suppressors will have to be carefully adjusted.

Because of the more complicated nuclear and electromagnetic processes that can occur when lead ions interact with the material of the collimators, collimation efficiency will be lower than for protons and quite different loss patterns are expected [13]. Here, again, the energy deposition from the losses may approach or exceed quench levels and may necessitate the installation of dispersion suppressor collimators in IR7.

16.6.1.2 p-Pb operation

Asymmetric collisions of protons with $^{208}Pb^{82+}$ nuclei are requested by the ATLAS, ALICE, CMS and LHCb experiments. The smaller forward detectors installed around the ATLAS and CMS interaction points also study these collisions. These runs are scheduled in place of the Pb-Pb runs, in the same way, in some fraction of the operating years.

The feasibility of this complex mode of operation, unforeseen in the original LHC baseline design, was demonstrated by the first runs in 2012 and 2013 [14]. Proton beams will be injected first since the Pb beams suffer more from intra-beam scattering at injection energy. The RF frequencies corresponding to capture of the two beams on their central orbits are significantly different at injection energy requiring the RF systems of the two rings to operate independently. At collision energy the frequencies will be locked together, displacing the proton orbit outwards and the Pb orbit inwards, by a small fraction of a

millimetre, onto off-momentum orbits. A "cogging" procedure, using the RF frequencies again, will be used to move the collision points to their proper locations in the experiments [15].

Proton-lead runs place a number of requirements on the filling schemes. The basic bunch spacing must be created by both the heavy-ion and proton pre-injector chains to ensure that the bunch patterns largely match each other. The trains must be distributed to provide an appropriate share of collisions in each experiment. As seen in 2013, this can result in a complicated set of beam-beam encounter classes, bunch parameters and lifetimes. In general, the proton beam size at the collision points will be smaller than the Pb beam, a circumstance which further reduces the lifetime of the Pb beam. Mitigation of this problem would be a second, less obvious, benefit of a stochastic cooling system.

As in Pb-Pb operation a new squeeze process will have to be commissioned, including all four experiments, with different end-points. This will generally be prepared and corrected first using on-momentum proton beams. Pre-computed chromatic corrections [15] will be incorporated for the final off-momentum squeeze.

Rapid luminosity burn-off of the Pb beam on the proton beam will determine the length of fills. The luminosity will be essentially proportional to the Pb beam intensity and the integrated luminosity delivered per fill summed over all experiments will be a fraction of N_{Pb}/σ_b where N_{Pb} is the total number of Pb ions in the beam at the start of collisions and σ_b is the cross section for luminosity burn-off in p-Pb collisions. The role of the proton bunch intensity is only to determine the lifetime of the Pb beam and the length of the fill. Values a few times less than in proton operation produce fills of reasonable length and satisfy operational constraints related to the functioning of the beam-positions monitors with unequal beams.

16.6.1.3 Other species

Collisions of lighter nuclei may eventually be requested by the experiments. At the time of writing, the injector chain is being commissioned with argon ions (for fixed target operation) for the first time. When this process is well-advanced, the beam quality and intensity data will allow performance projections for Ar-Ar and p-Ar collisions in the LHC.

Since most of the performance limitations for ion beams depend on high powers of the nuclear charge as well as beam intensity, their relative importance may shift considerably. First indications are that collimation losses from lighter ions will be more of a concern than for lead while losses from collision processes will be less serious.

16.7 References

[1] A. Ballarino et al., "Chapter 6 – Cold Powering", HL-LHC PDR

[2] A. Ballarino et al., "Test of the Superconducting Links in SM18

[3] M. Bednarek et al., "ElQA Qualification of the Superconducting Circuits During Hardware Commissioning", LHC-DE-TP-0007 rev 2.0, EDMS doc.no. 788197.

[4] E. Todesco et al., "Chapter 3 – Insertion magnets", HL-LHC PDR.

[5] Th. Weiler et al. "LHC Collimation system Hardware Commissioning", PAC07, Albuquerque, New Mexico, USA, 1625-1627

[6] R.Assmann et al. "Accelerator Physics Concept for Upgraded LHC Collimation Performance" PAC09, Vancouver, May 2009

[7] S. Claudet et al., "Chapter X – HL-LHC cryogenic systems", HL-LHC PDR.

[8] J.M. Jowett, G. Arduini, R.W. Assmann, P. Baudrenghien, C. Carli, et al, "First Run of the LHC as a Heavy-ion Collider", IPAC 2011, San Sebastian (2011), pp. 1837–1839.

[9] R Alemany-Fernandez, G H Hemelsoet, J M Jowett, M Lamont, D Manglunki, S Redaelli, M Schaumann, R Versteegen and J Wenninger, "ALICE spectrometer polarity reversal", CERN-ATS-Note-2012-039 MD, 2012.

[10] J.M. Jowett et al., "Future Heavy-Ion Performance of the LHC", Review of LHC and Injector Upgrade Plans Workshop (RLIUP), Archamps, France, 29-31 October 2013.

[11] R. Bruce, D. Bocian, S. Gilardoni, and J.M. Jowett, "Beam losses from ultraperipheral nuclear collisions between $^{208}Pb^{82+}$ ions in the large hadron collider and their alleviation", Phys. Rev.ST Accel. Beams **12**, 071002 (2009).

[12] M. Schaumann et al., "Potential of stochastic cooling of heavy ions in the LHC", IPAC 2014, Dresden (2014), pp. 76-78.

[13] H.-H. Braun, R. W. Assmann, A. Ferrari, J.-B. Jeanneret, J. M. Jowett, and I. A. Pshenichnov. "Collimation of heavy ion beams in LHC", IPAC2004, Lucerne (2004) pp. 551–3.

[14] J.M. Jowett, R. Alemany-Fernandez, P. Baudrenghien, D. Jacquet, M. Lamont, D. Manglunki, S. Redaelli, M. Sapinski, M. Schaumann, M. Solfaroli, Camillocci, R. Tomas, J. Uythoven, D. Valuch, R. Versteegen, and J. Wenninger, "Proton nucleus collisions in the LHC", IPAC 2013, Shanghai (2013), pp. 49-51.

[15] R Alemany, P Baudrenghien, D Jacquet, J M Jowett, M Lamont, D Manglunki, S Redaelli, M Sapinski, M Schaumann, D Valuch, R Versteegen, and J Wenninger, "p-Pb Feasibility Test and Modifications of LHC Sequence and Interlocking", CERN-ATS-Note-2012-052 MD, 2012.

[16] R Versteegen, R Bruce, JM Jowett, MJ McAteer, EH McLean, AS Langner, YI Levinsen, T Persson, S Redaelli, B Salvachua, PK Skowronski, M Solfaroli, Camillocci, R Tom´as, G Valentino, J Wenninger, and SM White, "Operating the LHC Off-Momentum for p-Pb Collisions", ", IPAC 2013, Shanghai (2013) pp. 1439–1441.

Chapter 17

Safety

C. Adorisio[5], I. Bejar Alonso[5], JC. Gascon[5], T. Otto[5], S. Roesler[5]
CERN, Geneva, Switzerland

17   Safety

17.1   Radiation to personnel

17.1.1 Design constraints

Design constraints for new or upgraded facilities should ensure that the exposure of persons working on the CERN sites, the public and the environment will remain below the specified dose limits [1] under normal as well as abnormal conditions of operation and that the optimization principle is implemented [2, 3]. In particular, the following design constraints apply:

The design of components and equipment must be optimized such that installation, maintenance, repair and dismantling work does not lead to an effective dose, e.g., as calculated with Monte Carlo simulations, exceeding 2 mSv per person and per intervention. The design is to be revised if the dose estimate exceeds this value for cooling times compatible with operational scenarios.

The annual effective dose to any member of a reference group outside of the CERN boundaries must not exceed 10 μSv. The estimate must include all exposure pathways and all contributing facilities.

The selection of construction material must consider activation properties to optimize dose to personnel and to minimize the production of radioactive waste. In order to guide the user a web-based code (ActiWiz) is available for CERN accelerators [4].

17.1.2 ALARA in the design of the Long Straight Sections

Proton-proton collisions in the LHC experiments produce a secondary radiation field that penetrates into the adjacent accelerator tunnels and can cause severe activation of beam-line elements. Consequently, in such areas the design of components and infrastructure has to be optimized to follow the As Low As Reasonably Achievable (ALARA) principle. The optimization of the design and later intervention is an iterative process: dose equivalent maps per unit time of exposure (that will be called dose rate maps in the following) of the concerned area(s) are compiled from measurements and/or simulations with Monte Carlo particle transport codes such as FLUKA [5, 6]. Based on these maps, the personal and collective doses of the intervention teams are calculated by using an intervention plan which then allows identifying and optimizing critical work steps in order to reduce doses. If the latter involves a change in design or work-scenario doses are re-evaluated by repeating the above steps.

17.1.3 The FLUKA Monte Carlo code for radiation protection studies

The use of general-purpose particle interaction and transport Monte Carlo codes is often the most accurate and efficient choice for assessing radiation protection quantities at accelerators. Due to the vast spread of such codes to all areas of particle physics and the associated extensive benchmarking with experimental data, the modelling has reached an unprecedented accuracy. Furthermore, most codes allow the user to simulate all aspects of a high energy particle cascade in one and the same run: from the first interaction of a TeV particle to the transport and re-interactions (hadronic and electromagnetic) of the produced secondaries, to detailed nuclear fragmentation, the calculation of radioactive decays and even of the electromagnetic shower caused by the radiation from such decays.

FLUKA is a general-purpose particle interaction and transport code with roots in radiation protection studies at high energy accelerators [5, 6]. It therefore comprises all features needed in this area of application:

Detailed hadronic and nuclear interaction models cover the entire energy range of particle interactions at the LHC, from energies of thermal neutrons to interactions of 7 TeV protons. Moreover, the interface with DPMJET3 [7] also allows the simulation of minimum-bias proton-proton and heavy ion collisions at the experimental interaction points which enormously facilitates calculations of stray radiation fields around LHC experiments.

FLUKA includes unique capabilities for studies of induced radioactivity, especially with regard to nuclide production, their decay and the transport of residual radiation. Particle cascades by prompt and residual radiation are simulated in parallel based on microscopic models for nuclide production and a solution of the Bateman equations [8] for activity build-up and radioactive decay. The decay radiation and its associated electromagnetic cascade are internally flagged as such in order to distinguish them from the prompt cascade. This allows the user to apply different transport thresholds and biasing options to residual and prompt radiation and to score both independently.

Particle fluence can be multiplied with energy-dependent conversion coefficients to effective dose or ambient dose equivalent [9] at scoring time. Prompt and residual dose equivalent can thus be computed in three-dimensional meshes, the latter for arbitrary user-defined irradiation and cooling profiles.

An integral part of the FLUKA code development is benchmarking of new features against experimental data. It includes both the comparison of predictions of individual models to measurement results (e.g., nuclide production cross sections) as well as benchmarks for actual complex situations as, for example, arising during accelerator operation.

17.1.4 FLUKA simulations

Comprehensive dose rate maps were calculated with FLUKA for the part of the Long Straight Section 1 (LSS1) that extends from the Target Absorber Secondary (TAS) to the separation dipole D1 (so-called "inner triplet area"), including the inner triplet quadrupole magnets and the corrector package (CP) according to the latest HiLumi LHC layout [10]. The results may also serve as guideline values for dose planning at inner triplet regions of LSS5, due to the similar design of the two LSSs.

The simulations were limited to the high energy secondary radiation field arising from the pp collisions as they dominate the activation in these areas. The influences due to losses of the beam directed towards the interaction point (IP) and beam-gas interactions are not considered. The FLUKA geometry shown below represents the tunnel on the right side of the LSS1.

The studies were done for 7+7 TeV pp-collisions at two different average luminosity values of $5{\times}10^{34}$ cm^{-2}s^{-1} (for the so-called "nominal scenario") and $7.5{\times}10^{34}$ cm^{-2}s^{-1} (for the so-called "ultimate scenario") with a 295 µrad half-angle vertical crossing in IP1 using DPMJET-III as the event generator.

The irradiation profiles used are based on the operational scenarios reported in Table 17-1.

Table 17-1: LHC operational parameters. The second and third columns refer to the so-called "nominal scenario", which will lead to a total integrated luminosity of 3060fb⁻¹. The fourth and fifth columns refer to the so-called "ultimate scenario". This scenario will lead to a total integrated luminosity of 3910fb⁻¹. For the total integrated luminosity 310fb⁻¹ are taken into account as integrated in the operational period before LS3.

Year of LHC Operation	Levelled luminosity [cm⁻²s⁻¹]	Integrated luminosity [fb⁻¹]	Levelled luminosity [cm⁻²s⁻¹]	Integrated luminosity [fb⁻¹]
LS3				
2026	5.00E+34	250	7.50E+34	300
2027	5.00E+34	250	7.50E+34	300
2028	5.00E+34	250	7.50E+34	300
LS4				
2030	5.00E+34	250	7.50E+34	300
2031	5.00E+34	250	7.50E+34	300
2032	5.00E+34	250	7.50E+34	300
LS5				
2034	5.00E+34	250	7.50E+34	300
2035	5.00E+34	250	7.50E+34	300
2036	5.00E+34	250	7.50E+34	300
LS6				
2038	5.00E+34	250	7.50E+34	300
2039	5.00E+34	250	7.50E+34	300
2040			7.50E+34	300

For the inelastic pp cross section the value of 85 mb is used, on the basis of the extrapolation [11]. Cycles of three years of continuous operation followed by a Long Showdown (LS) of a duration of one year were repeated until integrated luminosities of about 3000 fb⁻¹ and 4000 fb⁻¹ are reached for the nominal and ultimate scenarios, respectively.

The studies use a FLUKA implementation of the High Luminosity LHC inner triplet region developed by the FLUKA team [12] according to the latest design, mechanical layout and specifications, including a detailed model of the inner triplet region with new large-aperture Nb_3Sn magnets (150 mm coil aperture), field maps, corrector packages and segmented tungsten inner absorbers. As mentioned above, the inner triplet regions at LSS1 and LSS5 are radiologically equivalent and symmetrical around the interaction point. Thus, the simulations were performed for the right side of LSS1 only.

17.1.5 Results

Three-dimensional residual dose rate maps have been calculated from around 18 m distance from the interaction point up to around 82 m distance (i.e., from TAS to D1), and for six different cooling times: 1 hour, 1 day, 1 week, 1 month, 4 months and 1 year after the beam stop for both the nominal and the ultimate scenarios, i.e., when 3000 fb⁻¹ and 4000 fb⁻¹ have been reached, respectively.

In order to give examples for the available results, residual dose equivalent rates are reported in the following as two-dimensional maps for the one month cooling time as well as profile plots at four different cooling times (one week, one month, four months and one year). The values correspond to the average over 30 cm around the beam pipe height and between 40 and 50 cm distance from the outer surface of the cryostat (closest possible working distance).

Figure 17-1 shows the ambient dose equivalent rate maps in the inner triplet area after one month of cooling time and Figure 17-2 shows the residual dose rate profiles in the aisle at 40 cm distance from the cryostat at four different cooling times, when a total integrated luminosity of 3060 fb^{-1} is reached.
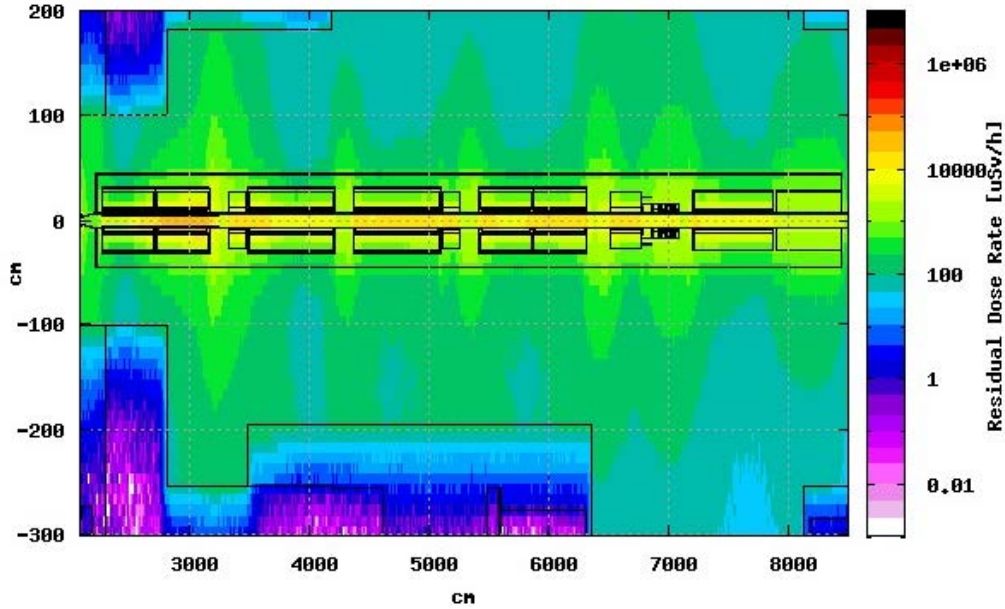
Figure 17-1: Residual dose equivalent rates in units of µSv/h around the inner triplet and D1 magnets when 3060 fb-1 has been reached after one month of cooling time. Doses are shown for a horizontal section at the level of the beam lines. The origin of the coordinate frame is at the interaction point.

Figure 17-3 shows the ambient dose equivalent rate maps in the inner triplet area after one month of cooling time and Figure 17-4 shows the residual dose rate profiles in the aisle at 40 cm distance from the cryostat at four different cooling times, for a total integrated luminosity of 3910 fb^{-1}.
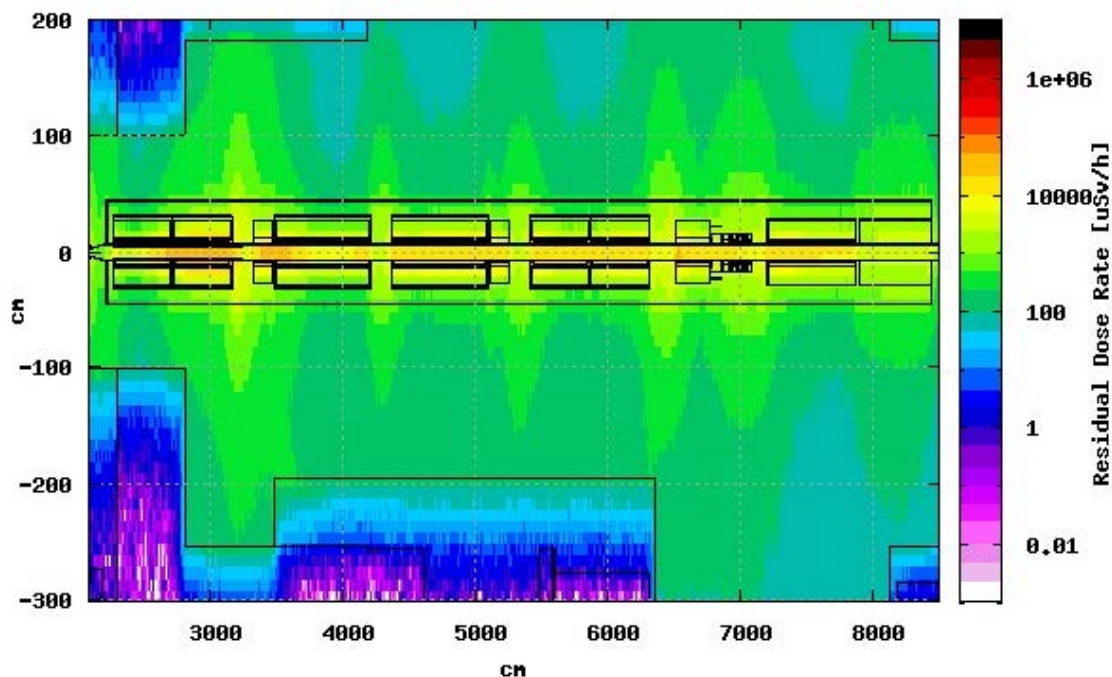
Figure 17-3: Residual dose equivalent rates in units of μSv/h around the inner triplet and D1 magnets when 3910 fb^{-1} has been reached after one month of cooling time. Doses are shown for a

horizontal section at the level of the beam lines. The origin of the coordinate frame is at the interaction point.
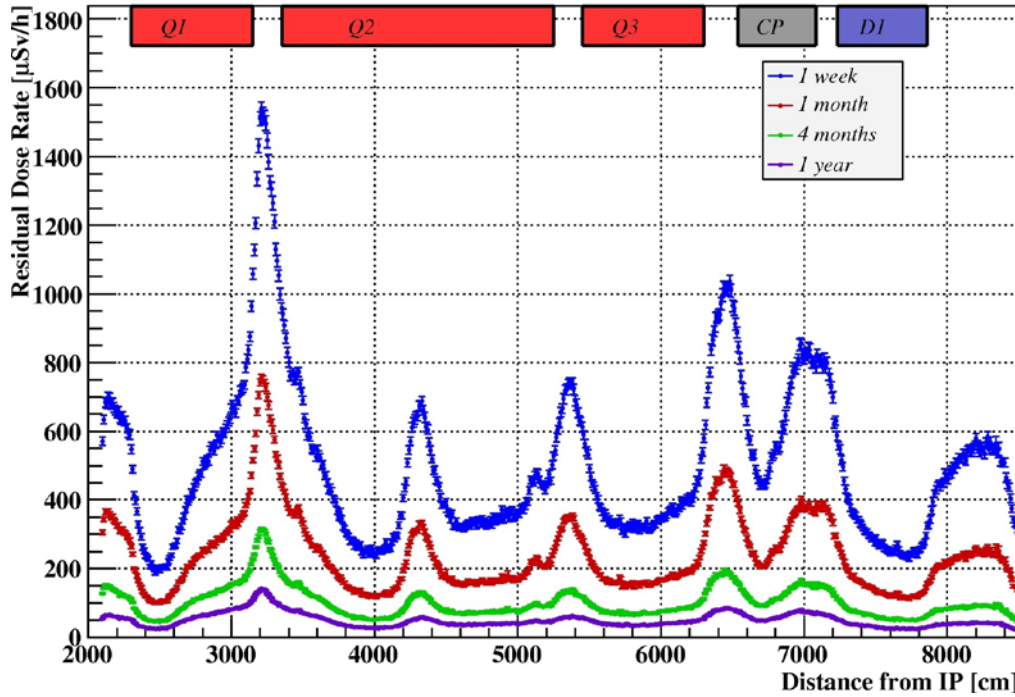
Figure 17-4: Ambient dose equivalent rate profiles for the ultimate scenario in the aisle at 40 cm from the cryostat at four different cooling times: one week in blue, one month in red, four months in green and one year in violet

The highest radiation levels will be found next to the magnet interconnections and in front of the TAS due to the "self-shielding" provided elsewhere by the magnets themselves.

The plot in Figure 5 shows the residual dose rate profiles at one month cooling times along the inner triplets, for the ultimate scenario in pink and for the nominal scenario in light blue. The average ratio between the two profiles is 1.35. This average ratio varies with cooling time and it depends purely on the instantaneous luminosity in case of short cooling times while for longer cooling times the ratio starts depending also on the total integrated luminosity.
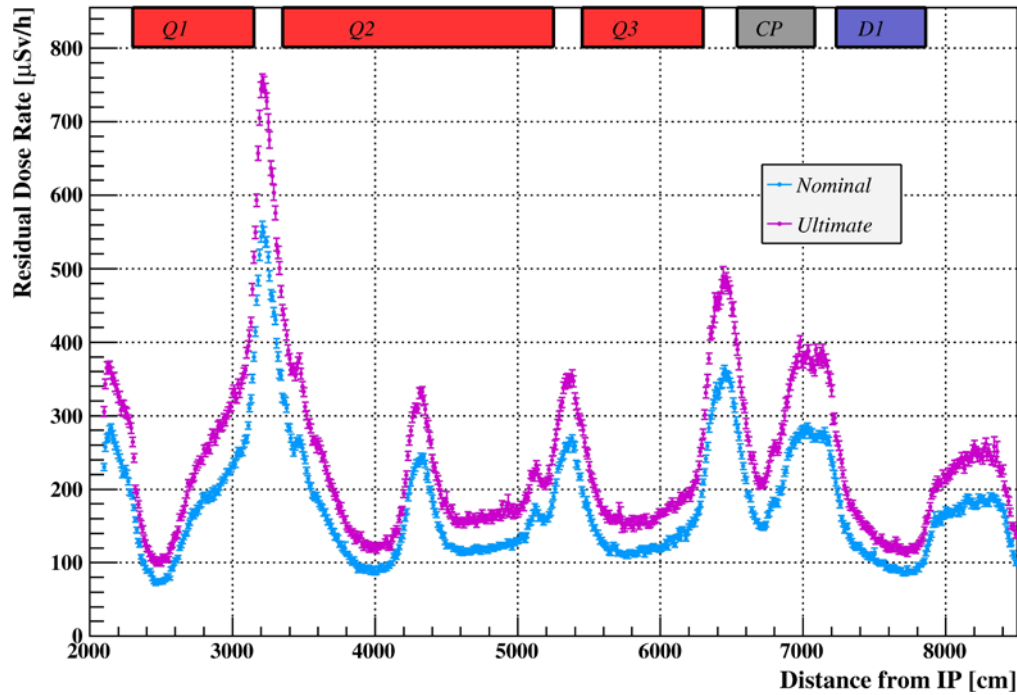
Figure 17-5: Ambient dose equivalent rate profiles along the aisle at 40 cm distance to the cryostat at one month cooling time. The profile in light blue is for the nominal scenario (about 3000 fb⁻¹ total integrated luminosity), the profile in pink is for the ultimate scenario (about 4000 fb⁻¹ total integrated luminosity)

17.1.6 Conclusions

Three-dimensional ambient dose equivalent rate maps were calculated with the FLUKA Monte Carlo code for the inner triplet region (from the TAS up to the D1 dipole magnet) for nominal and ultimate HiLumi LHC operational parameters and the latest upgrade layout. These predictions are now available and can be considered for the design of components. For example, the results will be used to assess the radiological impact, in terms of individual and collective dose, for typical interventions in the area and, thus, help in optimizing the design and the material choice as required by the ALARA principle. Further studies are also required to address airborne activation and the related environmental impact of the upgrade.

17.2 General Safety

17.2.1 Implementation of safety in HL-LHC

The HL-LHC presents a number of potential hazards that could pose serious safety risks. - The consequences could include the loss of life, damage to HL-LHC systems and facilities, or damage to the environment. Consequently all the HL-LHC WPs are classified as projects with major safety implications.

In practice the systems/processes of the HL-LHC WPs shall be submitted to a compulsory safety verification by the HSE Unit and shall only operate once the HSE Unit has granted safety clearance.

In the framework of the HL-LHC project, clearance will be given for the project phase, i.e. any development tests that will be performed on given systems or processes. After the HL-LHC project phase, a second clearance stage may become necessary once the system/process is ready for operation in the LHC.

17.2.2 Launch Safety agreement (LSA)

For each HL-LHC work package a launch safety discussion shall take place with the participation of the WP members the Project Safety Officer (PSO) and the correspondent from the safety unit (HSE-CO). After the launch safety discussion, the HSE-CO shall release the Launch Safety Agreement that provides the following information:

- Description of the WP systems/processes;

- Preliminary identification of the hazards and safety risks;

- Identification of the CERN Safety rules and Host State regulations applicable to the systems/processes;

- Tailored Safety advice on hazard control measures;

- List of Safety checks (including Safety checks required to grant Safety clearance) on the relevant systems/processes that shall be carried out by the HSE Unit during the WP life cycle;

- Minimal Contents of the WP Safety file needed to meet the Safety requirements

The Launch Safety Agreement may be reviewed and updated during the different phases of the systems/sub-system's life-cycle. Any changes to the safety requirements will be subjected to change control for integration, as required, in the baseline requirements.

17.2.3 Safety Folder, Safety Files and Safety documentation

The HL-LHC project will be documented as indicated in the quality management procedure "Safety Documentation Management" [13]. In this framework a Safety folder for the HL-LHC project shall be established and maintained during the project life cycle. In order to achieve this objective:

- The WPEs, based on the applicable Safety requirements, shall provide the Safety documents necessary to demonstrate compliance of the systems/processes (or sub-systems/sub-processes) that they are responsible for.

- The WPE provides a description for systems and processes under her responsibility, with focus on the Safety aspects. This forms the basis for the descriptive part of the WP Safety File

- The WPL shall establish and maintain the WP Safety file. The WP Safety file shall serve as an umbrella document where the relevant Safety documents, provided by the WPE, are referred to;

- The PSO shall establish and maintain the HL-LHC Safety folder. The HL-LHC Safety folder shall refer to the Safety files of the HL-LHC work packages.

The HL-LHC Safety Folder will consist of the collection of approved Safety Files of the HL-LHC WPs. The PSO shall ensure that the HL-LHC Safety Folder is kept up-to-date and available to the HSE Unit and Host CERN Safety Officers.

The Safety Folder for HL-LHC-LHC shall be provided to the HSE Unit for purposes of granting Safety clearance. The Safety Folder for HL-LHC will cover the Project Phase, which will extend until the end of LS3. Many of the material or organisational contributions realised in the WPs will be installed in the LHC accelerator. At this stage their Safety Files will become part of the LHC Accelerator Safety Folder.

Figure 17-6 shows the Organization of the HL-LHC Safety Documentation.
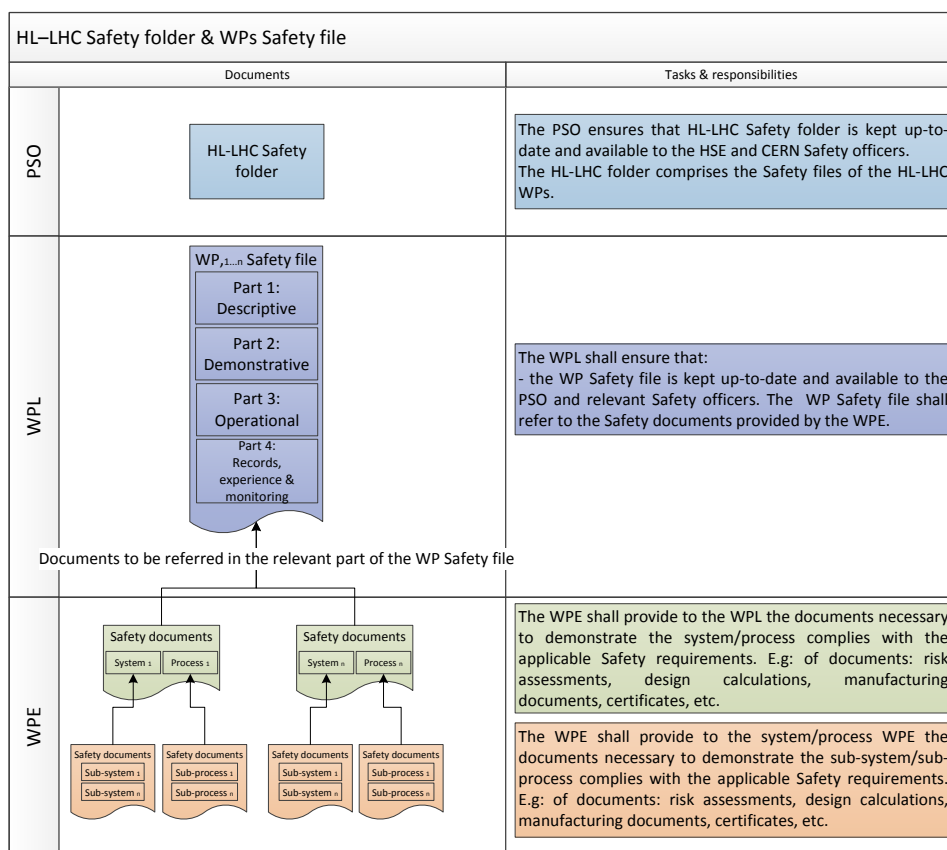
Figure 17-6: Organization of the Safety documentation

17.3 References

[1]   Safety Code F Radiation Protection, (2006). CERN.

[2]   Critères et exigences ALARA applicables aux interventions, (2006). CERN.

[3]   ALARA Review Working Group, (2012) Final report. CERN,

[4]   Vincke, H. and Theis, C., ActiWiz – optimizing your nuclide inventory at proton accelerators with a computer code. Proceedings of the ICRS-12 & RPSD 2012 conference, Nara, Japan, 2-7 September 2012, Progress in Nuclear Science and Technology, in press, 2013.

[5]   Battistoni, G., Muraro, S., Sala, P.R., Cerutti, F., Ferrari, A., Roesler, S., Fasso, A., and Ranft, J. The FLUKA code: description and benchmarking. Proceedings of AIP Conference. 2007.

[6]   Fassó, A., Ferrari, A., Ranft, J., and Sala, P.R., (2005) Fluka: a multi particle transport code. CERN. CERN-2005-10, INFN/TC_5/11, SLAC-R-773.

[7]   S.Roesler, R.Engel, J.Ranft, The Monte Carlo Event Generator DPMJET-III, Proceedings of the Monte Carlo 2000 Conference, Lisbon, 23-26 October 2000, A. Kling, F. Barao, M. Nakagawa, L. Tavora, P. Vaz eds., Springer-Verlag Berlin, 1033-1038 (2001).

[8]   H. Bateman, Solution of a system of differential equations occurring in the theory of radioactive transformations, Proc. Cambridge Philos. Soc. 15 , 423-427, (1910).

[9]   M. Pelliccioni, "Overview of fluence-to-effective dose and fluence-to-ambient dose equivalent conversion coefficients for high energy radiation calculated using the FLUKA code," Radiation Protection Dosimetry 88, pp. 279-297 (2000).

[10]   Mechanical layout, LHCLSXH_0010, (YEAR).

[11]   Csörgő, T. et al. Elastic Scattering and Total Cross-Section in p+p reactions measured by the LHC Experiment TOTEM at sqrt(s) = 7 TeV. In Progress of Theoretical Physics Proceedings of XLI International Symposium on Multiparticle Dynamics. 2012.

[12]   Brugger, M., Cerutti, F., and Esposito, L.S., (2013) The "environmental" challenges: impact of radiation on machine components. Accepted for publication in the "The High Luminosity LHC project". Under publication by World Scientific.

[13]   EDMS 1177755 v1.1.

List of Machine and Beam Parameters

A. List of Machine and Beam Parameters

A.1. Nominal Beam Parameters

Table A- 1: HL-LHC nominal parameters for 25 ns operation [1] for two production modes of the LHC beam in the injectors described in [2]

Parameter	Nominal LHC (design report)	HL-LHC (standard)	HL-LHC (BCMS)
Beam energy in collision [TeV]	7	7	7
Particles per bunch, N [10^{11}]	1.15	2.2	2.2
Number of bunches per beam	2808	2748	2604
Number of collisions in IP1 and IP5 [12]	2808	2736	2592
N_{tot} [10^{14}]	3.2	6.0	5.7
Beam current [A]	0.58	1.09	1.03
Crossing angle in IP1 and IP5 [µrad]	285	590	590
Normalized long range beam-beam separation [σ]	9.4	12.5	12.5
Minimum β^* [m]	0.55	0.15	0.15
ε_n [µm]	3.75	2.50	2.50
ε_L [eVs]	2.50	2.50	2.50
r.m.s. energy spread [0.0001]	1.13	1.13	1.13
r.m.s. bunch length [cm]	7.55	7.55	7.55
IBS horizontal [h]	105	18.5	18.5
IBS longitudinal [h]	63	20.4	20.4
Piwinski parameter	0.65	3.14	3.14
Total reduction factor R_0 without crab-cavity	0.836	0.305	0.305
Total reduction factor R_1 with crab-cavity	-	0.829	0.829
Beam-beam / IP without crab cavity	0.0031	0.0033	0.0033
Beam-beam / IP with crab cavity	0.0038	0.011	0.011
Peak luminosity without crab-cavity [10^{34} cm^{-2}s^{-1}]	1.00	7.18	6.80
Virtual luminosity with crab-cavity $L_{peak} \times R_1/R_0$ [10^{34} cm^{-2}s^{-1}]	(1.18)	19.54	18.52
Events/crossing without levelling and without crab-cavity	27	198	198
Levelled luminosity [10^{34} cm^{-2}s^{-1}]	-	5.00 [13]	5.00 [2]
Events/crossing (with levelling and crab-cavities for HL-LHC) [14]	27	138	146
Maximum line density of pile up events during fill [event/mm]	0.21	1.25	1.31
Levelling time [h] (assuming no emittance growth) [3]	-	8.3	7.6
Number of collisions in IP2/IP8	2808	2452/2524 [15]	2288/2396 [4]
N at LHC injection [10^{11}] [16]	1.20	2.30	2.30
Maximum number of bunches per injection	288	288	288
N_{tot} / injection [10^{13}]	3.46	6.62	6.62
ε_n at SPS extraction [µm] [17]	3.40	2.00	< 2.00 [18]

---

[12] Assuming one batch less from the PS for machine protection (pilot injection, TL steering with 12 nominal bunches) and non-colliding bunches for experiments. Note that due to RF beam loading the abort gap length must not exceed the 3µs design value.

[13] For the design of the HL-LHC systems (collimators, triplet magnets, etc.), a margin of 50% on the stated peak luminosity has been agreed.

[14] The total number of events/crossing is calculated with an inelastic cross-section of 85 mb (also for nominal), while 100 mb is still assumed for calculating the proton burn off and the resulting levelling time.

[15] The lower number of collisions in IR2/8 compared to the general purpose detectors is a result of the agreed filling scheme, aiming as much as possible at a democratic sharing of collisions between the experiments.

[16] An intensity loss of 5% distributed along the cycle is assumed from SPS extraction to collisions in the LHC.

[18] For the BCMS scheme emittances down to 1.4 µm have already been achieved at LHC injection which might be used to mitigate excessive emittance blow-up in the LHC during injection and ramp.

A.2. Main Machine parameters

Table A- 2: HL-LHC nominal machine parameters for proton operation

		Injection	Collision
Geometry			
Ring circumference	[m]	26658.883	
Ring separation in arcs	[mm]	194	
Bare inner vacuum screen height in arcs	[mm]	46.5	
Effective vacuum screen height (incl. tol.)	[mm]	44.04	
Bare inner vacuum screen width in arcs	[mm]	36.9	
Effective vacuum screen width (incl. tol.)	[mm]	34.28	
Main Magnet			
Number of main bends		1232	
Length of main bends	[m]	14.3	
Field of main bends	[T]	0.535	8.33
Bending radius	[m]	2803.95	
Lattice			
Maximum dispersion in arc	[m]	2.387 (H) / 0.281 (V)	2.789 (H)/0.632 (V)
Minimum dispersion in arc	[m]	0.959(H)/-0.281 (V)	0.832 (H)/-0.581(V)
Maximum β in arc	[m]	178 (H)/ 178 (V)	524 (H)/523(V)
Minimum β in arc	[m]	31.4 (H) / 32.1 (V)	25.2(H)/26.4 (V)
Horizontal tune		62.28	62.31
Vertical tune		60.31	60.32
Momentum compaction	[10^{-4}]	3.447	3.467
Slip factor η	[10^{-4}]	3.404	3.467
Gamma transition γ_{tr}		53.86	53.70
RF System			
Revolution frequency	[kHz]	11.2455	
RF frequency	[MHz]	400.79	
Harmonic number		35640	
Number of bunches		2748 (Standard) / 2604 (BCMS)	
Total RF voltage	[MV]	8	16
Synchrotron frequency	[Hz]	66.0	23.8
Bucket area	[eVs]	1.38	7.63
Bucket half height ($\Delta E/E$)	[10^{-3}]	0.965	0.343

---

[18] For the BCMS scheme emittances down to 1.4 μm have already been achieved at LHC injection which might be used to mitigate excessive emittance blow-up in the LHC during injection and ramp.

Table A- 3: HL-LHC nominal machine parameters at the collision points for proton operation. The crossing angle and separation refer to Beam 1.

		Injection	Collision
Interaction Data			
Number of collision points		-	4
Half crossing angle at the IP for ATLAS (IP1)	[μrad]	±295 (V)	±295 (V)
Half parallel separation at the IP for ATLAS (IP1)	[mm]	-2.0 (H)	0.0 (H)
Half external crossing angle at IP for ALICE (IP2)[8]	[μrad]	±170 (V)	±170 (V)
Half crossing angle at the IP for ALICE (IP2)[19]	[μrad]	±1259 (V)	±240 (V)
Half parallel separation at the IP for ALICE (IP2)	[mm]	+2.0 (H)	+0.144[20](H)
Half crossing angle at the IP for CMS (IP5)	[μrad]	+295 (H)	+295 (H)
Half parallel separation at the IP for CMS (IP5)	[mm]	±2.0 (V)	0.0 (V)
Half external crossing angle at the IP for LHCb (IP8) [8]	[μrad]	-170(H)	-250(H)
Half crossing angle at the IP for LHCb (IP8) [8]	[μrad]	1930(H)	-115 (H)
Half parallel angle at the IP for LHCb (IP8) [3]	[μrad]	±30(V)	0
Half parallel separation at IP for LHCb (IP8) [3]	[mm]	±3.5(V)	0.0(V)
Minimum β at IP1 and IP5	[m]	6	0.15
Minimum β at IP2	[m]	10	10
Minimum β at IP8	[m]	10	3

A.3. Main Insertion Region Magnet parameters

Table A- 4: New or refurbished quadrupoles for HL-LHC, all operating at 1.9 K. The orientation of the Rectellipse aperture [4] can be changed to optimise the mechanical aperture.

	Inner triplet (single aperture)			Matching section (2-in-1)		
Magnet	Q1	Q2	Q3	Q4	Q5	Q6
Number per side and per insertion	2	2	2	1	1	1
Type	MQXFA	MQXFB	MQXFA	MQYY	MQY	MQML
Magnetic length [m]	4.0	6.8	4.0	3.8	3.4	4.8
Gradient [T/m]	140			115	200	200
Coil aperture [mm]	150			90	70	56
Aperture separation [mm]	n/a			194	194	194
Beam screen (BS) shape	Octagon			Rectellipse		
BS aperture (H/V) [mm]	98/98	118/118		64/74	44/57.8	35.3/45.1
Mech. tolerances (R/H/V)[21] [mm]	0.6/1/1	0.6/1/1		0.84/1.26/0.6	0.84/1.26/0.6	as built

---

[19] The crossing angle in IP2 and IP8 is the sum of an external crossing angle bump and an 'internal' spectrometer compensation bump and it depends on the spectrometer polarity. The values quoted above correspond to the configuration with the spectrometer ON providing to the minimum long-range beam-beam normalized separation. The external bump extends over the triplet and D1 and D2 magnets. The internal spectrometer compensation bump extends only over the long drift space between the two triplet assemblies left and right from the IP. For IP2 the vertical external crossing angle sign can be changed and therefore the same sign of the internal and external angle can be chosen to be the same. This is not possible for IP8 as the sign of the crossing angle must be compatible with the recombination scheme.

[20] This corresponds to a full separation of 5 σ required to reduce the luminosity down to 10^{31} cm^{-2}s^{-1}.

[21] The definition of the parameters of the mechanical tolerances is given in [5].

Table A- 5: New dipole magnets for HL-LHC, all operating at 1.9 K. The orientation of the Rectellipse aperture can be changed to optimise the mechanical aperture. The orbit correctors can be nested or consecutive as indicated.

	Separation/ recombination dipoles		Orbit correctors			
Magnet	D1	D2	Q1/Q3	Q2	D2	Q4
Number per side and per insertion	1	1	2 [HV nest.]	1 [HV nest.]	2 [HV cons.]	2 [HV cons.]
Type	MBXF	MBRD	MCBXFA	MCBXFB	MCBRD	MCBYY
Magnetic length [m]	6.27	7.78	1.2	2.2	1.5	1.5
Integrated field [Tm]	35	35	2.5	4.5	4.5	4.5
Coil aperture [mm]	150	105	150	150	100	100
Aperture separation [mm]	n/a	188	n/a		194	194
BS shape	Octagon					Rectellipse
BS aperture (H/V) [mm]	118/118	84/84	118/118		79/79	64/74
Mech. tolerances (R/H/V) [mm]	0.6/1/1	0.84/1.36/1	0.6/1/1		0.84/1.36/1	0.84/1.26/0.6

Table A- 6: New multipolar superferric correctors for HL-LHC, all operating at 1.9 K.

Number	1	1	1	1	1	1	1	1	1
# poles	4	12	12	10	10	8	8	6	6
Normal/Skew	skew	normal	skew	normal	skew	normal	skew	normal	skew
Type	MQSXF	MCTXF	MCTSXF	MCDXF	MCDSXF	MCOXF	MCOSXF	MCSXF	MCSSXF
Mag. length [m]	0.807	0.43	0.089	0.095	0.095	0.087	0.087	0.111	0.111
Integrated field [mT·m] @50 mm	1000	86	17	25	25	46	46	63	63
Coil ap. [mm]	150								
BS shape	Octagon								
BS aperture (H/V) [mm]	118/118								
Mech. tolerances (R/H/V) [mm]	0.6/1/1								

The implementation of the ATS scheme in the HLLHCV1.0 requires hardware changes in other parts of the LHC ring. In particular, an additional sextupole (MS) magnet should be installed in Q10 in IR1 and 5. Moreover, Q5 in IR6 should be upgraded. The current baseline layout envisages the installation of a second MQY-type quadrupole close to each existing Q5.

A.4. Field Error Specification for the new Insertion Region Magnets

In this section the error tables used in the tracking simulations (as described in Chapter 2 - Section 3.2) for the various classes of new magnets are collected. Whenever the expected values of the multipoles turned out to cause an unacceptable reduction of the DA, the tables also give the requested values (in red) based on the beam dynamics studies. Note that the expected error tables at injection turned out to be already compatible with the criterion based on DA computation.

Table A- 7: Expected field quality errors at injection energy for the new IT (r_0 = 50 mm). These values represent the so-called IT_errortable_v66 in [6].

skew	mean	uncertainty	random	normal	mean	uncertainty	random
a3	0	0.800	0.800	b3	0	0.820	0.820
a4	0	0.650	0.650	b4	0	0.570	0.570
a5	0	0.430	0.430	b5	0	0.420	0.420
a6	0	0.310	0.310	b6	-16.0	1.100	1.100
a7	0	0.190	0.190	b7	0	0.190	0.190
a8	0	0.110	0.110	b8	0	0.130	0.130
a9	0	0.080	0.080	b9	0	0.070	0.070
a10	0	0.040	0.040	b10	4.15	0.200	0.200
a11	0	0.026	0.026	b11	0	0.026	0.026
a12	0	0.014	0.014	b12	0	0.018	0.018
a13	0	0.010	0.010	b13	0	0.009	0.009
a14	0	0.005	0.005	b14	-0.040	0.023	0.023

Table A- 8: Expected (blue) and target (red) field quality errors at top energy for the new IT (r_0 = 50 mm). These values represent the so-called IT_errortable_v66 in [6].

skew	mean	uncertainty	random	normal	mean	uncertainty	random
a3	0	0.800	0.800	b3	0	0.820	0.820
a4	0	0.650	0.650	b4	0	0.570	0.570
a5	0	0.430	0.430	b5	0	0.420	0.420
a6	0	0.310	0.310	b6	0.800	0.550	0.550
a7	0	0.152	0.095	b7	0	0.095	0.095
a8	0	0.088	0.055	b8	0	0.065	0.065
a9	0	0.064	0.040	b9	0	0.035	0.035
a10	0	0.040	0.032	b10	0.075	0.100	0.100
a11	0	0.026	0.0208	b11	0	0.0208	0.0208
a12	0	0.014	0.014	b12	0	0.0144	0.0144
a13	0	0.010	0.010	b13	0	0.0072	0.0072
a14	0	0.005	0.005	b14	-0.020	0.0115	0.0115

Table A- 9: Expected field quality at injection energy for the new D1 (r_0 = 50 mm). These values represent the so-called D1_errortable_v1 in [6].

skew	mean	uncertainty	random	normal	mean	uncertainty	random
a2	0	0.679	0.679	b2	0	0.200	0.200
a3	0	0.282	0.282	b3	-16.0	0.727	0.727
a4	0	0.444	0.444	b4	0	0.126	0.126
a5	0	0.152	0.152	b5	-0.500	0.365	0.365
a6	0	0.176	0.176	b6	0	0.060	0.060
a7	0	0.057	0.057	b7	0.900	0.165	0.165
a8	0	0.061	0.061	b8	0	0.027	0.027
a9	0	0.020	0.020	b9	-0.660	0.065	0.065
a10	0	0.025	0.025	b10	0	0.008	0.008
a11	0	0.007	0.007	b11	0.440	0.019	0.019
a12	0	0.008	0.008	b12	0	0.003	0.003
a13	0	0.002	0.002	b13	0	0.006	0.006
a14	0	0.003	0.003	b14	0	0.001	0.001
a15	0	0.001	0.001	b15	-0.040	0.002	0.002

Table A- 10: Expected (blue) and target (red) field quality at top energy for the new D1 (r_0 = 50 mm). These values represent the so-called D1_errortable_v1 in [6].

skew	mean	uncertainty	random	normal	mean	uncertainty	random
a2	0	0.679	0.679	b2	0	0.200	0.200
a3	0	0.282	0.282	b3	-0.900	0.727	0.727
a4	0	0.444	0.444	b4	0	0.126	0.126
a5	0	0.152	0.152	b5	0	0.365	0.365
a6	0	0.176	0.176	b6	0	0.060	0.060
a7	0	0.057	0.057	b7	0.4→0.2	0.165	0.165
a8	0	0.061	0.061	b8	0	0.027	0.027
a9	0	0.020	0.020	b9	-0.59→-0.295	0.065	0.065
a10	0	0.025	0.025	b10	0	0.008	0.008
a11	0	0.007	0.007	b11	0.470	0.019	0.019
a12	0	0.008	0.008	b12	0	0.003	0.003
a13	0	0.002	0.002	b13	0	0.006	0.006
a14	0	0.003	0.003	b14	0	0.001	0.001
a15	0	0.001	0.001	b15	-0.040	0.002	0.002

Table A- 11: Expected field quality at injection energy for the new D2 (r_0 = 35 mm). These values represent the so-called D2_errortable_v4 in [6].

skew	mean	uncertainty	random	normal	mean	uncertainty	random
a2	0	0.679	0.679	b2	0	0.200	0.200
a3	0	0.282	0.282	b3	3.8	0.727	0.727
a4	0	0.444	0.444	b4	±8.0	0.126	0.126
a5	0	0.152	0.152	b5	3.0	0.365	0.365
a6	0	0.176	0.176	b6	0	0.060	0.060
a7	0	0.057	0.057	b7	0.100	0.165	0.165
a8	0	0.061	0.061	b8	0	0.027	0.027
a9	0	0.020	0.020	b9	0.020	0.065	0.065
a10	0	0.025	0.025	b10	0	0.008	0.008
a11	0	0.007	0.007	b11	0	0.019	0.019
a12	0	0.008	0.008	b12	0	0.003	0.003
a13	0	0.002	0.002	b13	0	0.006	0.006
a14	0	0.003	0.003	b14	0	0.001	0.001
a15	0	0.001	0.001	b15	0	0.002	0.002

Table A- 12: Expected (blue) and target (red) field quality at top energy for the new D2 (r_0 = 35 mm). These values represent the so-called D2_errortable_v4 in [6]. The value of b_2 requires correction to prevent impact on machine performance due to the large beta-beating induced.

skew	mean	uncertainty	random	normal	mean	uncertainty	random
a2	0	0.679	0.679	b2	±25→~1	2.5→~1	2.5→~1
a3	0	0.282	0.282	b3	3.0→1.5	1.5	1.5
a4	0	0.444	0.444	b4	±2.0	0.2	0.2
a5	0	0.152	0.152	b5	-1.0	0.5	0.5
a6	0	0.176	0.176	b6	0	0.060	0.060
a7	0	0.057	0.057	b7	-0.200	0.165	0.165
a8	0	0.061	0.061	b8	0	0.027	0.027
a9	0	0.020	0.020	b9	0.090	0.065	0.065
a10	0	0.025	0.025	b10	0	0.008	0.008
a11	0	0.007	0.007	b11	0.030	0.019	0.019
a12	0	0.008	0.008	b12	0	0.003	0.003
a13	0	0.002	0.002	b13	0	0.006	0.006
a14	0	0.003	0.003	b14	0	0.001	0.001
a15	0	0.001	0.001	b15	0	0.002	0.002

Table A- 13: Expected field quality at injection energy for the new Q4 (r₀ = 30 mm). These values represent the so-called Q4_errortable_v1 in [6]

skew	mean	uncertainty	random	normal	mean	uncertainty	random
a3	0	0.682	1.227	b3	0	1.282	1.500
a4	0	0.428	0.893	b4	0	0.483	0.465
a5	0	0.177	0.406	b5	0	0.203	0.431
a6	0	0.484	0.277	b6	-10.373	10.373	2.974
a7	0	0.094	0.189	b7	0	0.094	0.189
a8	0	0.193	0.257	b8	0	0.193	0.257
a9	0	0.088	0.088	b9	0	0.088	0.088
a10	0	0.120	0.120	b10	0	3.587	0.956
a11	0	0.326	0.489	b11	0	0.326	0.489
a12	0	0.445	0.222	b12	0	0.445	0.222
a13	0	0.606	0.303	b13	0	0.606	0.303
a14	0	0.827	0.413	b14	0	2.067	0.413
a15	0	1.127	0.564	b15	0	1.127	0.564

Table A- 14: Expected field quality at top energy for the new Q4 (r₀ = 30 mm). These values represent the so-called Q4_errortable_v1 in [6].

skew	mean	uncertainty	random	normal	mean	uncertainty	random
a3	0	0.682	1.227	b3	0	1.282	1.500
a4	0	0.428	0.893	b4	0	0.483	0.465
a5	0	0.177	0.406	b5	0	0.203	0.431
a6	0	0.484	0.277	b6	0	5.187	1.487
a7	0	0.094	0.189	b7	0	0.094	0.189
a8	0	0.193	0.257	b8	0	0.193	0.257
a9	0	0.088	0.088	b9	0	0.088	0.088
a10	0	0.120	0.120	b10	0	3.587	0.956
a11	0	0.326	0.489	b11	0	0.326	0.489
a12	0	0.445	0.222	b12	0	0.445	0.222
a13	0	0.606	0.303	b13	0	0.606	0.303
a14	0	0.827	0.413	b14	0	2.067	0.413
a15	0	1.127	0.564	b15	0	1.127	0.564

Table A- 15: Expected field quality at injection energy for the new Q5 (r_0 = 17 mm). These values represent the so-called Q5_errortable_v0 in [6].

skew	mean	uncertainty	random	normal	mean	uncertainty	random
a3	0	0.500	0.900	b3	0	0.940	1.100
a4	0	0.230	0.480	b4	0	0.260	0.250
a5	0	0.070	0.160	b5	0	0.080	0.170
a6	0	0.140	0.080	b6	-3.000	3.000	0.860
a7	0	0.020	0.040	b7	0	0.020	0.040
a8	0	0.030	0.040	b8	0	0.030	0.040
a9	0	0.010	0.010	b9	0	0.010	0.010
a10	0	0.010	0.010	b10	0	0.300	0.080
a11	0	0.020	0.030	b11	0	0.020	0.030
a12	0	0.020	0.010	b12	0	0.020	0.010
a13	0	0.020	0.010	b13	0	0.020	0.010
a14	0	0.020	0.010	b14	0	0.050	0.010
a15	0	0.020	0.010	b15	0	0.020	0.010

Table A- 16: Expected field quality at top energy for the new Q5 (r_0 = 17 mm). These values represent the so-called Q5_errortable_v0 in [6].

skew	mean	uncertainty	random	normal	mean	uncertainty	random
a3	0	0.500	0.900	b3	0	0.940	1.100
a4	0	0.230	0.480	b4	0	0.260	0.250
a5	0	0.070	0.160	b5	0	0.080	0.170
a6	0	0.140	0.080	b6	0	1.500	0.430
a7	0	0.020	0.040	b7	0	0.020	0.040
a8	0	0.030	0.040	b8	0	0.030	0.040
a9	0	0.010	0.010	b9	0	0.010	0.010
a10	0	0.010	0.010	b10	0	0.300	0.080
a11	0	0.020	0.030	b11	0	0.020	0.030
a12	0	0.020	0.010	b12	0	0.020	0.010
a13	0	0.020	0.010	b13	0	0.020	0.010
a14	0	0.020	0.010	b14	0	0.050	0.010
a15	0	0.020	0.010	b15	0	0.020	0.010

A.5. References

[17] HL-LHC Parameter and Layout Committee Parameter table v 4.1.0 (27/8/2014) https://espace.cern.ch/HiLumi/PLC/_layouts/xlviewer.aspx?id=/HiLumi/PLC/SiteAssets/Parameter%20Table.xlsx

[18] G. Arduini, O. Brüning, R. De Maria, R. Garoby, S. Gilardoni, B. Goddard, B. Gorini, M. Meddahi, G. Rumolo, R. Tomás, "Beam parameters at LHC injection", CERN-ACC-2014-0006.

[19] S. Fartoukh, "LHCb crossing scheme for Run II & III", LHC Machine Committee Meeting n. 167, 19/6/2013, https://espace.cern.ch/lhc-machine-committee/Presentations/1/lmc_167/LHCb%20crossing%20scheme%20for%20Run%20II%20and%20III_S.Fartoukh.pdf

[20] O. S. Brüning, P. Collier, P. Lebrun, S. Myers, R. Ostojic, J. Poole, P. Proudlock (eds.), "LHC Design Report , v.1: the LHC Main Ring", CERN-2004-003-V-1, 2012.

[21] J.-B. Jeanneret, "Geometrical Tolerances for the Qualification of LHC magnets", LHC Project Report 1007, 2007

[22] /afs/cern.ch/eng/lhc/optics/HLLHCV1.0/errors/

Acronyms

B. HL-LHC Acronyms

a-C	Amorphous Carbon
ADT	Transverse Damper
ALARA	As Low As Reasonable Achievable
ASIC	Application Specific Integrated Circuit
ATS	Achromatic Telescopic Squeezing
AUG	emergency stop buttons
BCMS	Bach Compression and beam Merging Scheme
BETS	Beam Energy Tracking System
BFPP	Bound-Free Pair Production
BGV	Beam Gas Vertex Profile Monitor
BIS	Beam Interlock System
BLM	LHC Beam Loss Monitoring system
BPM	Beam Position Monitor
BRAN	TAN Luminosity monitor
BS	Beam Screen
BSRT	Synchrotron Radiation Telescope Monitor
CC	Crab Cavities
CCB	Cold compressor box
CDD	Cern Design Directory
CDP	Conductor Development Program
CFC	Carbon-fibre Carbon composites
CMOS	Complementary Metal-Oxide-Semiconductor
COTS	Commercial-Off-The-Shelf
CVD	Chemical Vapour Deposition
DA	Dynamic Aperture
DAC	Digital-to-Analogue Converter
DAQ	data acquisition
DF	Distribution Feed Box
DFBAM	Distribution Feed Box for Arc - IR 7/L
DFBAN	Distribution Feed Box for Arc - IR 7/R
DPA	Displacements-Per-Atom
DQW	Double Quarter Wave cavity
DSs	Dispersion Suppressors
DVB	cryogenic Distribution Valve Box
DWR	extraction resistors
EC	Electron Cloud
EE	energy extraction systems
ElQA	high voltage qualification
EMD	ElectroMagnetic Dissociation
ERA	European Research Area
ESFRI	European Strategy Forum on Research infrastructure

EUCARD	Enhanced European Coordination for Accelerator Research & Development
EYETS	Extended yearly Technical Stop
FMCM	Fast Magnet Current Change Monitors
FNAL	Fermi National Accelerator Laboratory
HEB	Hollow Electron Beam
HL-LHC	High Luminosity Large Hadron Collider
HFM	High Field Magnet
HOM	High-Order Modes
HTS	High Temperature Superconductor
IBS	Intra-Beam Scattering
IP	Interaction Point
IR	Interaction region
IT	Inner Triplet magnets
LARP	LHC Accelerator Research Program
LBDS	LHC Beam Dumping System
LCB	Lower Cold Box
LIU	LHC Injector complex Upgrade
LLRF	Low Level RF
LRBB	Long-Range Beam-Beam
LS[X]	Long Shutdown [Id Number]
LSS	Long straight Section
LVDT	Linear Variable Differential Transformer
MB	Main LHC Dipoles
MBH	11T Dipole
MBU	Multiple Bit Upsets
MCDO	Magnet Corrector Decapole/Octupole
MCS	Magnet Corrector Sextupole
MD	Machine Development
MIM	Multi-band Instability Monitor
MKB	Diluter Dump Kicker
MKI	Magnet Injection Kicker
MP3	Magnet circuits, Powering and Performance Panel
MPP	Machine Protection Panel
MPS	Machine Protection System
MQY	Insertion Region Wide Aperture Quadrupole
MS	Matching Section
NEG	Non-Evaporable Getter
NIEL	Non-Ionizing Energy Losses
NIMS	National Institute of Materials Science
P5	Particle Physics Project Prioritization Panel
PIC	powering interlock system
PIT	Powder-In-Tube process
PLC	programmable logic controller

PU	Pile-Up
QPS	Quench Protection System
QRL	cryogenic distribution line
QV	Quench buffer
r.m.s.	Root mean square
R2E	Radiation To Electronics
RF	Radio Frequency
RFD	RF Dipole cavity
RHQT	Rapid-Heating, Quenching Transformation
RRP	Restacked Rod Process
SC	Super Conductor
SCL	Super Conducting Link
SCRF	Superconducting Radio frequency
SEE	Single Event Effects
SEU	Single bit upsets
SEY	Secondary Electron Yield
SIL	Safety Integrity Level
SM	Service Module
SPS	Super Proton Synchrotron
SPT	Scheduled proton physics time
SR	Synchrotron radiation
SRF	Superconducting Radio frequency
TAXN	Target Absorber for Insertion Region Neutrals
TAXS	Target Absorber for Insertion Region Secondary
TCAP	Target Collimator Absorber Passive
TCDQ	Collimator for Q4 Protection
TCL	Long Collimator
TCLA	Target Collimator Long Absorber
TCLD	Auxiliary Collimators in DS Area
TCPP	Primary Collimator with BPM
TCSG	Target Collimator Secondary Graphite
TCSMP	Secondary Collimator Metallic Prototype
TCSP	Secondary Collimator with Pick-Up
TCSPM	Secondary Collimator with Pick-Up Metallic
TCT	Target Collimators Tertiary
TCTP	Target Collimator Tertiary with Pick-up
TCTPM	Target Collimator Tertiary with Pick-up Metallic
TDE	Target Dump for Ejected Beam
TDI	Beam Absorber for Injection
TID	Total Ionizing Dose
TMCI	Transverse Mode Coupling Instability
TS[X]	Technical stop [Id Number]
UA[X]	Service and access tunnel [Point Number]

UCB	Upper Cold Box
UFO	Falling particles
UJ[X]	Service cavern [Point Number]
UPS	Uninterruptable Power Supplies
VCT	Vacuum Chamber Transition
VDWB	Vacuum - Dump lines - Window
VELO	Vertex Locator
WBTN	Wide Band Time Normalizer
WCS	Warm Compressor Station
WIC	warm magnet interlock system

Glossary and Definitions

C. Glossary and Definitions

β^*	Optical β-function at the IP.
η	Machine slip factor.
η_D	Normalized dispersion: $\eta D = D/\sqrt{\beta}$, where D is the machine dispersion.
γ	Optic gamma function: $\gamma(s) = (1 + \alpha 2(s))/\beta(s)$ where $\beta(s)$ is the optical betatron function along the machine and $\alpha(s) = -\dfrac{d\beta}{2\,ds}$.
γ_r	The relativistic gamma factor.
abort gap	Area without any bunches in the bunch train that fits the time required for building up the nominal field of the LHC dump kicker.
arc	The part of the ring occupied by regular half-cells. Each arc contains 46 half cells. The arc does not contain the dispersion suppressor.
arc cell	It consists of two arc half-cells and presents the basic period of the optic functions.
arc half-cell	Periodic part of the LHC arc lattice. Each half-cell consists of a string of three twin aperture main dipole magnets and one short straight section. The cryo magnets of all arc half-cells follow the same orientation with the dipole lead end pointing upstream of Beam 1 (downstream of Beam 2).
batch	**PS batch:** Train of 72 bunches that is injected into the SPS in one PS to SPS transfer. **SPS batch:** Train of 4×72 or 3×72 bunches that is injected into the LHC in one SPS to LHC transfer.
Beam 1 and Beam 2	Beam 1 and Beam 2 refer to the two LHC beams. Beam 1 circulates clockwise in Ring 1 and Beam 2 circulates counter clockwise in Ring 2. If colors are used for beams, Beam 1 is marked blue and Beam 2 red.
beam cleaning	Removal of the large amplitude (larger than 6 sigma) particles from the beam halo. The LHC has two beam cleaning insertions: one dedicated to the removal of particles with large transverse oscillation amplitudes (IR7) and one dedicated to the removal of particles with large longitudinal oscillation amplitudes (IR3). These insertions are also referred to as the betatron and momentum cleaning or collimation insertions.
beam crossing angle	Dedicated orbit bumps separate the two LHC beams at the parasitic beam crossing points of the common beam pipe of Ring 1 and Ring 2. The crossing angle bumps do not separate the beams at the IP but only at the parasitic crossing points. These orbit bumps generate an angle between the orbit of Beam 1 and Beam 2 at the IP. The full angle between the orbit of Beam 1 and Beam 2 is called the crossing angle. In IR2 and IR8 the crossing angle orbit bumps consist of two separate contributions. One external bump generated for the beam separation at the parasitic beam crossing points and one internal bump generated by the experimental spectrometer and its compensator magnets. The LHC baseline foresees vertical crossing angles in IR1 and IR2 and horizontal crossing angles in IR5 and IR8.

beam screen	Perforated tube inserted into the cold bore of the superconducting magnets in order to protect the cold bore from synchrotron radiation and ion bombardment.
beam types	**Pilot beam:** Consists of a single bunch with 0.5×10^{10} protons. It corresponds to the maximum beam current that can be lost without inducing a magnet quench. **Commissioning beam:** Beam tailored for a maximum luminosity with reduced total beam power (i.e. increased operational margins related to beam losses and magnet quenches) and possibly smaller beam sizes (i.e. increased mechanical acceptance in terms or the transverse beam size and larger tolerances for orbit and β-beat). **Intermediate beam:** Beam tailored for a high accuracy of the beam measurements with reduced total beam power (i.e. increased operational margins related to beam losses and magnet quenches). **Nominal beam:** Beam required to reach the design luminosity of $L = 10^{34}$ cm^{-2}s^{-1} with $\beta^* = 0.55$ m ($\rightarrow$ normalized emittance $\varepsilon_n = 3.75$ μm; $N_b = 1.15 \times 10^{11}$; $n_b = 2808$). **Ultimate beam:** Beam consisting of the nominal number of bunches with nominal emittances (normalized emittance of 3.75μm) and ultimate bunch intensities ($I = 0.86A \rightarrow N_b = 1.7 \times 10^{11}$). Assuming the nominal value of $\beta^* = 0.55$ m and 2808 bunches, the ultimate beam can generate a peak luminosity of $L = 2.3 \times 10^{34}$ cm^{-2}s^{-1} in the two high luminosity experiments.
BPM	Beam Position Monitor.
bunch	Collection of particles captured within one RF bucket.
bus bar	Main cable that carries the current for powering the magnets outside the magnet coil.
channel	The two apertures of the double bore magnets form two channels of the LHC. Each arc has one outer and one inner channel.
cold mass	The cold mass refers to the part of a magnet that needs to be cooled by the cryogenic system, i.e. the assembly of magnet coils, collars, iron yoke and Helium vessel.
crossings	The two machine channels cross at the experimental insertions, i.e. at IP1, IP2, IP5 and IP8.
cryo magnet	Complete magnet system integrated into one cryostat, i.e. main magnet coils, collars and cryostat, correction magnets and powering circuits.
DA	See dynamic aperture
damper	Transverse or longitudinal feedback system used to damp injection oscillations and / or multi bunch instabilities of a beam.
decay and snap back	Persistent current decay is a change in the persistent current contribution to the total magnetic field in superconducting magnets powered at constant current (e.g. at injection). This effect varies among magnets and is a function of the powering history (i.e. previous current cycles). When the magnet current is changed (e.g. during the acceleration ramp) the magnetic field comes back to the original value before the decay. This effect is called snap

	back and occurs for the LHC main dipole magnets within the first 50 A change of the LHC ramp.
dispersion suppressor	The dispersion suppressor refers to the transition between the LHC arcs and insertions. The dispersion suppressor aims at a reduction of the machine dispersion inside the insertions. Each LHC arc has one dispersion suppressor on each end. The length of the dispersion suppressors is determined by the tunnel geometry. Each LHC dispersion suppressor consists of four individually powered quadrupole magnets which are separated by two dipole magnets. In the following this arrangement of 4 quadrupole and 8 dipole magnets is referred to as two missing dipole cells. For the machine lattice these two missing dipole cells are referred to as one dispersion suppressor. However, reducing the dispersion at the IPs to zero requires a special powering of two more quadrupole magnets on each side of the arc. In terms of the machine optics the dispersion suppressor refers therefore to the two missing dipole cells plus one additional arc cell.
dog leg magnets	Special dipole magnet used for increasing the separation of the two machine channels from standard arc separation. The dogleg magnets are installed in the cleaning insertions IR3 and IR7 and the RF insertion IR4.
dynamic aperture	Maximum initial oscillation amplitude that guarantees stable particle motion over a given number of turns. The dynamic aperture is normally expressed in multiples of the RMS beam size (σ) and together with the associated number of turns.
eddy currents	Eddy currents are screening currents that tend to shield the interior of a conductor or a superconducting cable from external magnetic field changes. In the case of a strand the eddy currents flow along the superconducting filaments in the strand (without loss) and close across the resistive matrix of the strand (copper for the LHC). In the case of a cable the eddy currents flow along the strands (without loss) and close resistively at the contact points among strands in the cable. Eddy currents are also referred to as coupling currents.
experimental insertion region	Insertion region that hosts one of the four LHC experiments.
filament	Superconducting filaments are fine wires of bulk superconducting material with typical dimension in the range of few microns. The superconducting filaments are embedded in the resistive matrix in a strand.
hourglass effect 'H'	Luminosity loss due to longitudinal modulation of beta function over the length of the bunch for small $\beta*$.
insertion region (IR)	Machine region between the dispersion suppressors of two neighboring arcs. The insertion region consists of two matching sections and, in the case of the experimental insertions, of two triplet assemblies and the separation / recombination dipoles.
interaction point (IP)	Middle of the insertion region (except for IP8). In the insertions where the two LHC beams cross over the IP indicates the point where the two LHC beams can intersect. In IR8 the experimental detector is shifted by 3/2 RF wave length and the IP refers to the point where the two LHC beams can intersect and does not coincide with the geometric center of the insertion.

ions	The LHC foresees collisions between heavy ions, $^{208}Pb^{82+}$ (fully stripped) during the first years (208 is the number of nucleons, 82 the number of protons of this particular nucleus).
ions, nominal scheme	Approximately 600 bunches per beam, with 7×10^7 Pb ions each, are colliding at 2.76 TeV/u to yield initial luminosity of $L = 1.0 \times 10^{27}$ cm^{-2}sec^{-1} with ($\beta^* = 0.5$ m).
Ions, early scheme	Approximately 60 bunches per beam, with 7×10^7 Pb ions each, are colliding to yield initial luminosity of $L = 5.0 \times 10^{25}$ cm^{-2}sec^{-1} with ($\beta^* = 0.5$ m).
lattice correction magnets	Correction magnets that are installed inside the Short Straight Section assembly.
lattice version	The lattice version refers to a certain hardware installation in the tunnel. It is clearly separated from the optics version and one lattice version can have more than one optics version.
left and right	See the definition under 'right and left'.
long range interactions	Interaction between the two LHC beams in the common part of the Ring 1 and Ring 2 where the two beams are separated by the crossing angle orbit bumps.
Long Straight Section (LSS)	the quasi-straight sections between the upstream and downstream dispersion suppressor of an insertion, including the separation / recombination dipole magnets.
luminous region	The 3-dimensional distribution of the collision event vertices
Luminosity reduction	**Geometric luminosity reduction factor due to beam offset 'R':** Reduced beam overlap due to transversal offset of collisions, frequently used for reduction of luminosity (levelling) and VdM scans. **Luminosity reduction factor due to crossing angle 'S':** Reduced beam overlap due to tilted bunch shape due to crossing angle. **Total luminosity reduction factor 'F' = R*H*S[22]**
machine cycle	The machine cycle refers to one complete operation cycle of a machine, i.e. injection, ramp up, possible collision flat top, ejection and ramp down. The minimum cycle time refers to the minimum time required for a complete machine cycle.
machine statistics	**run time:** annual time allocated to running with beam [days]. **scheduled physics time:** annual time allocated to physics (excluding initial beam commissioning, scrubbing, TS, recovery from TS, MDs, special physics) [days]. **physics efficieny:** time with both beams present and stable beams, versus scheduled physics time [%]. **machine availability:** time when machine is in a state allowing operations to take beam and run through nominal physics cycle, versus run time [%]. **turnaround time:** Time between the end of one and the start of the next physics run / data taking by the experiments (delimited by the loss of

---

[22] Strictly speaking no direct multiplication, but providing a reasonable indication of the different contributions (while dominated by crossing angle contribution).

	beam presence/beam dump back to declaration of STABLE_BEAMS) [hours]. **recovery time:** Time between the end of one and the readiness for injection of new particles of the next (delimited by the loss of beam presence/beam dump and resuming of the normal operational cycle) [hours].
magnet quench	Loss of the superconducting state in the coils of a superconducting magnet.
main lattice magnets	Main magnets of the LHC arcs, i.q. the arc dipole and quadrupole magnets.
matching section	Arrangement of quadrupole magnets located between the dispersion suppressor and the triplet magnets (or the IP for those insertions without triplet magnets). Each insertion has two matching sections: one upstream and one downstream from the IP.
n_1	The effective mechanical aperture n_1 defines the maximum primary collimator opening in terms of the rms beam size that still guarantees a protection of the machine aperture against losses from the secondary beam halo. It depends on the magnet aperture and geometry and the local optics perturbations.
N_b	Number of particles per bunch.
n_b	Number of bunches per beam.
nominal bunch	Bunch parameters required to reach the design luminosity of $L = 10^{34} \text{cm}^{-2} s^{-1}$ with $\beta^* = 0.55$ m. The nominal bunch intensity is $N_b = 1.15 \times 10^{11}$ protons.
nominal powering	Hardware powering required to reach the design beam energy of 7 TeV.
octant	An octant starts in the center of an arc and goes to the center of the next downstream arc. An octant consists of an upstream and a downstream half-octant. A half-octant and a half-sector cover the same part of the machine even though they may not have the same number.
optical configuration	An optical configuration refers to a certain powering of the LHC magnets. Each optics version has several optical configurations corresponding to the different operation modes of the LHC. For example, each optics version has different optical configuration for injection and luminosity operation and for the luminosity operation the optics features different optical configurations corresponding to different β^* values in the four experimental insertions of the LHC.
optics version	The optics version refers to a consistent set of optical configurations. There can be several different optics versions for one lattice version.
pacman bunches	Bunches that do not experience the same number of long-range beam-beam interactions left and right from the IP.
parallel separation	Dedicated orbit bumps separate the two LHC beams at the IP during injection, ramp and the optics squeeze. The total beam separation at the IP is called the parallel separation. The LHC baseline foresees horizontal parallel separations in IR1 and IR2 and vertical separations in IR5 and IR8.

parasitic crossing points	Positions in the common part of the Ring 1 and Ring 2 where the two beams can experience long range interactions.
persistent currents	Persistent currents are eddy currents with (ideally) infinitely long time constants that flow in the bulk of the superconducting filaments of a strand and tend to shield the interior of the filament from the external magnetic field changes. These screening currents close inside the superconducting filament, with zero resistance (in steady state). Hence, for practical purposes, they do not decay in time and for this reason they are referred to as 'persistent'.
physics run	Machine operation at top energy with luminosity optics configuration and beam collisions.
pile-up	**Event pile-up μ:** Number of visible inelastic proton-proton interactions in a given bunch crossing. **Average pile-up:** Mean value of the pile-up over a fill (averaged over all bunch crossings). **Peak pile-up:** Maximum pile-up in any bunch crossing at any time (usually at the start of the fill). **Peak average pile-up:** Mean pile-up at the beginning of the fill. It corresponds to the peak luminosity of the fill. In practice, it is determined as the maximum of the pile-up values obtained by averaging over all bunch crossings within time intervals of typically one minute. **Average pile-up density:** Number of inelastic proton-proton interactions in a given bunch-crossing divided by the size of the luminous region in Z.
pilot bunch	Bunch intensity that assures no magnet quench at injection energy for an abrupt loss of a single bunch but is still large enough provide BPM readings. The pilot bunch intensity of the LHC corresponds to 0.5×10^{10} protons in one bunch.
Piwinski parameter	Parameterisation of reduced beam overlap due to finite crossing-angle.
ramp	Change of the magnet current during. During the beam acceleration the magnets are 'ramped up' and after the end of a physics store the magnets are 'ramped down'.
resistive matrix	One of the two main constituents of the strand. The resistive matrix embeds the filaments in the strand and provides a low resistance current shunt in case of quench (transition of the superconducting material to the normal state).
RF bucket	The RF system provide a longitudinal focusing which constrains the particle motion in the longitudinal phase space to a confined region called the RF bucket.
Ring 1 and Ring 2	There are two rings in the LHC, one ring per beam. Ring 1 corresponds to Beam 1 which circulates clockwise and Ring 2 corresponds to Beam 2 which circulates counter clockwise in the LHC.
right and left	Describes the position in the tunnel relative to an observer inside the ring looking out (same definition as for LEP).
satellite bunch	Collection of particles inside RF buckets that do not correspond to nominal bunch positions. The nominal bunch spacing for the LHC is 25 ns while the

	separation of RF buckets is 2.5 ns. In other words, there are 9 RF buckets between two nominal LHC bunch positions that should be empty.
sector	The part of a ring between two successive insertion points (IP) is called a sector. Sector 1-2 is situated between IP1 and IP2.
separation / recombination magnets	Special dipole magnets left and right from the triplet magnets that generate the beam crossings in the experimental insertions.
Short Straight Section (SSS)	Assembly of the arc quadrupole and the lattice corrector magnets. Each SSS consists of one quadrupole magnet, one Beam Position Monitor (BPM), one orbit corrector dipole (horizontal deflection for focusing and vertical deflection for defocusing quadrupoles), one lattice correction element (i.e. trim or skew quadrupole elements or octupole magnets) and one lattice sextupole or skew sextupole magnet.
SPecial Straight Section (SPSS)	Quadrupole assemblies of the insertion regions. The SPSS features no lattice corrector and sextupole magnets and has only orbit correction dipole magnets and BPMs.
spool piece correction magnets	Correction magnets directly attached to the main dipole magnets. The spool piece correction magnets are included in the dipole cryostat assembly
strand	A superconducting strand is a composite wire containing several thousands of superconducting filaments dispersed in a matrix with suitably small electrical resistivity properties. The LHC strands have NbTi as superconducting material and copper as resistive matrix.
superconducting cable	Superconducting cables are formed from several superconducting strands in parallel, geometrically arranged in the cabling process to achieve well controlled cable geometry and dimensions, while limiting the strand deformation in the process. Cabling several strands in parallel results in an increase of the current carrying capability and a decrease of the inductance of the magnet, easing protection. The LHC cables are flat, keystoned cables of the so-called Rutherford type.
super pacman bunches	Bunches that do not collide head-on with a bunch of the other beam in one of experimental IPs.
TAN	Target Absorber Neutral: absorber for the neutral particles leaving the IP. It is located just in front of the D1 separation / recombination dipole magnet on the side facing the IP.
TAS	Target Absorber Secondaries: absorber for particles leaving the IP at large angles. It is located just in front of the Q1 triplet quadrupole magnet on the side facing the IP.
tune	Number of particle trajectory oscillations during one revolution in the storage ring (transverse and longitudinal).
triplet	Assembly of three quadrupole magnets used for a reduction of the optical β-functions at the IPs. The LHC triplet assembly consists in fact of 4 quadrupole magnets but the central two quadrupole magnets form one functional entity. The LHC has triplet assemblies in IR1, IR2, IR5 and IR8.

ultimate bunch intensity	Bunch intensity corresponding to the expected maximum acceptable beam-beam tune shift with two operating experimental insertions. Assuming the nominal emittance (normalized emittance of 3.75μm) the ultimate bunch intensity corresponds to 1.7×10^{11} protons per bunch.
ultimate powering	Hardware powering required to reach the ultimate beam energy of 7.54 TeV, corresponding to a dipole field of 9 T.
upstream and downstream	Always related to the direction of one of the two beams. If no beam is specified Beam 1 is taken as the default. This implies that stating a position as being 'upstream' without indicating any beam is equivalent to stating that the position is to the left.

beam half-life	Time during beam collision after which half the beam intensity is lost.
luminosity half-life	Time during beam collision after which the luminosity is halved. The luminosity half-life is generally smaller than the beam half-life.
bunch duration	The bunch duration is defined as $$\sigma_t = \frac{\sigma_s}{v},$$ where σ_s is the bunch length and v is the speed of the particles in the storage rings.
bunch length	The bunch length is defined as the 'RMS' value of the longitudinal particle distribution in one RF bucket. The bunch length is denoted as σ_s.
damping times	Time after which an oscillation amplitude has been reduced by a factor $1/e$. **longitudinal emittance damping time:** Half of the longitudinal amplitude damping time for a Gaussian approximation of the bunch distribution. **transverse emittance damping time:** Half of the transverse amplitude damping time for a Gaussian approximation of the transverse bunch distribution. If no explicit mentioning of the types of damping times is given the damping times refer to the amplitude damping times.
synchrotron radiation damping times	**longitudinal amplitude damping time:** The ratio of the average rate of energy loss (energy lost over one turn divided by the revolution time) and the nominal particle energy. **transverse amplitude damping time:** Time after which the transverse oscillation amplitude has been reduced by a factor $1/e$ due to the emission of synchrotron radiation. For a proton beam it is just twice the longitudinal amplitude damping time due to the emission of synchrotron radiation. If no explicit mentioning of the types of damping times is given the damping times refer to the amplitude damping times.
energy spread	The energy spread is defined as the 'RMS' value of the relative energy deviations from the nominal beam energy in a particle distribution. The energy spread is denoted as $\sigma_{\delta E/E0}$.

longitudinal emittance	The longitudinal emittance is defined as: $$\epsilon_s = 4\pi\sigma_t\sigma_{\delta E/E0}E_0,$$ where σ_t is the bunch duration in seconds, $\sigma_{\delta E/E0}$ the relative energy spread.
transverse beam size	The transverse beam size is defined as the 'RMS' value of the transverse particle distribution.
transverse emittance	The transverse emittance is defined through the invariance of the area enclosed by the single particle phase space ellipse. The single particle invariant under the transformation through the storage ring is given by $$A = \gamma x^2 + 2\alpha x x' + \beta x'^2,$$ where α, β and γ are the optical functions. The area enclosed by the single particle phase space ellipse is given by $$\text{area of ellipse} = \pi A$$ For an ensemble of particles the emittance is defined as the average of all single particle invariants (areas enclosed by the single particle phase space ellipsoids divided by π). The transverse betatron beam size in the storage ring can be written in terms of the beam emittance as $$\sigma_{x,y}(s) = \sqrt{\beta_{x,y}(s)\epsilon_{x,y}},$$ where $\beta_{x,y}(s)$ is the optical β-function along the storage ring. The transverse emittance is given by the following expression: $$\epsilon_z = \sqrt{\langle z^2\rangle\langle z'^2\rangle - \langle zz'\rangle^2}; z = x, y,$$ where it is assumed that the particle coordinates are taken at a place with vanishing dispersion and where $\langle\ \rangle$ defines the average value of the coordinates over the distribution. z and z' are the canonical transverse coordinates ($z = x,y$).
normalized transverse emittance	The beam emittance decreases with increasing beam energy during acceleration and a convenient quantity for the operation of a hadron storage rings (and linear accelerators) is the 'normalized emittance' defined as $$\epsilon_n = \epsilon\gamma_r\beta_r,$$ where γ_r and β_r are the relativistic gamma and beta factors:

$$\beta_r = \frac{v}{c}$$

$$\gamma_r = \frac{1}{\sqrt{1-\beta_r^2}}$$

(v is the particle velocity and c the speed of light in vacuum).

The nominal normalized transverse emittance for the LHC is

$$\epsilon_n = 3.75 \ \mu\text{m}.$$

(1:250)

Legend

LENGTH OF CELL	LC
DISTANCE BETWEEN INTERCONNECT VIRTUAL PLANES	DIP
LENGTH OF COLD MASS	LCM
DISTANCE COLD MASS/INTERCONNECT VIRTUAL PLANE	CM/IP
LENGTH OF MAGNET	LM
DISTANCE MAGNET/COLD MASS	DM/CM
MAGNETIC LENGTH (OPERATING CONDITIONS)	LMLI
DISTANCE BETWEEN MAGNETIC LENGTHS, OR BETWEEN MAGNETIC LENGTH AND INTERCONNECT VIRTUAL PLANE (OPERATING CONDITIONS)	DMLI
DISTANCE BETWEEN MAGNETIC CENTERLINES OR INTERCONNECT VIRTUAL PLANE (OPERATING CONDITIONS)	DMC
DISTANCE BETWEEN SUPPORT POSTS	DSP
DISTANCE BETWEEN VACUUM VESSEL JACKS	DVJ
DISTANCE VACUUM VESSEL/INTERCONNECT VIRTUAL PLANE	DVV/IP
LENGTH OF VACUUM VESSEL	LVV

IP5 CMS Q1 Q1A Q1B Q2A Q2A Q2B Q2B

UJ56 22000mm

LQXFA   LQXFC   LQXFD

TAXS–Q1: LHC Modules implemented to provide required functionalities, but the zone needs to be redesigned
(19000; 22112mm/IP)

C1.R5   C2.R5   C3.R5

Q3 Q3A Q3B CP D1 D1

LQXFB   LCXT   LDXT   DFBXJ

C3.R5   C4.R5

UJ57 25000mm

BBLR   BBLR

For collimators only active length.
Mechanical assembly and interfaces to be redesigned to fit the available space

C4.R5

D2 D2 CRAB MODULE Q4 Q4

LBRD   LQYY

Space reserved for
possible reposition of TCTV, TCTH and TCL

C4.R5

Q5 Q5

LQYCJ

C5.R5

Q6 Q6 DFXJ Q7 Q7A Q7B

LQNDF   RR57 20000mm   LQNFA

BIE: BEAM 1 EXTERIOR B2I: BEAM 2 INTERIOR

C6.R5   C7.R5

Distance from the IP

Assembly	Sub-Assembly	Start (mm)	End (mm)	Magnetic length (mm)
Q1 (LQXFA)	MQXFA	23000	27000	4000
	MQXFA	27500	31500	4000
Q2A (LQXFC)	MQXFB	33500	34700	1200
	MQXFB	35200	42000	6800
Q2B (LQXFD)	MQXFB	44000	50800	6800
	MQXFB	51300	52500	1200
Q3 (LQXFB)	MQXFA	54500	58500	4000
	MQXFA	59000	63000	4000
CP (LCXP)	MQXFA	65344.44	67544.44	2200
	MQSXF	67840.44	88647.44	807
	MQTXF	68788.82	69218.82	430
	MCTSXF	69356.70	89445.70	89
	MCDXF	69580.07	89675.07	95
	MCDSXF	69806.44	69904.44	95
	MCDXF	70036.82	70123.82	87
	MCDSXF	70254.20	70341.20	87
	MCSXF	70471.57	70582.57	111
	MCSSXF	70712.94	70823.94	111
D1 (LDXF)	MBXF	72320	78590	6270
TAXN		126986	130488	3500

Distance from the IP

Assembly	Sub-Assembly	Start (mm)	End (mm)	Magnetic length (mm)
D2 (LBRD)	MBRD	138506	146286	7780
	MCBRD	148766	148266	1500
	MCBRD	148746	150246	1500
CRAB MODULE	ACFCA.AR5.BTE	153574	153574	0
	ACFCA.AR5.BTE	154624	154624	0
	ACFCA.CR5.BTE	160174	160174	0
	ACFCA.DR5.BTE	161224	161224	0
Q4 (LQYY)	MCBYY	171855	173355	1500
	MCBYY	173835	175335	1500
	MQYY	176685	179015	3630
Q5 (LQYCJ)	MCBY	201926	202826	900
	MCBY	203222	204122	900
	MCBY	204518	205418	900
	MQY	205790	208190	3400
Q6 (LQNDF)	MCBC	224898	225798	900
	MQML	225990	230790	4800
Q7 (LQNFA)	MQM	260004	263434	3400
	MQM	263771	267171	3400
	MCBC	267362	268262	900

Roughing Pump (400mm)

Sector valves (655mm)

520mm space between collimators: Bellow "xy" for the fifth axis (VAMTA)

NOTE: Lay-out consistent with optics (HLLHCV1.1)

B1E: BEAM 1 EXTERIOR
B2I: BEAM 2 INTERIOR

IT IS ASSUMED AN INTEGRATED COEFFICIENT OF THERMAL CONTRACTION
FROM ROOM TEMPERATURE TO 1.9 K OF 3 mm/meter

High Luminosity Long Straight Section Mechanical Layout
IR5 RIGHT, CELLS C1.R5 TO C7.R5
HL-LHC
IR5 DROIT, CELLULES C1.R5 A C7.R5
HL-LHC

LHCLSXH_0010